

ISBN: 978-81-952903-6-9

Proceedings Book in Mechanical Engineering

Arijit Kundu · Md Naim Hossain

Sadhan Ghosh · Santanu Das

Prasanta Sahoo · P.K. Dan

Advances in Mechanical Engineering

Select Proceedings of ICTEMA2022



Arijit Kundu • Md Naim Hossain
Sadhan Kumar Ghosh • Santanu Das
Prasanta Sahoo • Pranab Kumar Dan

Advances in Mechanical Engineering

Select Proceedings of ICTEMA2022

ADVANCES IN MECHANICAL ENGINEERING (Select Proceedings of ICTEMA 2022)

Editors: Arijit Kundu, Md Naim Hossain, Sadhan Kumar Ghosh, Santanu Das, Prasanta Sahoo, Pranab Kumar Dan

Published Online by: NOLEGEIN, an imprint of Consortium E-Learning Network Pvt. Ltd.

Address: A-118, First Floor, Sector-63, Noida - 201301, Uttar Pradesh, India

Edition: First

Publication Year: 2022

ISBN: 978-81-952903-6-9

Copyright @2022 Jalpaiguri Government Engineering College, West Bengal India All right reserved.

No part of this book shall be reproduced or transmitted in any form or by any means, electronic or mechanical, including photocopying, recording, or by any information retrieval system without written permission of the publisher.

This publication is designed to provide accurate and authoritative information. It is sold under the express understanding that any decisions or actions you take as a result of reading this book, must be based on your own judgment and will be at your sole risk. The author will not be held responsible for the consequences of any actions and/or decisions taken as a result of any information given or recommendations made.

Organizing Committee

Patron

Prof. Amitava Ray, Principal

Organising Secretary

Dr. Md Naim Hossain

Joint Organising Secretary

Dr. Arijit Kundu

Executive Members

Prof. Subrata Bhattacharya

Prof. Soupayan Mitra

Prof. Sudip Mukherjee

Prof. Pradip Kumar Saha

Prof. Goutam Panda

Prof. Santanu Das

Prof. Jishan Mehedi

Prof. Arindam Saha

Prof. Asim Mahapatra

Prof. Nimai Mukhopadhyay

Prof. Gora Chand Chell

Prof. Subhranta Roy Chowdhury

Prof. Nripen Mondal

Prof. Samir Das

Prof. Sandipan Ganguly

Prof. Suman Mondal

Mr. Aniruddha Basu

Tresurer

Prof. Madhab Mandal

Smt. Elora Rakshit

Advisory Committee

Prof. Suman Chakraborty, IIT Kharagpur
Prof. Swarnendu Sen, Jadavpur University
Prof. Koushik Ghosh, Jadavpur University
Prof. Arup Kumar Das, IIT Roorkee
Prof. D.B. Jani, Gujarat Technological University, Ahmedabad
Prof. Pallab S. Mahapatra, IIT Madras
Prof. Sadhan Ghosh, Jadavpur University
Prof. P.K. Das, IIT Kharagpur
Prof. Prasanta Sahoo, Jadavpur University
Prof. P.K. Dan, IIT Kharagpur
Prof. Pankaj Biswas, IIT Guwahati
Prof. Ravi Kumar, IIT Roorkee
Prof. I.V. Singh, IIT Roorkee
Prof. S. P. Singh, IIT Delhi
Prof. Prasanta Sahoo, Jadavpur University
Prof. Santanu Das, KGEC, India
Prof. Uday S. Dixit, IIT Guwahati, India
Prof. Ashis Kumar Sen, IIT Madras, India
Prof. M. P Maiya, IIT Madras, India
Prof. Rangan Banerjee, IIT Bombay, India
Prof. A. Mani, IIT Madras, India

International Advisors

Prof. George Em Karniadakis, Brown School of Engineering, Brown University, USA
Prof. J.P. Meyer, University of Pretoria, South Africa
Prof. J. Paulo Davim, University of Aveiro, Portugal
Prof. Khoo Boo Cheong, NUS, Singapore

Session Chairs

Dr. D.B. Jani, Gujarat Technological University, Ahmedabad
Dr. Nripen Mandal, Jalpaiguri Govt. Engineering College
Dr. Ashok Kumar Dewangan, NIT Delhi
Dr. Sanjib Sajjan, Vaagdevi College of Engineering, Warangal
Mr. Suman Mandal, Jalpaiguri Government Engineering College

Our Editors

Prof. Sadhan Ghosh, Jadavpur University

Prof. Santanu Das, Kalyani Government Engineering College

Prof. Prasanta Sahoo, Jadavpur University

Prof. P.K. Dan, IIT Kharagpur

Corresponding Editor

Dr. Arijit Kundu, Jalpaiguri Government Engineering College

Dr. Md Naim Hossain, Jalpaiguri Government Engineering College

Preface

We on behalf of the organizing committee welcome you all to the International Conference on Thermal Engineering and Management Advances ICTEMA2022. Our great pride and pleasure are that we have been ultimately victorious in organizing this second International Conference in the Department of Mechanical Engineering in Jalpaiguri Government Engineering College under the weeping situations of pandemic incident continuing from March'20 after the very first International Conference ICTEMA 2020. However, the nation and its economy have to conform running to whatever the challenging circumstances it may face, as we know that, in the middle of each trouble lies a scope. Organizing committee and we, with the support of the top management of this institute collectively made this event a reality, and we are proud that this Institute is being hosting this conference with a great honour, though the output is only in such an online mode of the ceremony due to these current unfavorable conditions around the globe.

The annual conference is one of the effective reflections of its scientific, academic and social contributions. Not only does it allow us to meet and greet, but it also provides a unique forum for exchange of ideas, offers and opportunities. With this background, ICTEMA2020 has been planned to introduce in the market of research and education to present and discuss the current ideas of conventional engineering ground namely thermal and manufacturing engineering and production management, though we are conscious of the high risk of failure and attracting criticism in introducing such event in this very remote places of northern Bengal.

We wish to express our gratitude and respectful thanks to our international advisory committee, national advisory board, reviewer committee, editors, and all those who involved in organizing this conference.

We are also thankful to all the authors who have contributed their valuable research work to this conference. We also acknowledge the contributions of all session chairs and co-chairs without whom it won't be possible to conduct the technical sessions. All the submitted papers are reviewed by the eminent faculties and researchers from NITs and IITs, we are grateful to them also.

The information about the conference was largely sent to the authors using the internet. A collective number including foreign contributions were registered, though due to remote location, initially we were not so definitive in successful happening of the program. However, we have now planned to organize the program in future in every alternative year.

We appeal to the research community to extend their continued support and cooperation to the future activities of ICTEMA. We wish every participant a very affluent ICTEMA2022 and hope that this conference be a good source of reference for their future research.

Jalpaiguri, India

Dr. Md Naim Hossain Dr. Arijit Kundu
Organizing Secretaries and Corresponding Authors

Contents

Comparison of performance parameters and characteristics between diesel and biodiesel for four-stroke single cylinder diesel engine	1
Drug Type Classification using Logistic Regression and Decision Tree based Machine Learning Models	7
Comparison of Thermohydraulic Performance Prediction of Perforated Rectangular PFHE by Various Machine Learning Models & ANN	17
Disease Detection and Classification of Medicinal Leaves using Digital Image Features and Random Forest Technique	25
Innovatization of Entrepreneurship in Virtual Reality: Digital Duplicates, Internet of Things, Robotics	33
Effect of Battery Cell Arrangement on Thermal Management of Air-Cooled Battery Pack	43
Investigation of the Printability of Living Cell with Different Process Parameters of 3D Bio-Additive Manufacturing Process (Bioprinting)	55
Numerical Study of Electroosmotic Flow over A Hydrophobic Wavy Plate	63
Characterization of Some Non-edible Vegetable Oils Lubricants by Their Thermal Properties	69
Aerostatic Bearing Performance Analysis Based on CFD Study	77
Development of Mathematical Model for Ultimate Tensile Strength of TIG Welded Duplex Stainless Steel	83
Study the Application of Nanofluid in Solar CPVT/PVT system	95
An Implementation of Failure Mode and Effect Analysis (FMEA) in a Fibre Industry for Loss Reduction	103
Analysis of Tribological behaviour of Epoxy based Chopped Carbon Fibre Composite using Taguchi Technique	107
Deformation of Tumor Cell with Variation of Extracellular Matrix Density and Cytoskeleton: Cellular Growth, Migration Behavior	115
Prediction of Surface Roughness in Grinding Using Artificial Neural Networks	129
Simulation of microchannel heat exchangers with triangular and circular cavities	139
Thermal Management of a Cubical Building using Hydrated Salt 24	147
Numerical Investigation of Heat Transfer of a Thermosyphon varying the Filling Ratios	153
Performance Optimization Techniques for Micro Heat Sinks: A Review	159
Experimental investigation of heat transfer fluids for solar thermal collectors	171
A SWOT analysis approaches to implementation of renewable energy applications in West Bengal	177
Analysing the Barriers for Implementation of Industry 4.0 in Indian Dairy Industry: An ISM-MICMAC Approach	187
Identifying The Significant Barriers for Implementation of I4.0 In Indian Casting Industries Using ISM-MICMAC Approach	195

Numerical Analysis of a CPU Mainboard Chip to Study the Influence of Working Fluids in Heat Transfer Performance of Micro-Pin-Fin Heat Sink	203
Prediction of Thermal Comfort and Performance Comparison of Various Machine Learning Models	209
CFD simulation of atmospheric reentry of the FIRE-II capsule under supersonic conditions	211
Casting Simulation, Manufacturing and Validation for Railway Coupler	229
Computer Aided Manufacturing using Fusion 360	237
Assessment of Micro-mixing Process of Electroosmotic Flow in a Microchannel	247
Quantitative Analysis of Climatic Influence on the Cooling Tower Performance	257
Magneto-nanofluid flow evolution in a heart-shaped special cavity	263
ANN Modeling to Estimate Cutting Forces in Turning Operation	273

About the Editors



Dr. Arijit Kundu is currently Associate Professor in the Department of Mechanical Engineering, Jalpaiguri Government Engineering College, Jalpaiguri, West Bengal, India. He obtained his B.Tech (Mechanical Engineering) and M.Tech (Heat Power) from Jadavpur University, Kolkata, India, and Ph.D. (Refrigeration and Air Conditioning; Thermal Engineering) from the Indian Institute of Technology, Roorkee, India. His research interests include heat transfer, multiphase flow, boiling and condensation of eco-friendly refrigerants in re-entrant tubes, environmental protection, sustainability, etc. He has more than 10 years of teaching experience in Mechanical Engineering. He has published five international journals, twenty international and national conferences and completed one technical project sanctioned from the Department of Higher Education, Science and Technology and Biotechnology, Government of West Bengal. Three research scholars are doing Ph.D. under him. Currently, he is an editorial board member of the Proceedings of International Conference on Multidisciplinary Innovation in Academic Research (ICMIAR) 2019.



Dr. Md Naim Hossain is currently Assistant Professor in the Department of Mechanical Engineering, Jalpaiguri Government Engineering College, Jalpaiguri, West Bengal, India. He obtained his B.Tech (Mechanical Engineering) from Jalpaiguri Govt. Engineering College and M.Tech (Heat Power) and Ph.D. (Boiler Thermal Analysis and Multi-phase flow) from from Jadavpur University, Kolkata, India. His research interests include design of thermal components, boiler, heat transfer and multiphase flow, thermo-syphon analysis, waste to energy conversion etc. He has published four international journals, 15 international and national conferences.



Dr. Sadhan Kumar Ghosh is currently Professor in Department of Mechanical Engineering, Jadavpur University, Kolkata, India. He obtained his B. Tech (Mechanical Engineering), M. Tech and Ph.D. from Jadavpur University, Kolkata, India. His major areas of research interests include waste management, circular economy, environmental protection, quality environment safety and energy management systems, green manufacturing, supply chain management, SME sustainability, and total quality management. He has published 03 patents, 42 peer-reviewed journal articles, 167 conference proceedings, 11 books, 02 book chapters and principal investigator of 32 projects. Dr. Ghosh delivered 56 Lectures in various countries. Recently, he was an editorial board member of the Waste Management and Resource Efficiency, Proceedings of 6th IconSWM 2016, Sustainable waste management: Policies & Case Studies: Proceedings of 7th IconSWM, Waste Water Recycling and Management: Proceedings of 7th IconSWM 2017.



Dr. Santanu Das is currently Professor and Head of the Department of Mechanical Engineering, Kalyani Government Engineering College, India. He obtained his B.Tech (Mechanical Engineering) and M. Tech from Jadavpur University, Kolkata, India, and Ph.D. from Indian Institute of Technology, Kharagpur, West Bengal, India. His major areas of research interests include manufacturing technology: machining, grinding, welding, weld cladding, coating, production and inventory management, etc. He has published 132 journal papers, 80 international conferences, 100 national conferences/seminars, 16 national magazines, 10 workshops, 09 short term training course papers, 07 books edited, 07 books reviewed. He has received the 'Shiksha Ratna Award' in 2018 as an 'Outstanding Teacher' from Education Department, Government of West Bengal. Currently, he is an Editor, Journal of The Association of Engineers, India; Member of Editorial Board, Indian Welding Journal; Chief Editor, Indian Welding Journal; and Editor-in-Chief, Bulletin of the Association of Machines and Mechanisms.



Dr. Prasanta Sahoo received a Ph.D. degree in Mechanical Engineering and M.Tech. degree in Mechanical Engineering (Machine Design) both from Indian Institute of Technology, Kharagpur, and Bachelor of Mechanical Engineering (Honours) degree, from Jadavpur University, Kolkata. Currently, he is Professor at the Department of Mechanical Engineering of Jadavpur University, Kolkata, India. He has more than 25 years of teaching and research experience in Mechanical Engineering. He has supervised over 30 Ph.D. thesis so far as well as coordinated & participated in several financed research projects. He has visited and collaborated with Institutes from countries like United Kingdom, Portugal, France, Greece, Italy, Egypt etc. Presently, he acts as reviewer for more than 75 prestigious Web of Science journals. In addition, he has also authored 2 books (PHI and Springer), edited 3 volumes (Springer and IGI-Global), and written over 30 book chapters and published more than 500 articles in peer-reviewed journals and conference proceedings (h-index 31/5000+ citations).



Dr. Pranab Kumar Dan is currently Associate Professor, Indian Institute of Technology, Kharagpur, in the Rajendra Mishra School of Engineering Entrepreneurship, Kharagpur, West Bengal, India. He obtained his B.Tech (Mechanical Engineering) and M.Tech from the Institute of Engineering Science and Technology (IEST), Shibpur, West Bengal, India, and Ph.D. from Jadavpur University, Kolkata, India. His major research interests include production management and industrial Engineering, engineering design process and product innovation and development. He has published 34 journal papers, 12 international conferences, 08 books chapters, 08 national journals, 12 national conferences and 01 patent filed. Currently, he is a reviewer of International Journal of Advanced Manufacturing Technology (Springer) and Journal of Engineering Manufacture (Sage).

Comparison of performance parameters and characteristics between diesel and biodiesel for four-stroke single cylinder diesel engine

Trishit Janah*, Abhimanyu Kumar, Prabir Biswas

1 Introduction

Biofuels are commonly known as agro fuels, it is a sort of fuel that is generated from organic matter such as plants and animals (obtained directly from plants or indirectly from agricultural, commercial, domestic, and industrial wastes). These fuels are produced by the biomass conversion process. This biomass conversion can lead to fuel production in solid, liquid, or gaseous forms. Biodiesel is the most common form of biofuel used [1]. Biodiesel is a vegetable oil or animal fat-based fuel used in diesel engines produced by a process known as Transesterification [2]. Scientists E. Duffy and J. Patrick conducted Transesterification as early as 1853 [3]. After the commencement of the Industrial Revolution in the late 18th and 19th-century energy has become the new currency, which helps us to maintain economic growth and proper standard of living. Fossil fuels have been one of the most in-demand items for global primary energy production. Fossil fuels have accounted for 85% of the primary energy consumption, with oil (33% share), coal (28%), and natural gas (24%) as the major fuels, while nuclear energy, hydroelectricity, and renewables accounting for 4%, 7% and 4% of the total primary energy consumption, respectively worldwide [4]. For the last few decades, the world has seen an increased risk associated with the use of fossil fuels as the primary source of energy because of two crucial reasons i.e., fast depletion of existing fossil fuels and the other one pollution. As a result of these reasons, an alternative source of energy has drawn great attention in recent years [5]. Due to these factors, a considerable amount of attention is being focused on biofuel productions, especially referring to Biodiesel. There are several reasons why Biodiesel is a better alternative to the traditional conventional sources of energy. Due to the similarities of combustion properties of both Biodiesel and fossil-based diesel, it has provided a more renewable and sustainable solution for the future of the automotive industry. According to the International Energy Agency's(IEA) report on biodiesel production, global biodiesel production is expected to increase 25% over the next three years up to 2024 [6]. The use of Biodiesel has a lot of benefits firstly, with the approaching global energy crisis biodiesel will play a crucial role in reinforcing a nation's energy security. Secondly, biodiesel being renewable energy as it is derived from plant materials can help in the reduction of greenhouse gas emissions.

Aghbashlo et al. [9] studied the use of machine learning technology for modelling transesterification process and biodiesel research. Mathew et al. [10] found that production of biodiesel using renewable feedstocks and enzymes as catalysts could be used for commercial work. Ong et al. [11] studied the use of ionic liquid both as solvents as well as catalysts for biodiesel production from agricultural feedstocks. Hamza et al. [12] studied the presence of homogeneous and heterogeneous catalyst on transesterification process of biodiesel production.

2 Experimental Analysis

We have performed a series of experiments using a four-stroke single-cylinder diesel engine with the help of a Rope brake Dynamometer in our Internal Combustion Engine laboratory. Here using this experiment we have obtained the data for various performance parameters like RPM, Load, Brake

T. Janah, A. Kumar, P. Biswas

Department of Mechanical Engineering, Techno International Newtown, Kolkata - 700156

power, Indicated power, Specific fuel consumption, brake thermal efficiency, indicated thermal efficiency, and Mechanical efficiency for diesel and biodiesel respectively.

Table 1. Data recorded during a test of normal diesel

Applied load, W_1 (kg)	Specific Fuel Consumption, SFC (kg/Kws)	Calorific Value, CV	Brake Thermal Efficiency, BTE	Indicated Thermal Efficiency, ITE	η_{mech}
4	0.000130	46057	16.69	41.21	0.405
6	0.000104	46057	20.89	41.77	0.500185
10	0.000080	46057	27.23	45.08	0.604035
12	0.000077	46057	28.16	43.45	0.64808

Table 2. Data recorded during a test of biodiesel fuel

App. Load, W_1 (kg)	Specific Fuel Consumption, SFC (kg/Kws)	Calorific Value, CV	Brake Thermal Efficiency, BTE	Indicated Thermal Efficiency, ITE	η_{mech}
4	0.00013	37270	20.58	50.75	0.405467
6	0.000106	37270	25.27	50.65	0.498883
10	0.0000919	37270	29.21	48.35	0.604192
12	0.0000811	37270	33.08	51.05	0.64808

3 Comparison in between Diesel and Bio-Diesel Load Testing

3.1 Variation of engine rpm with applied load in between diesel fuel and biodiesel load testing

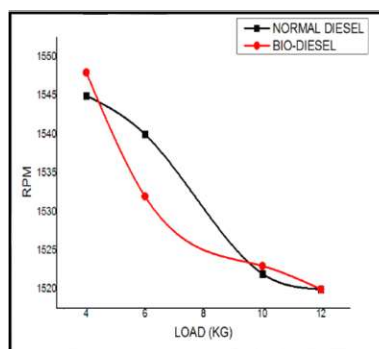


Fig. 1. Load vs Revolutions per minute (RPM)

Fig.1 shows the load vs rpm graph by comparing the performance of normal diesel and bio-diesel. Here we find that on increasing the applied load the rpm is reduced.

3.2 Variation of brake power with an applied load between diesel fuel and bio-diesel load testing

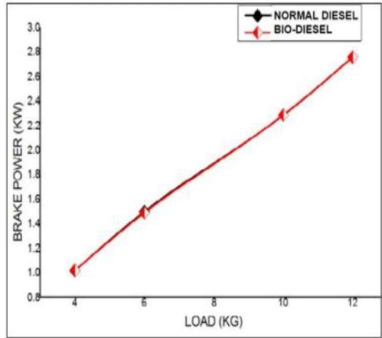


Fig. 2. Load vs Brake Power (BP)

Fig.2 illustrates the load vs brake power graph by comparing normal diesel and bio-diesel performance. Here we find that the performance of bio-diesel and normal diesel is more or less the same

3.3. Variation of the engine indicated power with applied load in between diesel fuel and bio-diesel load testing

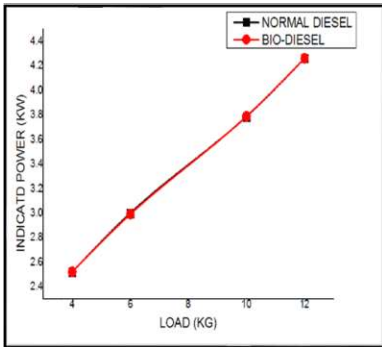


Fig. 3. Load vs Indicated Power (IP)

Fig.3 shows the load vs indicated power graph by comparing normal diesel and bio-diesel performance. Here we find that the performance of bio-diesel and normal diesel is more or less the same.

3.4. Variation of engine specific fuel consumption with applied load in between diesel fuel and bio-diesel load testing

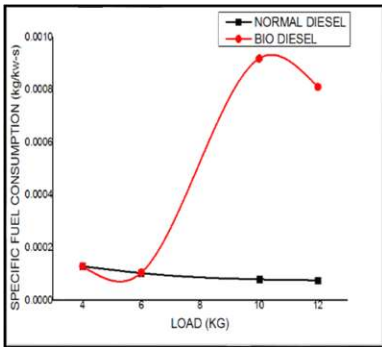


Fig. 4. Load vs Specific Fuel Consumption (SFC)

Fig.4 shows the load vs specific fuel consumption graph by comparing normal diesel and bio-diesel performance. Here we find that the performance of bio-diesel is greater than normal diesel.

3.5. Variation of the engine brake thermal efficiency with applied load in between diesel fuel and bio-diesel load testing

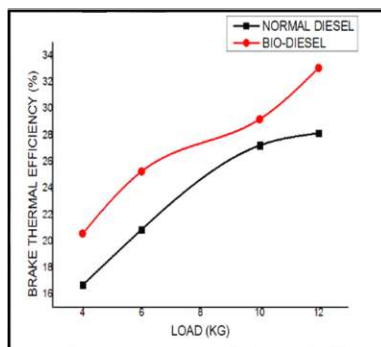


Fig. 5. Load vs Brake Thermal Efficiency (BTE)

Fig.5 shows the load vs brake thermal efficiency graph by comparing normal diesel and bio-diesel performance. Here we find that the performance of bio-diesel is greater than normal diesel.

3.6. Variation of engine mechanical efficiency with applied load in between diesel fuel and bio-diesel load testing

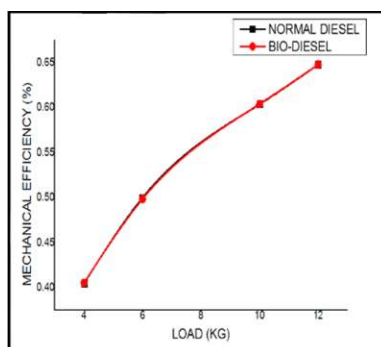


Fig. 6. Load vs Mechanical Efficiency

Fig.6 shows the load vs mechanical efficiency graph by comparing normal diesel and bio-diesel performance. Here we find that the performance of bio-diesel and normal diesel is more or less the same.

4 Conclusion

Here we have analyzed the performance of the four-stroke single-cylinder diesel engine using a rope brake dynamometer. Different types of graphs related to Volumetric Efficiency, Brake Power, Fuel Consumption, Applied load, Mechanical Efficiency, Brake thermal efficiency, etc. were obtained. With the help of these graphs, we have tried to analyze the performance characteristics of the said engine using diesel and biodiesel respectively. Then we have combined both the results and provided an explicit presentation of the above characteristics using graphical analysis thereby leading us to a logical conclusion for each case. After performing the above analysis we can say that using biodiesel as a substitute for normal diesel does not provide give us significant increase in the mechanical efficiency of the diesel engine. Even if there are minor variations in the data for indicated thermal efficiency and brake thermal efficiency but the overall mechanical efficiency remains the same. On the contrary, we

have seen that biodiesel being a renewable source of energy provides us with a more convenient option compared to normal diesel due to its eco-friendly nature.

References

1. Luque, R., Herrero-Davila, L., Campelo, J. M., Clark, J. H., Hidalgo, J. M., Luna, D. & Romero, A. A. (2008). Biofuels: a technological perspective. *Energy & Environmental Science*, 1(5), 542-564.
2. Ganesan, V. (2012). Internal combustion engines. McGraw Hill Education (India) Pvt Ltd.
3. Demirbas, A. (2008). Biodiesel (pp. 111-119). Springer London.
4. by fuel type-Exajoules, C., & Emissions, C. D. (2006). bp Statistical Review of World Energy June 2020.
5. Lin, L., Cunshan, Z., Vittayapadung, S., Xiangqian, S., & Mingdong, D. (2011). Opportunities and challenges for biodiesel fuel. *Applied Energy*, 88(4), 1020-1031
6. Biofuel production forecast; IEA, 2018. <https://www.iea.org/fuels-and-technologies/bioenergy>
7. Hansdah, D., Murugan, S., & Das, L. M. (2013). Experimental studies on a DI diesel engine fueled with bioethanol-diesel emulsions. *Alexandria Engineering Journal*, 52(3), 267-276.
8. Adaileh, W. M., & AlQdah, K. S. (2012). Performance of diesel engine fuelled by biodiesel extracted from a waste cooking oil. *Energy Procedia*, 18, 1317-1334.
9. Aghbashlo, M., Peng, W., Tabatabaei, M., Kalogirou, S. A., Soltanian, S., Hosseinzadeh-Bandbafha, H., & Lam, S. S. (2021). Machine learning technology in biodiesel research: A review. *Progress in Energy and Combustion Science*, 85, 100904
10. Mathew, G. M., Raina, D., Narisetty, V., Kumar, V., Saran, S., Pugazhendhi, A., & Binod, P. (2021). Recent advances in biodiesel production: challenges and solutions. *Science of The Total Environment*, 794, 148751
11. Ong, H. C., Tiong, Y. W., Goh, B. H. H., Gan, Y. Y., Mofijur, M., Fattah, I. R., ... & Mahlia, T. M. I. (2021). Recent advances in biodiesel production from agricultural products and microalgae using ionic liquids: Opportunities and challenges. *Energy Conversion and Management*, 228, 113647
12. Hamza, M., Ayoub, M., Shamsuddin, R. B., Mukhtar, A., Saqib, S., Zahid, I., & Ibrahim, M. (2021). A review on the waste biomass derived catalysts for biodiesel production. *Environmental Technology & Innovation*, 21, 101200

Drug Type Classification using Logistic Regression and Decision Tree based Machine Learning Models

Amit Chatterjee, Sujay Biswas, Arka Prava Das, Vineet Kumar Borashi

1 Introduction

In this era of automation, Industry 4.0 (I4.0) is developing rapidly as a substitute of current manual industry models. I4.0 involves various smart technologies like artificial intelligence (AI), hi-tech sensors, advanced robotics, cloud computing, cyber-physical systems, cognitive computing, mobile devices, and others. Due to its numerous advantages (like reduced production cost, flexibility and agility, improved efficiency, improved productivity, and many more), I4.0 is getting popularized as sustainable development model [1, 2].

Healthcare is one of the major industrial sectors that contributes significantly to enhance the economy and employment worldwide. Drugs and medicines are considered as one of the major pillars of healthcare industry. This is a vital factor for maintaining health, reducing disability and premature death, managing disease, and achieving health equity. To improve the performance and productivity in this sector, few research efforts have been conducted by utilizing AI and machine learning (ML) techniques over past few years. In this direction, Napolitano et al. [3] proposed a novel drug repositioning strategy using AI based approach. Several layers of data integration were used for model development using data of similarity in chemical structure, closeness of the targets within the protein-protein interaction network, and correlation of the gene expression patterns. The classifier provided high level of accuracy, after rigorous statistical evaluation. Chen et al. [4] proposed hierarchical classification scheme and several representative methods towards identifying drug-target interactions (DTI) for candidate medication and drug discovery. Lima et al. [5] applied ML in several steps of the drug discovery practice, such as estimating target structure, predicting movements of new ligands through model construction, detection or optimization of hits, and building the model that predict pharmacokinetic and toxicological profile of drug compounds. ML was also employed in different steps of ligand-based drug design (LBDD) and structure-based drug design (SBDD) studies. In a similar work, Lavecchia et al. too had utilized machine-learning techniques in the context of ligand-based virtual screening (LBVS) of drugs. Byvatov et al. [6] have compared support vector machine (SVM) and artificial neural network (ANN) based learning techniques for drug/non-drug classification in early-phase virtual compound filtering and screening. The results obtained by SVM training was more robust with smaller standard error compared to ANN training. Burbidge et al. [7] investigated SVM classification algorithm for structure-activity relationship analysis of pharmaceutical data. The classification operation involved forecasting the inhibition of dihydrofolate reductase by pyrimidines. In a benchmark test, the SVM was also compared to different ML techniques which can also be used in this purpose. Abacha et al. [8] shown the application of ML for calculating Drug-Drug Interactions (DDI) and performing Pharmacovigilance (PV) operation. Specifically, drug name recognition, DDI extraction, and DDI classification tasks were performed using SemEval technique.

In rural communities, providing quality health service is still a great challenge to the government. Due to various factors, like shortage of physicians, lack of infrastructure, underinsured residents, and many more, people could not receive adequate healthcare facilities. A topical report of the 'Lancet Global Health Commission (LGHC)' on 'High Quality Health Systems' reported that, around 5.7 million people die in medium and low-income countries each year due to poor quality healthcare [9]. To solve this major social issue, in this communication we propose automated prediction of drug type (to be prescribed) based on health parameters of the patient, using ML approach. For automatic classification, logistic regression and decision tree classifiers were used. The drug dataset was

imported from Kaggle open database for performing model training operation. Finally, confusion matrix and accuracy score metric was used to assess the performance of the model.

2 Theory

Machine learning (ML) is a branch of computer science and AI, which emphasizes on the use of algorithms and data to replicate the way that humans learn [10, 11]. ML algorithms are mainly divided into two broad classes i.e., unsupervised learning (USL), and supervised learning (SL). SL utilizes a set of input attributes X and corresponding labels (Y). The attribute has several instances (I_1, I_2, \dots, I_n) containing values of attributes and corresponding labels, which are cumulatively termed as ‘data’. These data are used for training the learning algorithm and generate the ML model. Whenever new instance (input) is given to model, it produces corresponding label (Fig. 1).

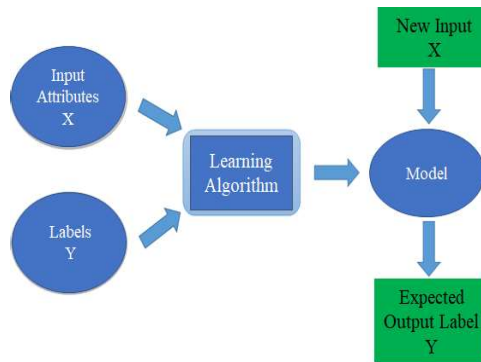


Fig. 1. Supervised learning model.

2.1 Logistic Regression

In statistics, the logistic model is utilized to predict the probability of a certain events or classes such as healthy/sick, win/lose, pass/fail, or alive/dead. In ML, this notion can be extended to classify several classes of events, such as anticipating whether an image contains an apple, banana, cat, dog, etc. [12]. Mathematically, logistic regression function can be described as (Fig. 2):

$$L(x) = \frac{1}{1+e^{-x}} \quad (1)$$

where, e =Euler's number= 2.71828

x =dependent variable

$L(x)$ =logistic function

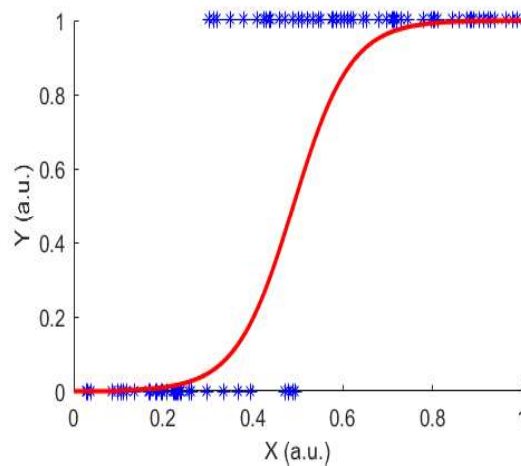


Fig. 2. Graphical representation of logit function

Usually, logistic regression is operated on binary target variables, but there can be more categories of target variables that can be predicted by it. Based on the number of classes, this model can be divided into two categories: binomial (i.e., classifying 2 groups), and multinomial (i.e., classifying 3 or more groups).

2.2 Decision Tree

Decision Trees can be categorised as a supervised ML, where the data is continuously fragmented according to a certain parameter. The tree is constructed by two entities, namely decision nodes and branches (Fig. 3). The node where first division in the dataset occurred is termed as root node. The terminal nodes that anticipate the results of the decision tree is known as leaf node. The component of the tree that directs the outcome of a split to the next node is called branches [13].

The core algorithm used for decision tree implementation is termed as ID3, developed by J. R. Quinlan [10, 11, 13]. The technique employs a greedy search top-down approach that channelize through the space of possible branches without implementing any backtracking. ID3 utilizes the concept of Entropy to construct a decision tree. Entropy can be mathematically expressed as:

$$E = \sum_{i=1}^c -p_i \log_2 p_i \quad (2)$$

where, p_i =probability of occurrence of an event i

c =total number of events

E =entropy.

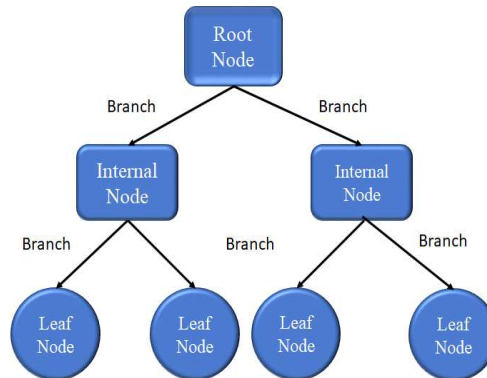


Fig. 3. Decision tree model.

The tree structure is constructed by splitting the dataset based on that attribute, for which entropy is minimal. Next, the same process is repeated for all other attributes, until leaves are reached. Alternative to entropy, information gain can also be used to construct the decision tree. However, for this parameter, maximum value is used for splitting the datasets. Due to its tree like structure (i.e., full of nodes and branches), decision trees can handle both categorical and numerical data.

3 Methodology

In this section, a brief discussion regarding dataset, train-test splitting, performance estimation parameters, and overall process flow is provided.

3.1 Dataset

For classification operation, Drug200 dataset was used. The database URLs are freely available from Kaggle, which can be easily downloaded by the researchers [14]. The specification of the dataset is shown in Fig. 4. The dataset contains five columns for independent variables, namely Age (integer variable, int64), Sex (string variable, object), BP (string variable, object), Cholesterol (string variable,

object), Na_to_K (floating point variable, float64), and a dependent variable namely Dtype (i.e. Drug type, string variable, object)). Each column has 200 non-null entries, which indicates that, no data cleaning operation will be required before model training. In this dataset, records of drug prescription of patients based on independent variables is provided. Details of different independent and dependent parameters, and their relationships are provided in Fig. 5, 6, and 7 respectively.

```

RangeIndex: 200 entries, 0 to 199
Data columns (total 6 columns):
#   Column          Non-Null Count  Dtype
---  ---
0   Age              200 non-null    int64
1   Sex              200 non-null    object
2   BP               200 non-null    object
3   Cholesterol       200 non-null    object
4   Na_to_K          200 non-null    float64
5   Drug             200 non-null    object
dtypes: float64(1), int64(1), object(4)
memory usage: 9.5+ KB

```

Fig. 4. Specification of Drug200 dataset.

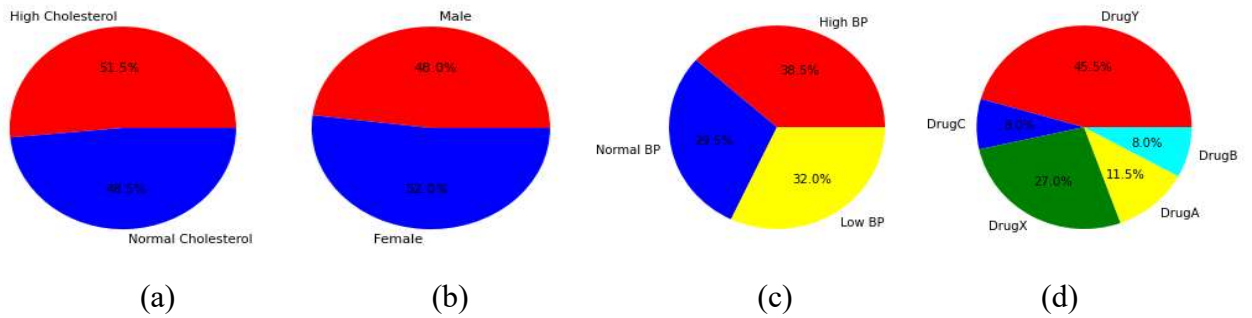


Fig. 5. Pie chart for Drug200 dataset: (a) cholesterol level, (b) Sex, (c) blood pressure, and (d) type of drug prescribed.

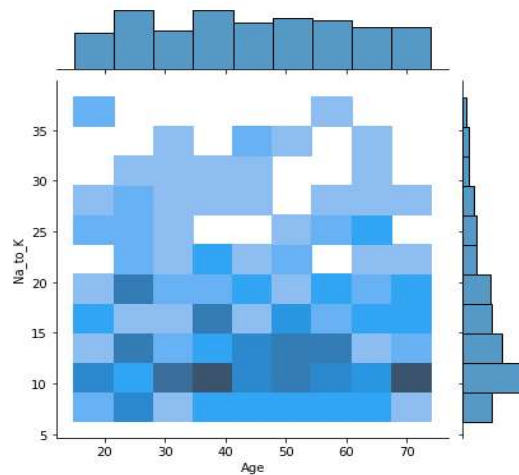


Fig. 6. Jointplot of patient age vs Na-to-K content.

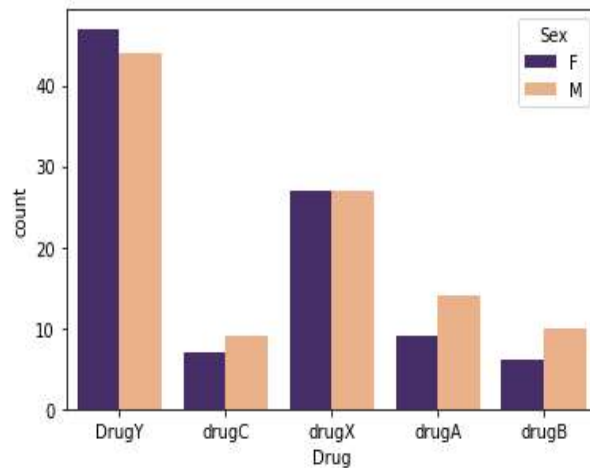


Fig. 7. Bar graph for drugs prescribed according to gender of the patient.

3.2 Train-test splitting

After generation/acquisition of dataset, training and testing datasets are constructed for construction and validation of the ML model (Fig. 8):

(a) Training Data: The data in the training set is utilized to generate the experience using which that the algorithm learns to respond.

(b) Test Data: The data in test set is used to estimate the performance of the model in conjunction with performance matrices.

To avoid unexpected errors that hinder the machine's accuracy, it is important that, no data points from the training set are included in the test set. If the data points of training set is also resides in test set, it will be problematic to evaluate whether the algorithm has learned from the training set or merely memorized it. Generally, more than 60% of the overall data is used to train the model, and remaining data is used to test it. Practically, the train-test ratio can be 80:20, 70:30, 65:35, 60:40, and others.



Fig. 8. Data splitting: training and testing.

3.3 Performance Estimation

For performance estimation of the learning models, confusion matrix approach was utilized. Confusion matrix can be defined as a summary of prediction results in a classification problem. The number of correct and incorrect predictions are summarized in a $N \times N$ matrix with count values and broken down by each class (where, N =total number of classes). This is shown in Fig. 9.

Terminology used here are as follows:

- True Positive: Observation is positive, and is predicted to be positive.
- False Negative: Observation is positive, but is predicted negative.

- True Negative: Observation is negative, and is predicted to be negative.
- False Positive: Observation is negative, but is predicted positive.

Confusion matrix is very useful for measuring different parameters such as accuracy score, precision, recall and F1 score.

		<i>Actual Values</i>	
		Positive (1)	Negative (0)
<i>Predicted Values</i>	Positive (1)	True Positive	False Positive
	Negative (0)	False Negative	True Negative

Fig. 9. Confusion matrix.

Accuracy score: The most common metric for classification is accuracy, which is the fraction of samples predicted correctly.

$$\text{Accuracy} = \frac{TP+TN}{\text{Total}} \quad (3)$$

Here, Total = TP+TN+FP+FN.

3.4 Process flow

The process flow illustration of drug classification process is shown in Fig. 10. Firstly, drug prescription data with different parameters is acquired with the help of medical practitioners. Collected data are then organized in MS Excel and labelled for supervised learning.

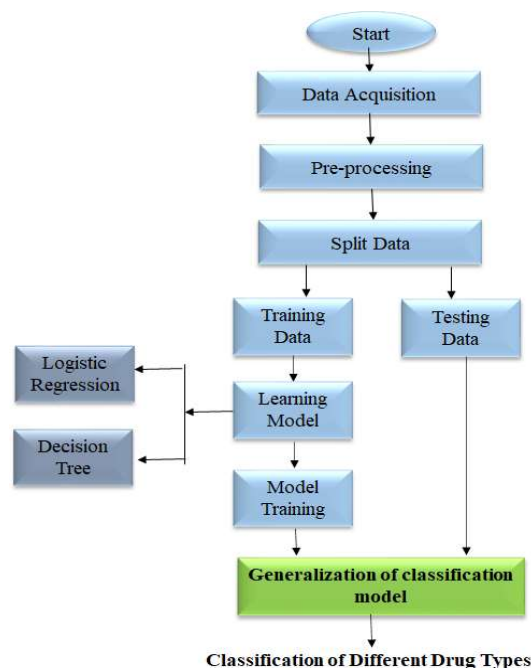


Fig. 10. Block diagram of ML operation.

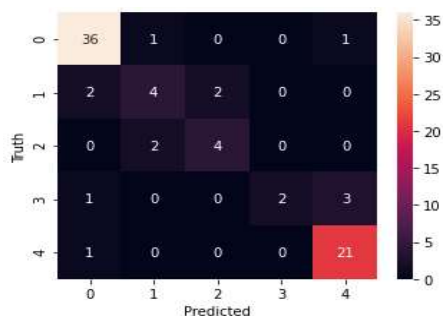
Next, the dataset is divided into training and testing datasets. The train test ratio was kept as 60:40. The training data (60%) is fed to learning models, and model training operation is accomplished. Two classification algorithms namely logistic regression and decision tree are tested for performing supervised ML classification. After model training operation is completed, final classification model is generated. Towards testing the appropriateness of a certain model for a particular data, remaining 40% test data was used. The performance of the classification model was tested using confusion matrix, and accuracy score metric. Based on the dataset, the model will classify among different sets of samples.

4 Results and Discussion

PYTHON JUPITAR NOTEBOOK v6.4.1 of ANACONDA NAVIGATOR was used for processing the data for ML. In this direction, the type of different parameters were checked using `pandas.head()` library function. It was observed from that, the values of Age, Sex, Cholesterol, BP, and Drug columns were categorical. However, categorical values could not be used for learning the model. Hence, label encoding operation was performed on the columns using `LabelEncoder()` and `fit_transform()` method of `sklearn.preprocessing` library.

This step converts character or string-based labels into numeric values i.e. machine-readable form. Afterwards, ML algorithms can decide in a meaningful way on how the labels must be operated to train the model accurately. It is a significant pre-processing step in supervised ML for the dataset containing string or character data type.

For train-test splitting, the ratio of train and test data was kept as 60:40. Two classifiers, i.e., logistic regression and decision tree were trained using the training data; and testing was performed on rest of the datasets. Towards this, classifiers were imported from respective library. For logistic regression the library was `sklearn.linear_model`; and decision tree was imported from `sklearn.tree`. Next, an instance of the classifier was created, and model fitting operation was performed using `x_train` (i.e. independent training data), and `y_train` (i.e. dependent training data). To test the model, `predict` method, followed by `x_test` (i.e. independent testing data) was used. For performance evaluation of both the learning models, confusion matrix was calculated. This is shown in Fig. 11 (a) and 12 (a) respectively. The confusion matrix results evidently indicate that, logistic regression produces more false results as compared to decision tree. Obtained accuracy for logistic regression and decision tree was 83.75%, and 98.75%, respectively (Fig. 11 (b) and 12 (b)). Hence, for drug detection, decision tree classifier should be used due to its higher performance accuracy.



(a)

```
In [50]: model.score(x_test,y_test)
```

```
Out[50]: 0.8375
```

(b)

Fig. 11. Results for logistic regression, (a) confusion matrix, and (b) accuracy score.

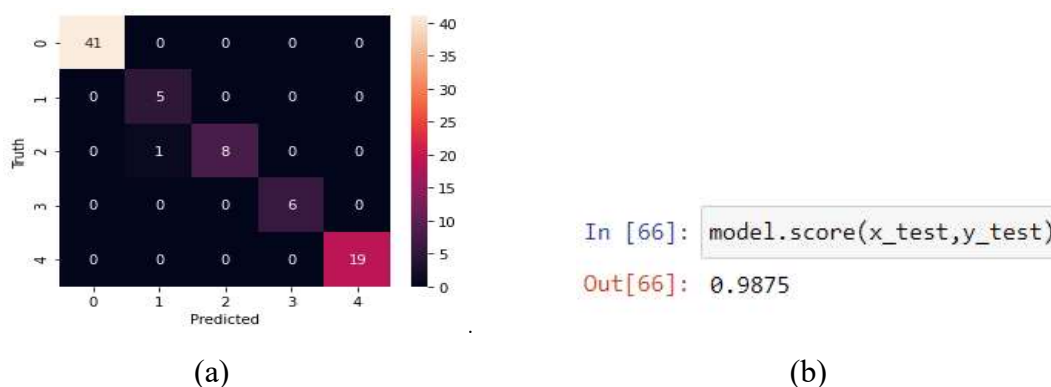


Fig. 12. Results for decision tree, (a) confusion matrix, and (b) accuracy score.

5 Conclusions and Future Work

In conclusion, application of AI has been demonstrated for healthcare industry. Overall, the ML algorithms used for automated classifications of different categories of drug (depending on different medical factors) are simple, robust, and computationally efficient. Following inferences can be drawn from this investigation:

- i) Applications of ML for predicting drug type prescribed to the patents, depending on different factors (sex, BP, Cholesterol Level and Na to K ratio) is demonstrated. For classification, logistic regression and decision tree based ML algorithms were used.
- ii) The dataset used for classification was imported from Kaggle Drug200 database. To split train-test dataset, the ratio between training and testing was kept as 60:40.
- iii) For classification of five different type of drugs, logistic regression classifier produced an accuracy of 83.75%; whereas, decision tree produced a score of 98.75%. Hence, for multiclass classification (viz. more than two), higher accuracy was achieved using decision tree based ML technique.

In future, other ML and DL based algorithms, viz. Naïve Bayes, K-mean clustering, support vector machine, artificial neural network, and others will also be investigated and the performance will be compared in terms of accuracy and programming complexity. Using these AI based techniques and industrial microcontrollers (Raspberry Pi, Arduino, PLC, and others), advanced robots can be constructed which will assist medical practitioners in upcoming years.

References

1. Lasi, H., Fettke, P., Hans-Georg, K., Feld, T., and Hoffmann, T. 2014. Industry 4.0. Business & Information Systems Engineering 6: 239-242.
2. Lucas, S. D., Guilherme, B. B., Néstor, F. A., and Alejandro, G. F. 2018. The expected contribution of Industry 4.0 technologies for industrial performance. International Journal of Production Economics 204: 383-394.
3. Napolitano, F., Zhao, Y., Moreira, V. M., Tagliaferri, R., Kere, J., D'Amato, M., & Greco, D. (2013). Drug repositioning: a machine-learning approach through data integration. Journal of cheminformatics, 5(1), 1-9.
4. Chen, R., Liu, X., Jin, S., Lin, J., & Liu, J. 2018. Machine learning for drug-target interaction prediction. Molecules, 23(9), 2208.

5. Lima, A. N., Philot, E. A., Trossini, G. H. G., Scott, L. P. B., Maltarollo, V. G., & Honorio, K. M. 2016. Use of machine learning approaches for novel drug discovery. *Expert opinion on drug discovery*, 11(3), 225-239.
6. Byvatov, E., Fechner, U., Sadowski, J., & Schneider, G. 2003. Comparison of support vector machine and artificial neural network systems for drug/nondrug classification. *Journal of chemical information and computer sciences*, 43(6), 1882-1889.
7. Burbidge, R., Trotter, M., Buxton, B., & Holden, S. 2001. Drug design by machine learning: support vector machines for pharmaceutical data analysis. *Computers & chemistry*, 26(1), 5-14.
8. Abacha, A. B., Chowdhury, M. F. M., Karanasiou, A., Mrabet, Y., Lavelli, A., & Zweigenbaum, P. 2015. Text mining for pharmacovigilance: Using machine learning for drug name recognition and drug–drug interaction extraction and classification. *Journal of biomedical informatics*, 58, 122-132.
9. Lewis, T. P., & Kruk, M. E. (2019). The Lancet Global Health Commission on High Quality Health Systems: countries are seizing the quality agenda. *Journal of Global Health Science*, 1(2).
10. Jordan, M. I., and Tom, M. 2015. Machine learning: trends, perspectives, and prospects. *Science* 349: 255-260.
11. Mohri, M., Afshin, R., and Ameet, T. 2018. *Foundations of machine learning*. MIT press.
12. Hosmer, J., David, W., Stanley, L., and Rodney, X. S. 2013. *Applied logistic regression*. John Wiley & Sons, 398.
13. Song, Y. Y., and Ying, L. U. 2015. Decision tree methods: applications for classification and prediction. *Shanghai Archives of Psychiatry* 2: 130.
14. <https://www.kaggle.com/jeevanrh/drug200csv>

Comparison of Thermohydraulic Performance Prediction of Perforated Rectangular PFHE by Various Machine Learning Models & ANN

Anirban Bose, Kailash Roy, Sayan Pramanik, Sayar Rakshit

1 Introduction

Because of its high area to volume ratio, compact heat exchangers are an excellent way to increase heat transfer. A plate fin heat exchanger is a common type of heat exchanger that is utilized in a variety of industries, including chemical, petrochemical, power generation, petroleum industry, aviation, cryogenic applications, and many more. The PFHE's performance is determined by the fin's geometry, the working fluid's characteristics, and flow parameters. In PFHEs, energy savings can be achieved by reducing waste energy or, in other words, improving the PFHE's thermo-hydraulic performance. To improve the performance of PFHEs, optimization is required, and this is currently being worked on. Using tools such as artificial intelligence machine learning will not only aid in the optimization of PFHEs models, but will also assist in the prediction of various essential parameters with optimal values, lowering development costs and time.

Because of their high area to volume ratio, PFHEs are an effective way to boost heat transfer. M. Khoshvaght-Aliabadi et al. [1] used a parametric CFD study method to examine the performance of PFHE using a manufactured experiment setup. When compared to triangular and trapezoid wings, the channel with rectangular wings improves heat transfer performance of the PFHE by 58.3 percent and 26.2 percent, respectively. A. Bose et al. [2] conducted a comparative investigation. By combining passive methods, such as nanofluids and various fin geometry, it can be made more efficient. J.M. Reneaume et al. [3] used the COLETH programme to optimize the heat exchanger by incorporating mathematical programming techniques. As a result of the programme, the fin geometry was optimized, lowering the cost. Manish Mishra et al. [4] established a GA-based methodology for multilayer plate-fin heat exchanger optimization. It calculated the best length and width parameters before calculating the overall annual cost. A.C. Caputo et al. [5] used the genetic algorithm to improve a shell and tube heat exchanger design, resulting in a 7.4% reduction in capital expenditure, a 93 percent reduction in operational costs, and a 52 percent reduction in total cost. Hamidreza Najafi et al. [6] used a multi-objective evolutionary algorithm to optimize a plate and frame heat exchanger. The method was able to provide a large number of optimal solutions that delivered the best results in terms of application, capital cost, and operational cost. Using a multi-objective genetic algorithm, Pouria Ahmadi et al. [7] optimized the design of a crossflow plate-fin PFHE. The work's initial two objective functions were to minimize the number of entropies generating units and total annual cost. R. V. Rao et al. [8] improved the Teaching-learning-based optimization (TLBO) algorithm for multi-objective optimization of heat exchangers with two competing objectives: efficacy and total cost. Zhe Wang et al. [9] used an enhanced multi-objective cuckoo search (MOCS) algorithm to optimize multi-objective optimization of PFHEs based on the -NTU model. They took into account eleven optimization factors as well as a penalty function for negotiating restrictions. A.K. Gupta et al. [10] investigated the results of compact heat exchanger prediction using ANN and ANFIS. The ANN and ANFIS models, which relate to Genetic Algorithm and Simulated Annealing, were determined to be valid.

More research is needed to optimize PFHEs, according to the literature review. Artificial intelligence is used to anticipate a rectangular perforated shaped plate-fin heat exchanger with changing fin spacing, perforated diameter, and fin height. The working fluid in the model is air, and the Reynolds Number was modified for laminar and turbulent flow areas. Linear Regression, XGBoost, Random Forest, Decision Tree, and ANN models are among the machine learning models compared here. The j-factor

and f-factor, which are heat transfer performance characteristics for laminar and turbulent flow zones, are predicted using these models. It is possible to optimize a prediction model using that method.

2 Methodology

2.1 Data Source

Velagapudi Vasu et al. [11] provided the data samples for perforated rectangular PFHEs with air as the working fluid. They used Ansys FLUENT to run a numerical simulation utilizing the Finite Volume Method (FVM). Figure 1 depicts the exact geometry and flow channels. In addition, Table 1 shows the specific parameters of the testing samples (PFHEs).

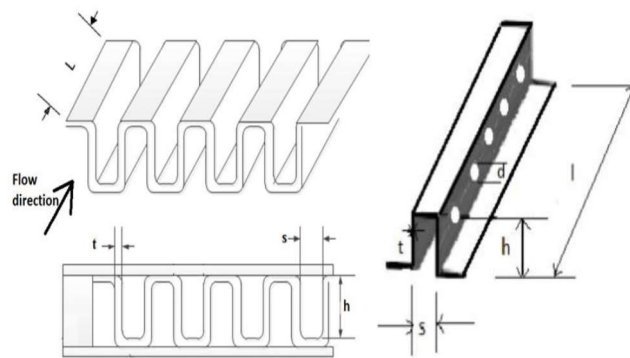


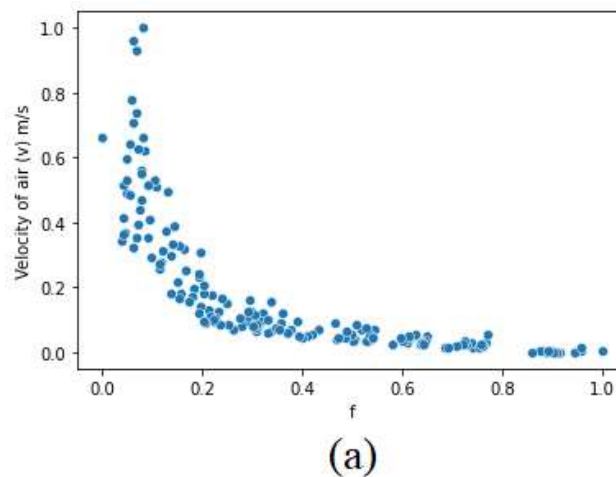
Fig. 1 Geometry of the flow channel for rectangular perforated shape

Table 1. Parameter ranges of the simulation data

Parameters	Flow Channel
Reynolds number	$100 \leq Re \leq 7000$
Length of the fin	$l = 100$ [mm]
Height of the fin	$h = 2, 4, 6, 8, 10$ [mm]
Fin spacing	$s = 2, 4, 6$ [mm]
Thickness of the fin	$t = 0.254$ [mm]
Perforation diameter	$d = 2, 4, 5$ [mm]

2.2 Data Visualization

The data was visualized using various pair plot and confusion matrix.



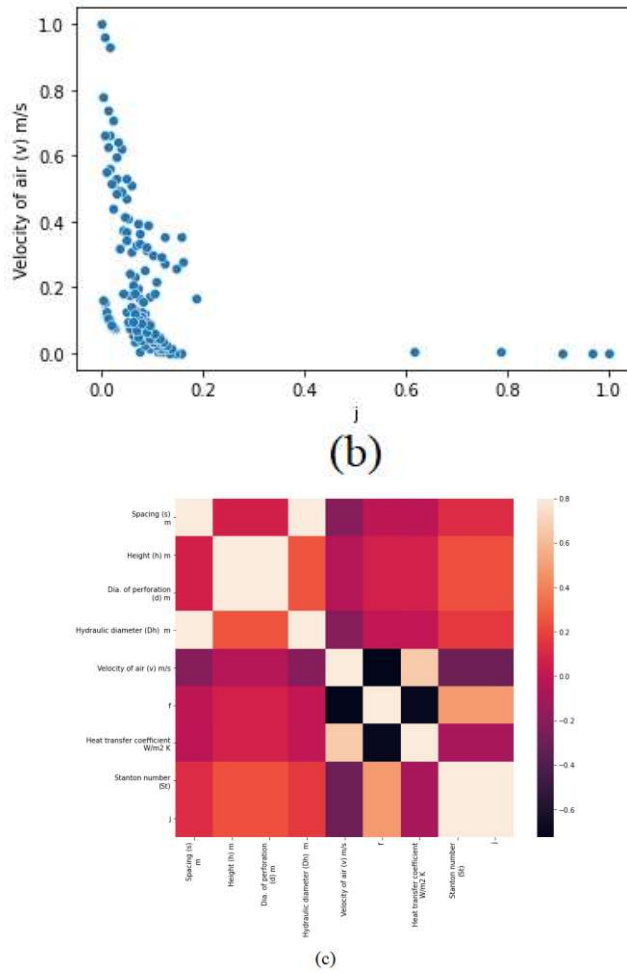


Fig. 2. Data Visualization where (a) scatter plot of velocity vs f-factor, (b) scatter plot of velocity vs j-factor, (c) heat map

2.3 Model platform

The code was written on python platform.

2.4 Learning Models

2.4.1 Linear Regression

Linear Regression is a predictive technique that establishes a linear relationship between input and prediction. The straight-line equation $y=mx+b$ is used for prediction, where y are the predicted values, x are the inputs, m is the slope, and b is the intercept. The least square method is used to minimize the error.

$$LSM = \frac{\sum_{i=1}^n (x_i - \bar{x})(y_i - \bar{y})}{\sum_{i=1}^n (x_i - \bar{x})^2} \dots (1)$$

2.4.2 XGBoost

XGBoost has been praised for its demonstrated mettle in terms of performance – and speed – since its launch in 2014. XGBoost builds trees using the loss function, which minimizes the following value:

$$L(\phi) = \sum_i \iota(\hat{y}_i, y_i) + \sum_k \Omega(f_k) \dots (2)$$

$$\text{where } \Omega(f) = \gamma T + \frac{1}{2} \lambda \|\omega\|^2$$

In this equation, the first part represents for loss function which calculates the pseudo residuals of predicted value \hat{y}_i and true value y_i in each leaf. The last part in $\Omega(f)$ contains the regularization term λ which is intended to reduce the prediction's insensitivity to individual observations, ω is the leaf weights which could be considered as the output value for the leaf, T is the number of terminal nodes or leaves and γ is the user defined penalty which is meant to encourage pruning.

2.4.3 Random Forest

The Random Forest Algorithm is a versatile model that is commonly used by engineers. It can tackle both regression and classification issues. It's made up of a variety of decision trees, each having the same nodes but distinct data that results in various leaves. It combines the outcomes of numerous decision trees to arrive at a single solution that represents the average of all of them. The mean squared error (MSE) is utilized for data branches from each node in regression.

$$MSE = \frac{1}{N} \sum_{i=1}^N (f_i - y_i)^2 \dots (3)$$

Here y_i is the value of the data point of testing at a certain node and f_i is the value returned by the decision tree. The formula determines the distance between each node and the projected actual value, which aids in determining which branch is the best choice for the forest.

2.4.4 Decision Tree

A decision tree is a fast approach for traversing a dataset and defining a tree-like path to the desired outcome. The data points stand on either side of the splitting node, depending on the value of a given feature, and this branching on a tree is based on control statements or values. To optimize the information gain at each split, an objective function is employed to split the nodes at the most informative characteristics, which is specified as follows.

$$IG(D_p, f) = I(D_p) - \left(\frac{N_{left}}{N_p} I(D_{left}) + \frac{N_{right}}{N_p} I(D_{right}) \right) \dots (4)$$

Here, f is the feature to perform the split, $D_p, D_{left}, \& D_{right}$ are the datasets, I is the impurity measure, N_p is the total number of the parent node and N_{left} and N_{right} are the number of sample in the child nodes.

2.4.5 Artificial Neural Network

Due to their structural flexibility, high representational capabilities, and availability of a wide variety of training algorithms, feed-forward neural networks are the most used designs. Here the individual element inputs are I_1, I_2, \dots, I_R multiplied by weights $w_{11}, w_{12}, \dots, w_{1R}$ and the weighted values are fed to the summing junction. The neuron has a bias b , which is summed with the weighted inputs to form the net input n . In this sum, n , is the argument of the transfer function F :

$$a = F(n) = F(w_{11}I_1 + w_{12}I_2 + \dots + w_{1R}I_{1R} + b) \dots (5)$$

This network consists of neurons arranged in layers in which every neuron is connected to all neurons of the next layer.

Table 2. The neural network layers for our work

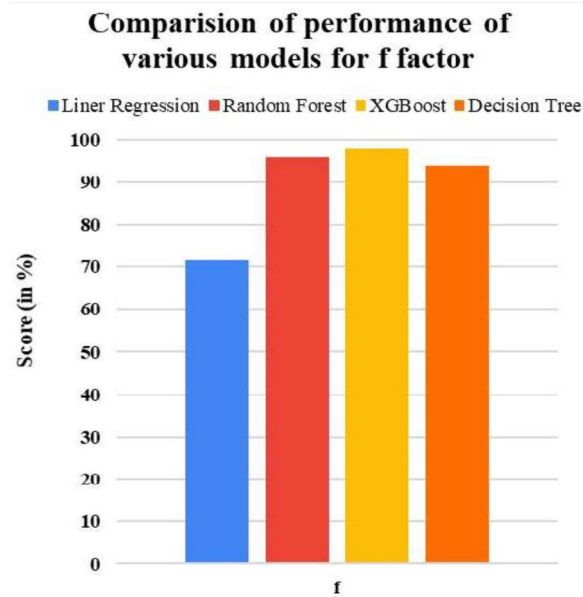
Model: "sequential"

Layer (type)	Output Shape	Param #
dense (Dense)	(None, 14)	112
dense_1 (Dense)	(None, 256)	3840
dense_2 (Dense)	(None, 256)	65792
dense_3 (Dense)	(None, 256)	65792
dense_4 (Dense)	(None, 1)	257
Total params: 135,793		
Trainable params: 135,793		
Non-trainable params: 0		

3 Result and Discussions

3.1 Simulation work

The Figure 3 represents the comparative bar plot for the four model's performance used are the Linear Regression, Random Forest, Decision Tree and XGBoost for prediction of f-factor. The best score was found using the XGBoost model with 98.037% as model score followed by Random Forest 95.742% model score, model score for Decision Tree was 93.769% and 71.451% model score for Linear Regression only.

**Fig. 3.** Comparison of performance of various models for f-factor

For prediction for j-factor with the same learning techniques is shown in Figure 4. The best model score was observed for Linear Regression with 100% then XGBoost with 98.715%, Decision Tree with 98.534% and 97.82% for Random Forest.

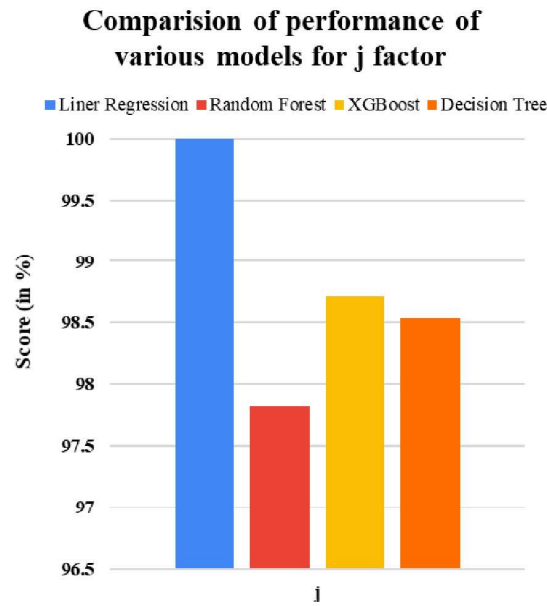


Fig. 4. Comparison of performance of various models for j-factor

Using artificial neural network for predicting the f-factor and j-factor also showed promising results. It is observed from the Figure 6 for f-factor and Figure 7 for j-factor total 50 epochs were executed. Comparing the Mean Absolute Error and Mean square error obtained in the f-factor and j-factor training, the curve decreased to almost zero which indicates for better prediction result.

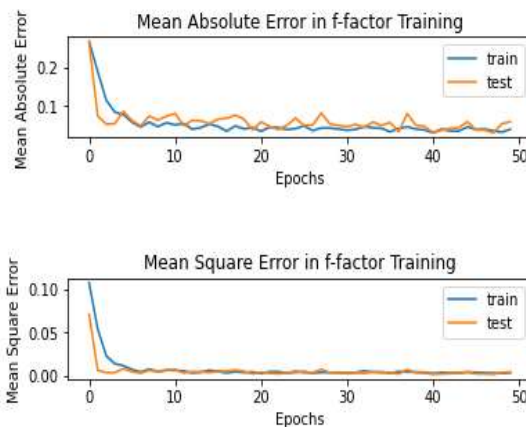


Fig. 6. MAE and MSE in f-factor Training

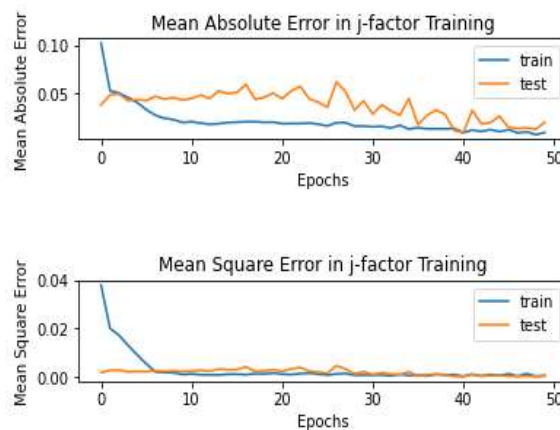


Fig. 7. MAE and MSE in j-factor Training

3.2 Experimental validation of the CFD model

Validation was done to check the authenticity of the CFD model dataset obtained by Velagapudi Vasu et al. [11] have validated by comparing with the results of the experiment done by Kays and London [12].

Table 3. Error observed

Decision Data	Error
Friction Factor	2-7%
Colburn j Factor	3-6%

4 Conclusion

In this research work performance of PFHE with perforated rectangular fin with working fluid as air at laminar and turbulent range was predicted using Artificial Neural Network and ML models Linear Regression, XGBoost, and Decision Tree. The accuracy score found by XGBoost was best for f-factor prediction while Linear regression showed best score for j-factor prediction among the ML models. Therefore, these best models for predicting performance parameters of Rectangular PFHE in the prescribed range of operating parameters can be used for optimization.

Acknowledgment

We are thankful to the college authority of Meghnad Saha Institute of technology (M.S.I.T.) to carry out this research work.

References

1. Khoshvaght-Aliabadi, M., S. Zangouei, and F. Hormozi. "Performance of a plate-fin heat exchanger with vortex-generator channels: 3D-CFD simulation and experimental validation." *International Journal of Thermal Sciences* 88 (2015): 180-192.
2. Bose, Anirban, Anupal Banerjee, and Utpal Maji. "Thermo-Hydraulic Performance Analysis of CNT-H₂O Nanofluid Flow in Turbulent region through Rectangular Plate Fin Heat Exchangers-A Numerical Study."
3. Reneaume, J-M., Hervé Pingaud, and N. Niclout. "Optimization of plate fin heat exchangers: a continuous formulation." *Chemical Engineering Research and Design* 78, no. 6 (2000): 849-859.
4. Mishra, Manish, Prasanta Kumar Das, and S. K. Sarangi. "Optimum design of crossflow plate-fin heat exchangers through genetic algorithm." (2004).
5. Caputo, Antonio C., Pacifico M. Pelagagge, and Paolo Salini. "Heat exchanger design based on economic optimisation." *Applied thermal engineering* 28, no. 10 (2008): 1151-1159.
6. Najafi, Hamidreza, and Behzad Najafi. "Multi-objective optimization of a plate and frame heat exchanger via genetic algorithm." *Heat and mass transfer* 46, no. 6 (2010): 639-647.
7. Ahmadi, Pouria, Hassan Hajabdollahi, and Ibrahim Dincer. "Cost and entropy generation minimization of a cross-flow plate fin heat exchanger using multi-objective genetic algorithm." (2011): 021801.
8. Rao, R. Venkata, and Vivek Patel. "Multi-objective optimization of heat exchangers using a modified teaching-learning-based optimization algorithm." *Applied mathematical modelling* 37, no. 3 (2013): 1147-1162.
9. Wang, Zhe, and Yanzhong Li. "Irreversibility analysis for optimization design of plate fin heat exchangers using a multi-objective cuckoo search algorithm." *Energy conversion and management* 101 (2015): 126-135.

10. Gupta, Ajay Kumar, Pankaj Kumar, Ranjit Kumar Sahoo, Anoop Kumar Sahu, and Sunil Kumar Sarangi. "Performance measurement of plate fin heat exchanger by exploration: ANN, ANFIS, GA, and SA." *Journal of Computational Design and Engineering* 4, no. 1 (2017): 60-68.
11. Velagapudi Vasu, Kumar, A C S, RamaKrishna, K, Shodhganga@INFLIBNET: Determination of heat transfer and flow friction characteristics of compact heat exchanger surfaces by CFD analysis, doi:<https://shodhganga.inflibnet.ac.in/handle/10603/2682>
12. Kays, W. M., and A. L. London. "Compact Heat Exchangers, 2nd Edn., 1964."

Disease Detection and Classification of Medicinal Leaves using Digital Image Features and Random Forest Technique

Amit Chatterjee, Arka Prava Das, Sujay Biswas, Vineet Kumar Borashi

1 Introduction

In present era, manual assembly systems are still mostly used due to its wide flexibility. However, they possess poor productivity levels, when compared to automated assembly systems. To circumvent this drawback, in last few years, Industry 4.0 (I4.0) has emerged as the fourth industrial revolution targeting to achieve higher productivity, and flexibility standards. To achieve acceptable performances I4.0 utilizes various smart technologies like artificial intelligence (AI), advanced robotics, cyber-physical systems, hi-tech sensors, cloud computing, cognitive computing, mobile devices, and others [1]. Agriculture is one of the prime industrial sectors, where I4.0 can be implemented extensively. Agriculture industry in India is remarkably pointed as the “sunrise sector”, which accounts for nearly 18% of India's gross domestic product (GDP). This sector poised for immense growth and greater contribution to the Asian as well as world food trade. However, productivity of different crops in rural area is significantly hampered due to disease and infections generated by various bacteria, fungus, and pathogens [2]. Hence, disease detection for crops needs significant research effort to improve agricultural productivity.

Leaf inspection is one of the prominent approaches for plant disease detection. Towards this, Ansari et al. [3] investigated leaf characteristics using laser based biospeckle technique. Authors successfully detected the infected regions of the leaves, which displayed a relatively lower dynamic activity as compared to the healthy tissue. Oerke et al. [4] used infrared thermography for detecting diseases at various stage of development, depending on the host-pathogen system. Generated thermal signatures were processed using different spatial approaches to distinguish between healthy and infected plants. Wang et al. [5] introduced hyperspectral imaging in the range of 328–1115 nm for the rapid prediction of tea leaf disease based on moisture, total nitrogen, and crude fiber contents. Using hyper spectral apparatus, ninety samples of eight tea-leaf types and two picking standards were investigated.

Ayurveda is a branch of agriculture that is undergoing tremendous growth owing to the rising awareness about the harmful side effects of conventional allopathic drugs. Market size for ayurvedic products was valued approximately 6.50 Billion USD in 2020, and is anticipated to reach 21.12 Billion USD by 2028 (rising at a CAGR of 15.63% from 2021 to 2028) [6]. For production of Ayurvedic medicine, high quality disease-free leaves are required. However, conventional leaf sorting techniques are manual, time-consuming, and require direct human intervention. The techniques used for disease detection of agricultural leaves, (viz. biospeckle, thermography, hyperspectral imaging) are complex, expensive, time consuming, require scientific expertise, and are susceptible towards environmental perturbations. Hence, to increase profitability of this industry, there is a need of simple automated technique to perform this task. To circumvent these drawbacks of conventional systems (to distinguish between fresh and diseased leaves for ayurvedic industry), in present communication, digital image features and random forest based machine learning technique were used. Data corresponding to fresh and diseased sample for two classes of medicinal leaves namely basil and periwinkle were utilized to train the model. Confusion matrix and accuracy score metric was used to assess the performance of the model.

In this section, brief description regarding image processing (top-hat filtering), feature extraction, and random forest classifier has been provided.

A. Chatterjee*, A. P. Das, S. Biswas, V. Borashi

*Independent Researcher (Formerly with Dept. of Electrical Engineering, IIT-Indore) Indore, India-452017

2 Theory

2.1 Top-hat filtering

In mathematical morphology, top-hat transform operation extracts details, and balance the overall luminescence of a given image [7]. This transform is used for various processing tasks, including background equalization, image enhancement, feature extraction, and many more. The classes of filters in this transform are built using several Fourier space or real space low pass filter functions. The name ‘top-hat’ originates from the hat like shape of the filter, when observed in the domain on which the filter function is constructed (Fig. 1).

To get the clear view of leaf image, and equalize background luminescence, this operation was used.

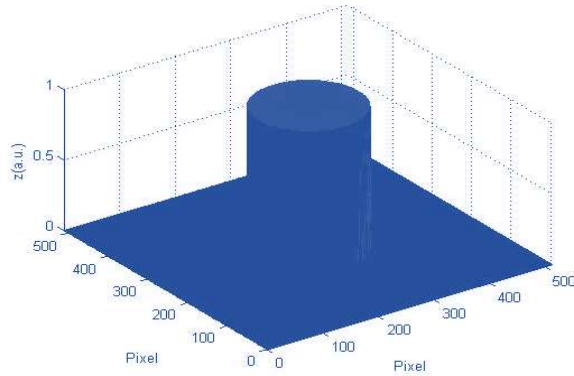


Fig. 1. Top-hat filtered image.

2.2 Feature extraction

Two image features namely ‘mean intensity’ and ‘contrast’ are calculated from top-hat filtered image [8].

(a) Mean Intensity: This parameter indicates the over-exposure (pixel saturation) or under-exposure by inferring the pixel values of the speckle images. Mathematically, this is expressed as

$$M = \text{mean}(\text{mean}(i(x, y))). \quad (1)$$

If the pixel values of grayscale image are towards 0 (under-exposure) or 255 (over-exposure), image properties cannot be traced precisely. Hence, the intensity of the illumination should be adjusted to avoid such conditions.

(b) Contrast: Contrast can be defined as the difference in luminance that makes representation in an image distinguishable. As compared to absolute luminance, human visual system is more sensitive to contrast.

Contrast estimates the integration of the luminance, and is calculated mathematically as:

$$C = \frac{\sigma}{\langle i \rangle}. \quad (2)$$

where $\langle i \rangle$ and σ denote the spatial average and standard deviation of the gray level intensity for each selected analysis window, respectively.

After feature extraction, random forest-based machine learning classifier is utilized for distinguishing fresh and diseased leaf samples.

3.5 Random Forest Classifier

Machine learning (ML) is a branch of AI, which accentuates on the use of algorithms and data to replicate the decision making system of human brain. ML algorithms are primarily divided into two broad categories i.e., supervised learning (SL) and unsupervised learning. SL uses a set of input attributes X and corresponding labels (Y) for its operation. Whenever new input is provided to the model, it produces corresponding label.

Random forest can be categorized as a supervised ML, where the decision making is performed using N-Decision tree approach. Each decision tree is constructed by two units, namely branches and nodes (Fig. 2). The node from which first division in the dataset takes place is termed as root node. The terminal nodes that forecast the outcomes of the decision tree is called as leaf node. The element of the tree which guides the outcome of a split to the next node is termed as branches [9, 10].

Conventionally, ID3 algorithm developed by J. R. Quinlan is used for decision tree implementation [10]. The technique uses a greedy search top-down approach for traversing possible branches without implementing any backtracking. The algorithm utilizes the concept of Entropy to generate a decision tree. This can be mathematically expressed as:

$$E = \sum_{i=1}^c -p_i \log_2 p_i. \quad (3)$$

where, E =entropy

p_i =probability of occurrence of an event i

c =total number of events

The tree structure is built by dividing the dataset based on that attribute, for which entropy is minimum. Next, the same process is repeated for all other attributes, until leaves are reached.

In random forest classifier, N number of decision tree are used (Fig. 3). The dataset is fed to all the decision trees, and corresponding results are calculated. Finally, classification result is evaluated by majority voting or averaging of all tree outcomes.

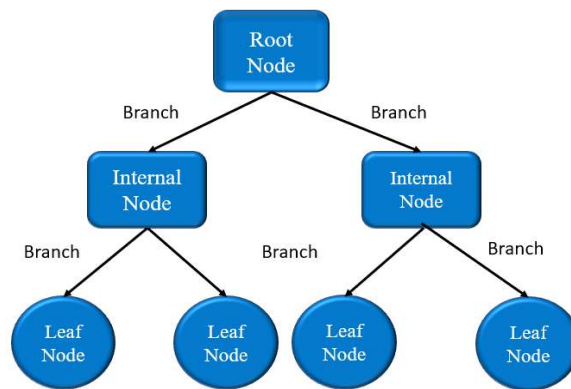


Fig. 2. Decision tree model.

3 Methodology

In this section, a brief discussion regarding dataset, train-test splitting, performance estimation parameters, and overall process flow is provided.

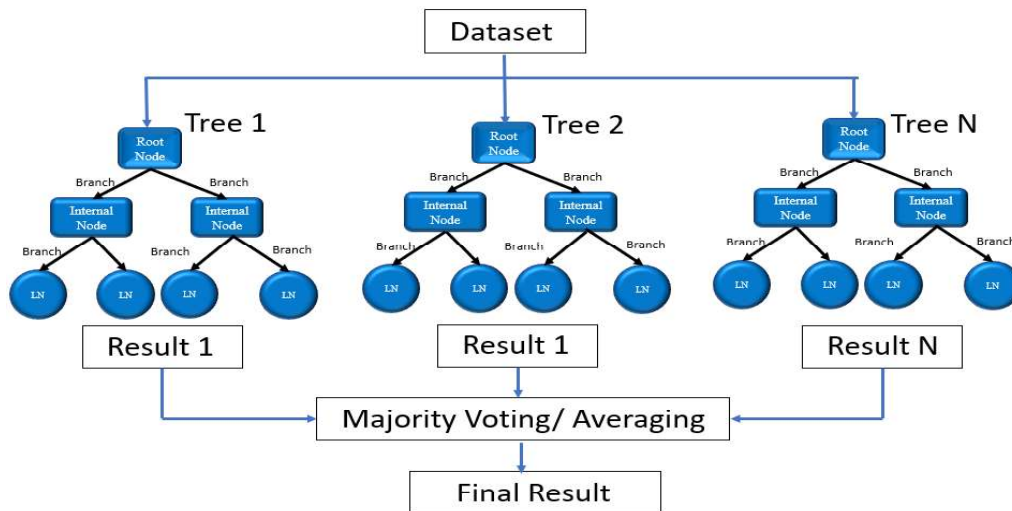


Fig. 3. Random forest model.

3.1 Dataset

For classification operation, two medicinal leaves namely basil (*Ocimum basilicum*) and periwinkle (*Catharanthus roseus*) were used. Both herbs are used for preparing several Ayurvedic medicines. Images of 250 fresh and infected leaves for each plant group are captured using Samsung M30 mobile camera (specification: 13MP sensor with f/1.9 aperture lens, 5MP wide-angle shooter with f/2.2 aperture). Numeric dataset is created from the captured images using top-hat filtering and image features.

3.2 Data splitting and performance estimation

For generation and validation of the ML model, acquired dataset is divided into training and testing datasets. Training data is utilized to generate the experience through which the algorithm learns to respond. Test data, in conjunction with performance matrices, is used to estimate the performance of the model [9].

		<i>Actual Values</i>	
		Positive (1)	Negative (0)
<i>Predicted Values</i>	Positive (1)	True Positive	False Positive
	Negative (0)	False Negative	True Negative

Fig. 4. Confusion matrix.

Confusion matrix approach was utilized as performance matrix for random forest based classification model. Confusion matrix is defined as a summary of prediction results for any classification model. The number of true and false predictions are segregated in a $N \times N$ matrix with count values, and fragmented by each class (where, N =total number of classes, Fig. 4). This matrix is

very useful for measuring the performance for the model as well as different classification parameters (such as accuracy score, precision, recall and F1 score) [10].

The most common metric for performance evaluation of a model is ‘accuracy’. This can be defined as the fraction of samples predicted correctly.

$$\text{Accuracy} = \frac{\text{True Positive} + \text{True Negative}}{\text{Total}} \quad (4)$$

Here, Total = (True Positive + True Negative + False Positive + False Negative).

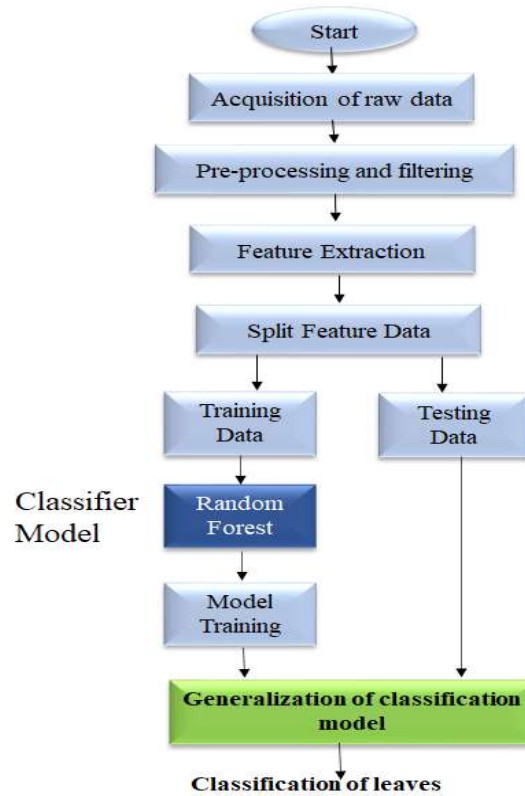


Fig. 5. Block diagram of ML operation.

3.3 Process flow

The process flow illustration for leaf quality classification process is shown in Fig. 5. Firstly, images of healthy and diseased leaves are acquired with the help of imaging device, and are converted to numeric data using image features. Numeric data are then organized in MS Excel and labelled as ‘fresh’ and ‘diseased’. Next, overall dataset is splitted into training and testing datasets. The ratio of train and test was kept as 3:2. Firstly, the training data (60%) is provided to learning models, and model training process is performed. Random forest based algorithms is used for performing supervised ML classification. After model training is completed, final classification model is created. Towards testing the relevance of the model for leaf classification, remaining test data was used. The performance of the classification model was verified using confusion matrix, and accuracy score.

4 Results and Discussion

Fresh and diseased leaves (as acquired using mobile camera) for basil and periwinkle plant are shown in Fig. 6 and 7 respectively. It is evident from the images that, two types of infection can be observed for infected leaf i.e. dark or white patches, and pale yellow discoloration. Hence, to distinguish between

fresh and infected leaf, digital image features are utilized. Towards this, RGB leaf image is converted to grayscale image using spatial averaging in MATLAB R2016a environment. For enhancement and background equalization, top-hat filtering is performed on grayscale image. 2D and 3D intensity distribution of gray scaled leaf, and top-hat filtered leaf is shown in Fig. 8 and 9 respectively.

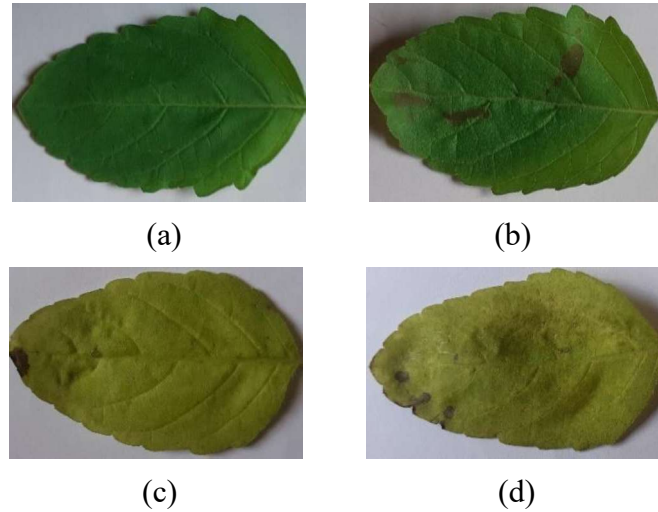


Fig. 6. Basil leaves: (a) fresh leaf, (b) infected leaf (sample 1), (c) infected leaf (sample 2), and (d) infected leaf (sample 3).

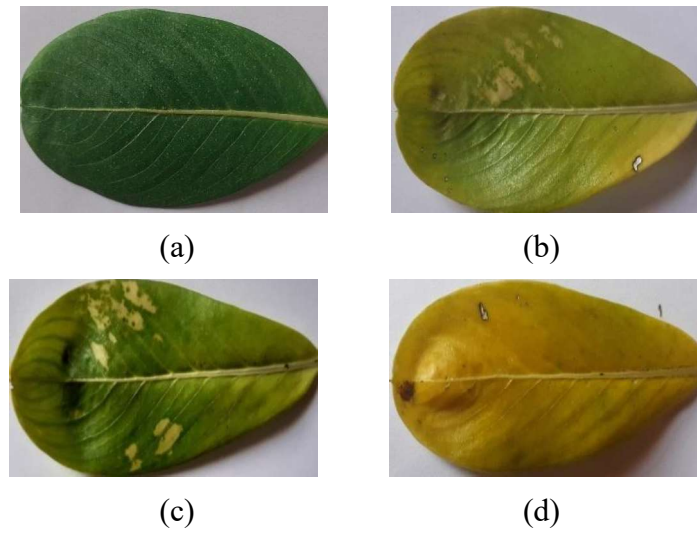


Fig. 7. Periwinkle leaves: (a) fresh leaf, (b) infected leaf (sample 1), (c) infected leaf (sample 2), and (d) infected leaf (sample 3).

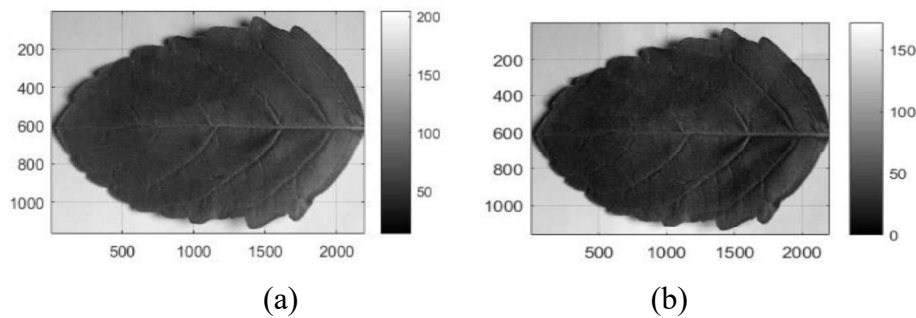


Fig. 8. (a) Gray-scaled leaf, and (b) top-hat filtered leaf.

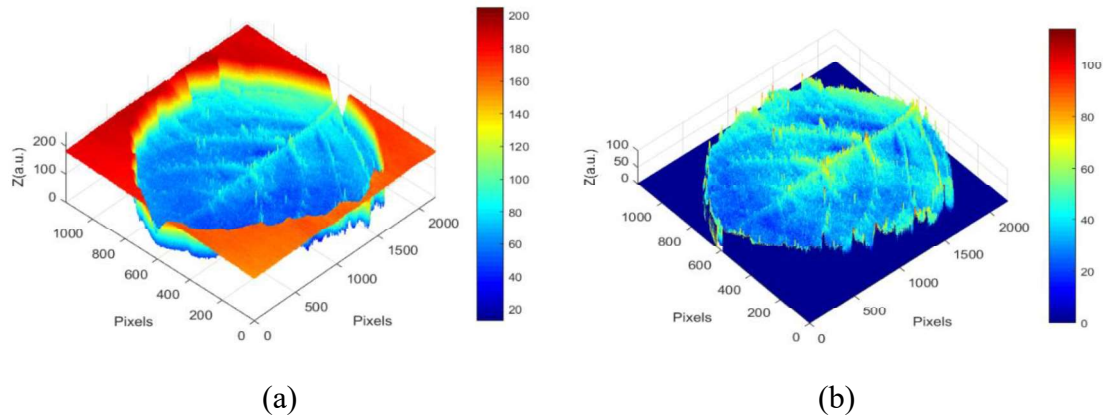


Fig. 9. 3D intensity distribution for (a) gray scaled leaf, and (b) top-hat filtered leaf.

Table 1. Features for different types of leaves.

Class	Type	Mean Intensity (a.u.)	Contrast (a.u.)
Basil Leaf	Fresh	55.9	0.32
	Infected	106.16	0.15
Periwinkle Leaf	Fresh	53.56	0.19
	Infected	85.38	0.12

Next, mean intensity and contrast feature for each leaf is calculated using Eq. 1 and 2. Numerical values of the features for both basil and periwinkle leaves are shown in Table 1. It is evident from the table that, both the features are capable of distinguishing between fresh and infected one. For using the data towards ML model training, calculated features are arranged in MS Excel with corresponding label.

Random forest classifier was trained using the training data; and testing was performed on rest of the datasets. Towards this, classifier was imported from *sklearn.ensemble* library. Next, an instance of the classifier was generated, and model fitting was accomplished using independent training data (x_{train}), and dependent training data (y_{train}). For testing the model, predict method, followed by independent testing data (x_{test}) was used. For performance evaluation of the learning model, confusion matrix was calculated. This is shown in Fig. 10 (a) and (b), for basil and periwinkle leaves respectively. The confusion matrix results evidently indicate that, random forest model can efficiently distinguish between fresh and diseased leaves. Obtained accuracy for basil and periwinkle leaf was 91%, and 89%, respectively.

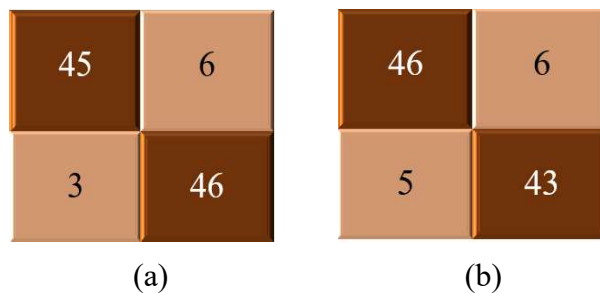


Fig. 10. Confusion matrix for (a) basil leaf, and (b) periwinkle leaf.

5 Conclusions and Future Work

In conclusion, application of AI has been demonstrated for classification of healthy and diseased leaves. Overall, digital image features and random forest algorithm used for automated classification technique is simple, computationally efficient, and robust. Following points can be obtained from this investigation:

- i) For predicting leaf quality, a combination of ML, digital image filtering, and feature extraction technique was utilized. Random forest-based ML algorithm was used for performing classification operation.
- ii) The dataset used for classification was acquired using RGB imaging device. For splitting train-test dataset, the proportion between training and testing was kept as 3:2.
- iii) For classification of fresh and infected class of basil leaf, classifier produced an accuracy of 91%; whereas, for periwinkle leaf, the accuracy score was 89%.

In future, different supervised and unsupervised learning techniques (e.g. Naïve Bayes, K-mean clustering, support vector machine, artificial neural network, and others) will also be investigated in terms of accuracy and programming complexity. Using industrial microcontroller (Raspberry Pi, Arduino, PLC, and others) based robots in conjunction with AI algorithms can be used for automated quality inspection of medicinal leaves.

References

1. Lasi, H., Fettke, P., Hans-Georg, K., Feld, T., and Hoffmann, T. (2014). Industry 4.0. Business & Information Systems Engineering 6: 239-242.
2. [Agriculture in India: Industry Overview, Market Size, Role in Development...| IBEF](#)
3. Ansari, M. Z., Mujeeb, A., & Nirala, A. K. (2018). Assessment of biological leaf tissue using biospeckle laser imaging technique. Laser Physics, 28: 065608-065614.
4. Oerke, E. C., & Steiner, U. (2010). Potential of digital thermography for disease control. In Precision crop protection-the challenge and use of heterogeneity (pp. 167-182). Springer, Dordrecht.
5. Wang, Y. J., Li, L. Q., Shen, S. S., Liu, Y., Ning, J. M., & Zhang, Z. Z. (2020). Rapid detection of quality index of postharvest fresh tea leaves using hyperspectral imaging. Journal of the Science of Food and Agriculture, 100: 3803-3811.
6. [India Emerging As A Global Wellness And Ayurveda Hub | IBEF](#)
7. Solomon, C., & Breckon, T. (2011). Fundamentals of digital image processing: a practical approach with examples in Matlab. John Wiley & Sons.
8. Chatterjee, A., Singh, P., Bhatia, V., & Prakash, S. (2020). An efficient automated biospeckle indexing strategy using morphological and geo-statistical descriptors. Optics and Lasers in Engineering, 134: 106217-106226.
9. Jordan, M. I., and Tom, M. (2015). Machine learning: trends, perspectives, and prospects. Science 349: 255-260.
10. Mohri, M., Afshin, R., and Ameet, T. (2018). Foundations of machine learning. MIT press.

Innovatization of entrepreneurship in virtual reality: digital duplicates, Internet of Things, robotics

Kateryna Kraus, Nataliia Kraus, Oleksandr Marchenko

1 Introduction

In modern business in Ukraine are widely used technologies of information retrieval systems Internet, advertising and sale of goods on Internet, electronic payments, electronic tenders, electronic card payments (including payroll), automated systems of salary accounting and reporting processes, electronic systems of protection and fire safety, electronic systems of information collection of control and measuring devices, mobile and selector communication, etc.

The concept of digital twinning has already become widespread in industrial production, but its benefits for the logistics industry are just beginning to show. For example, DHL in its Next Generation Wireless Logistics Review identified digital twinning as a new direction for growth. Digital duplicate is useful where access to main system is difficult or impossible (as in the case of a spacecraft), or it is costly (creating a costly product with a high degree of complexity: a large conveyor, powerful turbine or aircraft engine, and the cost of design error is very high), or it is associated with destructive phenomena (crash tests of new car models involve the destruction of expensive physical samples).

Digital double allows to reduce as much as possible delay time at natural tests. During the Fourth Industrial Revolution, digital duplicates became part of the “perfect storm” that combined the Internet of Things, robots, artificial intelligence, and automation. But interest in digital duplicates has spread far beyond production. A study by analysts at Markets&Markets indicates that digital counterpart market will grow from \$ 3.8 billion in 2019 to \$ 35.8 billion by 2025 due to the great interest in this technology from the pharmaceutical and defense industries [2].

2 EXPERIMENTAL ANALYSIS

Valuable in the scientific sense of research in digital entrepreneurship are the scientific works and practical works of such well-known scientists as R. Azum, W. Isaacson, D. Lichtblau, T. Stock and J. Seliger. It deserves due attention in terms of studying the prospects, directions and mechanisms of smart-industry development in the era of digitalization, which was engaged in well-known researchers and economists, namely: G. Androschuk, K. Alekseeva, Y. Bazhal, V. Vyshnevsky, V. Vitlinskyi, V. Geets, G. Davtyan, J. Zhalilo. Economists from Ukraine are also actively involved in research and development in terms of doing business that seeks to combine digital technology, security and economic success and issues of quality digital business management.

Among them are the names of J. Arnautov [3], E. Avdeev [4], N. Andrusyak [5], L. Boldyreva, A. Vichugova [6], O. Goloborodko, M. Zgurovsky, O. Kryvoruchko [7], N. Kraus, K. Kraus [8], P. Leonenko, O. Manzhura [9–10], A. Maslov [11], O. Marchenko [12–15], V. Osetskyi [16–17], V. Shtepa [18–19] and others. But, at the same time, a significant number of topical issues such as: characteristics of the problems and management of digital duplicates; preliminary recommendations in terms of quality control and management of digital duplicates in production; the process of creating and using digital duplicates; the content of work of digital duplicates in new and operating enterprises remains little studied in the future.

The aim of the article is to study the advantages of digital duplicates in terms of virtual reality. Representation of factors that should be considered before the introduction of digital duplicates in virtual reality. Finding out the peculiarities of the implementation of projects involving digital

K. Kraus*, N. Kraus, O. Marchenko

*Department of Management of Borys Grinchenko Kyiv University. Kyiv. Ukraine. 08137

duplicates, the criteria for this type of duplicates. Substantiation and disclosure of successful experience in the implementation of digital duplicate technologies.

3 RESULTS

3.1 *The concept of digital duplicates*

Digital duplicate is a virtual copy of a physical product, process, or ecosystem. It is used to create a simulation that can be updated and changed to a greater extent in the real world, and to reflect any actions that occur with physical object. Digital dual device consists of making decisions based on various assumptions. Tests are performed on virtual analogue without the need to interfere with the work of real, usually expensive, objects [2].

In today's business environment, the principles of digitalization of business are as follows: interoperability, operational interaction, integration (interoperability), virtualization, decentralization, real-time interaction, service orientation, modularity, training and continuing professional education, synergy and emergencies. So, it is not surprising that the concept of digital duplicates is attributed to Industry 4.0 and digitalization of production, the origins of this concept originated much earlier than the 2010s. This concept continues the CALS and PLM methodologies that emerged in the early 21st century. Product Life Cycle Support or CALS (Continuous Acquisition and Life Cycle Support) involves the continuous integration of CAD, CAE, CAM, MRP, ERP, SCM and CRM systems used in design, manufacture and operation of high-tech products. Product data management systems (PDM) are responsible for data integration.

The product lifecycle management technology itself fits into the concept of PLM (Product Lifecycle Management) – an organizational and technical system that supports all information about the product and related processes from design and production to decommissioning. One of the goals of CALS/PLM technologies is to create virtual productions, where the development of specifications for software-controlled process equipment is distributed in time and space between several autonomous organizations to accelerate and optimize the development and production of products. In the leading countries of the world for the development of CALS/PLM-technologies standards for electronic data exchange, electronic technical documentation and manuals for process improvement are being developed [20].

However, since 2010, when the term Big Data appeared, the popularity of CALS/PLM has been rapidly declining. The concept of virtual production is embodied in the form of a digital double, because it is from the second half of 2010 that computing power allowed to create almost identical copies of real physical objects and processes in real time [21]. Due to this, as well as the development of Big Data and the Internet of Things (IoT), the ideas of CALS/PLM were continued in Industry 4.0. Interactive data collection from IoT devices allows you to monitor and even control an object or process online. For example, Apache Kafka together with Spark, Storm, Flink or NiFi provide continuous aggregation and online processing of operational data. And the Apache Hadoop ecosystem is responsible for the reliable storage of this information and data from CAD, CAE, CAM, MRP, ERP, SCM, CRM, and even SCADA systems.

In addition, digital duplicates are actively using another trend technology Industry 4.0 – augmented and virtual reality (AR/VR). This allows you to simulate almost any situation and clearly represent the internal structure of complex systems, from living organisms to space satellites. Thus, digitalization of industrial enterprises, which develops digital duplicates of industrial objects and processes, has become a modern embodiment of CALS/PLM-ideas, significantly expanding their original scope [4].

Digital duplicates are created on the basis of a specialized platform. Such platforms are manufactured by both global fans such as Siemens and Dassault Systemes, and small companies such as Xcelgo. The choice of vendor depends, first, on the specific tasks of the digital duplicate. For example, Siemens is targeting its digital dual hardware platform, and Xcelgo's solution is better suited

for modeling production systems. In particular, the conditions for checking the operating modes of the platform are formed in the execution of instructions that can be edited.

3.2 Features of the process of using digital duplicates

Having digital duplicate for the created object provides a significant increase in efficiency for all project participants. The developer creates a quality system faster, radically reducing system debugging time. The client receives a thoroughly tested system in all possible modes with increased reliability. In this sense, digital counterpart is a tool to radically reduce the risks of large technical systems projects. The use of digital duplicate changes the application to the knowledge and experience of a specialist in the subject area of the customer's business: these specialists write scenarios to test the future system, form a checklist, which is then irradiated in full finished digital dual system [22].

Digital enterprise offers tangible benefits through the operation of digital duplicates, which are a virtual representation of the actual system. They allow you to get an idea of the entire life cycle of equipment and optimize it – both for new and existing plants and projects [23].

The creation of a digital duplicate takes place at the design stage of a new system. After that, as the object is completely designed, a static model of digital dual device is created on the basis of CAD-models in the CAD system or 3D-models of objects. It essentially describes the architecture of the object, the location of the system equipment in the workspace. In the next stage, the static model “comes to life” describes the workflows, moving to a dynamic model system. This is not just a visualization of what is happening in the system. Digital dual must reproduce systematic control in the same way as the physical system. In order to write algorithms for controlling digital dual devices, such algorithms are created for the purpose of a real system. If you connect algorithms on digital duplicates, you can get algorithms that will work exactly on a real system (Figure 1).

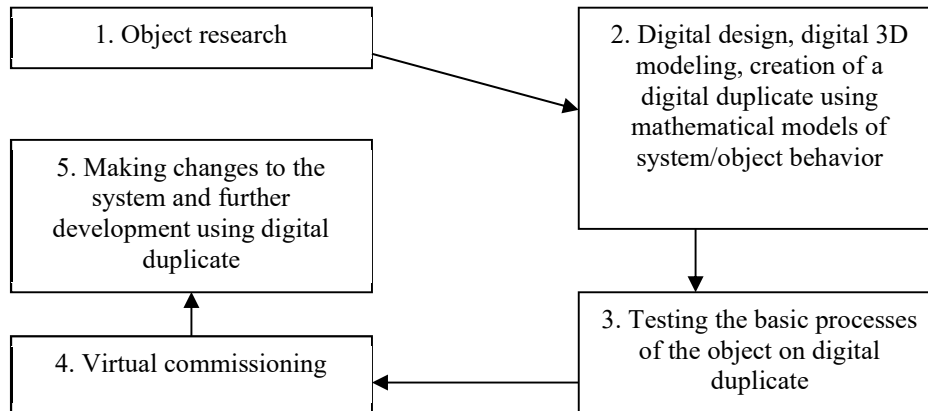


Fig. 1. The process of creating and using a digital duplicate (*author's development*)

Internet of Things (IoT) technology allows you to control devices remotely. In addition, the new method of digital duplicates can create copies of these devices. Digital duplicates are virtual copies of real objects that can be used to test the performance and efficiency of an item or system. Using digital duplicates, engineers can now quickly and easily test new sensors and products, as well as maintain and monitor their condition in a timely manner. Practitioners suggest that digital twin is a virtual interactive copy of a real physical object or process that helps to effectively manage it by optimizing business operations. For example, digital duplicate of the plant allows you to simulate the location of equipment, employee movements, work processes and emergency situations [6].

In essence, digital duplicate is a model of a real-time system that provides a virtual representation of physical assets. It allows you to manage both digital and physical assets as a whole. Digital duplicates have revolutionized the aerospace, manufacturing, engineering and energy sectors by

optimizing design, development, production and management of all aspects of a physical product throughout its life cycle [1].

3.3 Experience and benefits of using digital duplicates

The integrated concept of digital business duplicates consists of three forms: digital product duplicate, digital production duplicate and digital product and production performance duplicate. With extensive expertise in this field and optimized tool, Siemens is the only company to offer a holistic approach. The value of digital duplicate lies in the execution of scenarios and forecasting future performance (Table 1).

Table 1. Contents of digital duplicates at new and working enterprises (grouped by authors based on source 23)

Digital duplicates for new businesses	Digital duplicates for working enterprises
Creation of virtual production is carried out at the stage of designing processes and installations. Siemens provides a comprehensive set of tools for the design, modeling and construction of manufacturing enterprises. Using as a basis for collaboration platforms such as COMOS, and ensuring full data integration in the stages from design to design and commissioning, the system developers automatically create a digital duplicate installation with process automation, ready for implementation in real production with minimal effort, which allows you to reduce design costs and reduce production time.	At existing enterprises, technological processes, hardware and software can be used unchanged for decades. However, even in this case, digital duplicate can be very useful for optimizing existing processes and facilities. This digital duplicate allows you to analyze information on the operation of the plant. In this case, modernization and maintenance measures are based on the documentation in its original form and the relevant data on the operation of the plant. This significantly reduces the search time and the number of errors.
In the real world, Siemens' Process Management and Production Operations Management (MOM) systems ensure reliable production operations and help collect the data needed to create digital duplicate. This duplicate, created on the basis of real production systems and enriched with data obtained from Internet of Things, optimizes the production and maintenance of critical facilities.	Thanks to the integrated workflows, created digital duplicate is constantly updated until the end of the service life of the installation – the connection between virtual and real production is carried out in a closed loop.

Digital duplicate technology is one of the fastest growing concepts in Industry 4.0. It is the growth of the IoT industry and cloud technologies that has a significant impact on digital counterpart market. According to Gartner, digital duplicates are used in 13% of organizations implementing IoT projects, while 62% are either already implementing the technology or planning to do so. According to the latest Markets&Markets report, digital counterpart market will grow to \$ 35.8 billion by 2025 with an average annual growth rate of 37.8%. Digital duplicate technology is already widely used in industry, but it is no less important for manufacturers. Table 2 presents the advantages of using digital model of duplicates and the factors that should be considered before its implementation [3].

Table 2. Advantaches of using digital duplicates in virtual reality (group be outsours based on surce 2; 3)

Advantage	Content and characteristics during the application
Operational assessment of risks and production time	With the help of digital duplicate, companies can control the quality of a product before it appears in the real world. Because digital duplicate is a copy of the planned production process, experts may notice any process failures before the product goes into production. Thanks to digital duplicates, you can increase the intensity of testing by 10 times and reduce by 85% the labor resources involved in design process. In general, engineers can restructure the system by generating unexpected scenarios, studying the system's response, and creating mitigation strategies. Thus, new technology allows for better risk assessment, accelerate the development of new products and increase the reliability of production lines.
Improving	Process automation and round-the-clock access to system information can increase productivity

interaction within teams	and efficiency. Yes, in the team, developers can pay more attention to creating new elements, rather than monitoring and checking once again already running.
Intelligent service	Because digital duplicate IoT sensors generate big data in real time, businesses will be able to analyze internal statistics and detect any system failures in advance. This allows companies to move to intelligent service, while increasing the efficiency of the production line and reducing operating costs.
Improving financial decision-making process	In the virtual model, you can also specify the cost of materials and labor costs. As a result, companies can make faster and more efficient decisions in financial sense: whether the value is calculated correctly, what can affect it, and so on. You can also use digital duplicates to avoid financial losses due to reduced productivity. For example, previously business owners had to stop all workflows to test new warehouse modules. Now it all happens virtually and the effectiveness of the settings is easy to check again.
Remote real-time monitoring	When working with a large system, it is simply impossible to check any of its elements at once. However, digital duplicate can be accessed anywhere, allowing users to remotely monitor and control system performance. In practice, engineers have created a warehouse structure with all the necessary technical characteristics. Yes, digital duplicates mimic the operation of a warehouse. Thanks to it is possible to estimate productivity better and to choose the optimum approach at the organization of industrial warehouses in reality.

In logistics industry, the development of digital duplicates for complex infrastructure supply chains, such as ports and large warehouses, is still at an early stage. However, major ports around the world, including Singapore and Rotterdam, are turning to digital counterparts to design, plan and manage their operations. Having digital duplicate, such as a storage room, can significantly increase operational efficiency. Every process that takes place on the site and every piece of equipment will be reflected in a digital mirror, ensuring a constant flow of operational data. There are many advantages: you can quickly detect the inefficiency of certain areas of handling or identify problems with the maintenance of equipment before they affect the throughput [1].

3.4 Main conditions and levels of implementation of digital duplicates in enterprises

In addition, digital duplicate is not limited to collecting data obtained during product development and manufacturing, but continues to collect and analyze information throughout the life cycle of a real object, for example, using Internet of Things (IoT) devices [6]. Factors to consider before implementing digital duplicates in virtual reality are presented in Table 3.

From a practical point of view, it matters for what essence digital duplicate is created. For example, an aircraft engine is a separate object, which would correspond to a very difficult set of complex mathematical descriptions of how it works. This digital duplicate is necessary in order to test on a mathematical model all its capabilities and performance in various situations, including freelance. Another example is the logistics company's sorting center automation system. The sorting system consists of many relatively simple elements (for example, for transporting the conveyor), but for a logistics company it is important not one element, but the entire sorting system, and a digital duplicate is created for the entire production system [22].

Table 3. Factors to consider before implementation digital duplicates in virtual reality (grouped by authors based on source 3; 1)

Factors	Characteristic features
Update data security protocols	<p>Gartner estimates that by 2023, 75% of digital duplicates for OEM products connected to the IoT will use at least five different types of integration endpoints.</p> <p>The amount of data collected from the many endpoints is huge, and each is potentially vulnerable. Therefore, before implementing digital duplicate technology, companies need to analyze and update their security protocols. It is worth paying special attention to:</p> <ul style="list-style-type: none"> - data encryption; - access rights, including a clear definition of user roles; - principles of the least privileges; - elimination of known defects of the device;

	- regular security checks.
Team training	Companies need to make sure that their staff have the necessary skills and tools to work with digital duplicate models.
Data quality management	Duplicate digital models use data from thousands of remote sensors through unsecured connections. Companies should be able to exclude irrelevant data and manage gaps in data flows.

The benefits that an enterprise receives from digital transformation of business processes depend on the type of tasks performed by employees. The more complex the task, the deeper the level of digital transformation the company needs to increase overall efficiency. According to the level of complexity, the tasks are ranked as follows (from the simplest to the most complex):

- repetitive tasks;
- administrative tasks;
- unit level tasks;
- tasks of the enterprise level;
- expert tasks.

Ultimately, main goal of digital transformation is to ensure that employees perform only expert, ie the most unique tasks that are difficult to copy or accurately replicate. The rest of tasks can be performed with minimal employee participation and with the maximum involvement of powerful digital tools and increase the efficiency of their work. Features of the implementation of projects involving digital duplicates in terms of virtual reality in terms of stages are disclosed in Table 4.

Table 4. Peculiarities of project implementation with the participation of digital duplicates in the conditions of virtual reality (grouped by authors based on source 22; 20)

Stages of the project	Content and characteristics
Technical	Digital dual platforms are an objectively new phenomenon in the market. In particular, it provides clarity that not all pieces of equipment used in a particular project can be adequately represented by the platform. Then, these or those complex elements either come to create (construct) independently, which is not always a trivial task, or to ask the vendor to work with the platform. However, it should be noted that the vendor platform responds to operational requests at all times if they are interested in ensuring that their product is optimal as required.
Financial	If only the company decides to create digital duplicate, then this project will have to defend before the CFO in part the need to purchase licenses on the platform, and obviously a foreign vendor, and therefore the costs will be quite significant. If the production system is created by external contractors, such as an integrator, then the cost of acquiring a license is borne by the company's partner. To do this, it is important that the integrator constantly executes projects using digital duplicate platforms: then the cost of the platform will not become a separate item in the cost item required by the project. Because customers are often not ready to increase project budgets, for the sake of digital duplicates in the design services.
Terms of designing with the participation of digital duplicates	The timing of such projects depends on the system. In general, they are equated to the duration of the design phase. The expert conducts an empirical pattern: in the project, which takes 8 months, work on digital double adds to the duration of the first phases of development from 2 to 4 weeks, ie a maximum of 1 month. In the future, work with the digital double is carried out in parallel with the planned work on the system.
Improving the quality of design	Improving quality systems using digital duplicate is reflected in the best solutions at an early stage.

For example, DHL named three main challenges in promoting digital duplicates in logistics: cost, accurate asset representation, and data quality. Next-generation wireless and 5G can solve the last two problems. The exact reproduction of digital duplicates depends on the ability to communicate in real time between the physical asset and its virtual display. Given the complexity of modern warehouses and the growing number of automated logistics tools, the collection, transmission and visualization of data into dynamic virtual models have so far been limited by the capabilities of existing wireless networks. Now, thanks to 5G, this problem can be solved.

3.5 Successful experience in the implementation of digital duplicate technology

Digital duplicate can be thought of as a virtual prototype of a real object or process that contains all the data about it, including history and information about the current state. The criteria for digital duplicates are given in Table 5. Interactive analysis of this data using Big Data technologies allows you to effectively perform the following important management functions:

- obtaining accurate information about system performance;
- forecasting future conditions using ML-models of predictive analytics;
- remote control of the object in real time [6].

In terms of data quality, digital duplicates today have to collect data from many sources, both traditional IT systems and many sensors in the physical world. These can be boxes with RFID tags, AVG (cars with automatic control) or pallets with Bluetooth support. All this needs to be coordinated and coordinated through a single high-speed wireless network, which DHL suggests will be based on 5G [1].

Table 5. Categories of digital duplicates (grouped by authors based on source 6; 2)

Categories	Characteristic features
<i>Duplicate (Digital Twin Instance, DTI)</i>	data describing the physical object. For example, an annotated three-dimensional model, information about materials and components of the product, information about work processes, test results, records of repairs, operational data from sensors, monitoring parameters, etc.
<i>Prototype (Digital Twin Prototype, DTP)</i>	virtual analogue of a real physical object. It contains all the data for this product, including information from design and production stages, such as product requirements, three-dimensional model of the object, description of technological processes, disposal conditions, etc.
<i>Aggregate double (Digital Twin Aggregate, DTA)</i>	a system that integrates all digital duplicates and their real prototypes, allowing data to be collected and exchanged in real time.

Successful scenarios for the introduction of digital duplicate technology in different sectors of the economy are presented in Table 6. The ultimate goal of digital duplicate in manufacturing industry is to create a closed feedback loop between virtual and real production through the use of the right digital infrastructure. Due to this connection, the duplicate characteristics of real production allows you to develop optimization scenarios in virtual production. After successful modeling and implementation of these scenarios, the cycle begins again.

Table 6. Successful experience in the implementation of digital duplicate technology (compiled by authors based on source 2; 1)

Field of application	Brief description, content of the work
<i>Energy sector</i>	In the energy sector, digital duplicates are used to create virtual wind farms, or as they are sometimes called, "wind farms" based on cloud technology. Each wind farm has its own unique structure, like DNA or a fingerprint. Thanks to digital twin technology, engineers can combine and select different turbine configurations, depending on the conditions of the wind farm. As soon as the turbine is put into operation, its virtual copy begins to collect and analyze environmental data in real time, which leads to the creation of more efficient models.
<i>Sphere of hospitality and service</i>	Digital duplicates help to create simulations of real events and situations, and this creates a significant impact on the development of the Industry. For example, in the CKE Restaurants Holdings fast food chain, digital duplicates allow restaurants to work more productively. Digitization has affected the halls for visitors and kitchens, so companies are testing different options, thereby reducing staff rotation and creating more favorable conditions for visitors.
<i>Urban environment</i>	The technology helps city planners better understand and refine factors such as energy consumption. Digital copy of Singapore already exists, and copies of other cities are expected in the future.
<i>Retail</i>	The technology of digital duplicates has recently entered the field of retail, but could be very useful, especially when it comes to modeling the behavior of shoppers. Analytical firm Pygmalios singles out virtual duplicate technology as part of the Retail 4.0 digital retail transformation process, an

	approach that collects detailed real data from the physical retail environment and then uses it to better understand visitor behavior and actions.
<i>Healthcare</i>	Since a virtual image of any real object or environment is created, it is possible to create a “digital patient” – a model of the human body that gives an idea of the state of human health during his life. This is how Philips sees the future of healthcare. The idea of creating a whole digital patient is still far from being realized, but the technology is already being applied to certain parts of the body, which is encouraging. Philips has developed the HeartModel application, which creates a detailed 3D image of the human heart based on ultrasound images. One day, a virtual heart can help save the real thing.

Based on the analysis of literature sources, we concluded that digital transformation of the enterprise is the introduction of modern technologies in its business processes. This understanding involves not only the installation of modern hardware or software, but also fundamental changes in approaches to management, corporate culture, external communications. As a result, the productivity of each employee and the level of customer satisfaction increase, and the company gains a reputation for progressive and modern. The latest digital technologies of the “digitization” process lead to innovative transformations in all spheres of enterprise activity and encourage the creation of new business models.

4 CONCLUSIONS

In conclusion, it is worth noting that new technologies help companies reduce costs, increase productivity and efficiency, as well as optimize maintenance. In particular, it is the technology of digital duplicates in combination with the tools of machine learning and artificial intelligence allows to achieve this without compromising workflows. With this content, digital technology makes it possible not to stop the line to test a new element. Therefore, for manufacturers, the technology of digital duplicates is important not only to improve efficiency, but also to bring the product to market faster.

Guided by a number of topical issues that we have tried to focus on in this article, we remain true to the opinion that it is still important to conduct future research aimed at presenting the effects of digital transformation. Among them, we believe: significant release of working time of employees to focus on more important tasks, reducing the number of specific tasks, improving the coherence of business processes within digital enterprise, accelerating the processing of analytical information for management decisions, etc.

References

1. “Digital duplicates” – a new level of development of supply chains (2020), available at: <https://logist.fm/news/cifrovi-dviyniki-noviy-riven-rozvitku-lancyugiv-postachannya> (Assessed 17 September 2021).
2. Digital twins: 5 case studies from non-manufacturing companies (2021), available at: <https://nfp2b.ru/2020/11/18/tsifrovye-dvojniki-5-primerov-iz-praktiki-neproizvodstvennyh-kompanij/> (Assessed 27 September 2021).
3. Arnautova Ya. (2020), How technology allows you to control things remotely, available at: <https://nv.ua/ukr/techno/technoblogs/cifrovi-dviyniki-shcho-ce-za-tehnologiya-i-yak-vona-pracyuye-50089100.html> (assessed 17 September 2021).
4. Avdeev E. (2017), Digital twins. Design through reflection, available at: <https://habr.com/ru/post/331562/> (assessed 17 September 2021).
5. Andrusiak N.O., Kraus N.M., and Kraus K.M. (2020), Digital Cubic Space as a New Economic Augmented Reality. *Sci. innov.*, Vol. 16. № 3. pp. 92–105.
6. Vichugova A. (2021), Digitalization of production and digital twins: combining PLM, IoT and Big Data, available at: <https://www.bigdataschool.ru/blog/digital-twin-plm-iot-big-data.html> (Assessed 17 September 2021).
7. Kryvoruchko O.S., Kraus N.M., and Kraus K.M. (2018), Virtual reality of the national information and innovation space. *Economy and society*, no. 14. pp. 22–35, available at: <http://economyand.society.in.ua>

(Accessed 14 January 2021).

8. Kraus N.M., and Kraus K.M. (2018), What changes does Industry 4.0 bring to the economy and production? *Formation of market relations in Ukraine*, no. 9 (208), pp. 128–136.
9. Manzhura O., Kraus K., and Kraus N. (2021), Digitalization of Business Processes of Enterprises of the Ecosystem of Industry 4.0: Virtual-Real Aspect of Economic Growth Reserves. *WSEAS Transactions on Business and Economics*, Vol. 18, Art. #57. pp. 569–580, available at: [https://www.wseas.org/multimedia/journals/economics/2021/b165107-021\(2021\).pdf](https://www.wseas.org/multimedia/journals/economics/2021/b165107-021(2021).pdf) (Assessed 15 July 2021).
10. Manzhura O.V., Kraus N.M., and Kraus K.M. (2021), Training in digital entrepreneurship in the conditions of virtual mobility: tasks, methods, advantages. *Market infrastructure*, vol. 51, pp. 3–8, available at: http://www.market-infr.od.ua/journals/2021/51_2021_ukr/3.pdf (Accessed 15 June 2021).
11. Maslov A.O., Kraus N.M., and Kraus K.M. (2021), Institutional-evolutionary frames of the mentality of “digital man” as a “genetic code” of digital entrepreneurship. *Efficient economy*, no 3, available at: <http://www.economy.nayka.com.ua/?op=1&z=8734> (Accessed 30 March 2021).
12. Marchenko O., and Kraus N. (2021), Innovative-digital entrepreneurship as key link of Industry X.0 formation in the conditions of virtual reality. *Baltic Journal of Economic Studies*, Vol. 7. № 1. pp. 47–56, available at: <http://baltijapublishing.lv/index.php/issue/article/view/952/1006> (Accessed 30 June 2021).
13. Marchenko O., Kraus N., and Kraus K. (2020), The impact of servation on the results of economic digital entrepreneurship activities. *Ukraine in the context of global and national modern servisation processes and digital economy*: monograph. Praha: OKTAN PRINT. 2020. 265 p. (pp. 81–91).
14. Marchenko O.V., Kraus N.M., and Kraus K.M. (2021), Digital gradients as key attributes of the formation of Education 5.0 and Industry X.0. *Economic space*, no 165, pp. 13-17.
15. Marchenko O.V., Kraus N.M., and Kraus K.M. (2021), Skills and competencies produced by the course “Digital Entrepreneurship” at the University 5.0. *State and regions*, no 1 (118), pp. 6-11.
16. Osetskyi V.L., Kraus N.M., and Kraus K.M. (2021), Sharing economics: dialectical development of reciprocal exchange in the conditions of virtual reality and digital transformation. *Economic theory*, no 2, pp. 5–19.
17. Osetskyi V.L., Kraus N.M., and Kraus K.M. (2021), Sharing economics: institutional mode, universality and novelization of business development on virtual digital platforms. *Efficient economy*, no 4, available at: <http://www.economy.nayka.com.ua/?op=1&z=8786> (Accessed 05 June 2021).
18. Shtepa O.V., Kraus K.M., and Kraus N.M. (2021), Industry X.0 and Industry 4.0 in the context of digital transformation and innovative strategy of national economy development. *Efficient economy*, no 5, available at: <http://www.economy.nayka.com.ua/?op=1&z=8901> (Accessed 27 May 2021).
19. Shtepa O.V., Kraus K.M., and Kraus N.M. (2021), Methods of teaching digital entrepreneurship in the system of economic education at an innovative university. *Entrepreneurship and innovation*, no 16, pp. 7–14.
20. CALS- and PLM-technologies (2021), available at: <https://helpiks.org/6-11760.html> (Accessed 17 September 2021).
21. Digital duplicate (2021), available at: https://ru.wikipedia.org/wiki/Digital_duplicate (Accessed 18 September 2021).
22. TAdviser: Everyone is talking about digital twins. What does it mean and what it looks like in practice? (2021), available at: <https://www.reksoft.ru/blog/2021/03/11/digital-twins/> (Accessed 17 September 2021).
23. Digital enterprise for continuous production (2021), *SIEMENS*, available at: <https://new.siemens.com/ua/uk/kompaniya/klyuchovi-temy/tsifrovaya-promyshlennost/bezperervne-vyrobnytstvo.html> (Accessed 27 June 2021).

Effect of Battery Cell Arrangement on Thermal Management of Air-Cooled Battery Pack

Arnab Pattanayak , Sourav Sarkar*, Achintya Mukhopadhyay

1 Introduction

The Automobile industry has started to shift its drive system from engine to motor due to the growing air pollution and also a shortage of fossils fuels. Electric vehicles (EVs) as well as Hybrid electric vehicles (HEVs) have become future of the transportation industry since it is eco-friendly and zero-emission. In Electric vehicles (EVs) as well as Hybrid Electric Vehicles (HEVs) Li-ion battery is used worldwide. Li ion battery has high charge density, thermal stability, no memory effect between charging and discharging cycle and also environmental friendliness. These characteristics of li- ion cell gave it's an extra edge compared to other batteries of different materials. The working reliability and also long-term durability of LIB highly depend on its internal as well as external temperature. Not only high temperature but also too low temperature affect the degradation process of battery material and also shorten its lifespan. To get high power or to charge the battery at a very short time we have to run the battery at a higher charging/discharging cycle which increases battery heat generation. As a consequence battery temperature will increase.

It is observed in many scientific studies by several researchers that the efficiency of charging cycle and also lifecycle will be reduced if battery is working above 50-55°C [1]. Usually, optimal temperature range of LIB is of 30–40 °C. Above 80-90°C there is a chance of severe thermal failure also called thermal runaway [2-4]. So, we need a robust Battery thermal management systems (BTMS) which can regulate the maximum temperature reached during the process and also control temperature differences between the battery cells within the battery pack under their operating conditions [5].

There are various methods of BTMS. Among them, air-cooled BTMS is perhaps the simplest, both conceptually and mechanically. Since natural convection air cooling system is generally insufficient to cool the battery to a large extent. So we use a fan for forced convection air cooling. Its warm-up period is shorter than the liquid type system which has larger thermal inertia with the liquid coolant in the system. With the advantage of lightweight, forced air cooling is widely used in some automotive companies to control the battery pack temperature. So around the globe, many studies have been carried out to upgrade the air-cooled BTMS. Fan et al [6] studied numerically the effect of airflow rate and also gap between the batteries on the cooling performance of battery pack. They found that when gap space was increased from 1 mm to 5 mm then temperature difference between the batteries was decreased by 0.41°C on fixed volume flow of air of 20.4 m³/h and with increase the flow rate from 20.4 m³/h to 40.8 m³/h, the maximum temperature of batteries decreased by 1.8 °C on fixed gap distance of 3 mm between the batteries. Chen et al [7] carried out a configuration optimization for a parallel air-cooled battery pack system. From their result, it was suggested that to find the optimum arrangement the space around the highest temperature battery should increase and minimize the space around the lowest temperature one. Chen et al [8] had done a numerically comparative study between five battery pack configurations with repositioning air inlet and outlet position. They found that in symmetrical configurations maximum temperature rise was reduced by at least 43% and energy consumption was reduced by 33% for different airflow inlets. However, a considerable amount of research is required to properly understand the effect of battery cells arrangement within the battery pack without changing the battery pack size.

S. Sarkar
Jadavpur University, Kolkata-700032

The aim of the present work is to develop a numerical model of the battery pack and investigate the effect of air inlet velocity on thermal management parameters like battery temperature, battery cells temperature difference, fan power requirement. Initially, a 2-D model of nine 18650 Li-ion cells is considered for investigating the effect of inlet air velocity in cooling performance. Another four battery pack configurations are considered by arranging the battery cell without changing pack size to understand the effect of battery arrangement on thermal management of air-cooled battery pack. The results are discussed through a Comparative analysis of favorable battery temperature condition i.e. 30°C to 40°C as well as minimum temperature variation between cells i.e. 3-5 K between these five batteries.

2 NUMERICAL MODELING

2.1 Geometry for Numerical Model

The computational domain selected for the present work to numerically simulate heat transfer from battery cells to forced air coming to the battery pack is presented in Figure 1. The module shown contains nine lithium-ion cells with $LiFePO_4$ cathode, graphite anode. The nine cells are positioned within the module with evenly spaced apart cells. As it is a 2D model so cylindrical battery cell represented here as circular structure. Air as a coolant comes from the left side of the module to lower the temperature of the battery. The cell are numbered from 1 to 9, the airflow then exits the module from the right side, which is exposed finally to the atmosphere. For the sake of simplicity, the tabs on the cells, bus bar to connect the batteries and other electronic components which are present actually are excluded from this model. The Air is coming at a constant speed constraint at the inlet, while the outlet is specified as the pressure output constraint. Non-slip boundary condition is applied on side walls. The ambient temperature i.e the temperature at which air is coming from the inlet is consider here as 20°C. In this modelling, the heat transfer in radiation is assumed to be very negligible and so it is not taken into account.

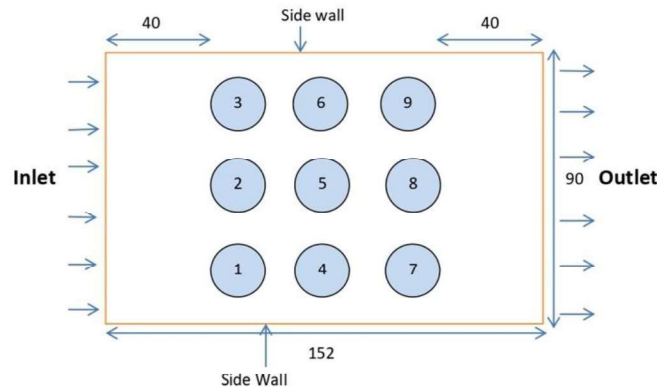


Fig. 1. Geometrical model of the battery pack

2.2 Assumptions

The solution is obtained by simulation in ANSYS software and the following assumptions are considered:

- 1) Material of the battery is considered as isotropic.
- 2) Fluid and also heat transportation are two dimensional and steady.
- 3) Battery generates constant heat.
- 4) Thermo-physical properties for air are constant.
- 5) Density variation is considered as constant.

2.3 Governing Equations

The general purpose CFD code software Fluent 18.1 is used for the present numerical simulation which utilized the finite volume method to discretize the governing equations and a pressure-based solver to handle the pressure-velocity coupling. Assuming a steady and incompressible flow the governing equations of the flow and heat transfer are continuity, momentum and energy equations and can be written in the inertial frame of reference as follows.

3.3.1 Battery:

As we consider battery as an isotropic material. So for this the generalised energy equation for specific thermo- physical properties is-

$$\frac{\partial}{\partial t}(\rho C_p T) = \nabla \cdot (K \nabla T) + Q_{gen} \quad (1)$$

Where, T represents battery temperature, C_p represents specific heat capacity of the battery, K stands for radial thermal conductivity of the battery material. Q_{gen} is the rate of heat generation per unit volume.

3.3.2 Fluid domain:

The fluid domain is governed by the continuity, momentum, and also energy equations which are given below:

3.3.2.1 Continuity equations

$$\frac{\partial \rho}{\partial t} + \nabla \cdot (\rho \vec{V}) = 0 \quad (2)$$

3.3.2.2 Momentum equations

$$\frac{\partial}{\partial t}(\rho \vec{V}) + \nabla \cdot (\nabla \vec{V} \vec{V}) = -\nabla P + \nabla \cdot (\mu \nabla \vec{V} + \nabla \vec{V}^T) \quad (3)$$

3.3.2.3 Energy equations

$$\frac{\partial}{\partial t}(\rho C_p T) + \nabla \cdot (\rho C_p \vec{V} T) = \nabla \cdot (K \nabla T) \quad (4)$$

where, \vec{V} represents velocity of fluid, μ represents viscosity of the fluid, ρ is the density of the fluid, T is the temperature of the fluid.

2.4 Boundary Conditions

This battery pack is considered as inlet Air flow is coming to module in a steady manner i.e. no variation of air flow according to time. Battery pack at extreme left side as well as extreme right side is open for inflow and outflow respectively. At inlet velocity inlet boundary condition and outlet side pressure outlet boundary condition are assigned. At inlet temperature of air as a cooling medium is taken 20°C (293 K). In this CFD model of battery pack Air act as a fluid zone and li-ion battery cells are fixed zone. An interface is created between the battery cells and the surrounding air domain and the interface is meshed as a coupled wall boundary condition. The interface acts as a wall zone and does not allow fluid to pass through it but permits heat transfer across the interface. All other surfaces are in no-slip constraint.

2.5 Discretization Scheme

A pressure based finite volume discretization algorithm is employed to solve the governing equations. The SIMPLE algorithm is used for the pressure-velocity coupling. The Least Squares Cell based

gradient discretization and for pressure discretization second order scheme is used. For momentum and energy discretization second order upwind scheme is used. Turbulent kinetic energy and turbulent dissipation rate are discretized using first order upwind scheme.

2.6 Battery Cell Properties

Table 1: Battery Cell (18650) Specification (Thermal)

Sl no.	Parameters	Details/Value
1	Battery	Li-ion battery, anode: Carbon cathode: LiFePO ₄ ,
2	Capacity	3.6 Ah
3	Diameter (D)	18 mm
4	Length (L)	65 mm
5	Density	2007(kg/m ³)
6	Radial Thermal conductivity	1 (W/m-K)
7	Specific heat capacity	998 (J/kg-K)

2.7 Battery Heat Generation

Generally, battery is operated at variable charging and discharging cycle. As a consequence heat generation also vary time to time as well as operating cycle to cycle. So first we have to know the heat generation range for parametric study in BTMS. Saw et al [9] have studied about different C rate of a battery and from their numerical result they estimated heat generation by a li-ion battery for several C rates. From their study Saw et al [9], it is found that at 5C rate average heat generation rate from a battery is 9.48 W.

$$\begin{aligned}
 \text{As for 18650 cell, Volume (V)} &= \frac{\pi}{4} D^2 L \\
 &= \frac{\pi}{4} (.018)^2 \times .065 \\
 &= 1.65 \times 10^{-5} \text{ m}^3
 \end{aligned}$$

$$\begin{aligned}
 \text{Heat generation rate } (Q_{gen}) &= \frac{9.48}{1.65 \times 10^{-5}} \text{ W/ m}^3 \\
 &= 5.75 \times 10^5 \text{ W/ m}^3
 \end{aligned}$$

3 RESULTS AND DISCUSSIONS

3.1 Grid Independence Study

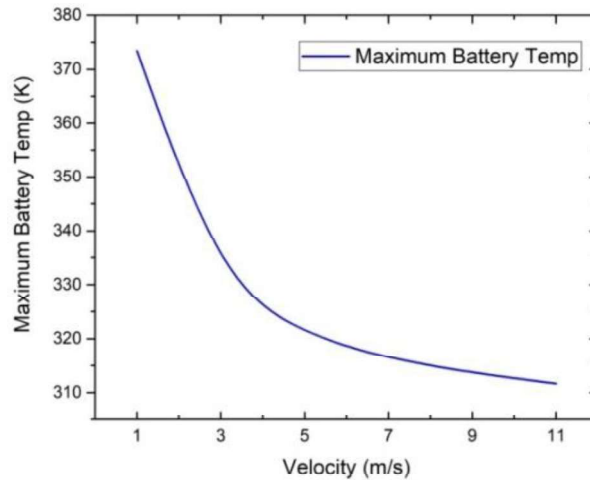
In our study we perform a grid independence study on the battery pack with air velocity inlet 9 m/s at 20°C temperature. We take temperature of battery number 2 and battery number 8 as a variable. In the TABLE 2, it is seen that temperature of the battery will not significantly vary beyond the mesh element number 145054. Therefore grid 5 (145054 element) is taken for simulation study to reduce the time without compromising solution result dependency on grid size.

Table 2: Details of Grid Independence Study

Grid Number	Mesh Elements	Average Temperature Of Battery 2 [K]	Average Temperature Of Battery 8 [K]
Grid 1	57146	319.1167	328.2706
Grid 2	62723	317.9827	325.5877
Grid 3	70754	317.6341	323.3443
Grid 4	131446	315.1203	317.1421
Grid 5	145054	313.3038	316.9864
Grid 6	154917	313.3665	316.6077
Grid 7	160764	313.8555	316.3712

3.2 Effect of Velocity in Temperature

In the figure 2, it is easily seen that battery temperature decreases with gradual increase of the air flow velocity. It signifies that heat exchange process from battery to fluid is increasing. When air flow velocity is below 5 m/s then battery temperature is reducing in a very rapid manner but when air inlet velocity is more than 9 m/s the trend of battery temperature reduction is not that much. It can be explained that at very high velocity of air the temperature difference between battery cell and fluid is reduced.

**Fig. 2.** Temperature vs. inlet velocity

3.3 Pressure Loss and Power Requirement

To supply the air to the battery pack we need a fan or blower which consumes power. It is desirable to know the amount of fan power needed to move the air from inlet to outlet through the battery pack. If fan needed excessive power that means energy efficiency of the vehicle will be less because fan will take power from the battery itself. Excess power requirement means fan size will be large which may not be physically accommodated in vehicle. Power requirement can be estimated from the pressure drop and also the volumetric flow rate of air coming to battery pack.

Fan or pumping (for liquid cooling) power can be estimated by-

$$P = \Delta p \times Q$$

$$= (p_{in} - p_{out}) \times Q$$

Where Δp represents pressure drop in battery pack in Pascal, Q is volumetric flow rate of cooling fluid (air) in m^3/s . Pressure drop is calculated based on total average pressure at the inlet and also outlet of this battery pack. From the figure 3 it is seen that fan power varies with velocity in this study.

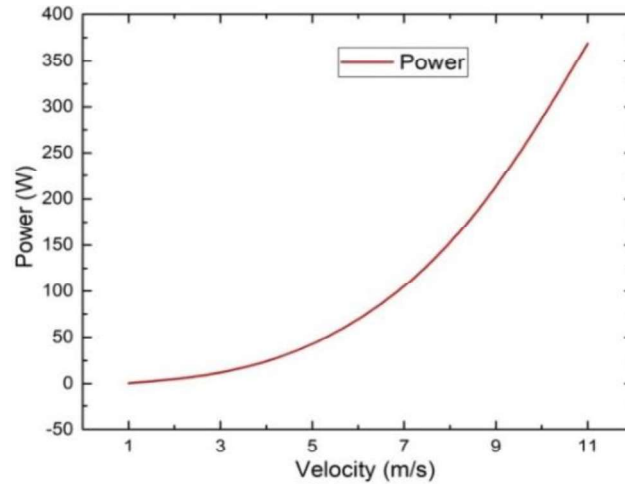


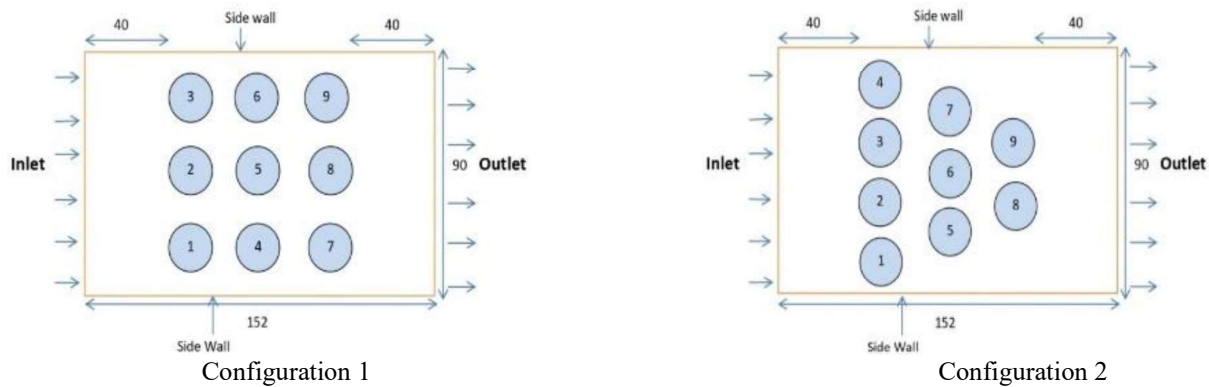
Fig. 3. Power Requirement vs. Velocity

3.4 Different Battery Pack Configurations

Following criteria have been chosen to construct five configurations of battery cell arrangement in a battery pack and also its consequence in battery thermal management system:

- To develop 5 different configurations of a battery pack.
- Distance between inlet and 1st cell row and also distance between last cell row and outlet will be same for all configurations.
- Heat generation of each battery for all configurations will be same.
- To obtain the temperature of the battery cell that is desired for maximum power efficiency.
- To obtain minimum operating cell to cell temperature difference for highest battery life.

Different Battery Pack Configurations are shown in figure 4.



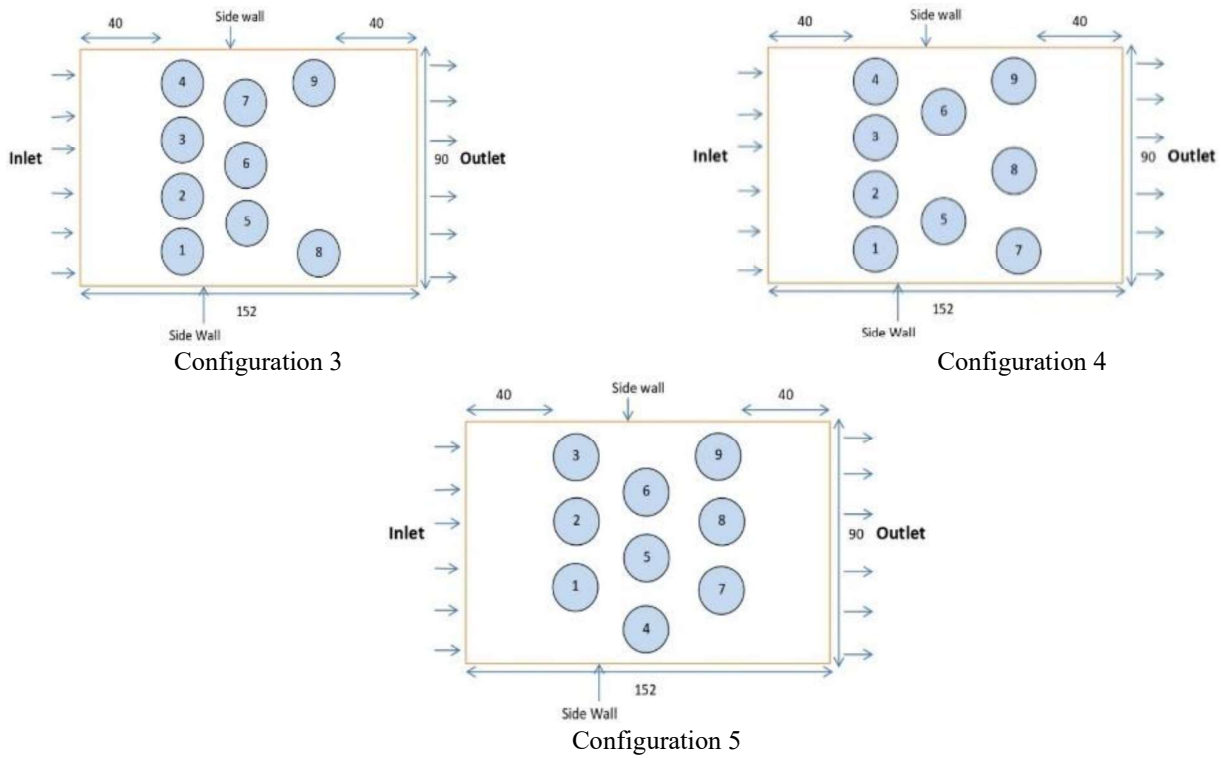


Fig. 4. Different arrangement of battery cell in battery pack

From the simulation result of maximum temperature for different configuration graphical representation is shown in Figure 5.

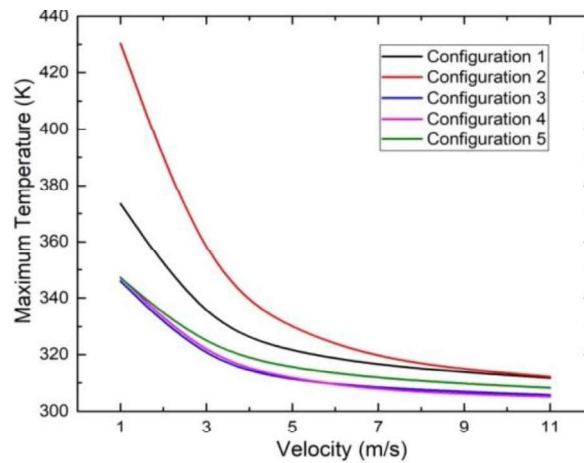


Fig. 5. Temperature vs. velocity (m/s)

According to figure 5, it is clear that when air inlet velocity increases then the temperature decrease trend of all battery pack designs is more all less the same. However, it is easily identified that heat dissipation in battery configuration 2 is less so the maximum temperature of the battery pack of configuration 2 is highest among other configurations. And it is also identified that the maximum battery temperature of configuration 3 and configuration 4 is quite the same.

From the previous study by many researchers, it is found that the battery will perform at its maximum efficiency in the temperature range of 303K -313K. And from this study, it is found that battery temperature will be maintained in this range in all configurations between 9 m/s to 11 m/s velocity inlet of air. However, the above favourable temperature range can be achieved for battery configuration

3 and configuration 4 in between 5 to 7 m/s velocity inlet range. To achieve the same temperature range for primary configuration i.e. configuration 1, air inlet velocity has to maintain at 9 – 11m/s range. The requirement of less velocity means fan power requirement also be less which will decrease the cost of cooling. For a better understanding of the temperature difference for different battery pack configuration temperature and velocity, contours have been plotted and the same as shown in figure 6.

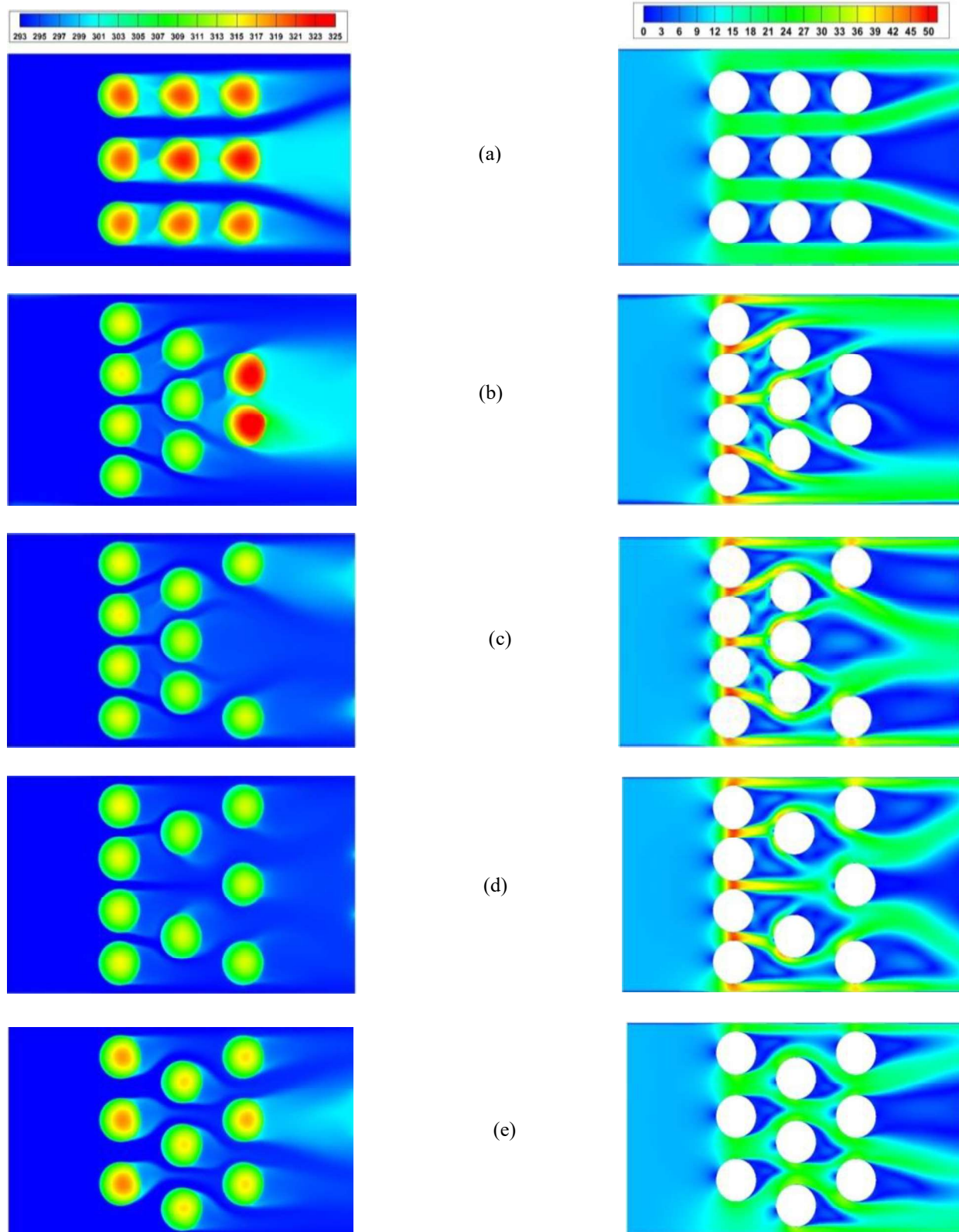


Fig. 6. Temperature and velocity contour of different configuration (a) configuration1, (b) configuration 2, (c) Configuration 3, (d) configuration 4, (e) configuration 5

From the simulation result of fan power requirement for different configuration graphical representation is shown in figure 7.

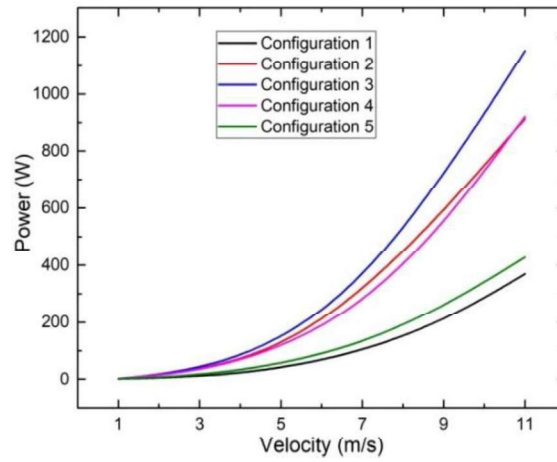


Fig. 7. Power vs. velocity graph

From figure 7, it is clear that when we increase the velocity of the air at the inlet the parametric trend of fan power requirement for all the battery pack arrangements are more or less the same. It is seen that the power requirement for configuration 1 is the least among all other designs. The power requirement for configuration 3 is highest followed by configurations 2, 4, and 5 respectively. From the temperature requirement, it is clear that although the power requirement for configuration 3 is high, this configuration can maintain the temperature of the battery pack at low velocity i.e. 5-7 m/s also. To maintain the same temperature range i.e. 303-313K for configuration 1 inlet velocity will be high i.e. above 9 m/s. In this velocity range, the power requirement will be high compared to configurations 3 and 4. As for 5-7 m/s air inlet, the power requirement for configuration 4 is lesser than configuration 3. So, it can be said that battery configuration 4 is more suitable than configuration 3.

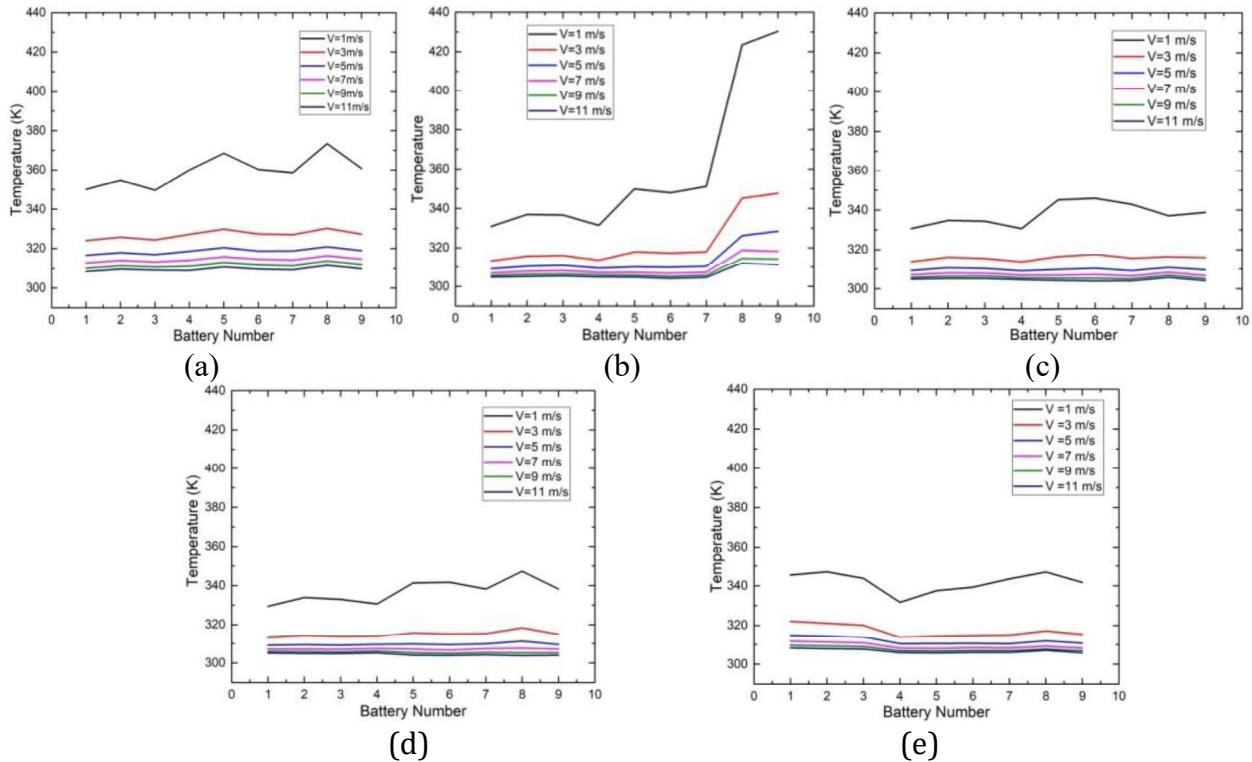


Fig. 8. Cell to cell temperature difference for different configuration; (a) configuration 1, (b) configuration 2, (c) configuration 3, (d) configuration 4, (e) configuration 5

3.4 Cell To Cell Battery Temperature Difference

From the Figure 8, it can be seen that at low velocity of air inlet the battery pack temperature homogeneity is very less. When the velocity of air increases it is clearly seen that in all configuration difference between battery cell temperatures within battery pack is decreasing gradually. From figure 8 it is clear that in higher velocity (9 -11 m/s) also there is more than 5K temperature difference between the cells in configuration 2. It is not a favourable condition for battery health in long run. Battery configuration 3 and battery configuration 4 give us maximum temperature homogeneity. For these two configurations, we can achieve our desired temperature difference i.e. less than 5K in lesser velocity of air inlet (between 5-7 m/s). Between 3 and 4 configuration battery arrangement, battery configuration 4 gives us little more temperature equality at the lower velocity of the air inlet.

4 Conclusions

In this study, five battery pack configurations are designed by arranging the nine 18650 lithium ion battery cells without changing the battery pack size. These five different arrangements with similar structural parameters are simulated to reveal the effect of battery arrangement on the performance of BTMS. The conclusions drawn from this study are:

- (1) With the increase of the air velocity at the inlet the cooling performance i.e. the maximum temperature of the battery cell decreasing at very high rate. However, when the air velocity crosses a certain range (5-7m/s) then the rate of temperature decrease is very less.
- (2) Power requirement also increasing exponentially with increasing velocity of air.
- (3) Configuration 4 can maintain the same favorable temperature range (i.e., 303-313 K) in lesser air velocity (5-7 m/s) than the primary structure i.e. configuration 1 which requires 9 - 11m/s air inlet velocity.
- (4) Configuration 4 has the lowest power consumption up to 30-35% less than configuration 1.
- (5) Temperature difference between the battery cells is also easily achieved in Configuration 4 at 5-7m/s velocity range.

References

1. A. Pesaran, "Battery thermal management in EVs and HEVs: Issues and Solutions", Battery Management, volume 43, pp. 34-49, 2001.
2. G. Kim, A. Pesaran, and R. Spotnitz, "Three-Dimensional Thermal Abuse Model for Lithium-Ion Cells", Journal of Power Sources, volume 170, pp. 476-489, 2007.
3. J. Xu, C. Lan, Y. Qiao and Y. Ma, "Prevent thermal runaway of lithium-ion batteries with mini-Channel cooling", Applied Thermal Engineering, volume 110, pp. 883-890, 2017.
4. T. Hatchard, D. MacNeil, A. Basu, and J. Dahn, "Thermal Model of Cylindrical and Prismatic Lithium-Ion Cells", Journal of The Electrochemical Society, volume 148, pp. A755. 2001.
5. J. Kim, J. Oh, H. Lee, "Review on Lithium-Ion Battery Thermal Management System for Electric Vehicle", Applied Thermal Engineering, volume 149, pp.192- 212, 2018.
6. L. Fan, J.M. Khodadadi, A.A. Pesaran, "A parametric study on thermal Management of an air-cooled lithium-ion battery module for plug-in Hybrid electric vehicles", Journal of Power Sources, volume 238, pp. 301-312, 2013.
7. K. Chen, S. Wang, M. Song, L. Chen, "Configuration optimization of battery pack in parallel air-Cooled battery thermal management system using an optimization strategy", Applied Thermal Engineering, volume 123, pp. 177-186, 2017.
8. K. Chen, Y. Chen, Y. She, M. Song, S. Wang, L. Chen, "Construction of effective symmetrical air-Cooled system for battery thermal management". Applied Thermal Engineering, volume 166. pp.114679, 2019.

9. L. H. Saw, Y. Yonghuang, A.O.T. Andrew, W. T. Chong, S. H. Kuan, M.C. Yew, "Computational Fluid dynamic and thermal analysis of Lithium-ion battery pack with air cooling", *Applied Energy*, volume 177, pp. 83-792, 2016.
10. K. Yu, X. Yang, Y. Cheng, C. Li "Thermal analysis and two-directional air flow thermal management for lithium-ion battery pack", *Journal of Power Sources*, volume 270, pp.193-200, 2014.

Investigation of the printability of living cell with different process parameters of 3D bio-additive manufacturing process (bio-printing)

Ranjit Barua, Ankita Das, Amit Roy Chowdhury, Pallab Datta

1 Introduction

Latest advances in Additive Manufacturing (AM) technology have offered promising opportunities for mechanical and biomedical technologies. The materials are joined layer by layer to construct desired objects [1]. The most broadly used bio-manufacturing and biomedical applications of AM contains the fabrication of exact anatomical models, organ and tissue development of tailored implants and prosthetics, etc. In addition, AM technology can be incorporated into modern manufacturing engineering and medical science. AM methods are being used clinically to advance treatment ideas, and especially in the field of artificial vascular network construction by bio-additive manufacturing or bio-printing process. It utilizes effective resolution deposition of biomaterials, special cell types, and different growth factors. Those simultaneous appearances as bio-inks, which are the inputs of the bio-printing process, correspond to traditional inks concerning the inkjet printing process. Bio-additive manufacturing or bio-printing methods are based on the same principles as traditional additive manufacturing procedures, such as inkjet process, extrusion process, etc. These procedures, though, have faced modifications and variations stated by the character of the base materials, operational environment, and incorporated living cells [2]. Transplantation of Tissue and organ, can expand and advance features of survival, but patients (transplanted) need the long time use of antineoplastic or immunosuppressive medicines. Individual concern and medication are also required for the patient of the prosthesis, for example, knee arthroplasty, which does not recommend an ultimate solution and is now dependent on the chance of rejection, mechanical malfunctions, and anatomical flexibility. The incapability to control refutation inspires the investigation of another to traditional transplantation of tissue and organ. Bio-printing is one capable region, which plans to employ living cells and the basics of additive manufacturing to fabricate important tissues and organs. With the help of computer-controlled bio-printing devices to accurately deposit biocompatible inks, which includes hydrogels [3], living cells [4], and growth factors [5]. Especially in extrusion-based methods, a continuous deposit of bio-ink filaments through an extruder nozzle employing pneumatic pressure or syringe pump. The amount of bio-ink (deposited) can be modified by monitoring the translation of the piston. The fabricated object by extruded bio-ink on the surface plate layer by layers [6]. Printability is one of the most significant factors applied to the quantity of the modification between the fabricated object and the designed model [7-9]. This variance could be affected by the physical immovability and formability of printed objects, and the extrudability of bio-ink [10]. This variance could be affected by the physical immovability and formability of printed objects, and the extrudability of bio-ink [11]. Here, we investigate how the different parameters influence printability during the cell bio-printing process experimentally.

R. Barua^{1*}, A. Das, A. Roy Chowdhury, P. Datta

^{*}CHST, IEST-Shibpur, Howrah

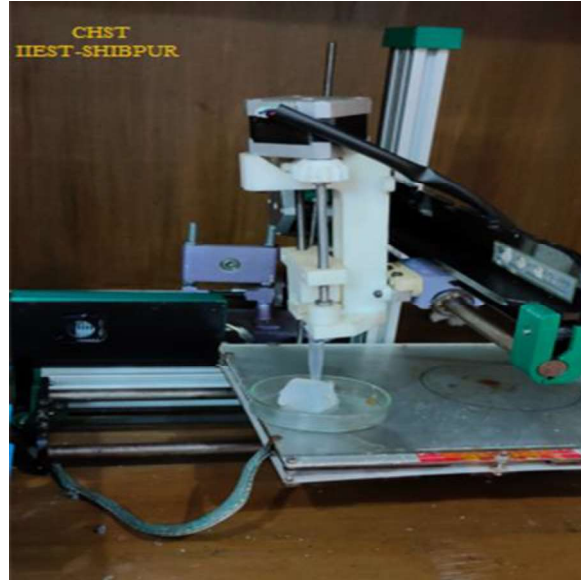


Fig.1 Bio-printer machine (CHST, Heaton Hall, IEST-Shibpur, Howrah).

2 Materials and Methods

To study the cell viability to procedure parameters, a model (quantitative) was established from the experimental data. The process parameters of the cell viability model along with the shear stress model, an analytical result can be found to establish the % of live cells for particular shear stress. Throughout the bio-printing procedure, cells were suspended in the hydrogel solution (alginate), also the shear stress was influenced by the applied pressure. A large number of parameters affect the maximum shear stress, as well as the applied pressure, concentration of hydrogel solution, geometrical size of bio-printer nozzle, etc. In a systematic model for calculating the maximum shear stress, it was assumed that the solution of hydrogel and cells behave as a non-Newtonian fluid. The model associated the process parameters of cell printing for the maximum shear stress. In this investigation, the model was completed to analyze the cell viability as a function of maximum shear stress.

2.1. Bio-ink rheological model

The rheological properties of the extruded bio-ink were considered as a non-Newtonian fluid, which has a shear thinning viscous characteristics for improve printability and good cross-linking phenomenon to make appropriate stiffness for the fabricated material to sustain its geometrical shape after extruding. Therefore, the bio-ink was prepared as a density equivalent to 997.4 kg.m⁻³. As here, it is considered a non-Newtonian fluid, the vicious character was defined by the power-law of viscosity model, which is shown in Equation (1).

$$\eta = k \cdot \dot{\gamma}^{n-1} e^{t_0/t} \quad (1)$$

$$\eta = \frac{\tau}{\dot{\gamma}} \quad (2)$$

Where, η is the viscosity, $\dot{\gamma}$ is the shear rate, τ is the shear stress, t is the temperature, and k is the consistency index [108.92 Pa·s^{0.154}]. It was assumed that the viscosity of the bio-ink not dependent on the temperature.

The shear rate also depends on the nozzle diameter.

$$\gamma = \frac{v}{r} \quad (3)$$

Where, v is the deposition velocity, and r is the radius of the bio-printer nozzle. The flow rate (q) will be:

$$q = v \cdot \pi r^2 \quad (4)$$

And,

$$q = \left(\frac{n}{3n+1}\right) \pi \gamma^{\frac{n-1}{n}} \left(\frac{\partial p / \partial z}{2\eta}\right)^{1/n} r^{\frac{3n+1}{n}} \quad (5)$$

As, the cell-hydrogel bio-ink is basically incompressible non-Newtonian fluid, the dispensing pressure (p), then the flow through bio-printer nozzle can be expressed as:

$$\left(\frac{\partial v}{\partial r_n}\right)^n = \frac{r_n \gamma^{n-1}}{2\eta} \frac{\partial p}{\partial z} \quad (6)$$

The maximum wall shear stress can be find from the equation 2, 3 and 5 will be:

$$\tau_{max} = \left(\frac{n}{3n+1}\right)^n \frac{r}{4} \frac{\partial p}{\partial z} \quad (7)$$

The effects of printing speeds and wall shear stress instigated by the bio-ink flow inside the bio-printer nozzles throughout bio-printing and $\partial p / \partial z$ is the pressure gradient. Shear stresses and shear rates were calculated for altered nozzle models considering 50 psi in place of a pressure boundary situation at the inlet of the nozzle. The static inlet pressure affects dissimilar speeds dependent on the nozzle geometrical design. The boundary condition of the exit point was fixed to be the normal atmospheric pressure.

2.2. Cell culture model

High glucose Dulbecco's modified Eagle medium (DMEM) (ThermoFisher Scientific; USA) was used as the growth medium for culturing human dermal fibroblast cells in the bio-ink for 3 days. The cell line was procured from NCCS Pune, India. The cell viability was determined by employing a live/dead assay (Live/Dead Double Staining Kit (Merck, USA)). For performing the live/dead assay, the staining solution was prepared by mixing 1.0 μ L of 1.0 mM propidium iodide and 1.0 μ L of 2.5 mM Cyto-dye in 1.0 mL of staining buffer. Cell-laden bio-ink constructs were treated with 100 μ L of staining solution and incubated in dark at 37 °C and 5% CO₂ for 15 min. The live/dead fluorescence microscopic images were captured using a fluorescence microscope (Nikon eclipse Ti U, Japan) at 20x magnification. For the green and red emission, the excitation wavelengths were set at 465-495 nm and 512-552 nm which emitted at 515-555 nm and λ_{em} 565-615 nm, respectively.

3 Experimental Setup

The experimental setup of the extruder cell bio-printer is shown in Fig. 1. A high-speed camera (Techobucks, 1080P), which was focused on the nozzle and helped to capture the trajectory of bio-inks (cells + alginate) droplet at a 35000 frame rate and also recorded the process of droplet formation. Throughout the bio-printing (cell) process, initially, the bio-ink was full in the nozzle chamber. Negative pressure was then created by an air compressor balancing the bio-ink gravity, avoiding the outflow of bio-ink from the orifice.

4 Results and Discussion

The results of the nozzle angle (convergence) and the departure diameter showed that the shaft section is vital when improving nozzles design for the bio-printing process to stability the resolution of printing quality and also the cell viability.

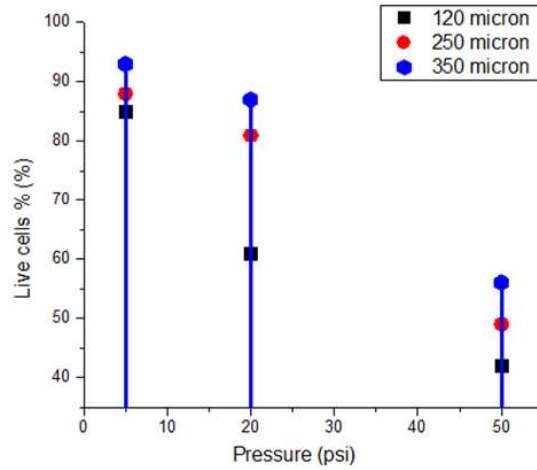


Fig. 2 Live cells (%) of different diameters of nozzle-tip at different dispensing pressure.

If it is required to enhance the printing speed without obstructing cell viability and printing resolution. The minimum convergence angle of the nozzle generates the maximum wall shear stresses. Fig. 2 shows the increase in the percentage of live cells with decreasing the pressure and increasing diameter of nozzle-tip and maximum shear stress was noticed at 588 KPa for 350-micron diameter of the nozzle, and maximum shear stress is noticed at 50 psi (Fig. 3). The printing resolution is improved in minor exit diameter. Correspondingly to bio-inks and many living tissues are essential to maintain viscoelastic properties. For the development of the cell and variation, the stiffness property of the bio-printed material. Typical cells react to applied pressure during the bio-printing process, and they are incapable to adjust the undergo cell injury and later the cell death. Cell injury can be reversible in which usual homeostasis is repaired or irreversible where cells death. This study investigates characterizing the percentage cell viability with injury made by bio-printing. The cell viability reduces as the pressure raises and the diameter of the nozzle decreases. It is observed that the result of pressure is extensively better than the result of the diameter of the nozzle.

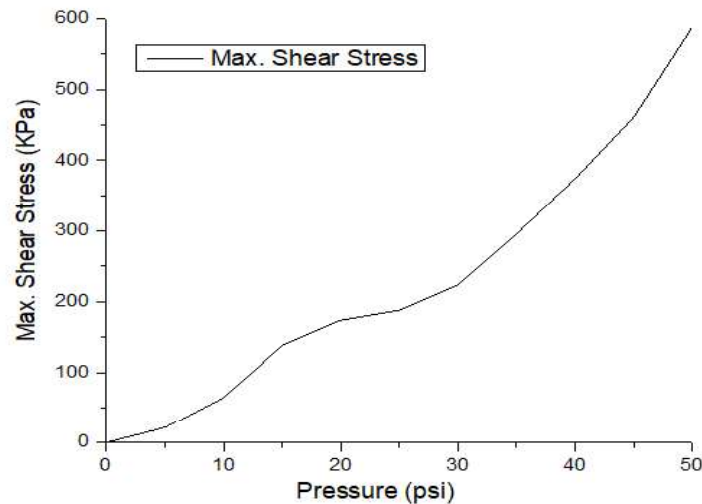


Fig. 3 Maximum shear stress at different releasing pressure for of 350 microns diameter of nozzle-tip.

Which has a significant effect and is related to the normal living biological tissue, specifically for skin tissue and cartilages. Alternatively, bio-inks are usually essential to have low viscosities to flow through bio-printer nozzles. The effects of printing speeds and wall shear stress instigated by the bio-ink flow inside the bio-printer nozzles. The maximum living cell (87%) was noticed at a 350 micron diameter nozzle (Fig. 4).

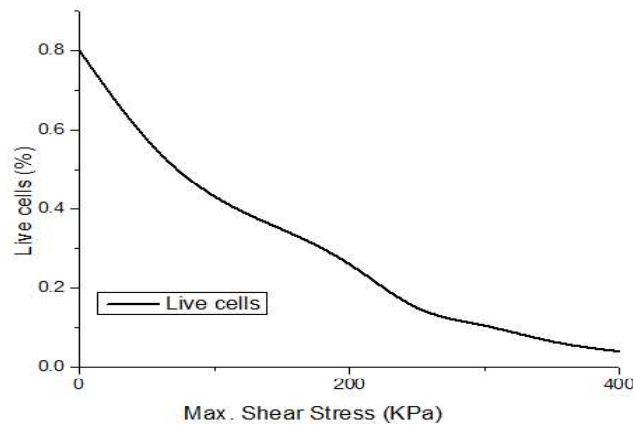


Fig. 4 Effects of the maximum shear stress on % cell viability.

For analysis the effect of viscosity of bio-ink on shear stress, three different viscosities were considered at constant applied voltage 45V. The maximum shear stress was raised with the increases of bio-ink viscosity (Fig. 5).

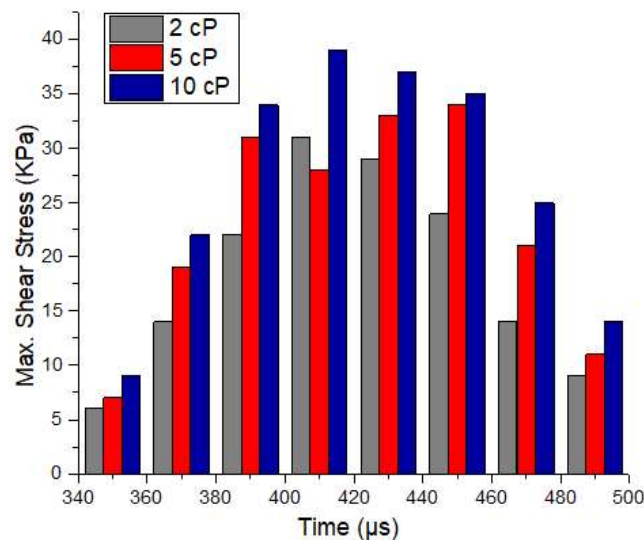


Fig. 5 Effects of the viscosity of bio-ink on shear stress.

For analysis the effect of nozzle diameter on shear stress, three different nozzle diameters were considered during the experimental process. The maximum shear stress was decreased with enhances of the nozzle diameter (Fig. 6).

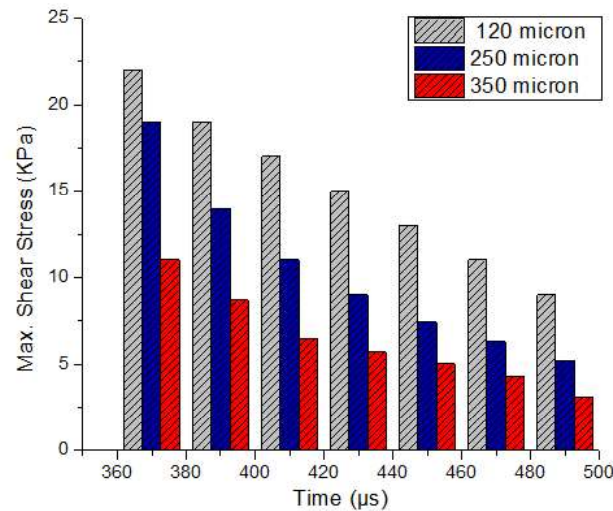


Fig. 6 Effects of the different nozzle diameters of bio-printer on shear stress.

The cell viability was observed to be significantly high as has been shown in Fig. 7 where the green cells represent live whereas the red cells depict death.

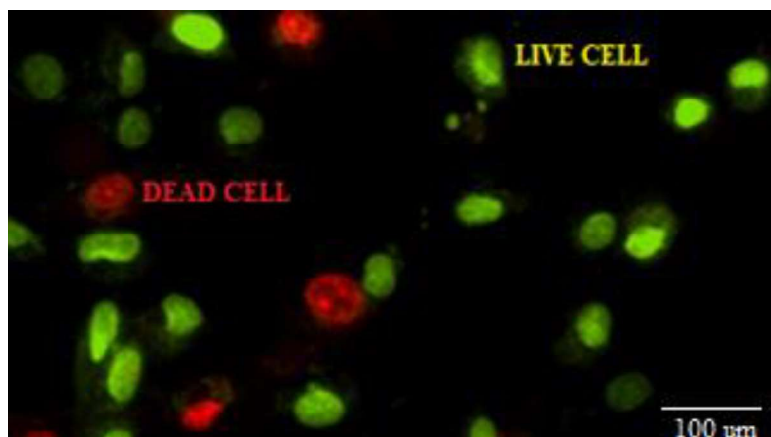


Fig. 7 Microscopic image of live and dead cell.

5 Conclusion

The experimental analysis of bio-ink flow along with two different nozzle models, ideal settings for nozzle geometrical shape and design could be recognized, to improve the suitable printability. This investigational analysis has offered shear stresses minimum values which would promise satisfactory cell viability, allowing for the stationary nozzle inlet (dia. 350 microns) pressure at 21 psi, which has offered an improved qualitative relationship among the different nozzle models. This indicates the geometry of the nozzle is most important to facilitate develop the bio-printing process. However, precise measurable results would require a mesh modification analysis, which is suggested as upcoming work. Cell viability could be improved by varying shear stress, which can be achieved by optimizing the printing parameters by using this 3D bio-printing model. The insights gained here can help guide the rational design of scalable constructs designated for its application in the field of 3D bio-printing and bio-additives manufacturing process.

Acknowledgment

The authors would like to thank IIEST-Shibpur, CHST, Heaton Hall Lab.

References

1. Barua, R., Datta, P., & Chowdhury, A. R. (2022). The Impact of 3D Printing Technology on the COVID-19 Pandemic. In A. Moumtzoglou (Ed.), *Quality of Healthcare in the Aftermath of the COVID-19 Pandemic* (pp. 135-154). IGI Global. <https://doi.org/10.4018/978-1-7998-9198-7.ch008>
2. W. Sun, B. Starly, A. C. Daly, J. A. Burdick, J. Groll, G. Skeldon, W. Shu, Y. Sakai, M. Shinohara, M. Nishikawa, J. Jang, D.-W. Cho, M. Nie, S. Takeuchi, S. Ostrovidov, A. Khademhosseini, R. D. Kamm, V. Mironov, L. Moroni, I. T. Ozbolat, *Biofabrication* 2020, 12, 022002.
3. R. Chang, J. Nam, W. Sun. Effects of dispensing pressure and nozzle diameter on cell survival from solid freeform fabrication-based direct cell writing. *Tissue engineering. Part A*, 14(1), 41–48. 2008.
4. H. Hwangbo, H. Lee, E. J. Jin, J. Lee, Y. Jo, D. Ryu, G. Kim. Bio-printing of aligned GelMa-based cell-laden structure for muscle tissue regeneration. *Bioactive materials*, 8, 57–70. 2021.
5. F. Zhou, Y. Hong, R. Liang, X. Zhang, Y. Liao, D. Jiang, J. Zhang, Z. Sheng, C. Xie, Z. Peng, X. Zhuang, V. Bunpetch, Y. Zou, W. Huang, Q. Zhang, E. V. Alakpa, S. Zhang, H. Ouyang. Rapid printing of bio-inspired 3D tissue constructs for skin regeneration. *Biomaterials*, 258, 120287. R. Nicole, “Title of paper with only first word capitalized,” *J. Name Stand. Abbrev.*, in press. 2020.
6. Barua, R., Datta, S., Datta, P., & Chowdhury, A. R. (2019). Scaffolds and Tissue Engineering Applications by 3D Bio-Printing Process: A New Approach. In K. Kumar, & J. Davim (Ed.), *Design, Development, and Optimization of Bio-Mechatronic Engineering Products* (pp. 78-99). IGI Global. <http://doi:10.4018/978-1-5225-8235-9.ch004>
7. Barua, R., Datta, S., Datta, P., & Roychowdhury, A. (2022). Study and Application of Machine Learning Methods in Modern Additive Manufacturing Processes. In S. Salunkhe, H. Hussein, & J. Davim (Ed.), *Applications of Artificial Intelligence in Additive Manufacturing* (pp. 75-95). IGI Global. <https://doi.org/10.4018/978-1-7998-8516-0.ch004>
8. Barua, R., Datta, S., Roychowdhury, A., & Datta, P. (2019). Importance of 3D Printing Technology in Medical Fields. In K. Kumar, D. Zindani, & J. Davim (Ed.), *Additive Manufacturing Technologies From an Optimization Perspective* (pp. 21-40). IGI Global. <http://doi:10.4018/978-1-5225-9167-2.ch002>
9. F. Zhao, J. Cheng, M. Sun, H. Yu, N. Wu, Z. Li, J. Zhang, Q. Li, P. Yang, Q. Liu, X. Hu, Y. Ao. Digestion degree is a key factor to regulate the printability of pure tendon decellularized extracellular matrix bio-ink in extrusion-based 3D cell printing. *Biofabrication*, 12(4), 045011. 2020.
10. P. Shi, A. Laude, W. Y. Yeong. Investigation of cell viability and morphology in 3D bio-printed alginate constructs with tunable stiffness. *Journal of biomedical materials research. Part A*, 105(4), 1009–1018. 2017.
11. H. K. Baca, E. C. Carnes, C. E. Ashley, D. M. Lopez, C. Douthit, S. Karlin, C. J. Brinker. Cell-directed-assembly: directing the formation of nano/bio interfaces and architectures with living cells. *Biochimica et biophysica acta*, 1810(3), 259–267. 2011.

Numerical study of electroosmotic flow over a hydrophobic wavy plate

Sumit Kumar Mehta, Sukumar Pati

1 Introduction

The electroosmotic flow (EOF) has several engineering applications in chemical and medical industries [1, 2]. The EOF is generated by the application of an external electric field together with the presence of an electric-double-layer (EDL) for an electrically conductive fluid [3-6]. Further, the use of the wavy or corrugated surfaces is helpful for heat transfer enhancement [7-12] and efficient micromixing [13-15].

In the past few decades, the EOF over the larger surface has been investigated by a number of researchers [1, 2, 16, 17]. Chang and Wang [1] studied the rotating EOF over a larger flat surface by varying the angular speed of the rotation. It is found that the vertical locations where axial and transverse flow velocities attain maxima decrease with the increase in angular speed. Erickson and Li [17] studied EOF over the heterogeneous charged surface. They concluded that the augmentation in the degree of heterogeneity enhances the distortion of the flow, and this effect is mild in the core region. Recently, Silkina et al. [2] investigated electroosmotic flow over the permeable porous film. They found that the augmentation in absorption capacity in porous film enhances the strength of EOF actuation.

Numerous research works have been conducted to investigate the effect of wavy surfaces on EOF [18-21]. Cho et al. [22] studied the flow and heat transfer characteristics for combined EOF and pressure-driven flow through a complex wavy channel. They found that the maxima of the Nusselt number augment with the increase in wavy amplitude. Banerjee and Nayak [15] investigated electroosmotic mixing for the flow of non-Newtonian power-law fluid through a wavy micromixer. They found that the increase in wavy surface amplitude augments the mixing efficiency. Recently, Mehta et al. [14] explored the electroosmotic mixing of Carreau fluid for flow through the wavy micromixer considering the surface charge heterogeneity and the effect of the finite size of ion.

Further, the surface of the microfluidic system has been coated with the polymeric material intentionally to achieve greater hydrophobicity; thus advection strength enhances [23]. Zhao [24] conducted a numerical simulation to study EOF over the patterned superhydrophobic surface and found that the electroosmotic actuation augments when the interface of liquid-gas is charged. Also, the superhydrophobic nano-grooved structure reduces the fluid friction.

From the extensive literature review, it appears that no one has investigated the effect of interfacial slip on electroosmotic flow over a larger wavy plate, which is the objective of the present study.

2 Theoretical Formulation

We investigate the EOF over a large hydrophobic wavy plate numerically. The physical domain is depicted in Fig. 1. The profile of the wavy surface is taken as: $S(X) = A \sin(2\pi X/L)$. Here, A and L are the amplitude and wavelength of the wavy surface, respectively. The flow is steady, incompressible, and two-dimensional and the fluid is Newtonian. The point charge assumption of ions is invoked. The Joule heating effect is neglected [14].

S.K. Mehta, S. Pati

Department of Mechanical Engineering, National Institute of Technology Silchar, Silchar, Assam-788010, India

Using these assumptions, the dimensionless governing transport equations can be written as follows [14]:

$$\nabla^2 \phi = 0 \quad (1)$$

$$\nabla^2 \psi = \kappa^2 \sinh(\psi) \quad (2)$$

$$\nabla \cdot \mathbf{u} = 0 \quad (3)$$

$$\text{Re}(\mathbf{u} \cdot \nabla) \mathbf{u} = -\nabla p + \nabla^2 \mathbf{u} + [\kappa^2 \sinh(\psi)](\nabla(\phi + (\psi/\Omega))) \quad (4)$$

Here, Eq. (1) to (4) are the Laplace equation for the external electric field, the Poisson-Boltzmann equation for EDL potential field, continuity and momentum equations for the flow field, respectively.

The imposed boundary conditions are as follows:

at the wavy surface: $\mathbf{n} \cdot \nabla \phi = 0$, $\psi = \zeta$, $\mathbf{u} = \beta(\tau_{n,t})$;

at the left and right boundary: $\phi_L = 0$, $\phi_R = \phi_o$, $\mathbf{n} \cdot \nabla \psi = 0$, $\mathbf{u}_L = \mathbf{u}_R$, $p_L = p_R$ (periodic condition);

at the upper part $\mathbf{n} \cdot \nabla \phi = 0$, $\mathbf{n} \cdot \nabla \psi = 0$, $\mathbf{n} \cdot (-p\mathbf{I} + \nabla \mathbf{u}) = 0$ (open boundary).

Here, $\phi(=\phi'/\phi'_{ref})$, $\psi(=\psi/\psi'_{ref})$, $\mathbf{u}(=\mathbf{u}/u'_{ref}=u\hat{i}+v\hat{j})$, $p(p'L/\mu u'_{ref})$, and $\text{Re}=(\rho u'_{ref}L/\mu)$ are dimensionless external potential, electric double layer (EDL) potential, velocity vector, pressure, and Reynolds number respectively; ρ and μ are the fluid density and viscosity, respectively; $u'_{ref}(=E_\infty \varepsilon \psi'_{ref}/\mu)$ and $\psi'_{ref}(=k_B T_o/ze)$ are reference velocity and EDL potential, respectively [3, 4];

$\nabla \equiv (\hat{i}\partial/\partial x, \hat{j}\partial/\partial y)$; $x=X/L$; $y=Y/L$; $\Omega=(\phi'_{ref}/\psi'_{ref})$, $\beta=\beta'/L$, $\kappa=L/\lambda_D$; $\lambda_D=(2n_o z^2 e^2/\varepsilon k_B T_o)^{-0.5}$;

n_o , k_B , T_o , ε , z and e are the bulk ionic concentration, Boltzmann constant, reference temperature, valency of ions, and charge on an electron, respectively [3-5].

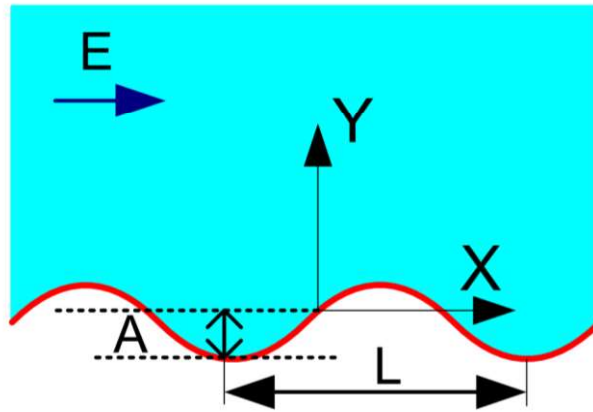


Fig. 1. Physical domain

3 Numerical Methodology and Validation

The governing equations have been solved numerically using a finite element method based numerical solver. We also perform the grid independence test and select the mesh having number of elements equal to 47140 such that there is less than 0.01% relative difference in maximum transverse velocity with respect to the extremely fine mesh. The numerically computed dimensionless velocity field

matches well with the analytical solution of $u(y) = 1 - (\zeta \exp(-\kappa y))$ [16]. at $\zeta = 1$, $\kappa = 5$, and with the limiting case $\alpha (= A/L) = 0$. The validation is depicted in Fig. 2 for EOF over a flat surface.

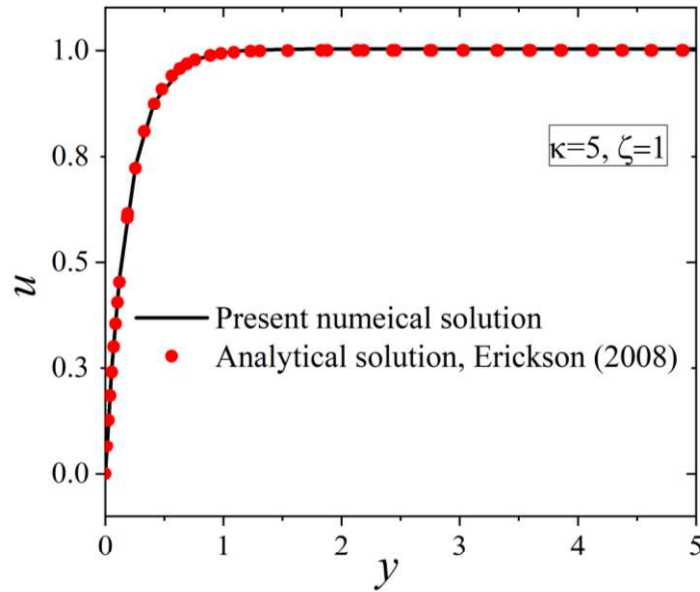


Fig. 2. Comparison of the present numerical solution with the analytical solution obtained by Erickson [16] .at $\zeta = 1$, $\kappa = 5$, and with the limiting case $\alpha (= A/L) = 0$.

4 Results and Discussion

The flow characteristics have been investigated for an electroosmotic flow over a large hydrophobic wavy plate by varying the dimensionless amplitude ($\alpha (= A/L)$) and dimensionless slip length (β) in the range of $0.0125 \leq \alpha \leq 0.5$ and $0 \leq \beta \leq 0.1$, respectively [3-5, 14, 25, 26].

The dimensionless electric field and velocity vectors are shown in Fig. 3. It is observed that the denser electric field line density at the convex surface causes the higher intensity of the electric field. In comparison, an opposite effect is observed at the concave wavy surface. Further, it is noted that the higher electric field strength at the convex surface causes the larger intensity of the velocity vector, which is attributed to the augmentation in the electroosmotic actuation strength. Although close to the wavy surface, there exists transverse velocity, it is seen that far from the wavy wall, the transverse velocity component is zero and causes a unidirectional flow.

The variation of axial flow velocity (u) is depicted in Fig. 4(a) at section AB (See Fig. 3). It is observed that the value of u decreases with α . It is attributed to the decrease in the electroosmotic flow strength with the electric field intensity near the concave surface. Further, the transverse flow velocity (v) decreases with α near the wall region, and enhances with α far from the wall, and approaches to zero in the core, as depicted in Fig. 4(b). These observations can be explained as follows. The decrease in electric field intensity with α near the concave wall decreases the value of v . While, at the intermediate region, the influence of the increase in velocity vector strength with α at the convex surface (See Fig. 3) augments the value of v with α . Moreover, the negligible effect of waviness in the core causes zero value of v .

The variation of core axial velocity (u_∞) with β is depicted in Fig. 5 for different values of α . It is observed that the increase in the value of β augments the value of u_∞ . The augmentation in the hydrophobicity with β , decreases the flow resistance near the wall. Moreover, the value of u_∞ decreases with α due to the decrease in axial flow velocity (See Fig. 4(a)).

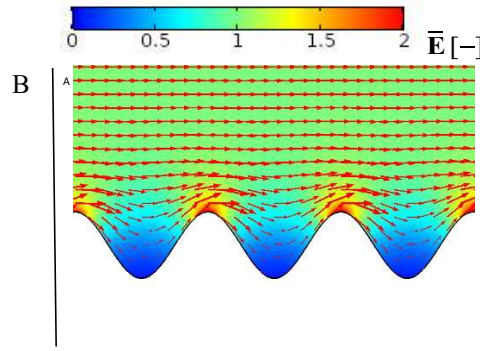


Fig. 3. Velocity vector (arrow size in the bulk region represents, $u=2.97$) and dimensionless external electric field contour at $\alpha = 0.25$, $\kappa = 20$ and $\beta = 0.1$.

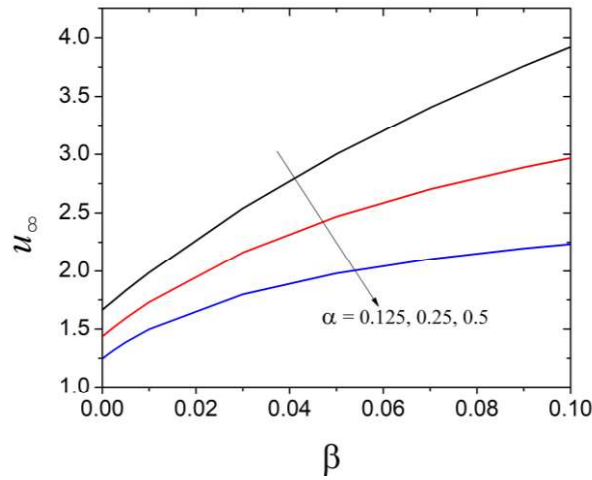


Fig. 5. Variation of bulk axial flow velocity (u_{∞}) with β for the different values of amplitudes at $\kappa = 20$.

The variation of maximum transverse flow velocity (v_{Max}) with β is depicted in Fig. 6 for different values of α . It is observed that the increase in β also augments the value of v_{Max} due to the decrease in the flow resistance. Moreover, v_{Max} augments with α . It is because of the increase in velocity vector magnitude with α at the convex surface due to the increase in electric field strength. It is noted that the percentage increases in v_{Max} are obtained as 36.39% and 11.62% for change in α from 0.125 to 0.5 at $\beta = 0$ and 0.1, respectively.

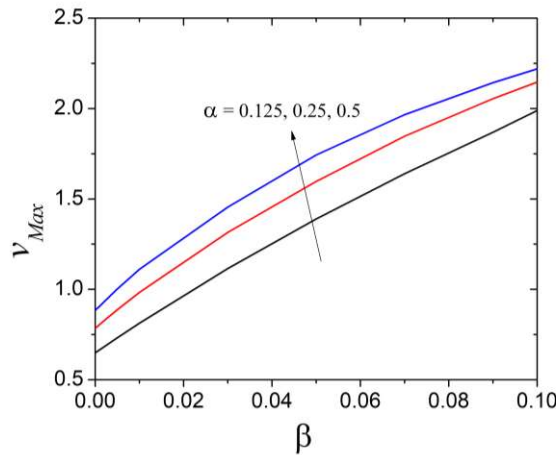


Fig. 6. Variation of maximum transverse flow velocity with β for different values of amplitude at $\kappa = 20$.

5 Conclusions

In the present study, we investigate dynamics for an electroosmotic flow over a large hydrophobic wavy plate by varying the dimensionless amplitude (α) and dimensionless slip length (β) in the range of $0.0125 \leq \alpha \leq 0.5$ and $0 \leq \beta \leq 0.1$, respectively. The important findings from the present work are summarized as follows:

- The flow is induced in the transverse direction by the wavy surface, and the velocity is higher at the convex surface. Moreover, the axial flow velocity decreases with an increase in amplitude.
- The core axial flow velocity (u_x) increases with β and decreases with α .
- An increase in β and α augments the value of maximum transverse flow velocity (v_{Max}). The percentage increases in v_{Max} are obtained as 36.39% and 11.62% for change in α from 0.125 to 0.5 at $\beta=0$ and 0.1, respectively.

References

1. Chang, C., Wang, C. (2011) Rotating electro-osmotic flow over a plate or between two plates. *Physical Review E*, 84, 056320.
2. Silkina, E.F., Bag, N., Vinogradova, O.I. (2020). Electro-osmotic properties of porous permeable films. *Physical Review fluids*, 5, 123701.
3. Pabi, S., Mehta, S.K., Pati, S. (2021). Analysis of thermal transport and entropy generation characteristics for electroosmotic flow through a hydrophobic microchannel considering viscoelectric effect. *International Communications in Heat and Mass Transfer*, 127, 105519.
4. Pabi, S., Mehta, S.K., Pati, S. (2021). Effect of slip on vortex formation near two-part cylinder with same sign zeta potential in a plane microchannel. *Techno-Societal 2020*. In: Pawar PM, Balasubramaniam R, Ronge BP, Salunkhe SB, Vibhute AS, Melinamath B, editors. Cham: Springer International Publishing, 1013–22.
5. Sujith, T., Mehta, S.K., Pati, S. (2021). *Effect of non-uniform heating on electroosmotic flow through microchannel*. *Recent Advances in Mechanical Engineering*. In: Pandey KM, Misra RD, Patowari PK, Dixit US, editors. Singapore: Springer Singapore, 499–508.
6. Mondal, B., Mehta, S.K., Patowari, P.K., Pati, S. (2021). Numerical analysis of electroosmotic mixing in a heterogeneous charged micromixer with obstacles. *Chemical Engineering and Processing - Process Intensification*, 168, 108585.
7. Pati, S., Mehta, S.K., Borah, A. (2017). Numerical investigation of thermo-hydraulic transport characteristics in wavy channels: Comparison between raccoon and serpentine channels. *International Communications in Heat and Mass Transfer*, 88, 171–176.
8. Mehta, S.K., Pati, S. (2019). Analysis of thermo-hydraulic performance and entropy generation characteristics for laminar flow through triangular corrugated channel. *Journal of Thermal Analysis and Calorimetry*, 136, 49–62.
9. Mehta, S.K., Pati, S. (2020). Numerical study of thermo-hydraulic characteristics for forced convective flow through wavy channel at different Prandtl numbers. *Journal of Thermal Analysis and Calorimetry*, 141, 2429–2451.
10. Mehta, S.K., Pati, S. (2021). Thermo-hydraulic and entropy generation analysis for magnetohydrodynamic pressure driven flow of nanofluid through an asymmetric wavy channel. *International Journal of Numerical Methods for Heat & Fluid Flow*, 31, 1190–213.
11. Mehta, S.K., Pati, S., Ahmed, S., Bhattacharyya, P., Bordoloi, J.J. (2021) Analysis of thermo-hydraulic and entropy generation characteristics for flow through ribbed-wavy channel. *International Journal of Numerical Methods for Heat & Fluid Flow*. <https://doi.org/10.1108/HFF-01-2021-0056>
12. Mehta, S.K., Pati, S. (2018). Effect on non-uniform heating on heat transfer characteristics in wavy channel. In: *Fifth international conference on computational methods for thermal problems ThermaComp 2018*, Indian Institute of Science, Bangalore, Fifth Edition, 498–501.

13. Mondal, B., Mehta, S.K., Patowari, P.K., Pati, S. (2019). Numerical study of mixing in wavy micromixers: comparison between raccoon and serpentine mixer. *Chemical Engineering and Processing - Process Intensification*, 136, 44–61.
14. Mehta, S.K., Pati, S., Mondal, P.K. (2021). Numerical study of the vortex-induced electroosmotic mixing of non-Newtonian biofluids in a nonuniformly charged wavy microchannel: Effect of finite ion size. *Electrophoresis*, 42, 2498-2510
15. Banerjee, A., Nayak, A.K. (2019). Influence of varying zeta potential on non-Newtonian flow mixing in a wavy patterned microchannel. *Journal of Non-Newtonian Fluid Mechanics*, 269, 17–27.
16. Erickson, D. (2008). Electroosmotic flow (DC). Li D. (eds) *Encyclopedia of Microfluidics and Nanofluidics*. Springer, Boston. https://doi.org/10.1007/978-0-387-48998-8_446
17. Erickson, D., Li, D. (2003). Three-dimensional structure of electroosmotic flow over heterogeneous surfaces. *The Journal of Physical Chemistry B*, 107, 12212–12220.
18. Xia, Z., Mei, R., Sheplak, M., Fan, Z.H. (2009). Electroosmotically driven creeping flows in a wavy microchannel. *Microfluidics and Nanofluidics*, 6, 37–52.
19. Shu, Y.C., Chang, C.C., Chen, Y.S., Wang, C.Y. (2010). Electro-osmotic flow in a wavy microchannel: Coherence between the electric potential and the wall shape function. *Physics of Fluids*, 22, 082001.
20. Yoshida, H., Kinjo, T., Washizu, H. (2016). Analysis of electro-osmotic flow in a microchannel with undulated surfaces. *Computers & Fluids*, 124, 237–245.
21. Chen, C.K., Cho, C.C. (2007) Electrokinetically-driven flow mixing in microchannels with wavy surface. *Journal of Colloid and Interface Science*, 312, 470–80.
22. Cho, C.C., Chen, C.L., Chen, C.K. (2012) Characteristics of combined electroosmotic flow and pressure-driven flow in microchannels with complex-wavy surfaces. *International Journal of Thermal Sciences*, 61, 94–105.
23. Soong, C.Y., Hwang, P.W., Wang, J.C. (2010). Analysis of pressure-driven electrokinetic flows in hydrophobic microchannels with slip-dependent zeta potential. *Microfluidics and Nanofluidics*, 9, 211–223.
24. Zhao, H. (2010). Electro-osmotic flow over a charged superhydrophobic surface. *Physical Review E* 81(6), 066314-1-066314-9.
25. Vasista, K. N., Mehta, S. K., Pati, S. (2021). Numerical assessment of hydrodynamic and mixing characteristics for mixed electroosmotic and pressure-driven flow through a wavy microchannel with patchwise surface heterogeneity, *Proceedings of the Institution of Mechanical Engineers, Part E: Journal of Process Mechanical Engineering*. <https://doi.org/10.1177/09544089211051640>.
26. Vasista, K. N., Mehta, S. K. Pati, S., Sarkar S. (2021). Electroosmotic flow of viscoelastic fluid through a microchannel with slip-dependent zeta potential. *Physics of Fluids*, 33, 123110.

Characterization of some Non-edible Vegetable Oils Lubricants by their Thermal Properties

S.C.Sharathchandra, Dr.R.Harishkumar, Dr.S.Manu, Dr.Basavaraj Ganiger

1 Introduction

All over the world, petroleum based reserves will be depleted in few decades which result in frequent price hike and bad impacts on environment; pollution, global warming, acid rain etc. Further the lubricants are very essential control wear and tear of internal combustion engine components and to increase life and mileage of automobiles. So the researchers have been putting more effort to develop an emission free, non toxic and biodegradable eco friendly lubricants. Navdeep Sharma Dugala et al., [1] have studied the kinematic viscosity, flash point, fire point, pour point, cloud and some other thermal properties of esterified Mahua and Jatropha biodiesel oils. The best blend of above biodiesels were noticed through above mentioned characteristics. It has concluded that the kinematic viscosity and density values of blends B10, B20, B30 and B40 found better than their purest forms. Further B40 blend showed upper-end limit of desirable values and B50 showed lower-end limit of desirable property values. Leonardo Israel et al., [2] have assessed lubricity and oxidation of Jatropha oil subjected to thermal ageing. It has reported that thermal aging noticeably oxidises the Jatropha oil and also increases the viscosity hence coefficient of friction rises considerably. Z. M. Zulfattah et al., [3] have experimentally studied the effect of a bio lubricant on engine emission and spark plug fouling. It was observed that bio lubricant blends burn cleaner compared to mineral oil lubricant thus no unburnt lubricant and lesser fouling of spark plug were occurred. Arianti N. et al., [4] have made a review on production of bio lubricants from vegetable oils through transesterification process and their limitations. It has comprehensively noticed that the properties of bio-lubricants extracted from vegetables easily get damaged hence there is a need extensive research to enhance the life of bio-lubricants. M. A. Kalam et al., [5] have studied the thermal stability and lubricating performance of olive oil employed to a heavy duty diesel engine. In the experimentation, olive oil performance parameters were compared and with commercial lube oil and analyzed. It is reported that Olive oil because of its high percentage of oleic acid content offers an excellent oxidation stability. Further Olive oil showed ample kinematic viscosity which made its usage for boundary lubrication. The olive oil possess thermal stability even at 390 °C. It is also reported that Olive oil exhibited a lower friction coefficient and worn scar surface area than that with commercial lube oil. S. Arumugam et al., [6] have investigated on a biofuelled engine optimum performance parameters with the bio-lubricant. The rapeseed oil was used for bio-lubricant and biofuel. The Taguchi-grey relational analysis was followed to assess the optimal parametric combination to observe better engine performance along with minimal emissions. The compression ratio, lubricant type and engine load were subjected to optimization using L18 orthogonal array. It has concluded that an improvement in engine performance characteristics was noticed with the usage of using rapeseed oil lubricant and rapeseed biodiesel combination. Masoud Dehghani et al., [7] have developed neural network model to estimate the effect of different bio lubricants onto the emissions and performance of a two stroke spark ignition engine. The relationship between input parameters and engine performance and emissions are estimated using the artificial neural network (ANN) model. The lubricant type, engine speed were the inputs to the ANN model. The brake power, BSFC and CO, CO₂, UBHC, O₂ and NO_x emissions were the output of the model. K. S. V. Krishna Reddy et al., [8] have experimentally studied the brake thermal efficiency, brake specific fuel consumption and mechanical efficiency of an engine using commercial SAE20W40 and blended palm oil as lubricants. It is reported that there were no such variations in engine performance and emissions with the usage of SAE20W40 and palm oil. However 25% palm oil blend resulted the

lower NO_x emission levels than that with SAE20W40 oil. S. Arumugam and Siram [9] have experimentally assessed the friction and wear behavior of diesel engine cylinder liner–piston ring combination under presence of rapeseed oil bio-lubricant and commercial SAE20W40 lubricant with the aid of reciprocating type tribometer test rig. It has concluded that the rapeseed oil bio-lubricant exhibited better friction coefficient and good oxidative stability. S. Bekal and N. R. Bhat [10] have studied the performance characteristics and emissions of diesel engines lubricated by blends of Pongamia oil and neat mineral oil. The smoke, NO_x, CO, HC, EGT, BSEC and friction power were noticed with different blends of pongamia lubricant as well as with neat mineral oil lubricant and results were compared. Gopalasamy Sriram and Abhishek Kumar [11] have studied the diesel engine emissions when lubricated by blended Fish oil methyl ester and mineral oil. It has concluded that the 20% blended Fish oil methyl ester lubrication showed better emission levels compared to all other lubricants used. The study of non edible vegetable oils thermal properties is of utmost importance in assessing their suitability as lubricating oils for internal combustion engines. So in the current research work three non edible oils extracted from Honge, Neem and Mahua seeds were taken and esterified. The thermal properties of non esterified and esterified lubricating oils blends were assessed and the compared. Finally a comparison has also done with commercial SAE15W40 synthetic oil.

2 Experimentation

2.1 Measurement of Specific gravity

The specific gravity of all the lubricating oils and oil blends were measured using the instrument called hydrometer. Hydrometer consists of glass and a cylindrical stem filled with mercury to make it float upright and contains paper scale inside the stem to display the specific gravity directly. The Specific gravity of all the different oils and their blends were calculated by following ASTM D5355 procedure. It is also experienced that higher the aromatic compounds in the oils result higher specific gravity while higher the saturated compounds result lower specific gravity. Further used engine oils specific gravity found higher because of the presence of more quantity of dissolved solids.

2.2 Measurement of Kinematic Viscosity

The Saybolts viscometer instrument was used to calculate the kinematic viscosity of the lubricating oils. The Kinematic viscosity of lubricating oils were calculated as per ASTM D2161 procedure. The oil cup was filled with 60 ml lubricating oil and the bowl surrounding the oil cup was filled with normal water. The coil type water heater heats the water and thus the oil to the temperature of 450C. The bottom screw of the oil cup was lifted to allow the oil to flow down and collected it into a measuring jar of 60ml. The time taken for the blow down of the hot oil present in cup into measuring jar was noted with the help of digital stop watch. The kinematic viscosity was calculated using the empirical relation; Kinematic viscosity = $[0.22 \cdot t - (180 / t)]$ mm²/sec.

3 Results and Discussions

3.1 Specific Gravity of Non Esterified Oil Blends

Figure 1 shows the variations observed in specific gravity with non esterified oil blends. It is calculated that specific gravity of non-esterified neat Neem oil, Honge oil and Mahua oil were 0.925, 0.930 and 0.9 respectively. It can also be observed that as vegetable oil percentage in the blend increases, there is an increase in the specific gravity. This is attributed to presence of more quantity of mono alkyl esters and fatty acids of vegetable oils. Further free fatty acids (FFA) of Neem oil Mahua (FFA 3.0)

Oil and Honge oil are found 3.0, 7.0 and 5.0 tespectively hence the specific gravity of Neem oil found lower than Honge oil and Mahua oil.

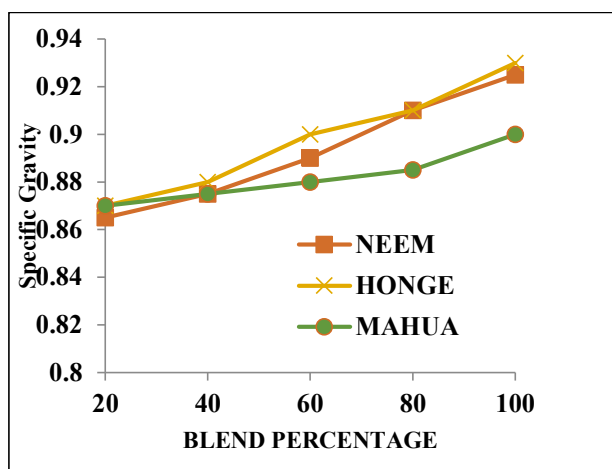


Fig. 1. Variation of Specific gravity with non esterified oil blends.

3.2 Specific Gravity of Esterified Oil Blends

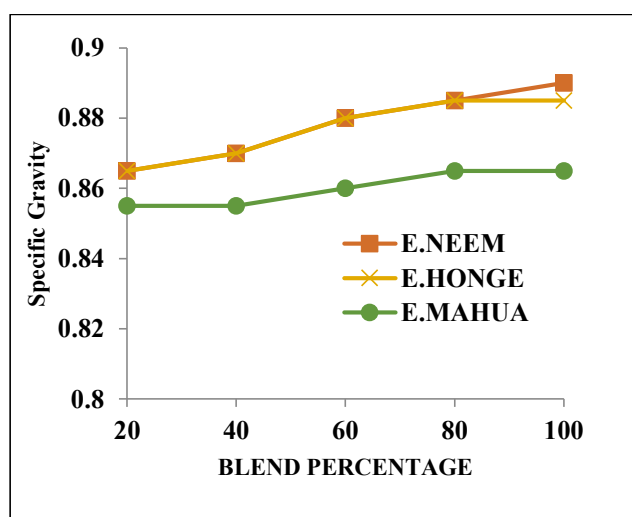


Fig. 2 Variation of Specific gravity with esterified oil blends.

Figure 2 shows the variations observed in specific gravity with different percentage esterified oil blends. It is calculated that specific gravity of esterified neat Neem oil, Honge oil and Mahua oil were 0.89, 0.885 and 0.865 respectively. It can be observed that as vegetable oil percentage in the blend increases, there is an increase in the specific gravity. This is due to presence of more quantity of mono alkyl esters and fatty acids of vegetable oils. Further esterified Honge oil, Neem oil showed higher specific gravity compared to esterified Mahua Oil. This is because of higher molecular weight of triglycerides and more quantity fatty acids presence in esterified Neem and Honge comparatively.

3.3 Comparison of Specific Gravity of Non Esterified and Esterified Oil Blends.

Figure 3 shows the comparison among variations observed in specific gravity with non esterified and esterified oil blends. It can be observed that the esterified Mahua and Honge oils showed least specific gravity among the tested oils.

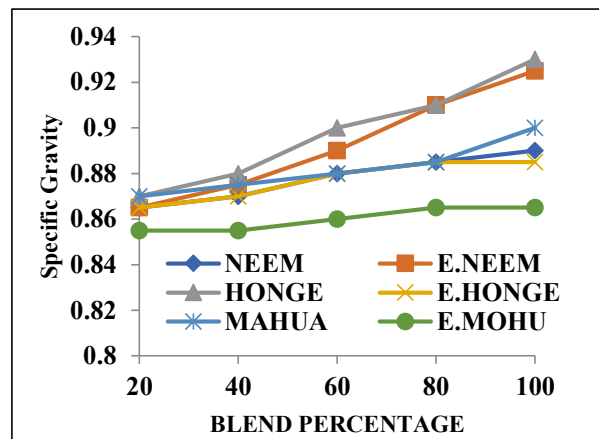


Fig 3. Variation of Specific gravity with non esterified & esterified oil blends.

3.5 Comparison of Specific Gravity of Non Esterified and Base Oil (SAE15W40)

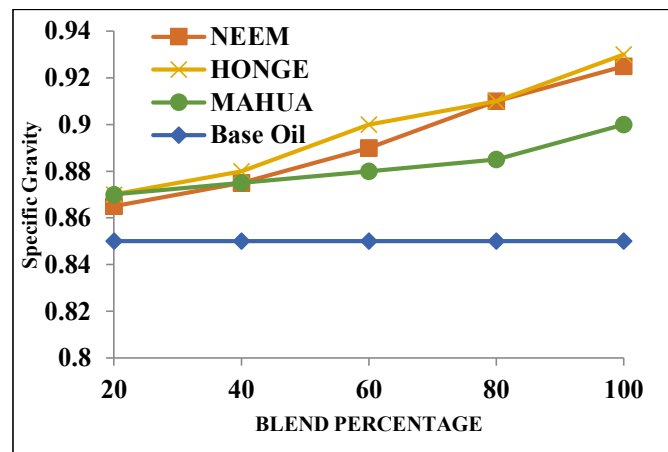


Fig. 4. Comparison of Specific gravity with non esterified oil blends and base oil.

Figure 4 shows the comparisons among specific gravity of non esterified oil blends and base synthetic oil SAE15W40. It can be observed that after the synthetic oil specific gravity rank, Mahua, Neem and Honge find the preferential rank.

3.5 Comparison of effect of esterified oil with base oil on specific gravity

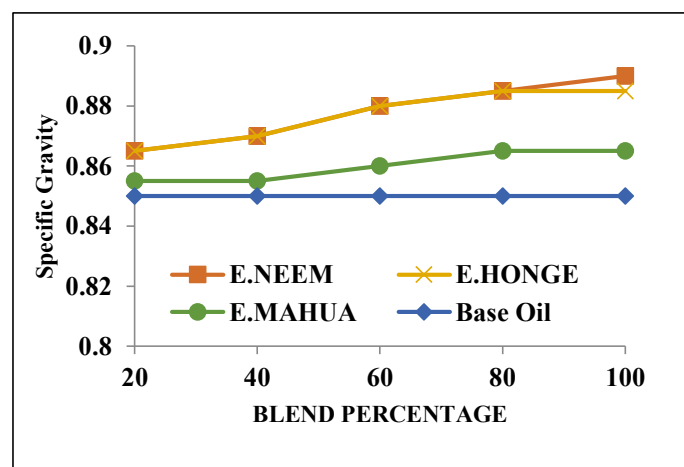


Fig. 5. Comparison of Specific gravity of Esterified oil blends with Base oil.

Figure 5 shows the comparisons among specific gravity of esterified oil blends and base synthetic oil SAE15W40. It can be observed that after the synthetic oil specific gravity rank, Mahua, Neem and Honge find the preferential rank.

3.6 Kinematic Viscosity of Non Esterified Oil Blends

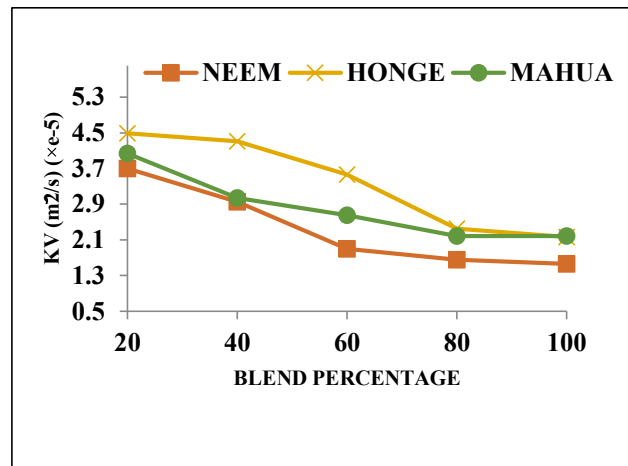


Fig. 6. Variation of Kinematic viscosity with non esterified oil blends.

Figure 6 shows the variation of kinematic viscosity with non esterified oil blends. It is calculated that kinematic viscosity of non esterified neat Neem oil, Honge oil and Mahua oil were $1.584 \times 10^{-5} \text{ m}^2/\text{s}$, $2.16 \times 10^{-5} \text{ m}^2/\text{s}$ and $1.707 \times 10^{-5} \text{ m}^2/\text{s}$ respectively. It can also be observed that as vegetable oil percentage in the blend increases, there is decrease in the kinematic viscosity. This is attributed to lower volatility of vegetable oils.

3.7 Kinematic Viscosity of Esterified Oil Blends.

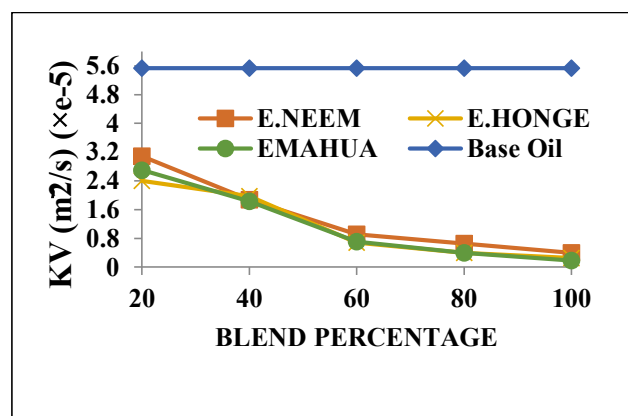


Fig. 7. Variation of Kinematic viscosity of Esterified oil blends.

Figure 7 shows the variation of kinematic viscosity with non esterified oil blends. It is calculated that kinematic viscosity of esterified neat Neem oil, Honge oil and Mahua oil were $0.3964 \times 10^{-5} \text{ m}^2/\text{s}$, $0.2557 \times 10^{-5} \text{ m}^2/\text{s}$ and $0.1805 \times 10^{-5} \text{ m}^2/\text{s}$ respectively. It can also be observed that as vegetable oil percentage in the blend increases, there is decrease in the kinematic viscosity. This is attributed to lower volatility of vegetable oils and also due to the removal of fat and glycerine during esterification process.

3.8 Comparison of Kinematic Viscosity of Non Esterified and Esterified Oil Blends.

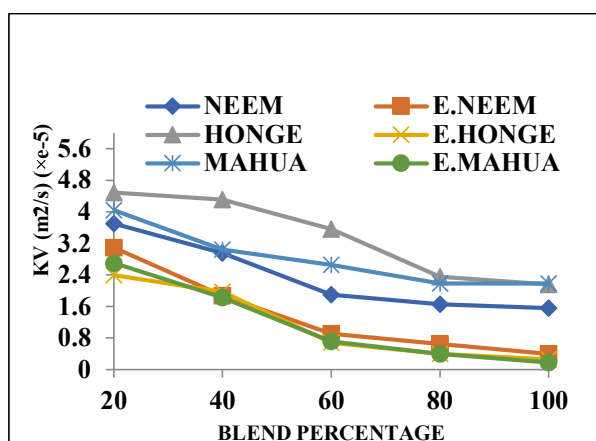


Fig. 8. Comparison of Kinematic viscosity non esterified and esterified oil blends.

Figure 8 shows Comparison of Kinematic viscosity non esterified and esterified oil blends. It can be observed that the non-esterified Honge oil possesses more kinematic viscosity which is due to presence of higher triglycerides and fatty acids lower volatility of non edible oil. Further it can be observed that the esterified Mahua oil possesses lower Kinematic viscosity compared with other oils tested which is due to separation of triglycerides and fatty acids during esterification.

3.9 Comparison of Kinematic Viscosity of Non Esterified and Base Oil (SAE15W40).

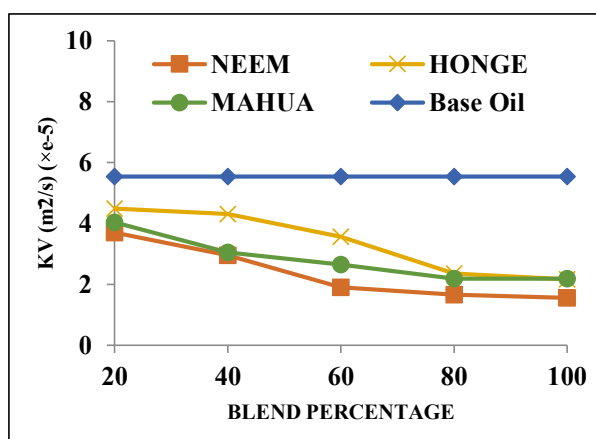


Fig. 9. Comparison of Kinematic Viscosity of non esterified oil blends with base oil.

Figure 9 shows the comparisons among kinematic viscosity of non esterified oil blends and base synthetic oil SAE15W40. It can be observed that after the synthetic oil kinematic viscosity rank, Honge, Mahua and Neem find the preferential rank. It can be observed that the decrease in the kinematic viscosity with the rise blend percentage and this is due to lower volatility of non edible oil. The 20% Honge oil blend value has kinematic viscosity value nearer to base oil.

3.10 Comparison of Kinematic Viscosity of Esterified and Base Oil (SAE15W40).

Figure 10 shows the comparisons among kinematic viscosity of esterified oil blends and base synthetic oil SAE15W40. It can be observed that after the synthetic oil kinematic viscosity rank, Honge, Mahua and Neem find the preferential rank. It can be observed that the decrease in the kinematic viscosity

with the rise blend percentage and this is due to lower volatility of non edible oil. The 20% Honge oil blend value has kinematic viscosity value nearer to base oil.

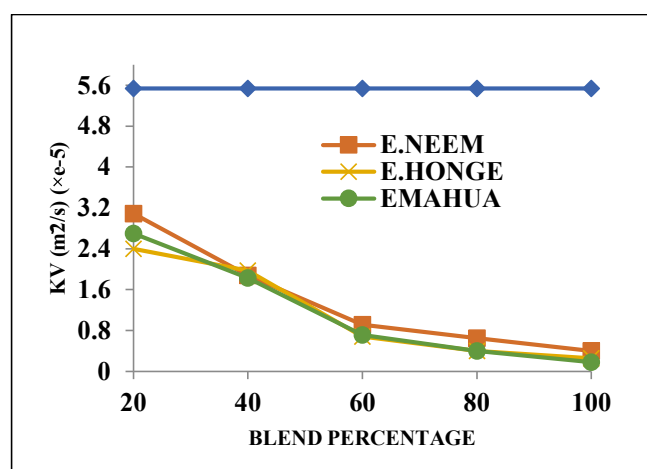


Fig. 10. Comparison of Kinematic Viscosity of esterified oil blends with base oil.

4 Conclusions

There is an increase in the specific gravity with the increase of vegetable oil proportion in the blends. The presence of more mono alkyl esters and fatty acids of vegetable oils is the due factor. The specific gravity of non esterified oils higher than that of esterified oils due to loss of dilution of fatty acids during esterification.

There is increase in the kinematic viscosity with the increase of vegetable oil proportion in the blends. This is attributed to lower volatility of vegetable oils. The kinematic viscosity of non esterified oils found higher than that of esterified oils. The esterified Honge oil 20% blend possesses comparatively good kinematic viscosity and it is close to synthetic mineral oil.

Acknowledgment

The authors are very much grateful to the Sri Siddhartha Academy of Higher Education Tumkur, Karnataka, India for providing requisite facilities to successfully carry out this research work.

References

1. Navdeep Sharm Dugalaa, Gyanendra Singh Goindi, Ajay Sharma, "Evaluation of physicochemical characteristics of Mahua (*Madhuca indica*) and Jatropha (*Jatropha curcas*) dual biodiesel blends with diesel", Journal of King Saudi University-Engineering Sciences, 2020.
2. Leonardo Israel, Farfan-Cabrera, Ezequiel Alberto Gallardo-Hernández, Mario Gomez-Guarneros, Jose Perez-Gonzalez, Jesus Gilberto Godínez-Salcedo, "Alteration of lubricity of Jatropha oil used as bio-lubricant for engines due to thermal ageing", Renewable Energy, Vol. 149, 2020, pp.
3. R.Z.M.Zulfattah, N.W.M.Zulkifli, H.H.Masjuki, M.H.Harith, A.Z.Syahira I. Norain, R.Jumaidin, M.N.A.M. Yusoff, Azham Alwi, M.Jamshaid, A.Arsilanc, "Effect of bio-based lubricant towards emissions and engine breakdown due to spark plug fouling in a two-stroke engine", Journal of Cleaner Production, Vol. 221, 2019, pp.215-223
4. Arianti N. Annisa1, Widayat Widayat, "A Review of Bio-lubricant Production from Vegetable Oils Using Esterification Transesterification Process", MATEC Web Conf. Vol. 156, 2018.
5. M. A. Kalam, H.H.Masjuki, HaengMukCho, M.H.Mosarof, Md. IqbalMahmud, Mohammad Asaduzzaman Chowdhury, N.W.M.Zulkifli, "Influences of thermal stability, and lubrication performance of biodegradable oil as an engine oil for improving the efficiency of heavy duty diesel engine", Fuel, Vol. 196, 2017, pp. 36-46.

6. S. Arumugam, G. Sriram, T. Rajmohan, J. Paulo Davim, "Multi-objective Optimization of Engine Parameters While Bio-lubricant–Biofuel Combination of VCR Engine Using Taguchi-Grey Approach", *Ecotribology*, 2016, pp 105-123.
7. Masoud Dehghani, Soufi Barat Ghobadian, Gholamhassan Najafi, Mohammadreza Sabzimaleki, Farzad Jaliliantabar, "Performance and Exhaust Emissions of a SI Two-stroke Engine with Bio lubricants Using Artificial Neural Network", *Energy Procedia*, Volume 75, 2015, pp, 3-9.
8. K. S. V. Krishna Reddy, Naval Kabra, Umesh Kunchum, and T. Vijayakumar, "Experimental Investigation on Usage of Palm Oil as a Lubricant to Substitute Mineral Oil in CI Engines", *Chinese Journal of Engineering*, Vol. 2014, pp.1-5.
9. S. Arumugam, Sriram, "Synthesis and characterisation of rapeseed oil bio-lubricant – its effect on wear and frictional behaviour of piston ring–cylinder liner combination", *Journal of Engineering Tribology*, Vol.227(1), 2013, pp. 3-15.
10. S. Bekal and N. R. Bhat, "Bio-lubricant as an Alternative to Mineral Oil for a CI Engine—An Experimental Investigation with Pongamia Oil as a Lubricant", *Energy Sources, Part A: Recovery, Utilization, and Environmental Effects*, Vol. 34(11), 2012, pp. 1016-1026.
11. Gopalasamy Sriram, Abhishek Kumar, "Evaluation of Performance of Crankcase Oil in a Biodiesel Engine - A Case Study", *Tribology online*, Vol.6(5), 2011, pp. 235-238.

Aerostatic bearing performance analysis based on CFD study

Nripen Mondal, Tanumoy Banerjee, Sourav Das

1 Introduction

Air bearing is increasingly used for electronic industry, chemical industry, coordinate measurement machine, dentist drill, micro-machining, chemical etching, food processing, wafer-steppers, moment of inertia measurement system. Advantage of using air bearing is no-friction between the contact surface and clean operation condition compare to the conventional ball and roller bearing. Using computational Fluid Dynamics (CFD), aerostatic bearing performance has been analyzed and observed that double slot is the best performance [1]. Aerostatic bearing static characteristics have been analyzed using single and multiple type orifices using CFD analysis. It is found that multiple restrictors have better stiffness [2]. Using CFD analysis aerostatic bearing with flat pad and different orifice shape, comparison has been performed and experimentally validated the CFD based result [3]. The numerically and experimentally aerostatic bearing stiffness and stability has been validated [4-5]. The two different shape of air bearing one is the inherent orifice restrictor, another pocketed orifice model have been analyzed by numerically and CFD methods [6]. Miyatake and Yoshimoto [7] investigated that the small air hole feeding with changing the orifice diameters and changing number of feed hole, air bearing performance is evaluated by finite difference method (FDM) and CFD approach. Chen and He [8] by CFD method, it is found that small vortices of the orifice recess caused the bearing instability. Aerostatic bearing has been designed for the measuring moment of inertia of aerospace vehicles Mondal et al.[9]. Renn and Hsiao [10] made experimental and CFD study on aerostatic bearing. They observed that the mass flow rate characteristic through an orifice is different with the flow in nozzle. They modified the critical pressure ratio based on the experimental and simulation study. Talukder and Stowell [11] investigated that the pneumatic hammer mainly occurred based on the depth of the pocket, orifice diameter etc. Karkoub and Elkamel [12] using artificial neural network, pressure distribution of rectangular aerostatic bearing is evaluated for higher performance design. The basic static and dynamics of aerostatic bearing design carried out firstly numerically, and then validated through CFD analysis has been performed Mondal et al. [13-15].

In this research paper a simplified geometrical shape aerostatic bearing performance has been analyzed using CFD method.

2 Air Bearing Geometry Descriptions

The figure 1 shows the sectional view of an aerostatic bearing for present research work. In generally inlet is connected through an external compressor and the outlet is atmosphere condition. The inlet is centrally located which inner radius r_1 0.025m and height is 0.04m. Compressed air passes through central air hole and goes to atmosphere through bearing stator and rotor part. The outer radius r_3 of the bearing is 0.027m and inner recess radius r_2 is 0.012m. The gap between stator and rotor part is about 15 micron.

N. Mondal, T. Banerjee*, S. Das

*Department of Mechanical Engineering and Mechanics Lehigh University Pennsylvania-18015, USA

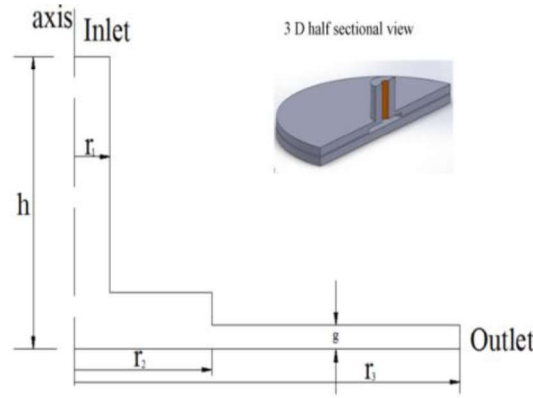


Fig.1 Air bearing schematic sectional view

3 Governing Equations

The fluid motion is generally governed by the laws of mass and momentum in the fluid mechanics which can be formed by Navier-Stokes equations (N-S). The mass conservation and the momentum conservation equation are given bellow.

Continuity equation:

$$\frac{\partial \rho}{\partial t} + \text{div}(\rho \vec{u}) = 0 \quad (1)$$

Where, ρ is the air density and t is time, \vec{u} is the vector velocity in the Cartesian coordinate.

According to Navier-Stokes equations or momentum equation:

$$\begin{aligned} \frac{\partial \rho}{\partial t} + \frac{\partial(\rho u)}{r \partial r} + \frac{\partial(\rho v)}{r \partial \theta} + \frac{\partial(\rho w)}{\partial z} &= 0 \\ \frac{\partial \rho}{\partial r} &= \mu \frac{\partial^2 u}{\partial z^2} \\ \frac{\partial \rho}{\partial z} &= 0 \\ \frac{\partial \rho}{\partial \theta} &= r \mu \frac{\partial^2 v}{\partial z^2} \end{aligned} \quad (2)$$

4 Results and Discussion

Mesh has been generated on the surface of flow domain with the help of ANSYS CFD Fluent Solver (CFX) and special care was taken for refinement of meshes near corners and near the outlet cross-section area by fine meshing and edge sizing refinements shows in figure 2. The enlarge view of the inlet, corner and outlet are shows in the figure 3, figure 4 and figure 5 respectively.

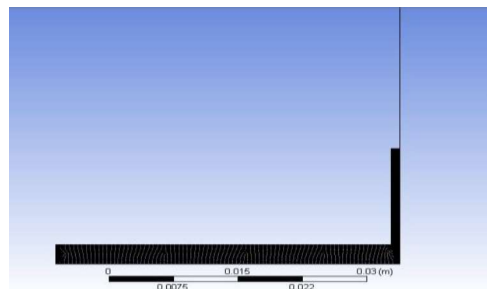


Fig.2: Grid system used for CFD analysis

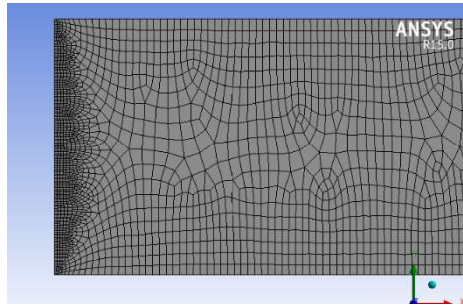


Fig.3: Enlarge view of the inlet mesh domain

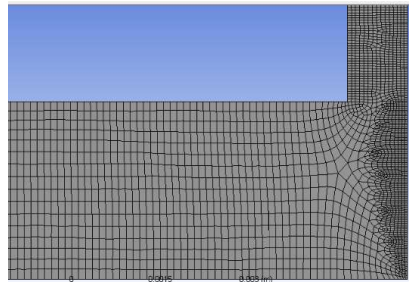


Fig.4: Enlarge view of the sharp corner mesh domain

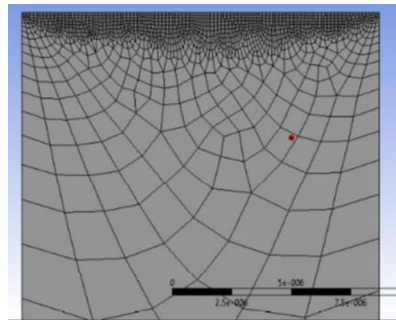


Fig.5: Enlarge view of the outlet mesh domain

The boundary condition has been chosen for this analysis inlet pressure supply 0.6 Mpa and outlet is the atmospheric condition and flow is isothermal and temperature chosen as 300k. The bearing walls are considered to be adiabatic and no-slip condition. Axis is taken for one side hence it is an axis-symmetric model. Total 1000 iterations are performed for the convergence study. The gravitational effects have been neglected for the present study and the flow is laminar flow condition.

Figure 6 shows the static pressure contour plot, it is observed that pressure from inlet to inner recess radius r_2 pressure is almost same after that pressure gradually decreasing.

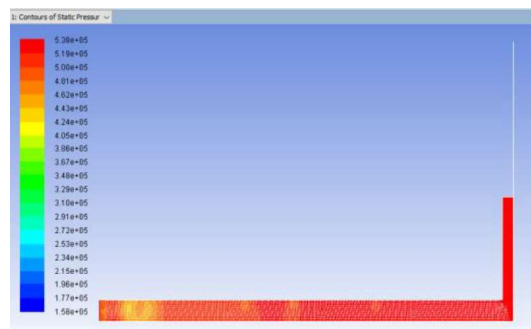


Fig.6: Pressure distribution of the bearing

From figure 7 it is shows that horizontal section from inlet to the length (h) of the central air hole pressure is constant it is about 5.3×10^5 Pa.

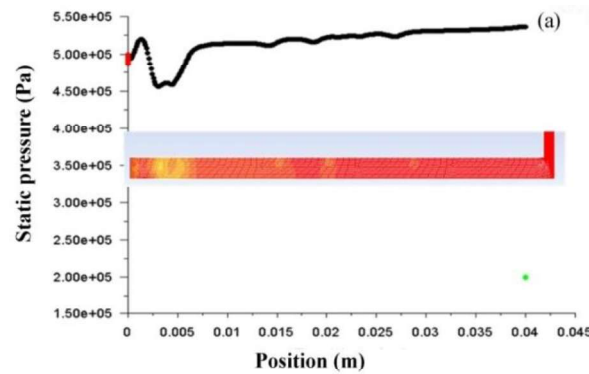


Fig.7: Pressure distribution of the bearing horizontal section

From figure 8 it is clearly observed that from bottom of the central air hole static pressure gradually decreasing to reach about 2×10^5 pa.

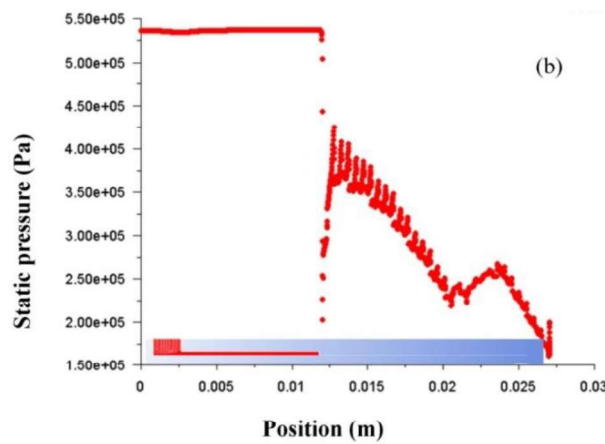


Fig.8: Pressure distribution of the bearing vertical section

Figure 9 shows that the velocity variation of the bearing passage. It is observed that at central air hole passage, velocity fluctuation occurs.

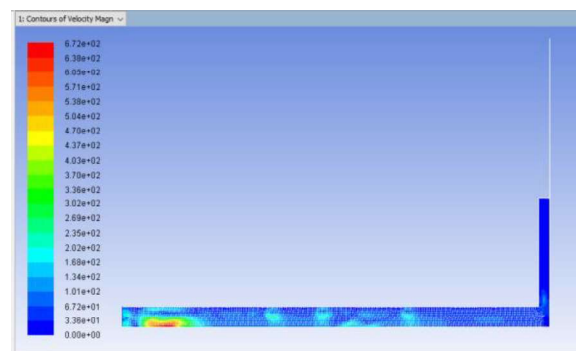


Fig.9: Velocity distribution of the bearing

From figure 10 it is shows that the inlet velocity variation for the horizontal section.

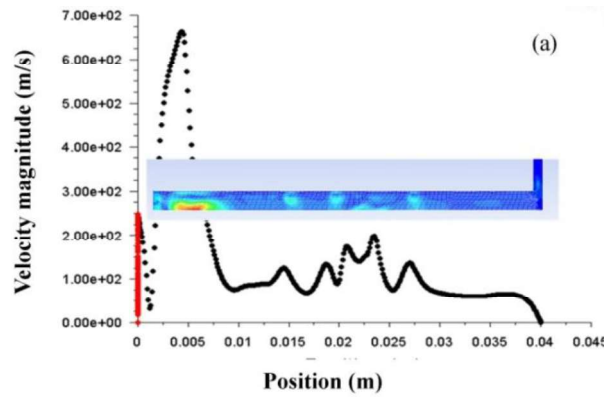


Fig.10: Velocity distribution of the bearing horizontal section

From figure 11 it is shown that the bearing velocity variation for the vertical section.

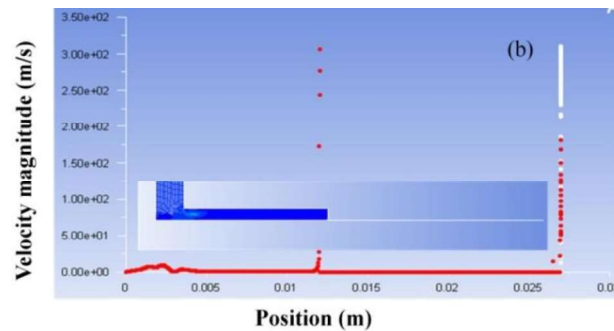


Fig.11: Velocity distribution for vertical section of the bearing vertical section

4 Conclusions

In this paper simplified aerostatic bearing performance analysis was studied using CFD analysis. The following conclusions are made:

- (1) From bearing inlet to length of the air hole, pressure is same after that it is decreasing nature and it reaches to atmospheric condition at outlet.
- (2) Initially from inlet, velocity fluctuating is observed and velocity is gradually decreasing and at outlet of the bearing passage, velocity becomes very low.
- (3) From this present air bearing CFD analysis, it is observed that total force generate 212 N and mass flow rate 2.6×10^{-4} kg/s.
- (4) In future study air bearing performed analysis can be performed with experimental as well as CFD study.

Acknowledgements

This research did not receive any specific grant from funding agencies in the public, commercial, or not-for-profit sectors.

References

1. H.Zhu, Y.Lin, Y.Li and D.Li, "CFD Investigation on the performance of Aerostatic Thrust Bearing with Exhaust Slots Used in Low-vacuum Condition" Proceeding of 2012 International Conference on Mechanical Engineering and Materials Science (MEME 2012).

2. M.P.Muhammad, W.Wang, M.Imran, L.He, G. Weiwei, "Modeling and Simulation of Aerostatic Thrust Bearings" IEEE, 2020,DOI: 10.1109/ACCESS.2020.2999748.
3. G.Belforte, T.Raparelli,A.Trivella,V.Viktorov, C.Viscont,"CFD analysis of aerostatic pads with simple orifice-type feeding system" Tribology Letters, 58(2), (2015),DOI:10.1007/s11249-015-0503-8.
4. H.L.Cui, Y.Wang, B.R.Wang, H.Yang and H.Xia, "Numerical Simulation and Experimental Verification of the Stiffness and Stability of Thrust pad Aerostatic Bearings"J.Mech.Eng. (2018)31:23, <https://doi.org/10.1186/s10033-018-0228-3>.
5. Y.Li and H.Dang, "Influences of the geometrical parameters of aerostatic thrust bearing with pocketed orifice-type restrictor on its performance" Tribology International 40 (2007), pp.1120-1126.
6. S.H.Chang, C.W.Chang, and Y.R.Jeng, " Numerical analysis of discharge coefficients in aerostatic bearing with orifice-type restrictors" Tribology International, 90(2015), pp.157-163.
7. M. Miyatake and S.Yoshimoto, "Numerical investigation of static and dynamic characteristics of aerostatic thrust bearing with small feed hole" Tribology International, 43(2010), pp.1353-9.
8. X, Chen, X. He, "The effect of the recessshapeon performance analysis of the gaslubricated bearing in opticallylithography", *Tribology International*, **39**(2006), pp. 1336–1341.
9. N.Mondal, S. Acharya, R.saha, D.Sanyal and K.Majumder, "Optimum Design of Mounting Components of a Mass property Measurement" Measurement,78(2016),pp.309-321.
- 10.J.C.Renn, C.H.Hsiao," Experimental and CFD study on the mass flow rate characteristic of gas through orifice-type restrictor in aerostatic bearing .Tribology International,37(2004),pp.309-15.
- 11.H.M,Talukder, T.B.Stowell," Pneumatic hammer in an externally pressurized orifice compensate air journal bearing" Tribology International,36(2003),pp.585-91.
- 12.M.Karkoub and A.Elkamel,"Modelling pressure distribution in a rectangular gas bearing using neural network" Tribology International, 30(1997), pp.139-50.
13. N.Mondal, R.Saha and D.Sanyal, "Designing Aerostatic Bearing With Counterbalancing Gaps for lifting a Heavy Payload" ASMEJ.Tribology, 136(2014), pp.031701.
14. N.Mondal, B.K. Saha, R.Saha and D.Sanyal, " High-Thrust Aerostatic Bearing Design Through Transient Perturbation Modeling with numerical Validation" ASME J.Tribology,140(2017),pp.041012.
15. N.Mondal, R.Saha and D.Sanyal, "Modeling and performance analysis of aerostatic bearing for lifting heavy payload" Procedia Engineering, 90(2014), pp.123-128.

Development of mathematical model for ultimate tensile strength of TIG welded Duplex stainless steel

Sandip Mondal, Goutam Nandi, Pradip Kumar Pal

1 Introduction

Duplex Stainless Steel (DSS) is made by exceptional blend of double phase configuration of ferrite with austenite. 50% ferritic and 50% austenitic phase structure has generally been observed in grain configuration of DSS. It has got high yield strength, good ductility, ability to withstand high working temperature and good corrosion resistance. Application of DSS is increasing day to day due to the favourable weldability property of duplex stainless steel. Duplex stainless steels are sometimes used as a substitute to austenitic stainless steels (ASS) in different areas of application like reaction vessels and pipelines of chemical, oil refinery and gas industries. Austenite structure provides a unique arrangement of strength. Ferrite phase provides local corrosion resistance.

Murugan et al. prepared a mathematical model for five levels factorial technique. Using this method, bead geometry of welding of 316L stainless steel into IS2062 structural steel had been investigated and illustrated in graphical form. They searched for the selection of appropriate levels of process parameters to reach the desired quality for the welded product [1]. Badji et al. investigated phase structure configuration and different properties of 2205DSS materials. They performed heat treatment on DSS materials by annealing, using temperature 800°C - 1000°C . They showed that the most of ferritic phase structures were positioned around the HAZ zone [2]. Sotomayor et al. determined the adhesive property of duplex stainless steel on a thermoplastic. They also examined the rupture failures of that material. Several conditions like humidity had significant role to evaluate the effectiveness of surface treatment [3]. Palani and Murugan investigated the cladding effect using different parameters such as welding current, nozzle-to-plate, and welding speed distance on the weld bead geometry [4]. J. J. Del Coz Diaz et al. shows the important role of the material properties in the final deformed shape of two different stainless steels using finite element method including the birth and death technique. They also investigated that opposite angular deformation and longitudinal bending occur when these steels are welded with a similar TIG procedure [5]. Pandya and Menghani prepared a mathematical model for prediction of tensile properties of dissimilar AA6061-T6 to Cu welds. They used friction stir welding process with Zn interlayer [6]. Tarng and Yang applied Taguchi technique to optimize weld pool structure [7]. Tarng et al. investigated on the optimal weld bead structure of TIG welded stainless steel to determine the process parameters by using modified Taguchi method [8]. Tarng et al. researched related to grey-based Taguchi technique to decide optimal process factors of submerged arc welding, concern of various weld properties [9]. Murta et al. developed Mathematical model for predicting mechanical properties in rebar manufacturing. They showed that an artificial neural network can be useful in evaluating and choosing the most adequate parameters to achieve the desired steel properties [10].

Literature survey suggests that there is a need of further extensive research in the area of TIG welding of duplex stainless steel. DSS is being extremely used in oil and chemical industry. But the sufficient research work has not been done on this emerging field. In so far as TIG welding of duplex stainless steel is concerned, knowledge-base is not sufficiently rich. More and extensive research may lead to develop a sound knowledge-base which will help better understanding of the various aspects relating to duplex stainless-steel welding. For that reason, mathematical modeling, metallographic characterization, parametric optimization, analysis of joint performance etc. are very much important.

S. Mondal

Department of Mechanical engineering, Haldia Institute of Engineering, Haldia

Investigation related to these fields will lead to create a strong knowledge-base which will help use of TIG welding in more predictable way with the desired quality of weld.

In the present work, duplex stainless-steel plates are joined by TIG welding. Nine butt-welding joints are made by TIG welding under varied input parameters. The Taguchi's L9 orthogonal array design is used to design the experiments, with three controllable factors, viz. current, welding speed and shielding gas flow rate. Factor levels are chosen on the basis of trial runs and the knowledge of text book. Welding excellence is evaluated by X-ray radiography test. Then, tensile test has been done. A new mathematical model is developed using non-linear regression analysis for the prediction of ultimate tensile strength. The variables used in the prediction models are selected welding parameters like welding current, gas flow rate and speed of welding. A residual plot for UTS has been developed. Calculation of percentage deviation for UTS has been made. Comparison of measured and predicted UTS value has been done by graphical representation. The relationship between ultimate tensile strength and the welding parameters has been illustrated graphically by surface plots and contour plots as well. Combined effects of any pair of input parameters on UTS are represented graphically with the help of three-dimensional surface plots. According to this analysis, the models provide good UTS with the data used in this study.

2 Experimental Works

In this experiment, TIG welding was performed on duplex stainless-steel plates. The dimension of each welding plate was taken as 75 mm \times 50 mm \times 3 mm. Butt welding joint was completed. Filler rod was not utilized at the time of welding process. Argon gas was used as the shielding gas. The diameter of Tungsten electrode was 2.4mm. TIG welding on DSS was completed with the help of IGBT digital welding inverter (400A, III phase) of Electra Engineering (India) Pvt. Limited. Materials were welded with suitable welding parameters like current, gas flow rate, welding speed. The photographic view of the arrangement of TIG welding equipment is shown in figure 1. Photographic view of welding sample no. 4 is shown in figure 2. The trial runs of welding joints and final welding joints were completed successfully with the help of these welding equipments.



Fig.1. TIG welding setup



Fig. 2. Welding sample no. 4

2.1 Base Metal

In this study the base metal was a duplex stainless steel (ASTM/UNS: 2205). The chemical composition of this DSS material is shown in table 1. The microstructural feature of the base metal exhibits a duplex structure with embedded grains of austenite and ferrite.

Table 1. Composition of DSS

Composition of elements in %	C	Si	Mn	P	S	Cr	Mo	Ni	Al
	0.0210	0.2800	1.7200	0.0220	0.0140	22.6500	3.1800	4.7300	0.0100
	Co	Cu	Nb	Ti	V	Pb	Fe	N	
	0.0780	0.0090	0.0400	0.0080	0.0110	0.0030	67.123	0.1010	

2.2 Process Parameters and Their Levels

The process factors were decided based on several experimental trials. Here, 3 levels of current, 3 levels of gas flow rate and 3 levels of welding speed were taken to complete the joining process. Welding process factors with their levels are listed in table 2.

Table 2. Welding process factors with their levels

Factors	Units	Notations	Levels		
			1	2	3
Welding Current	A	C	80	85	90
Gas Flow Rate	l/min	F	7	7.5	8
Welding speed	mm/s	S	2.3	2.8	3.5

3 Results and Discussion

3.1 Tensile Test and Results

Completing X-ray radiography investigation, tensile testing samples were created from the TIG welding plates, by Electronica sprintcut-734 wire electrical discharge machining (WEDM) (input

power supply 3 Phase, AC 415 V, 50 Hz, linked load 15 KVA). Photographic view of tensile specimen preparation by WEDM is shown in figure 3(a) Photographic view of tensile test specimens as per ASTM E8 is shown in figure 3(b) and tensile sample after test is shown by figure 3(c).



Fig. 3(a) Tensile specimen preparation by WEDM



Fig. 3(b) Tensile test specimen



Fig. 3(c) Tensile sample after test

The tensile testing samples were investigated with the help of tensile testing machine Instron by Blue star engineering & electronics Ltd, Model no. : BSUT-60-JD-SERVO, serial no. : 2016/048, maximum capacity: 600 KN. Data related to tensile strength are listed in table 3. These results were used for preparing the mathematical model which was very much necessary to realize the desire excellence of TIG weld within the experimental domain.

Table 3. The results of Ultimate tensile strength with welding parameters

Sample no.	Welding parameter with value			Ultimate tensile strength (MPa)
	Current (A)	Welding speed (mm/s)	Shielding gas flow rate (l/min)	
1	80	2.3	7	460
2	80	2.8	7.5	595
3	80	3.5	8	635
4	85	2.8	7	610
5	85	3.5	7.5	645
6	85	2.3	8	630
7	90	3.5	7	640
8	90	2.3	7.5	610
9	90	2.8	8	650

4 Regression Analysis of Ultimate Tensile Strength Data (UTS)

In this section, data have been used to generate regression equations, contour and surface plots. These have been also used to develop and interpret the residue plots. The experimentally measured results i.e., actual observations and results obtained through mathematical model i.e. predictions are compared. The analyses have been done for ultimate tensile strength of TIG welded duplex stainless steel, UNS 2205.

At first, mathematical modeling through non linear regression analysis, of ultimate tensile strength observations has been made using MINITAB 16 software. Surface plots and contour plots for UTS are developed along with residual plots.

4.1 Mathematical Modeling

Ultimate tensile strength is been expressed in terms of the process variables: welding current (C), gas flow rate (F) and speed of welding (S) as

$$UTS = \theta_1 + \theta_2 (C) + \theta_3 (F) + \theta_4 (S) + \theta_5 (C * F) + \theta_6 (C * S) + \theta_7 (F * S) \quad (1)$$

Where θ_1 is the constant coefficient, θ_2 , θ_3 and θ_4 are the coefficients of welding current, gas flow rate and speed of welding respectively.

The final mathematical model to estimate UTS is given as

$$UTS = -3563.39 - 9.85396 * C - 116.687 * F + 3414.09 * S + 8.87746 * C * F - 19.7828 * C * S - 220.538 * F * S \quad (2)$$

Where UTS is in MPa, C is in A, F is in l/min and S is in mm/s.

Gauss-Newton algorithm method is applied to develop this mathematical equation. This equation is prepared keeping maximum iterations 200 and tolerance 0.00001. From θ_1 to θ_7 , starting value for every parameter is 1. The mathematical model is successfully prepared with the help of calculating the estimation of parameters and correlation matrix for parameter estimates. The parameter estimates and correlation matrix for parameter estimates are given in tables 4 and 5 respectively. Residual plots for UTS are also given in figure 4. These residual plots validate the regression model. From residual plots it is clearly observed that maximum data are satisfied and regression model is, therefore, considered valid. In this analysis, the Sum of Squared Errors (SSE) gets minimized by the set of parameter

estimates when the algorithm is converged on the parameter values correctly. The correct interpretation for each parameter depends on the expectation function and the parameter's place in it. So, the relationship between the predictor and the response has been determined with the help of nonlinear model. The Standard Error of the estimate (SE estimate) is used to measure the precision of the parameter estimate. The smaller standard error describes the more precise estimate. The Confidence Intervals (CI) are ranges of values that are likely to contain the true value of each parameter in the model. The confidence intervals are used to assess the estimate of each parameter estimate. Here, the correlation between parameter estimates is displayed by the correlation matrix. For highly correlated parameter estimates, the number of parameters must be reduced for the simplification of the model.

Table 4. Parameter estimates for UTS

Parameter	Estimate	SE Estimate	95% CI
Theta1	-3563.39	3115.87	(16969.9, 9843.12)
Theta2	-9.85	43.87	(198.6, 178.91)
Theta3	-116.69	508.24	(2303.5, 2070.11)
Theta4	3414.09	1034.57	(1037.3, 7865.49)
Theta5	8.88	7.23	(22.2, 39.98)
Theta6	-19.78	6.77	(48.9, 9.33)
Theta7	-220.54	67.67	(511.7, 70.63)

Table 5. Correlation matrix for parameter estimates for UTS

	Theta1	Theta2	Theta3	Theta4	Theta5	Theta6
Theta2	-0.935479					
Theta3	-0.919549	0.952964				
Theta4	0.276715	0.565030	0.601917			
Theta5	0.833432	0.955626	0.967129	0.760499		
Theta6	-0.245371	0.476026	0.604180	-0.950949	-0.712105	
Theta7	-0.260376	0.582596	0.512188	-0.936752	-0.712105	0.782967

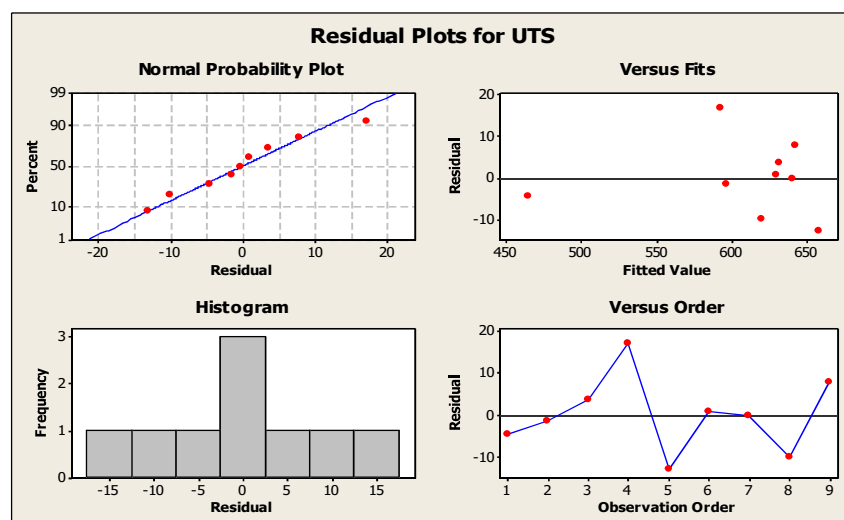


Fig. 4 Residual plots for UTS

4.2 Calculation of Percentage Deviation for UTS

After generating the mathematical model, it is required to compare between experimentally measured results and results obtained through mathematical model. This comparison or accuracy of the model has been presented by percentage deviation and graphical plots given in table 6 and figure 5 respectively.

Table 6. Calculation of percentage deviation for UTS

Sample no.	Experimental result for UTS (measured result) in MPa	Result for UTS obtained through Mathematical model (prediction result) in MPa	Percentage of Deviation in %
1	460	464.5718	-0.99387
2	595	596.4235	-0.23924
3	635	631.4386	0.56085
4	610	592.9039	2.802639
5	645	658.06115	-2.02498
6	630	629.1706	0.131651
7	640	640.2964	-0.04631
8	610	619.9735	-1.635
9	650	642.164	1.205538

From table 6, it is seen that percentage deviation for UTS is in within $\pm 3\%$. This can be considered as acceptable. Figure 5 also indicates that the mathematical model works satisfactorily for the prediction of the response within the range of the experimental domain.

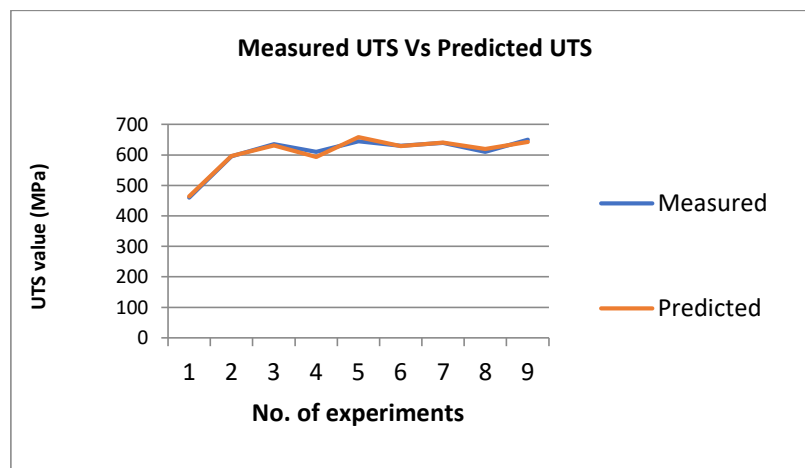


Fig. 5. Comparison of measured and predicted UTS value

4.3 Surface Plots and Contour Plots for UTS

The relationship between ultimate tensile strength and the welding parameters has been illustrated graphically by surface plots and contour plots as well. Combined effects of any pair of input parameters

on UTS are represented graphically with the help of three-dimensional surface plots. In surface plots, a response is plotted against any two input variables when the other variable, the third one, is held constant. The contour plots are two-dimensional graphs that show contours of constant response, with the axis system being a specific pair of the process variables, while the other variable is held invariable. The plots are particularly necessary when the stationary point is a saddle point or is remote from the design region. But it should be kept in mind that the contour plots are only estimator, they are not generated by deterministic equations. Every point on a contour has a standard error. Interaction effects of the input process parameters on the response(s) are also identified with the help of these plots. The surface plots are shown in figures 6-8 and contour plots are shown in figures 9-11.

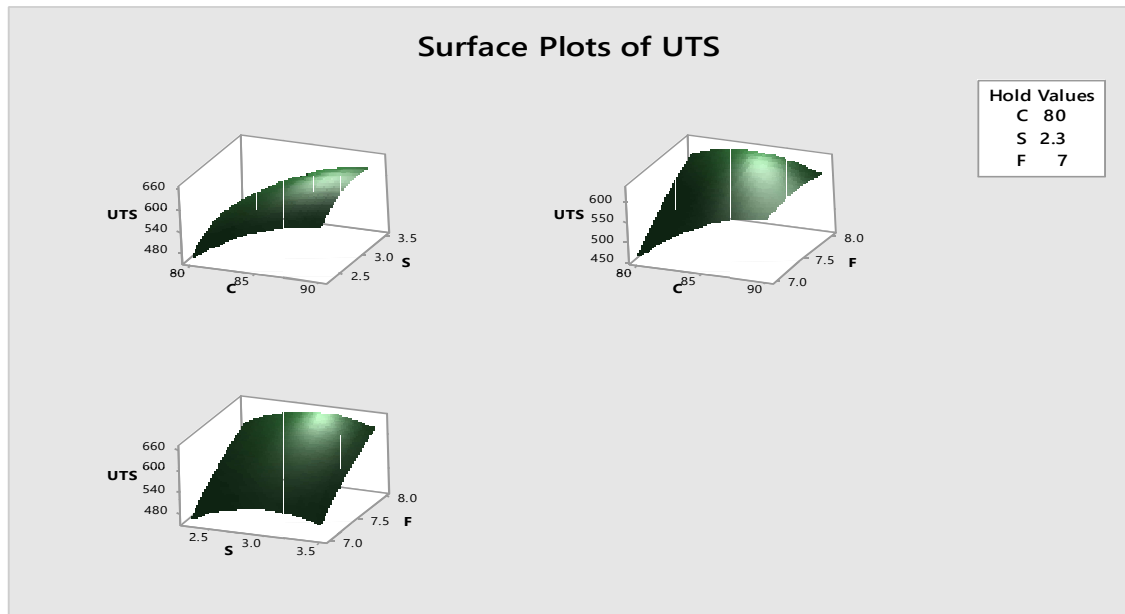


Fig. 6. Surface plots of UTS when welding current (C), gas flow rate (F) and speed of welding (S) constant at lowest level

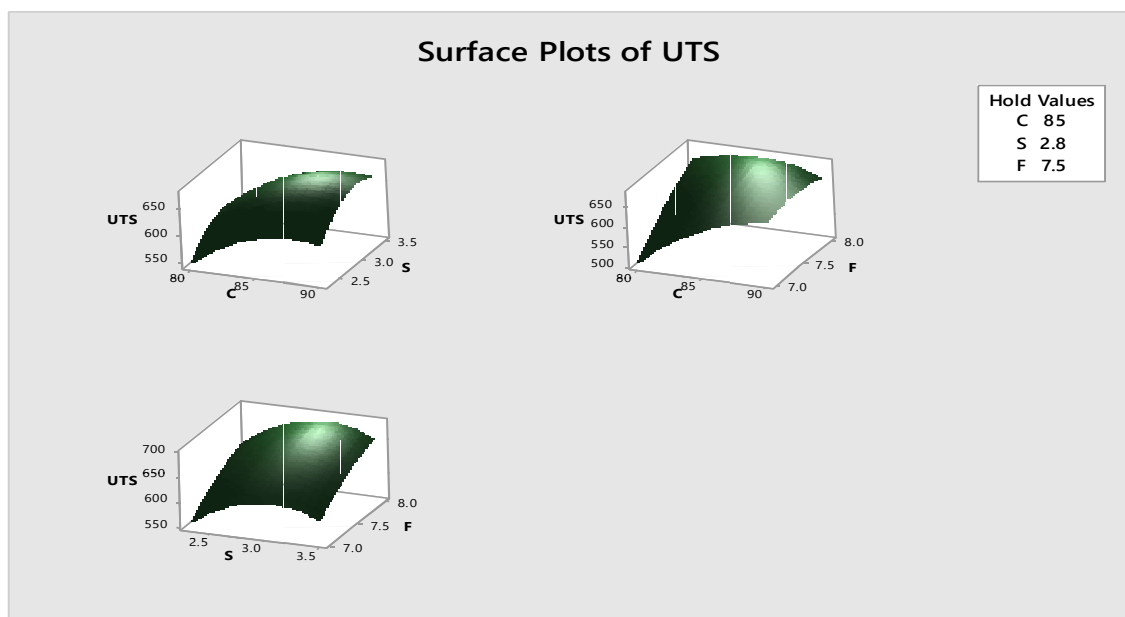


Fig. 7. Surface plots of UTS when welding current (C), gas flow rate (F) and speed of welding (S) constant at middle level

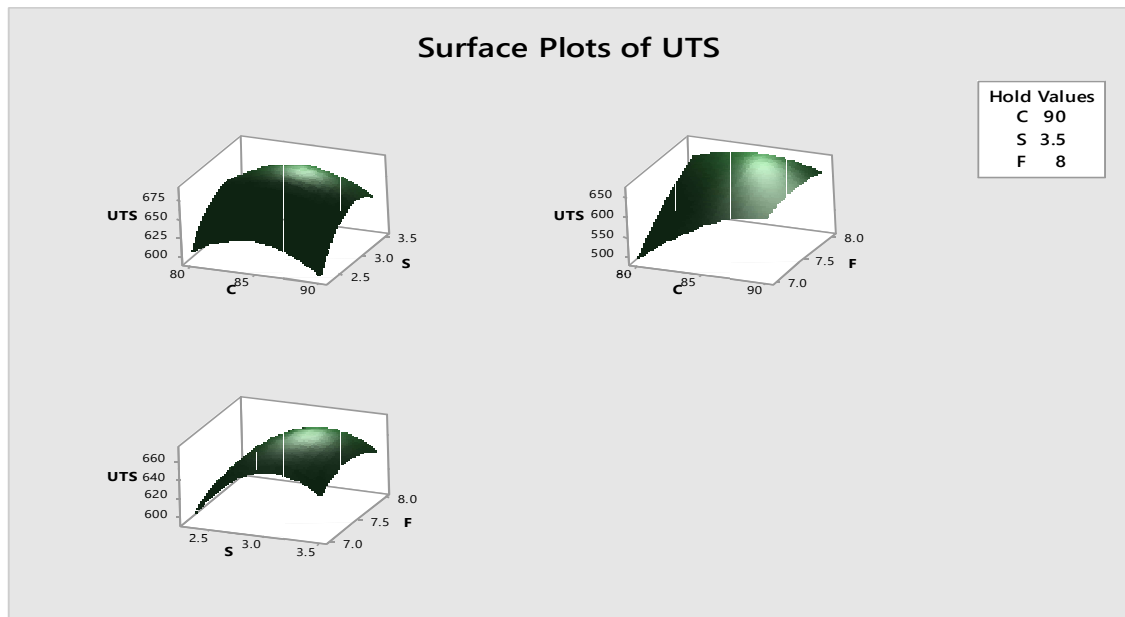


Fig. 8. Surface plots of UTS when welding current (C), gas flow rate (F) and speed of welding (S) constant at highest level

If the response surface exhibits appreciable bend, curvature or undulation, then interaction effect is considered to be significant. No or very little bend/curvature or undulation of response surface plots leads to the fact that interaction effect is less or insignificant. In figure 6, 7 and 8, less bend or curvature in surface plots has been clearly observed when speed of welding is in held at level 2.3 mm/s, 2.8 mm/s and 3.5 mm/s, medium bend or curvature has been observed when welding current is in held at level 80 A, 85 A, 90 A and higher bend or curvature is found when gas flow rate is in held position i.e. level 7 l/min, 7.5 l/min and 8 l/min. Here, interaction effects between gas flow rate and welding current with UTS revealed as less significant than the interaction effects of other combination of two process parameters like gas flow rate and speed of welding with UTS, current and speed of welding with UTS. This means interaction among the welding factors, welding current (C) and gas flow rate (F) causes lesser influence on the response UTS as compared to the interactions among the factors gas flow rate (F), speed of welding (S) and welding current (C), speed of welding (S).

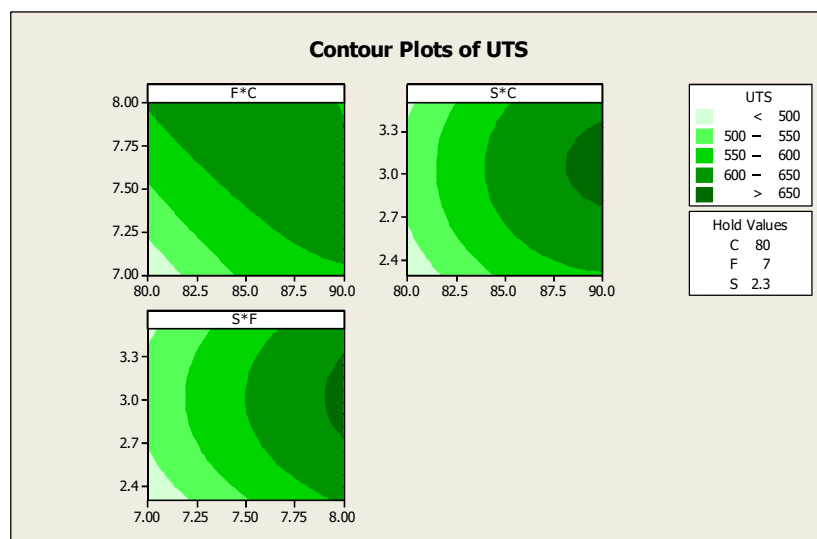


Fig. 9. Contour plots of UTS when welding current (C), gas flow rate (F) and speed of welding (S) constant at lowest level

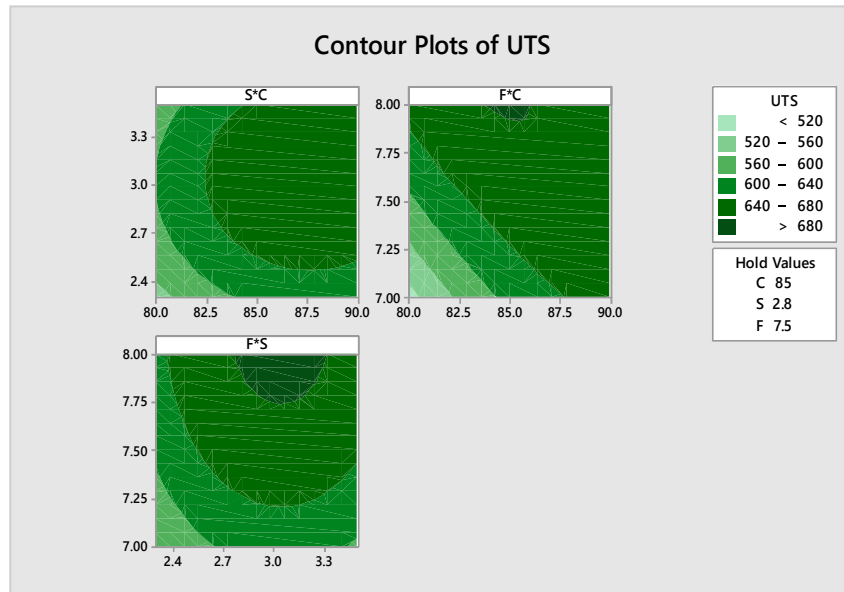


Fig. 10. Contour plots of UTS when welding current (C), gas flow rate (F) and speed of welding (S) constant at middle level

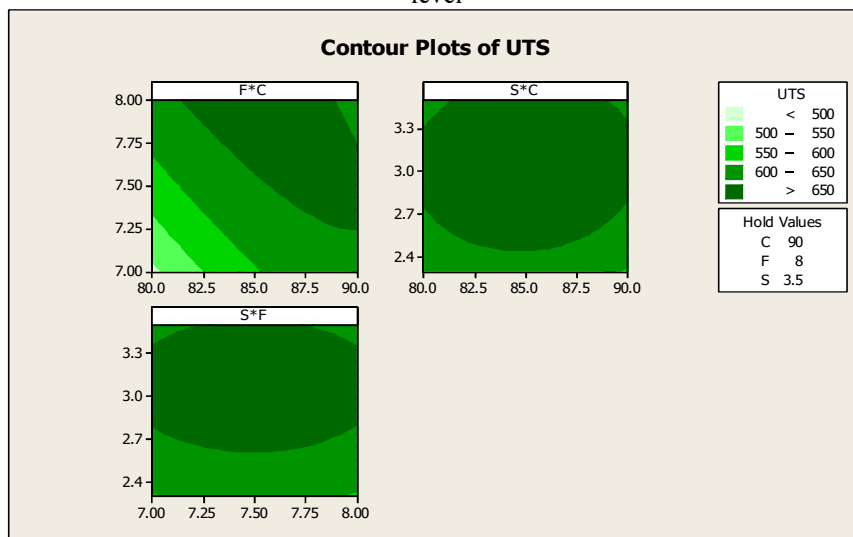


Fig. 11 Contour plots of UTS when welding current (C), gas flow rate (F) and speed of welding (S) constant at highest level

Contour plots (shown in figures 9-11) are helpful for estimating the combined effects of any two parameters on the response. The contour lines, with little or no curvature indicate lesser or no interaction effect; whereas bent or circular contours suggest interaction effect to be significant on the response. For example, interaction among the factors welding current (C) and speed of welding is found to be significant in so far as the effect of this interaction on UTS is concerned. Interaction effect of welding current (C) and gas flow rate (F) on UTS is not so much significant, as revealed in figures 9– 11, while speed of welding (S) is kept in constant position. All other surface and contour plots can be evaluated in the same manner.

5 Conclusions

Based on the results of present investigation and analysis of the experimental data, the following

conclusions are drawn in respect of TIG welding of Duplex Stainless-Steel ASTM/UNS: 2205, of 3 mm thickness, within the range and the limit of the study.

1. Mathematical model for ultimate tensile strength has been prepared satisfactorily through non linear regression analysis.
2. Residual plots validate the regression model. From residual plots it is clearly observed that maximum data are satisfied and regression model is, therefore, considered valid.
3. Percentage deviation for UTS is in within $\pm 3\%$. This can be considered as acceptable. Figure 5 also indicates that the mathematical model works satisfactorily for the prediction of the response within the range of the experimental domain.
4. For surface plots, interaction among the welding factors, welding current (C) and gas flow rate (F) causes lesser influence on the response UTS as compared to the interactions among the factors gas flow rate (F), speed of welding (S) and welding current (C), speed of welding (S).
5. For contour plots, interaction among the factors welding current (C) and speed of welding is found to be significant in so far as the effect of this interaction on UTS is concerned. interaction effect of welding current (C) and gas flow rate (F) on UTS is not so much significant, as revealed in figures 9–11, while speed of welding (S) is kept in constant position.

References

1. Murugan, N., Parmar, R. S., & Sud, S. K. (1993). Effect of submerged arc process variables on dilution and bead geometry in single wire surfacing. *Journal of Materials Processing Technology*, 37(1-4), 767-780.
2. Badji, R., Bouabdallah, M., Bacroix, B., Kahloun, C., Belkessa, B., & Maza, H. (2008). Phase transformation and mechanical behavior in annealed 2205 duplex stainless steel welds. *Materials characterization*, 59(4), 447-453.
3. Sotomayor, M. E., Sanz, J., Cervera, A., Levenfeld, B., & Várez, A. (2015). Surface modification of a duplex stainless steel for plastic-metal hybrid parts. *Archives of Materials Science and Engineering*, 72(2), 86-93.
4. Palani, P. K., & Murugan, N. (2006). Sensitivity analysis for process parameters in cladding of stainless steel by flux cored arc welding. *Journal of manufacturing processes*, 8(2), 90-100.
5. del Coz Díaz, J. J., Rodríguez, P. M., Nieto, P. G., & Castro-Fresno, D. (2010). Comparative analysis of TIG welding distortions between austenitic and duplex stainless steels by FEM. *Applied Thermal Engineering*, 30(16), 2448-2459.
6. Pandya, S. N., & Menghani, J. V. (2018). Developments of mathematical models for prediction of tensile properties of dissimilar AA6061-T6 to Cu welds prepared by friction stir welding process using Zn interlayer. *Sādhanā*, 43(10), 1-18.
7. Tarng, Y. S., & Yang, W. H. (1998). Optimisation of the weld bead geometry in gas tungsten arc welding by the Taguchi method. *The International Journal of advanced manufacturing technology*, 14(8), 549-554.
8. Tarng, Y. S., Yang, W. H., & Juang, S. C. (2000). The use of fuzzy logic in the Taguchi method for the optimisation of the submerged arc welding process. *The International Journal of Advanced Manufacturing Technology*, 16(9), 688-694.
9. Tarng, Y. S., Juang, S. C., & Chang, C. H. (2002). The use of grey-based Taguchi methods to determine submerged arc welding process parameters in hard facing. *Journal of materials processing technology*, 128(1-3), 1-6.
10. Murta, R. H., Braga, F. D., Maia, P. P., Diógenes, O. B., & De Moura, E. P. (2021). Mathematical modelling for predicting mechanical properties in rebar manufacturing. *Ironmaking & Steelmaking*, 48(2), 161-169.

Study the Application of Nano-fluid in Solar CPVT/PVT system

Ranjit Barua, Arindam Banerjee, Sumit Bhowmik, Debasish Banerjee

1 Introduction

Solar energy has a significant role in protecting our earth from the effects of weather change affected by the usage of fossil fuels to fulfill the energy demands. Thus, improving the enactment of solar energy expertise is of important significance. Nowadays, solar PV is shown to play equally with fossil fuels. An important challenge though is the rise in the temperature of the solar cells which influences their electrical proficiencies. Therefore, scientists have established a new approach to eliminate the extra heat from these methods to reduce their heat by using modern nanotechnology which can solve this problem [1, 2]. Nanotechnology is an interdisciplinary area that merges engineering, science, and technology all together at the nano-scale [3]. There is an extensive choice of uses where nanotechnology can happen, for example, biology, engineering, and material science. In the field of solar energy, nanotechnology can confidently contribute by substituting the functioning element with nano-fluids, which is a new category of heat transfer fluid that permits extra heat to be detached from the solar system. The perception of applying nanoparticles with the base fluids is to raise the thermal conductivity which can source a better heat transfer coefficient in addition to higher thermal efficiency. Nano-fluid has been described in dissimilar approaches in the research journal but several researchers have the same opinion that it is a combination of nanoparticles, which have a 1 to 100 nm ranging diameter, dispersed resourcefully in a base fluid [4–6]. This type of base fluids can be refrigerant, water, thermal oils, or ethylene glycol [7]. By applying nano-fluid, the heat transfer throughout the fluid can be improved over and above the whole system's thermal performance [8]. Additionally, nano-fluids can use as optical filters for the photovoltaic cells as they can catch all of the unneeded solar energy which is not functional for these cells within working range in addition to reducing the temperature [9].

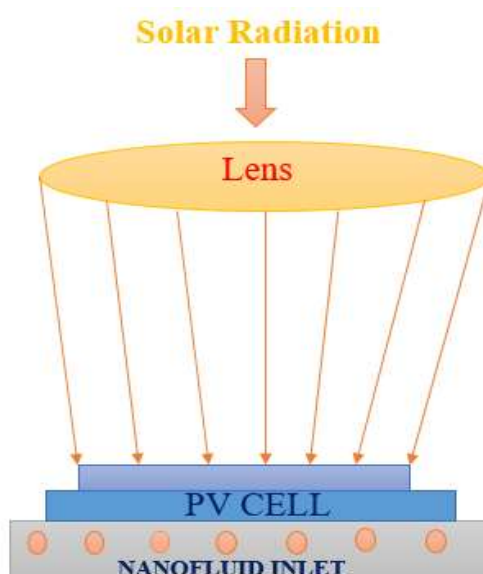


Fig. 1. CPVT systems.

2. Nanofluid Preparation

There are two ways to prepare nano-fluids, for example (a) Single Step Method, and (b) Two-Step Method.

2.1. Single Step Method

In this procedure, the dispersal and making of nanoparticles arise in a similar step. The single-Step Method can be performed chemically or physically [10]. The chemical process depends on computing a reducing agent to the combination of base fluid and nanoparticles by stirring and heating [11]. Alternatively, in a physical way, the ultrasonic-aided submerged arc system is applied for nanoparticle syncretization. The electrical energy created from titanium electrodes which are fused in the dielectric liquid is applied to melt the nanoparticles and vaporize the deionized water. Hereafter, in the vacuum chamber, the nano-fluid, which is the combination of deionized water and melted nanoparticles, is formed [12].

2.2. Two-Step Method

In this procedure, the nanoparticles are arranged as an initial step and then mixed with the base fluid by applying ultrasound or a high shear process. To make sure that the nanoparticles are steady within the base fluid, dissimilar methods have been utilized. Initially, by applying ultrasonication procedure, this advance is suitable for nano-fluid volumes from 0.2 to 2000 mL and creates a nano-fluid with better stability and is measured as the most useful technique for preparation [11]. This method can be classified into direct or indirect ultrasonication.

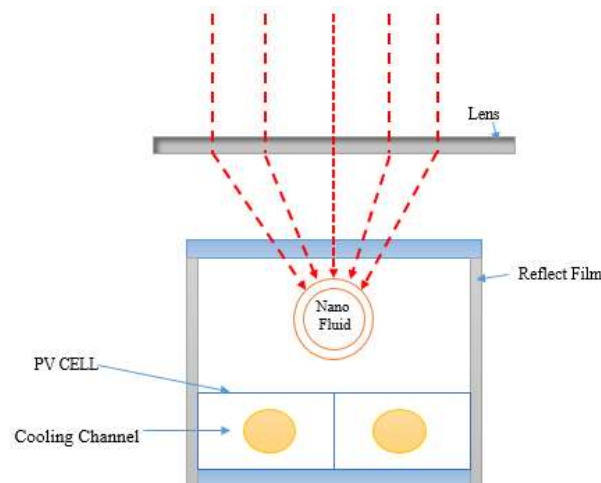


Fig. 2 CPVT systems with optical filter.

3 Applications of Nanotechnology in CpvT Systems

Application of concentrators or mirrors is done only in concentrated photovoltaic systems and not in photovoltaic solar cells as shown in Fig. 1. These concentrators or mirrors concentrate the sunlight on a small area of the highly efficient solar cells. This increases the thermal and electrical efficiencies. The temperature of the system also increases, which has a deterrent effect on the efficiency of the system. Nano-fluids can be used as coolants, could be used to decrease the temperature of the overall system and increase the efficiency of the system even more. And not a lot of research has been carried out in this field. Most of the studies on nano-fluids which are used for cooling purposes are on metal, metal oxide, and silicon carbide nanoparticles in the nano-fluid. Hassani et al. [13] and Rahbar et al. [14] investigated the effect of using metal nanoparticles in the nano-fluids on the enhancement of the efficiency of the CPVT. Numerical studies on two types of concentrated PVT system designs were

carried out by Hassani et al. [13] using two different types of nano-fluids with separate nano-fluids for the optical filtering and the cooling process. The first design configuration mentioned in Hassani et al. [13] (D-1) had two separate channels, one channel for the optical nano-fluid and the other channel for the thermal nano-fluid. The second design configuration was a double pass channel (D-2). In the study, the optical nano-fluid consisted of Ag nanoparticles dispersed in Therminol VP-1 9 (base liquid) which is suitable for high-temperature applications because the terminal can absorb the long wavelength, whereas silver nanoparticles can absorb the shorter wavelength. The thermal nano-fluid used in the separate channels (D-1) is having Silver nanoparticles suspended in water. The authors concluded through simulation results that when the volume fraction of the silver nanoparticles grew from 0.001% to 1.50%, the overall efficiency showed a sharp increase for GaAs and SI at a solar concentration of 160 and 100. Furthermore, the study also concluded that using two different types of fluids in a separate channel design is more efficient than a double pass design. Rahbar et al. [14] presented a mathematical model of a system, which consisted of solar concentrating receivers using Nano-fluids as a method of spectral splitting working on Ag/water to run on an Organic Rankine Cycle. A mathematical 1-D thermal model was done with the help of the Engineering Equation Solver (EES). The nanofluid in the mathematical model was used both as a cooling fluid and as an optical filter for the CPVT system. The optical filter is used to extract only the useful part of the solar spectrum for the concentrated photovoltaic system. The research concluded that using nano-fluid as the working medium in the NFCPV/T system had a great effect on overall efficiencies. The efficiencies were greater at especially at concentration ratios greater than 7 (the increase inefficiencies are found to be 1.8%, 3.3%, and 5.1%, respectively, as compared to CPVT). Various other configurations were studied by Srivastava and Reddy [15] of a parabolic trough concentrator (PTC) along with a Compound Parabolic Collector (CPC) to help homogenize the heat flux. Both the cases of a compound parabolic collector integrated with PTC and the one without the integration of CPC were discussed. Also, various effects of using a different number of cells along with various types of base fluids such as Syltherm 800, Therminol VP-1, and Therminol VP-59 has studied An investigation was done by An et al. [16] by applying nano-fluid as an optical filter in concentrating photovoltaic thermal (Fig. 2), where the base fluid of Oleylamine solution consists of nanoparticles detached in it. The ranged of the particle diameter was from 50.5 to 73.7 nm, and the standard diameter was 60.2 nm.

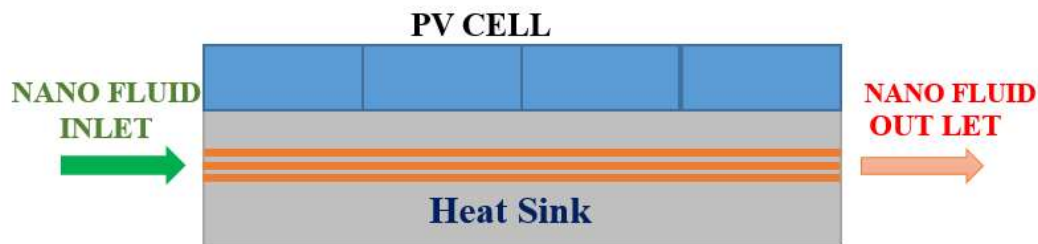


Fig. 3 Photovoltaic Solar Thermal System.

4. Applications of Nanotechnology in PV/T Systems

Till recently, studies on a very limited number on the effects of nano-particles have been done on the Photo Voltaic Thermal Systems. And the nanoparticles on which research has been done are silicon carbide and metal oxides. An even small number of studies have been conducted to study the effect of using carbon-based nanoparticles on the efficiency of the PVT systems. In this portion, the studies carried out in this area applying the aforesaid nanoparticles are summarized (Fig. 3), where the working plan of performing a nano-fluid to cool down a solar cell has been focused on solar radiation. By applying this type of cooling medium attached with the photovoltaic thermal systems permits the removal of heat to be used for other thermal purposes. It also reduces the photovoltaic thermal cells temperature throughout the day which in turn raises the effectiveness which in the future directs to higher electric production. Major development inefficiencies are seen by adding the Metal oxide

nanoparticles when used with dissimilar base fluids. An experimental study of a photovoltaic thermal system was conducted by Sardarabadi and Passandideh-Fard [17] wherein the system was cooled by special types of nanoparticles and water as a base fluid flowing from beginning to end copper tubes at the back of the photovoltaic thermal cell.

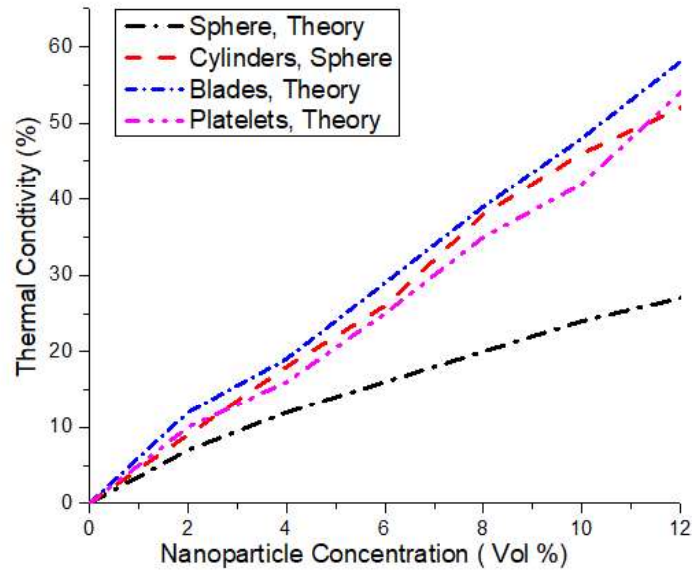


Fig. 4 Influence of nanoparticle shape on the thermal conductivity of alumina nano-fluid.

5. Parameters That Have a Strong Effect on the Thermal Conductivity of the Nano-fluid

Nano-Particles are used with a base fluid with the idea that it increases the thermal conductivity of the resulting nano-fluid, which increases the heat transfer phenomenon within the system. In this section, some important parameters that have a significant influence on the thermal conductivity of the nano-fluid are discussed as mentioned in the published studies.

5.1 Volume Concentration of Nanoparticle

An effective improvement has been noticed with the increase of the thermal conductivity of the nano-fluid by increasing the nanoparticle volume concentration. Various studies have investigated that increasing the volume fraction up to 5% [12], can enhance the thermal conductivity of the resulting nano-fluid, as studied by Iranmanesh et al. [18] and Verma et al. [19].

5.2 Temperature

The thermal conductivity of the nano-fluid also raises quite considerably by raising the temperature of the nano-fluid which has been revealed [18-22]. Though, the accurate opposite characteristics were noticed for viscosity. In contrast to the above studies, Bellos and Tzivanidis [24] in their current research assured that the temperature increase by decreasing the thermal conductivity of the nano-fluid. Additional research on this can be analyzed to clear the uncertainty.

5.3 Particle Size

Nano-fluid are those fluids that consist of base fluid and nanoparticles which have a diameter less than 100 nm. Therefore, it is normally preferred to use nanoparticles with small sizes to achieve a better

enhancement in the thermal conductivity as well as in heat transfer as the smaller size of the nanoparticles increases the overall surface area required for thermal conduction. The effect of increasing the diameter of the nanoparticles on the efficiency of a flat plate solar collector is discussed in Kang et al. [25].

5.4 Base Fluid Type

Base fluids are such types of fluid where the nanoparticles are dissolved. The thermal characteristics of this type of fluid are equally significant. There are many types of base fluids. It was found that base fluid with low thermal conductivity was more efficient than base fluids with high thermal conductivity in Xie et al. [26]. However, Rejeb et al. [27] argued that using water as a base fluid that has higher thermal conductivity is more efficient than ethylene glycol as a base fluid, which has a lesser thermal conductivity. The same nanoparticles and the same operating temperatures were used in the study.

5.5 Nanoparticle Shape

The shape of the nanoparticles has a significant effect on the thermal conductivity and working of nano-fluids. Many scientists have analyzed the effect of the shape of nanoparticles and their relationship with thermal conductivity [28]. Murshed et al. [29] have investigated two different types of structures which are cylindrical shape and spherical shape. The cylindrical-shaped nanoparticles showed better thermal conductivity than the spherical-shaped nano-particles through experiments. An assessment of the enhancement of the thermal conductivity is shown in Fig. 4 when applying differently shaped nanoparticles [30]; the several shapes include cylinders, spheres platelets, blades, and bricks. The shape which had the most excellent thermal conductivity was attained when using the blade's shape.

6 Conclusion

It is quite natural, in the area of solar energy, usage of nano-fluid has a growing future. Consequently, new investigational work essentials to be conducted particularly with concentrated photovoltaic thermal systems. Several studies for solar thermal systems would be significant with the purpose of confirming the amount which the nano-fluids can increase the performance. This analysis should be led accompanied by a cost investigation of the system. Moreover, experimental and theoretical investigates are required for analyzing the effects of applying nano-fluids in dissimilar solar systems. The interface between the dissimilar nano-fluids factors and characteristics, for example, particles shape, volume fraction, thermal absorptivity, thermal conductivity, particles size, etc., is essential to be considered.

Acknowledgment

The authors would like to thanks IEST-Shibpur and OmDayal Group of Institutions, Uluberia, Howrah.

References

1. X. Ju, C. Xu, Z. Liao et al., "A review of concentrated photovoltaic-thermal (CPVT) hybrid solar systems with waste heat recovery (WHR)," *Scientific Bulletin*, vol. 62, no. 20, pp. 1388–1426, 2017.

2. T. M. Sathe and A. S. Dhoble, "A review on recent advancements in photovoltaic thermal techniques," *Renewable and Sustainable Energy Reviews*, vol. 76, pp. 645–672, 2017.
3. S. K. Das, S. U. S. Choi, and H. E. Patel, "Heat transfer in nanofluids—a review," *Heat Transfer Engineering*, vol. 27, no. 10, pp. 3–19, 2006.
4. K. V. Wong and O. De Leon, "Applications of nanofluids: current and future," *Advances in Mechanical Engineering*, vol. 2, Article ID 519659, 2010.
5. E. Bellos, Z. Said, and C. Tzivanidis, "The use of nanofluids in solar concentrating technologies: a comprehensive review," *Journal of Cleaner Production*, vol. 196, pp. 84–99, 2018.
6. F. Yazdanifard, M. Ameri, and E. Ebrahimnia-Bajestan, "Performance of nanofluid-based photovoltaic/thermal systems: a review," *Renewable and Sustainable Energy Reviews*, vol. 76, pp. 323–352, 2017.
7. V. Trisaksri and S. Wongwises, "Critical review of heat transfer characteristics of nanofluids," *Renewable and Sustainable Energy Reviews*, vol. 11, no. 3, pp. 512–523, 2007.
8. I. M. Mahbubul, "Preparation of nanofluid," in *Preparation, Characterization, Properties and Application of Nanofluid*, W. Andrew, Ed., p. 374, Elsevier Inc., 2019.
9. N. E. Hjerrild, S. Mesgari, F. Crisostomo, J. A. Scott, R. Amal, and R. A. Taylor, "Hybrid PV/T enhancement using selectively absorbing Ag-SiO₂/carbon nanofluids," *Solar Energy Materials & Solar Cells*, vol. 147, pp. 281–287, 2016.
10. I. M. Mahbubul, E. B. Elcioglu, R. Saidur, and M. A. Amalina, "Optimization of ultrasonication period for better dispersion and stability of TiO₂–water nanofluid," *Ultrasonics Sonochemistry*, vol. 37, pp. 360–367, 2017.
11. H. Chang, C. S. Jwo, P. S. Fan, and S. H. Pai, "Process optimization and material properties for nanofluid manufacturing," *International Journal of Advanced Manufacturing Technology*, vol. 34, no. 3-4, pp. 300–306, 2007.
12. H. A. Mohammed, A. A. Al-Aswadi, N. H. Shuaib, and R. Saidur, "Convective heat transfer and fluid flow study over a step using nanofluids: a review," *Renewable and Sustainable Energy Reviews*, vol. 15, no. 6, pp. 2921–2939, 2011.
13. S. Hassani, R. A. Taylor, S. Mekhilef, and R. Saidur, "A cascade nanofluid-based PV/T system with optimized optical and thermal properties," *Energy*, vol. 112, pp. 963–975, 2016.
14. K. Rahbar, A. Riasi, H. Khatam Bolouri Sangjoei, and N. Razmjoo, "Heat recovery of nano-fluid based concentrating photovoltaic thermal (CPV/T) collector with organic Rankine cycle," *Energy Conversion and Management*, vol. 179, pp. 373–396, 2019.
15. S. Srivastava and K. S. Reddy, "Simulation studies of thermal and electrical performance of solar linear parabolic trough concentrating photovoltaic system," *Solar Energy*, vol. 149, pp. 195–213, 2017.
16. W. An, J. Wu, T. Zhu, and Q. Zhu, "Experimental investigation of a concentrating PV/T collector with Cu9S5 nanofluid spectral splitting filter," *Applied Energy*, vol. 184, pp. 197–206, 2016.
17. M. Sardarabadi and M. Passandideh-Fard, "Experimental and numerical study of metal-oxides/water nanofluids as coolant in photovoltaic thermal systems (PVT)," *Solar Energy Materials & Solar Cells*, vol. 157, pp. 533–542, 2016.
18. S. Iranmanesh, H. C. Ong, B. C. Ang, E. Sadeghinezhad, A. Esmaeilzadeh, and M. Mehrali, "Thermal performance enhancement of an evacuated tube solar collector using graphene nanoplatelets nanofluid," *Journal of Cleaner Production*, vol. 162, pp. 121–129, 2017.
19. S. K. Verma, A. K. Tiwari, S. Tiwari, and D. S. Chauhan, "Performance analysis of hybrid nanofluids in flat plate solar collector as an advanced working fluid," *Solar Energy*, vol. 167, pp. 231–241, 2018.
20. A. H. A. Al-Waeli, K. Sopian, M. T. Chaichan, H. A. Kazem, H. A. Hasan, and A. N. Al-Shamani, "An experimental investigation of SiC nanofluid as a base-fluid for a photovoltaic thermal PV/T system," *Energy Conversion and Management*, vol. 142, pp. 547–558, 2017.
21. S. Lee, S. U. S. Choi, S. Li, and J. A. Eastman, "Measuring thermal conductivity of fluids containing oxide nanoparticles," *Journal of Heat transfer*, vol. 121, no. 2, p. 280, 1999.
22. S. S. Chougule, A. T. Pise, and P. A. Madane, "Performance of nanofluid-charged solar water heater by solar tracking system," in *IEEE-international conference on advances in engineering, science and management*, pp. 247–253, India, 2012.
23. S. K. Verma, A. K. Tiwari, S. Tiwari, and D. S. Chauhan, "Performance analysis of hybrid nanofluids in flat plate solar collector as an advanced working fluid," *Solar Energy*, vol. 167, pp. 231–241, 2018.

24. E. Bellos and C. Tzivanidis, "Investigation of a nanofluid-based concentrating thermal photovoltaic with a parabolic reflector," *Energy Conversion and Management*, vol. 180, pp. 171–182, 2019.
25. W. Kang, Y. Shin, and H. Cho, "Economic analysis of flat-plate and U-tube solar collectors using an Al_2O_3 nanofluid," *Energies*, vol. 10, no. 11, p. 1911, 2017.
26. H. Xie, J. Wang, T. Xi, Y. Liu, and F. Ai, "Dependence of the thermal conductivity of nanoparticle-fluid mixture on the base fluid," *Journal of Materials Science Letters*, vol. 21, no. 19, pp. 1469–1471, 2002.
27. O. Rejeb, M. Sardarabadi, C. Ménézo, M. Passandideh-Fard, M. H. Dhaou, and A. Jemni, "Numerical and model validation of uncovered nanofluid sheet and tube type photovoltaic thermal solar system," *Energy Conversion and Management*, vol. 110, pp. 367–377, 2016.
28. E. V. Timofeeva, J. L. Routbort, and D. Singh, "Particle shape effects on thermophysical properties of alumina nanofluids," *Journal of Applied Physics*, vol. 106, no. 1, article 014304, 2009.
29. S. M. S. Murshed, K. C. Leong, and C. Yang, "Enhanced thermal conductivity of TiO_2 — water based nanofluids," *International Journal of Thermal Sciences*, vol. 44, no. 4, pp. 367–373, 2005.
30. H. Xie, J. Wang, T. Xi, Y. Liu, and F. Ai, "Dependence of the thermal conductivity of nanoparticle-fluid mixture on the base fluid," *Journal of Materials Science Letters*, vol. 21, no. 19, pp. 1469–1471, 2002.

An Implementation of Failure Mode and Effect Analysis (FMEA) in a Fibre Industry for Loss Reduction

Mayank Jatwa, VK Sukhwani

1 Introduction

Every industry's main objective is to reduce losses and getting profit. With the rapid increase of industries in the market the competitive environment developed. This development pushes the industries to reduce their losses or try eliminate the waste as minimum as possible and implement the strategies and innovative methods to which the waste could minimize. In fibre industry, cellulose sheet is the main raw material in the manufacturing process of fibre (staple fibre). The cellulose pulp is processed by hard wood with the help of chemical like sodium hydroxide, Sulphur dioxide etc. [1]. FMEA method used to fetch and detect the probable failure modes of the particular process [2].

On the basis of background of the industry we planned research focusing to explore the governing cause of failure in the quantity & quality of cellulose sheet by using FMEA. The output of the study as able to judge the most dominate factor as the cause of losses in the cellulose sheet. Then, offered improvement suggestions to eliminate the cellulose sheet losses in the industry.

2 Literature Review

Failure mode and effect analysis (FMEA) is a procedure to prevent and detect as many as failure modes. FMEA helps to find the root causes of quality issues [3]. A failure mode includes failure of design, conditions beyond the limits or changes in the product that disrupts the function of production line. FMEA can be done by evaluating the potential failure of the product or eliminate the chance of failure by recording the observation [4]. The following steps are identified for implementing the process of FMEA [5].

- a. Functions of business process
- b. Potential failures modes
- c. Potential failures effects
- d. Causes of failure
- e. Modes of detection
- f. Calculate the rating of severity, occurrence, detection and RPN (Risk Priority Number)
- g. Rectification in industry

To calculate the value of severity, occurrence and detections as follows [6][7].

1. Severity value:
Severity value calculates how much impact or intensity of the incident will affect to the final outcome in the process because one failure mode subsequently affects another activity. The impact factor on the rating scale ranges from 1 to 10 shown in table 1.
2. Occurrence value:
The possibility of occurrence which leads to the major cause of the failures happened and during the running process of industry. To identify the value occurrence, look at the table 2.
3. Detection value:
Detection functions as a preventing potential failure during the process of research and reduce the failure level in the industry. Detection rate can be seen in table 3.

M. Jatwa*, V.K. Sukhwani

Master of Engineering, Industrial Engineering & Management, Department of Mechanical Engineering, Ujjain Engineering College, India 456010

Table 1. Severity Value

Representation	Scale	Example
None	1	No effect on quality
Very small	2	Cellulose sheet quality not change
small	3	Little change in quality
Very low	4	Cellulose sheet small impaired
Low	5	Dissatisfaction on the quality of cellulose sheet
Moderate	6	Failure cause trouble
High	7	Cellulose sheet quality unsatisfactory
Very high	8	Cellulose sheet quality very unsatisfactory
Hazardous alarm	9	Potential failure cause bad effect on cellulose sheet
Hazardous no alarm	10	Failure mode effect is fatal to the quality of cellulose sheet

Table 2. Occurrence value

Representation	Scale	Example
Never	1	No history of failure
Rarely	2	Failure is rare
Very little	3	Possibility of failure is very little
Little	4	Cellulose sheet suffered minor irritancy
Low	5	Some of the possible failure
Moderate	6	Possibility of failure occurs
Quite High	7	Possibility of failure is high enough
High	8	High number of failures
Very high	9	Extremely high possibility of failure
Almost certain	10	Failure is almost certain

Table 3. Detection value

Representation	Scale	Example
Almost certain	1	Detected conformed
Very high	2	Detected mostly
High	3	Chances of detection is greater
Moderate high	4	Detection may be sufficiently high
Moderate	5	Detection may be moderate
Low	6	Detection may be low
Very low	7	Dependency of very low juncture to detect
Distant	8	Possessed very little opportunities to detect
Very Distant	9	Might no detects
Impossible	10	Merely no detects

3 Methodology

This study was able to determine the most major activity as the cause of losses of cellulose sheet. Data collection methods that used are interviews, group discussion. Observations are carried out to observe the process of cellulose sheet supply chain activities, orderings process in the industry and the needs of quality of cellulose sheet that must be met up to supplier's specifications of cellulose sheet quality. Its specifications were obtained by quality control department. Follow up with the interviews were conducted to identify the cause of the failure to the losses in the cellulose sheet as well as to get an assessment of the five respondents and group discussion who have been determined. The research process to solve the problem was represented by diagram in figure 1.

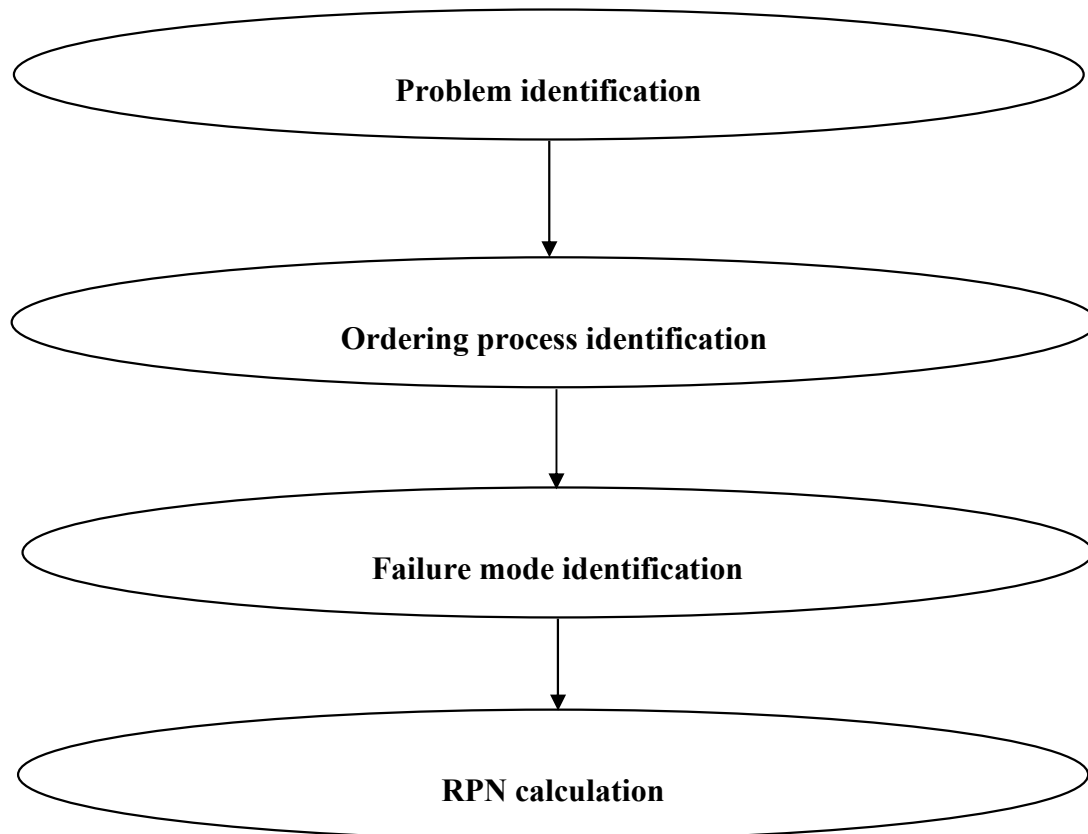


Fig. 1. Research Process

3 Results and Conclusions

The identification of failure modes conducted the experts. The researches determine five experts who are from procurement department of the industry. Estimates of the severity, occurrence and detection of failure modes are inoculated with the five experts that are shown below in the table. After that, the expert will estimate the risk priority number (RPN). This value determines the cause of the most cardinal issues in the cellulose sheet losses. Risk Priority Number (RPN) value calculations are conducted with help of interviews and group decision. The results of the evaluation are based on the table below can be seen the 10 different types failure modes of risk priority number (RPN) value and the potential failures are ranked accordingly.

The results depict the following losses which will help the industry to cater the problems of cellulose fibre sheet losses:

- The ware housing facility should be increased
- Proper management plan for the storage to sheets for avoidance water and rotten spoilage
- Alternation of the layout of storage facilities for reduction for the drainage of the sheets.

The above advice for the industry to reduce the losses in the plant and increase the profitability of the industry.

Components	Severity					Occurrence					Detection					RPN					Average RPN	Ranking
	1	2	3	4	5	1	2	3	4	5	1	2	3	4	5	RPN1	RPN2	RPN3	RPN4	RPN5		
Sheet spoilage	8	5	7	7	8	9	7	8	6	4	6	4	7	7	8	432	140	382	294	256	300.8	3 rd
Unfavourable quality	9	5	8	4	8	5	7	8	8	4	5	4	5	2	7	225	140	320	64	224	194.6	5 th
Unloading location	6	6	5	7	7	3	4	5	6	4	4	3	5	4	2	72	72	125	168	56	98.5	10 th
Wet sheets	7	6	9	8	8	4	5	4	7	4	4	5	2	4	4	112	150	72	224	128	137.5	7 th
Logistics error	4	6	3	7	8	2	5	3	7	6	6	7	8	7	8	48	210	72	343	384	211.4	4 th
Sample test	8	7	4	8	5	7	7	2	4	5	4	4	5	3	4	224	196	40	96	100	131.2	8 th
Human Inspection	7	8	8	6	8	5	4	3	5	5	5	7	6	7	4	175	224	144	210	160	182.6	6 th
Storage area	9	9	8	7	8	7	8	9	8	8	8	7	5	7	5	504	504	360	392	320	416	1 st
Drainage stockpiling	9	8	7	8	8	8	7	7	8	6	8	5	6	6	7	576	280	294	384	336	374	2 nd
Spilling sheets at loading	3	4	3	5	4	5	5	4	7	4	5	5	7	5	4	75	100	84	175	64	99.6	9 th

References

1. Surabhi Sengar and S. B. Singh (2012) Operational behaviour and reliability measures of viscose staple fibre plant including deliberate failures: *Int. J. of Reliability and Applications*, Vol. 13, No. 1, pp. 1-17.
2. Rastayesh, S.; Bahrebar, S.; Blaabjerg, F.; Zhou, D.; Wang, H.; Dalsgaard Sorensen, J. (2020) A System Engineering Approach Using FMEA and Bayesian Network for RiskAnalysis—A Case Study: *Sustainability*, 12, 7
3. Narayanagounder 2009 A New Approach for Prioritization of Failure Modes in Design FMEA using ANOVA *J World Academy of Sc., Eng. of Tech.*, vol 25, pp 95-98
4. V Gasperz 2002 Pedoman Implementation Program Six Sigma (*Jakarta: Gramedia Pustaka Utama*)
5. Mikulak JE, McDermott R E, and Beauregard MR 1996 *The Basics of FMEA* (New York: Productivity Press)
6. Prajapati D R 2012 Implementation of Failure Mode and Effect Analysis: A Literature Review *Int. J. Of Management, IT and Engineering IJMIE Vol.2 Issue 7* ISSN: 2249-0558 pp 264-292.
7. Stamatis, D.H. (2003) Failure Mode and Effect Analysis FMEA from Theory to Execution, 2nd ed.; *ASQ Quality Press: Milwaukee, WI, USA*, ISBN 0-87389-598-3.

Analysis of Tribological behaviour of Epoxy based Chopped Carbon Fiber Composite using Taguchi Technique

Dharmendra Kumar Madhukar, Nipu Modak, Pujan Sarkar

1 Introduction

The material designing today is shifted from monolithic to composite materials because of various characteristics like weight reduction, low cost, better quality, corrosion resistance and good performance in structural materials [1]. The rapid progress in applications and industries created a distinction between the demands of available materials and advanced applications. Thus, it becomes important for developing new materials with upgrade properties to fulfill the requirements. Composite materials have great prospective as a substitute product for metal-based ones as Polymer-based composites require less maintenance, low cost, have good tribological properties, and possess longer durability compared to traditional material. Engineering or natural materials comprised of two or more components with diverse physical or chemical characteristics and possessing a superior outcome are referred to as composites. The composites properties are governed by the properties of the fiber likely to reinforce it. Composite substances are extensively used in present-day engineering fields, i.e. marine industries, automotive industries, aerospace industries, defense, drilling and biomedical because of their appealing properties because of high specific strength, high resistance to corrosion, high specific modulus and low weight [2-3]. The kind of fibers, resin used, fiber weight/volume percent, fiber orientation, and other parameters all have an impact on mechanical and tribological properties of composite materials. Various fibers like carbon fiber, Kevlar fiber, glass fiber, cellulose fiber, etc., have been used to examine the effect on both mechanical and tribological Characterization [4-7]. Many investigations of the mechanical, friction, and wear properties of fiber-epoxy composites have been undertaken, and it has been revealed that employees of polymeric materials are immobile owing to weak mechanical qualities and a lack of wear resistance [8].

Carbon fiber is one among the foremost useful reinforcement materials in composites and its major usage in manufacturing of the components of automotive, aerospace industries and many more due to the unique feature like low density, lightweight, high strength, high hardness and high modulus [9]. The usage of Nanofillers in epoxy composites increases applications in the construction industry sector like floorings and airport runway that is repaired as a protective coating against severe wear. Nanofillers in epoxy composites are increasingly being used in the construction sector, such as in the restoration of airport runways and flooring as a protective layer against high wear. Furthermore, epoxy's mix of characteristics permits it to be used in polymer-based heavily loaded sliding bearings. [10]. Many kinds of research stated that the component made up of carbon fiber reinforced epoxy composites shows high efficiency when compared to steel material because of good machinability, high specific strength, high damping ratio, and lightweight [11].

Many researchers stated that mechanical and erosion wear behaviour of polymer composites is highly affected by several parameters such as fiber loading, orientation, length, concentration, sliding distance, sliding speed, fiber geometry, angle of impingement, and particles shapes and, if any, inconsistent will affect the material loss rate [8, 11-16]. In light of these issues, this study used an abrasive disc/wheel experimental setup to optimize the impact of parameters including loads, sliding velocity(speed), and fiber quantity on the wear behaviour of carbon fiber reinforced epoxy composites [17, 18]. Taguchi's experimental procedures are commonly employed to modify the wear behaviour of various composites, and ANOVA is utilized to analyze the results [19-21].

2 Material and Fabrication

Chopped carbon fiber (fig. 1) is used as reinforcement, while epoxy LY556 with hardener HY-951 is used as the matrix material in this study. To initiate appropriate mixing and exothermic reaction, Araldite LY556 epoxy was mixed with HY951 hardener in a 10:1 proportion (fig. 2), and starred for about twenty minutes. Fabrication is done with the hand layup method in different contents of fiber reinforcement. A Mild steel mold (fig. 3) of dimension (180 mm x 120 mm x 10 mm) is used. The interior side of the mold is coated with a micron-thick tear-resistant plastic sheet [22].



Fig. 1 Chopped Carbon Fiber



Fig. 2 Araldite LY556 + HY951 hardener (10:1 ratio)



Fig. 3 Fabrication of Chopped CFREC

Table 1. Details of composite sample

Test Piece	Matrix	Reinforcement
TP- 1	70%	30%
TP- 2	60%	40%
TP- 3	50%	50%

Epoxy (resin and hardener) is lapped on the chopped fibers uniformly. The full assembly is squeezed in a hydraulic press (30 kg) and kept at room temperature for 20 (twenty) hours to allow the surplus resin to eliminate the entrapped air bubbles. Post-curing is performed at ambient temperature for 30 hours after de-molding to achieve the production process [23]. The specific of composites fabricated are shown in table 1.

The principal objective of this research is to use the ANOVA technique to find the most significant parameter by examining at the influence of process variables (loads, speed of the slide, and content of Fiber) mostly on wear and friction behaviour of carbon fiber epoxy composites.

3 Result and Analysis

Taguchi technique is one of the most widely used for improving the efficiency of various mechanical processes [24]. Three different parameters were used in the dry sliding wear tests: Normal load (20N, 30N and 40N), Sliding Speed (0.6m/s, 0.8m/s, and 1 m/s), and proportion of fiber (30 wt. %, 40 wt. % and 50 wt. %). The L9 orthogonal array was chosen with the understanding that the DF of the orthogonal array must be greater than or equal to the total wear criterion [25]. The wear rate and COF were the response variables to be investigated [26]. The tests were carried out according to the run sequence of the Taguchi model, and thus the results obtained.

The experimental data was analyzed using the MINITAB 18 programme, which is especially built for the analyses of experimental data and transformed to signal-to-noise ratios (S/N) [27, 28]. In the existence of noise, the S/N ratio determines how predictable a product or process is. The greatest S/N ratio process parameter settings always produce the best quality with the least variation. The following is the S/N ratio for wear rate and coefficient of friction utilizing "smaller is better" characteristics, which may be computed using a logarithmic conversion of the gradient descent:

$$S/N = -10 \log \left[\frac{1}{t \sum_{i=1}^t R_i^2} \right] \quad (1)$$

Table 2. L9 Orthogonal Array CFREC

F_L (in N)	V (in m/sec)	F_{bC} (in wt. %)	W_r (in mm³/m)	SNRA (W_r)	COF	SNRA (COF)
20	0.6	30	0.00332	49.57724	0.54164	5.325785
20	0.8	40	0.00274	51.24499	0.63813	3.901817
20	1	50	0.00364	48.77797	0.62216	4.121958
30	0.6	40	0.00509	45.86564	0.635	3.944525
30	0.8	50	0.00539	45.36822	0.61214	4.262985
30	1	30	0.00424	47.45268	0.65613	3.660202
40	0.6	50	0.00669	43.49148	0.67912	3.36107
40	0.8	30	0.00781	42.14698	0.72367	2.809189
40	1	40	0.00853	41.38102	0.7459	2.546388

Table 2 demonstrates that the second experiment and the first experiment, respectively, have the best wear rate and friction coefficient. These trials yielded the highest S/N ratios. The difference between the greatest and lowest values of the average of S/N ratios was used to identify the most influential control parameter [29]. The effect of the control parameter becomes stronger as the difference in average S/N ratios grows.

Tables 3 and 4 demonstrate the ordering of parameters in the response table for wear rate and friction coefficient using signal - to - noise ratio obtained at various attribute [30]. With the aid of this table, we can quickly visualize the influence of numerous circumstances. The table provides rankings based on delta stats, primarily compare effect magnitudes.

Minitab assigns rankings based on delta values, with rank one being the greatest delta value, rank two representing the second highest, and so on. According to Tables 3 and 4, the most important factor in determining the wear rate and coefficient of friction is load.

Table 3. Table Of Response For S/N Ratio for Wear Rate

Level	F _L (in N)	V(in m/sec)	F _{bc} (wt. %)
1	49.87	46.31	46.39
2	46.23	46.25	46.16
3	42.34	45.87	45.88
Delta	7.53	0.44	0.51
Rank	1	3	2

Table 4. Table Of Response For S/N Ratio For COF

Level	F _L (in N)	V(in m/sec)	F _{bc} (wt. %)
1	4.45	4.21	3.932
2	3.96	3.658	3.464
3	2.91	3.443	3.915
Delta	1.54	0.768	0.467
Rank	1	2	3

5.1 Analysis of Variance

Using analysis of variance, the influence of wear factors such sliding velocity/ speed, force/ load applied, and fiber weight percent on tribological parameters like wear and coefficient of friction is examined. These analyses were conducted using a ten percent level of significance and a ninety percent degree of confidentiality.

Table 5 reveals that the most important element determining wear rate is load (91.57 percent). The wear rate is basically unaffected by sliding speed or carbon fiber weight percent. The load applied (68.66 percent) is the most relevant component, followed by sliding velocity (17.308 percent) and carbon fiber weight percentage (7.77 percent), as per the analysis of variance for friction coefficient in Tables 6.

Table 5. ANOVA for Wear Rate

Source	DF	Seq SS	Adj SS	Adj MS	Int. F	P (%)
F _L (in N)	2	85.013	85.013	42.507	12.0054	91.57
V(in m/sec)	2	0.3443	0.3443	0.1722	0.0484	0.3708
F _{bc} (wt. %)	2	0.3965	0.3965	0.1982	0.0559	0.427
R. E.	2	7.0812	7.0812	3.5406		
Total	8	92.835				

Table 6. Anova for Cof

Source	DF	Seq SS	Adj SS	Adj MS	Int. F	P (%)
F _L (in N)	2	3.7321	3.7321	1.8661	10.986	68.66
V(in m/sec)	2	0.9407	0.9407	0.4704	2.769	17.308
F _{bc} (wt. %)	2	0.4223	0.4223	0.2111	1.243	7.77
R. E.	2	0.3397	0.3397	0.1699		
Total	8	5.4349				

Figure 4 shows, a response diagram for S/N ratio (principal effects plot), that visually depicts the effect of control settings on composite wear rate. The combination of elements that provide the lowest composite wear rate is determined by the examination of the data. Figure 1 shows that a combination of 40 N applied load (A₃), 50 wt% fiber content (C₃), and 1m/sec sliding speed (B₃) results in the lowest wear rate. Whereas Figure 5 shows that, a combination of 40 N applied load (A₃), 1 m/sec sliding speed (B₃) and 40 wt% fiber content (C₂) produces the lowest coefficient of friction. In addition, the major effects plot provides an estimate of the relative importance of the factors on the system response. If a factor's line is close to horizontal, it has little impact. A component with the highest inclination, on the other hand, will have the most impact.

Figures 1 & 2 illustrate that load is the key component for both wear rate and COF, with the steepest slope, followed by fiber content and sliding speed, as evidenced by the ANOVA and response table mentioned previously.

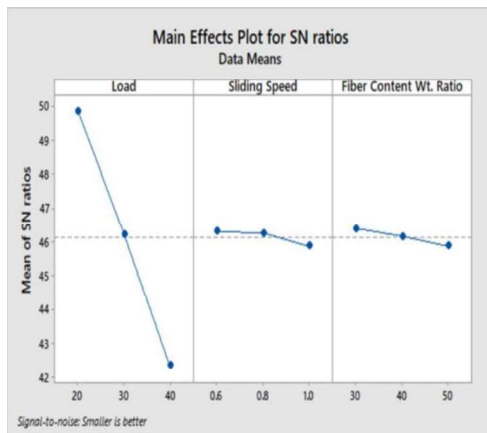


Fig. 4 Control factor's influence on wear rate

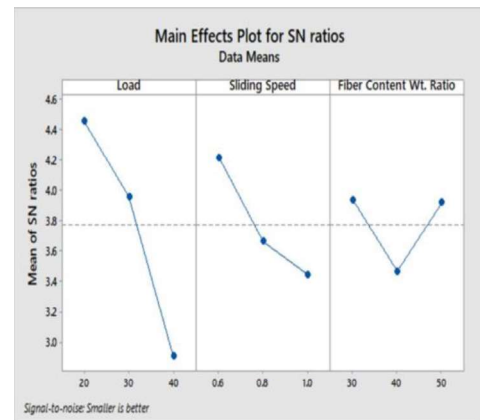


Fig. 5 Control factor's influence on COF

4 Confirmation Test

The confirmation test is the final stage in the Taguchi analysis. Taguchi analysis was performed to discover the best values of parameters in Tables 3 and 4. The confirmation tests were conducted using an arbitrary mix of variables, with $A_3B_3C_3$ representing wear rate and $A_3B_3C_2$ representing coefficient of friction. Eqs. (2) and (3) for wear rate and coefficient of friction, respectively, may be used to calculate the projected S/N ratio [31].

Table 7. Results of confirmation tests

S/N Ratio of W_r			S/N Ratio of COF		
Level A_3, B_3, C_3			Level A_3, B_3, C_2		
Predicted	Exp.	Error %	Predicted	Exp.	Error %
41.7993	44.863	6.829	2.27177	2.39175	5.016

$$\eta = \bar{T} + (\bar{A}_3 - \bar{T}) + (\bar{B}_3 - \bar{T}) + (\bar{C}_3 - \bar{T}) \quad (2)$$

$$\eta = \bar{T} + (\bar{A}_3 - \bar{T}) + (\bar{B}_3 - \bar{T}) + (\bar{C}_2 - \bar{T}) \quad (3)$$

Table 7 compares the expected wear rate and frictional force to the observed response. The difference between the actual and anticipated S/N ratio values is computed. The wear rate has a predicted error of 6.821 percent, while the friction coefficient has 5.01 percent. This demonstrates that the anticipated values are accurate.

5 Conclusion

In this work, the study's primary purpose was to fabricate the composite of CFREC. Then, tribological testing was carried out on CFREC. The Taguchi design of the experiment was used to examine the COF and dry sliding wear of CFREC under various weights and sliding speeds. It was discovered that the applied load influenced wear rate and COF by 91.57 percent and 68.66 percent, respectively. The S/N ratio was computed using the best testing parameters for wear rate and COF, and found that the anticipated and observed that the both wear rates and COF were almost identical.

References

1. Liang, X., & Wu, D. (2019), "Tribological properties of carbon-fibre-reinforced plastic against tungsten carbide under dry condition", *Tribology International*, 134, 118-128.
2. Singh, L., Ram, B. & Singh, A. (2013), "Optimization of Process Parameter for Stir Casted Aluminium Metal Matrix Composite Using Taguchi Method". *International Journal of Research in Engineering and Technology*, 02, 375-383.
3. Patil, S. D., Bhalerao, Y., & Takale, A. M. (2020), "Optimization of design variables for carbon/glass hybrid composites laminates using the Taguchi Technique", *World Journal of Engineering*, 17, 309-323.
4. He, X., Zhang, W. & Yang, R. (2017), "The characterization of DOPO/MMT nanocompound and its effect on flame retardancy of epoxy resin", *Composites Part A-applied Science and Manufacturing*, 98, 124-135.
5. Ruggiero, A., Merola, M., Carlone, P. & Archodoulaki, V. (2015), "Tribo-mechanical characterization of reinforced epoxy resin under dry and lubricated contact conditions" *Composites Part B-engineering*, 79, 595-603.
6. Xie, Y., Hill, C. A., Xiao, Z., Militz, H. & Mai, C. (2010)" Silane coupling agents used for natural fiber/polymer composites: A review", *Composites Part A-applied Science and Manufacturing*, 41, 806-819.
7. Wu, J., & Cheng, X. H. (2006) "The tribological properties of Kevlar pulp reinforced epoxy composites under dry sliding and water lubricated condition", *Wear*, 261, 1293-1297.
8. Sarkar, P., Modak, N., & Sahoo, P. K. (2018) "Mechanical and Tribological Characteristics of Aluminium Powder filled Glass Epoxy Composites". *Materials Today: Proceedings*, 5(2), 5496-5505.
9. Gupta, A., Kumar, A., Patnaik, A. & Biswas, S. (2011) "Effect of Different Parameters on Mechanical and Erosion Wear Behavior of Bamboo Fiber Reinforced Epoxy Composites", *International Journal of Polymer Science*, 2011, 1-10.
10. Masuelli, M. A. (2013), "Fiber Reinforced Polymers - The Technology Applied for Concrete Repair", IntechOpen.
11. Chauhan, S. R., Kumar, A., Singh, I. & Kumar P. (2010)," Effect of Fly Ash Content on Friction and Dry Sliding Wear Behavior of Glass Fiber Reinforced Polymer Composites - A Taguchi Approach", *Journal of Minerals and Materials Characterization and Engineering*, 09, 365-387.
12. Clark, H. M. (2002), "Particle velocity and size effects in laboratory slurry erosion measurements OR... do you know what your particles are doing", *Tribology International*, 35, 617-624.
13. Kim, J., Lee, J. J. & Lee, D. (2005)" Effect of Fiber Orientation on the Tensile Strength in Fiber-Reinforced Polymeric Composite Materials", *Key Engineering Materials*, 297-300, 2897 – 2902.
14. Ross, P. J. (1996) "Taguchi Techniques For Quality Engineering: Loss Function, Orthogonal Experiments, Parameter And Tolerance Design", 2nd Edition, McGraw-Hill, New York.
15. Peace, G.S. (1993), "Taguchi Methods: A Hand-on Approach", Addison-Wesley, Reading, MA.
16. Barbero, E. J. (2018) "Introduction to Composite Materials Design", 3rd Edition, CRC Press.
17. Moorthy, S. S., Manonmani, K. & Elangovan, T. (2015), "An Optimization Approach to the Dry Sliding Wear Behavior of Particulate Filled Glass Fiber Reinforced Hybrid Composites", *Journal of Engineered Fibers and Fabrics*, 10(2), 113-120.
18. Sarkar, P., Modak, N., & Sahoo, P. K. (2016), Reciprocating Friction and Wear Characteristics of Al Particulate Glass Epoxy Composites, *International Journal of Surface Engineering and Interdisciplinary Materials Science*, 4(1), 25-44.
19. Böger, L., Sumfleth, J., Hedemann, H. & Schulte, K. (2010), "Improvement of fatigue life by incorporation of nanoparticles in glass fibre reinforced epoxy", *Composites Part A-applied Science and Manufacturing*, 41, 1419-1424.
20. Rahman, M. M., Zainuddin, S. M., Hosur, V., Malone, J., Salam, M. B., Kumar, A. D. & Jeelani, S. A. (2012) "Improvements in mechanical and thermo-mechanical properties of e-glass/epoxy composites using amino functionalized MWCNTs", *Composite Structures*, 94, 2397-2406.
21. Seretis, G., Nitodas, S., Mimigianni, P., Kouzilos, G. N., Manolakos, D. E. & Provatidis, C. G., (2018) "On the post-curing of grapheme nanoplatelets reinforced hand lay-up glass fabric/epoxy nanocomposites" *Composites Part B-engineering*, 140, 133-138.

22. Sarkar, P., Modak, N., & Sahoo, P. K. (2017), Effect of Normal Load And Velocity on Continuous Sliding Friction and Wear Behavior of Woven Glass Fiber Reinforced Epoxy Composite, *Materials Today: Proceedings*, 4(2)(A), 3082-3092.
23. Sarkar, P., Modak, N., & Sahoo, P. K. (2018), Mechanical and Tribological Characteristics of Aluminium Powder filled Glass Epoxy Composites, *Materials Today: Proceedings* 5, pp. 5496–5505, 2018.
24. Wu, Y. & Wu, A. (2000), “Taguchi Methods for Robust Design”, ASME Press.
25. Deshpande, S. & Rangaswamy, T. (2016), "A Comparative Study on Dry Sliding Wear Characteristics of Al_2O_3 and Bone Powder Filled Hybrid Composites” *Journal of Minerals and Materials Characterization and Engineering*, 4 (2), 164-180.
26. Dharmalingam, S., Subramanian, R. and Kok, M. (2013), “Optimization of abrasive wear performance in aluminium hybrid metal matrix composites using Taguchi–grey relational analysis “, *Proceedings of the Institution of Mechanical Engineers, Part J: Journal of Engineering Tribology*, 227(7) 749–760.
27. Padhi, P.K., & Satapathy, A. (2012), “Prediction and Simulation of Erosion Wear Behavior of Glass-Epoxy Composites Filled with Blast Furnace Slag”, *Advanced Materials Research*, 585, 549 – 553.
28. Bhatia, S., Khan, S. & Angra, S.(2021), “Dry sliding wear characterization of SGM/boron carbide hybrid polymer matrix composite”, *Polymers and Polymer Composites*, 29(7), 961-970.
29. Ozsoy, N., Ozsoy, M. & Mimaroglu, A. (2017), “Taguchi Approach to Tribological Behaviour of Chopped Carbon Fiber-Reinforced Epoxy Composite Materials” *ActaPhysicaPolonica A*, 132, 846-848.
30. Radhika, N., & Subramaniam, R. (2013), "Wear behaviour of aluminium/alumina/graphite hybrid metal matrix composites using Taguchi's techniques", *Industrial Lubrication and Tribology*, 65 (3), 166-174.
31. Patnaik, A., Biswas, S. & Mahapatra, S.S. (2007), “An evolutionary approach to parameter optimisation of submerged arc welding in the hard facing process”, *International Journal Manufacturing Research*, 2(4), 462-483.

Nomenclature

CFREC	:	Carbon Fiber Epoxy Reinforced Composite
COF	:	Coefficient of Friction
DF	:	Degree of Freedom
TP	:	Test Piece
S/N	:	Signal to Noise
V	:	Sliding Speed/ Sliding Velocity (in m/sec)
W_r	:	Wear Rate (in mm^3/m)
F_L	:	Load (in N)
R. E.	:	Residual Error
F_{bc}	:	Fiber Content (in %Wt. Ratio)
t	:	number of trial/ tests
R_i	:	i^{th} experiment's response value
Exp.	:	Experimental
Adj. MS	:	Adjusted mean of squares,
Seq SS	:	Sequential sum of squares
ANOVA	:	Analysis of variance
Cont.	:	Contribution (in %)
η	:	Estimated Average
\bar{T}	:	Average of all the tests/ experiments
A_3, B_3, C_3 & C_2 :	:	Average response for variables and interactions at the chosen level

Deformation of tumor cell with variation of extracellular matrix density and cytoskeleton: cellular growth, migration behavior

Sriram Mahitha, Apurba Das*, Amit Roy Chowdhury, Pallab Datta

1 Introduction

Microtubules, intermediate filaments, and actin filaments make up the cytoskeleton and is a complex hierarchical network. From the cell nucleus to the membrane boundary, the cytoskeleton is present. The cytoskeleton is responsible for preserving cellular form and structure, supplying mechanical assistance, and assisting in cellular movement. It is the main protective element for intrinsic cellular functions [1]. Cellular integrity and functionality were affected by cytoskeleton deformation in various pathological conditions [2,3]. Different research groups have examined the impact of individual cytoskeleton components on various cellular properties [4-6]. For example, different simulation models were used to investigate the load-bearing properties of F-actins and their effect on cellular stiffness [7,8]. Furthermore, to properly understand the changes in pathological conditions, the effect of degraded cytoskeleton components on cellular elasticity under such opioid therapy has been reported. It has been found that when F-actins are disrupted, cellular elasticity drops by 2 to 6 times [9]. Mechanical properties of the cytoskeleton play the most important role in cell deformation against any type of mechanical loading. The cellular microenvironment exerts forces that change the internal equilibrium of the cell and help in the maintenance of cellular geometry and motion [10,11]. Mechanical properties of the extracellular matrix (ECM) (especially the stiffness of collagen fibers) adjacent to the malignant cells are quite different compared to the extracellular matrix adjacent to the normal cell. Numerous experiments [12] have revealed that cellular behavior differs depending on substrate stiffness, roughness, and other factors. However, in the FE models developed so far, only matrix stiffness has been taken into account and other important parameters are not considered. Several filamentous networks spread from the plasma membrane to the nuclear envelope and even the interior of the nucleus in cytoskeletal structures through specialized cell junctions that cross the plasma membrane, the cytoskeleton also helps to anchor the cell to its neighbors and the extracellular matrix. The cytoskeleton is now understood to be made up of hundreds of different (associated) proteins that work together to organize the intricate machinery that is involved in almost every structural and dynamic part of living cells, such as cell maintenance, cell movement, cell proliferation, apoptosis, cell differentiation, and cell signaling. Many cellular functions, like cell proliferation, differentiation, apoptosis, motility, signal transduction, and gene expression, are now understood to be controlled by and reliant on a mechanically intact cytoskeleton to sustain cell structure and structural integrity. The cytoskeletal structure determines cellular deformability, while force and signal signals resulting from an applied load are thought to include complex interactions among integrins, cytoskeletal components, and the nucleus. As a result, gaining a thorough understanding of mechanotransduction in disease and tissue growth requires a clear understanding of the role cytoskeletal constituents play in regulating cell mechanics. A more thorough understanding of this information necessitated the development of a basic but reliable multi-structural model to help measure cellular viscoelastic behavior and accurately describe a wide variety of experimental results. Several statistical models are used to measure the impact of the cytoskeleton on cellular intrinsic properties. Among them, a finite element model based on the mechanical reaction of the cell under various experimental parameters has been used to analyze experimental results [13].

If the models are sufficiently tested, simulation models for predicting cellular response are especially useful because real-time experiments are not always feasible for such research. Two of the most widely used simulation methods for defining the mechanical reaction of cells are the tensegrity method and finite element modeling [14]. A tensegrity model has been depicted using cytoskeleton components that have been pre-stressed [15]. The use of finite element modeling to simulate force operation in various experimental setups such as indentation, surface interactions, and so on has been commonly published [16]. By individually considering their elastic properties in the computational model, some of these studies have identified the role of individual cytoskeletal components in the overall mechanical response of cells. The strain produced inside the cell as a result of external forces (for example, AFM indentation) has also been incorporated into FEA models. The contribution of each cytoskeletal factor to the overall cell response under AFM indentation was determined in this analysis. The FEA findings were compared to the results of a parallel experimental study. AFM studies have also shown that cell elasticity changes dramatically during cancer metastasis and is linked to the degradation of cytoskeletal elements [17]. Under compression and shear (sinusoidal in nature) forces, FE models of a cell have also shown cellular responses. To simulate the experimentally observed variations in cell elasticity with cytoskeleton degradation, Katti and Katti[18] used nN level forces in the FEA technique to simulate the experimentally observed variations in cell elasticity with cytoskeleton degradation. The loading-unloading force on a cell was applied in a longitudinal direction in all nano-indentation situations, but the effect of surface roughness, which plays an important role in demonstrating cell response under mechanical loading, was not considered in this analysis. The mechanical reaction of the cell due to cyclic strains on the cytoskeleton is another significant factor ignored in current FEA models. It has been discovered that mechanical distension of the underlying surface plays a role in cell migration at injury sites [19]. Similarly, Livne et al. [20] observed cell reorientation in response to cyclic stretching of the underlying substrate, both experimentally and theoretically. Strains that form on a cell's periphery cause the cell to move in a specific direction and impair cell-cell interaction. The stress transfer in the nucleus occurs through microtubules, which then travel through the pool of cytoplasm, allowing mechanical stress to spread across the cytoplasm [21]. At 1 Hz cyclic loads, cells often align parallel to the direction of substrate stretching, and changes in shape and orientation are recorded.

The deformation pattern of malignant cells differs compared to normal cells. Finite simulation studies of this deformation pattern are limited in the open literature. It reveals that, in the existing finite element analyses related to cells under mechanical loading, the effect of cyclic loading of extracellular matrix on the cell and the deformation of tumor cells under these loads were not given proper attention. In the present study, a finite element model of 16 cells attached to an extracellular matrix has been developed and analyzed to observe the tumor cell deformation pattern under cyclic strain applied on the substrate surface with degradation of cytoskeleton along with a variation of collagen volume fraction.

2. Materials and Methods

2.1. *Different components of the proposed FE model:*

Different forms of the cytoskeleton, different sections of cytoplasm, nucleus, and membrane were described using the same types of beam, solid, and shell components throughout the development of the finite element model. The cytoskeleton network was built using the 2-noded beam portion (Fig.1). Figure 1 depicts the proposed cytoskeleton arrangement and intermediate filaments (IFs). IFs are modeled as 2-noded beam elements having a solid cylinder cross-section of diameter 10 nm. Actin filaments (AFs) are modeled as stable cylindrical cross-section beam elements with a diameter of 7 nm, as seen in Fig.1. Microtubules (MTs) (Fig. 1), which are modeled as a hollow cylindrical cross-section with an outer diameter of 25 nm and an inner diameter of 11 nm as seen in the structure. With typical nodes, the cytoskeletons are bound to other cellular organelles (Fig.2). The number of overall

elements in the tumor cell model is 7,51,577, out of which 2,20,584 are twenty node tetrahedral solid elements and the rest are 2 noded beam elements.

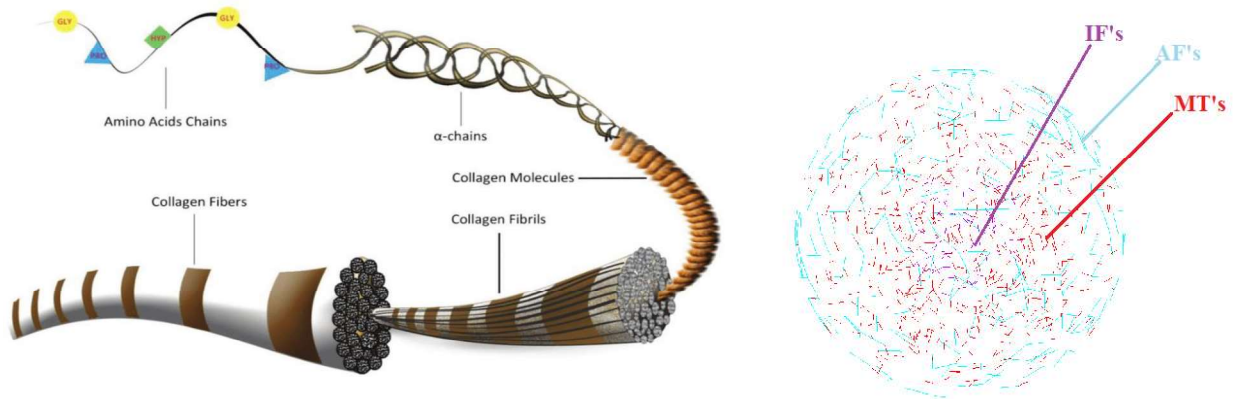


Fig. 1 Collagen fibre and Cytoskeletal arrangement (IF-Intermediate Filaments, AF-Actin Filaments, MT-Microtubules)

2.3 FE modelling:

Finite element (FE) analysis is a quantitative scientific computational technique used to simulate mechanics and biophysics at different scales. With FE models, one can define loads and boundary conditions applied to a structure with defined material properties. FE analysis has been applied with success to modeling and determining the strain distributions within tissues and organs, including studies of mechano-transduction to predict fracture healing in bone. Some FE models also include the non-homogeneous property of the cell, as the cells are very dynamic in terms of material property and structure. FE analysis has been used to model single cell structural mechanics: the idea that the cortical membrane that surrounds the cytoplasm of the cell was the main component responsible for cell structural stability, led to simple homogeneous models for cell mechanics.

A tumor of 16 cells (4cell divisions) is modeled using ANSYS APDL. The elastic properties of the cellular components used in the present study are shown in Table 1. In the FE model, the tumor is surrounded by an extracellular matrix and is considered as a cube of dimension 60,000 μm , consisting of blood and collagen fibers (Figure 1(b)) meshed as tetrahedral and beam elements respectively in ANSYS APDL. The collagen fiber density is high near the tumor cell and it decreases up to 60% away from the tumor-affected cell. The entire model is shown in Figures 2a to 2d. The model is prepared in HP Z640 workstation (3.20 GHz, 8-core processors, 64GB RAM total 2400 MHz memory) using ANSYS APDL software.

Table 1. Material properties for FE analysis

Component	Young's Modulus (E)	Poisson's Ratio	Yield	Ref.
Cytoplasm	0.25KPa	0.49	2%	[22]
Microtubule	2GPa	0.3	60%	[23]
Actin filament	1GPa	0.3	20%	[23]
Intermediate filament	1GPa	0.3	20%	[23]
Nucleus	1KPa	0.3	-	[24]
Collagen fiber	1.2GPa	0.3	-	
Blood	66.7GPa	0.48	-	

The presence of tumor cells can degrade the stiffness of the cells up to 70% compared to normal cells. In reality stiffness of the malignant cells decreases due to the decrease of stiffness of entire cell

elements, but assumptions are made to degrade the cytoskeletal stiffness only. 4 different percentages of degradation of cytoskeletal material properties are considered. In the present model cytoskeletal material properties are 82.5%, 65%, 47.5%, and 30% of normal cells are considered for modeling of the malignant cell with reduced stiffness.

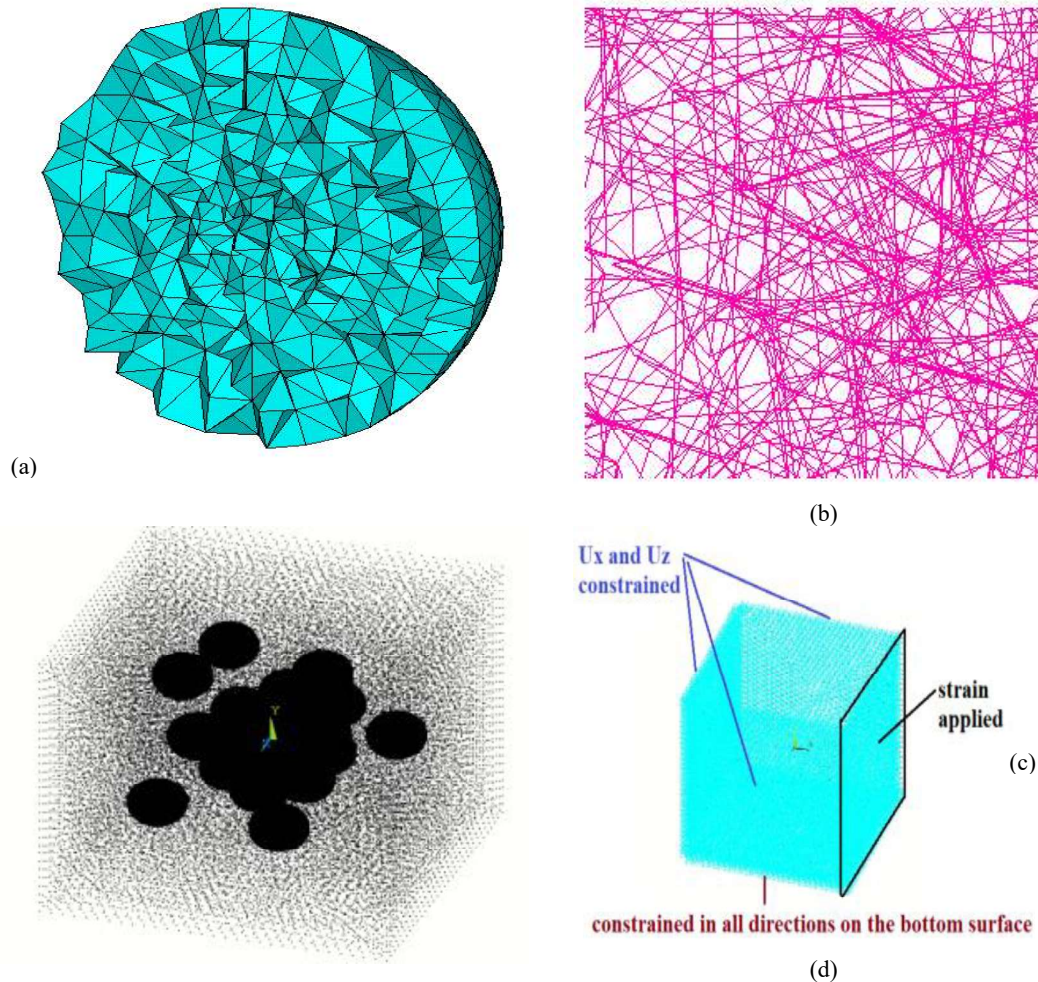


Fig. 2 (a) Cytoplasm surrounded by Cell membrane (b) Collagen Fibers (c) Entire model represented by the nodes (d) Boundary conditions of the surface nodes

2.3 Loading condition:

Loads are one of the inputs which need to be provided on FE models [25]. An external strain of 0.001 to 0.01 varies in 4 cycles and is applied on a full model. Figure 2d shows the applied strain on nodes corresponding to one of the vertical sides of the cube with the nodes corresponding to bottom horizontal nodes as fixed nodes. A ramped strain with a minimum value of 0.001 in 0.1sec and the maximum value was applied in 10sec. The unloading process occurred in between 10 sec to 20sec. 4 complete cycles for 80 sec of this loading and unloading process were applied on the cell model. Therefore, a total of 4 loading and unloading cycles will process. Figure 7 represents the Time vs Strain plot.

different collagen radii of 75nm,100nm,125nm,150nm are considered for the present analysis. The cytoskeleton mechanical properties in terms of percentage are varied and the variation of the collagen volume fraction is shown in table 3.

Table 3. Percentage of cytoskeleton mechanical properties with Collagen Volume Fraction

Sl No	Collagen Volume Fraction	Percentage of cytoskeleton mechanical properties (in %)
1	0.015	100
2	0.04875	82.5
3	0.0825	65
4	0.11625	47.5
5	0.15	30

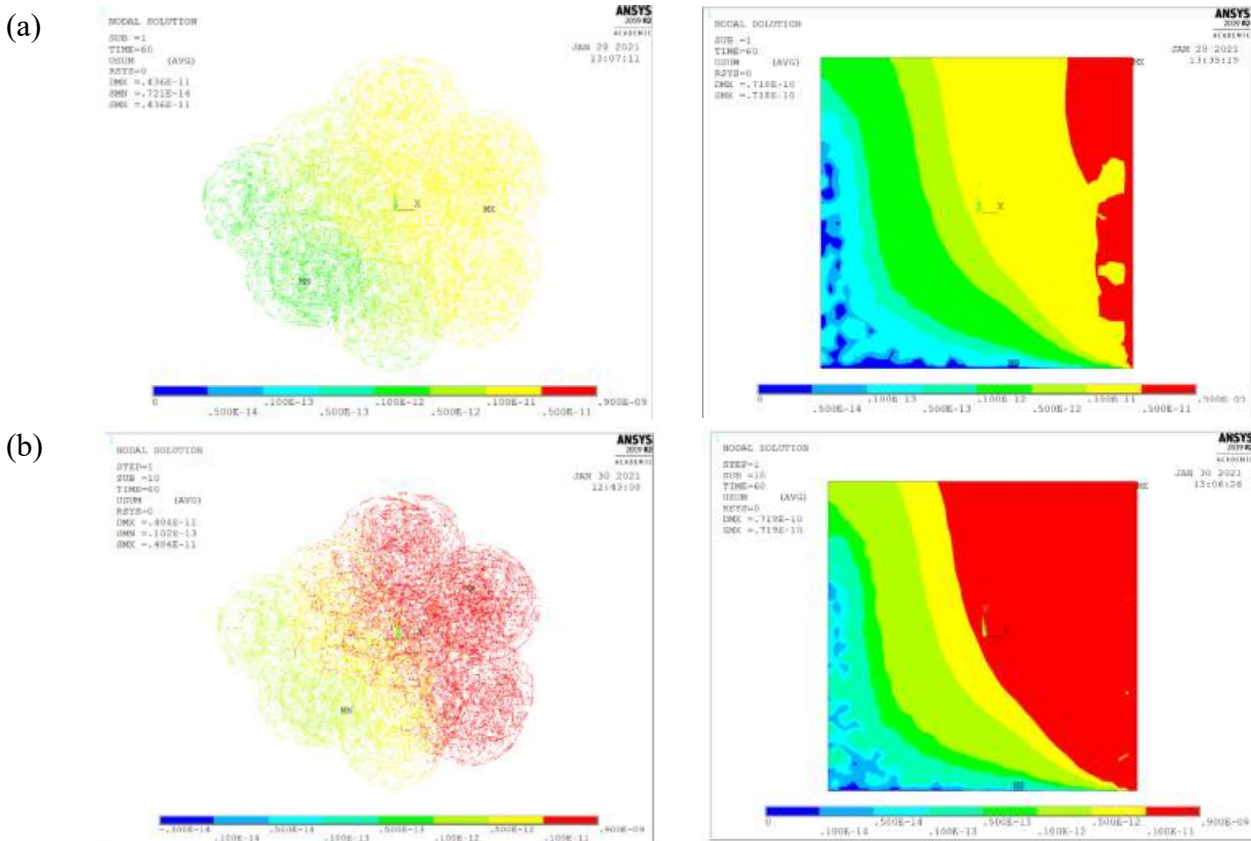
2.4 Boundary conditions:

The nodes corresponding to the other 3 vertical sides of the cube are constrained to move in horizontal i.e., X and Z directions. The nodes corresponding to the top horizontal surface of the cube are not constrained in any direction. All the nodes of the model are constrained in rotation in all directions. The cyclic strain is applied on the model on nodes corresponding to one of the vertical sides of the cube.

3. Analysis Data

3.1 Cellular response to cyclic loading

Figure 3(a) to 3(e) represents the deformation of nodes corresponding to a tumor and the entire model for collagen radius of 75nm. Figure 4(a) to 4(e) represents the deformation of nodes corresponding to a tumor and the entire model for collagen radius of 100nm. Figure 5(a) to 5(e) represents the deformation of nodes corresponding to a tumor and the entire model for collagen radius of 125nm. Figure 6(a) to 6(e) represents the deformation of nodes corresponding to a tumor and the entire model for collagen radius of 150nm.



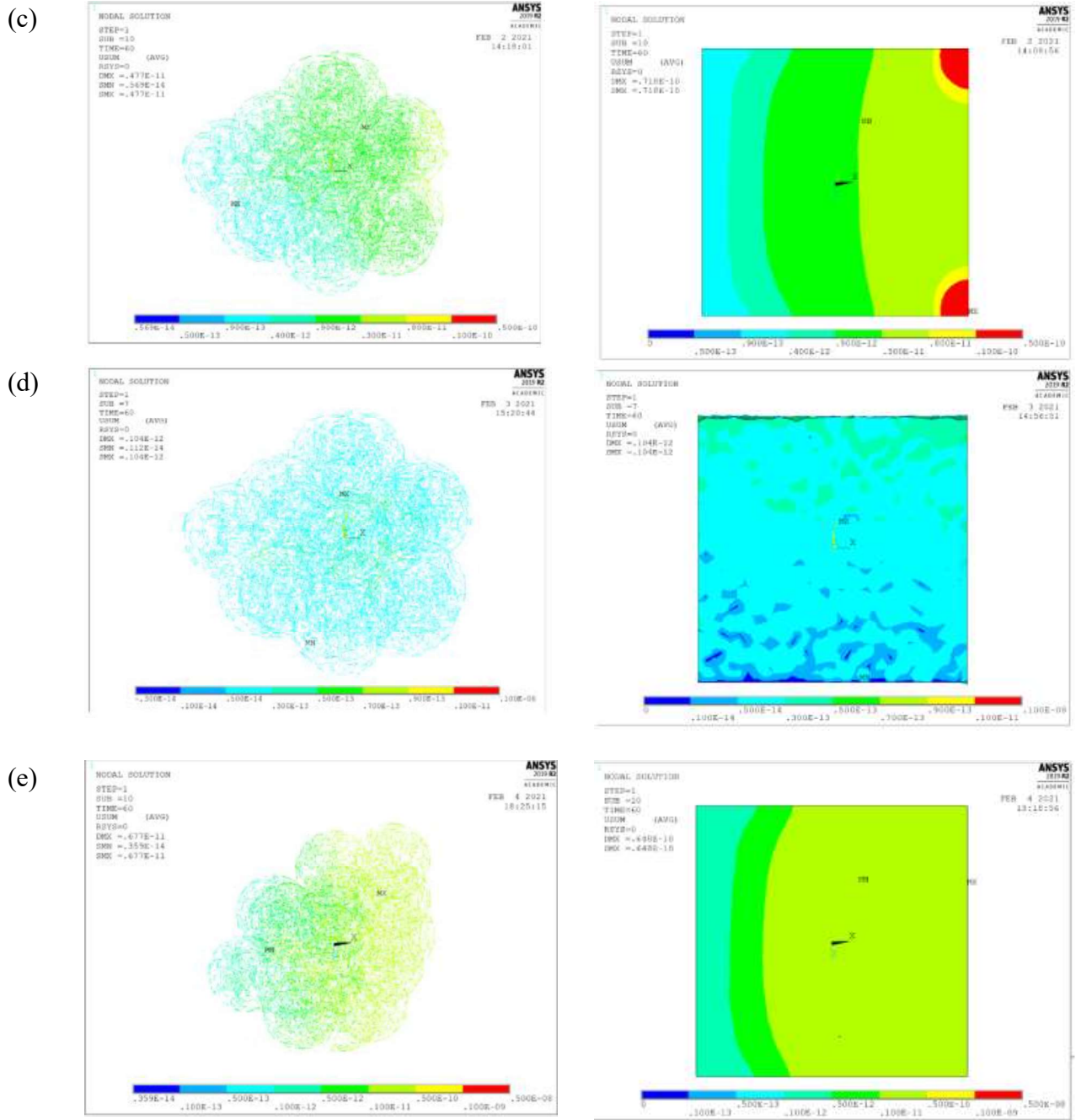
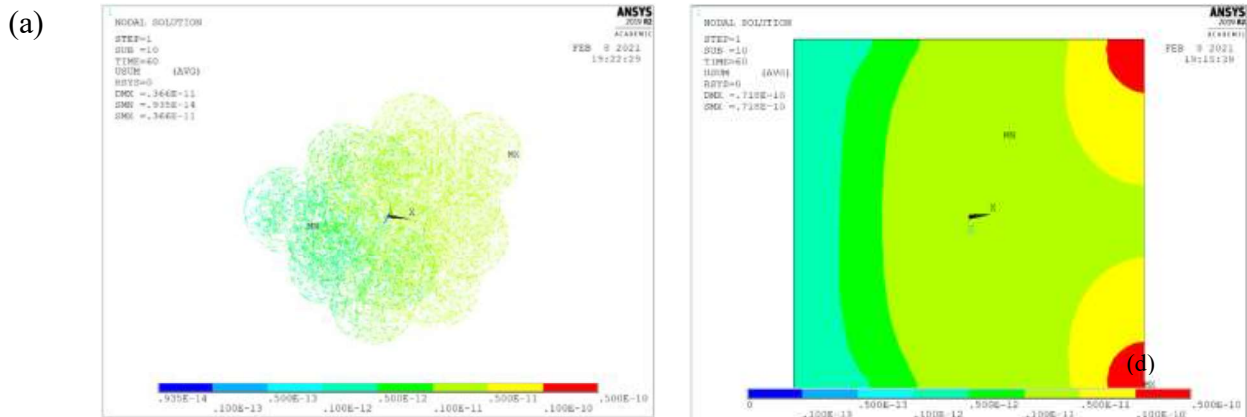


Fig. 3 Deformation of nodes corresponding to tumour and entire model for collagen radius of 75nm for collagen volume fraction of (a) 0.015 (b) 0.04875 (c) 0.0825 (d) 0.11625 (e) 0.15



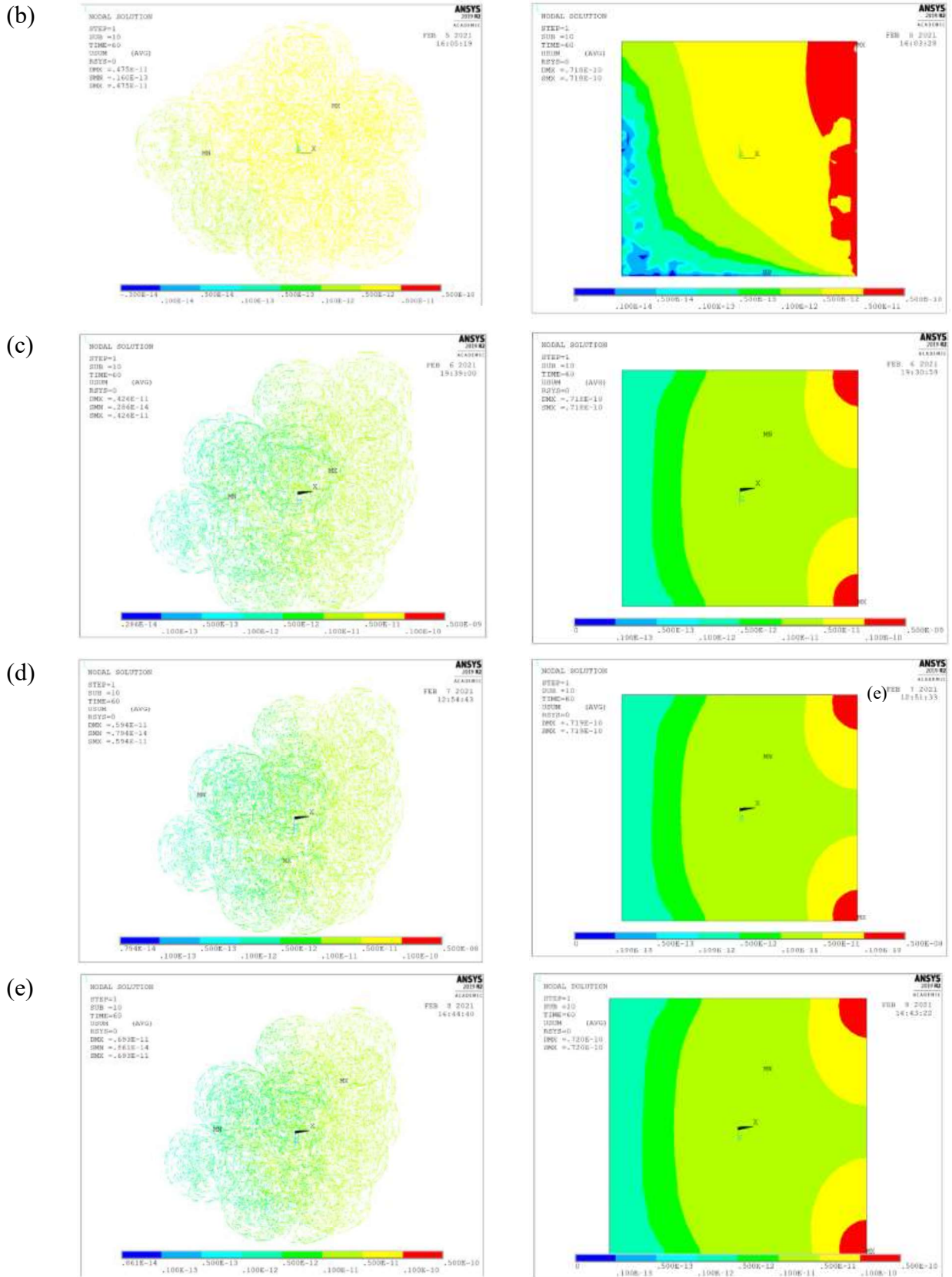
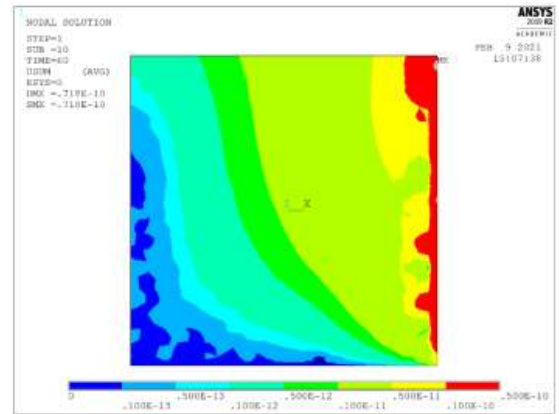
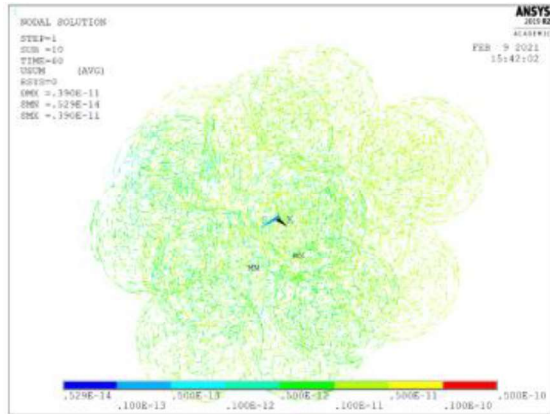
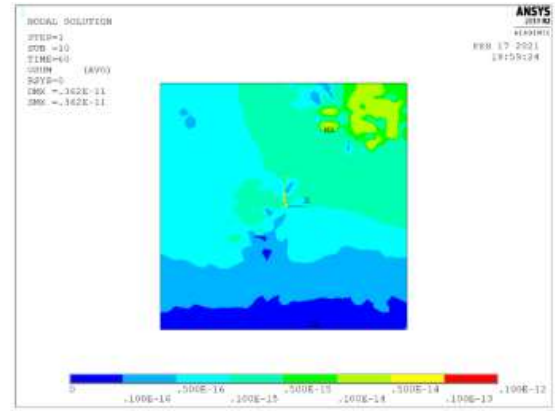
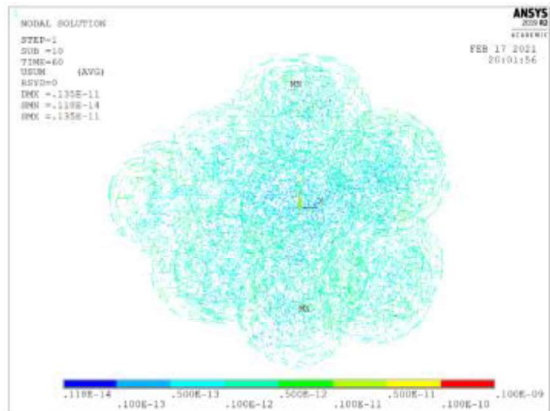


Fig 4 Deformation of nodes corresponding to tumour and entire model for collagen radius of 100nm for collagen volume fraction of (a) 0.015 (b) 0.04875 (c) 0.0825 (d) 0.11625 (e) 0.15

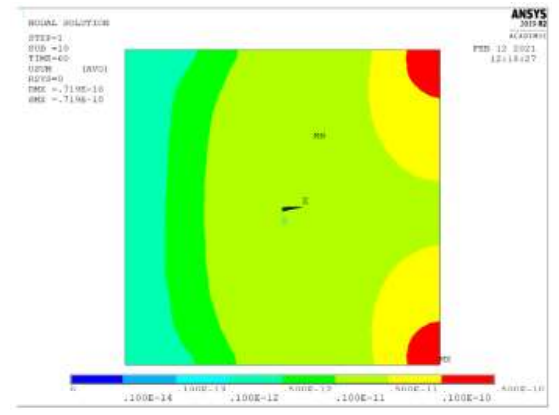
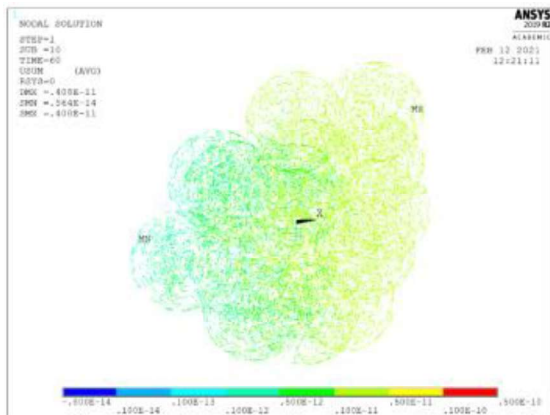
(a)



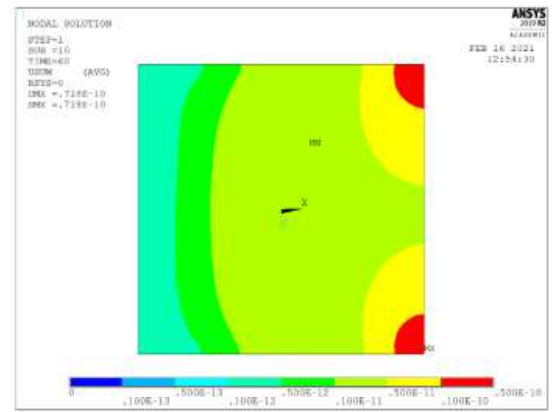
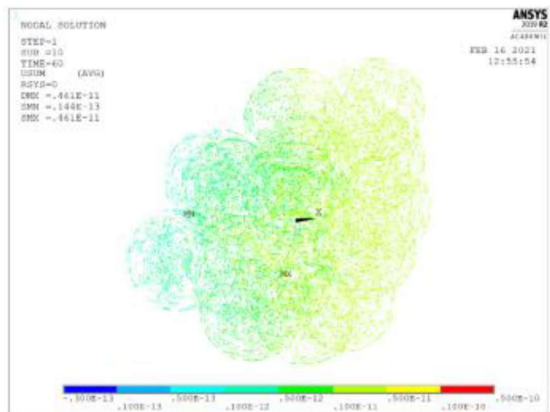
(b)



(c)



(d)



(e)

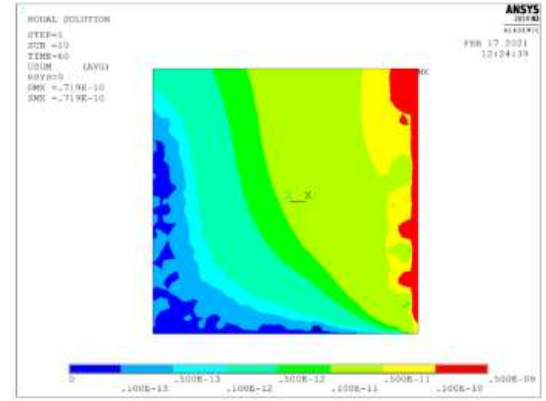
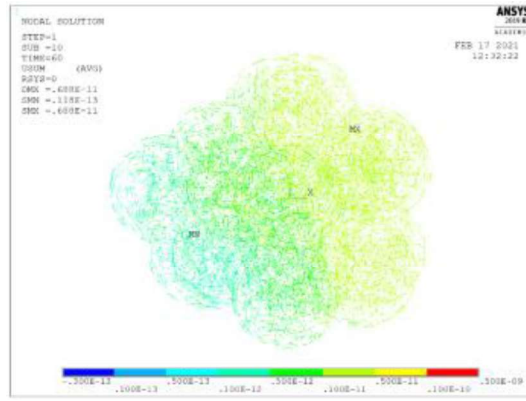
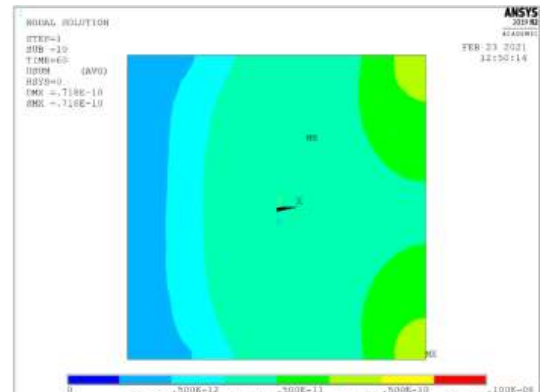
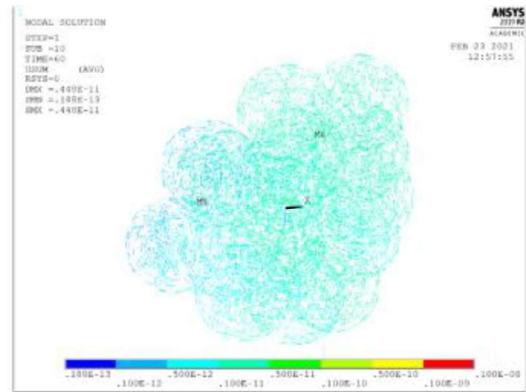
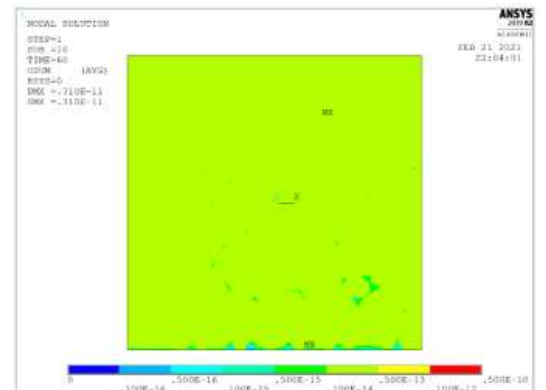
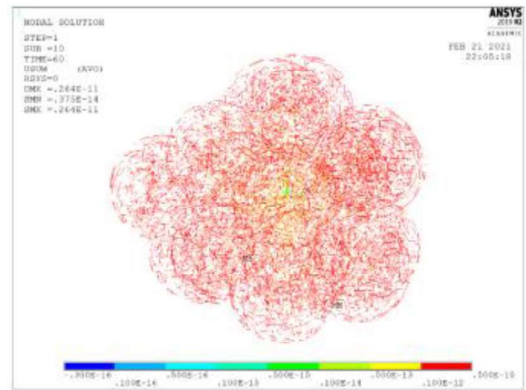


Fig 5 Deformation of nodes corresponding to tumour and entire model for collagen radius of 125nm for collagen volume fraction of (a) 0.015 (b) 0.04875 (c) 0.0825 (d) 0.11625 (e) 0.15

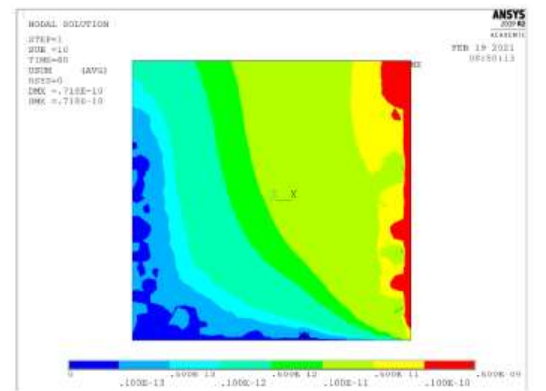
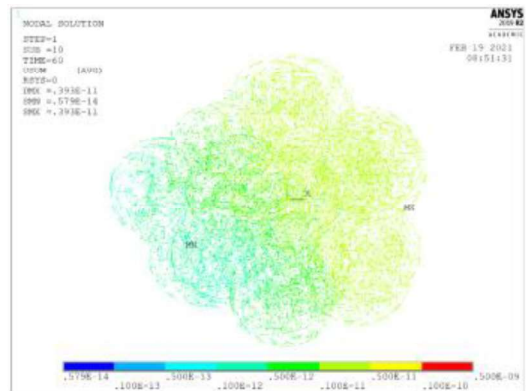
(a)



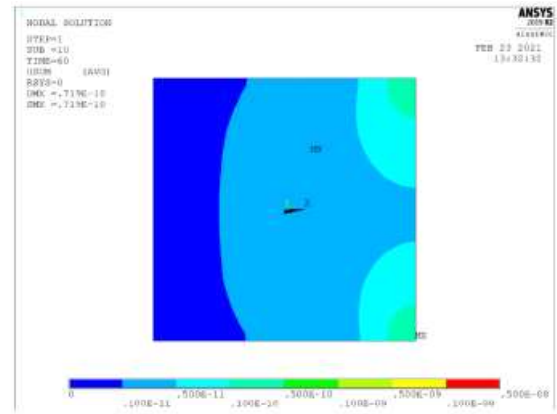
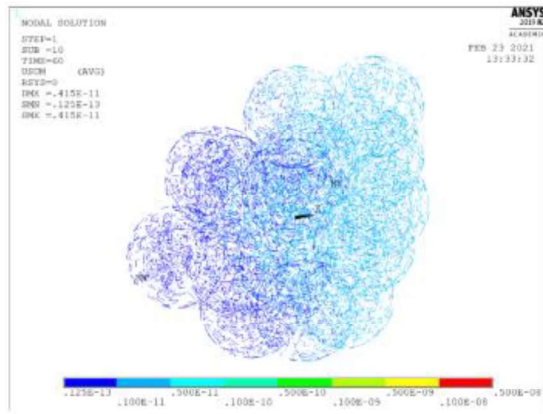
(b)



(c)



(d)



(e)

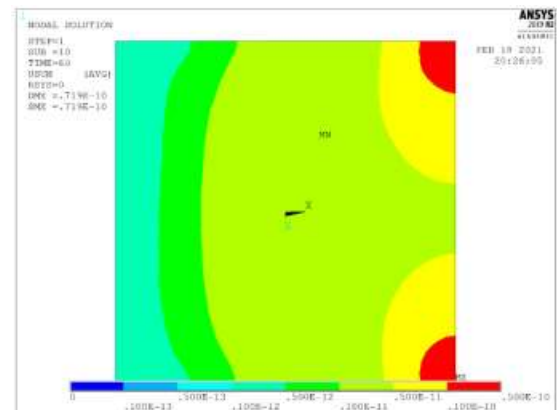
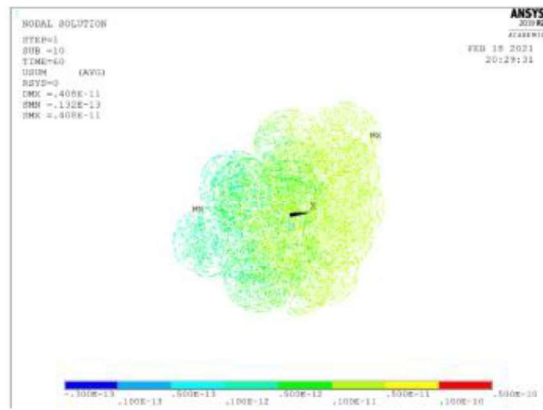


Fig. 6 Deformation of nodes corresponding to tumour and entire model for collagen radius of 150nm for collagen volume fraction of (a) 0.015 (b) 0.04875 (c) 0.0825 (d) 0.11625 (e) 0.15

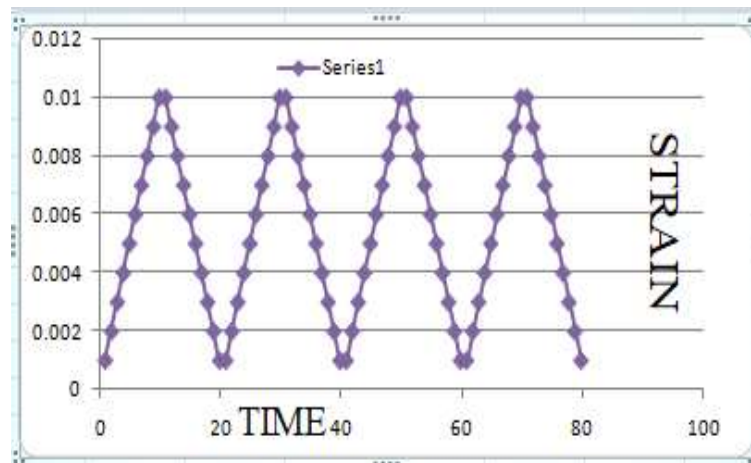


Fig. 7 Time vs Strain plot

4. Result and Discussion

Cytoskeleton elements consist of around 0.24% volume fraction of the overall cellular volume. Depending upon the cell type, the volume fraction of the cytoskeleton can vary up to 20% in a cell. In addition, the cytoskeleton can be degraded under the action of various drugs and the influence of certain other biochemical changes associated with cancer like activation of caspase [26-28], and such variation can have a significant effect on the overall mechanical response of the cell. This shows the

importance of elastic property of cells is an important parameter and need to study in detail to find the deformation pattern of tumor cells. Though the influence of matrix stiffness has been studied widely in simulation studies [29, 30] combined models incorporating substrate roughness have not been yet explored. In the present study, the deformation pattern of the tumor cell with reduced stiffness has been performed and the cases are presented. The plastic deformation of the cell was also constantly increased with the increase in the degradation percentage of the cytoskeleton. As the cytoskeleton gets degraded, the stress distribution across various cellular components becomes uniform. For assessment of cytoskeletal loading, cyclic loading is applied on the substrate, and the strain transferred to the cell due to this cyclic loading is measured. It is observed that when the cyclic loading is applied, it causes permanent cell deformation. With the increased number of cycles, the plastic strain accumulation in cells is increased and as a result, the mean value of equivalent strain is also increased with each loading cycle. From this observation, it can be opined that the application of cyclic loading causes the continual shape change in cells which may also promote cellular movement. Maximum strain induced in the case of cyclic loading is $\sim 7\%$, which can initiate cellular shape change [31]. Most of the forces acting on a cell are through indirect loading via surfaces thus, this kind of cyclic loading is important to understand and the cell-substrate interaction.

5. Conclusion

A 3D-finite element model of a tumor cell has been modeled that includes the cytoskeletal elements, discrete cytoskeleton architecture, and other components including the nucleus, cell membrane, and cytoplasm. The cell deformation pattern has been simulated to understand the mechanical response of the cell and the possibility of tumor cell migration from the tumor affected zone. Based on the present work the following points can be concluded.

- a. The vertical displacements are limited to less than 2.2% of the cell diameter for normal healthy cells. As the cytoskeleton gets degraded, the maximum plastic deformation is observed very significantly. It is found that normal vertical deformation for even a degraded cell goes to 5.6% of its diameter.
- b. The accumulation of plastic deformation due to cyclic loading is very significant. It is observed that only in 4 cycles of 20% strained amplitude loading at the substrate, the cells can suffer from huge deformations (6-8% strain), which can accumulate in the cell when cyclic loading is applied.
- c. Once the cyclic load reach the plastic zone, then each subsequent loading cycle enhances the cumulative accumulated strain in each cycle, leading to a change of the shape of the cell. Therefore, it can be concluded that cyclic loading plays a pivotal role in shape change of the cells and to achieve cell migration.
- d. From the above results, it is observed that the cell of diameter 5000 nm undergoes a maximum deformation of 108 nm and then undergoes plastic deformation. As the cytoskeleton gets degraded, the maximum plastic deformation is observed very significantly.
- e. It is found that normal vertical deformation for even a degraded cell goes to 5.6% of its diameter. The accumulation of plastic deformation due to cyclic loading is very noteworthy.
- f. The percentage of deformation is also dependent on the mechanical properties and surface properties of the substrates. From the above results, it is observed that the cells undergo more deformation, as the collagen volume fraction increases around the cells.
- g. It is also observed that, the cells undergo more deformation when the collagen diameter is increasing.

Reference

1. Fletcher DA (2010) ASCB 50TH ANNIVERSARY ESSAY On Force and Function. 21:3795–3796.
2. Liu Y, Mollaeian K, Shamim MH, Ren J (2020) Effect of F-actin and Microtubules on Cellular Mechanical Behavior Studied Using Atomic Force Microscope and an Image Recognition-Based Cytoskeleton Quantification Approach. *Int J Mol Sci* 21:392.
3. Pachenari M, Seyedpour SM, Janmaleki M, Shayan SB, Taranejoo S, Hosseinkhani H (2014) Mechanical properties of cancer cytoskeleton depend on actin filaments to microtubules content: Investigating different grades of colon cancer cell lines. *J Biomech* 47:373–379. E
4. Eletcher DA, Mullins RD (2010) Cell mechanics and the cytoskeleton. *Nature* 463:485–492. <https://doi.org/10.1038/nature08908>
5. Ispanixtlahuatl-Meráz O, Schins RPF, Chirino YI (2018) Cell type specific cytoskeleton disruption induced by engineered nanoparticles. *Environ Sci Nano* 5:228–245. <https://doi.org/10.1039/C7EN00704C>.
6. Liu Y, Mollaeian K, Shamim MH, Ren J (2020) Effect of F-actin and Microtubules on Cellular Mechanical Behavior Studied Using Atomic Force Microscope and an Image Recognition-Based Cytoskeleton Quantification Approach. *Int J Mol Sci* 21:392.
7. Fallqvist B, Fielden ML, Pettersson T, Nordgren N, Kroon M, Gad AKB (2016) Experimental and computational assessment of F-actin influence in regulating cellular stiffness and relaxation behaviour of fibroblasts.
8. Wang K, Cheng J, Cheng SH, Sun D (2013) Probing cell biophysical behavior based on actin cytoskeleton modeling and stretching manipulation with optical tweezers. *Appl Phys Lett* 103(8).
9. Rotsch C, Radmacher M (2000) Drug-induced changes of cytoskeletal structure and mechanics in fibroblasts: An atomic force microscopy study. *Biophys J* 78:520–535.
10. Mohammed D, Versaevel M, Bruyère C, Alaimo L, Luciano M, Vercruysse E, Procès A, Gabriele S (2019) Innovative Tools for Mechanobiology: Unraveling Outside-In and Inside-Out Mechanotransduction. *Front Bioeng Biotechnol* 7:162.
11. Zhang X, Liu M, Li Y, Dong Y, Pingguan-Murphy B, Lu T, Xu F (2015) Engineering cell microenvironment using novel functional hydrogels. *Eur Polym J* 72:590–601.
12. Borau, C., Kamm, R. D., & García-Aznar, J. M. (2011). Mechano-sensing and cell migration: a 3D model approach. *Physical biology*, 8(6), 066008.
13. Langrand B, Casadei F, Marcadon V, Portemont G, Kruch S (2017) Experimental and finite element analysis of cellular materials under large compaction levels. *Int J Solids Struct* 128:99–116.
14. Kardas D, Nackenhorst U, Balzani D (2013) Computational model for the cell-mechanical response of the osteocyte cytoskeleton based on self-stabilizing tensegrity structures. *Biomech Model Mechanobiol* 12:167–183. <https://doi.org/10.1007/s10237-012-0390-y>.
15. Xue F, Lennon AB, McKayed KK, Campbell VA, Prendergast PJ (2013) Effect of membrane stiffness and cytoskeletal element density on mechanical stimuli within cells: an analysis of the consequences of ageing in cells. *Comput Methods Biomech Biomed Engin* 18:468–476.
16. Barreto S, Perrault CM, Lacroix D (2014) Structural finite element analysis to explain cell mechanics variability. *J Mech Behav Biomed Mater* 38:219–231.
17. Cross SE, Jin YS, Rao J, Gimzewski JK (2007) Nanomechanical analysis of cells from cancer patients. *Nat Nanotechnol* 2:780–783.
18. Katti DR, Katti KS (2017) Cancer cell mechanics with altered cytoskeletal behavior and substrate effects: A 3D finite element modeling study. *J Mech Behav Biomed Mater* 76:125–134.
19. Desai LP, White SR, Waters CM (2010) Cyclic mechanical stretch decreases cell migration by inhibiting phosphatidylinositol 3-kinase- and focal adhesion kinase-mediated JNK1 activation. *J Biol Chem* 285:4511–4519.
20. Livne A, Bouchbinder E, Geiger B (2014) Cell reorientation under cyclic stretching. *Nat Commun* 5:1–8.
21. Lim CT, Zhou EH, Quek ST (2006) Mechanical models for living cells - A review. *J Biomech* 39:195–216.
22. Ingber DE, Heidemann SR, Lamoureux P, Buxbaum RE (2000) Opposing views on tensegrity as a structural framework for understanding cell mechanics. *J Appl Physiol* 8:1663–1678.
23. Suresh S (2007) Biomechanics and biophysics of cancer cells. *Acta Mater* 55:3989–4014.
24. Barreto S, Clausen CH, Perrault CM, Fletcher DA, Lacroix D (2013) A multi-structural single cell model of force-induced interactions of cytoskeletal components. *Biomaterials* 34:6119–6126.

25. Bao G, Suresh S (2003) Cell and molecular mechanics of biological materials. *Nat Mater*, 2:715-725.
26. Povea-Cabello S, Oropesa-Ávila M, de la Cruz-Ojeda P, Villanueva-Paz M et al (2017) Dynamic Reorganization of the Cytoskeleton during Apoptosis: The Two Coffins Hypothesis. *Int J Mol Sci* 18:2393.
27. Rotsch C, Radmacher M (2000) Drug-induced changes of cytoskeletal structure and mechanics in fibroblasts: An atomic force microscopy study. *Biophys J* 78:520–535.
28. Vakifahmetoglu-Norberg H, Norberg E, Perdomo AB, et al (2013) Caspase-2 promotes cytoskeleton protein degradation during apoptotic cell death. *Cell Death Dis* 4:e940–e940.
29. Kraning-Rush CM, Reinhart-King CA (2012) Controlling matrix stiffness and topography for the study of tumor cell migration. *Cell Adh Migr* 6:274–279.
30. Pathak A, Kumar S (2012) Independent regulation of tumor cell migration by matrix stiffness and confinement. *Proc Natl Acad Sci* 109:10334 LP – 10339.
31. Livne A, Bouchbinder E, Geiger B (2014) Cell reorientation under cyclic stretching. *Nat Commun* 5:1–8.

Prediction of Surface Roughness in Grinding Using Artificial Neural Networks

Sayan Bag, Santanu Das, Bandana Barman

1 Introduction

Maintaining proper quality of ground surface is essential in manufacturing. Grinding is a high speed machining process. It is complex and often fails to achieve desired accuracy. Prediction, or Estimation, is a logical guess about what will happen in the next future event based on historical information, previous regular data, evidence, background experience, knowledge and psychological hypothesis. There is no such surety as 100% matching of predicted value and true data. There is a probability that the predicted value and true data would be quite close. In this regard, ANN was employed in condition monitoring of cutting tool wear [1-3], estimation of drilling burr [4], assessment of viscosity of dual phase flow system [5], estimation of surface roughness in grinding, etc. [6-9]. The Neural Networks (NN) is trained through Back Propagation (BP) algorithm. Mondal et al. presented [6] how Artificial Neural Networks (ANN) could be used to estimate surface roughness in a centreless grinding process. Kwak et al. used [7] neural networks to achieve an intelligent diagnosis for chatter and burning phenomena on grinding operation, when Shrivastava et al. developed [8] an intelligent modelling of surface roughness during grinding of ceramics. They compared regression analysis with ANN to evaluate estimation accuracy of surface roughness among them. Aguiar et al. developed [9] a model to predict surface roughness in grinding using Neural Networks. Kumar et al. implemented [10] a model to predict wheel wear, tool wear, and surface roughness in electro-discharge diamond grinding using Neural Networks. Lipinski et al. developed [11] a neural network model for the grinding process to determine surface roughness under different workpiece-wheel combinations. Chaudhury et al. selected [12] appropriate fluid delivery technique for grinding titanium using the AHP. Different types of nozzle systems were used. The criteria were wheel load, surface characteristics and force. They noticed compound nozzle setup of fluid delivery to have penetrated the air layer around the wheel. Mahata et al. explored [13] grindability of Ti-6Al-4V using an indigenously developed eco-friendly micro pump-based cooling system. The main objective of this work is to investigate the applicability of Artificial Neural Networks (ANN) to estimate surface roughness of the ground surface at the proper state of experimental conditions in surface grinding.

2 The Artificial Neural Networks (ANN)

2.1 Introduction to ANN

The concept of ANN is derived mostly from the field of human science, in which human nervous system plays a critical role in human body. The work of human body is regulated by brain. A neuron is a unique natural cell that transfers data from one neuron to the next neuron via electrical and chemical change. The cell body has a core that stores data and a plasma that does the processing on the data in a neuron. The entire procedure of accepting and sending signs to the cell body is done through dendrites.

S. Bag^{*1}, S. Das¹, B. Barman²

¹Department of Mechanical Engineering, Kalyani Government Engineering College, India 741235

²Department of Electronics & Communication Engineering, Kalyani Government Engineering College, India 741235

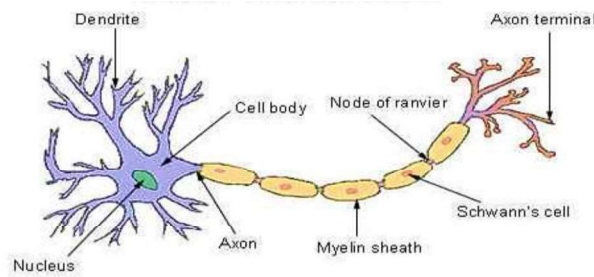


Fig. 1 Human Neuron Structure [14]

The ANN is a computational model based on structure and functions of biological neural networks. Information that flows through the network affects structure of ANN as neural network changes or learns in a sense based on that input and output information or data.

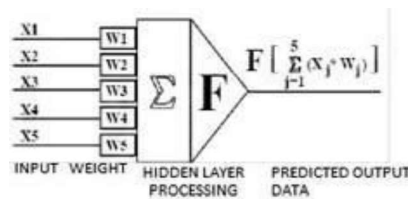


Fig. 2 Artificial Neural Networks algorithmic structure [14]

2.2 Types of Training in ANN

Different types of training are applied in ANN; supervised, unsupervised, and adaptive training respectively.

2.3 Algorithmic Structure of a Typical ANN [5]

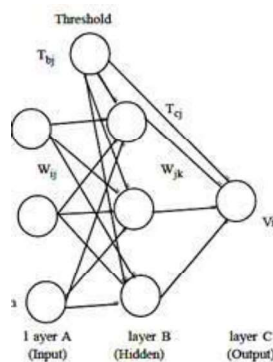


Fig. 3 Typical structure of an Artificial Neural Networks [5]

In a typical standard structure of the ANN, the activation function employed may be a sigmoid function as shown in Eq. 1.

$$f(x) = 1 / (1 + \exp(-x)) ; \quad (1)$$

Neuron transforms signals to the next layer by summation of weighted node values added with threshold weight through sigmoid function.

The values of hidden nodes, b_j in hidden layer B, are found by Eq. 2;

$$b_j = 1/(1 + \exp -(\sum_{i=1 \text{ to } m} (W_{ji} a_i) - T_{bj})); \quad j=1 \text{ to } n \quad (2)$$

W is weight, n is No. of hidden nodes, m is No. of input nodes, a is input node value and T is threshold weight. Also values of the nodes of output layer C, c_j are computed by Eq. 3;

$$c_j = 1/(1 + \exp -(\sum_{i=1 \text{ to } n} (W_{ji} b_i) - T_{cj})); \quad j=1 \text{ to } k \quad (3)$$

Where, k is No. of nodes at output.

Random numbers in the range of -1 to +1 were used to initialize weights between each of the two nodes and threshold weight. The ANN is retrained, so that appropriate weights are determined, using the training data set, which consist of input data set and associated data set corresponding to experimental observation.

Compared with the target value, d_j. The avg. square error is calculated by Eq. 4.

$$E = \sum_{i=1}^n \sum_{j=1}^k (d_{ij} - c_{ij})^2 / (pk); \quad (4)$$

p is the total No. of input data set and k is the No. of output nodes.

The weights are modified using the back propagation if the average square error value exceeds the stated limit.

If error, E is large then an error gradient, e_{2ij} between output and hidden layer is calculated by Eq. 5.

$$e_{2ij} = c_{ij}(1 - c_{ij})(T_{ij} - c_{ij}); \quad j = 1 \text{ to } k, \quad i = 1 \text{ to } p \quad (5)$$

For different hidden layers, and between first hidden layer and input layer, the error gradient, e_{ij} is found out by using Eq. 6.

$$e_{1ij} = b_{iq}(1 - b_{iq}) \sum_{j=1}^k (e_{2ij} W_{jq}); \quad q=1 \text{ to } n, \quad i=1 \text{ to } p \quad (6)$$

An iterative technique is used to manage weights. The incremental change in weight between output and the hidden layer is derived using Eq. 7.

$$\Delta W_{jq}(N) = q_b \Delta W_{jq}(N-1) + q_c \cdot \sum_{i=1}^p e_{2ij}; \quad j=1 \text{ to } k, \quad q=1 \text{ to } n \quad (7)$$

Positive constants, q_b and q_c, are known as momentum factor and learning rate, respectively. The weight increment is calculated by Eq. 8 after collecting error gradient between hidden and input layers.

$$\Delta W_{qi}(N) = q_b \Delta W_{qi}(N-1) + q_c \cdot \sum_{j=1}^k e_{1ij}; \quad i=1 \text{ to } k, \quad q=1 \text{ to } n \quad (8)$$

The following equations are used to determine new weights W(N) [As in Eq.9.], as well as the threshold weights T(N) [as in Eq. 10].

$$W(N) = W(N-1) + \Delta W(N); \quad (9)$$

$$T(N) = T(N-1) + \Delta T(N); \quad (10)$$

This method for change in weight continues till the error falls below a specified value or total number of iterations reaches the specified number.

3 Application of ANN In Predicting Surface Roughness Using Experimental Data

In this section, the technique to predict surface roughness for grinding is discussed. Four input grinding parameters are taken under fifteen conditions as shown in Table I. The ANN model is constructed based on of experimental data of surface roughness. The validity of the model is determined by comparing predicted and experimental surface roughness measurements within a predetermined range of parameters. Fig. 4 and Fig. 5 show the ANN structures used in this particular grinding problem to predict surface roughness.

3.1 Experimental Investigation

3.1.1 Experimental Condition

Experimental data were collected from the paper of Agarwal et al. [15]. Cutting velocity was taken as 36.6 m/sec, workpiece feed rate was taken as 5 m/min, 7.5 m/min, 10 m/min, 12.5 m/min and 15 m/min. Infeed chosen was 5 μm , 10 μm and 15 μm . Experiments were conducted on a hydraulic surface grinding machine with a diamond grinding wheel. Wheel diameter used was 250 mm. The diamond-grinding wheel was Norton made with modulus of elasticity 70 GPa and aluminium as core material. The modulus of elasticity of grit is 925 GPa and Poisson's ratio of aluminium and diamond grit are taken as 0.33 and 0.20 respectively. Silicon carbide was used as the workpiece material. Density of workpiece material is 3.17 gm/cm³, and Hardness is 2700 Kg/mm².

3.1.2 Experimental Observation

Table I shows the detail of the grinding parameters, observed average chip thickness and surface roughness as obtained from 15 sets of experiments. These data are utilized in constructing the ANN structure for the purpose of predicting surface roughness.

Table 1. Data used for the ANN [15].

Input Layer Data into ANN					Target Layer Data into ANN
Sl. No.	Grinding Wheel Velocity (Vg) m/s	Work Piece Feed rate (Vw) m/min	Depth of cut (d) μm	Average Chip Thickness (tm) μm	Experimental Surface Roughness (Ra) μm
1	36.6	5	5	1.204	0.164
2	36.6	7.5	5	1.458	0.269
3	36.6	10	5	1.515	0.277
4	36.6	12.5	5	1.683	0.311
5	36.6	15	5	1.818	0.329
6	36.6	5	10	1.675	0.221
7	36.6	7.5	10	2.032	0.234
8	36.6	10	10	2.071	0.287
9	36.6	12.5	10	2.300	0.321
10	36.6	15	10	2.501	0.389
11	36.6	5	15	2.002	0.213
12	36.6	7.5	15	2.468	0.291
13	36.6	10	15	2.604	0.328
14	36.6	12.5	15	2.889	0.361
15	36.6	15	15	3.138	0.389

3.2 Application of ANN on the Experimental Results

According to Table I, the input layer matrix consists of three grinding parameters and one observed response indicated by four input nodes in the ANN structure and there are 15 sets of experimental conditions that are represented by a matrix of the size of 4×15 to feed into the network model.

Average chip thickness values observed during grinding are one of the input layer data under fifteen experimental conditions. The input layer matrix of ANN network model is formed as 4×15 corresponding to 15 sets of experiments. Experimental surface roughness values are set as target data in artificial neural networks architecture. So, the target layer matrix of ANN model is formed as 1×15 . The outline of the ANN used is given in table II.

Two types of models are used by varying numbers of hidden nodes. The first model consists of 10 hidden nodes, that is a 4-10-1 ANN model (Fig. 4), and the second model is as shown in Fig. 5 that consists of 15 hidden nodes (that is, 4-15-1 ANN model) in hidden layer to compute the algorithm. Hidden nodes were varied twelve times from 5 upto 16 with an increment of one. The values that seem desirable are highlighted here. In ANN, attempts are made to bring the percentage of error close to zero. If the percentage of error is equal to zero for each and every condition then it is called as a purely ideal ANN structure. Training and retraining the network were done by following Trial and Error method to get the regression (R) value near about one. When the R value was near about one, running of the program was stopped and the predicted data were collected. According to table I, target layer matrix is of size 1×15 that is fed into the network model architecture.

Ten and fifteen hidden nodes are placed in hidden layer at two different ANN model architectures. After building input layer, target layer, and one hidden layer, training-learning process started until obtaining the satisfactory values of training error.

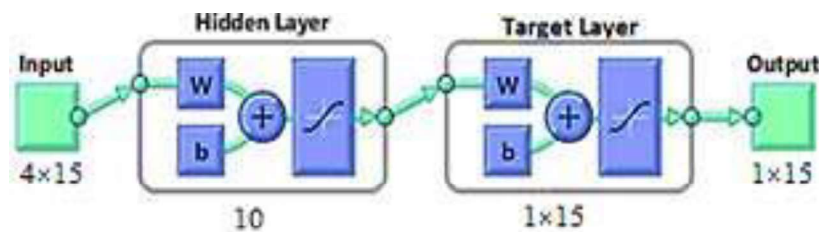


Fig. 4 Designmodel-1 of ANN for grinding with ten hidden nodes.

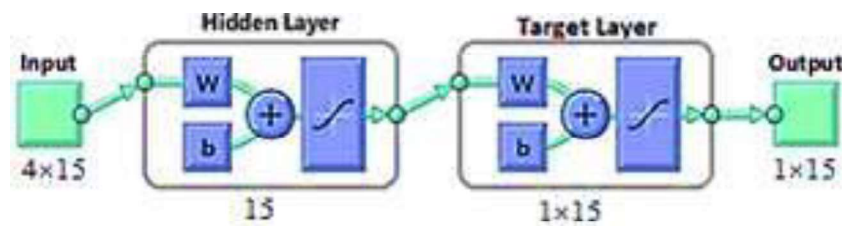


Fig. 5 Designmodel-2 of ANN for grinding with fifteen hidden nodes

Table 2. Algorithms used in ANN

Data Division:	Random (dividerand)
Training:	Lavenberg-Marquardt back propagation (trainlm)
Performance:	Mean squared error (mse)
Calculation:	MEX program
Function	Sigmoid
Histogram:	Ploterrhist

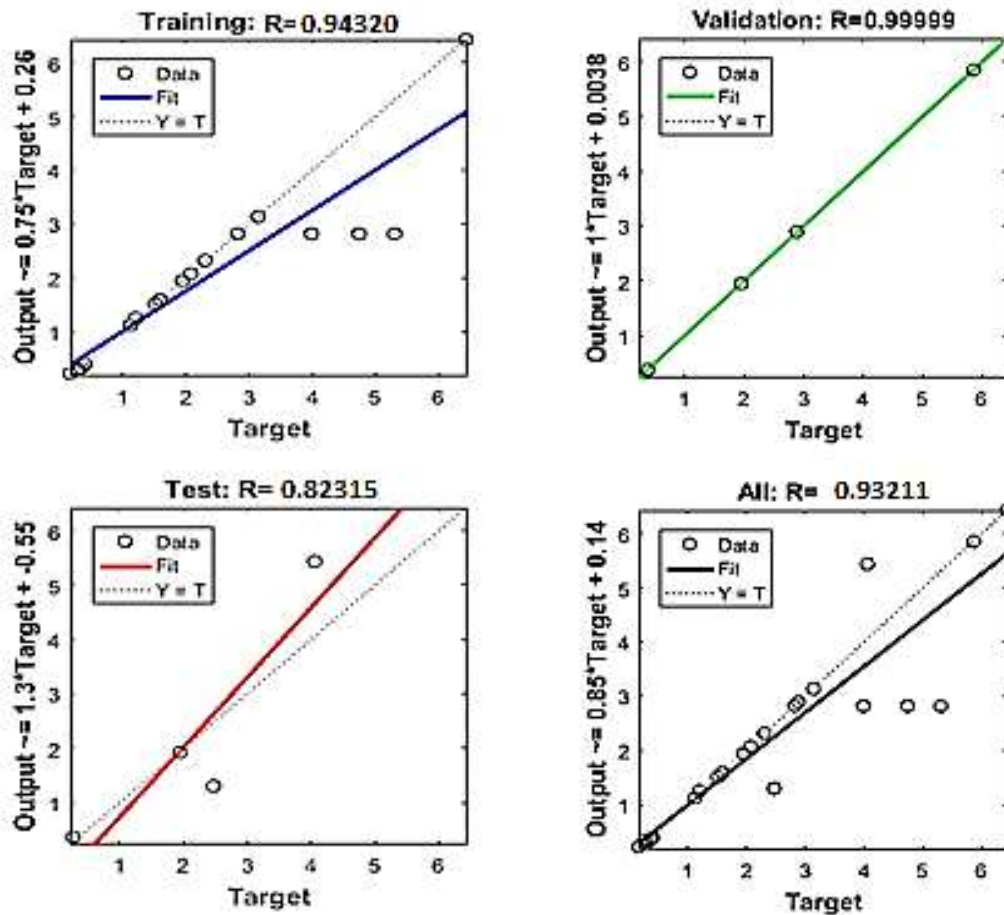


Fig. 6 Final trained (at 14 epoch) regression plot of first model with ten hidden nodes.

Table 3. values of R and slope angle from first model and second model of ANN.

Type of Data set	For first ANN model (4-10-1)		For second ANN model (4-15-1)	
	Value of R	Slope angle	Value of R	Slope angle
Training Data set	0.94320	Less than 45 degree	1	45 degree
Validation Data set	0.99999	Close to 45 degree	1	45 degree
Test Data set	0.82315	Greater than 45 degree	1	45 degree
All-Mean Data Set	0.93211	Less than 45 degree	0.9908	Greater than 45°

With the standard regression value of plot, $R=1$ and slope with 45 degree angle with target axis, estimation is considered to be quite accurate. When training data, validation data, test data and all-mean data maintain these standardized values, the output will be considered to be quite accurate naturally with quite low estimation error.

With the first ANN structure with 4-10-1 ANN model, comparison of target data set with the ANN output dataset appeared not much desirable on Regression plot (Fig. 6) after training stage got over. Therefore, the predicted output data were not also much close to the experimental data expectedly, that is why this Regression plot was needed to improve upon further. Because ANN is a long and continuous improvement process by varying different types of optimization parameters in structural system.

To reduce estimation error to the desirable extent, the second model of ANN was created by increasing the numbers of hidden nodes from ten to fifteen and the network was retrained again.

With the second ANN model (4-15-1), regression value (R) becomes 1 or almost 1 for all the datasets as indicated in Table III, and slope angles obtained are almost 45 degree for all the data sets including training data set, validation data set, testing data set and all-mean data set.

Accordingly, predicted output data become much close to the experimental data showing quite less estimation error as detailed in Table IV. Therefore, this 4-15-1 ANN model showing the Regression plot in Fig. 7 can be considered to be acceptable.

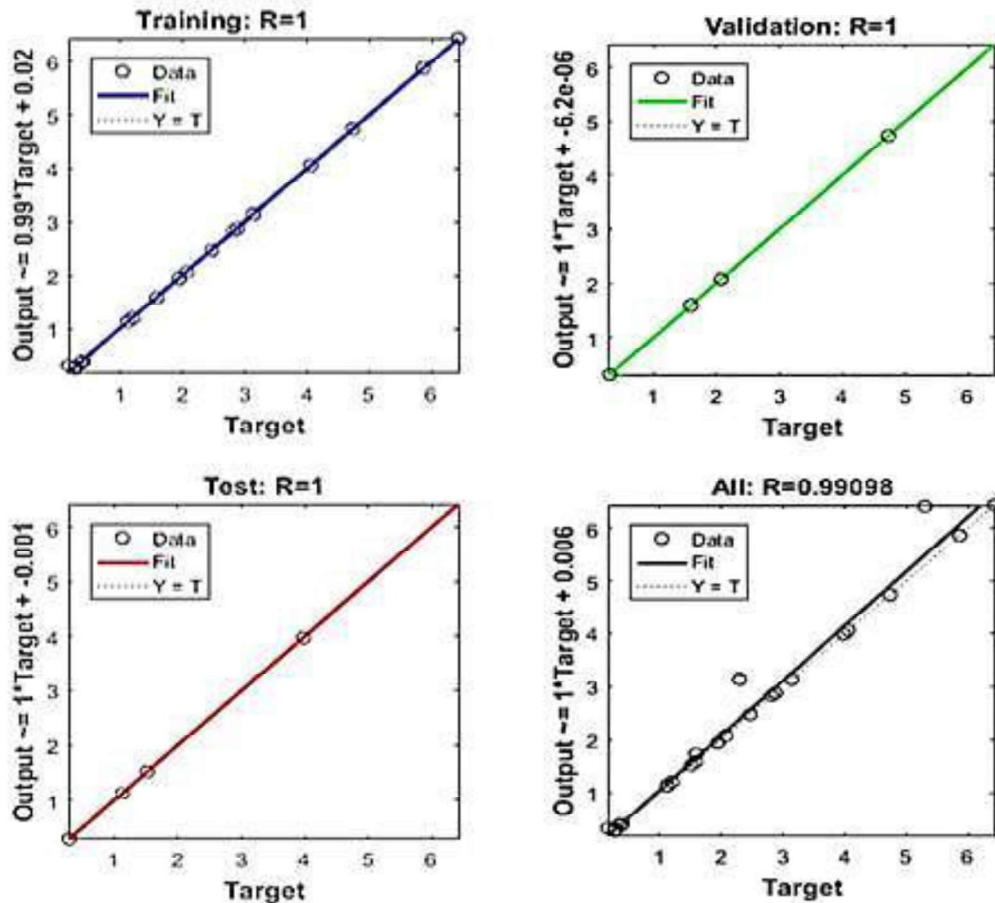


Fig. 7 Final trained regression (at epoch 12) plot of second model, with fifteen hidden nodes.

3.3 Results

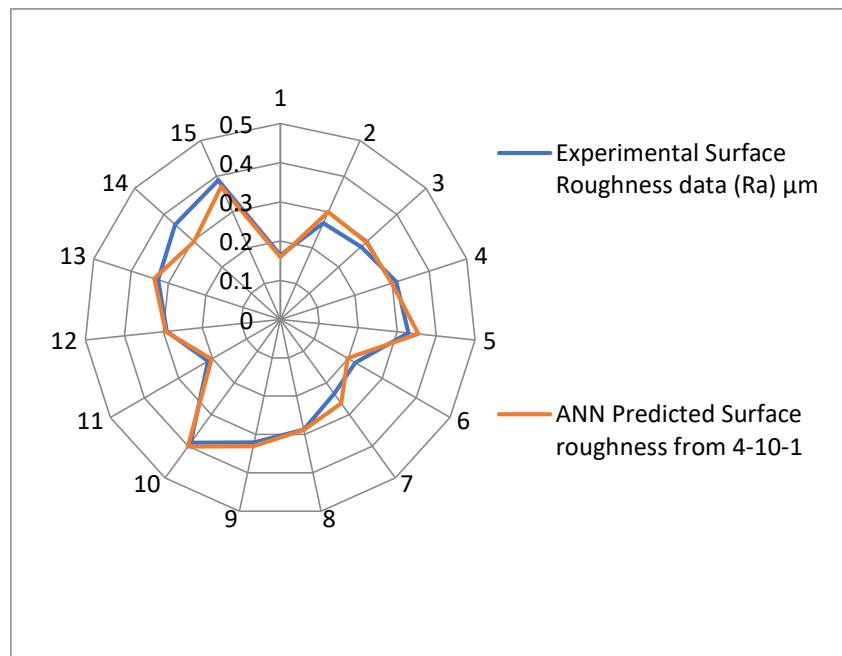
Based on the target layer matrix, the output layer matrix is also 1×15 in network model architecture. The results shown in Fig. 8 in the form of Radar net plot of first ANN-model with 4-10-1 network structure sometimes show considerable deviation between two radial lines meaning the data sets are not often fully matching at certain points for some state of experimental condition. So, this ANN predicted output data and experimental data need improvement further as stated earlier also.

Radar net plot results shown in Fig. 9 of the second ANN-model having 4-15-1 architecture show that mostly two radial lines are overlapping; it means the data sets are almost fully matching at most of the points related to different states of experimental condition. So, this ANN predicted output data and experimental data are found to be much close to each other, and hence, its applicability.

Table 4. Comparison of predicted output values from the two ANN models.

Sl. No.	For the 1st ANN Model with 4-10-1 structure		For the 2nd ANN Model with 4-15-1 structure	
	ANN Predicted Surface roughness	Percentage error	ANN Predicted Surface roughness	Percentage error
1	0.159	3.048	0.163	0.609
2	0.3	11.524	0.267	0.743
3	0.295	6.498	0.281	1.444
4	0.299	3.858	0.313	0.643
5	0.354	7.598	0.323	1.823
6	0.198	10.407	0.209	5.429
7	0.265	13.247	0.243	3.846
8	0.288	0.348	0.287	0
9	0.331	3.115	0.311	3.115
10	0.401	3.084	0.398	2.313
11	0.202	5.164	0.212	0.469
12	0.294	1.030	0.3	3.092
13	0.338	3.048	0.333	1.524
14	0.296	18.005	0.347	3.878
15	0.371	4.627	0.4	2.827

The bar chart depicted in Fig. 10 shows the comparison of percent prediction error corresponding to both the ANN models considered. This bar chart reiterates that for the first ANN model, percent prediction errors are quite more than the second ANN model. Therefore, the second ANN model with 15 hidden nodes can be considered for recommendation for adoption.

**Fig. 8** Radar net plot of ANN to compare experimental data with predicted values from first model.

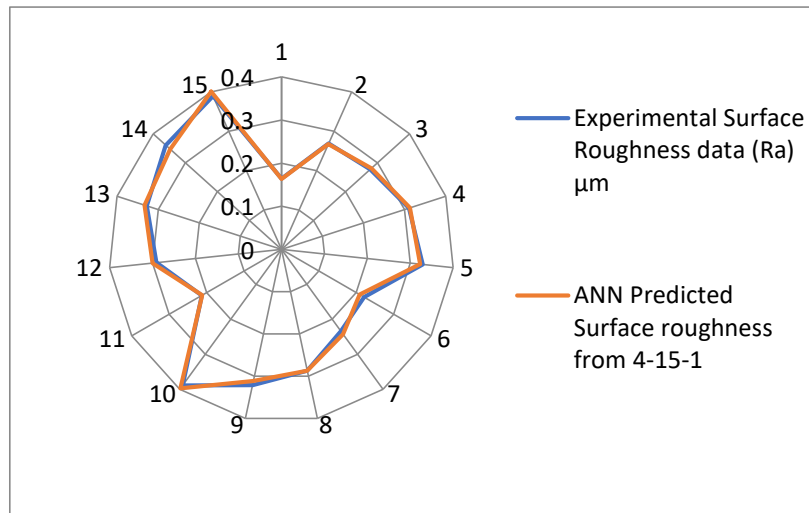


Fig. 9 Radar net plot of ANN to compare experimental data and predicted values of the second model.

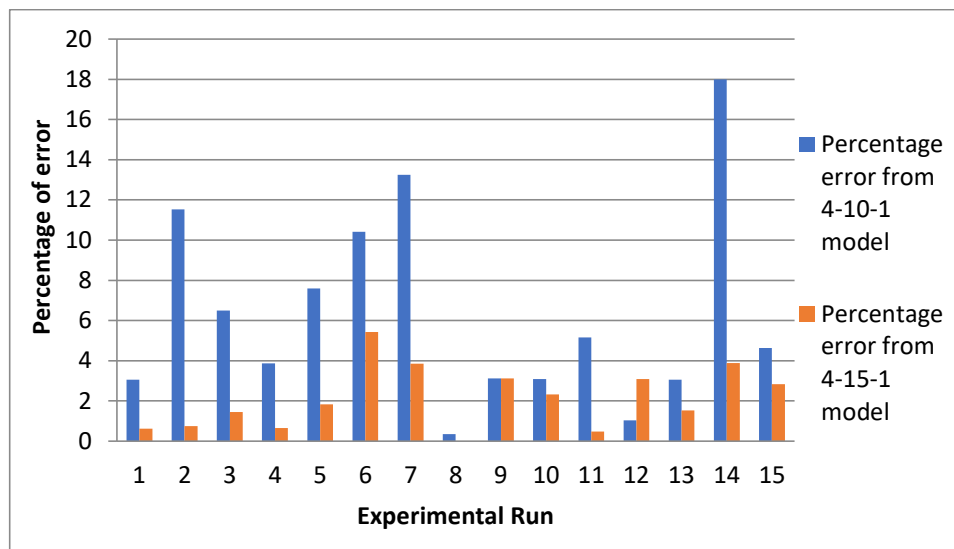


Fig. 10 Comparison chart of Percentage error of estimation on experimental surface roughness data, in between two ANN Model.

4 Conclusion

The Artificial Neural Networks with 4-15-1 architecture could predict well the target data set according to input matrix and output matrix available on MATLAB worksheet. At most of the grinding conditions, the experimental data and ANN estimates were found to be quite close with this ANN structure and maximum prediction error was detected to be 5.429%. Therefore, the ANN finds its applicability well in predicting average surface roughness in surface grinding.

References

1. Das, S., Roy, R., and Chattopadhyay, A.B. (1996). Evaluation of wear of turning carbide inserts using neural networks. *International Journal of Machine Tools and Manufacture*, 36(7), 789-797.
2. Das, S., Bandyopadhyay, P.P., and Chattopadhyay, A.B. (1997). Neural-networks-based tool wear monitoring in turning medium carbon steel using a coated carbide tool. *Journal of Materials Processing Technology*, 63(1-3), 187-192.

3. Mukherjee, A., and Das, S. (2021). A simple online tool condition monitoring system using artificial neural networks. IOP Conference Series: Materials Science and Engineering, 1080(012020).
4. Misra, D., Das, S., Mondal, N., and Saha, P.P. (2020). Estimation of drilling burr formation with artificial neural network analysis. Indian Science Cruiser, 34(3), 23-31.
5. Ghanta, K., and Das, S. (2013). Neural Networks Based Modeling of Viscosity for Facilitating Transportation of Magnetite Orewater Slurry. Journa of the Association of Engineers, India, 83(2). 43-54.
6. Mondal, S.C., and Mondal, P. (2014). Application of Artificial Neural Network for Modeling Surface Roughness in Centerless Grinding Operation. International All India Manufacturing Technology, Design and Research Conference, 6081-6086.
7. Kwak, J.S., and Ha, M.K. (2004). Neural Network Approach for Diagnosis of Grinding Operation by Acoustic Emission and Power Signals. Journal of Materials Processing Technology, 147(1), 65-71.
8. Shrivastava, P.K., and Dudey, A.K. (2011). Intelligent Modeling of Surface Roughness During Diamond Grinding of Advanced Ceramics. Proceedings of the World Congress on Engineering, 1, 1-8.
9. Augier, P.R., Cruz, E.D.C., Paula, W.C.F., and Bianchi, C.E. (2008). Predicting Surface Roughness in Grinding using Neural Networks. Advances in Robotics, Automation and Control, 33-44.
10. Kumar, S., and Choudhury, S.K. (2007). Prediction of Wear and Surface Roughness in Electro-Discharge Diamond Grinding. Journal of Materials Processing Technology, 191. 206-209.
11. Lipinski, D., Balasz, B., and Rypina, L. (2018). Modelling of Surface Roughness and Grinding Forces using Artificial Neural Networks with Assessment of the Ability to Data Generalisation. Int J Adv Manuf Technology, 1335-1347.
12. Chaudhury, A., Mandal, B., and Das, (2015). Selection of Appropriate Fluid Delivery Technique for Grinding Titanium Grade-1 using The Analytic Hierarchy Process. International Journal of Analytic Hierarchy Process, 7(3). 454-469.
13. Mahata, S., Mukhopadhyay, M., Banerjee, A., Kundu, A., Mandal, B., and Das, S. (2020). Exploring Grindability of Ti-6Al-4V using an Indigenously Developed Environment Friendly Micro Pump Based Cooling System. Indian Journal of Engineering and Materials Sciences, 27(3). 724-729.
14. Dambatta, Y., Sayuti, M., Sarhan, A., Shukor, A., and Derahman, N. (2018). Prediction of Specific Grinding Forces and Surface Roughness in Machining of AL6061-T6 Alloy using ANFIS Technique. Industrial Lubrication and Tribology, 1-9.
15. Agarwal, S., Khare, Kr. S., Pandey, P.V., and Patel, M. (2017). An Analytical Chip Thickness Model for Performance Assessment in Silicon Carbide Grinding. Procedia Manufacturing, 10, 298-306.

Nomenclature

A	input layer
a_i	i^{th} component of input vector entering a neuron
B	hidden layer (s)
b_j	calculated output for j^{th} neuron
C	output layer
c_k	calculated output for k^{th} neuron
d_k	desired output for k^{th} neuron
i, j, q	subscripts to denote a particular layer
m, n, k	number of nodes in A, B and C
T_i	threshold weight for i^{th} neuron
W_{ij}	weight between i^{th} and j^{th} nodes

Simulation of microchannel heat exchangers with triangular and circular cavities

K. Mohana Rao, Amit Kumar, Dipak Chandra Das, Pritam Das

1 Introduction

In recent decades, the invention of systems with improved performance of integrated circuits requires very effective and efficient heat removal to avoid any disturbances and to maintain the proper operation of chips. For solving this problem one has to provide more surface area exposed to the working fluid such that the chances of dissipating heat from the integrated circuit will be more. Considering this problem one can employ Microchannels heat exchangers (MCHXs) in the place of conventional heat exchangers which have wide industrial applications such as medical equipment, electronic chips, etc. [1]. MCHXs with cavities can improve heat transfer characteristics [2]. Parallel micro-channels heat sinks using a working fluid can be served as emerging techniques for efficient cooling [3].

MCHX is firstly proposed by Tuckerman and Pease [1] to address the forced convection cooling of integrated circuits. Herman and Kang [2] investigated the enhancement of heat transport using the grooved. Peng and Peterson [4] reported the noteworthy effect on the heat transfer using MCHXs with rectangular channels. Jiang et al. [5] conducted experimental studies of MCHXs with or without porous media and reported that the heat exchanges using porous media are more whereas the pressure drop is higher for the later one. Qu and Mudawar [6] extended the study to visualize the flow characteristics of water in trapezoidal microchannels. Tiselji et al. [7] conducted experiments and numerical investigations to gauge the heat transfer of water flowing through triangular silicon. Kim and Kim [8] developed an analytical model for the microchannel heat sinks. Mishan et al. [9] investigated the pressure drop and heat transfer for a rectangular microchannel experimentally using water. Wang et al. [10] investigated the effects of partial and full heating for offset strip fin microchannels network heat sinks. Gunasegaran et al. [11] analyzed the characteristics of geometrical parametric variations of MCHXs. Dharaiya and Kandlikar [12] studied the significance of structured roughness on heat transfer. Chai et al. [13] simulated the MCHXs with triangular reentrant cavities. Capua et al. [14] analyzed an MCHX of the photovoltaic system numerically. Huang et al. [15] reported the enhancement of heat transfer in microchannels with cavities. Pan et al. [16] have investigated the heat transport phenomena for fan-shaped cavities of an MCHX.

In this present work, considering the advancements in the integrated circuits, there is a consequent rise in the heat flux which causes the chips to damage. To solve this problem one needs to employ MCHXs with structured cavities along the length of the channel having more surface area in the design model, which helps in dissipating more heat and helps to the proper working of the chips. A numerical model is proposed to address the heat flows and the pressure drop reduction using Ansys 19 and the model results are validated with the Huang et al. experiment [15].

2 Numerical Modelling

Following the multiphase mixture model, the mass, momentum, and energy balances can be expressed as

$$\frac{\partial}{\partial t}(\rho_m) + \nabla \cdot (\rho_m \mathbf{v}_m) = 0 \quad (1)$$

K. M. Rao, A. Kumar*, D. C. Das, P. Das

Department of Mechanical Engineering, NIT Agartala, Agartala - 799046, India

$$\frac{\partial}{\partial t}(\rho_m v_m) + \nabla \cdot (\rho_m v_m v_m) = -\nabla p + \nabla \cdot \left[\mu_m (\nabla v_m + \nabla v_m^T) \right] + \rho_m g + F + \nabla \cdot \left(\sum_{k=1}^n \alpha_k \rho_k v_{dr,k} v_{dr,k} \right) \quad \dots(2)$$

$$\frac{\partial}{\partial t} \left(\sum_{k=1}^n \alpha_k \rho_k E_k \right) + \nabla \cdot \sum_{k=1}^n (\alpha_k v_k (\rho_k + E_k) + p) = \nabla \cdot (k_{eff} \Delta T) + S_E \quad \dots(3)$$

where S_E represents the rest of the volumetric heat sources and

$$E_k = h_k - \frac{p}{\rho k} + \frac{v_k^2}{2} \quad \dots(4)$$

For an incompressible phase

$$E_k = h_k \quad \dots (5)$$

The volume fraction of phase p can be derived from the mass balance and expressed as

$$\frac{\partial}{\partial t} (\alpha_q \rho_q) + \nabla \cdot (\alpha_q \rho_q v_m) = -\nabla \cdot (\alpha_p \rho_p v_{dr,p}) + \sum_{q=1}^n (m_{pq} - m_{qp}) \quad \dots(6)$$

The amount of energy the fluid can absorb can be written as

$$Q_{absorb} = m_f c_f (T_{f,out} - T_{f,in}) \quad \dots (7)$$

The local convective heat transfer coefficient (HTC) [15] is reported as

$$h = \frac{Q_{absorb}}{A(T_w - T_f)} \quad (8)$$

where T_f is the mean of $T_{f,out}$ and $T_{f,in}$.

2.1 Geometry of the computational domain

The dimensions of the computationally designed test section as depicted in Fig. 1 are 40 mm in length, height and width of the channels are 300 μm . The corresponding meshing of the computational domains is shown in Fig. 2. Similarly, 10 channels are present parallel to each other in horizontal orientation. Therefore, 10 channels present in each Microchannel heat exchanger test section. The triangular cavities test section is shown in Fig. 1. (b) is having a sudden expansion and sudden

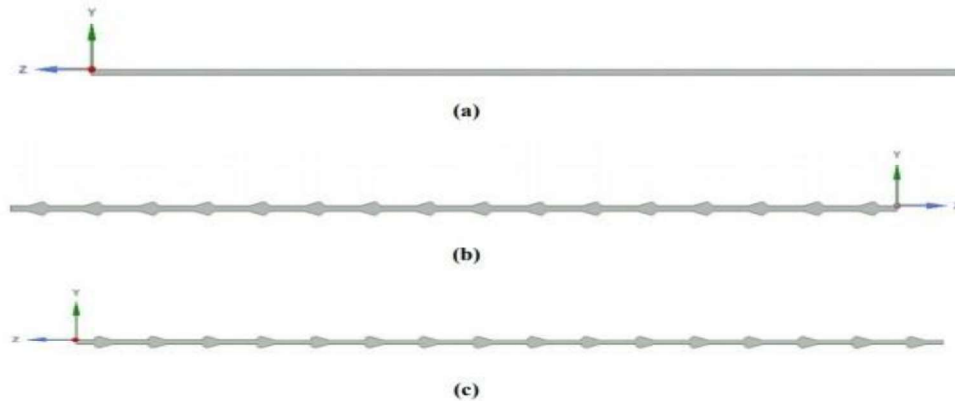


Fig. 1. Microchannels with (a) no cavity (straight microchannel), (b) triangular cavities, and (c) circular cavities

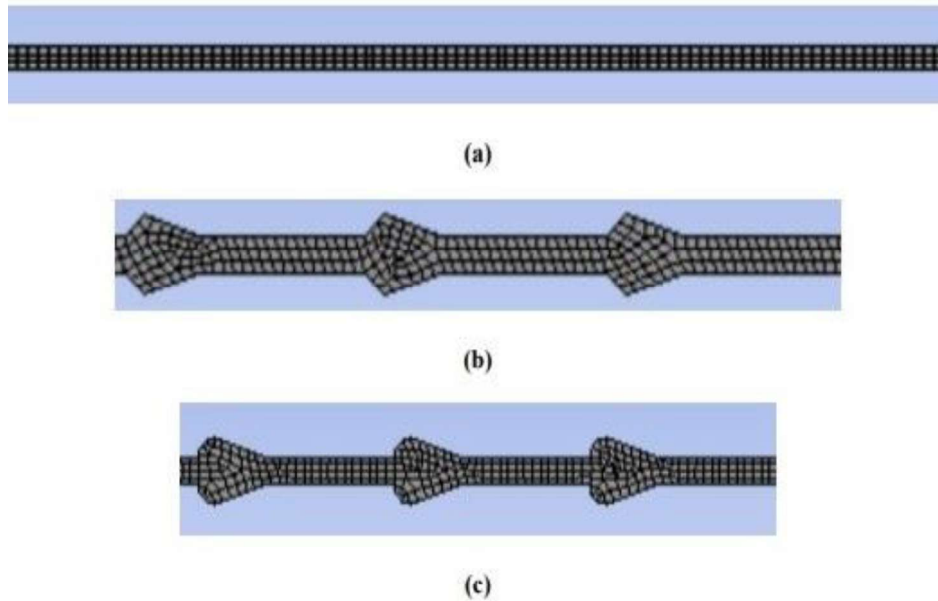


Fig. 2. The meshing of the computational domain of microchannels with (a) no cavity (straight microchannel), (b) triangular cavities, and (c) circular cavities.

contraction for a length of 600 μm and 200 μm respectively. The adjacent gap between the cavities present along the length of the channel is 2400 μm . The extended projection outwards the channel is 200 μm . The circular cavities test section is shown in Fig. 1. (c) is having a circular arc of 200 μm and the sudden contraction continues for a length of 600 μm . The adjacent distance between the circular cavities along the length of the channel is 2400 μm .

The simulation is done in ANSYS Fluent workbench for all three test sections at different Reynolds numbers 40, 60, 80 with a heat source of 0.22 MW/m². The pressure-based solver, absolute velocity formulation, and transient state conditions are applied. The model used here is the multiphase-mixture model with energy equation and the flow along the channel is laminar viscous flow. The solution method pressure-velocity coupling SIMPLE scheme is used. The spatial discretization for the gradient is least squares cell-based, for pressure PRESTO. The spatial discretization method for the momentum, volume fraction, and energy is the first-order upwind.

2.2 Material properties

The working fluid used in the micro-channel of silicon is deionized water. The property values of the working fluid are taken at room temperature i.e., 27°C is reported in Table 1[17].

Table 1. Properties of the Materials

Material	k (w/m.k)	ρ (kg/m ³)	μ (kg/m.s)	C_p (KJ/kg)
Deionized Water	0.579	997.8	0.0009532	4.184
Silicon	170	2330	-	0.71

3 Results and Discussions

3.1 Validation of HTC

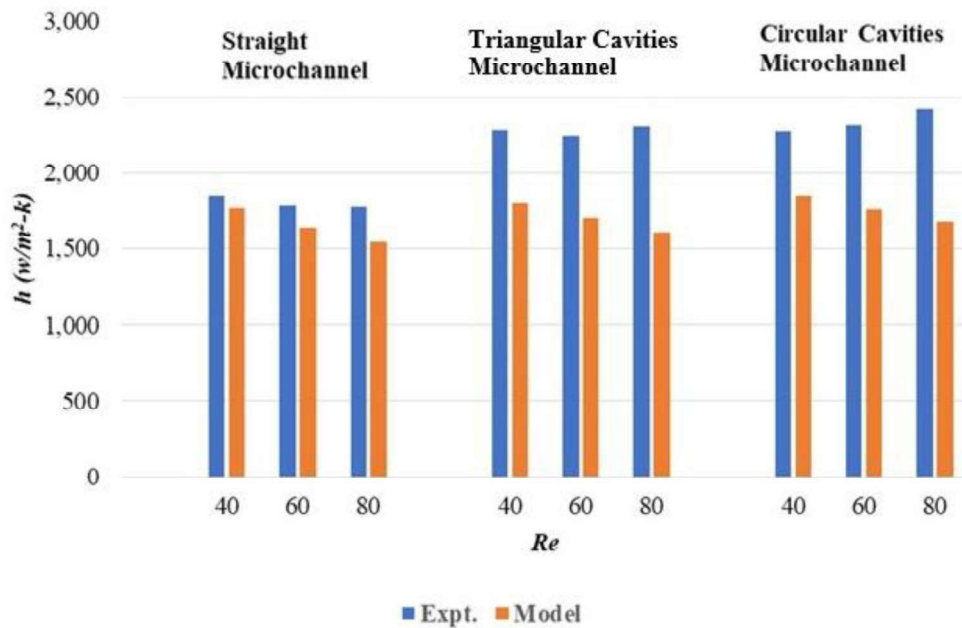


Fig. 3. Prediction of model HTC with Huang et al. experiment [15] for different shaped cavities of a microchannel varying the Reynolds numbers

Figure 3 depicts the present numerical model validation with the Huang et al. experiment [15]. The working fluid passes through one end of the channel whose bottom surface is generating a constant heat flux, due to this the fluid evaporates and vapor is formed at the other end. The temperatures are noted along the length of the channel, with these values the HTC is calculated. It is observed that there is a deviation in the numerical model values as compared to the experimental values of the HTC. The addition of the cavities along both sides of the channel will redirect the flow into the extended structured cavities. There are increased velocities in the cavities region and the flow changes from steady to oscillating. The oscillating flow causes the enhancement of heat transfer. Overall, there is a 3.5% enhancement in the HTC. Table 2 represents the error measurement associated with the present model. The error percentage deviation for straight channels is in the range of 4% to 13%. For the Triangular cavities test section, the error percentage deviation is in the range of 21% to 29%. And for the Circular cavities test section, its range is between 19% to 29%. An overall mean error of 19% is observed in the validation of the model with the experiment.

Table 2. Error percentages of HTC

Test Section	Re-40	Re-60	Re-80
Straight Channel	4%	8%	13%
Triangular Cavities channel	21%	24%	29%
Circular Cavities channel	19%	24%	29%

3.2 Validation of pressure drop reduction

The pressure drop reduction factor is associated with the input pumping power required to run the flow along the channel. So, this factor is important in improving the economy of the MCHXs. The model predictions are promising concerning the experiment [15] as depicted in Fig. 4. The improved performance is in the range of 4% to 15% as reported in Table 3. As the fluid flows along the channel and pair of cavities, there is a sudden increase of cross-sectional area which causes the reduction of the acceleration of the flow and thereby causes less resistance along with the flow. The model captures the experimental trend of reduction of pressure drops with an overall mean error of 9%.

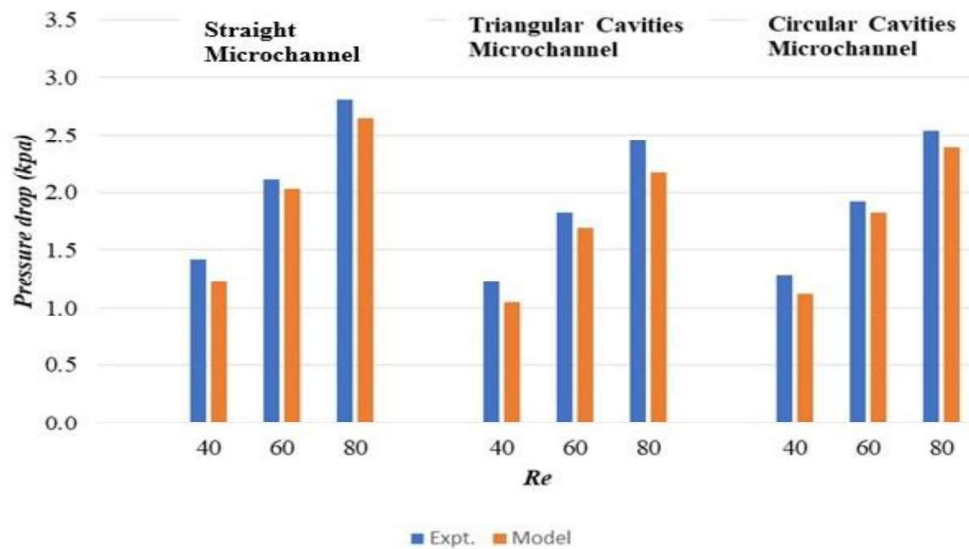


Fig. 4 Prediction of model pressure drop reductions with Huang et al. experiment [15] for different shaped cavities of a microchannel varying the Reynolds numbers.

Table 3. Improvement in Pressure Drop Reduction

Test Section	Re-40	Re-60	Re-80
Straight channel	13%	4%	6%
Triangular cavities channel	15%	8%	11%
Circular cavities channel	13%	5%	6%

3.3 Parametric variation

Parametric variation is studied to capture the physical configurations of the flow field. Figure 5 represents the variation of the HTC at $Re = 40$ for the three test sections. It shows that there is an enhancement of HTC for the test sections with cavities. The oscillating flow causes the enhancement of heat transfer as it prevails more in the case of the presence of circular cavities than the triangular shape. The model is extended to carry out the simulations at different wall temperatures to observe the effect of HTC in the microchannels as shown in fig. 6. From the results, it is observed that the HTC is more at the subcooled temperature of 20°C as sensible heat transfer plays a dominant role and further decreases with the increase in ambient temperature.

Figure 7 represents the variation of pressure drop reduction for the three different test sections at Reynolds Number 40. It shows that the pressure drop is less for triangular cavities channel i.e., 1.05 kpa, followed by circular cavities channel with 1.12 kpa. Compared with the straight microchannel, the pressure drop reduction is improved with cavities. Whereas fig. 8 revealed the pressure drop reduction for the straight microchannel at Re-40 for the surrounding temperature of 20 degrees is 0.56 kpa. The pressure drop reduction decreases with an increase in the ambient temperature.

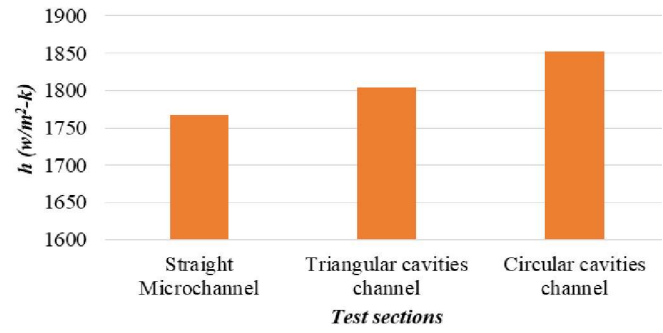


Fig.5. Variation of HTC for straight, triangular, and circular cavities at Reynolds number = 40.

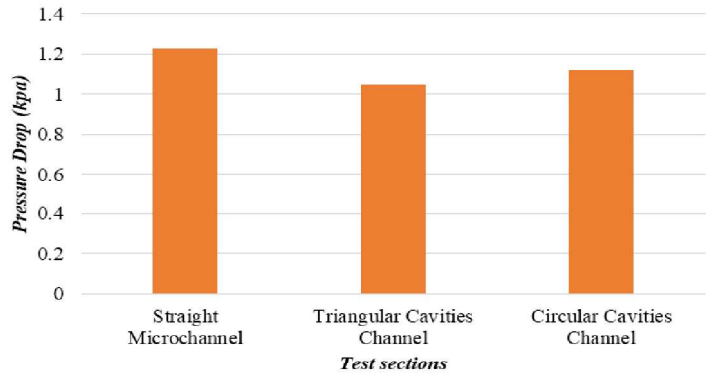


Fig. 6. Variation of HTC for different subcooling for straight microchannel at Reynolds number = 40.

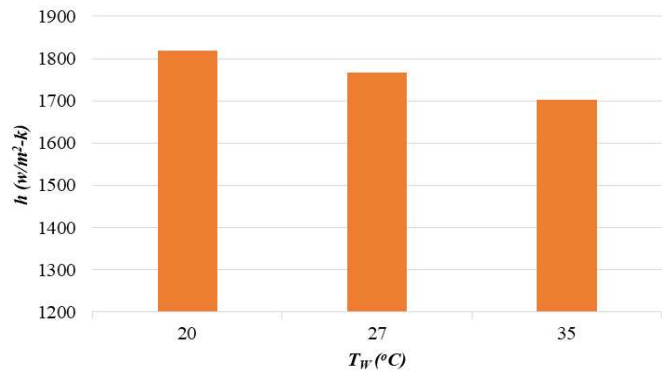


Fig.7. Variation of reduction of pressure drops for straight, triangular, and circular cavities at Reynolds number = 40.

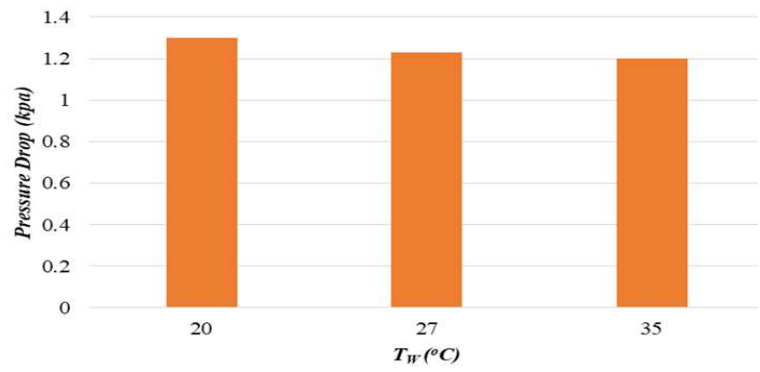


Fig. 8. Variation of reduction of pressure drops for different subcooling for straight microchannel at Reynolds number = 40.

4 Conclusions

In this investigation, simulation for MCHXs with different shaped cavities along the length of the channel is done.

- Cavities can enhance the HTC up to 4% by providing different geometries of cavities like triangular, circular, expansion, and contraction types along the length of the MCHX. The addition of the cavities along both sides of the channel will redirect the flow into the extended structured cavities. There are increased velocities in the cavities region and the flow changes from steady to oscillating. The oscillating flow causes the enhancement of heat transfer.
- With the increase in the Reynolds number, there is an enhancement of the HTCs as heat escapes at a faster rate.
- The pressure drop reduction for the test sections with the cavities is more as compared to the straight test section microchannels. The decreasing of pressure drop is observed for the test sections. Because, as the fluid flows along the channel and pair of cavities, there is a sudden increase of cross-sectional area which causes the reduction of the acceleration of the flow and thereby causing less resistance along with the flow.
- The HTC and reduction in the pressure drop are improved with these contraction, expansion, and circular cavities along the length of the channel.

Acknowledgement

The authors acknowledge Chemical Engineering Department, NIT Agartala for providing the computational facilities.

Nomenclature

A	Convective heat transfer area(m ²)	Re	Reynolds number
c_f	Fluid specific heat capacity (kJ/kg-K)	T_w	Wall temperature (K)
C_p	Specific heat (kJ/kg-K)	$T_{f,in}$	Inlet Temperature (K)
E_k	Enthalpy for phase k (kJ/kg)	$T_{f,out}$	Outlet Temperature (K)
F	Gravity (N)	ϑ_m	Mass-averaged velocity (m/s) = $\frac{\sum_{k=1}^n \alpha_k \rho_k \vartheta_k}{\rho_m}$
h	HTC (W/m-K)	$\vartheta_{dr,k}$	Drift velocity for secondary phase k (m/s) = $\mu_k - \mu_m$
h_k	Sensible enthalpy for phase k (kJ/kg)	ρ	Density
k	Thermal conductivity (W/m-K)	ρ_m	Mixture density (kg/m ³) = $\sum_{k=1}^n \alpha_k \rho_k$
k_{eff}	Effective conductivity (W/m-K)	α_k	Volume fraction of phase k
m_f	Mass flux (kg/s)	μ	Viscosity
n	Number of phases	μ_m	Viscosity of the mixture (kg/m-s) = $\sum \alpha_k \rho_k$
Q_{absorb}	Energy absorbed by fluid (W)		

References

1. D. B. Tuckerman and R. F. W. Pease, "High-performance heat sinking for VLSI", *IEEE Electron Device Lett.*, vol. 2, no. 5, 1981, pp. 126-129.
2. C. Herman and E. Kang, "Heat transfer enhancement in a grooved channel with curved vanes", *Int. J. Heat Mass Transfer*, vol. 45, no. 18, 2002, pp. 3741-3757.
3. F. Hong and P. Cheng, "Three-dimensional numerical analyses and optimization of offset strip-fin micro-channel heat sinks", *Int Commun Heat Mass*, vol. 36, 2009, pp. 651-656.

4. X. F. Peng and G. P. Peterson, "Convective heat transfer and flow friction for water flow in microchannel structures", *Int. J. Heat Mass Transfer*, vol. 39, no. 12, 1996, pp. 2599–2608.
5. P. Jiang, M. Fan, G. Si and Z. Ren, "Thermal–hydraulic performance of small-scale micro-channel and porous-media heat-exchangers", *Int. J. Heat Mass Transfer*, vol. 44, 2001, pp. 1039–1051.
6. W. Qu, and I. Mudawar, "Experimental and numerical study of pressure drop and heat transfer in a single-phase microchannel heat sink", *Int. J. Heat Mass Transfer*, vol. 45, 2002, pp. 2549 – 2565.
7. I. Tiselj, G. Hetsroni, B. Mavko, A. Mosyak, E. Pogrebnyak and Z. Segal, "Effect of axial conduction on the heat transfer in microchannels", *Int. J. Heat Mass Transfer*, vol. 47, 2004, pp. 2551–2565.
8. D.K. Kim and S.J. Kim, "Averaging approach for micro-channel heat sinks subject to the uniform wall temperature condition", *Int. J. Heat Mass Transfer*, vol. 49, 2006, pp. 695–706.
9. Y. Mishan, A. Mosyak, E. Pogrebnyak and G. Hetsroni, "Effect of developing flow and thermal regime on momentum and heat transfer in micro-scale heat sink", *Int. J. Heat Mass Transfer*, vol. 50, 2007, pp. 3100 – 3114.
10. G. Wang, L. Hao and P. Cheng, "An experimental and numerical study of forced convection in a microchannel with negligible axial heat conduction", *Int. J. Heat Mass Transfer*, vol. 52, 2009, pp. 1070–1074.
11. P. Gunnasegaran, H. Mohammed, N. Shuaib and R. Saidur, "The effect of geometrical parameters on heat transfer characteristics of the micro-channels heat sink with different shapes", *Int Commun Heat Mass*, vol. 37, 2010, pp. 1078–1086.
12. V.V. Dharaiya and S.G. Kandlikar, "A numerical study on the effects of 2d structured sinusoidal elements on fluid flow and heat transfer at the microscale" *Int. J. Heat Mass Transfer*, vol. 57, no. 1, 2013, pp. 190–201.
13. L. Chai, G.D. Xia and H.S. Wang, "Parametric study on thermal and hydraulic characteristics of laminar flow in a microchannel heat sink with fan-shaped ribs on sidewalls Part 2: Pressure drop", *Int. J. Heat Mass Transfer*, vol. 97, 2016, pp. 1081–1090.
14. H M. D. Capua, R. Escobar, A.J. Diaz and A. M Guzmán, "Enhancement of the cooling capability of a high concentration photovoltaic system using micro-channels with forwarding triangular ribs on sidewalls", *Appl. Energy*, vol. 226, 2018, pp. 160–180.
15. B. Huang, H. Li, S. Xia and T. Xu, "Experimental investigation of the flow and heat transfer performance in micro-channel heat exchangers with cavities", *Int. J. Heat Mass Transfer*, vol. 159, 2020, pp. 120075.
16. M.Q. Pan, H.Q. Wang, Y.J. Zhong, M.L. Hu, X.Y. Zhou, G.P. Dong and P.N. Huang, "Experimental investigation of the heat transfer performance of microchannel heat exchangers with fan-shaped cavities", *Int. J. Heat Mass Transfer*, vol. 134, 2019, pp. 1199–1208.
17. J. H. Keenan and F. G. Keyes, "Thermodynamic Properties of Steam" *John Wiley, New York*, 1949.

Thermal Management of a Cubical Building using Hydrated Salt 24

Dipak Chandra Das, Kumar Gourav, Pritam Das

1 Introduction

Phase change materials (PCMs) have various engineering applications, such as building cooling [1], industry thermal energy storage (TES) [2], battery thermal management [3], electric/power peak regulation [4], for its suitable thermal and eco-friendly characteristics. Confronted with the shortages of energy resources, using PCM attracts more attention to improve the thermal and human comfort inside a room by balancing the temperature variation inside the room. PCM also offers to minimize the extreme heatwave inside the non-airconditioned rooms. The PCM absorbs heat during the melting when room temperature increases in daytime and releases heat during the solidification as temperature decreases at night and also balances the use of renewable and non-renewable energies by reducing the consumption of fossil fuels.

The enhancement of the energy performance of buildings is carefully analyzed along with the energy consumption issues associated with the improvement of living standards that makes the energy policy for the local and global community for the upcoming days. [4,5,6]. Detailed analyses were carried out for ensuring thermal comfort associated with the greenhouse effect, operational cost. In order to rationalize the energy for domestic use and export, gulf nations have started to reduce the consumption of energy of houses [7]. Kousksou et al. [8] reviewed the primary challenges and applications of TESs extensively. Soares et al. [9] carried out experimental investigations of passive TESs with PCMs and analyzed the thermal characteristics of an envelope of the building and energy consumption issues concerning operational cost and heat load calculation. The minimization of CO₂ emissions during heating and cooling is also observed. Lin et al. [10] performed a simulation study on houses of different sizes for different PCMs and found that the fluctuation of the temperature inside the house is reduced. They also observed that the system gives higher efficiency with an increase in the thickness of the PCMs. Hasnain [11] analyzed the insulating characteristics of the different PCMs which can cause problems of a heat recovery cycle leads to raise the melting temperature and degrade the performance of that system. The use of extended surfaces can minimize the problem. Cardenas and Leon [12] showed the path of overcoming the lowering of transfer area associated with low thermal conductivity of the PCM as compared to micro and macro encapsulation by incorporation of fins which are in direct contact with the heating wall and mixing the low thermal conductivity PCM with the high conductivity one. Jin and Zhang [13] utilized the PCM into residential applications and reported that the variation of temperatures measured throughout the year at different seasons and weather conditions. The mentioned issue can be solved by introducing multi-layered PCMs. Belmonte et al. [14] performed a numerical analysis on a configuration where a PCM is incorporated into a floor. They have used a hydronic radiant ceiling as an energy discharge equipment and found that system reduces the energy consumption by more than 50% by incorporating an air-to-air heat recovery device. Lin et al. [15] designed a ceiling ventilation device combined with solar PV thermal collectors and PCMs. The system could deliver the maximum air temperature rise of 23.1°C without using the air conditioning system in winter. Kamkari and Shokouhmand [16] performed a set of experiments to characterize the melting of a PCM with and without the inclusion of horizontal fins and predicted the heat transfer associated with the melting process. They also observed that overall fin effectiveness

D. C. Das*, K. Gourav, P. Das

Department of Mechanical Engineering, NIT Agartala, Agartala - 799046, India

Yan et al. [17] characterized the dehydrating and the melting process of four different salt hydrates which is essential to design a TES. Wong-Pinto et al. [18] reviewed the mixing of nanoparticles with PCM to enhance the thermo-physical performance of the PCM and the addition of nanoparticles is elaborately described. Kumar et al. [19] summarized the different enhancement techniques to improve stability and thermal performance of salt hydrates using nanoparticles and expanded graphite. The investigations of PCM to enhance the thermal performance, reliability, and stability to use were carried out during different timeframes [20-23].

The present paper deals with the measurement of temperature variation between the outside and inside of a cubical building using hydrated salts HS24. The inorganic HS24 is chosen for its high thermal conductivity and high enthalpy associated with phase change processes. Another advantage of choosing HS24 is that thermo-physical properties resemble the climate of Tripura, India. The investigations are conducted for three distinct modes associated with inlet-outlet conditions, and natural-forced convection of airflow for winter, spring, and summer seasons.

2 Experimental Procedure

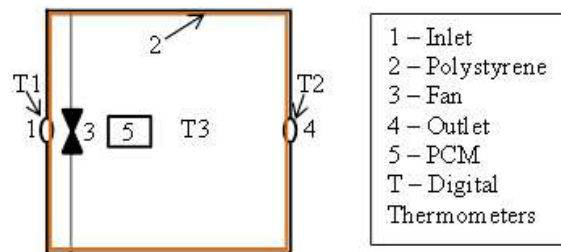


Fig. 1. Schematic of the experimental setup

A small TES is installed at the CASE Lab (Computational Analysis and Simulation for Experiment), Mechanical Engineering Department, National Institute of Technology Agartala as shown in fig. 1 to evaluate the thermal environment of the building. The temperature readings through the small TES unit are experimentally analyzed in terms of both melting and solidification processes. It contains three zones namely inlet, a small cubical container, and outlet zones. The cubical box has dimensions of $0.675 \times 0.675 \times 0.675 \text{ m}^3$ and the boundaries are made up of 0.02 m thick ply with inner insulation of polystyrene of 0.005 m thickness to insulate the system from the surrounding. Two circular holes on vertical parallel walls are made for airflow into the building. A supportive ventilating fan of 100 rpm is installed inside the cubical to force the airflow through the inlet and outlet. The PCM is placed inside the inlet wall at a distance xx mm from the outlet to the normal direction. Three digital thermometers that are calibrated at room temperature are used for measurements of temperature at the inlet, outlet, and inside the cube respectively. Four HS24 HDPE [25] insulated packets of PCMs are used for the given volume. HDPE encapsulation gives aluminium like thermal conductivity as claimed by the manufacturer.

For the PCM to work efficiently the temperature difference of 12 to 15°C is necessary between day and night. The PCM is used passively to get air conditioning. The climate of Tripura exhibits a strong seasonal rhythm. The state is characterized by a warm and humid tropical climate with the summer season extending from March to the half of October [24]. The temperature difference between day and night of Tripura is generally between 10 - 16°C [24] which is perfect for the PCM to be used. The average temperature of Tripura is roaming around 22-28°C so a PCM of the melting point of 24°C is selected for the experimentation. The properties of PCM are shown in Table 1.

The PCM is charged at day by taking the latent heat from solar energy. In the summer season, the PCM is charged during the day by taking the latent heat from solar energy to maintain the temperature fluctuations to a minimum and discharged at night. It is observed that the temperature variation of the building is steady and uniform with the application of the PCM.

Table 1. Thermophysical properties of the hydrated salt [25]

Property (savE 24)	Value	Property (savE 24)	Value
Melting Temp (°C)	26.0	Liquid Thermal Conductivity (W/mK)	0.55
Freezing Temp (°C)	25.0	Solid Thermal Conductivity (W/mK)	1.05
Latent Heat (kJ/kg)	199	Base Material	Inorganic
Liquid Density (kg/m ³)	1510	Congruent Melting	Yes
Solid Density (kg/m ³)	1621	Flammability	No
Liquid Specific Heat (kJ/kg K)	2.42	Thermal Stability (cycles)	~2000
Solid Specific Heat (kJ/kg K)	2.07	Maximum Operating Temperature (°C)	80

3 Result and Discussions

Readings are taken for three different seasons i.e., summer, winter, and spring seasons during the daytime from 0900 to 1600 hours for five days in every season, and mean temperature is calculated and presented in Table 2, 3, 4 respectively. The investigations are conducted for three distinct cases of inlet-outlet and natural-forced convection configurations of airflow i.e, Case A - Both inlet and outlet closed, Case B - Both inlet and outlet open with fan off (Natural Convection), and Case C - Both inlet and outlet open with the fan on (Forced Convection).

In winter, thermal gradient recorded are marginal for every case as expected due to the small temperature difference between the atmosphere, and freezing and melting point of HS24 PCM. The PCM raises the temperature of the building with a mean of 0.7°C. Natural convection case plays an important rule in winter as heat transfer escapes at a lower rate than the forced convection mode. The mean temperature increases by 0.9°C in natural convection against the 0.8°C and 0.5°C increase for forced convection and adiabatic condition respectively.

Table 2. Data Recorded in Winter 2019

Case	Thermometer	Temperature (°C) during time intervals							
		0900	1000	1100	1200	1300	1400	1500	1600
A	T1	16.5	18.4	21.1	22.3	23.5	22.7	21.9	20.1
	T2	16.7	18.8	21.4	22.5	23.6	22.9	22.0	20.3
	T3	17.0	19.0	21.7	22.8	23.9	23.1	22.2	20.4
	T1-T2	0.2	0.4	0.3	0.2	0.1	0.2	0.1	0.2
	T1-T3	0.5	0.6	0.6	0.5	0.4	0.4	0.3	0.3
B	T1	16.5	18.4	21.1	22.3	23.5	22.7	21.9	20.1
	T2	17.2	19.6	21.8	22.7	23.8	23.5	22.6	20.8
	T3	17.5	19.8	22.0	22.9	24.0	23.7	22.8	21.0
	T1-T2	0.7	1.2	0.7	0.4	0.3	0.8	0.7	0.7
	T1-T3	1.0	1.4	0.9	0.6	0.5	1.0	0.9	0.9
C	T1	16.5	18.4	21.1	22.3	23.5	22.7	21.9	20.1
	T2	17.3	19.1	21.8	22.6	23.7	23.1	22.4	21.1
	T3	17.6	19.3	22.1	22.8	23.9	23.2	22.7	21.3
	T1-T2	0.8	0.7	0.7	0.3	0.2	0.4	0.5	1.0
	T1-T3	1.1	0.9	1.0	0.5	0.4	0.5	0.8	1.2

Spring and summer season of Tripura show a similar trend of results as temperature decreases for every case. The mean temperature decreases by 1.3°C, 1.4°C, 3.2°C in adiabatic, natural convection and forced convection modes whereas for summer season it records 1.4°C, 1.3°C, and 4.1°C respectively. The dataset show the mean thermal gradient are 2°C and 2.3°C for spring and summer. The maximum temperature drops in forced convection i.e, 4.1°C and 3.2°C for summer and spring respectively lead to think that HS24 works predominantly in the local weather of Tripura. The mean temperature is summarized in Table 5.

Table 3. Data Recorded in Spring 2020

Case	Thermometer	Temperature (°C) during time intervals							
		0900	1000	1100	1200	1300	1400	1500	1600
A	T1	24.1	25.0	25.6	26.4	27.6	26.4	25.7	23.5
	T2	25.1	24.6	24.1	24.9	26.1	25.2	24.3	23.1
	T3	24.8	24.4	23.8	24.6	25.7	24.9	24.1	23.0
	T1-T2	1.0	0.4	1.5	1.5	1.5	1.2	1.4	0.4
	T1-T3	0.7	0.6	1.8	1.8	1.9	1.5	1.6	0.5
B	T1	22.1	22.4	22.6	22.9	23.3	22.8	22.4	21.9
	T2	22	21.8	21.7	21.4	21.7	21.2	21.1	20.8
	T3	21.7	21.4	21.3	21.1	21.4	21.0	20.9	20.6
	T1-T2	0.1	0.6	0.9	1.5	1.6	1.6	1.3	1.1
	T1-T3	0.4	1.0	1.3	1.8	1.9	1.8	1.5	1.3
C	T1	27.5	28.9	29.7	30.5	32.1	31.8	30.3	29.1
	T2	26.3	26.1	26.5	26.8	27.9	27.8	27.7	27.6
	T3	26.1	25.8	26.2	26.4	27.6	27.4	27.5	27.5
	T1-T2	1.2	2.8	3.2	3.7	4.2	4.0	2.6	1.5
	T1-T3	1.4	3.1	3.5	4.1	4.5	4.4	2.8	1.6

Table 4. Data Recorded in Summer 2020

Case	Thermometer	Temperature (°C) during time intervals							
		0900	1000	1100	1200	1300	1400	1500	1600
A	T1	29.6	30.2	32.2	33.8	36.2	35.5	32.6	29.9
	T2	28.9	29.7	31.4	32.6	34.8	33.6	32.4	29.2
	T3	28.6	29.3	30.8	32.0	34.0	33.1	32.1	29.1
	T1-T2	0.7	0.5	0.8	1.2	1.4	1.9	0.2	0.7
	T1-T3	1	0.9	1.4	1.8	2.2	2.2	0.5	0.8
B	T1	29.6	30.2	32.2	33.8	36.2	35.5	32.6	29.9
	T2	29.1	29.6	31.2	32.8	35.2	34.6	32.2	29.4
	T3	28.6	29.1	30.6	32.0	34.4	33.9	31.8	29.1
	T1-T2	0.5	0.6	1.0	1.0	1.0	0.9	0.4	0.5
	T1-T3	1	1.1	1.6	1.8	1.8	1.6	0.8	0.8
C	T1	29.6	30.2	32.2	33.8	36.2	35.5	32.6	29.9
	T2	28.0	28.2	27.7	28.8	30.7	30.4	28.5	26.8
	T3	27.7	28.0	27.3	28.5	30.6	30.1	28.3	26.5
	T1-T2	1.6	2.0	4.5	5.0	5.5	5.1	4.1	3.1
	T1-T3	1.9	2.2	4.9	5.3	5.6	5.4	4.3	3.4

Table 5. Average Modulus Temperature Differences (°C)

Season	Case A	Case B	Case C	Mean
Winter	0.5	0.9	0.8	0.7
Spring	1.3	1.4	3.2	2
Summer	1.4	1.3	4.1	2.3

Figure 2 depicts the temperature variation of Case A, Case B, and Case C separately throughout the winter, spring, and summer. It can be seen that the PCM tries to maintain the temperature within the human comfort zone. Forced convection cases play the vital rule that creates the maximum temperature difference leads to balance the human comfort temperature. PCM also reduces temperature fluctuations.

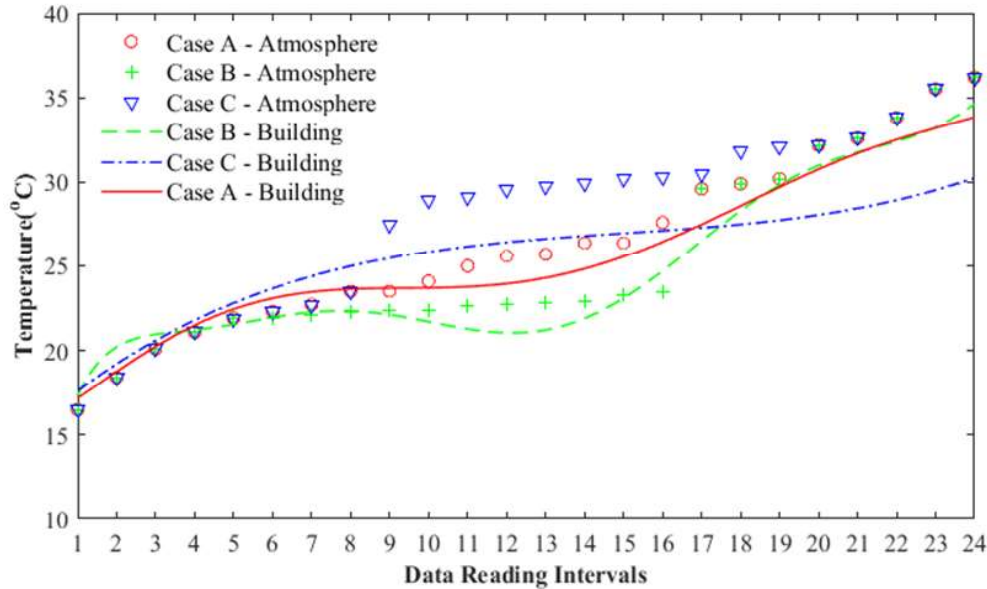


Fig. 2. Overall data readings for different flow situations

4 Conclusions

The temperature readings taken show the positive impact of the inclusion of PCM in the building. It also shows the fluctuations in temperature being reduced. Time delay in temperature change can be seen from readings. It is expected that the annual energy savings for heating and cooling will be increased as PCM generates a notable temperature difference. The notable findings from the experiment are detailed as

- The maximum temperature difference is recorded as 5.6°C which is obtained in the summer season and the temperature delay is increased.
- Though the PCM used for the winter season is not very effective in creating a warming effect it was able to delay the temperature change and hence maintaining the comfort of the building.
- The result of the temperature steadiness implies that the PCMs can be utilized in the non-air-conditioned building for creating a gradual cooling effect.

Acknowledgment

The authors express their gratitude towards the Deepraj Datta, Tuhinabha Chaudhuri, and Nilanjan Debbarma, UG Students, and Rahul Roy, PG Student, Department of Mechanical Engineering, NIT Agartala for their support and contributions in this experimental work.

References

1. S. Álvarez, L. F. Cabezas, A. Ruiz-Pardo, A. Castell, J. A. Tenorio, Building integration of PCM for natural cooling of buildings, *Applied Energy*, 109 (2013) 514-522.
2. P. Royo, L. Acevedo, V. J. Ferreira, T. García-Armingol, A. M. López-Sabirón, G. Ferreira, High-temperature PCM-based thermal energy storage for industrial furnaces installed in energy-intensive industries, *Energy*, 173 (2019) 1030-1040.

3. A. Verma, S. Shashidhara, D. Rakshit, A comparative study on battery thermal management using phase change material (PCM), *Thermal Science and Engineering Progress*, 11 (2019) 74–83.
4. L. Pérez-Lombard, J. Ortiz, C. Pout, A review on buildings energy consumption information, *Energy and Buildings* 40 (3) (2008) 394–398.
5. E. Asadi, M. Gameiro, C. Henggeler, L. Dias, Multi-objective optimization for building retrofit strategies: a model and an application, *Energy and Buildings* 44 (2012) 81–87.
6. C. Diakaki, E. Grigoroudis, D. Kolokotsa, towards a multi-objective optimization approach for improving energy efficiency in buildings, *Energy and Buildings* 40 (2008) 1747–1754.
7. S. Alotaibi, Energy consumption in Kuwait: prospects and future approaches, *Energy Policy* 39 (2011) 637–643.
8. T. Kousksou, P. Bruel, A. Jamil, T. El Rhafiki, Y. Zeraouli, Energy storage: applications and challenges, *Solar Energy Materials and Solar Cells* 120 (2014) 59–80.
9. N. Soares, J.J. Costa, A.R. Gaspar, P. Santos, Review of passive PCM latent heat thermal energy storage systems towards buildings' energy efficiency, *Energy and Buildings* 59 (2013) 82–103.
10. Lin, W.; Ma, Z.; Cooper, P.; Sohel, M.I.; Yang, L. Thermal performance investigation and optimization of buildings with integrated Phase Change Materials and solar photovoltaic thermal collectors. *Energy Build.* 2016, 116, 562–573]
11. S.M. Hasnain, on sustainable thermal energy storage technologies, Part I: Heat storage materials and techniques. *Energy Convers. Manag.* 1998, 39, 1127–1138.
12. B. Cardenas, N. Leon, High temperature latent heat thermal energy storage: Phase Change Materials, design considerations and performance enhancement techniques. *Renew. Sustain. Energy Rev.* 2013, 27, 724–737.
13. X. Jin, X. Zhang, Thermal analysis of a double layer Phase Change Material floor. *Appl. Therm. Energy* 2011, 31, 1576–1581.
14. J.F. Belmonte, P. Eguía, A.E. Molina, J.A. Almendros-Ibáñez, Thermal simulation and system optimization of a chilled ceiling coupled with a floor containing a phase change material (PCM), *Sustain. Cities Soc.* 14 (2015) 154–170.
15. W.Y. Lin, Z.J. Ma, M.I. Sohel, P. Cooper, Development and evaluation of a ceiling ventilation system enhanced by solar photovoltaic thermal collectors and phase change materials, *Energy Convers. Manage.* 88 (2014) 218–230.
16. B. Kamkari, H. Shokouhmand, Experimental investigation of phase change material melting in rectangular enclosures with horizontal partial fins, *International Journal of Heat and Mass Transfer* 78 (2014) 839–851.
17. T.S. Yan, T.X. Li, J.X. Xu, J.W. Chao, Understanding the transition process of phase change and dehydration reaction of salt hydrate for thermal energy storage, *Applied Thermal Engineering* (2019), doi: <https://doi.org/10.1016/j.applthermaleng.2019.114655>
18. L. S. Wong-Pinto, Y. Milian, S. Ushak, Progress on use of nanoparticles in salt hydrates as phase change materials, *Renewable and Sustainable Energy Reviews* 122 (2020) 109727.
19. N. Kumar, J. Hirschey, T. J. LaClair, K. R. Gluesenkamp, S. Graham, Review of stability and thermal conductivity enhancements for salt hydrates, *Journal of Energy Storage* 24 (2019) 100794.
20. Schmit H, Rathgeber C, Hooek P, Hiebler S, Critical review on measured phase transition enthalpies of salt hydrates in the context of solid-liquid phase change materials, *Thermochimica Acta* (2019), doi: <https://doi.org/10.1016/j.tca.2019.178477>
21. N. Xie, J. Luo, Z. Li, Z. Huang, X. Gao, Y. Fang, Z. Zhang, Salt hydrate/expanded vermiculite composite as a form-stable phase change material for building energy storage, *Solar Energy Materials and Solar Cells* 189 (2019) 33–42.
22. B.C. Zhao, R.Z. Wang, Perspectives for short-term thermal energy storage using salt hydrates for building heating, *Energy* 189 (2019) 116139.
23. A. Sharma, V. Tyagi, C. Chen, D. Buddhi, "Review on thermal energy storage with phase change materials and applications," *Renewable and Sustainable Energy Reviews*, pp. 318–345, February 2009.
24. The climate of Tripura, India, India Meteorological Department, <https://agartala.imd.gov.in/Tripura-Climatology/>
25. Salt Hydrates property, Pluss Advanced Technologies Pvt. Ltd., https://www.pluss.co.in/upload/technical-datasheets/2019/Doc%20325%20TDS_HS%2022.pdf

Numerical Investigation of Heat Transfer of a

Thermosyphon varying the Filling Ratios

Dipak Chandra Das, Tabrez Alam, Amit Kumar, Pritam Das

1 Introduction

Wickless heat pipe (WHP) follows the passive heat transfer mechanism using natural convection phenomena to circulate the liquid inside a vertical oriented closed-loop circuit without incorporating pumping power. Broader application areas include the electrical and electronic types of equipment cooling, heat exchanger, water heat recovery etc [1-5]. The WHPs consist of an evaporator, adiabatic and condenser sections which follow the evaporation and condensation of the working fluids to maintain the heat flows. Applied heat to the working fluid in the evaporator converts the liquid to vapour which get condensed in the condenser after passing through the adiabatic section. The condensate is returned to the evaporator by gravity effect to complete the loop.

There has been considerable research work done to model the steady-state and transient operation of the WHP. Shin et al. [1] studied the thermosyphon system using Tio₂-nanofluid with different volume ratios and heat fluxes and reported the 50% reduction in mean temperature difference. Jouhara and Robinson [2] examined the two-phase thermosyphon using water, FC-84, FC-77, and FC-3283. Jafari et al. [3] experimentally examined the thermosyphon system and developed heat transport correlations for various filling ratios (FR) and applied heat fluxes which predict the experimental results with tolerances of 30% and deviation of 10% in evaporator and condenser sections. Kusuma et al. [4] incorporated the RELAP 5/MOD 3.2 to simulate the WHP for the nuclear-spent fuel pool whereas Hasan and Abood [5] carried out the experimental investigation for the integrated WHP of a solar water heating system for various diameters of the evaporator. Singhal et al [6] investigated the copper thermosyphon implementing the volume of fluid (VOF) approach. The bubble formations are also recorded at time intervals. Andrzejck [7] incorporated the geyser boiling effects on the performance of a WHP using water, ethanol and SES36. Jubori and Jawad [8] developed an innovative CFD model to examine a WHP for different configurations. Zhang et al [9] numerically work on the wick construction of an annular heat pipe. Two type connection wick structures were designed, the axial direction wick structure and radial direction connection wick structure. A three-dimensional symmetrical model with liquid-vapour phase transition was built. Adnan et al [10] coupled the flat evaporator with a WHP for various FRs. Narendranathan [11] describe the CFD model of a thermosyphon, a type of heat exchanger and analyze its efficiency by varying its fill volume. El-Nasr and El-Haggar [12] studied the significance of the working fluids, container materials, number of wick layers and the wick structures on the heat transfer performance of the heat pipes. Ranjbar et al [13] numerically simulated the heat transport phenomenon in WHP using the VOF approach in a thermosyphon. Mukilarasan [14] experimentally investigated and compared the heat transfer characteristics of WHP using various heat inputs and found that the pipe made up of copper shows better characteristics. Aluminium is found to be effective while using ethanol and dichloromethane as the working fluid. Brass is found to be effective with acetone and for copper, toluene works better. Ahmad [15] experimentally investigated the WHP using water, acetone and mixtures of the two fluids at different ratios. Generally, the temperature of the evaporator outside surface increases from the bottom to peak at almost the middle of the evaporator and starts to decrease through the rest part of the evaporator and adiabatic section.

In this present work, a numerical model is developed using ANSYS FLUENT to study the thermal performance under various flow configurations at different filling ratios for applied heat inputs of a WHP. Filling ratio, defined as the ratio of the initial volume of fluid inside the evaporator section to the volume of the evaporator, is a vital input parameter that governs the performance of a thermosyphon. Heat transfers through evaporation and condensation processes are also examined. The work is extended to visualize the parametric variations through the temperature, water-liquid volume fraction, water vapour air volume fraction, pressure contours from a numerical perspective for the implementations of WHPs in vital applications.

2 Numerical Simulation

2.1 Governing Equation

The mixture model is developed by incorporating the governing equations detailed as follows:

The continuity equation can be expressed as

$$\partial/\partial t(\rho_m) + \nabla \cdot (\rho_m \mathbf{V}_m) = 0 \quad (1)$$

where

$$\mathbf{V}_m = \sum (\alpha_k \rho_k \mathbf{V}_k) / \rho_m \quad (2)$$

where

$$\rho_m = \sum \alpha_k \rho_k \quad (3)$$

The momentum equation can be obtained as

$$\partial/\partial t(\rho_m \mathbf{V}_m) + \nabla \cdot (\rho_m \mathbf{V}_m \mathbf{V}_m) = -\nabla P + \nabla \cdot [\mu_m (\nabla \mathbf{V}_m + \nabla \mathbf{V}_m^T)] + \rho_m \mathbf{g} + \mathbf{F} + \nabla \cdot (\sum \alpha_k \rho_k \mathbf{V}_{dr,k} \mathbf{V}_{dr,k}) \quad (4)$$

$$\mathbf{V}_{dr,k} = \mathbf{V}_k - \mathbf{V}_m \quad (5)$$

The energy equation is as follows

$$\partial/\partial t \sum (\alpha_k \rho_k E_k) + \nabla \cdot (\sum \alpha_k \mathbf{V}_k (\rho_k E_k + P)) = \nabla \cdot (K_{eff} \nabla T) + S_E \quad (6)$$

where

$$K_{eff} = \sum \alpha_k (K_k + K_t) \quad (7)$$

2.2 Computational Domain

The schematic and meshing of the computational domain of a WHP are presented in fig.1. A 2-D model having the dimension of $0.5 \times 0.025\text{m}$ is considered with 52065 nodes and 51200 elements. Mesh arrangement is examined by grid independence test for the mesh size 32×400 . Mesh independency test is more no of nodes that will take more time for calculation. The given table shows the mesh independency test result that there is no change in heat flux. The model is equipped with a liquid-water mixture. The specimen consists of condenser, adiabatic, and evaporator sections with vertical lengths of 150, 200, and 150 mm respectively. It has been assumed that the interface is permeable to liquid water. The simulation is carried out considering steady-state and implicit body force with appropriate factors. To counter pressure-velocity coupling, an algorithm called PISO is applied.

The gradient for spatial distribution is set as the Least Square cell-based method. To deal with pressure discretization, the PRESTO method is applied and to solve momentum and energy equations

first-order upwind scheme is employed assisted by the Quick scheme. As the species transport model and mixture are dealt with the help of the heat and mass transfer model, the relaxation factor should confirm the convergence.

A transient model was developed with a time step of 0.0001 seconds, while the flow is assumed to be laminar incompressible viscous flow. The boiling temperature of 373K was defined and the condenser temperature was set at 283K. 40%, 60%, and 80% FRs are considered with the inclinational angle of 90 degrees which is measured concerning the horizontal axis. The initial condition is set at no heating condition. No-slip boundary condition was fixed and constant heat flux is provided at the evaporator.

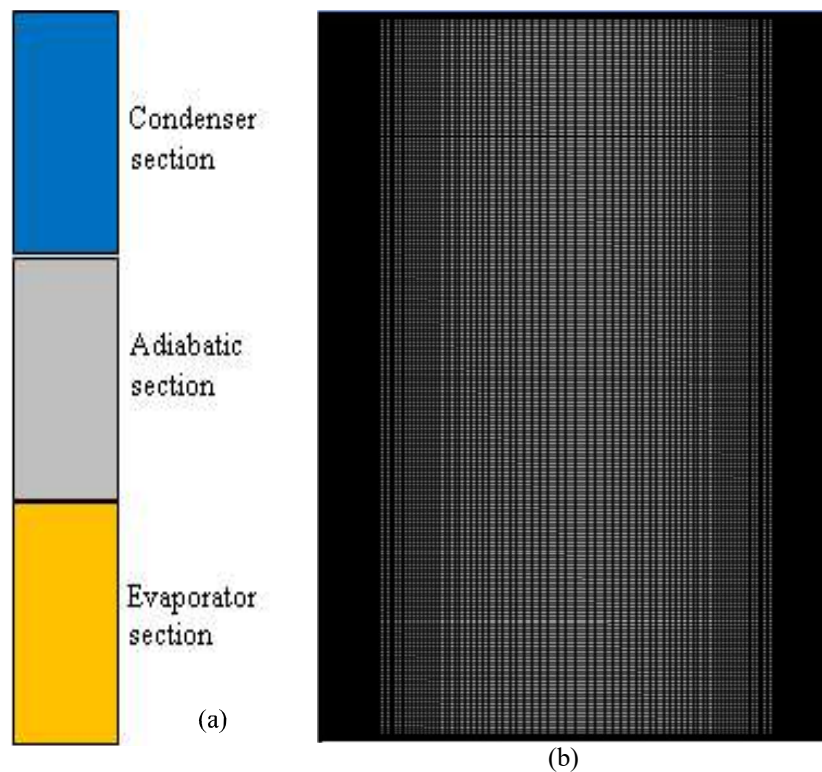


Fig. 1 (a) Schematic and (b) mesh distribution on the computational domain of a wickless heat pipe

3 Result and Discussion

The heat supplied at the evaporator converts the liquid to vapour at a later stage and goes to the condenser where it condenses and returns to the evaporator due to gravity. This process repeated again and again. Figure 2.(a) shows the temperature contour which represents temperature changes with time is indicating that there is a very low temperature in the evaporator section liquid. Condenser liquid has a higher temperature which shows that there is more vapour section in the Condenser section. It indicates that the vaporization of almost all the liquid has been done. The temperature of the evaporator section has given more initially, resulting in which water liquid gets evaporated.

Result as reported in fig. 2.(b) and 2.(c) show that at the evaporator section vapour volume fraction is 0.9982 which means almost all the water is converted into vapour and similarly at the condenser section vapour volume fraction is 0.9996, which means all the water is converted into the vapour. The pressure contour as depicted in fig. 2.(d) shows after the simulation which indicates that there is very low pressure in the evaporator as compared to the condenser.

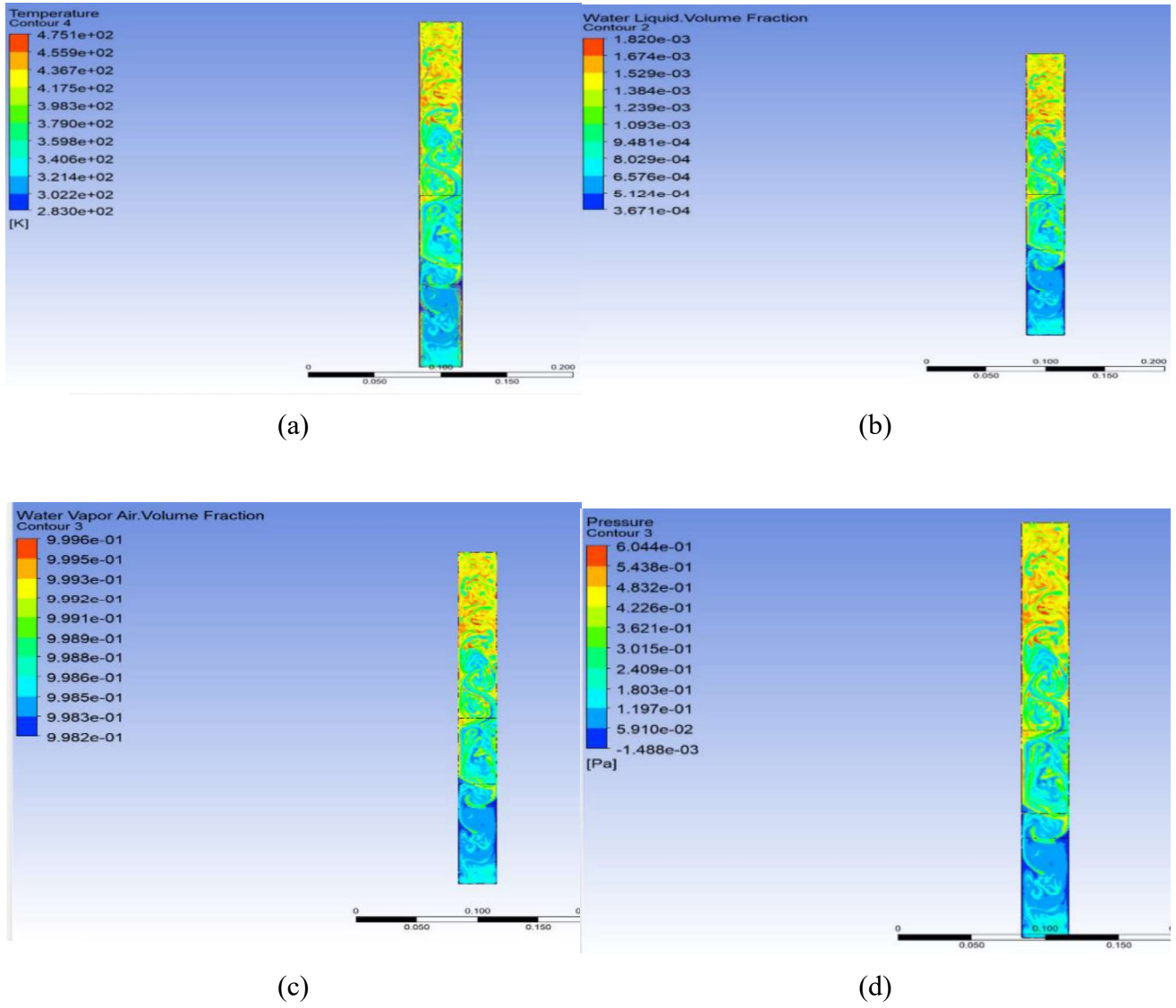


Fig. 2 (a) Temperature, (b) water-liquid volume fraction, (c) water vapour air volume fraction, (d) pressure contours

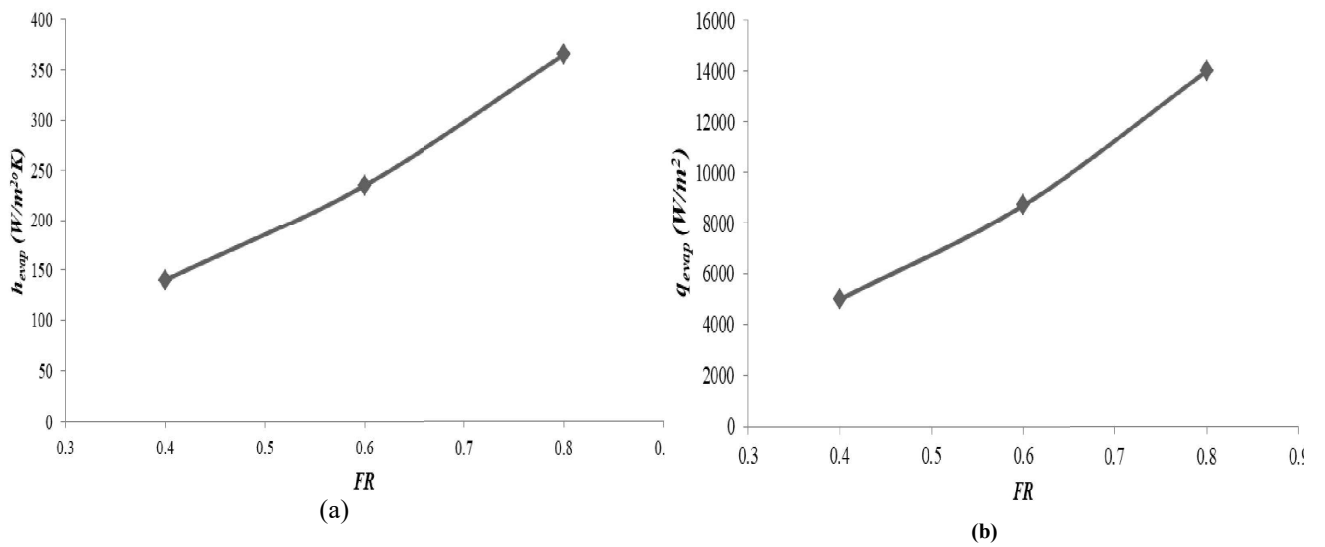


Fig. 3 Significance of filling ratio on evaporator section

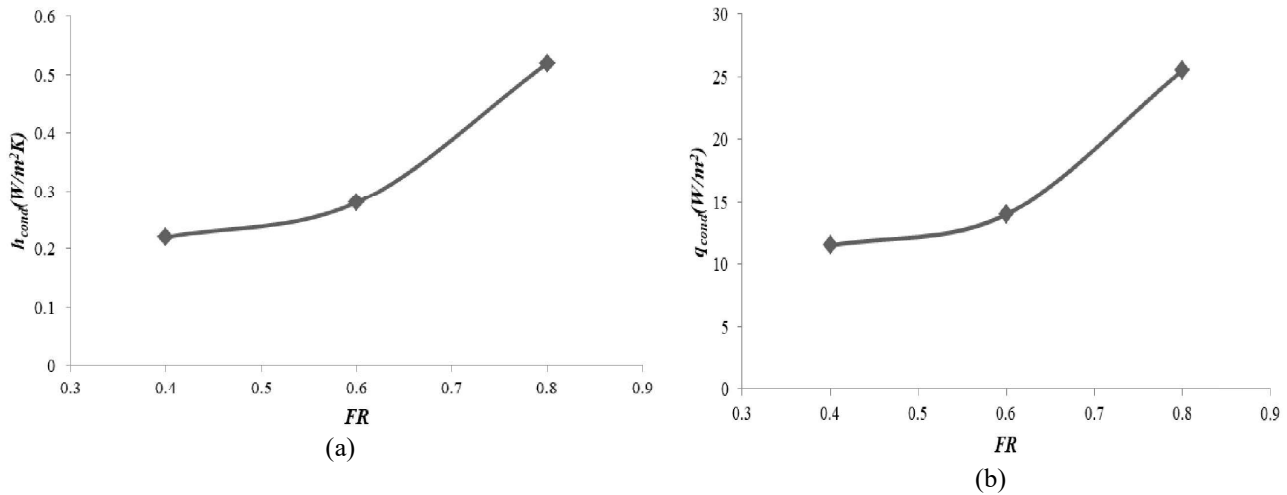


Fig. 4 Significance of filling ratio on condenser section

The fig. 3 and 4 show that the heat flux and the heat transfer coefficient increase with the FRs for the applied flow configurations inside the evaporator as well as condenser sections. Low FR also disturbs the operating of the heat pipe because, at low FR, the evaporator section liquid gets easily and early evaporated. With increasing the FR, the thermal resistance decreases which means heat transfer increases.

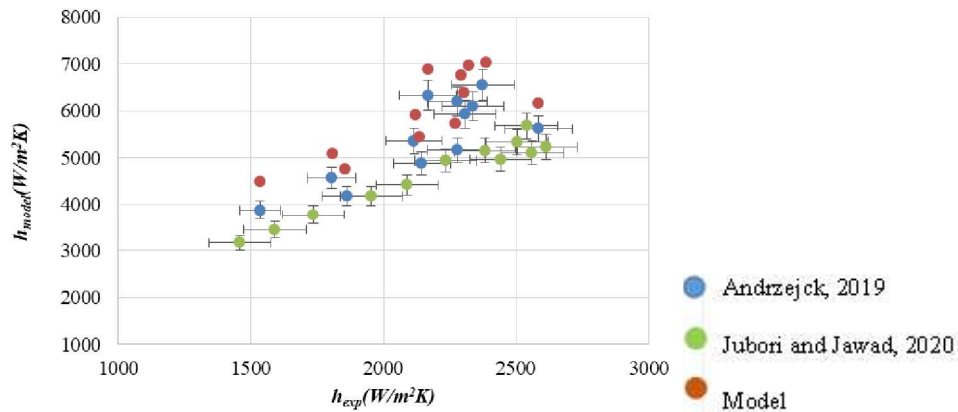


Fig. 5 Model vs experimental heat transfer coefficients

A comparison of experimental data for the heat transfer coefficient with the present numerical model provided a satisfying agreement as shown in fig. 5. The mean absolute errors are 7% and 12% concerning the experimental results of Andrzejek [7] and Jubori and Jawad [8] respectively.

4 Conclusions

A numerical model is developed using ANSYS FLUENT to study the thermal performance under various flow configurations at different filling ratios for applied heat inputs of a WHP for different FRs at fixed inclination angle. Heat transfers through evaporation and condensation processes are also examined. The work is extended to visualize the parametric variations through the temperature, water-liquid volume fraction, water vapour air volume fraction, pressure contours from a numerical perspective for the implementations of WHPs in vital applications. The predicted results reported that the heat flux in the evaporator and the condenser increases with an increase in the FR. At high FR, the heat transfer coefficient increases which mean heat transfer increases and thermal resistance decrease.

Acknowledgment

The authors express their gratitude towards the Chemical Engineering Department, NIT Agartala for their computational support.

Nomenclature

V_m	Mass Averaged Velocity (m/s)	u, v	Velocity components in x,y directions
ρ_m	Mixture Density (kg/ m ³)	V	Volume (m ³)
n	Number of Phases	α	Volume fraction
F	Body Force (N)	K	Thermal conductivity (W/m K)
μ_m	Viscosity of the mixture (Pa.s)	ν	Kinematic viscosity (m ² /s)
$V_{dr,k}$	Drift Velocity of the Secondary Phase K(m/s)	μ	Dynamic viscosity (Pa.s)
K_{eff}	Effective Thermal Conductivity (W/m K)	σ	Surface tension coefficient (N/m)
K_t	Turbulent Thermal Conductivity (W/m K)	ρ	Density (kg/m ³)
T	Temperature (K)		

References

1. D. R. Shin, S. H. Rhi, T. K. Lim and J. C. Jang “Comparative study on heat transfer characteristics of nanofluidic thermosyphon and grooved heat pipe”. *Journal of Mechanical Sciences and Technology* 25 (6) pp.1391-1398 (2011).
2. H. Jouhara, A. J. Robinson “Experimental investigation of small diameter two-phase closed thermosyphon charged with water, FC-84, FC-77 and FC-3283. *Applied Thermal Engineering*, 2009, 30 (2-3),pp-201
3. D. Jafari, P. D. Marco, S. Filippeschi, A. Franco, “An experimental investigation on the Evaporation and Condensation heat transfer of two phase closed thermosyphon”. *Experimental Thermal and Fluid Sciences* 88, pp. 111-123 (2017).
4. M. H. Kusuma, N. Putra, S. Ismarwanti, S. Widolo “Simulation of wickless Heat pipe as Passive cooling System in Nuclear Spent Fuel Pool using RELAP5/MOD3.2”.*International Journal on Advanced Science Engineering Information technology*.
5. A. J. Hasan, M. H. Abood “Experimental Investigation On Integrated Wickless Heat Pipe for Solar Water Heating”. *APRN Journal of Engineering and Applied Sciences*. Volume 13,NO 3 (2018).
6. S. Singhal, A. Gaikwad, J. Jaidi “CFD analysis of a wickless Heat Pipe”. IHMTTC (2017).
7. R. Andrzejck “Experimental Investigation of the thermal performance of a wickless heat pipe operating with different fluids: Water, Ethanol, and SES36. Analysis of influences of instability processes at working operation parameters”. *Energies* (2019)
8. A. M. A. Jubori and Q. A. Jawad “Computational evaluation of thermal behavior of a wickless heat pipe under various conditions”. *Case Studies in Thermal Engineering* 22 (2020).
9. H. Zhang, F. Ye, H. Guo, X. Yan, C. Ma, “Numerical study on the effects of the wick structure of an annular heat pipe on the isothermal performance”. *Proceeding of the 5th world congress on momentum, heat and mass transfer (MHMT 20)*.
10. S. I. Adnan, A. A. R. Ahmad and A. A. A. Rasool “Experimental study of wickless heat pipe with fat evaporator for used in cooling of electronic components”. *Journal of University of Babylon for engineering services*, Vol-27 (2019).
11. S.K Narendranathan “Analytical and Numerical analysis of thermosyphon”. *International Journal of Research in Mechanical Mechatronics and Automobile Engineering*, 2, Issue-5 pp.107-115.
12. A. A. El-Nasr and S. M. El-Haggar “Effective thermal conductivity of heat pipes”. *Heat and Mass Transfer*, 32, pp. 97-101, (1996).
13. B. Ranjbar “Numerical Simulation of Two-phase Flow and Heat Transfer Phenomenon in Wickless Heat Pipe”. *Specialty Journal Of Engineering and Applied Sciences*, 4, pp.1-12 (2019)
14. N. Mukilarasan, M. V. A. Romilton, S Ismath, I. Venkatraman, and R Vignesh “Experimental and Comparision Study of Heat Transfer Characteristics of Wickless heat pipes by using various heat input”. *International Journal for Research in Applied Sciences & Engineering Technology*, 6 (2018), pp. 758-769.
15. H. H. Ahmad “Heat Transfer Characteristics in a heat pipe using Water-Hydrocarbon Mixtures as a Working Fluid”. *Al-Rafidain Engineering*, 20 (2012), pp. 128-137.

Performance Optimization Techniques for Micro Heat Sinks: A Review

Sakshi Pandit, Amit Arora

1 Introduction

Electronic devices have wide range of applications like micro biomedical devices, small military gadgets, air conditioning systems, avionics technologies, automotive applications, and miniature robots. Integration of multiple circuit elements to increase functionality of these devices is a common industrial requirement. Electronic devices' efficient and prolonged working can be restrained by immense heat generation during their operation, eventually exceeding device temperature above critical limits. Overheating circuit components causes problems of crack formation, hairline fractures, voids formation, melting of solder, resulting in reduction of component's reliability [1] and causing premature device failure [2]. For every 1°C rise in temperature of an electronic component that is working between 70 to 80°C , its reliability declines up to 5% [3]. It is necessary to have a stringent thermal management solution to avoid breakdowns in electronic systems.

Various thermal management solutions such as heat pipe, cold plate, heat spreaders, Peltier cooling plate, jet impingement technique, thermoelectric cooler, heat sinks are studied in the last few decades. Heat sinks are one of the standard thermal solutions as it aims to dissipate heat from a hot device to a cooling medium and thus regulate device temperature within a threshold limit [4]. Conventional heat sinks are ineffective in satisfying the cooling requirement of miniaturized electronic devices [5,6]. In general, microdevices have hydraulic diameter between $1\text{ }\mu\text{m}$ to $1000\text{ }\mu\text{m}$ [7,8]. Therefore, emphasizing focus on heat transfer in microdomains, microchannel and micro pin fin heat sink possess great potential in solving the high heat flux problem. In general, a smooth microchannel heat sink can dissipate 790 W/cm^2 of heat flux with a maximum temperature rise of 71°C [9] because of its property of high heat transfer coefficient, high volume to surface area ratio and requirement of lower flow rate of fluid.

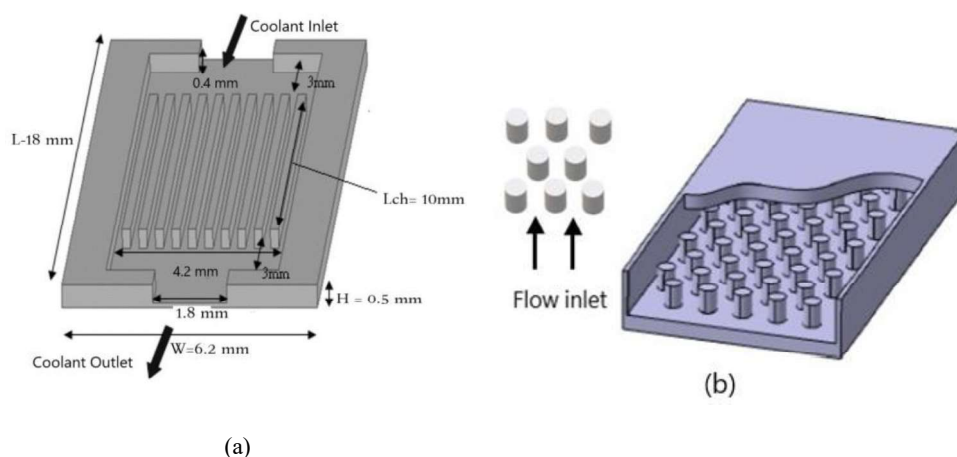


Fig. 1 Structure of (a) Microchannel heat sink [7], (b) Micro pin fin heat sink [11]

In this context, this article provides a state-of-the-art review on design optimization techniques of micro heat sink, discussed in standard benchmark investigations. Performance optimization of micro heat sink depends upon micro heat sink's 1) Types 2) Design characterizations (flow path arrangements, layout of fins, correctional shape, geometrical parameters, etc.) 3) Working fluid.

2 Critical performance parameters

This section enlists parameters which measure thermal and hydraulic performance of microchannel and micro pin fin heat sink. In numerous experimental and computational studies, thermal performance is evaluated by average heat transfer coefficient [10], Nusselt number [10], thermal resistance [11], and a temperature drop of the heat sink.

$$\text{Heat transfer coefficient } h = \frac{q''}{T_{avg} - T_l} \quad (1)$$

$$\text{Nusselt number } Nu = \frac{h D_h}{k_l} \quad (2)$$

$$\text{Maximum Thermal Resistance } R_{th,max} = \frac{T_{max} - T_{in}}{q''} \quad (3)$$

$$\text{Hydraulic diameter } D_h = \frac{2 W_c H_c}{W_c + H_c} = \frac{4 A}{P} \quad (4)$$

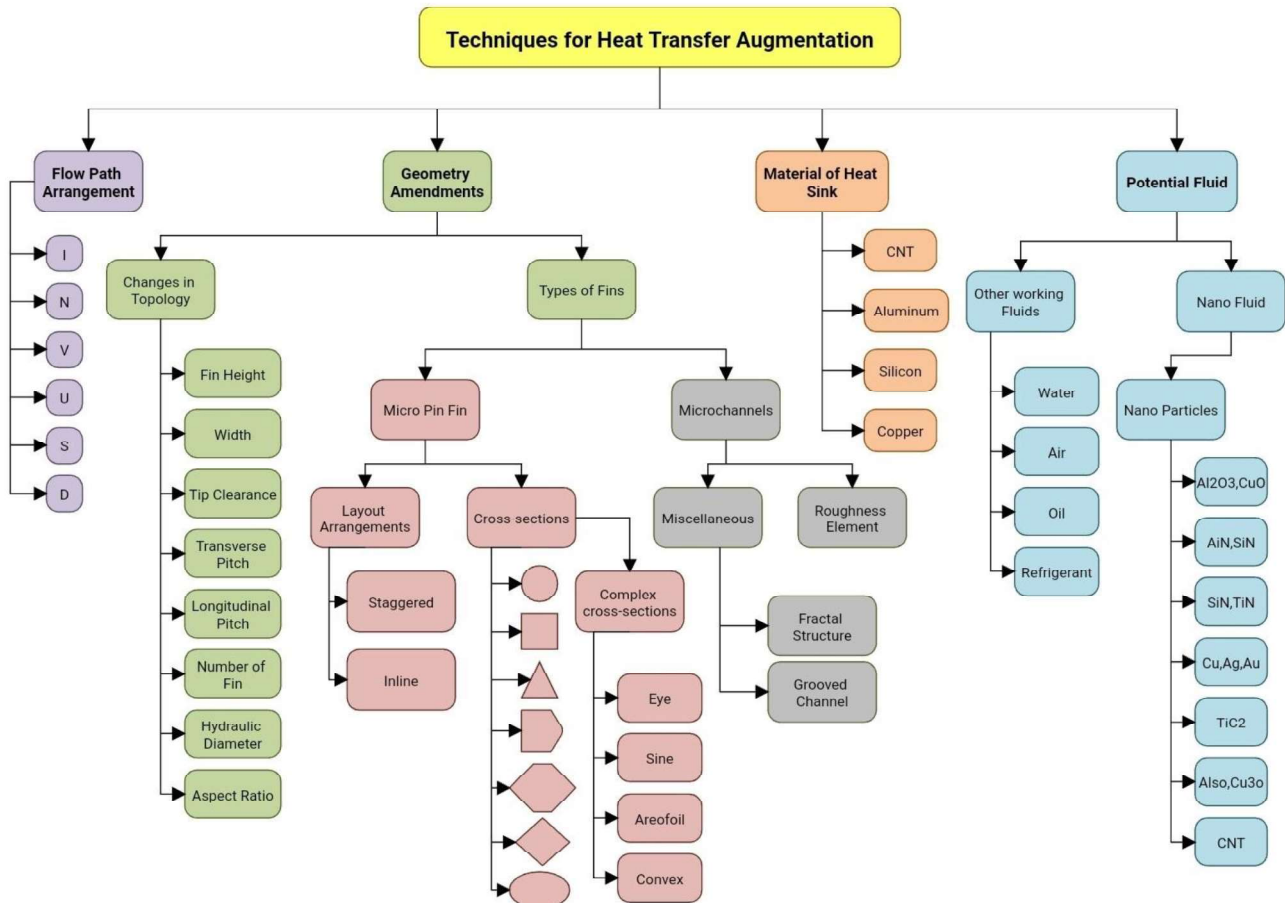


Fig. 2. Flow chart illustrating thrust areas for heat transfer augmentation.

Where Re is Reynolds number, Pr is Prandtl number and k_l is thermal conductivity of liquid, q'' is effective heat flux, T_{avg} is average temperature of solid-liquid contact surface and T_l is bulk fluid

temperature, T_{max} is maximum temperature of bottom substrate, T_{in} is fluid inlet temperature, A = area and W_c , H_c = width, height of microchannel.

Assessment of hydraulic performance is obtained by pressure drop [12,13], friction factor [14], and pumping power [15].

$$\text{Pressure drops } \Delta P = \frac{f \cdot N_x \cdot \rho \cdot U^2}{2} \quad (5)$$

$$\text{Friction factor } f = \frac{C}{Re^m} \quad (6)$$

$$\text{Pumping power } P = Q \cdot \Delta P \quad (7)$$

Where f is friction factor, ρ is fluid density, U is average velocity of fluid, N_x is number of rows of pin fins, C is geometry dependent friction factor coefficient, and m depends upon fluid flow regime, Q is volume flow rate of coolant.

Performance optimization depends on the micro heat sink's types, design characterizations (flow path arrangements, layout of fins, correctional shape, geometrical parameters, etc.), and material and working fluid used in the micro heat sink. Studies involving these techniques are discussed in upcoming sections. Thrust areas to have improved performance in micro heat sinks are shown in flow chart in Fig. 2.

3 Thermo-hydraulic characterization

The fundamental aim is to get a minimum value of temperature, thermal resistance, pressure drop (i.e., minimum pumping power requirements), and higher value of Nusselt number and heat transfer coefficient. This section includes characterization of heat sink based on evaluation of thermal and hydraulic performance parameters.

3.1 Comparison of microchannel and micro pin fin

Microchannel heat sink involves parallel channels constructed in alignment with fluid flow. The concept of microchannel was first proposed in an experimental study conducted by Tuckerman and Pease [9]. Progress in micromachining technologies leads to replacement of channels structure by pin fin arrays of staggered and inline configuration. A comparison made by Japerson et al. [16] revealed that micro pin fin heat sink has lower thermal resistance than microchannel heat sink at a fluid flow rate above 60 g/min and 30°C inlet temperature of fluid considering same characteristic dimensions and material of both heat sink. Micro pin fin arrays induce a higher flow mixing rate and create recirculation zones, increasing heat transfer [17]. Therefore, microchannel heat sink has poor thermal performance and less pressure drop than micro pin fin heat sink. The viscous shear and flow separation around pin fins increase the total pressure drop of the micro pin fin heat sink [11].

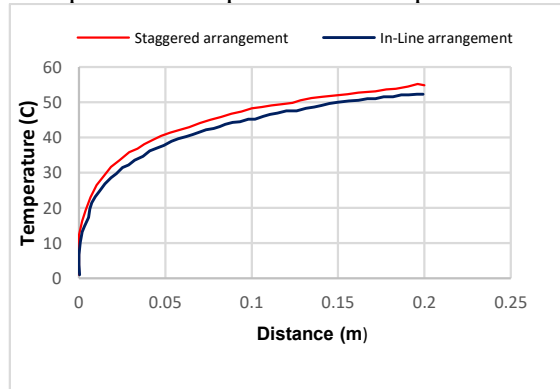


Fig. 3 Friction factor verses Reynolds number comparing in-line and staggered configuration [14].

3.2 Fin configurations

Inline and staggered are the two basic configurations of pin fins, studied experimentally and numerically by various researchers. Configurations of pin fin are the arrangement layout of pin arrays. Staggered configuration can be formed by offsetting alternate rows of inline configuration [13]. In a numerical study, Jalil et al.[4] found that staggered configuration improves thermal performance by 4.2% when tested with air velocity of 1m/s and 250 W input heat flux as depicted in Fig. 4. Fluid flow path in the staggered case has more obstruction that causes rise in fluid temperature at the exit section [4]. The staggered arrangement has the advantage of attaining higher Nusselt number. However, this arrangement results in higher pressure drop and friction factor, over inline configuration because of tortuous flow path of fluid around pins in staggered arrangement. This drawback can be overcome by using different shapes of pins or by changing fin dimensions and fin spacing. In a study, Vanapalli [14] took circle and square cross-section shapes of pin fin in staggered and in-line configuration and found that square staggered arrangements have lower friction factor than circular ones.

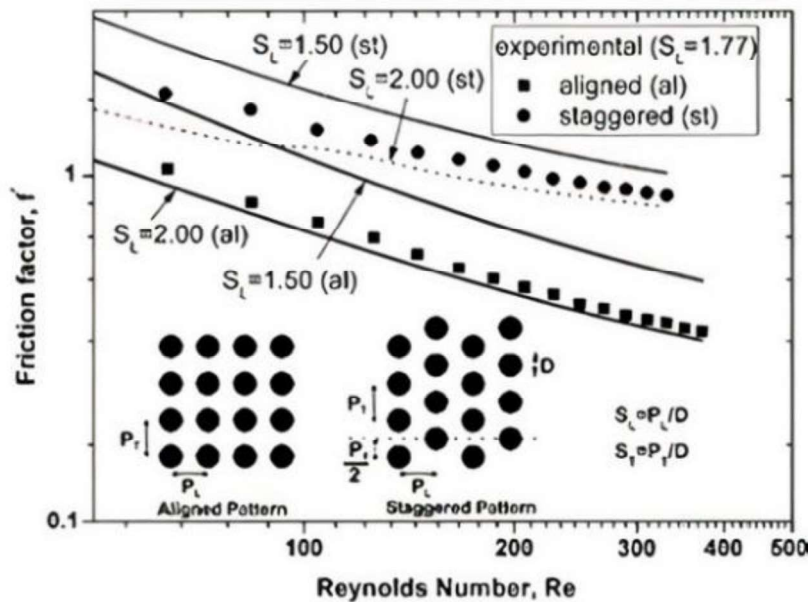


Fig. 4 Friction factor verses Reynolds number comparing in-line and staggered configuration [14].

3.3 Fractal structured microchannels

Fractal tree-like structures create branching for fluid flow in microchannels (as shown in Fig. 5.), which mimics the flow pattern followed in nature like fluid transport in leaf, airflow sacs in lungs. Under same flow rate and pumping power conditions, fractal-like bifurcated microchannels have reduced the temperature by 30 K and yielded 60% less pressure drop than basic straight microchannels [18].

Moreover, friction factor and Nusselt number both increase with increase in branching levels of fractal structures and decrease in aspect ratio of fractal structure channels within the same branching level. Many numerical studies investigated effects of bifurcation joint shapes, impact of bifurcation angles, and effect of bifurcations levels. An optimum value of bifurcation angle resulted in higher heat transfer capability and pressure drop. It was found that T joint bifurcation gives uniform cooling and reduced thermal resistance than Y joint bifurcation [15].

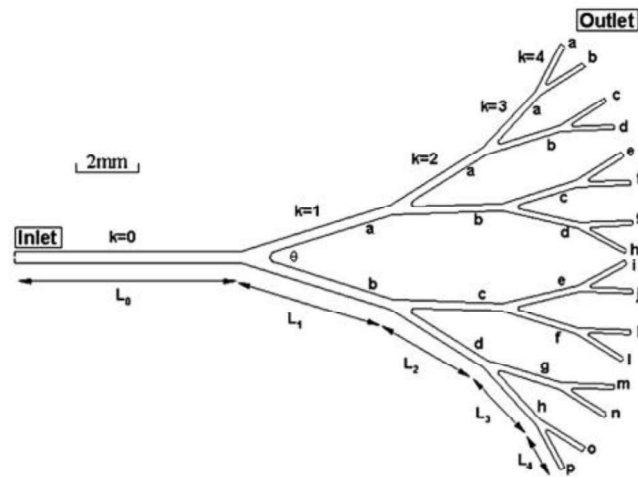


Fig. 5 Fractal structured microchannel [5].

3.4 Flow path arrangements

The design of inlet/outlet plenums for fluid flow is effective technique in improving cooling performance of micro heat sinks. Temperature uniformity in heat sink can be attained by inducing uniform flow conditions in micro heat sink. If non-uniform distribution of fluid exists, the performance of heat sink achieved in experiments will not be similar to that depicted in numerical studies. Six different microchannel heat sinks having different inlet/outlet arrangements in the way of I, N, S, D, U, V letters have been numerically analyzed by Chien and Chen [7] (fluid follows the shape of letters). The cases I, N, D, S have horizontal fluid entry and exit and have flow recirculation zones at corners. But in cases U, V heat sink, flow looks like impingement of jet at inlet with no recirculation zone formed. Also, at a fixed pressure drop of 35 kPa, values of flow rate were 2.3 m³/sec, 2.3 m³/sec, 2.4m³/sec, 2.6 m³/sec, 2.9m³/sec, 2.9m³/sec for N, S, D, I, U, V microchannel heat sink. Thus U, V heat sinks have higher temperature uniformity, pressure drop, lower velocity maldistribution, and lower thermal resistance than I, N, D, S type heat sinks, as seen in Fig. 6. Varying header shapes of microchannels can control flow non-uniformity. It was found that triangular, trapezoidal shapes give the best performance at lower flow rates and rectangular header shapes at higher flow rates [17].

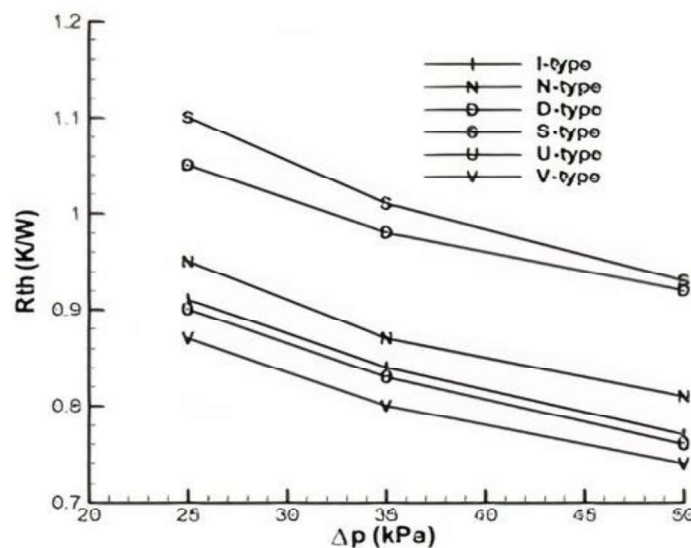


Fig. 6 Thermal resistance of different microchannel heat sinks as a function of pressure drop [7].

4 Design optimization of micro pin fins

Different researchers had made several amendments in design of micro pin fins to enhance heat transfer. Comparison of pin fin configuration and different cross-section shapes, optimization of pin fin dimensions, and pin fin spacing are various design improving techniques discussed below.

4.1 Effect of fin topology

Changes in topology features like height, width and hydraulic diameters of fins result in vague micro heat sinks' performance. Bhandari and Prajapati [10] numerically studied effect of varying fin height from 0.5 mm to 2.0 mm under uniform heat flux of 100 to 150 W/cm². They found that the fin height of 1.5 mm is optimum as increasing height beyond that doesn't result further increase in Nusselt number, as shown in Fig. 7. The reason for lower heat transfer potential after certain fin height is that it will decrease open space available on top of fins, preventing favorable flow behavior of fluid. Therefore, optimization of fin height is essential [12].

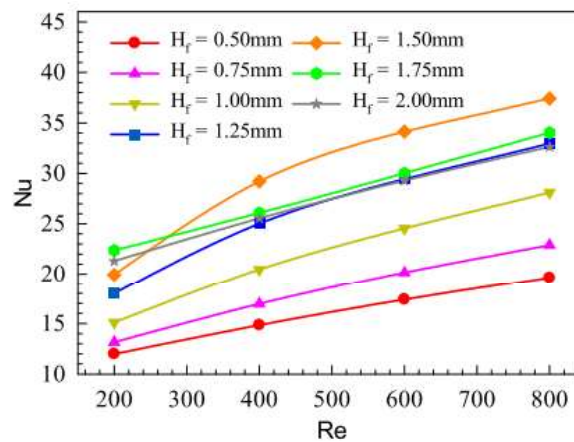


Fig. 7 Plot of Nusselt number at different values of Reynolds number comparing pin fin heights [12].

4.2 Effect of fins arrangement

John et al.[19] compared different cases of circular and square shape pins having transverse and longitudinal spacing varied between 350-650 μ m and 150-300 μ m respectively for performance evaluation using FOM parameter, which was weighted average of thermal resistance and pressure drop. In circle pin fins at lower Re number, FOM increased from 1.06 to 1.5 with the increase in longitudinal pitch from 350 to 650 μ m. Moreover, found no effect of increasing longitudinal spacing in square pin fins. There was increase in FOM with increase in transverse spacing of circular pins. But for square pins, there exist an optimum transverse spacing depending upon Reynolds number. Square pin fins were preferred at higher Reynold numbers over circle pin fins. Thus, the shape of pin fins and Reynolds number of fluids play an important role in determining performance along with changes in pin-fin spacing [19].

4.3 Effect of pin fin cross-section shapes

Cross-section shapes of pin fins are seen to affect thermo-hydraulic performance. Thus, various studies with their evaluation parameter magnitude are shown below in Table 1. In an experimental study by Yang et al. [20], triangular shape pins were found to have maximum temperature and pressure drop due to maximum blocking of fluid, whereas for circular shape pins

blocking was minimum, therefore minimum pressure drop occurs. Hexagonal pin fins guide the fluid flow and allow it to move in pin's back region, which improves cooling [20].























Vanapalli et al.[14] analyzed hydraulic performance of pillar matrices of different cross section shapes. They obtained that circle cross-section has more friction factor than lenticular (slim) shapes of rhombus, sine, ellipse. Circular pin fins cause abrupt changes in velocity of fluid due to extreme cross-sectional variations. To overcome disadvantages of flow separation, circular cross section was modified to airfoil shapes like hydrofoil, convex cross section shapes. In study Abdoli et al. [21] considered airfoil shapes with hotspot in heat sink, with input background heat flux at of 1000 W/cm², they found that hydrofoil shape and convex shape can improve pumping power by 30.4% and 47.3% respectively than circle shapes.

Tullius et al. [13] used computational simulation data to obtain correlation for Nusselt number across fins (Nu) as stated below considering fin height (hf), longitudinal spacing (SL), transverse spacing (St), clearance distance from the top (dh), Hydraulic diameter of fins (Df), (Prs) Prandtl number at surface for six basic pin fin cross-section shapes [13].

$$Nu = C_{Nu} \frac{S_L}{D_f}^{0.2} \frac{St}{D_f}^{0.2} \frac{h_f}{D_f}^{0.25} \left(1 + \frac{d_h}{D_f}\right)^{0.4} Re^{0.6} Pr^{0.36} \frac{Pr}{Pr_s}^{0.25} \quad (8)$$

Where C_{Nu} is a constant having value 0.08, 0.0937, 0.036, 0.0454, 0.0936, 0.0752 for circle, square, diamond, triangle, ellipse, hexagon cross sections respectively.

Table 1. Results of Yang et al. [20] having input heat transfer coefficient set as 10 W/m²K, Abdoli et al. [21] At 1000 W/cm² input heat flux , Vanapalli et al. [14] at Reynolds number 100, comparing different cross-section shape pin fins

	Parameters	Comparison of different cross-section shapes				
D. Yang et al.	Pressure drop (kPa)	17.7 	15.6 	15.5 	15.1 	14.7 
	Average Temperature (K)	321.1 	321.0 	320.5 	319.7 	319.2 
A. Abdoli et al.	Pumping power (W)	 Circle 0.13>	 Hydrofoil 0.09>	 Convex 0.06		
	Average Temperature (°C) @ 1000 W/cm ² heat flux	 Circle 74.9>	 Hydrofoil 73.0>	 Convex 70.0		
S. Vanapalli et al.	Friction factor @ Re=100	 Circle >	 Square >	 Rhombs >	 Eye >	 Ellipse >  Sine >

5 Potential working fluid

One of the ways to enhance thermal performance of micro heat sink is by improving characteristics of working fluid. It is essential to understand flow physics in order to elucidate fluid regime at micro-scale. Too small dimensions of microscale heat sinks are comparable with mean free path of fluid particles. Thus, flow physics is different than the macro-scale heat sink. An assessment

of fluid regime can be done by Knudsen number (Kn), which is ratio of mean free path of fluid to characteristics length of system. Microchannels with dimensions above 1 μm have Kn between (10⁻³, 10⁻¹), and it follows low macroscopic fluid behavior and can be solved using Navier stokes equation [6]. Coolants like water [19], air, oil, and refrigerants are commonly used in many applications. Heat transfer ability of conventional fluid-based microchannels is getting saturated [22], thus there is a need for alternative potential fluid.

5.1 Nanofluids

Nanofluids are colloidal suspensions of nano-sized particles in base fluid. Nanofluids are considered as a new family of coolants because they have high thermal conductivity and could result in ultra-high heat flux of 1350 W/cm² with an interface temperature of 80°C [23]. Metals (Au, Ag, Cu and its oxides (Al₂O₃, CuO), carbide/nitride ceramics (SiC, TiC, AlN, SiN) are used as nanoparticles. Higher concentration of nanoparticles accounts for increased Brownian motion in nanofluid, causing higher momentum of nanoparticles by which energy is carried for longer distances before releasing into colder areas [23].

Volume Fraction and nanoparticle size are two parameters that affect Nusselt number, dimensional pressure drop. The reason for higher coolant temperature (lower pin fin temperature) is due to increase in surface area for molecular collisions by increasing volume fraction. Increasing volume fraction about 0.01-0.04 of CuO and Al₂O₃ particles significantly increases Nusselt number 1.62%-4.5% and 8.37%-11.44%, respectively, and increases dimensional pressure drop has been reported in a study by Seyf and Feizbakhshi [24] as shown in Fig. 8. Differences in particle shape, morphology, and surface treatment of Al₂O₃ and CuO particles elucidate such differences in Nusselt number. Increase in volumetric fraction results in strong hydrodynamic interactions and high fluid internal shear stress, which causes fluid viscosity and pressure drop to increase [24, 6]. With heat flux of 300 W/cm² and input pumping power of 2.25 W, diamond (1 Vol%, 2nm) and copper (1 Vol%) based nanofluid with water as base fluid enhances cooling performance by 10%, 4%, respectively. As inferred from Fig. 9, nanofluid with diamond nanoparticles have low thermal resistance at a given pumping power [23].

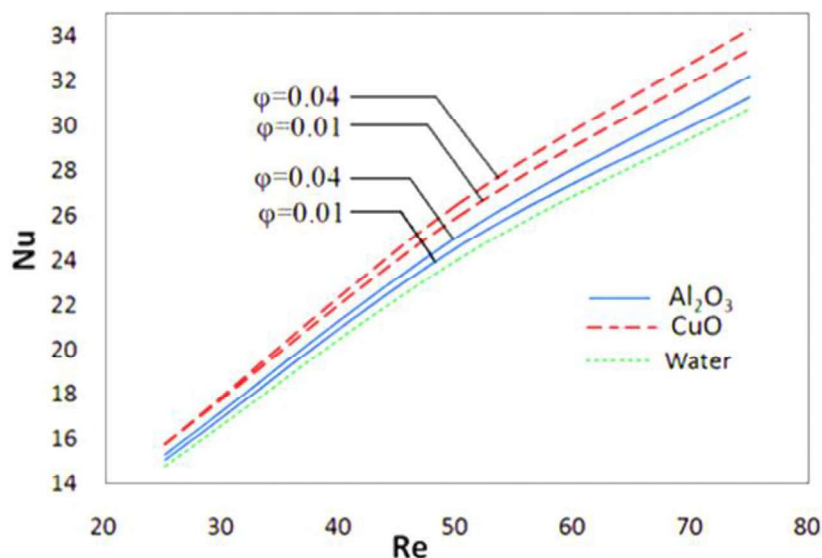


Fig. 8 Nusselt number as a function of Reynolds number with variation in volumetric fraction of Al₂O₃, CuO based nanofluid and comparison with pure water [21].

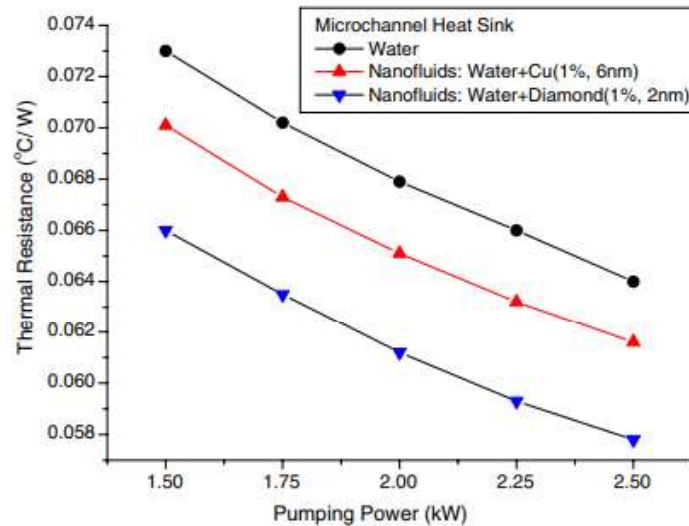


Fig.9 Variation of thermal resistance at different pumping power for Cu, Diamond-based nanofluids [23].

Effects of particle diameter on performance parameters are found to be different for CuO and Al₂O₃ nanoparticles. Reducing the size of Al₂O₃ nanoparticles causes formation of liquid layer (nanolayer) around smaller particles, aggregation of particles, enhanced surface area, which leads to higher Nusselt number, heat transfer coefficient, and thermal conductivity [24]. The case is opposite with CuO particles, on increasing size of particle, Nusselt number and thermal conductivity both decreases. Because of decreased Brownian motion of CuO particles, increased mass of aggregates and clustered particle concentration in confined regions, there is non-uniformity in distribution of particles, resulting in lower thermal conductivity [24].

5.2 Other working fluid

Nanofluids have some limitations like nanoparticle sedimentation, increase in pressure drop, erosion, clogging in channels, pipe wall abrasion due to suspension of particles. Therefore, many researchers investigate cooling performance with conventional cooling fluids like water, air, oil, N₂ gas, fluorinates and refrigerants. Among them, deionized water is most often used as a working fluid as it has a higher convection heat transfer coefficient. A study conducted by Hasan Mushtaq & Muter, Dhay [25] compared water, ethylene glycol, oil in pure form in micro heat sink with constant heat flux of 100 W/cm² at its base. In comparison, it was found that oil has better thermal performance than the other two because of higher velocity. Still, water performed best overall due to the positive factor of lower pressure drop[25].

6 Material selection for micro heat sink

Demand for a better cooling solution motivated researchers to study different substrate materials having high thermal conductive properties. Pertinent choices of material for heat sinks are silicon ($k = 148$ W/mK), CNT – carbon nanotube structure, aluminum ($k = 237$ W/mK) and copper ($k = 401$ W/mK). CNT material possesses high thermal conductivity (200-800 W/mK), high strength, and chemical stability. CNT material has porous media due to graphite rolled sheet structure, which allows fluid to penetrate. Tullius et al. [13] analyzed various mentioned materials by plotting Nusselt number v/s Reynolds number graph and found that CNT material performed best with no effects on pressure drop increments. Comparing the other three materials in a numerical study conducted by Uday Kumar et al. [26], it was found that silicon gives maximum temperature rise of coolants, as shown in Fig.10.

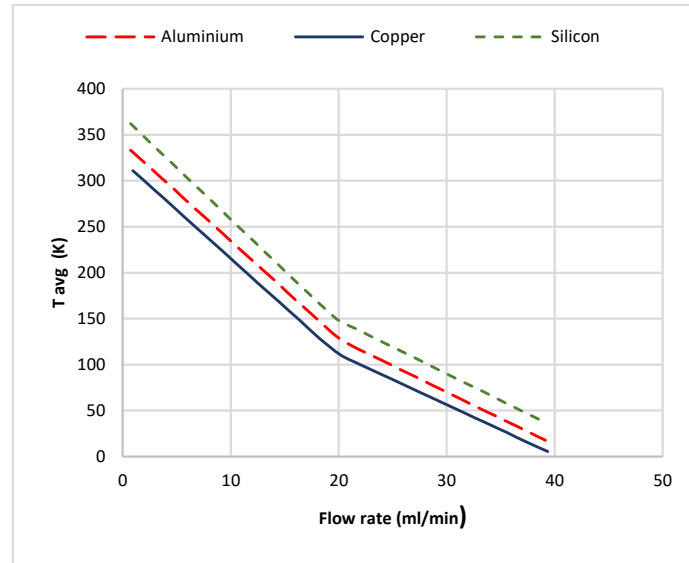


Fig. 10 Comparison of different material by plot of average temperature as a function of fluid flow rate [26]

7 Conclusions

Micro heat sink is found effective in rectifying problem of high heat flux generation in miniaturized electronic devices. Comparative analysis of literature extrapolates following key conclusions:

- On comparing at constant 30°C temperature, it found that at relatively higher flow rate of 60 g/min micro pin fins performs better.
- V, U fluid flow path arrangement could result in uniform flow distribution and lower thermal resistance than basic I path arrangement. Fractal-like microstructure structures result in reduced temperature and decreased pressure drop, in which T joint bifurcation was found better than Y joints.
- Among the two configurations, staggered pin fins improve overall performance than inline configuration, with a limitation of higher pressure drop, which can be mitigated by using different cross-section shapes or by altering fin topology.
- On studying the effect of fin height variation on cooling performance under heat flux, 100-150 W/cm²
- found an optimum fin height of 1.5 mm. Increase in transverse pitch increases FOM parameter in circle pin fins. At lower Re numbers, circular pins are preferred to have denser longitudinal arrangements. Moreover, square pin fins are preferred at a higher Re number.
- Cross-section of pin fins of convex shape reduces pressure drop and minimizes maximum temperature, thus giving better performance than circular and hydrofoil shapes. Also, among other considered shapes, hexagon cross-section gave the best performance, and triangular performed worst.
- Diamond-based nanofluid enhances performance of heat transfer more as compared to copper-based heat sink. Volumetric fraction can be increased up to a limit due to unfavorable viscosity rise of nanofluids resulting in high pumping power requirement. Effect of increasing nanoparticle diameter showed opposite trends for different nanoparticles.
- Carbon nanotube material is the best choice for heat sink material, which can make a massive difference in overall performance.

The conclusions made in this paper will be beneficial for readers in developing their clear understanding of the subject topic.

References

1. T. T. Mattila, J. Li, and J. K. Kivilahti, "On the effects of temperature on the drop reliability of electronic component boards," *Microelectron. Reliab.*, vol. 52, no. 1, pp. 165–179, 2012, doi: 10.1016/j.microrel.2011.07.085.
2. V. Lakshminarayanan and N. Sriraam, "The effect of temperature on the reliability of electronic components," *IEEE CONECCT 2014 - 2014 IEEE Int. Conf. Electron. Comput. Commun. Technol.*, pp. 1–6, 2014, doi: 10.1109/CONECCT.2014.6740182.
3. J. Zhou, X. Cao, N. Zhang, Y. Yuan, X. Zhao, and D. Hardy, "Micro-Channel Heat Sink: A Review," *Journal of Thermal Science*, 2020. .
4. J. M. Jalil, A. H. Reja, and A. M. Hadi, "Numerical Investigation of Thermal Performance of Micro-Pin Fin with Different Arrangements," *IOP Conference Series: Materials Science and Engineering*, 2020. .
5. G. Narendran, N. Gnanasekaran, and D. A. Perumal, "A Review on Recent Advances in Microchannel Heat Sink Configurations," *Recent Patents on Mechanical Engineering*, 2018. .
6. J. F. Tullius, R. Vajtai, and Y. Bayazitoglu, "A review of cooling in microchannels," *Heat Transfer Engineering*, 2011. .
7. R. Chein and J. Chen, "Numerical study of the inlet/outlet arrangement effect on microchannel heat sink performance," *International Journal of Thermal Sciences*, 2009. <http://dx.doi.org/10.1016/j.ijthermalsci.2008.12.019>.
8. G. L. Morini, "Single-phase convective heat transfer in microchannels: A review of experimental results," *International Journal of Thermal Sciences*, 2004. .
9. D. B. TUCKERMAN AND R. F. W. PEASE, "High-Performance Heat Sinking for VLSI," 1981.
10. P. Bhandari and Y. K. Prajapati, "Thermal performance of open microchannel heat sink with variable pin fin height," *International Journal of Thermal Sciences*, 2021. <https://doi.org/10.1016/j.ijthermalsci.2020.106609>.
11. V. Saravanan, C. K. Umesh, D. Hithaish, and K. Seetharamu, "Numerical investigation of pressure drop and heat transfer in pin fin heat sink and micro channel pin fin heat sink," *International Journal of Heat and Technology*, 2018. .
12. H. Zhao, Z. Liu, C. Zhang, N. Guan, and H. Zhao, "Pressure drop and friction factor of a rectangular channel with staggered mini pin fins of different shapes," *Experimental Thermal and Fluid Science*, 2016. <http://dx.doi.org/10.1016/j.expthermflusci.2015.10.010>.
13. J. F. Tullius, T. K. Tullius, and Y. Bayazitoglu, "Optimization of short micro pin fins in minichannels," *International Journal of Heat and Mass Transfer*, 2012. <http://dx.doi.org/10.1016/j.ijheatmasstransfer.2012.03.022>.
14. S. Vanapalli *et al.*, "Pressure drop of laminar gas flows in a microchannel containing various pillar matrices," *Journal of Micromechanics and Microengineering*, 2007. .
15. S. E. Ghasemi, A. A. Ranjbar, and M. J. Hosseini, "Numerical study on the convective heat transfer of nanofluid in a triangular minichannel heat sink using the Eulerian–Eulerian two-phase model," *Numer. Heat Transf. Part A Appl.*, vol. 72, no. 2, pp. 185–196, 2017, doi: 10.1080/10407782.2017.1358990.
16. B. A. Jaspersion, Y. Jeon, K. T. Turner, F. E. Pfefferkorn, and W. Qu, "Comparison of micro-pin-fin and microchannel heat sinks considering thermal-hydraulic performance and manufacturability," *IEEE Transactions on Components and Packaging Technologies*, 2010. .
17. A. R. B. Yousef Alihosseini and M. Mohammadi, "Effective parameter on increasing efficiency of micro scale heat sinks and application of liquid cooling in real life," .
18. C. P. Zhang *et al.*, "Numerical and experimental studies on laminar hydrodynamic and thermal characteristics in fractal-like microchannel networks. Part A: Comparisons of two numerical analysis methods on friction factor and Nusselt number," *International Journal of Heat and Mass Transfer*, 2013. <http://dx.doi.org/10.1016/j.ijheatmasstransfer.2013.06.073>.

19. T. J. John, B. Mathew, and H. Hegab, "Parametric study on the combined thermal and hydraulic performance of single phase micro pin-fin heat sinks part I: Square and circle geometries," *International Journal of Thermal Sciences*, 2010. <http://dx.doi.org/10.1016/j.ijthermalsci.2010.06.011>.
20. D. Yang, Y. Wang, G. Ding, Z. Jin, J. Zhao, and G. Wang, "Numerical and experimental analysis of cooling performance of single-phase array microchannel heat sinks with different pin-fin configurations," *Applied Thermal Engineering*, 2017. <http://dx.doi.org/10.1016/j.applthermaleng.2016.08.211>.
21. A. Abdoli, G. Jimenez, and G. S. Dulikravich, "Thermo-fluid analysis of micro pin-fin array cooling configurations for high heat fluxes with a hot spot," *International Journal of Thermal Sciences*, 2015. .
22. H. R. Seyf, Z. Zhou, H. B. Ma, and Y. Zhang, "Three dimensional numerical study of heat-transfer enhancement by nano-encapsulated phase change material slurry in microtube heat sinks with tangential impingement," *International Journal of Heat and Mass Transfer*, 2013. .
23. S. P. Jang and S. U. S. Choi, "Cooling performance of a microchannel heat sink with nanofluids," *Applied Thermal Engineering*, 2006. .
24. H. R. Seyf and M. Feizbakhshi, "Computational analysis of nanofluid effects on convective heat transfer enhancement of micro-pin-fin heat sinks," *International Journal of Thermal Sciences*, 2012. <http://dx.doi.org/10.1016/j.ijthermalsci.2012.02.018>.
25. M. I. Hasan and D. M. Muter, "Study the micro heat sink with pin fins and different coolants: a comparative study," *International Journal of Engineering & Technology*, 2019. .
26. A. Uday Kumar, A. Javed, and S. K. Dubey, "Material Selection for Microchannel Heatsink: Conjugate Heat Transfer Simulation," *IOP Conference Series: Materials Science and Engineering*, 2018. .

Experimental investigation of heat transfer fluids for solar thermal collectors

Pawan Kumar Kuldeep, Sandeep Kumar, Sunita Mahavar

1 Introduction

The heat temperature fluids (HTFs) have various applications in the industrial process of heat collection and transfer. These fluids may be natural or synthetic. Although synthetic fluids are a little expensive and are also hazardous to some extent due to the degradation by-products, yet they are preferred in many thermal applications due to their versatile temperature range. The properties of various types of HTFs for different applications are studied by a number of researchers. Hoffmann et. al. [1] have performed a study on different vegetable oils relative to a reference oil. The hot wire thermal probe method is used for thermal conductivity measurement. It was observed that the thermal conductivity is affected by the fatty acid composition. Ramos-Pallares et. al. [2] used an expanded fluid (EF) thermal conductivity model for the theoretical study of crude oils (mainly heavy oils). The predicted thermal conductivities based on various properties viz density, pressure, etc. were in good agreement with the experimental values. Three fuel blends having methyl laurate and n-undecane, n-dodecane, n-tridecane were prepared and liquid thermal conductivity was measured by the transient hot-wire method by Fenhong Song et. al. [3]. Mara K. Ustra et.al. [4] have determined density, viscosity, and thermal conductivity as a function of temperature and composition for fatty acid methyl esters (FAME) from soybean, castor, and Jatropha oils. They observed that as the temperature increases, values of all properties decrease. [4]. The transfer of heat in any system is largely affected by the type, design, and material of the heat exchanger. Sager et. al. [5] have investigated the effect of insert tape geometry on the heat exchanger tubes. A comparison of thermal characteristics of water flowing in a tube equipped with x-tape and the twisted tape was made. The x-shaped tape showed better performance than the twisted tape. A comparative analysis and performance evaluation of various properties of ethylene glycol (EG) and silicon carbide (SiC) using a one-shell-two tube heat exchanger was conducted by J. E. Igwe et. al. [6]. The MATLAB software was used for the analysis of the different combinations of EG and SiC with water. The highest heat transfer rate was found for

Table 1. The application of HTFs in solar thermal systems

Reference	Fluid	Solar thermal system	Aspect	Temp. (°C)
Fritsch et al. [8]	Molten-salt mixture	CSP solar receiver Parabolic trough power plants	Experimental	700
Conroy et al. [9]	Liquid Sodium, molten salt		Theoretical	
Trabelsi et al.[10]	Therminol VP-I and Molten Salt		Theoretical	
Boerema et al. [11]	Hitec	Central-receiver systems	Experimental	600/ 873
Kenda et al. [12]	Jatropha curcas crude oil	CSP	Experimental	210
Hoffman et al. [13]	Vegetable oils (seven different kinds)			250
Jung et al. [14]	Silicone fluid	Solar thermal power plant	Experimental	425

a combination of SiC and water. Nicholas Boerema et.al. [7] performed a comparative study between thermophysical properties of Hitec (a ternary molten salt 53% KNO_3 + 40% NaNO_2 + 7% NaNO_3) and liquid sodium (Na) as heat transfer fluid. They tested these fluids for use in high-temperature concentrated solar thermal central-receiver systems for power generation. It was found that liquid sodium might be a good alternative to molten salt (commonly used in STC) provided certain limitations that can be removed. For the solar thermal collector, depending upon system configuration, there may be a need for heat transfer fluids that act either as primary working fluids absorbing solar radiation in the collector directly or as secondary fluids that transfer the absorbed solar thermal energy to the working fluid through a heat exchanger [8]. Various HTFs have been tested and used in solar thermal appliances, a few of those are summarized in table 1. High heat conductivity, low viscosity, Good safety features viz. nonexplosive, easy replacement, and less contamination are some desired properties and features of an effective and efficient HTF to be used in the solar thermal collectors. Considering the importance of HTF in the solar thermal field, the present study is focused on testing two heat transfer fluids Silicon oil and Hytherm (thermic fluids). A detailed experimental study is performed in an indoor lab set-up and reported in the paper.

2 Experimental Setup & Instruments

A thermal fluid heating system is designed at the laboratory scale of the solar energy research laboratory (SERL), University of Rajasthan, Jaipur. The indoor experimental set-up includes a heat source, heat exchanger, heat storage, and other testing equipment. The water is chosen as a heat storage medium or secondary HTF. In a heat exchanger, silicone oil (SO) and Hytherm are used as direct heat collecting material/ primary HTFs/ working fluids through an electrically heating source. Through the circular copper pipe, the water is circulated in the heat exchanger and then water is also used as heat storage material. The effects of the temperature of SO and Hytherm and water amount in heat storage on heat transfer rate are studied through various experiments performed on a number of days. There are 4 main parts of this whole experimental setup. **Heat Receiver/Exchanger:** This is an insulated cylindrical copper-cavity box. A copper spiral tube is dipped in this receiver along with 1 L oil (HTF). This receiver is placed on a heat source (electrical heater). Two Temperature sensors are kept inside

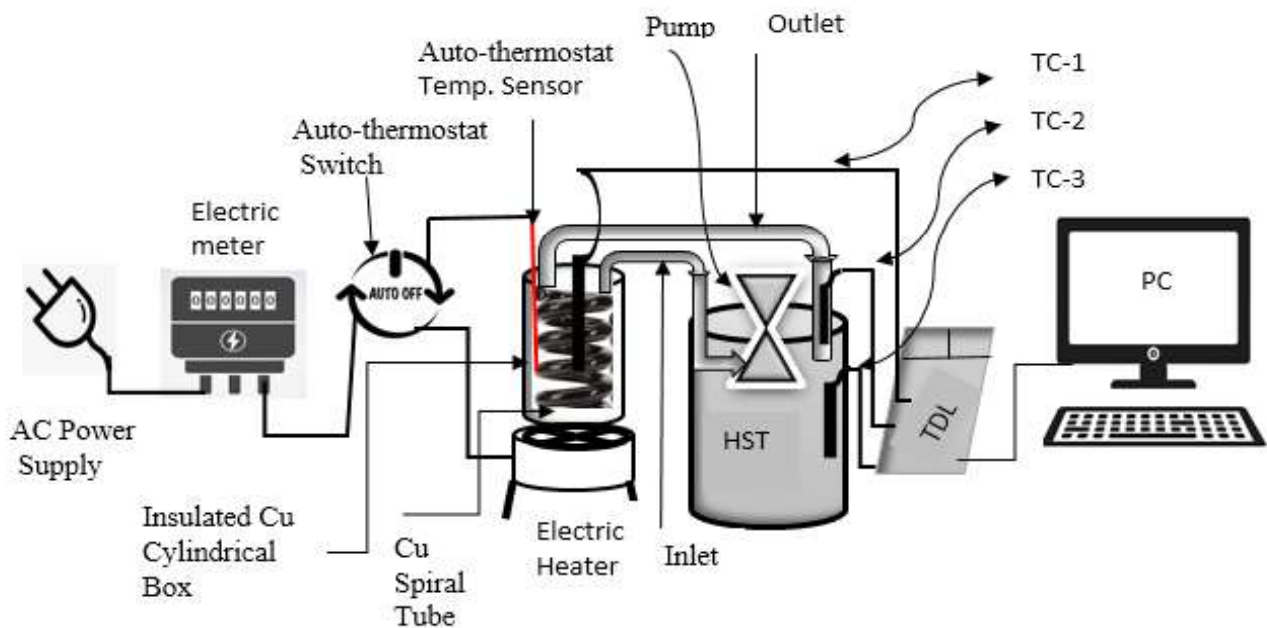


Fig. 1. The schematics of the indoor experimental setup for heat transfer (HST-Heat Storage Tank, TC-temperature of various locations, TDL-temperature data logger, PC-computer).

HTF. One K- type thermocouple (TC-1) is connected to an auto-cut thermostat switch and another TC is connected to the temperature data logger: **Heat Storage Tank (HST):** This tank has an 8 L maximum capacity of fluid storage. A modified pump is dipped inside the water (storage) to pump the water. Silicon tubes are used for water circulation, due to their high-temperature capacity. The water is pumped to the inlet of the copper spiral tube. The outlet of this copper spiral tube is immersed inside the heat storage tank. One TC-1 is adjoined inside the silicon tube and another TC-2 is wrapped around the silicon tube tightly. One another TC-3 is immersed inside the HST to measure the storage temperature. **Energy source/Power supply:** An electrical digital meter is connected to an A.C. power source is used to supply the heat to the receiver. Although, conventional heat does not provide an analogy of a solar thermal collect as a heat source, yet for comparative study and indoor study it is a good alternative. The electricity consumption is measured from the digital meter (0.1 unit). This meter is connected to an auto-thermostat switch. This switch is used for controlled heating of HTFs. Switch cut the power supply for a specific temperature value of the HTF. **Temperature data logger (TDL):** All the temperatures are measured through a K- type thermocouples and using a data logger (85XX+ Masibas data logger, 0.1 °C least counts). This TDL is connected to a computer and temperature data is recorded at the desired time interval. In the present study, this time interval is set to be 5 min. **Flow rate:** This is manually measured at the beginning of every set-up for collecting the fluid in the measuring jar for a fixed time period.

3 Measurements and Thermal Profiles

Using Static fluid Silicon oil (SO), firstly the effect of heat sources is tested. For this three auto cuts are sets at 125, 150, and 200 °C. The observed thermal profile is shown in Fig. 2. Through repeated observation it was found that an auto cut at 150 °C, is an optimized value to heat input, hence further all the experiments are performed only for this value of the auto cut set. Three sets of experiments are conducted for each HTF. In these sets, the water load values are kept at 4, 6, and 8 L. The thermal profile of HTFs (SO and Hytherm) are measured as well as the temperature of the storage tank is also measured. These are depicted in Fig. 2, 3, 4, and 5. All the experiments are performed at 5 mint intervals and continued till the water (Circulating fluid) in the storage tank reaches 90° C. As a part

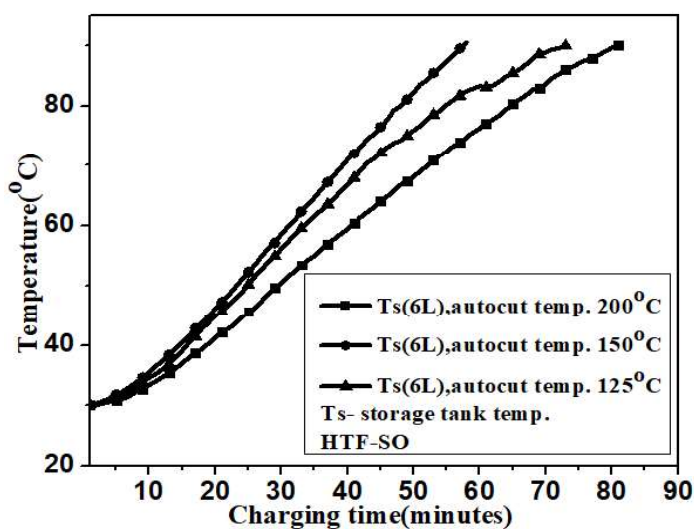


Fig. 2 Storage tank temperature (water load 6 L) with time curve for the different operating temperatures of Silicon oil (1 L)

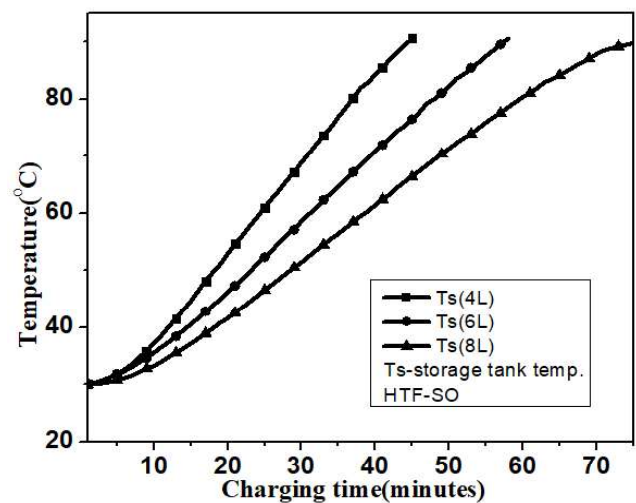


Fig.3. Storage tank temperature (water load 4, 6, and 8 L) with time curve at 150 °C operating temperature of Silicon oil (1 L)

of the durability study a 15 hour non-continuous heating of SO and Hytherm in various experiments are closely observed and reported in Fig. 6.

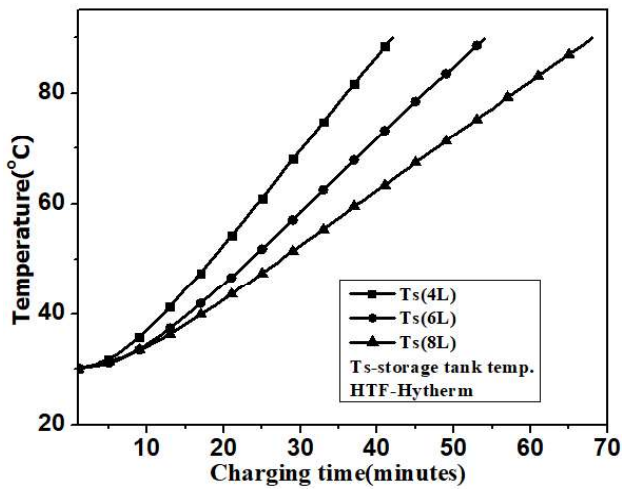


Fig. 4. Storage tank temperature (water load 4, 6, and 8 L) with time. The curve at 150 °C operating temperature of Hytherm (1 L)

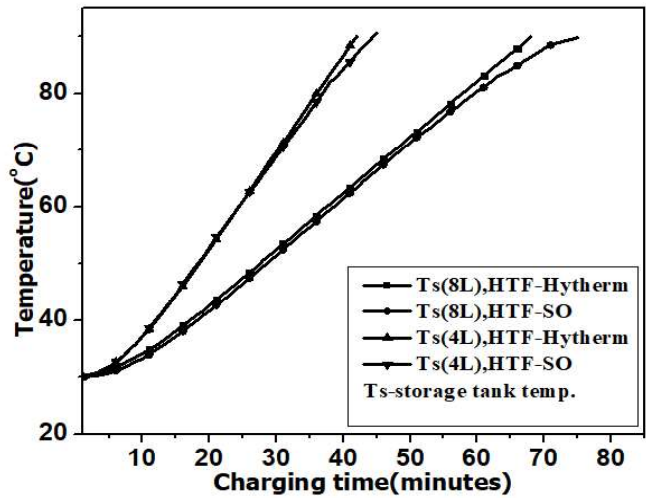


Fig. 5. The comparative curve of the rise of Storage tank temperature (water load 4 and 8 L) at 150 °C operating temperature of Hytherm and Silicon oil (1 L)

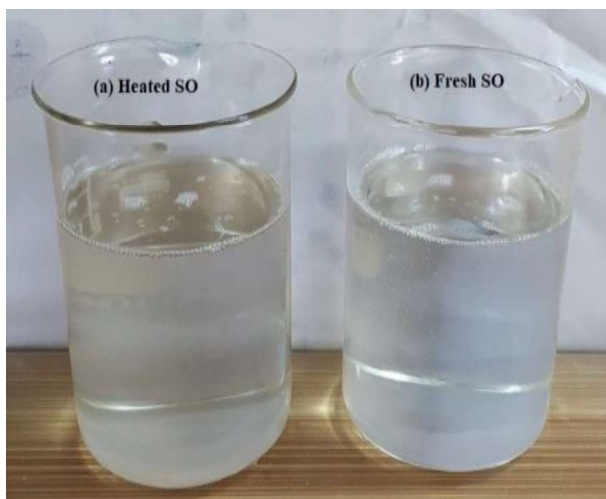


Fig. 6. The appearance of Silicon oil after 15 h of non-continuous heating

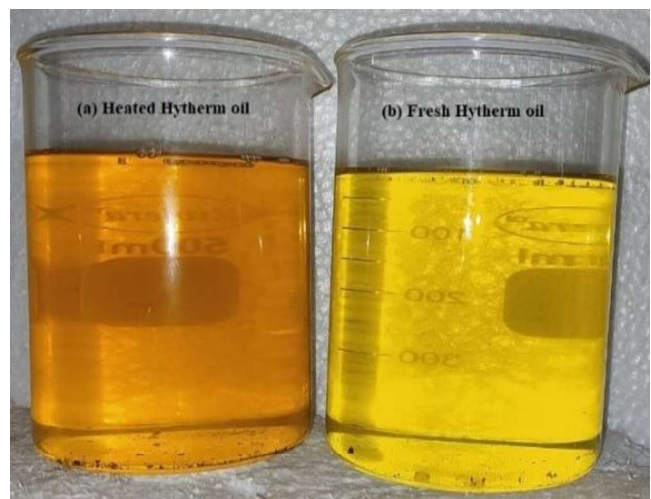


Fig. 7. The appearance of Hytherm after 15 h of non-continuous heating

Table 2. Charging time comparison of HTFs for three water load

Primary HTFs (1 L) type	Secondary HTF(water) amount (L)	Flow rates (ml/s)		Charging Time (min.)	Power consumed (Unit)
		at 30 °C	at 90 °C		
Silicon oil (SO)	4	7.3	7.8	44	1.0
	6	9.2	9.5	57	1.2
	8	10.7	10.9	75	1.6
Hytherm oil	4	9.6	9.7	41	1.0
	6	10.0	10.3	53	1.2
	8	10.0	10.3	68	1.5

4 Results

In the present study, Fig. 2 depicts that for the different operating temperatures of Silicon oil, the heat transfer rate to 6 l water load is different. The highest rate of heat transfer is observed for the operating temperature at 150 ° C, while for higher 200 ° C and lower 125 ° C, this rate is significantly less. It infers that the rate of heat transfer of primary fluid (SO) depends on the secondary heat transfer (water) and this transfer is maximum for a certain temperature of primary HTF. For this practical arrangement, this is 150 ° C, but for another set of experiments, it might be different. Determination of this optimum operating temperature (OPOT). This determination will considerably save the heat input. It is also observed that OPOT is independent of the water load amount. Therefore, for all other experiments, this OPOT is set for both primary HTFs. Fig. 3 and Fig. 4, infers that for both primary HTFs, as the secondary HTF amount is increased the rate of heat transfer also decreases as obvious. The results of this study are also summarized in Table 2. The comparative data shown in Fig. 5 infer the rate of heat transfer of both SO and Hytherm to the water load is almost near still a few changes in the charging period are found when things are closely observed (Table 2). Although SO and Hytherm have different-different physical properties but it is found that Hytherm has a higher heat transfer rate compared to SO at the laboratory conditions. Almost 3 to 7 min difference in observed i.e. Hytherm heat transfer is slightly higher than SO for almost same power consumption. The observed changes in colors in Fig. 6 and 7 show significant changes for Hytherm while no changes in silicon oil. The price of SO is about 380 INR/kg and for Hytherm it is 115 INR/liter. The comparative rate of heat transfer of Hytherm with SO and low price make it suitable for use in receiver part of solar thermal collectors, provided a change in physical properties over a period of time should be more studied for more conclusive results.

5 Conclusion

Effective and efficient heat transfer materials with low cost and large life cycle are desirable in the field of the solar thermal collector to receive heat through the receiver and transfer it to the user application. Aiming this, in the present study, an experimental study is performed on two HTFs (Silicon oil and Hytherm) as primary HTFs. The secondary HTF is a commonly used fluid i.e. water. This indoor experimental study concludes that Hytherm has a comparative heat transfer performance than Silicon oil, while it is relatively available at less price than Silicon oil. However, a durability test conducted for a shorter time period concludes that a long-term study should be conducted to check Hytherm for actual field use effectively with a longer period.

Acknowledgment

The authors are thankful to DST (New Delhi) and SERB (New Delhi) to provide project funds for this experimental study and to UGC (New Delhi) for a research grant to authors, Mr. Pawan and Mr. Sandeep. The authors also acknowledge the Department of Physics, University of Rajasthan, Jaipur to provide the necessary infrastructure.

References

1. J.-F. Hoffmann, J.-F. Henry, G. Vaitilingom, R. Olives, M. Chirtoc, D. Caron & X. Py, "Temperature dependence of thermal conductivity of vegetable oils for use in concentrated solar power plants, measured by 3omega hot wire method," *International Journal of Thermal Sciences*, 2016, 107, 105–110.
2. F. Ramos-Pallares, F. F. Schoeggl, S. D. Taylor & H. W. Yarranton, "Prediction of thermal conductivity for characterized oils and their fractions using an expanded fluid-based model," *Fuel*, 2018, 234, 66–80.
3. F. Song, Q. Wang, Q. Meng, H. Mu & J. Fan, "Measurements on the thermal conductivity of three fuel blends containing a biodiesel compound methyl laurate + diesel compounds: n-undecane, n-dodecane, n-tridecane," *Thermochimica Acta*, 2021, 178986.

4. M. K. Ustra, J. R. F. Silva, M. Ansolin, M. Balen, K. Cantelli, I. P. Alkimim, J. Vladimir Oliveira, "Effect of temperature and composition on density, viscosity, and thermal conductivity of fatty acid methyl esters from soybean, castor, and *Jatropha curcas* oils," *The Journal of Chemical Thermodynamics*, 2013, 58, 460–466.
5. S. Paneliya, S. Khanna, V. Mankad, A. Ray, P. Prajapati & I. Mukhopadhyay, "Comparative study of heat transfer characteristics of a tube equipped with X-shaped and twisted tape insert," *Materials Today: Proceedings*, 2020.
6. J. E. Igwe, C. S. Agu, "Comparative Analysis of Different Fluids in One Shell Pass And Two Tube Heat Exchanger. American Journal of Engineering Research (AJER) e-ISSN: 2320-0847 p-ISSN: 2320-0936 Volume-5, Issue-8, pp-81-87, 2016.
7. N. Boerema, G. Morrison, R. Taylor & G. Rosengarten, "Liquid sodium versus Hitec as a heat transfer fluid in solar thermal central receiver systems," *Solar Energy*, 2012, 86(9), 2293–2305.
8. A. Fritsch, C. Frantz, R. Uhlig, "Techno-economic analysis of solar thermal power plants using liquid sodium as heat transfer fluid," *Solar Energy* 177 (2019) 155-162.
9. T. Conroy, M. N. Collins, J. Fisher, R. Grimes, "Thermohydraulic analysis of single-phase heat transfer fluids in CSP solar receivers," *Renewable Energy*. 129, Part A, (2018) 150-167.
10. S. E. Trabelsi, L. Qaider, A. Guizani, "Investigation of using molten salt as heat transfer fluid for dry cooled solar parabolic trough power plants under desert conditions Investigation of using molten salt as heat transfer fluid for dry cooled solar parabolic trough power plants under desert conditions," *Energy Conversion and Management*, 15 (2018) 253-2.
11. N. Boerema, G. Morrison, R. Taylor, G. Rosengarten, "Liquid sodium versus Hitec as a heat transfer fluid in solar thermal central receiver systems," *Solar Energy* 86, 9, (2012) 2293-2305.
12. E. S. Kenda, K. Edem, N. Tsoukpoe, W. K. Igor, Y. Ouédraogo, Coulibaly, P. Xavier, F. Marie, W. Armel, "Jatropha curcas crude oil as heat transfer fluid or thermal energy storage material for concentrating solar power plants," *Energy for Sustainable Development* 40 (2017) 59–67.
13. J. F. Hoffmann, G. Vaitilingom, J. F. Henry, M. Chirtoc, R. Olives, V. Goetz, "Temperature dependence of thermophysical and rheological properties of seven vegetable oils in view of their use as heat transfer fluids in concentrated solar plants," *Solar Energy Materials and Solar Cells* 178, (2018), 129-138.
14. C. Jung, J. Dersch, A. Nietsch, & M. Senholdt, "Technological Perspectives of Silicone Heat Transfer Fluids for Concentrated Solar Power." *Energy Procedia*, 2015, 69, 663–671.

A SWOT analysis approaches to implementation of renewable energy applications in West Bengal

Debojit Roy, Suprit Bag, Soupayan Mitra

1 Introduction

The world needs energy to run. Energy is needed for sustain in day to day life. The world needs energy to drive the economic and human development. For India as well as West Bengal, The main sources of energy are still remaining as natural non-renewable type resources. But burning of fossil fuels has harmful effects on ecology and environment. It has a long lasting unavoidable health hazards issues. Here is the requirements of renewable resources are come into action. That's why the whole world is focused on the green and sustainable way to perform energy practices so that there will be no harmfulness of the systemic approach of energy use. The natural source of energy plays a major role in sociological and economic development of West Bengal as well as the country also. [1] All efforts should be therefore directed to gear alternate sources of energy as a supplement of our energy needs for domestic, institutional, commercial and industrial purposes.

2 Energy scenario in West Bengal:

In eastern India, West Bengal is the most important state and the third largest economics state of India. West Bengal is one of the centres of Indian agricultural hubs and huge reserve of old reputed Industries. Many hubs and sophisticated power consumption sectors are there in West Bengal. Asansol is a coal mining area and Durgapur is a zone of power plant industries and the state West Bengal has many other coal reserves as well. Govt. of West Bengal has taken initiative for reformation of power sector at 2005 with the reconstructing of west Bengal state Electricity board into a distribution company and a transmission company in 2007. West Bengal become a promising state which for making better energy situation in India and with the collaboration of the Central Govt., the state Govt. also done enormous transformation in power sector in a parallel way. The total installed capacity and the energy consumption rate is an important parameter to express the energy scenario of any particular region.

3 Methodology of SWOT analysis:

SWOT analysis is a method of planning in a strategic way, which mainly used to identify the person or organization for identify its Strengths, Weaknesses, Opportunities and Threats related to competition or project planning process. We can say it's a situational assessment or situational analysis. Using this situational analysis process we are checking the implementation of Renewable energy in West Bengal in recent situations or years and future scopes. We are taking information from different literature & government websites for collecting the data for implementation of renewable energy, level, different future scope, policies, limitations, possibilities, menacing etc. After collecting all information we are identify the internal and external factors, which are favorable or unfavorable to achieve the implementation of Renewable Energy in West Bengal.

4.1.2 Political and Economic Stability

India's demand for energy is set to outpace domestic supply, providing the largest contribution (30 per cent) to global energy demand growth to 2035 [5]. This integration of India into the world energy market may become a key shift in global economy. As a state of India West Bengal also trying to implement the renewable energy in various sectors in the state. India's Nationally Determined Contribution under the Paris Agreement sets goal to increase the share of non-fossil fuels in its power generation capacity and increase the forest and tree cover to support the additional carbon sink.

So in west Bengal also the implementation of green energy is having a significant role. By this new financial policy, Nodal agency can use this fund for promotion of RE which will generate sufficient revenue to make the fund self-sustainable. The Nodal Agency shall also be responsible for managing of the Green Energy Fund and will prepare the yearly budget for utilization of the fund [6].

4.1.3 Policy Environment Supporting Renewable Energy Implementation

The policy environment for renewable energy development in India as well as West Bengal is robust and provides an enabling environment in all tiers of government to effectively implement and deploy these policies and provide a platform for an enhanced effective energy sector to the citizens, government commitment in promoting renewable energy technologies dates back to the post-apartheid constitution.

The objectives as a whole of these policies are, but not limited to the followings:

- Increasing the access to inexpensive energy facilities in the state and improve the facilities.
- Manage the harmful environmental impacts from energy-related crisis;
- Diversification of energy supply;
- Economic growth calculation of the green energy implementation in the state.
- Merge the resources to make a solution to the constraints coming on the path of development of the renewable energy in the state.

Large number of programs has been taken by WBREDA related to the solar energy, wind energy, mini & micro hydel and bio-energy etc. Today, West Bengal is one of the leading states in the country in respect of utilization of Renewable Source of Energy. About 300 thousand families in rural areas of West Bengal are using Bio-Energy for their cooking purpose [2]. Several Energy Education Park has been set up by WBREDA in Kolkata, Siliguri and Durgapur.

Table 2. Achievement made by WBREDA on cumulative basis [2].

1	Installed Home Lighting Systems using Solar PV	2,00,000 Nos.
2	Installed Street Lighting System using Solar PV	10,000 Nos.
3	SP Power Plants	950 kWp
4	Installed Bio-gas plant	2,72,000 Nos.
5	Installed Wind Farm	2 MW
6	Biomass Gasifier used for the process of electrification in Village areas	1.5 MW
7	Power Generation using the Rice Husk	61.75 MW
8	Energy Parks	9 Nos.
9	Solar Housing Complex	30 Nos.
10	Mini Micro Hydel power generation system	2 MW
11	Battery Operated Vehicle	1,500 Nos.

Few important programs in West Bengal related to Non-renewable initiative are as follows [2]:

- Village electrification through Solar PV Systems
- Village electrification through decentralized generation like Biomass Gasified, Solar PV etc.,
- Wind Farm Project at Freserganj
- At Ganga Sagar, the Wind-Diesel- Gasified Hybrid Project.
- Electrification of schools by using renewable energy systems.
- Establishment of Energy Parks
- One of the Promotional activity for an rice mills is generating power from rice husk
- Installation of Bio-gas plants for households
- Solar hot water systems
- Tidal Energy Project
- Popularizing Battery Operated Vehicle.

Government of West Bengal paying more attention to generate more energy from green and renewable energy sources to overcome the gap between requirements and supply of energy and also try to use that as a supplement to grid power. In the near future WBREDA intends to take some following programs inter-alia regular program.

4.1.4 Govt. Subsidy

Central Government as well as State Government's Nodal Agencies (SNAs) offering various schemes for giving subsidy to the people who are willing to install the rooftop PV system. According to MNRE, the cost regarding the installation of rooftop PV system without any kind of subsidy is around INR 60,000 - 70,000 on an average. [15] For installing a rooftop PV system, after availing approx. 30% subsidy, consumer just have to pay INR 42,000 - 49,000. There is also generation-based incentives facility by the government. But to avail this, the consumer should generate 1100 kWh - 1500 kWh per year [13].

4.1.5 Research and institutional supports

Development of research processes, standardization of the research design and technological viability checking with demonstration is a core requirement for the growth of any renewable energy model. To develop the technological supports to the components, sub-systems, product & services, standards and resource management, the Ministry of New & Renewable Energy (MNRE) promotes Research, Development and Demonstration (RD&D) program. Such promotions on research and developments will leads to improvement of the renewable energy implementation process.

4.1.6 Open Market Investment

The Govt. of India as well as Govt. of West Bengal, through the Department of Energy, has unlocked the energy sector for public and private investment [3]. This external investment partnership plan is taken by the government to achieve the goal of providing clean, affordable and accessible energy to all the citizens. The government also aims at recapitalizing and financing the energy sector through private investment partnership. The strategy of the investment has a leading gesture to the off-grid use of the renewable energy resources, like water heating and cooking using the solar power as well as photovoltaic which is mostly used as a separate electricity source in areas that are too far away from the grid system. One project has been implemented in West Bengal's Sunshine School with the goal of lowering the carbon emissions and bring reliable and affordable energy to the classrooms of the state

by omitting the traditional grid electricity supplies for onsite produced solar power by grid-connected systems.[5] West Bengal Renewable Energy Development Agency (WBREDA) runs a project with the goal of achieving at least 250MW of solar power to the grid by 2030 [6].

4.2 Weaknesses

4.2.1 High power generating cost

The initial capital which is needed for implementing the renewable energy projects are very high with the comparison of the fossil fuels and this further leads to facing challenges and obstacles by the renewable projects. The renewable power generation cost in India is much higher than the conventional because of the high price imported technologies that are used to produce electricity. In west Bengal the Initial investment cost to build a renewable infrastructure is higher because lack of the state govt. subsidy. If the renewable projects that are shows low-performance are faces financial obstacles.

4.2.2 Miserable Household Electrification

Although near about 99.5% electrification of the villages in the state, only 42% of that rural household electrification indicates that a significant rise in energy demand may be shown in the future days and hence need for increasing the generating capacity and strengthening the transmission and distribution network [6]. The number of customers would increase a definite way and the energy provider must take care of this by improving the generation process and efficiency.

4.2.3 Government's Poor Bureaucratic Processes

Indications by different studies and stakeholders have revealed that the processes leading to license approval for the development of renewable energy are very challenging. They are also complex, lengthy and cumbersome. The requirement of different permits makes the process complex type and unnecessarily long. Another aspect is Renewable power was calculated based on cost-plus methods (adding direct material cost, direct labor cost, and product overhead cost). This does not include the environmental and socio-economic benefits of using the green energy resources. These may be a drawback of implementation of green resources of energy.

4.2.4 Land acquisition issues

Land acquisition has become a important issue. As we know that the efficiency of generated power from Renewable Energy sources is very less than the efficiency of conventional power sources. For covering this efficiency gap it's required more area for make big plant thus causes for high demand. But West Bengal is a agriculture based state which causes for limited availability of land. So it's become difficult to setting up big power plants as well as for transmission line.

4.2.5 Need for private participation

Private involvements in the power sector is a great necessity and Public Private Partnerships needs to be encouraged in the state to build competitive environment among the players and also for the improvement of the efficiency of the systems to provide the service to the customers in affordable rates. New updated policies have to be enabling by the state government for attracting more private investors in the sector.

4.2.6 Improving generation performance

The additional capacity added in the State Sector mainly by West Bengal Power Development Corporation has helped the state in meeting the increased demand and sell surplus energy outside the state. There is also lower generation issue facing by some of the plants due to erratic coal supplies. The improvement in generation performance would be critical to financial sustainability of the sector in West Bengal [14].

4.2.7 Lack of Awareness

There is also a lack of information and education regarding the huge sustainability and viability potential of renewable energy in most of the state including West Bengal. This limits investment in the sector [8]. There is a shortage of skilled and appropriate human resources in this green energy sector.

4.3 Opportunities

4.3.1 Global Awareness and exposure

Several countries, especially those generating energy from carbon-intensive sources have pledged their support of the abatement of carbon and India, as one of these countries. World Wind Energy Association (WWEA) and The Energy and Resources Institute (TERI), was arranged a conference named World Wind Energy Conference(WWEC2021), they will focus on the clean energy transition propelled by presentable progress of renewable energy with key focus on accelerating the capacity additions of wind and solar energy into the country's energy systems and reduce the use of conventional energy system in line with Paris agreements.WWEC2021 host country, India, is one of the leaders in availability of many renewable energy technologies and therefore is an ideal location to discuss progress, challenges, obstacles and achievements of the renewable energy world. [9]. This type of global exposure of India will drive the continuous development in renewable sector in the country as well as West Bengal.

4.3.2 Central Govt. and State govt. better Collaboration

Better collaboration of both the governments will increase the opportunity for renewable transformation for West Bengal. Better understanding and good communications between two governments will promote the implementations of the schemes and better ground level integration of renewable energy policies.

4.3.3 Financing the renewable sector

The both central and State government should provide enough budget for the clean energy sector. The government should concentrate on research & development sector and provide some excess fund for R&D. The government introduces Goods and Service Tax (GST) in 2017 which causes for worsened the industry performance and an increase in costs that causes a threat to the practicability of the ongoing projects, ultimately hampering the target achievement of the projects. These GST issues need to be addressed. Also Banks should allow an interest reduce on housing loans if the owner is installing renewable applications in the house such as solar lights, solar water heaters, and PV panels. This will encourage people to use more renewable energy. Furthermore, income tax rebates also can be given to individuals or companies or any organizations if they are implementing renewable energy applications.

4.3.4 Promote awareness

Govt. of west Bengal should pay attention about the ground level awareness about the needs of renewable energy use and global impact of the green energy implementation among the citizens. Regions where the renewable energy generation can have high potential, the local administration should hotspots those regions and by smooth and high awareness and facility the land acquisition must be done so that any plant of renewable energy can be situated.

4.3.5 Improvement in manufacturing/technology

The state should move to domestic manufacturing. It imports solar cell & module 90% of its requirements from Malaysia, China, and Taiwan [20]. Many foreign companies desiring to set up joint ventures in India provides only a little response because the given order in its current form presents inadequate safeguards. There are incremental developments in technology at regular and continuous periods, which need capital, and the State and Central Govt. should surplus the way to handle these factors.

4.3.6 Promote Research and development program

India has a magnificent power of young aspiring minds with good academic and skilled institutions. The Research & Development capability should be upgraded to solve critical problems in the clean energy sector for better future. West Bengal should take an initiative in industry-academia partnership, which might promote innovative R&D and support leading-edge Renewable power solutions to protect the globe for future generations & sustainability. Government should encourage to transferring of ideas between industry, academia, and policymakers from around the world to develop & increase adoption of renewable power.

4.3.7 Renewable energy jobs in India

The available jobs which are based on renewable are divided into many sub category like the technological development for renewable energy implementation, installation/de-installation, operation of parts, and maintenance operations. As technology quickly evolves and change the workers in all areas need to update their skills through continuing training/education or job training, and in several cases could benefit from professional certification. Our government and some private sector increase this training opportunity like TPSDI.

4 Threats

4.4.1) Fossil Fuel Dominance: Currently and in the near future, it is unlikely that the Government of India as well as West Bengal Government will completely eradicate its dependence on coal as a major or main source of energy supply. This is because besides the abundance of coal, it supports the energy-intensive, large scale mining industries that support and account for most of the state's gross domestic product.

4.4.2 Corruption

There has been damning evidence of corruption in most states in India, including the Department of Energy of West Bengal, which is the statutory body mandated with generating, transmitting and distributing electricity West Bengal [13]. These claim have bring about the government to set up a "Commission of Inquiry into State Capture", to properly and thoroughly investigate the alleged

corruption in all government and taking necessary steps. Such corrupt activities do not provide an enabling environment for the investment and implementation of renewable energy alternatives in the State.

4.4.3 Market obstacles

The biomass market in India as well as in West Bengal is facing a demand & supply gap which causes in a continuous and dramatic increase in biomass prices because the biomass supply is unreliable and there is no organized market for fuel, and the price fluctuations are very high compare to the other conventional energy. In India there are four markets of renewable, they are as follows the government market (providing budgetary support and purchase the output of the project), the government-driven market (provide budgetary support only), the loan market (taking loan for finance renewable based applications), and the cash market (buying renewable-based applications to meet personal essential energy needs) [20]. There is an inadequacy in promoting the loan market and cash market in India and this also give impacts on the implementation of Renewable energy resources in West Bengal.

4.4.4 Technological obstacles

Every installation of a renewable project comes up with complex risk challenges from environmental uncertainties, natural disasters, planning, equipment failure, and profit loss. On 11th of December 2017 MNRE issued the standardization process for renewable energy projects policy for testing, standardization, and certification. They are find they are still at an elementary level as compared to international practices. Quality assurance processes are still under beginning conditions. Each and every success in renewable energy implementation is based on specific action plans for the testing, standard and certification of performance.

4.4.5 Environmental obstacles

Making wind turbines motionless during times of low wind can protect birds and bats but is not practiced. One times wind turbine material production, transportation of materials, on-site construction, assembling, operation, maintenance, dismantlement, and decommissioning may be associated with global warming, and there is a lag in this consideration. The PV cell manufacturing process includes hazardous chemicals such as 1-1-1 Trichloroethene, HCL, H₂SO₄, N₂, NF, and acetone [20]. Inhaling silicon dust creates health hazardous situation or workers. Disposal of the manufacturing wastes are not done properly. The thin-film PV cells, which contain cadmium—telluride, gallium arsenide, and copper-indium-gallium-dieseline. These materials are creating public health threats and environmental threats. A hydro turbine blade kills aquatic ecosystems (fish and other organisms).

4.5 Analysis

Table no.3 provides a summary about the SWOT analysis on Renewable Energy Implementation in the state West Bengal.:

5 Conclusion

West Bengal is endowed with different renewable energy sources which are abundant and potentially viable. Renewable energy can meet the high energy demand in the state as well as the whole country and particularly households without electricity through off-grid connection and create a sustainable and feasible transition to the decarbonization of the present energy system which is coal or any other

conventional energy dependent. An exploration of renewable energy options has been beclouded by the abundance and high dependence on coal, which have dominated the energy market in West Bengal for decades. This study evaluated the different renewable energy sources and its potential, level, different future scope, policies, limitations, possibilities, menacing etc. using the SWOT analysis. This study has revealed several significant policy implications for future scope based on current situations. Some appropriate policies mentioned in this paper, from those thing policymakers highlight the need or requirements for promoting the programs for renewable energy sources to build a pathway into a sustainable transition of the Indian energy system as well as West Bengal.

Table 3. SWOT analysis matrix

Internal Factors	
<i>Strengths(+++)</i>	<i>Weaknesses(---)</i>
Suitable geographic position	High power generating cost
Political and Economic Stability	Miserable Household Electrification
Policy Environment Supporting Renewable Energy Implementation	Government's Poor Bureaucratic Processes
Govt. Subsidy	Land acquisition issues
Research institutions and institutional supports	Need for private participation
Open Market Investment	Improving generation performance
	Lack of Awareness
External Factors	
<i>Opportunities(+++)</i>	<i>Threats(---)</i>
Global Awareness and exposure	Fossil Fuel Dominance
Central Govt. and State govt. better Collaboration	Corruption
Financing the renewable sector	Market obstacles
Promote awareness	Technological obstacles
Improvement in manufacturing/technology	Environmental obstacles
Promote Research and development program	
Renewable energy jobs in India	

These include the fact that West Bengal has robust policies to tackle the energy challenges afflicting the country. There is potential in all the identified renewable energy options but harnessing energy from solar and wind is more advantageous as the State is very well-positioned geographically. It is hoped that both state and central government will strengthen the political gains by doing what is right for the economy and the citizens to avoid instability. This will help in opening the state and the country for local and international investments. There is a need for government intervention and participation in the issue of land due to its sensitivity. Large portions of land are sometimes required in the development of renewable energy projects so government must be taking some steps to find new free areas for implementation of new Renewable plant & where it's not available its causes for technology falling. Above all, corruption is a cankerworm in any society and poses a risk is the road of implementation of renewable Energy [13]. The government should find those threats and working over to reduce it. The Outcomes of the study can be used in all the states of India to modify the process of implementation of renewable energy or green energy initiatives.

References

1. West Bengal Renewable Energy Development Agency (WBREDA), Government of West Bengal, <http://www.wbreda.org/about-us/>
2. West Bengal Renewable Energy Development Agency (WBREDA), Government of West Bengal,

- Future plan of WBREDA, Govt. of West Bengal, <http://www.wbreda.org/future-plan/>
3. Ministry of New and Renewable Energy (MNRE), Govt. of India.
 4. Rajat Roy *West Bengal to focus on developing hydroelectricity*, Kolkata Last Updated at February 10, 2013.
 5. ENERGY STATISTICS India 2021, National Statistical Office, Ministry of Statistics and Program Implementation, Government of India.
 6. Policy on Co-generation and Generation of Electricity from Renewable Sources of Energy, Department Of Power & Nonconventional Energy Sources, Govt. of West Bengal, 5th June, 2012.
 7. BP Energy Outlook country and regional insights-India (2018), <https://www.bp.com/content/dam/bp/en/corporate/pdf/energy-economics/energy-outlook/bp-energy-outlook-2018-country-insight-india.pdf>
 8. The ECONOMIC TIMES Jun 02, 2021 edition entitled Schools go solar as West Bengal reaches for green goals, <https://economictimes.indiatimes.com/industry/renewables/schools-go-solar-as-west-bengal-reaches-for-green-goals/articleshow/83155744.cms>
 9. The 19th World Wind Energy Conference WWEC2021 has been scheduled to take place from 24-26 November 2021, with the theme Powering the World with Wind and Sun, <https://wwec2021.org/>
 10. A. Bergmann, N. Hanley, R. Wright *Valuing the attributes of renewable energy investments Energy Policy*, 34 (9) (2006), pp. 1004-1014 12217.
 11. N. Int, *What is clean energy transition and how does nuclear power fit in?*, Energy Agency Bull. 2020, 61, 3–5.
 12. Moorthy, K.; Patwa, N.; Gupta, Y. *Breaking barriers in deployment of renewable energy*, Heliyon 2019, 5, 01166.
 13. Meera Mahadevan *The Price of Power: Costs of Political Corruption in Indian Electricity*, January 14, 2019 Job Market Paper.
 14. "Profile and Challenges- North Eastern and Eastern States of India"- Pricewater House Coopers, 3rd North East & East Power Summit 2010, Indian Chamber of Commerce, 2010.
 15. The ECONOMIC TIMES May 15, 2019 edition, "Solar subsidies: Government subsidies and other incentives for installing rooftop solar system in India", https://economictimes.indiatimes.com/small-biz/productline/power-generation/solar-subsidiesgovernment-subsidies-and-other-incentives-for-installingrooftopsolarsysteminindia/articleshow/69338706.cms?utm_source=contentofinterest&utm_medium=text&utm_campaign=cppst
 16. Dr. S.P. Gon Choudhuri *Renewable Energy in West Bengal*, West Bengal green energy development corporation Limited (WBGEDCL)
 17. Will Kenton reviewed by GORDON SCOTT *Strength, Weakness, Opportunity, and Threat (SWOT) Analysis*, <https://www.investopedia.com/terms/s/swot.asp>
 18. SWOT Matrix, Concept Draw, <https://www.conceptdraw.com/examples/swot-matrix>
 19. Solomon E. Uhunamure and Karabo Shale, *A SWOT Analysis Approach for a Sustainable Transition to Renewable Energy in South Africa, Sustainability* 2021, 13, 3933. <https://doi.org/10.3390/su13073933>, MDPI journals.
 20. Charles Rajesh Kumar. J & M. A. Majid, *Renewable energy for sustainable development in India: current status, future prospects, challenges, employment, and investment opportunities*, ISSN: 2192-0567, 2021 BioMed Central Ltd unless otherwise stated. Part of Springer Nature.

Analysing the Barriers for Implementation of Industry 4.0 in Indian Dairy Industry: An ISM-MICMAC Approach

Sujay Biswas

1 Introduction

Industry 4.0 can be determined as the 4th industrial revolution that utilizes sophisticated robotics and AI, sensors, cloud computing, IoT, data collection and analytics, 3D printing, and other new types of models, mobile devices, etc. These are the upcoming smart development across the world. The 4th industrial revolution improves the system performance, the environment of the manufacturing systems, industrial stakeholders, customers, distributors, etc. will get benefit from the advanced technologies of industry 4.0 as it promises to change the production process severely. Industry 4.0 has enabled interaction between man-machine to produce customized products efficiently to meet the customer needs [1].

India plays a vital role in milk production in the upliftment of rural and socio-economy. The Dairy industry changes its technologies and business policies towards globalization [2]. The dairy animal population of India is the largest across the world through the milk production per animal is significantly lower than the other major dairy producers. Total 1,13,725.7 MT dairy products were exported over the world in the year 2018-2019. The total price of these dairy products is Rs. 2423 Crores 345.71 USD Million. Total worth gains by the Indian dairy market of INR 10,527 billion in 2019 will be helpful for Indian rural economic development [3].

There are several barriers to implementing I4.0 concepts in the industry, due to its extremely advanced approach. Over the last few years, few researchers have attempted to find out the nature and interrelationship among them. In this direction, [4] discussed a few barriers such as employment disruptions, deficiency in understanding about the benefits of IoT, flawless assimilation and compatibility issues, legal and contractual uncertainty for investigation of the driving and dependence power of barriers to adopting I4.0 in the Indian manufacturing industry.[5] investigated the applicability of I4.0 from workers' perspectives for German manufacturing plants.[6] analyzed driving factors, risks, and barriers for implementing I4.0 for generalized manufacturing models. The research methodology was a combination of particular reference bases with a research questionnaire inquiry conducted for industrial enterprises in the Czech Republic.[7] performed an empirical investigation of an emerging economy to find out barriers to I4.0. The work also evaluated how the obtained barriers stimulate the linkage between digitalization and the performance of the firm.

With the execution of industry 4.0, the production process of the Indian dairy industry will become more efficient. The productivity, quality of the product will increase and the resources will be optimized as well. Similar to other industries, while implementing industry 4.0, there arise few obstructions that the industries need to overcome. Therefore, in this communication, we aim to recognize the significant barriers to implementing industry 4.0 and the mutual relation among those barriers. To achieve our objective, the following questions were addressed in this work:

- I. What are the important barriers to implementing industry 4.0?
- II. What is the relationship between these barriers?
- III. What are the driving and dependence power of the barriers to implementing industry 4.0?

To answer these research questions, we developed an ISM approach to investigate the interrelationship between the barriers for the execution of industry 4.0 in the dairy industry.

S. Biswas

*Dept. of Industrial Engineering and Management, MAKAUT, WB
Simhat, Haringhata, Nadia, India-741249*

2 Theory and Methodology

2.1. Barrier Identification:

Through various literature surveys, and expert opinions, barriers for implementing I4.0 in the Indian dairy industry are identified. Developing a questionnaire from 21 experts (among which 17 were from various industries and 4 from academics), we collected data that was considered appropriate for our study. The participants are mainly engineers, senior technicians, managers, automation specialists, project managers, area managers, senior professors for our study. Seventeen barriers were suggested for the implementation of industry 4.0 by reputed experts, which are: the shortage of financial support (B1); high implementation cost (B2); absence of proper infrastructure (B3), unavailability of skilled/trained/qualified staff (B4); lack of knowledge in management systems (B5); communication gap between upper and lower levels of management (B6); lack of vision (B7); need of automation (B8); not up to standards (B9); deficiency of security and privacy (10); lack of research and development (B11); shortage of government subsidy (B12); absence of awareness about 4.0 (B13); deprivation of understanding of the significance of Industry 4.0 (B14); lack of professional culture in the company (B15); deficiency of implementation knowledge about 4.0 (B16); scarcity of proper waste management (B17).

2.2. ISM:

ISM is an analytical approach that is used to determine the interrelationship between the factors that affect the particular subject [8]. This investigative model can be used to examine the interdependency between the barriers and the drivers [9]. ISM model helps decision-makers in various decision-making environments such as analysis of supply chain, analyzing the enablers in the sustainable supply chain, barriers analyzing, and others [10].

(a). Development of structural self-interaction matrix (SSIM):

This is the first step towards the development of the ISM model. SSIM matrix is created using the following formula:

- **V:** If Barrier a will impact Barrier b, hence we can represent it as 'V' in the SSIM.
- **A:** If Barrier a will be impacted by Barrier b, hence we can represent it as 'A' in the SSIM.
- **X:** If Barrier a and Barrier b will impact each other, we can represent it as 'X' in the SSIM.
- **O:** If Barrier a and Barrier b are unrelated, therefore we can represent it as 'O' in the SSIM.

The SSIM matrix is presented in Table 1.

(b). Development of the Initial Reachability Matrix (IRM):

IRM (binary matrix) is calculated with the help of SSIM, and the values V, A, X, and O are substituted with 0 or 1, as per the following rules:

- i) if (a, b) value is denoted as 'V', then the (a, b) value in the IRM will be assigned as 1, and (b, a) value will be assigned as 0.
- ii) if (a, b) value is denoted as 'A', then the (a, b) value in the IRM will be assigned as 0, and (b, a) value will be assigned as 1.
- iii) if (a, b) value is denoted as 'X' then the (a, b) value in the IRM will be assigned as 1, and (b, a) value will be assigned as 1.

- iv) if (a, b) value is denoted as 'O' then the (a, b) value in the IRM will be assigned as 0, and (b, a) value will be assigned as 0.

(c). Implementation of the final reachability matrix (FRM):

After the implementation of the IRM, FRM is needed to be developed with the help of transitivity rules. The transitivity rules can be stated as: if a variable E is related to variable F, and variable F is related to variable G, then by default E is related to G. The transitivity is implemented as 1* in the FRM matrix.

(d). Creation of level partition for barriers:

In this step, from the FRM matrix, we evaluated the reachability set and antecedent set of individual barriers and with that, we developed an intersection set. To identify the level of barriers, we repeated the iterative process.

(e). Formation of ISM based model for the barriers:

The ISM-based model was developed after developing the level partitioning with the help of a digraph. A digraph is used to visualize the interrelation between the elements and their interdependencies.

2.3. MICMAC Analysis:

The abbreviation of MICMAC is Matriced' Impacts Croises-Multiplication Applique and Classement (cross-impact matrix multiplication applied to classification) which is evaluated from the multiplication property of matrices [11]. To analyze the driving power and dependence power of different barriers, this MICMAC analysis was initiated by Godet in the year of 1986 [12]. This analysis is used to find out the distinct effect between the barriers to determine the main barriers that drive the model in its full manner. There are four group representations, depending on analysis results:

- i) **Autonomous:** This group, represented in quadrant I include the barriers which have weak driving power and weak dependence power, least attached to the system.
- ii) **Dependent:** Quadrant II represents dependent barriers which consist of those barriers that have weak driving power and strong dependence power.
- iii) **Linkage:** Linkage barriers are represented in quadrant III and it includes barriers that have strong driving power and strong dependence power.
- iv) **Independent:** Quadrant IV represents independent barriers that contain strong driving power but weak dependence power.

3 results and discussion

From the ISM-based approach, we had determined the interrelationship between the barriers identified so that the authority can consider those barriers for eliminating and reducing for successful implementation of Industry 4.0 in the Indian Dairy Industry. In this direction, SSIM, IRM, FRM, and iteration matrices were calculated. This is shown in Tables 1, 2, and 3 respectively. Using these matrices, MICMAC analysis has been performed. From the MICMAC results (as shown in Fig. 2), 'Shortage of government subsidy (B12)', is the autonomous barrier with weak driving power and weak dependence power. The barriers 'Not up to standards (B9)', 'Deficiency of security and privacy (10)', 'Lack of professional culture in the company (B15)', and 'Scarcity of proper waste management (B17)' were placed at Level I, II in our ISM based hierarchy model. The management system should follow

Table 3. FRM matrix for barrier calculation for the Indian dairy industry.

Barrier a	Barrier b																	Driving Power
	B1	B2	B3	B4	B5	B6	B7	B8	B9	B10	B11	B12	B13	B14	B15	B16	B17	
B1	1	1	1	1	1	1	1	1	1*	1	1	1*	1*	1*	1*	1*	1	17
B2	0	1	0	0	0	0	0	1	1	1	1	1*	1*	1*	1*	1*	1	11
B3	0	1*	1	0	0	0	0	1	1	1	1	1*	1*	1*	1*	1*	1	12
B4	0	1*	1*	1	1*	1	1*	1*	1	1*	1	1*	1	1	1	1	1*	16
B5	0	1*	1*	1	1	1	1*	1*	1	1*	1*	0	1*	1	1*	1	1	15
B6	0	1*	1*	0	1*	1	1	1*	1	1*	1*	0	1*	1	1*	1	1*	14
B7	0	1*	1	1*	1	1*	1	1*	1	1	1	1*	1	1	1*	1	1	16
B8	0	1	1*	0	1*	1*	0	1	1*	1*	1*	0	1	1	1*	1	1	13
B9	0	1	0	0	0	1*	0	1*	1	1	1*	0	0	0	1	0	1	8
B10	0	1	0	0	0	0	0	1*	1*	1	1*	0	0	0	0	0	1*	6
B11	0	1	1*	0	1*	1*	0	1*	1	1*	1	1	1	1*	1*	1	1	14
B12	0	1*	0	0	0	0	0	0	1*	0	1	1	1*	0	0	1*	1	7
B13	0	1*	1	1*	1	1*	0	1	1	1*	1	1*	1	1*	1*	1	1*	15
B14	0	1*	1	0	1*	1	1*	1	1	1	1*	0	1	1	1	1	1*	14
B15	0	0	0	0	0	1	1*	0	1*	0	0	0	0	1*	1	1*	0	6
B16	0	1*	1	0	0	1	1*	1	1	1*	1*	0	1*	1	1*	1	1	13
B17	0	0	0	0	0	0	0	0	0	0	0	0	0	0	0	0	1	1
Dependence Power	1	15	11	5	9	12	8	14	16	14	15	8	13	13	14	14	16	

Table 4. Iteration to determine the level of barriers in the Indian dairy industry.

Barriers	Reachability	Antecedent	Intersection	Iteration no and level
B15	6,7,9,14,15,16	1,2,3,4,5,6,7,8,9,11,13,14,15,16	6,7,9,14,15,16	I
B17	17	1,2,3,4,5,6,7,8,9,10,11,12,13,14,16,17	17	I
B8	2,3,5,6,8,9,10,11,13,14,16	1,2,3,4,5,6,7,8,9,10,11,13,14,16	2,3,5,6,8,9,10,11,13,14,16	II
B9	2,6,8,9,10,11	1,2,3,4,5,6,7,8,9,10,11,12,13,14,16	2,6,8,9,10,11	II
B10	2,8,9,10,11	1,2,3,4,5,6,7,8,9,10,11,13,14,16	2,8,9,10,11	II
B11	2,3,5,6,8,9,10,11,12,13,14,16	1,2,3,4,5,6,7,8,9,10,11,12,13,14,16	2,3,5,6,8,9,10,11,12,13,14,16	II
B11	2,3,5,6,8,9,10,11,12,13,14,16	1,2,3,4,5,6,7,8,9,10,11,12,13,14,16	2,3,5,6,8,9,10,11,12,13,14,16	II
B13	3,4,5,6,12,13,14,16	1,3,4,5,6,7,12,13,14,16	3,4,5,6,12,13,14,16	III
B14	3,5,6,7,13,14,16	1,3,4,5,6,7,13,14,16	3,5,6,7,13,14,16	III
B16	3,6,7,13,14,16	1,3,4,5,6,7,12,13,14,16	3,6,7,13,14,16	III
B12	12	1,3,4,7,12	12	IV
B3	3	1,3,4,5,6,7	3	V
B5	4,5,6,7	1,4,5,6,7	4,5,6,7	VI
B6	5,6,7	1,4,5,6,7	5,6,7	VI
B7	4,5,6,7	1,4,5,6,7	4,5,6,7	VI
B4	4	1,4,5,7	4	VII
B1	1	1	1	VIII

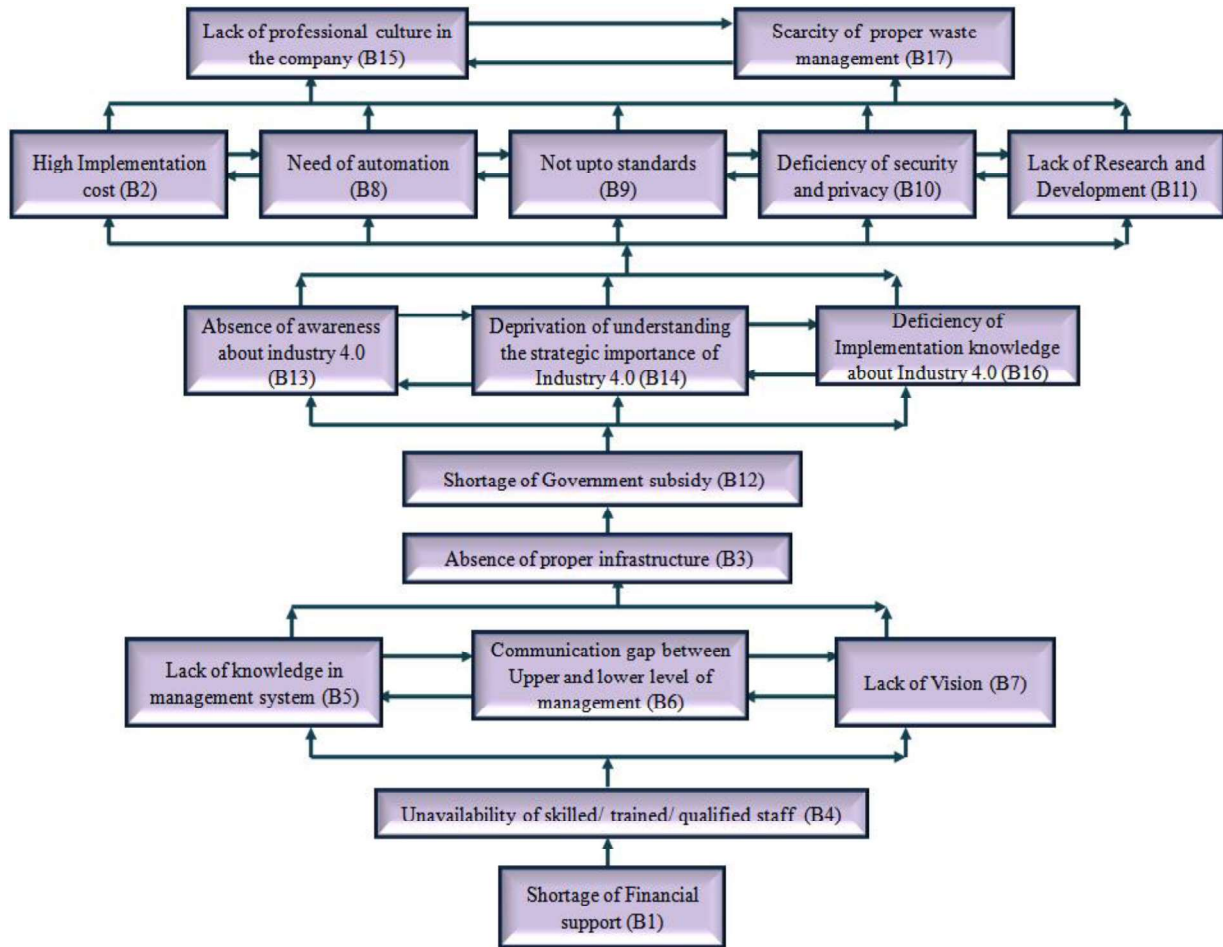


Fig.1 ISM based model for barriers in Indian Dairy Industry

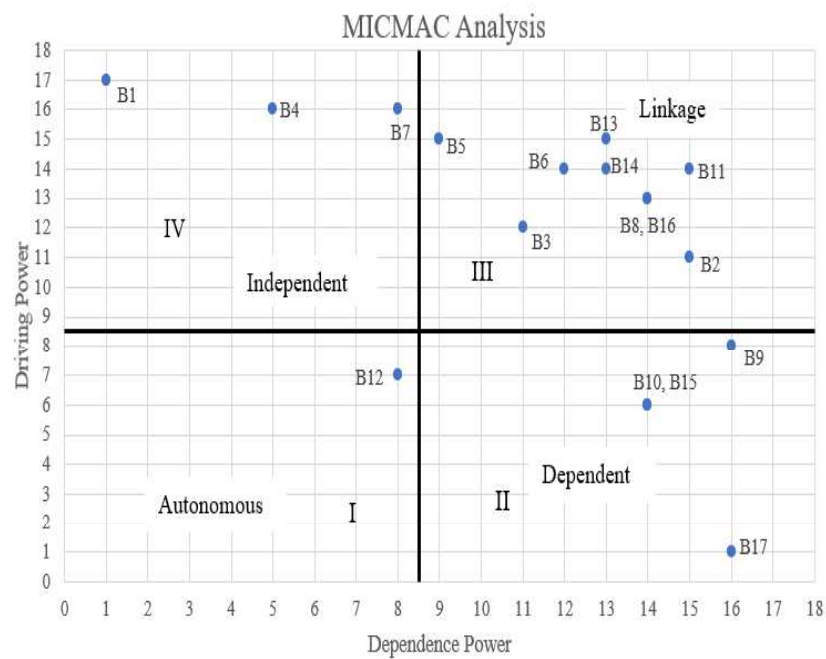


Fig. 2 MICMAC results: driving-dependence power for barriers.

Nine barriers i.e., ‘High implementation cost (B2)’, ‘Absence of proper infrastructure (B3)’, ‘Lack of knowledge in management systems (B5)’, ‘Communication gap between upper and lower levels of management (B6)’, ‘Need of automation (B8)’, ‘Lack of research and development (B11)’, ‘Absence of awareness about 4.0 (B13)’, ‘Deprivation of understanding of the significance of Industry (B14)’ and ‘Deficiency of implementation knowledge about 4.0 (B16)’ are having strong driving power and strong dependence power and they are placed in quadrant III and denoted as linkage barriers. Hence, the authority should encompass their positive attention to solve this barrier as these barriers are relatively unstable and any effect on them may cause problems to other barriers.

There are three remaining barriers which are located in quadrant IV due to strong driving power and weak dependence power (Fig. 2). ‘Shortage of financial support (B1)’, ‘Unavailability of skilled/trained/qualified staff (B4)’, ‘Lack of vision (B7)’ are addressed as independent barriers placed at the bottom of our ISM based hierarchy model. Among these three barriers, ‘Unavailability of skilled/trained/qualified staff (B4)’, ‘Shortage of financial support (B1)’ is at level VII and VIII respectively. Therefore, to implement Industry 4.0 in the Indian Dairy Industry the management must follow up these barriers to be solved out or to reduce with the help of formulation, strategies, etc. due to the high driving power of the barriers.

4 Conclusions and Future Work

In this research, based on the literature review and experts’ suggestion, seventeen barriers are identified as the relevant barriers for implementation industry 4.0 in the Indian Dairy industry. With the help of ISM based approach, we determine the interrelationship between the barriers. Using ISM-MICMAC analysis it was observed that, the barrier ‘Shortage of financial support (B1)’, is the most effective barrier which was placed at the bottom of ISM based model. Additionally, ‘Unavailability of skilled/trained/qualified staff (B4)’ and ‘Lack of vision (B7)’ are the independent barriers that may be considered as one of the most effective barriers for the implementation of industry 4.0.

Future studies can be extended using more numbers of barriers from a greater number of experts so that the research work can be broadened and Structural Equation Model (SEM) can be adopted for identifying efficiently the interrelationship between the barriers.

References

1. Geissbauer, R., Lubben, E., Schrauf, S., & Pillsbury, S. (2018). Digital Champions. *How industry leaders build integrated operations ecosystems to deliver end-to-end customer solutions*. Price water house Coopers.
2. Bhardwaj, A., Mor, R. S., Singh, S., & Dev, M. (2016). An investigation into the dynamics of supply chain practices in Dairy industry: A Pilot Study. In *Proceedings of the 2016 Int. Conf. on Industrial Engg. and Oper. Mgt., Detroit, Michigan, USA* (pp. 1360-1365).
3. Madhavan, M., Krishnakumar, K., & Karpagam, K. Performance of dairy industry in india: an analysis
4. Kamble, S. S., Gunasekaran, A., & Sharma, R. (2018). Analysis of the driving and dependence power of barriers to adopt industry 4.0 in Indian manufacturing industry. *Computers in Industry*, 101, 107-119.
5. Müller, J. M. (2019). Assessing the barriers to Industry 4.0 implementation from a workers’ perspective. *IFAC-PapersOnLine*, 52(13), 2189-2194.
6. Macurová, P., Ludvík, L., & Žwaková, M. (2017). The driving factors, risks and barriers of the industry 4.0 concept. *Journal of applied economic sciences*, 12(7).
7. Chauhan, C., Singh, A., & Luthra, S. (2021). Barriers to industry 4.0 adoption and its performance implications: An empirical investigation of emerging economy. *Journal of Cleaner Production*, 285, 124809.
8. Singhal, D., Tripathy, S., Jena, S. K., Nayak, K. K., & Dash, A. (2018). Interpretive structural modelling (ISM) of obstacles hindering the remanufacturing practices in India. *Procedia Manufacturing*, 20, 452-457.

9. Vigneshvaran, R., & Vinodh, S. (2020). Development of a structural model based on ISM for analysis of barriers to integration of lean with industry 4.0. *The TQM Journal*.
10. Khurana, S., Mannan, B., & Haleem, A. (2020). Total interpretive structural modelling of critical factors of sustainable-oriented innovation for Indian manufacturing MSMEs. In *Recent Advances in Mechanical Engineering* (pp. 95-106). Springer, Singapore
11. Sharma, S. Applied Multivariate Techniques; John Wiley & Sons, Inc.: Hoboken, NJ, USA, 1995.
12. Godet, M. (1986). Introduction to la prospective: seven key ideas and one scenario method. *futures*, 18(2), 134-157.

Identifying The Significant Barriers for Implementation of I4.0 In Indian Casting Industries Using ISM-MICMAC Approach

Sujay Biswas, Arka Prava Das

1 Introduction

In the modern era of the automation Industry, 4.0 (I4.0) is emerging rapidly as a substitute for the present labor-intensive industry model [1]. I4.0 can be viewed as the 4th industrial revolution that involves cloud computing, IoT, advanced robotics, machine learning (ML), artificial intelligence (AI), cyber-physical systems, advanced sensors, data collection and analytics, 3D printing, and other new types of models, mobile devices, etc. It is upcoming smart development across the globe. Advantages of automation (I4.0) include reduced production cost, increased overall system performance, improved efficiency, agility, and flexibility, and many others. [2]. Industry 4.0 has enabled interaction between man-machines [3]. Human empowerment plays a significant role in the production process of I4.0 but at instance, coloration with robots and habituating with the machines is a difficult challenge within the industry. To optimize the ramp-up time I4.0 has a significant impact as it increases the operator's performance and leads to efficient and safe production. Industry 4.0 includes the integration of smart sensors and smartphones together while collaborating with industries to achieve the desired objective and corresponding plan accurately. Industry 4.0 includes three mechanical patterns driving this transformation: connectivity, knowledge, and flexible manufacturing. After the declaration of the term 'Industry 4.0', many industrialists and governments worldwide adopted this to make necessary changes for making the industries digitalized [4], [5]. Consumers are provided the new digital solutions according to their problem such as internet-based services immersed in products with the help of smart technology [6]. The technology required for the implementation of I4.0 still required more attention techniques. Many prior types of research have been done about the implementation of industry 4.0, many models were approached by several researchers [7], [8],[9], whereas few types of research have been done about the significance of the technologies Industry 4.0 leads to produce a customized product in a huge amount [10].

Casting is a conventional machining process in which liquid material is poured into a mold that contains a hollow cavity of the desired shape and then allowed to solidify. Casting is most often used for making complex shapes that would be otherwise difficult or uneconomical to make by other methods. The casting metal method is one of the oldest processes. More innovations in technology are needed by the cost-effective ideas to generate goods of the best quality at minimum cost. These days, lots of work are going on in the research and development of the casting industry to improve the efficiency of the casting methods that have been defined as the parameters for shaping the casting industry. The effective study on the casting industry reveals that the countries like China, India, USA have made significant advancements in technologies in casting component manufacturing. These iterations of innovations are possible because the reason is there are sufficient ambient temperatures for the casting process. All Indian casting companies are actively participating in the manufacturing of casting goods in various applications.

S. Biswas¹, A. P. Das²

¹Dept. of Industrial Engineering and Management, MAKAUT, WB
Simhat, Haringhata, Nadia, India-741249

²Dept. of Mechanical Engineering
Institute of Engineering & Industrial Technology (IE & IT), MAKAUT Durgapur, West Bengal- 713212

Depending upon the specifications of the commodity and the area of usage effective measures must be taken from various methods. For the rapidly growing casting industry, the specific casting process will fulfill the significant requirements from the minimum cost of production. Before applications, mechanical properties such as hardness are given in the casting parameters for any essential casting component. For the selection of specific casting methods, there are important considerations and important parameters that must take for production [11].

With the execution of I4.0, the overall production process of the Indian casting industry will become more effective and efficient as well. The quality of the product, productivity will increase and the resources will be optimized as well. Therefore, in this communication, we aim to identify the significant barriers to implementing I4.0 and the interrelation among those barriers. To achieve our objective, the following questions were addressed in this study:

- I. What are the significant barriers to implementing industry 4.0 in the casting industry?
 - II. What is the mutual relationship between these barriers?
 - III. What is the dependence and driving and power of the barriers to implementing industry 4.0?
- To answer these research questions, we developed an ISM approach to investigate the mutual relationship between the barriers to the execution of I4.0 in the casting industry.

2 Theory and Methodology

2.4. *Barrier Identification:*

Through various experts' opinions and literature surveys, barriers to implementing I4.0 in the Indian casting industry are identified. Developing a questionnaire from 47 experts (among which 16 from academics and 31 from various industries), we collected data that was considered appropriate for our study. The participants are mainly senior managers, project managers, automation specialists, area managers, technicians, engineers, senior professors, and many others for our study. Eighteen barriers were suggested for the implementation of industry 4.0 by reputed experts, which are: communication gap among department (B1); lack of long-term vision (B2); high implementation cost (B3), absence of proper digital infrastructure (B4); deficiency of knowledge about industry 4.0 (B5); lack of funding for I4.0 (B6); resistance to change (B7); shortage of subsidy from the government (B8); risk of data and cyber security (B9); shortage of skilled/ trained/ qualified employed employee resources (10); lack of clear comprehension about IoT benefits (B11); lack of internet coverage and IT facilities (B12); deficiency of detailed and strategic planning (B13); absence of advanced manufacturing facilities (B14); lack of support from top management (B15); lack of waste management (B16); lack of worker motivation (B17); job loss due to automation (B18).

2.5. *Interpretive Structural Modeling (ISM):*

Interpretive Structural Modeling (ISM) analyzes the complexity between the variables. ISM is also used to develop a map of the interrelationship between the elements in flexible circumstances. The most effective application of ISM is to use the practical knowledge of experts and knowledge to break down the classification into the sub-structured model [12]. To analyses the interdependency between the elements, the analytical model can be used [13].

[14] discussed ISM approach to identify the mutual relationship between the enablers of sustainability in market-oriented firms. According to [15] the characteristics of ISM can be described as a methodology that is interpretive, structural to specify the relationship and complexity relationship between the elements of a system. There are a few limitations also such as the relationship between the variables is based upon the knowledge and priority provided by the identified experts' knowledge. Hence there is a chance of manipulation of the outcome. The major application of this ISM model is

to help the decision-makers in different decision-making environments [16] determine the enablers in the sustainable supply chain [17], analyze the potential of the supply chain [18], analyze the barriers of green lean six sigma implementation [19], etc.

(a). Development of structural self-interaction matrix (SSIM):

This is the first step towards the development of the ISM model. SSIM matrix is created using the following formula:

- **V:** Barrier a will influence barrier b; hence we can express it as 'V' in the SSIM.
- **A:** Barrier a will be influenced by barrier b; hence we can express it as 'A' in the SSIM.
- **X:** Barrier a and barrier b will influence each other; hence we can express it as 'X' in the SSIM.
- **O:** Barriers a and barrier b are unrelated; therefore, we can represent it as 'O' in the SSIM.

The SSIM matrix is presented in Table 1.

(b). Development of the Initial Reachability Matrix (IRM):

The Initial Reachability Matrix (IRM) is often considered as 'binary matrix' is developed using the SSIM and the values V, A, X, and O are substituted with 0 or 1, as per the rules which are given below:

- v) In the SSIM matrix, if the value in a cell (a, b) is represented as 'V' then the entry in the initial reachability matrix (IRM) of the cell (a, b) will be represented as 1 and the value of the cell (b, a) will be 0 in the initial reachability matrix.
- vi) In the SSIM matrix, if the value in a cell (a, b) is represented as 'A' then the entry in the initial reachability matrix (IRM) of the cell (a, b) will be represented as 0 and the value of the cell (b, a) will be 1 in the initial reachability matrix.
- vii) In the SSIM matrix if the value in a cell (a, b) is represented as 'X' then the entry in the initial reachability matrix (IRM) of the two cells both (a, b) and (b, a) will be denoted 1 in the initial reachability matrix.
- viii) In the SSIM matrix if the value in a cell (a, b) is represented as 'O' then the entry in the initial reachability matrix (IRM) of the two cells both (a, b) and (b, a) will be denoted 0 in the initial reachability matrix.

(c). Implementation of the final reachability matrix (FRM):

After the implementation of the IRM, FRM is needed to be developed with the help of transitivity rules. The transitivity rules can be stated as: if a variable I is related to variable J, and variable J is related to variable K, then by default I is related to K. The transitivity is implemented as 1* in the FRM matrix.

(d). Creation of level partition for barriers:

With the help of the final reachability matrix (FRM), we determined the reachability set and antecedent set of each barrier. Level partitioning is used to analyze the hierarchy of those elements. The reachability set of a barrier contains the barrier itself and other barriers which lead help to achieve it i.e., the set of barriers that have binary digit '1' in its respective row in the final reachability matrix and the antecedent set consists of that barrier itself and other barriers which might influence it and they are having binary digit '1' in their corresponding column of the final reachability matrix. Then, we developed the intersection set from the reachability and intersection set for all barriers. The barriers for which the reachability set and intersection set is similar are allocated level in the ISM hierarchy model. In the next process, the assigned barrier has been discarded from the subsequent level

partitioning process and the process lasts till the assignment of each barrier in the ISM hierarchy model. In our study, ten levels of barriers have been identified as presented in Table 4.

(e). Formation of ISM based model for the barriers:

After developing the final reachability matrix, we developed the ISM-based model to conceptualize the interrelationship between the variables. To develop the model, a digraph was introduced and the digraph is converted into ISM based model by substituting the nodes of enablers with statements as shown in Fig.1.

2.6. MICMAC (Matriced' Impacts Croises-Multiplication Applique and Classment) Analysis:

In the year of 1986, the MICMAC analysis was initiated by Godet to analyze the dependence and driving power of different barriers [20]. In MICMAC analysis, there are four group representations, depending on analysis results:

- v) **Autonomous:** This group contains the barriers which are having weak driving and dependence power and they are considered as least attachment with the system and placed at quadrant I.
- vi) **Dependent:** In this group, the barriers which have weak driving power and strong dependence power are denoted as dependent barriers and they are assigned at quadrant II.
- vii) **Linkage:** The barriers with strong driving power and strong dependence power are denoted as linkage enablers and they are placed at quadrant III.
- viii) **Independent:** Cluster IV represents the barriers of strong driving power and weak dependence power and they are termed as independent barriers.

The MICMAC analysis is presented in Fig. 2.

3 Results and Discussion

ISM approach and MICMAC analysis were used to determine the contextual relationship among the barriers and to identify the effective barrier to influence the implementation of industry 4.0 in the Indian casting industry.

Table 1. SSIM matrix for barrier calculation for Indian casting industry.

[illegible]

In this direction, SSIM, IRM, FRM, and iteration matrices were calculated. This is shown in Tables 1, 2, and 3 respectively. Using these matrices, MICMAC analysis has been performed. From the MICMAC results (as shown in Fig. 2), ‘shortage of subsidy from the government (B8)’, is the autonomous barrier with weak driving power and weak dependence power, which is placed in quadrant I. ‘lack of worker motivation (B17)’, ‘lack of internet coverage and IT facilities (B12)’, ‘resistance to change (B7)’, ‘risk of data and cyber security (B9)’, ‘absence of advanced manufacturing facilities (B14)’, ‘lack of waste management (B16)’, and job ‘loss due to automation (B18)’, are the dependent barriers with weak driving power and strong dependence power which are placed in quadrant II. Among these five barriers, (B17), (B12), (B7), (B19), (B14), (B16), and (B18) are at levels III, II, and I respectively. The management system should follow up the main cause of these occurring barriers and identify that the management should understand the level of dependency on other barriers.

Table 2. IRM matrix for barrier calculation for Indian casting industry

Barrier a	Barrier b																		
	B1	B2	B3	B4	B5	B6	B7	B8	B9	B10	B11	B12	B13	B14	B15	B16	B17	B18	
B1	1	0	0	0	0	0	1	0	0	0	1	1	1	0	1	0	1	0	
B2	0	1	0	1	0	1	1	0	1	1	1	1	1	1	1	1	1	1	
B3	0	0	1	1	0	1	0	1	0	0	0	1	0	1	1	1	1	0	
B4	0	0	0	1	0	0	0	0	1	0	0	1	1	0	0	1	0	0	
B5	1	1	0	1	1	0	0	0	1	1	1	1	1	1	0	1	0	0	
B6	0	0	0	1	0	1	0	0	1	1	0	1	0	1	0	1	1	0	
B7	0	0	0	0	0	0	1	0	0	0	0	0	0	0	0	0	0	1	
B8	0	0	0	1	0	0	0	1	0	0	0	0	0	1	0	0	0	0	
B9	0	0	0	0	0	0	0	0	1	0	0	0	0	0	0	0	0	0	
B10	1	1	0	0	0	0	1	0	0	1	1	0	0	0	0	0	0	1	
B11	0	0	0	1	0	0	1	0	1	0	1	1	1	0	0	0	1	1	
B12	0	0	0	0	0	0	0	0	1	0	0	1	0	1	0	0	0	0	
B13	1	0	0	0	0	0	0	0	1	0	0	1	1	1	1	1	1	1	
B14	0	0	0	0	0	0	0	0	0	0	0	0	0	1	0	0	0	0	
B15	1	0	0	0	0	0	0	0	1	1	0	1	1	1	1	1	1	1	
B16	0	0	0	0	0	0	0	0	0	0	0	0	0	0	0	1	0	0	
B17	0	0	0	0	0	0	0	0	0	0	1	0	0	0	0	0	1	1	
B18	0	0	0	0	0	0	0	0	0	0	0	0	0	0	0	0	0	1	

Table 3. FRM matrix for barrier calculation for Indian casting industry

Barrier a	Barrier b																			Driving Power
	B1	B2	B3	B4	B5	B6	B7	B8	B9	B10	B11	B12	B13	B14	B15	B16	B17	B18		
B1	1	0	0	1*	0	0	1	0	1*	1*	1	1	1	1*	1	1*	1	1*	13	
B2	1*	1	1*	1	0	1	1	0	1	1	1	1	1	1	1	1	1	1	16	
B3	1	0	1	1	0	1	0	1	1*	1	0	1	1	1	1	1	1	1	14	
B4	1*	0	0	1	0	0	0	0	1	0	0	1*	1	1*	1*	1	1*	1*	10	
B5	1	1	1*	1	1	0	1*	0	1	1	1	1	1	1	1*	1	1*	1*	16	
B6	1*	1*	1*	1	0	1	1*	0	1	1	1*	1	0	1	0	1	1	1*	14	
B7	0	0	0	0	0	0	1	0	0	0	0	0	0	0	0	0	0	1	2	
B8	0	0	0	1	0	0	0	1	1*	0	0	1*	0	1	0	0	0	0	5	
B9	0	0	0	0	0	0	0	0	1	0	0	0	0	0	0	0	0	0	1	
B10	1	1	0	1*	0	1*	1	1*	1*	1	1	1*	1*	1*	1*	1*	1*	1	16	
B11	1*	0	0	1	0	0	1	0	1	0	1	1	1	1*	1*	1*	1	1	12	
B12	0	0	0	0	0	0	1*	0	1	0	1*	1	1*	1	1*	0	1*	0	8	
B13	1	0	0	0	0	0	1*	0	1	1*	1*	1	1	1	1	1	1	1	12	
B14	0	0	0	0	0	0	0	0	0	0	0	0	0	1	0	0	0	0	1	
B15	1	1*	1*	0	0	0	1*	0	1	1	1*	1	1	1	1	1	1	1	14	
B16	0	0	0	0	0	0	0	0	0	0	0	0	0	0	0	1	0	0	1	
B17	0	0	0	1	0	0	1	0	1	0	1	1	1	0	0	0	1	1	8	
B18	0	0	0	0	0	0	0	0	0	0	0	0	0	0	0	0	0	1	1	
Dependence Power	10	5	5	10	1	4	11	3	14	8	10	13	11	13	10	11	12	13		

Table 4. Iteration to determine the level of barriers in the casting industry.

Barriers	Reachability	Antecedent	Intersection	Iteration no and level
B9	9	1,2,3,4,5,6,8,9,10,11,12,13,15,17	9	I
B14	14	1,2,3,4,5,6,8,10,11,12,13,14,15	14	I
B16	16	1,2,3,4,5,6,10,11,13,16	16	I
B18	18	1,2,3,4,5,6,7,10,11,13,15,17,18	18	I
B7	1	1,2,5,6,7,10,11,12,13,15,17	1	II
B12	11,12,13,15,17	1,2,3,4,5,6,8,10,11,12,13,15,17	11,12,13,15,17	III
B13	1,10,11,12,13,15,17	1,2,3,4,5,10,11,12,13,15,17	1,10,11,12,13,15,17	III
B17	4,11,12,13,17	1,2,3,4,5,6,10,11,12,13,15,17	4,11,12,13,17	III
B1	1,4,10,11,15	1,2,3,4,5,6,10,11,15,	1,4,10,11,15	IV
B15	1,2,3,10,11,15	1,2,3,4,5,10,11,15	1,2,3,10,11,15	IV
B4	4	2,3,4,5,6,8,10,11	4	V
B8	8	3,8,10	8	VI
B11	11	2,5,6,10,11	11	VI
B6	2,3,6,10	2,3,6,10,	2,3,6,10	VII
B10	2,6,10	2,3,5,6,10	2,6,10	VII
B3	3	3,5	3	VIII
B2	2	2,5	2	IX
B5	5	5	5	X

Five barriers i.e., ‘lack of clear comprehension about IoT benefits (B11)’, ‘absence of proper digital infrastructure (B4)’, ‘communication gap among department (B1)’, ‘lack of support from top management (B15)’, ‘deficiency of detailed and strategic planning (B13)’, are having strong driving power and strong dependence power and they are placed in quadrant III and denoted as linkage barriers.

Among these five barriers, (B11), (B4), (B1), (B15), and (B13) are at levels VI, V, IV, and III respectively. Hence, the authority should encompass their positive attention to solve this barrier as these barriers are relatively unstable and any effect on them may cause problems to another barrier.

There are five remaining barriers which are located in quadrant IV due to strong driving power and weak dependence power it is denoted as independent barriers (Fig. 2). ‘Deficiency of knowledge about industry 4.0 (B5)’, ‘lack of long-term vision (B2)’, ‘high implementation cost (B3)’, ‘shortage of skilled/ trained/ qualified employed employee resources (10)’, and lack of funding for I4.0 (B6)’, are addressed as independent barriers placed at the bottom of our ISM based hierarchy model. Among these five barriers, (B5), (B2), (B3), (B10), and (B6) are at levels, IX, VIII, and VII respectively. Therefore, to implement Industry 4.0 in the Indian casting industry the management must follow up these barriers to be solved out or to reduce with the help of formulation, strategies, etc. due to the high driving power of the barriers.

4 Conclusions and Future Work

In this research, based on the experts’ suggestions and literature review, eighteen barriers are identified as the relevant barriers for the implementation of I4.0 in the Indian casting industry. With the help of ISM based approach, we determine the mutual between the barriers. Using ISM-MICMAC analysis it was observed that, the barrier ‘deficiency of knowledge about industry 4.0 (B5)’, is the most effective

barrier which was placed at the bottom of ISM based model. Additionally, ‘lack of long-term vision (B2)’, ‘high implementation cost (B3)’, ‘shortage of skilled/ trained/ qualified employed employee resources (10)’, and ‘lack of funding for I4.0 (B6)’, is the independent barriers which may be considered as one of the most significant barriers for the implementation of industry 4.0.

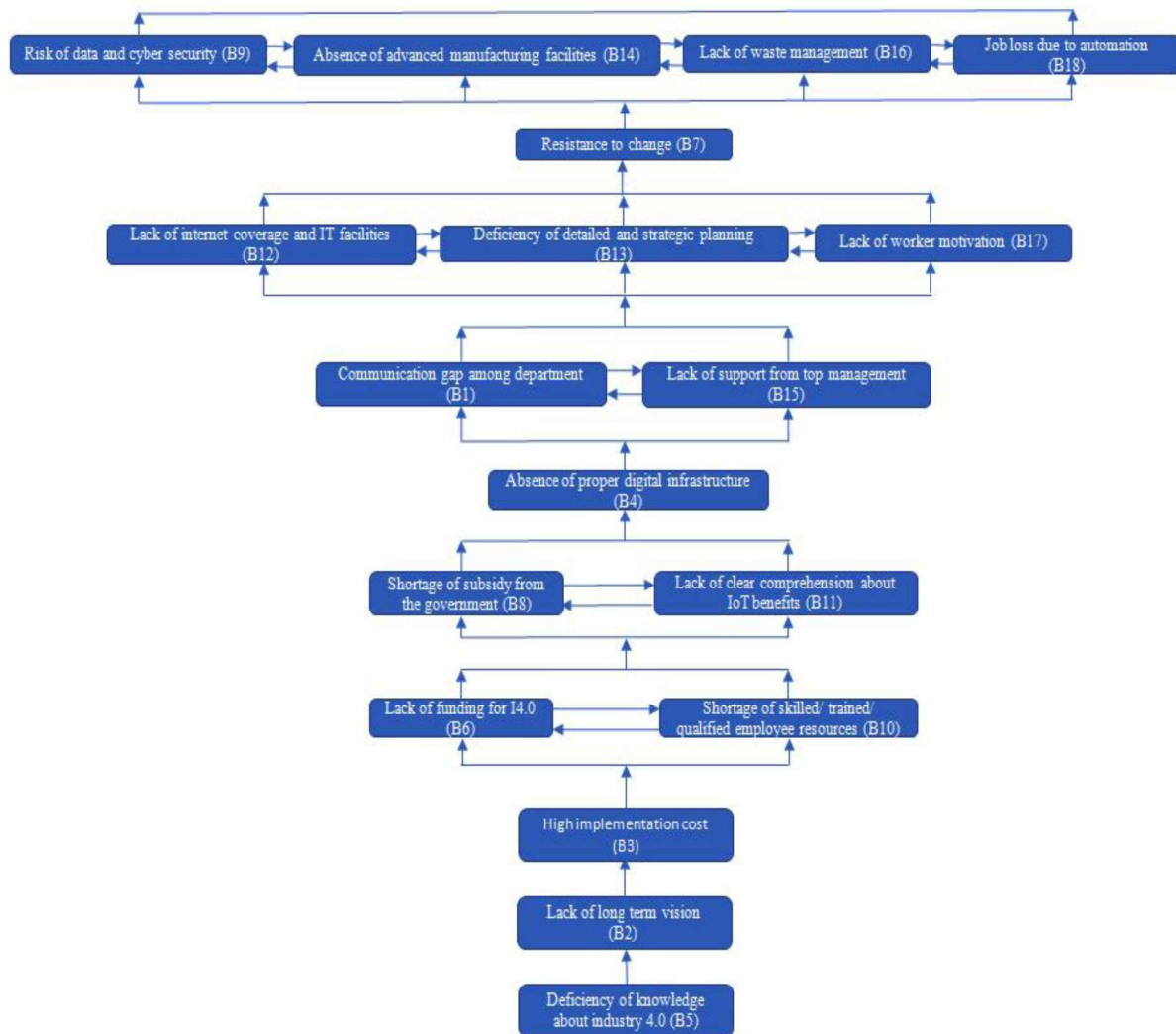


Fig.1 ISM based model for I4.0 implementation barriers in the Indian casting industry

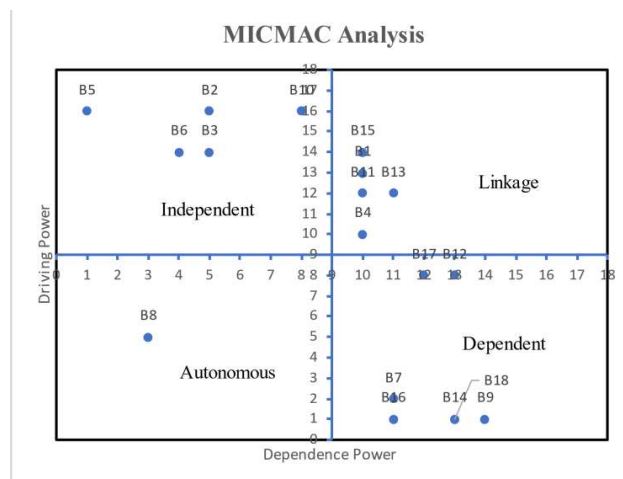


Fig. 2 MICMAC results: driving-dependence power for barriers.

We introduced the ISM approach for the implementation of I4.0 in the Indian casting industry and develop a structural model based on their interrelationship. Other methods can be employed for a better outcome and this research is generalized and limited to one state West Bengal, India. Therefore, further research work can be extended using more numbers of barriers from a greater number of experts and it can be implemented to a different region of the country with a different methodology such as Fuzzy Analytic Hierarchy Process (FAHP) and Structural Equation Modelling (SEM) to figure out the mutual relationships and to validate the structured model statistically.

References

1. Skobelev, P. O., & Borovik, S. Y. (2017). On the way from Industry 4.0 to Industry 5.0: From digital manufacturing to digital society. *Industry 4.0*, 2(6), 307-311.
2. Geissbauer, R., Lubben, E., Schrauf, S., & Pillsbury, S. (2018). Digital Champions. *How industry leaders build integrated operations ecosystems to deliver end-to-end customer solutions*. Price water house Coopers.
3. Brettel, M., Friederichsen, N., Keller, M., & Rosenberg, M. (2017). How virtualization, decentralization and network building change the manufacturing landscape: an industry 4.0 perspective. *FormaMente*, 12.
4. Ghobakhloo, M. (2018). The future of manufacturing industry: a strategic roadmap toward Industry 4.0. *Journal of Manufacturing Technology Management*.
5. Nascimento, D. L. M., Alencastro, V., Quelhas, O. L. G., Caiado, R. G. G., Garza-Reyes, J. A., Rocha-Lona, L., & Tortorella, G. (2019). Exploring Industry 4.0 technologies to enable circular economy practices in a manufacturing context: A business model proposal. *Journal of Manufacturing Technology Management*.
6. Ayala, N. F., Paslauski, C. A., Ghezzi, A., & Frank, A. G. (2017). Knowledge sharing dynamics in service suppliers' involvement for servitization of manufacturing companies. *International Journal of Production Economics*, 193, 538-553.
7. Schuh, G., Anderl, R., Gausemeier, J., ten Hompel, M., & Wahlster, W. (Eds.). (2017). *Industrie 4.0 maturity index: managing the digital transformation of companies*. Herbert Utz Verlag GmbH.
8. Bagheri, B., Yang, S., Kao, H. A., & Lee, J. (2015). Cyber-physical systems architecture for self-aware machines in industry 4.0 environment. *IFAC-PapersOnLine*, 48(3), 1622-1627.
9. Mittal, S., Khan, M. A., Romero, D., & Wuest, T. (2018). A critical review of smart manufacturing & Industry 4.0 maturity models: Implications for small and medium-sized enterprises (SMEs). *Journal of manufacturing systems*, 49, 194-214.
10. Dalenogare, L. S., Benitez, G. B., Ayala, N. F., & Frank, A. G. (2018). The expected contribution of Industry 4.0 technologies for industrial performance. *International Journal of Production Economics*, 204, 383-394.
11. Rajkumar, I., & Rajini, N. (2021). Influence of parameters on the smart productivity of modern metal casting process: An overview. *Materials Today: Proceedings*.
12. J.N. Warfield, Toward interpretation of complex structural models, *IEEE Trans. Syst. Man Cybern.* SMC-4 (5) (1974) 405-417.
13. Vigneshvaran, R., & Vinodh, S. (2020). Development of a structural model based on ISM for analysis of barriers to integration of lean with industry 4.0. *The TQM Journal*.
14. Agrawal, A. K., Kumar, D., & Rahman, Z. (2017). An ISM approach for modelling the enablers of sustainability in market-oriented firms. *International Journal of Business Excellence*, 12(1), 23-45.
15. Raj, T., Shankar, R., & Suhaib, M. (2008). An ISM approach for modelling the enablers of flexible manufacturing system: the case for India. *International Journal of Production Research*, 46(24), 6883-6912.
16. Goel, V., & Khurana, S. (2020). Analysis of factors for green supply chain in Indian timber market: an ISM approach. In *Advances in Intelligent Manufacturing* (pp. 59-66). Springer, Singapore.
17. Kumar, D., & Rahman, Z. (2017). Analyzing enablers of sustainable supply chain: ISM and fuzzy AHP approach. *Journal of Modelling in Management*.
18. Raut, R. D., Narkhede, B., & Gardas, B. B. (2017). To identify the critical success factors of sustainable supply chain management practices in the context of oil and gas industries: ISM approach. *Renewable and Sustainable Energy Reviews*, 68, 33-47.
19. Kaswan, M.S. and Rath, R. (2019), "Analysis and modeling the enablers of green lean six sigma implementation using interpretive structural modeling", *Journal of Cleaner Production*, Vol. 231, pp. 1182-1191.
20. Godet, M. (1986). Introduction to la prospective: seven key ideas and one scenario method. *futures*, 18(2), 134-157.

Numerical Analysis of a CPU Mainboard Chip to Study the Influence of Working Fluids in Heat Transfer Performance of Micro-Pin-Fin Heat Sink

Subham Ghosh, Debasish Biswas

1 Introduction

The advancement of electronic components and technology turned the computers into an essential thing almost in the every aspect in a current day to day life. Modern computers are capable of processing huge information efficiently in no time. But, with great efficiency comes greater heat dissipation and increased heat density, thus escalating the temperature i.e., the greatest foe of microprocessors in the electronics world. A good modern server should impart high performance at the expense of less power consumption, compact size and less noise, etc. This increases complexity while miniaturization the design, making the power distribution of microprocessors extremely unstable, leading to development of thermal hotspots. Hot spots are the regions which have locally high temperatures and huge temperature gradient, poorly affecting the microprocessor stability and performance thereby reducing the cooling capability of microprocessors as well. Cooling of CPU is of prime importance in order to maintain stable performance and get consistent working conditions for related IT equipment and electronic devices. There are several methods for cooling of electronic components such as impingement of cooling jet and heat pipe[1–5]. High pressure air flow can be considered as a conventional cooling technique and in terms of cost, complexity and reliability it can be considered as an effective technique.

To design an efficient cooling system there are various parameters which have to be taken into account but out of those heat transfer rate, low-pressure drop are the most important. When liquid is used as a medium instead of air, it can dissipate more heat at smaller footprints. Heat sink is an important component and it has key involvement on heat transfer path since convective heat plays the significant role on the heat transfer in net effective thermal resistance. Plate-fin HSs are efficient in transferring heat due to small pressure drops, effortless design and low-cost production. But, micro-pin-fin HSs are much better due to improved regions leading to outmatched HT rate and superior thermal performance regardless of the fluid dynamics [6, 7]. Earlier investigators had suggested HS with improved HT surfaces capable of reducing thermal resistance due to convective heat. Initial boundary layers can be reset as an induced secondary flow phenomenon and this can be treated as a common flow phenomenon. In order to achieve such a flow phenomenon in fluid flow field, heat sinks are needed to be designed taking the flow interferences and high pressure drop during operation into account. The pressure drop has to be made optimum as it tends to increase the pumping power although the heat-transfer rate increases.

The main objective of the present work is to analyze the fluid flow characteristics and heat transfer of the heat sink with micro-pin- fin and draw a comparison between the effects of two different working fluids (nanofluid and water). The proposed HS in the present work is employed in the CPU main board chip. The performance of Aluminum micro-pin-fin HS is analyzed at a particular Reynolds's Number (Re) and inlet turbulent intensity (TI). Based on the literature, earlier researchers had their basis of study on different fin materials. There are several researches considering the geometry of the pin fins but studies based on working fluid can be found hardly. In the present study two working fluids i.e. distilled water and CuO-water nanofluid are considered and a brief effect on heat transfer performance is presented.

2 Problem Formulation

The current study considers cooling via forced convection of a CPU main board chip. The main board chip has two narrow channels i.e., inlet and outlet channels having square cross sections of dimension $4.0 \text{ mm} \times 4.0 \text{ mm}$ each. Length of the channels has been considered as 3.5 mm . Fig. 1 depicts the rectangular dimension flow domain which has been chosen in the present study (length 13.0 mm and width 21.0 mm). Height of each fin is taken as 0.7 mm and this value is considered as constant for both types of fluids throughout the analysis. MPF diameter given by, $d = D/e = 0.8$ has been considered. Water and nanofluid (CuO-water) are considered as the working fluids for studying the comparison in this system [8].

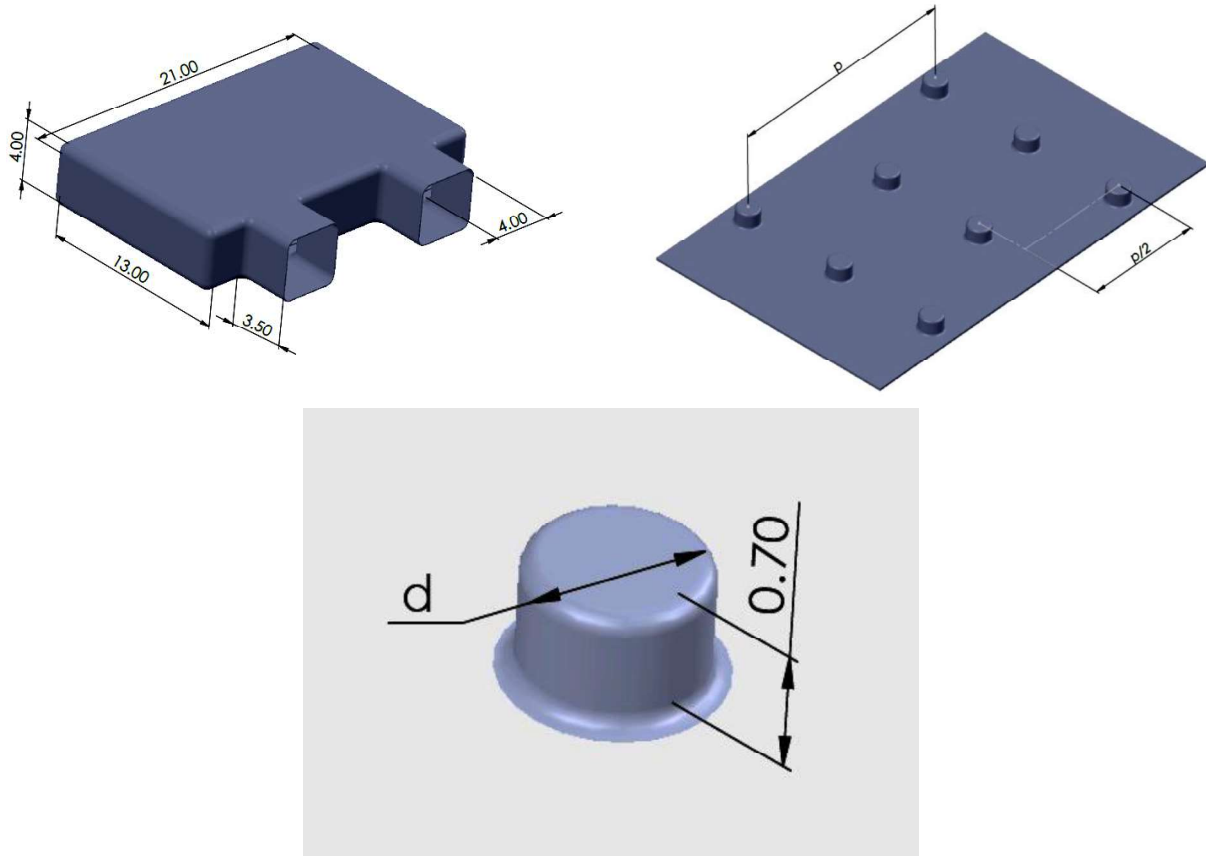


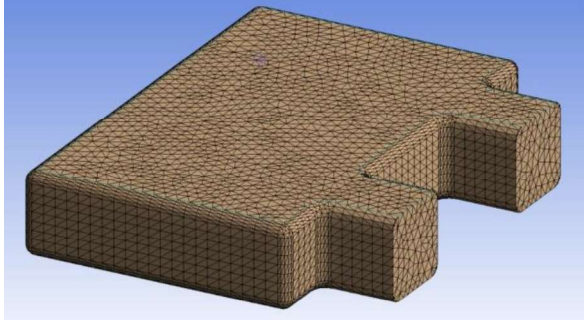
Fig. 1 Schematic diagram of the model.

3 Numerical Procedure

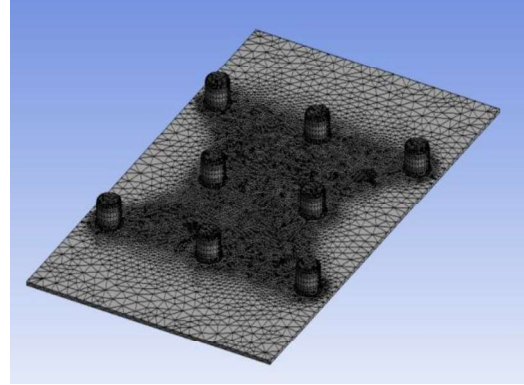
The geometry has been designed and meshed using the student version software, ANSYS Workbench 2020 R2. In order to reduce the computational time and number of grid cells only single channel is modeled for the study. Hexahedral mapped structure mesh is used for most of the computational domain except some corner places. Fig. 2 shows the generated image of the 3D model having uniform structured grid. The computation uses a mesh of 71616 nodes with 398435 elements ($Re=5000$, $d=0.8$, $TI=3\%$). The inlet temperature is constant during the experiment at 293.15K (20°C) and a steady wall heat flux modeled is used with the intensity of 2.0 KW/m^2 on the base of the heating plate to generate heat in electronics chips. Heat flux at the boundaries is not fluctuating and taken as a boundary condition with no slip boundary condition is considered at the heat receptors and contact surface of fluid domain. Velocity profile at inlet is considered uniform with 3% turbulent intensity (TI)

throughout the domain [9]. The fixed computational domain has been chosen and constant properties have been considered for both of the working fluid (water and nanofluid).

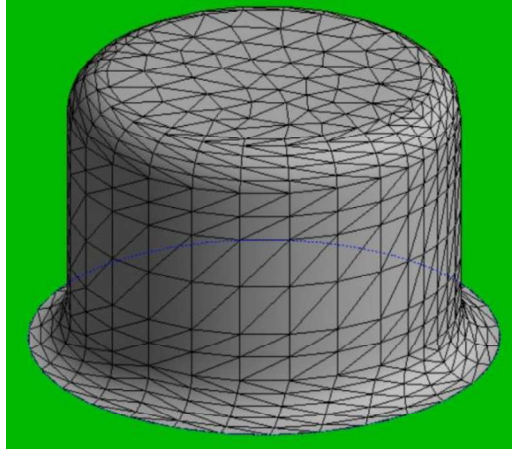
Governing equations have been solved by using CFD, ANSYS's Fluent 2020 R2 student versioned software with finite volume method. The exclusive solver is capable of solving governing equations independently, valid for incompressible flow. More detailed information on the mathematical and numerical modeling may be found out from previous research works [10–12].



(a) Fluid Domain



(b) Base Heating Plate



(c) Pin Fin

Fig. 2 Views of Grid.

4 Governing Equations

For the simplification of the analysis a single phase model has been considered for the nanofluid and the governing equations for this model are given below.

Continuity equation is given by:

$$\nabla \cdot \vec{V}_{nf} = 0 \quad (1)$$

Momentum equation is given by:

$$\nabla \cdot (\rho_{nf} \vec{V}_{nf} \vec{V}_{nf}) = -\nabla p + \nabla \cdot \left[\left(\mu_{nf} \vec{V}_{nf} + \vec{V}_{nf}^T \right) \right] \quad (2)$$

Energy equation is given by:

$$\nabla \cdot (\rho_{nf} c_{p_{nf}} T_{nf} \vec{V}_{nf}) = \nabla \cdot (k_{nf} \nabla T_{nf}) \quad (3)$$

The solid region heat conduction equation is:

$$k_s \nabla^2 T_s = 0 \quad (4)$$

In this study, the thermo-physical properties are taken as constant [13-18]. To solve these equations the nanofluid properties are also needed which is expressed below.

Density is given by [19]:

$$\rho_{nf} = (1 - \psi)\rho_f + \psi\rho_p \quad (5)$$

Specific heat is given by [20]:

$$C_{p_{nf}} = \frac{(1-\psi)(\rho C_p)_f + \psi(\rho C_p)_p}{\rho_{nf}} \quad (6)$$

Dynamic viscosity is given by [21]:

$$\mu_{eff} = \frac{\mu_f}{(1-\psi)^{2.5}} \quad (7)$$

Thermal conductivity is given by [22]:

$$k_{nf} = k_f \times \frac{k_f \times (n-1) - (k_f - k_p) \times (n-1) \times \psi + k_p}{k_f \times (n-1) + (k_f - k_p) \times \psi + k_p} \quad (8)$$

Table 1. CuO Nanoparticle and Water Thermo-physical Parameters

	C_p (J/kg. K)	k (W/m. K)	μ (N.s/m ²)	d_p (mm)	ρ (kg/m ³)
Distilled Water	4179	0.613	0.001003	-	997.1
CuO	540	18	-	29	6500

5 Boundary Conditions

In the finite volume method the conservation equations for energy, momentum, continuity and volume are solved for the each grid. And the boundary conditions are given below.

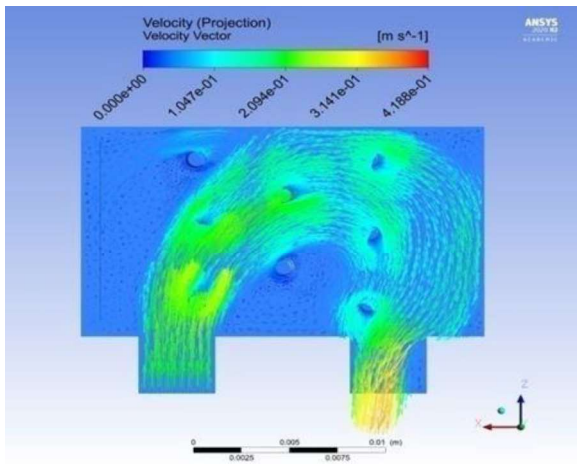
- The velocity of the working fluid is uniform and calculated for a particular Reynolds no.
- The inlet temperature, where the working fluid enters is maintained at $T_{in} = 293.15$ K.
- On the base plate uniform heat flux of intensity 2.0 KW/m^2 has been considered and on the other walls of the heat sink are considered as adiabatic walls.
- Thermal equilibrium and no slip velocity conditions at the contact positions of the walls and the working fluid are applied.
- Hydrodynamic and thermally fully developed flow at the outlet is considered.

6 Results And Discussion

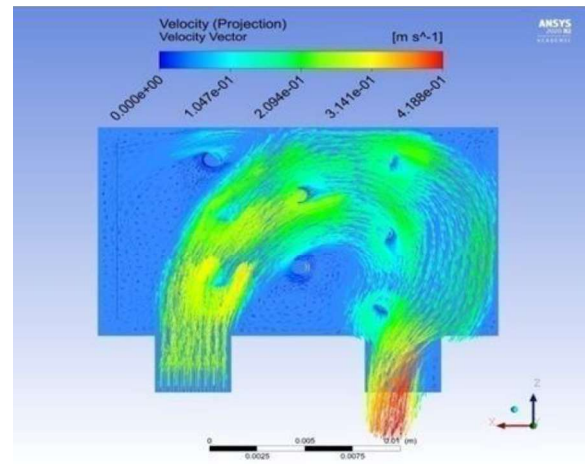
In the present work a nanofluid flow of a particular volume fraction 20% is considered and the simulation is done to analyze the thermal performance of the HS. Again another simulation is done where water is the working fluid and the important results such as heat transfer rate, friction factor, and pressure drop are compared with the previous one.

6.1 Velocity Vector and Velocity Contour

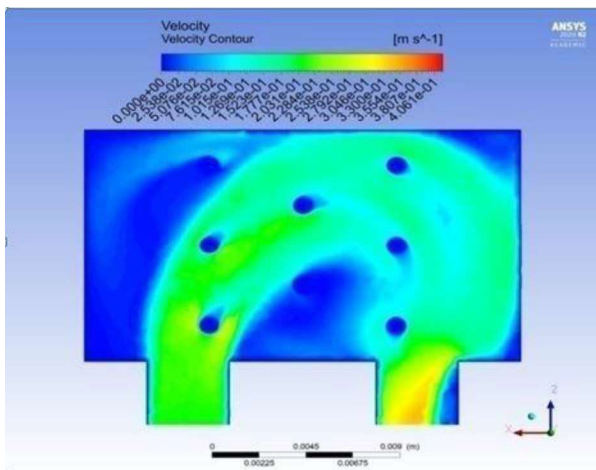
The streamlines are obtained for the heat sink with $d = 0.8$ at $Re = 5000$ at TI 3% which are shown Fig.3 and Fig.4. Both the figures show velocity vectors and velocity contours at the base of heat sink around the micro-pin-fins respectively. The density of the base fluid increases due to presence of nanoparticles and so a reduction in velocity is expected in case of nanofluid which is exactly how the fig: 3. Also the reduction will be more as the particle volume fraction is increasing. So, it is expected that the magnitude of fluid flow velocity at the sink outlet in case of nanofluid is less compared to distilled water.



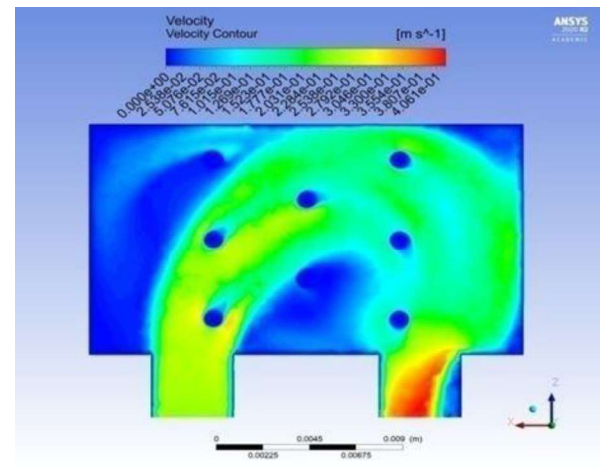
(a) For nanofluid



(b) For water

Fig. 3 Around micro-pin-fins velocity vectors.

(a) For nanofluid



(b) For water

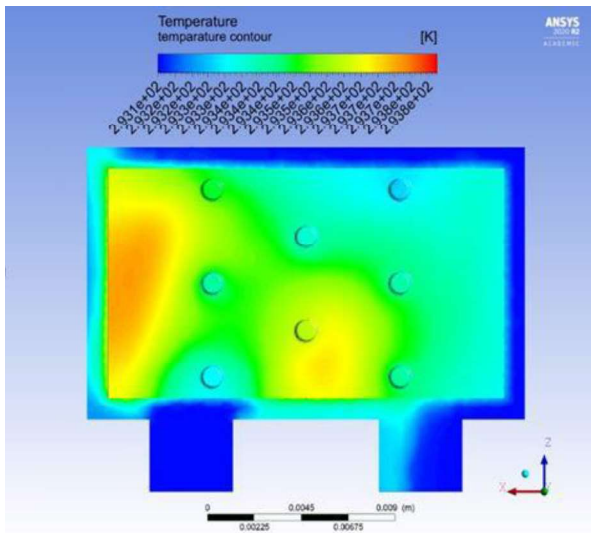
Fig. 4 Velocity contour around micro-pin-fins.

It can be observed from the governing equation that the velocity increases the velocity with the effective thermal conductivity but the temperature gradient on liquid-vapour interface decreases. So, considering all the factors the magnitude of fluid flow velocity decreases in case of nanofluid compared to the base fluid.

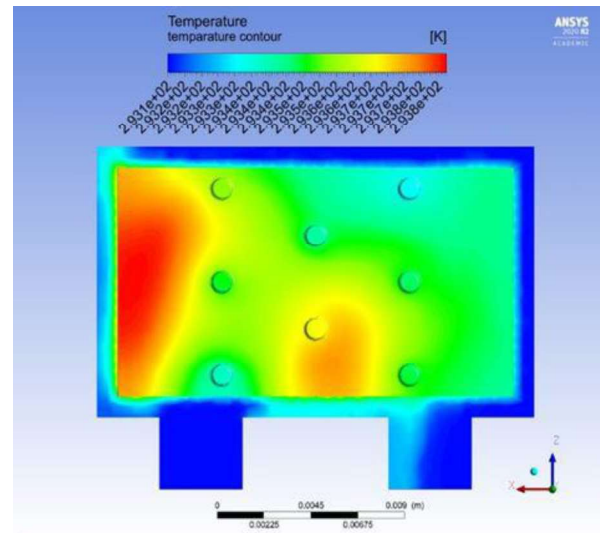
6.2 Distribution of Temperature

The distribution of temperature of the heating plate of HS is demonstrated in Fig. 5. The uses of nanofluid as the working fluid clearly give the positive effect due to higher thermal conductivity of the nanofluid than the base fluid. The colour-map of the temperature which is a non dimensional temperature contour plot also tells the same fact. Lower thermal resistance can be achieved by using nanofluids as compared to the base fluids. So, when the nanofluid is used as working fluid better heat reduction and more uniform temperature distribution can be achieved.

Due to the presence of the nano-particles thermal conductivity has been enhanced and so when more particles are present the thermal conductivity will be more. But there are some limitations as this also increases pressure drop which is another defining factor and discussed below. However, the thermal conductivity has temperature dependency. Higher heat transfer rate can be obtained when the temperature gradient is higher. For this reason nanofluid is also known as smart fluid.



(a) For nanofluid



(b) For water

Fig. 5 Distribution of Temperature for heat sink.

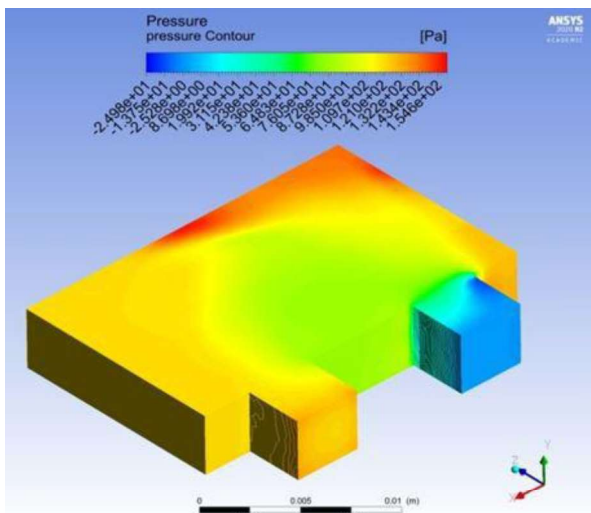
6.3 Pumping Power

If coolant passes through any channel, a pressure drop always occurs. So, for the continuous flow there is a requirement of external pumping power. This can be calculated by:

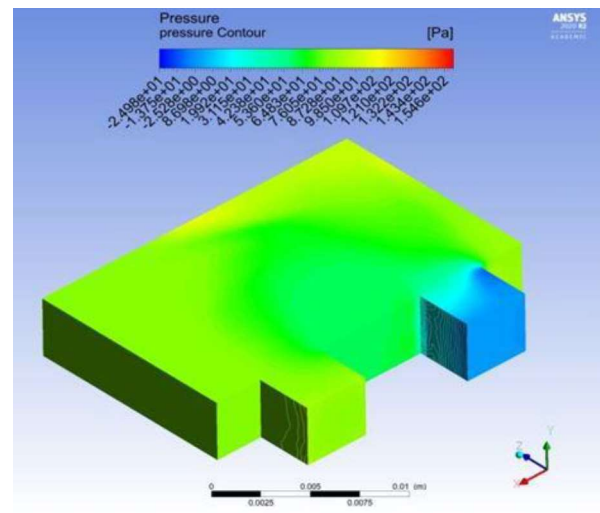
$$PP = \Delta p \cdot Q \quad (9)$$

Here, Q defines volume flow rate and Δp defines pressure drop through the heat sink.

Surface roughness is the main reason for this pressure drop but with the comparison to water a greater pressure drop can be observed in case of nano-fluid because of the enhancement of the viscosity due to the addition of nanoparticles, hence, the requirement of the pumping power will increase for the flow per unit length which can be shown from the fig.6.



(a) For nanofluid



(b) For water

Fig. 6 Pressure contour for heat sink.

To get the optimum result it is necessary to find the optimum volume fraction so that better heat transfer rate can be obtained without too much pressure drop.

6 Conclusions

After performing the simulation with the nanofluid and water as working fluid some important points are found which are given below.

- Higher heat transfer coefficient can be achieved for nanofluid as compared to the water as working fluid. With the volume fraction of the nanoparticles effective thermal conductivity also increases.
- The temperature distribution is also more uniform in case of nanofluid.
- Reduction in velocity at the outlet can be achieved due to higher viscosity and density in case of nanofluid.

More pumping power is also required while nanofluid is used compared to the water but for small volume fraction of the nanoparticles it can be sacrificed as the main objective is to achieve higher heat transfer rate to cool down the CPU efficiently.

References

32. S.Y. Yoo, D.S. Park, M.H. Chung, S.Y. Lee, Heat transfer enhancement for fin-tube heat exchanger using vortex generators. *KSME Int. J.* 16(1), 109–115 (2002)
33. S.E. Ghasemi, A.A. Ranjbar, M.J. Hosseini, Experimental evaluation of cooling performance of circular heat sinks for heat dissipation from electronic chips using nanofluid. *Mech. Res. Commun.* 84, 85–89 (2017)
34. H. Arya, M.M. Sarafraz, M. Arjomandi, Heat transfer & fluid flow of MgO/ethylene glycol in a corrugated heat exchanger. *J. Mech. Sci. Technol.* 32(8), 3975–3982 (2018)
35. K. Kim, Heat pipe cooling technology for desktop PC CPU. *Appl. Therm. Eng.* 23, 1137–44 (2003)
36. I. Khorunzhii, H. Gabor, R. Job, W.R. Fahrner, H. Baumann, Modeling of a pin fin heat converter with fluid cooling for power semiconductor modules. *Int. J. Energy Res.* 27, 1015–1026 (2003)
37. S.Y. Kim, R.L. Webb, Thermal performance analysis of fan-heat sinks for CPU cooling, in *Proceedings of the IMECE'03*, IMECE 2003-42172 (2003)
38. D. Kim, Thermal optimization of microchannel heat sink with pin fin structures, in *Proceedings of the IMECE'03*, IMECE 2003-42180 (2003)
39. H.C. Chiu, R.H. Hsieh, K. Wang, J.H. Jang, C.R. Yuc, The heat transfer characteristics of liquid cooling heat sink with micro pin fins. *Int. Commun. Heat Mass Transf.* 86, 174–180 (2017)
40. H. Chattopadhyay, S. Murmu, Transport phenomena over bluff bodies at varying inlet turbulent intensity. *Heat Transf. Res.* (Online Published). <https://doi.org/10.1615/HeatTransRes.2018019048>
41. S. Bhattacharyya, H. Chattopadhyay, S. Bandyopadhyay, Numerical study on heat transfer enhancement through a circular duct fitted with centre-trimmed twisted tape. *Int. J. Heat Technol.* 34(3), 401–406 (2016)
42. S. Bhattacharyya, H. Chattopadhyay, A.C. Benim, Computational investigation of heat transfer enhancement by alternating inclined ribs in tubular heat exchanger. *Prog. Comput. Fluid Dyn. Int. J.* 17(6), 390–396 (2017)
43. S. Bhattacharyya, H. Chattopadhyay, A. Guin, A.C. Benim, Investigation of inclined turbulators for heat transfer enhancement in a solar air heater. *Heat Transf. Eng.* (2018). <https://doi.org/10.1080/01457632.2018.1474593>
44. Ali Ijam, R. Saidur, P. Ganesan, Cooling of minichannel heat sink using nanofluids, *Int. Commun. Heat Mass Transfer* 39 (2012) 1188–1194.
45. H.A. Mohammed, P. Gunnasegaran, N.H. Shuaib, The impact of various nanofluid types on triangular microchannels heat sink cooling performance, *Int. Commun. Heat Mass Transfer* 38 (2011) 767–773.
46. Mostafa Keshavarz Moraveji, Reza Mohammadi Ardehali, CFD modeling (comparing single & two-phase approaches) on thermal performance of Al₂O₃/water nanofluid in mini channel heat sink, *Int. Commun. Heat Mass Transfer* 44 (2013) 157–164.
47. H.A. Mohammed, P. Gunnasegaran, N.H. Shuaib, Heat transfer in rectangular microchannels heat sink using nanofluids, *Int. Commun. Heat Mass Transfer* 37 (2010) 1496–1503.
48. Mushtaq Ismael Hasan, Investigation of flow & heat transfer characteristics in micro pin fin heat sink with nanofluid, *Appl. Therm. Eng.* 63 (2014) 598–607.

49. Mostafa Keshavarz Moraveji, Reza Mohammadi Ardehali, Ali Ijam, CFD investigation of nanofluid effects (cooling performance & pressure drop) in mini-channel heat sink, *Int. Commun. Heat Mass Transfer* 40 (2013) 58–66.
50. D.A. Drew, S.L. Passman, *Theory of Multicomponent Fluids*, Springer, Berlin, 1999.
51. S.M. Yang, W.Q. Tao, *Heat Transfer*, third ed., Higher Education Press, Beijing, China, 1998. 821
52. H.C. Brinkman, The viscosity of concentrated suspensions & solutions, *J. Chem. Phys.* 20 (1952) 571–581.
53. R.L. Hamilton, O.K. Crosser, Thermal conductivity of heterogeneous two- component systems, *Ind. Eng. Chem. Fundam.* 1 (1962) 187–191.

CFD simulation of atmospheric reentry of the FIRE-II capsule under supersonic conditions

Anik Mandal, Aveek Pal, Nirmal K. Manna, Sandip Sarkar

1 Introduction

One of the most challenging aspects of modern-day spaceships is their reentry into the atmosphere of any planet. There are three basic phases, which need to be taken into account for this reentry study. These include deceleration, heating, and accuracy of landing (impact). The payload and structure of the vehicle limit the maximum deceleration it can withstand. Minimizing the deceleration is not the only concern of re-entry designers, too little deceleration can also cause serious problems. It can cause the space shuttle to bounce off into the atmosphere and back into the cold reaches of space. During the re-entry phase, the atmosphere presents a dense fluid medium whose physical properties (like density, ambient temperature, viscosity, and thermal conductivity) change rapidly with time. Any object entering the atmosphere also has a huge amount of kinetic energy due to its speed and potential energy due to its position above the surface. This energy eventually is converted to heat, which needs to be dissipated in order to prevent the melting of the spacecraft.

Several researchers [1-3] have suggested the use of Phenolic Impregnated Carbon Ablator (PICA) and phenolic asbestos as some ideal materials that would enable the spacecraft to withstand these high thermal loads. In our present work, we have considered phenolic asbestos as the material.

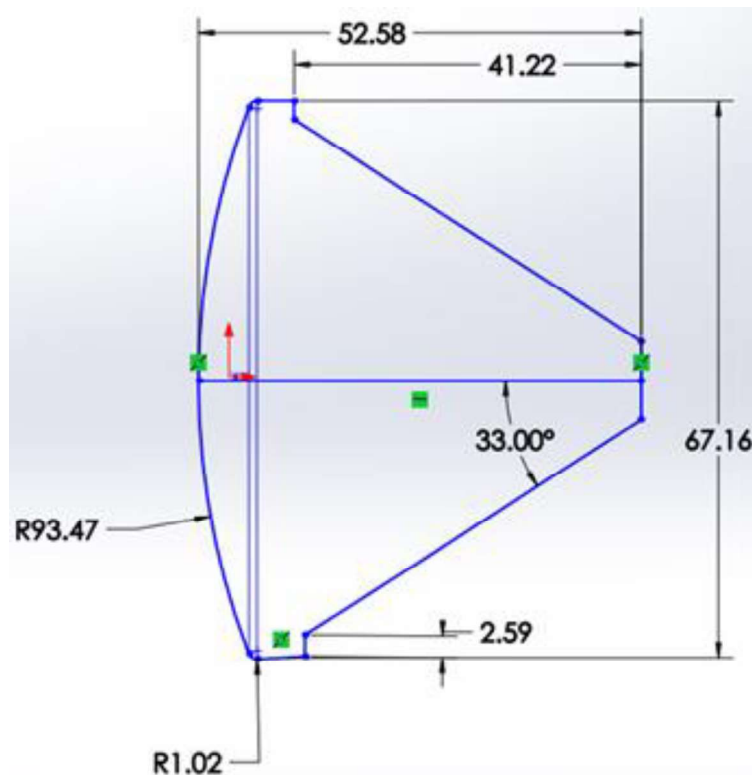


Fig. 1. FIRE-II dimensions.

A. Mandal, A. Pal, N. K. Manna, S. Sarkar*

Department of Mechanical Engineering, Jadavpur University, Kolkata, India.

2 Modeling

Bluff body approximation has been followed in this simulation study. Some modifications have been put forward into the geometry of the original FIRE-II spacecraft (Fig. 1). A three-dimensional view of the modified geometry has been shown in Fig. 2. The minor modifications put into the original geometry helped in the simplification of the model.

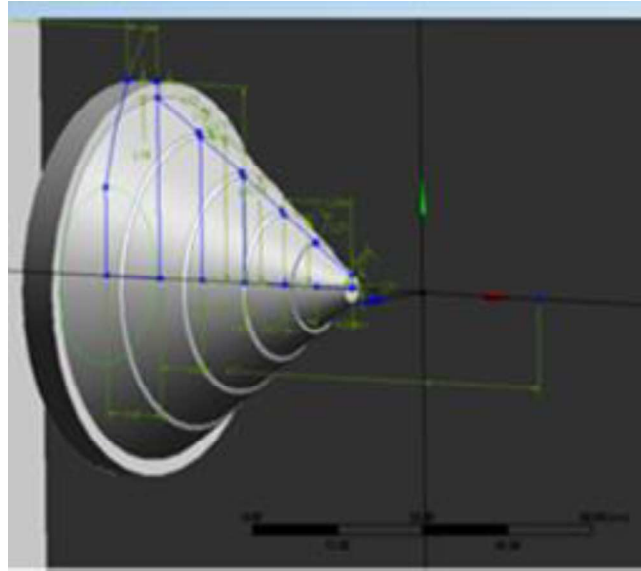


Fig. 2. 3D model considered in the present study.

Fig 3 shows the notation followed, namely X and L , where we define the axial position of the point of study in our work. We have conducted the study at an axial position of $X/L = 0.19$ in our present work.

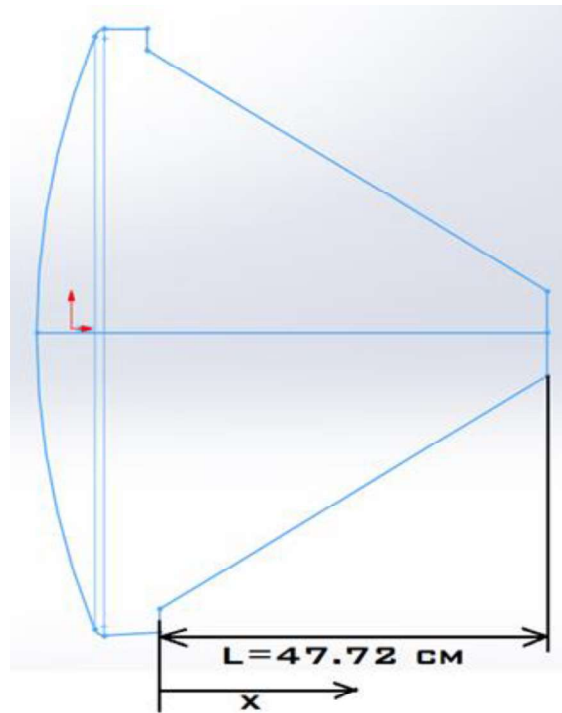


Fig. 3. Various axial positions of the spacecraft body (surface).

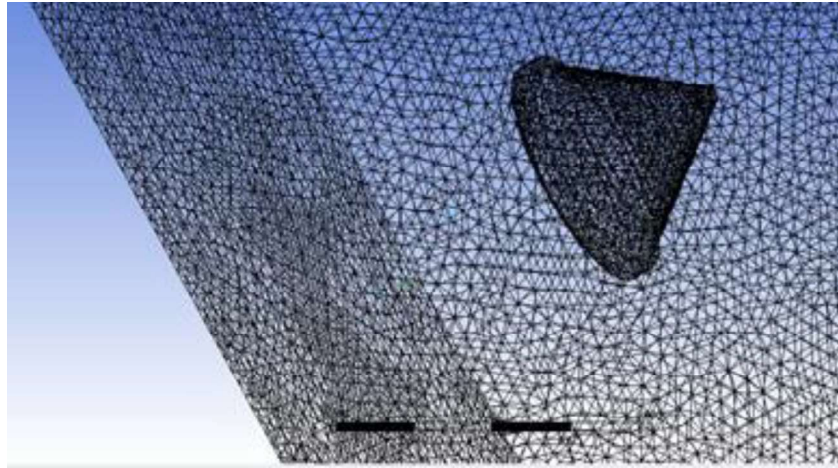


Fig. 4. Meshing of spacecraft geometry and surrounding fluid domain.

2.1 Meshing

Meshing has been done in the AMP environment. The physics preference was set as CFD with a solver preference of FLUENT. The inflation option was set as a smooth transition. The meshing has been performed using elements of size 0.04 mm. In order to get fair results, it is recommended that in ANSYS meshing the maximum skewness should be less than 0.95 with an average value less than 0.33. In our case, the maximum skewness is 0.85 and the average value is 0.24. Fig. 4 shows the 3D meshing of the spacecraft and the surrounding fluid domain. Simulation setup

The simulation is performed using Ansys Fluent R2021. 3D steady-state simulations are performed over a range of velocities, Reynolds number, and free stream temperature conditions. The boundary conditions put forth in the problem have been obtained from the experimental data listed. Since several studies [4] suggest the use of the Spallart Allmaras one equation turbulence model for Aerospace applications involving compressible flows, this has been used in this particular simulation. On intermediate grids, ($1 < y^+ < 30$), the formulation maintains its integrity and provides consistent wall shear stress and heat transfer coefficients. The solver type was selected as a density-based solver. In order to incorporate the modifications of the properties of air (since these properties vary with altitude over the surface of a planet), we have modified these in the material properties for fluid. Also, the material properties of the wall of the space capsule were entered as per those of phenolic asbestos. The initialization type was selected as hybrid initialization. An extract of the solver monitor showing the convergence of the solution to calculate the heat transfer rate is given below.

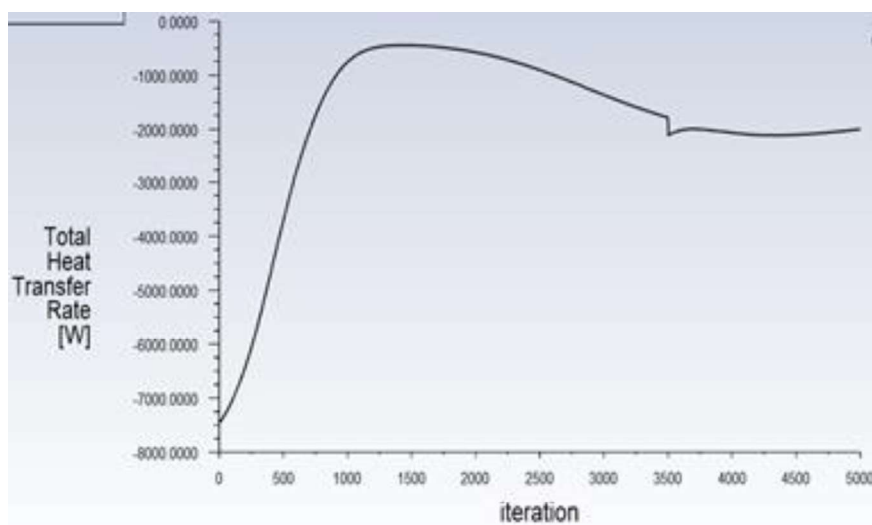


Fig. 5. Converging solutions for calculation of heat transfer rate.

Boundary conditions were applied as per flight data shown in Table 1. Velocity inlet was selected as an inlet boundary condition and pressure outlet was selected as outlet boundary condition with reference pressure as 0 Pa.

Table 1. Considered data for the present study

Time (s)	Altitude (km)	Re	Velocity (km/s)	Density (kg/m ³)	T_{∞} (K)	T_w (K)
1634	76.42	2×10^4	11.36	3.72×10^{-5}	195	615
1636	71.04	5×10^4	11.31	8.57×10^{-5}	210	810
1637.5	67.05	7×10^4	11.25	1.47×10^{-4}	228	1030
1639	63.11	1×10^5	11.14	2.41×10^{-4}	242	1325
1640.5	59.26	2×10^5	10.97	3.86×10^{-4}	254	1560

Wall temperature (T_w), ambient temperature (T_{∞}), and density were obtained from the data listed in Table 1. Since Reynolds number (Re) is also available and we know the velocity, density, and spacecraft dimensions, we could easily determine the value of dynamic viscosity, which is an important input parameter to the solver.

2.2 Validation

We are interested in estimating the heat flux at some axial position and the forebody stagnation point of the spacecraft. The simulation was run for 5000 iterations per run. The results obtained in the present work have been validated with the experimental data available from the work of other researchers [5]. This can be seen from Fig. 6. Heat flux at the forebody stagnation point is given in Fig. 7.

Table 2. Validation using experimental heat flux data (into the spacecraft) at $x/L = 0.19$.

Time [s]	1634	1636	1637.5	1639
Experimental heat flux [W/cm ²]	6	14	15.1	15.1
Heat flux from simulation [W/cm ²]	4.022	9.79	14.5045	18.1319

Table 3. The present and experimental data of heat flux into spacecraft at the forebody stagnation point

Time [s]	1634	1636	1637.5	1639
Experimental heat flux [W/cm ²]	3.75	6.25	8.7	11.25
Heat flux from simulation [W/cm ²]	1.37	2.04	2.39	2.43

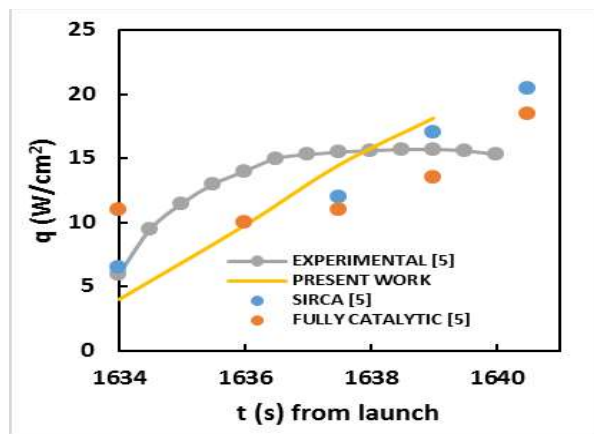


Fig. 6. Heat flux into the spacecraft at an axial position of $x/L = 0.19$.

In order to calculate the heat flux, we have first calculated the total heat transfer into the given area of interest. Then, we calculated the area of this zone. Dividing the total heat transfer by the area, we have obtained the heat flux into the region of study. All the calculations have been performed by the solver.

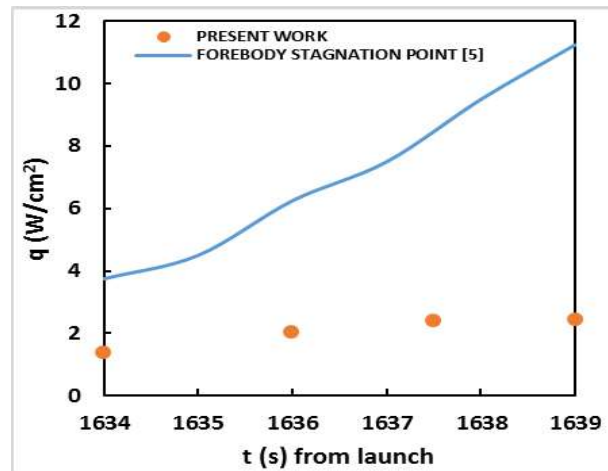


Fig. 7. Heat flux into the spacecraft at the forebody stagnation point.

3 Results and Discussion

During supersonic flow, when the velocity of an object exceeds the local acoustic velocity, the Mach number exceeds 1 and a shock layer is usually formed ahead of the moving body. The simulation shows this feature clearly. Given below are Fig. 8 and Fig. 10 which show extracts of the post-processed results which clearly show the shock layer.

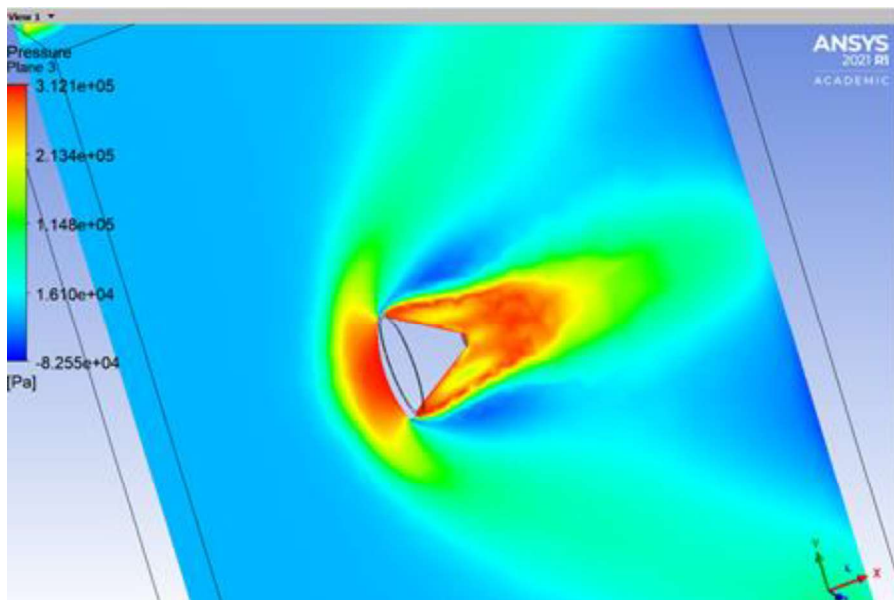


Fig. 8. Pressure variation in the flow field at a velocity of 660 m/s.

Across a shock wave, the physical properties of a fluid change abruptly. The shock layer formed on the forebody causes heating of the spacecraft, as discussed earlier. Recent research in this field has predicted several models [6] for this reentry process, where various other effects like thermal radiation, catalysis of the surface material of the spacecraft, and chemical transport are taken into consideration.

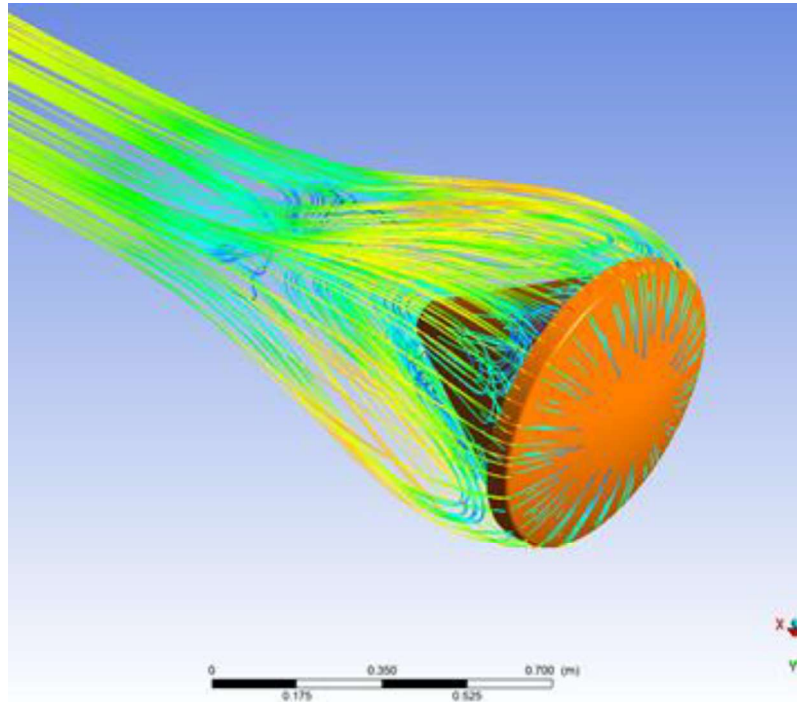


Fig. 9. Streamlines showing velocity variation over the spacecraft at a velocity of 660 m/s.

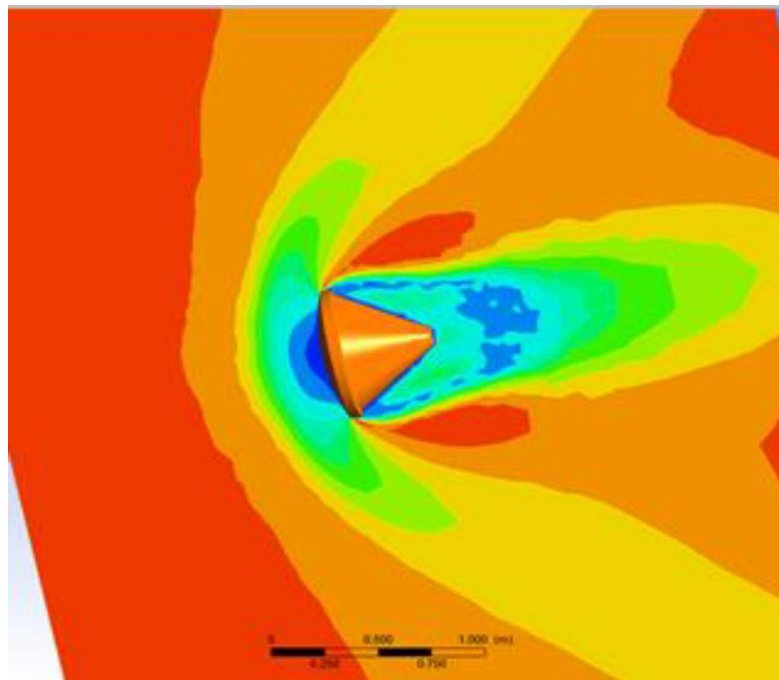


Fig. 10. Diagram showing variation of Mach no. in the flow field.

4 Conclusions

In the present study, we have only considered the basic model that considers aerothermal properties including density, thermal conductivity, temperature, heat flux, and molar mass of fluid. This study may provide usual data for providing initial solutions for the more advanced models just discussed.

Nomenclature

L	characteristic length, m	q	heat flux, W/cm ²
Re	Reynolds number	t	time, s
T_{∞}	ambient temperature, K	T_w	surface temperature, K
X	axial position, m		

References

1. S. Dhawan, M. Vishal and A. Taploo, "Thermal Protection for a Re-Entry Vehicle using Heat Ablation Process," *International Journal of Science and Research*, vol. 4, no. 11, pp. 1293-2095, 2015.
2. S.M. Johnson, "Thermal Protection Materials and Systems: Past, Present and Future," *Presentation at Missouri University of Science and Technology, Rolla, MO, USA*, 2013.
3. A.R. Bahramian and M. Kobaki, "Polymer Nanocomposites as ablative materials," In *Polymer green flame retardants*, pp. 461-502, Elsevier, 2014.
4. S.R Allmaras, F.T. Johnson and P.R Spalart, "Modifications and Clarifications for the Implementation of the Spalart-Allmaras Turbulence Model," In *Seventh international conference on computational fluid dynamics (ICCFD7)*, vol. 1902. 2012.
5. M. Wright, M. Loomis and P. Papadopoulos, "Aerothermal Analysis of the Project Fire II Afterbody Flow," *Journal of Thermophysics and Heat Transfer*, vol. 17, no. 2, pp. 240-249, 2003.
6. M.J. Wright, J.L. Brown, K. Sinha, G.V. Candler, F.S. Milos and D.K. Prabhu, "Validation of Afterbody Aeroheating Predictions for Planetary Probes: Status and Future Work," In *2nd International Planetary Probe Workshop*. 2005.

Prediction of Thermal Comfort and Performance Comparison of Various Machine Learning Models

Harshvardhan Singh, Gaurav Kumar Rai, Anirban Bose

1 Introduction

As per ASHRAE, thermal comfort is defined as that state of mind which expresses total satisfaction with the thermal environment. This thermal comfort is actually person specific. In the same environment, one person may feel comfortable and the other may feel uncomfortable. It is a very important parameter for the Heat Ventilation and Air Conditioning (HVAC) companies, as their ultimate target is to provide a comfortable indoor environment to the customers. This presents the need for the prediction of thermal comfort.

In thermal comfort dataset, there are two types of comfort, one is static thermal comfort, and another is adaptive thermal comfort. The adaptive comfort datasets contain both, environment related and occupant related data [1]. To build a more accurate dataset for predicting thermal comfort, outlier detection technique is used to eliminate the biased data or outliers. Outlier detection technique is also known as anomaly detection technique. This technique has two approaches, one is model based approach, and another is stochastic based approach. It will result an anomaly free dataset which produces more robust comfort models [2].

Reduction of power consumption is the need of the hour. It is known that the power consumption of the HVAC systems is nearly 40% of the total building power consumption. To minimize the cost and consumption, deep reinforcement learning technique was used in [3] for optimization of energy consumption and thermal comfort. To make a thermally comfortable environment for students, a statistical analysis was performed in which a thermal comfort database consisting of 4866 responses of students who were in primary, and from there it was known that students prefer 'cooler than neutral' sensation and also, they more likely prefer air-conditioned classrooms for their thermal comfort [4]. In day-to-day life, many workers have extreme work load and for the same reason, they feel stressed and this increases their heart rate variability (HRV). So, by distinguishing the changes in HRV with thermal discomfort, a multimodal SWELL knowledge work, can be built, with the help of stress dataset, achieving 99.25% to 99.75% accuracy. This delivers thermal comfort and also predicts work stress based on people's HRV [5].

The ASHRAE Global Thermal Comfort Database II project was launched in the year 2014, to foster the importance of open-source research databases in the advancements of HVAC sector. Instead of collecting data from climate chamber research, it was collected from field experiments. The data types were both, instrumental and subjective. This was done to increase the reliability of this database [6].

In this paper, the ASHRAE Global Thermal Comfort Database II was used for the making of thermal comfort predictive model using different Machine Learning algorithms. Finally, their performances were compared, and the best model was selected for the purpose of web deployment.

2 Data Analysis And Cleaning

After loading the data, it was observed that it had 107583 rows and 70 columns. The columns represent some features. It was seen that some of the features were redundant, such as temperatures in Fahrenheit and velocities in fpm.

H. Singh*, G. K. Rai, A. Bose

Department of Mechanical Engineering, Meghnad Saha Institute of Technology, India 700150

Also, some features had nothing to do with the thermal comfort prediction, such as “Publication (Citation)”, “Database” and “Data contributor”. Such kind of features were deleted from the dataset, for simplification. After this operation, 52 features (columns) were left with 107583 rows. It was understood from the feature description of this dataset that “Koppen climate classification” has been classified into 28 types. Thus, there is a need to simplify it. The first step towards simplification is to visualize the frequency of different classifications present in the dataset. As it can be observed in Fig.1, there are a total of 16 climate types present in our dataset. The full form of the climate-type names is presented in Table I. It can be observed that Csa (Hot-summer Mediterranean) has the maximum frequency in the dataset, whereas BSk (Cold semi-arid) has the minimum frequency.

Table 1. Full form of the climate-type names in Fig. 1.

Climate-type name in short form	Climate-type name in full form	Climate-type name in short form	Climate-type name in full form
BSk	Cold semi-arid	Dfb	Warm-summer humid continental
Cwb	Monsoon-influenced temperate oceanic	Csb	Warm-summer Mediterranean
Cwa	Monsoon-influenced humid subtropical	BWh	Hot desert
Af	Tropical rainforest	Cfb	Temperate oceanic
Am	Tropical monsoon	Aw	<i>Tropical wet savanna</i>
As	<i>Tropical dry savanna</i>	BSh	Hot semi-arid
Dwa	Monsoon-influenced hot- summer humid continental	Cfa	Humid subtropical
Csc	Cool-summer Mediterranean	Csa	Hot-summer Mediterranean

In general, climate can be classified into five distinct categories, namely, polar, temperate, tropical, continental and dry. It is to be noted that the first letter of abbreviation of the Koppen climate classification refers to one of the five generalized climates. This allows us to simplify the column “Koppen climate classification”, into only five categories. After simplification, it was found that only four generalized types of climates are present in this dataset. They are continental, dry, tropical and temperate. Fig. 2 shows the frequency of these generalized climates present in the dataset.

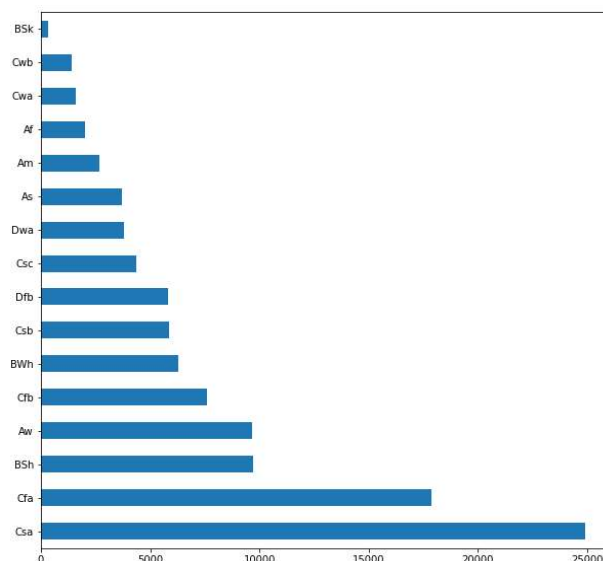


Fig. 1 Bar graph of the frequency of Koppen climate classification

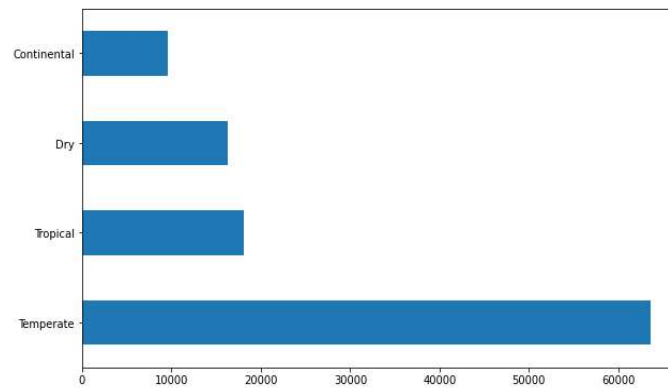


Fig. 2 Bar graph of the frequency of generalized climate classification

The frequency is maximum for temperate climate, and minimum for continental. Also, not even a single polar climate data is present.

Now, there was a need to analyze the missing values. Exploration of the missing values was done with the help of "missingno" library. There are two visualizations. The first visualization, in Fig. 3, would be for the numerical columns, and the second one, in Fig. 4, for the categorical columns. The missing values in the columns are represented by white. After having a look at the figure, it was decided to select only those features (columns) which are having less than 67% NaN values. This caused the resulting dataset to have a reduced number of columns, that is, 26. Also, any numerical value that should have been category/object, were also converted. Some missing values which could be replaced by median, were fixed. Such features whose missing values were fixed, are "Age", "Thermal Sensation", "Clo", "Met", "Air temperature (C)", "Relative humidity (%)", "Air velocity (m/s)", and "Outdoor monthly air temperature (C)". This replacement of some missing data by median was done in order to have a sufficiently big dataset for a reliable training of the machine learning predictive models. After some analysis, it was decided to select only the main features for the thermal comfort prediction. A total of seventeen features were selected for this purpose, namely, "Year", "Season", "Climate", "City", "Country", "Building type", "cooling_strategy_building", "Age", "Sex", "Thermal sensation", "Thermal preference", "Clo", "Met", "Air temperature (C)", "Relative humidity (%)", "Air velocity (m/s)", and "Outdoor monthly air temperature (C)".

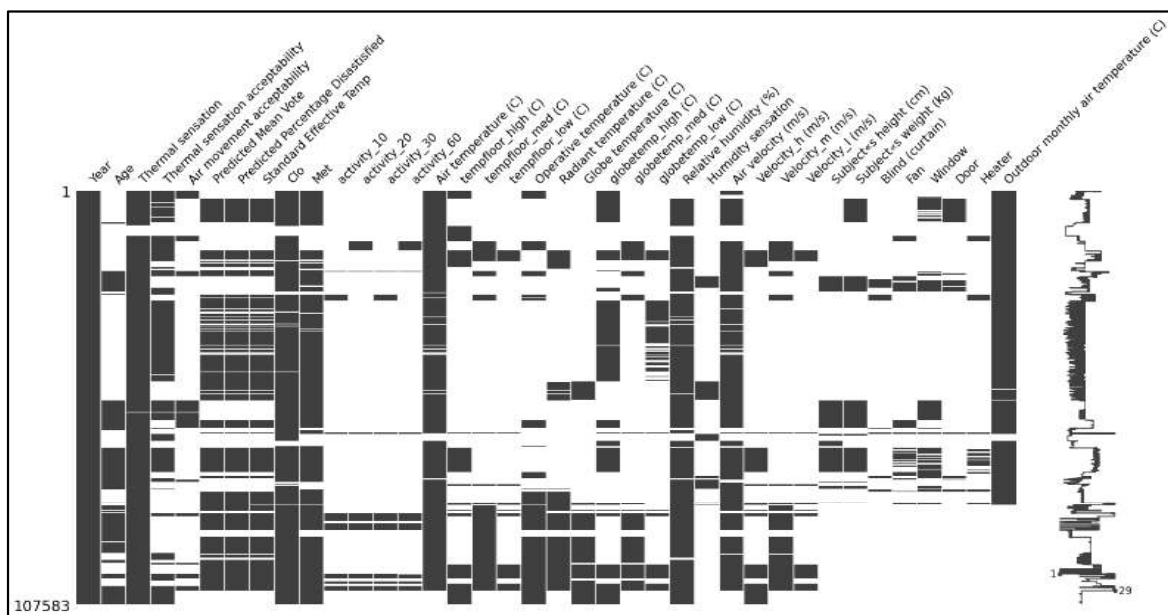


Fig. 3 Visualization of the missing values for numerical columns.

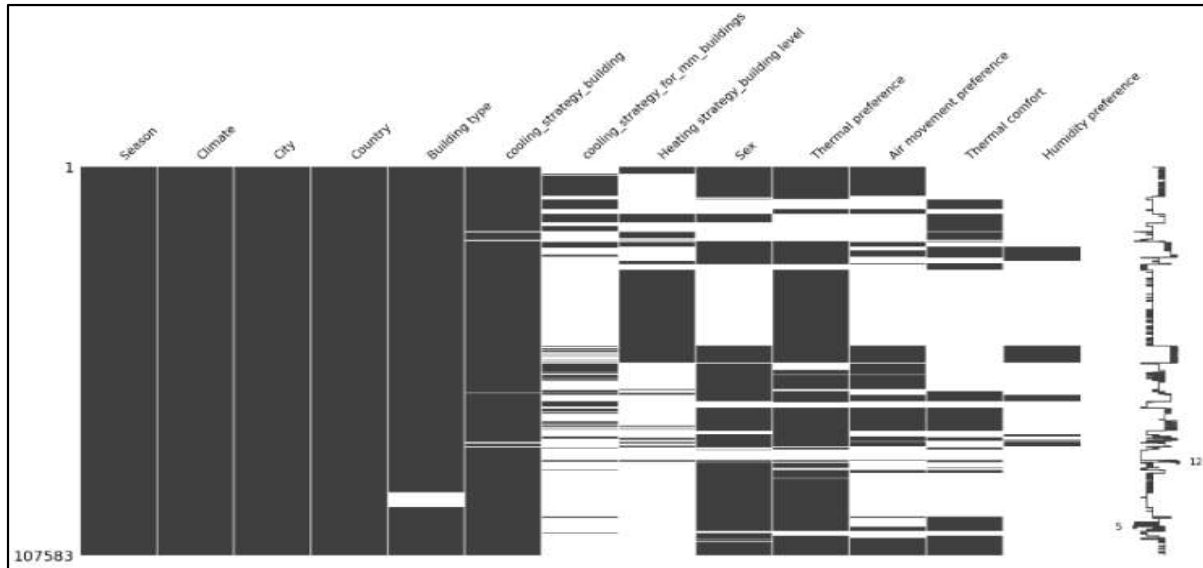


Fig. 4 Visualization of the missing values for categorical columns.

After this, all the rows which had NaN values, were deleted. The “Thermal comfort” column contains a rating on a scale of 1 to 6, where 1 signifies very uncomfortable, and 6 signifies very comfortable. The numbers in this column were converted to integer type, so that only six categorical outputs, 1 to 6, would be present.

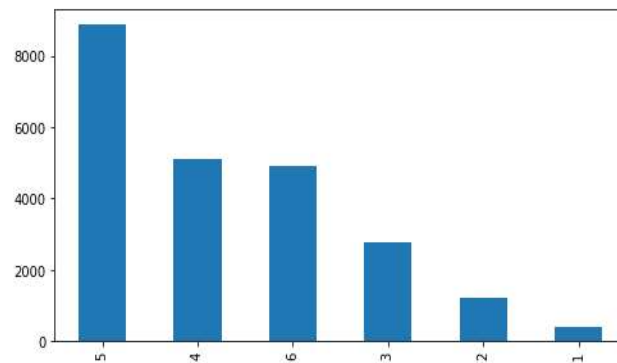


Fig. 5 Bar graph of the frequency of thermal comfort data (1 to 6)

Zero, if present, would be deleted from the dataset, since it would behave as an outlier because the rating itself starts from 1. After all these cleaning operations, the final dataset had 23,297 rows and 18 columns (features). For the visualization of the occurrence of thermal comfort data, a bar graph has been plotted in Fig. 5. It can be concluded from it, that in the final dataset, 5 has the maximum occurrence, and 1 has the minimum occurrence.

Finally, data was split into input and output variables. Here, the input variable was multi-dimensional. Thereafter, one hot encoding was done, due to the presence of categorical input data. It is to be noted that after one hot encoding, as expected, the number of input columns increased from 17 to 63. Using train-test-split technique, the remaining data was split for training and testing, in a ratio of 8:2, respectively. After this, it was decided to use Decision Tree, Random Forest, XG Boost, K-Nearest Neighbor, Bagging and Gaussian Naive Bayes algorithms for the making of thermal comfort predictive models. At the end, the performance of all the six models were compared, and the best model was selected for web deployment.

3 Prediction of Thermal Comfort Using Different Machine Learning Algorithms

3.1 Decision Tree Model

Decision tree algorithm falls under the category of supervised machine learning technique. It has the capacity to be used, both, for regression as well as classification problems. A target variable is identified, and this model tries to predict it, after sufficient training.

Here, a tree representation is used to solve the problems. In this algorithm, there is a leaf node that corresponds to a class label, and the internal nodes of the tree represent attributes. An important assumption in this algorithm is that at the very beginning, the entire training set is considered as a root. Statistical methods are used for assigning the attributes as an internal node or root node.

Splitting of data, in decision tree algorithm, is controlled by entropy. This entropy is a measure of the uncertainties or impurities in a dataset. Its value lies in a range of 0 to 1. A lower value of entropy signifies high certainty. Splitting goes on till we get a pure-subset. This pure-subset is a case where after splitting, entire data falls under the same category or class.

$$\text{Formula of entropy: } H(s) = -P_{(+)} \log_2 P_{(+)} - P_{(-)} \log_2 P_{(-)}$$

$P_{(+)} \rightarrow$ percentage of positive class

$P_{(-)} \rightarrow$ percentage of negative class

It is needed to decide which feature to split at each node, while building a tree. This decision is taken with the help of information gain. It gives us an idea of the amount of information which a feature gives about the class. In this algorithm, information gain is calculated for each split, and the split with maximum information gain is selected.

Formula of information gain:

$$\text{Gain}(S, A) = H(s) \sum \frac{|S_v|}{|S|} H(S_v)$$

$S_v \rightarrow$ Total sample after the split

$S \rightarrow$ Total sample

When this algorithm of decision tree was used to make a thermal comfort predictive model, with the previously cleaned dataset, an accuracy score of 43.03% was achieved. A confusion matrix of this model has been shown in Fig. 6. The markings, 0 to 5, along x and y-axes actually represent 1 to 6.

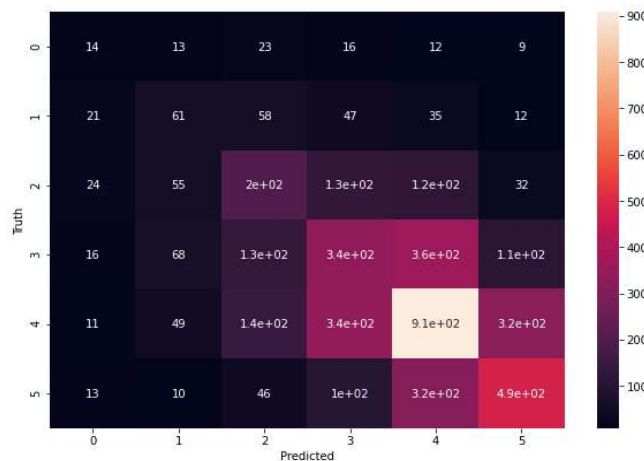


Fig. 6 Confusion matrix of decision tree model

3.2 Random Forest Model

Random forest is an ensemble learning type of algorithm. It is widely used due to its outstanding performance in both, regression and classification tasks. Also, it gives acceptable performance when the

training dataset is small to medium. It contains a lot of decision trees. It does not rely on the prediction of one decision tree, rather it goes by the majority vote of the decision trees. This results in a higher accuracy and reliability. The more the number of trees present in a random forest model, the accuracy increases.

On implementing this algorithm for the making of a thermal comfort predictive model, an accuracy score of 51.35% was achieved. A confusion matrix of this model has been shown in Fig. 7. The markings, 0 to 5, along x and y-axes, actually represent 1 to 6.

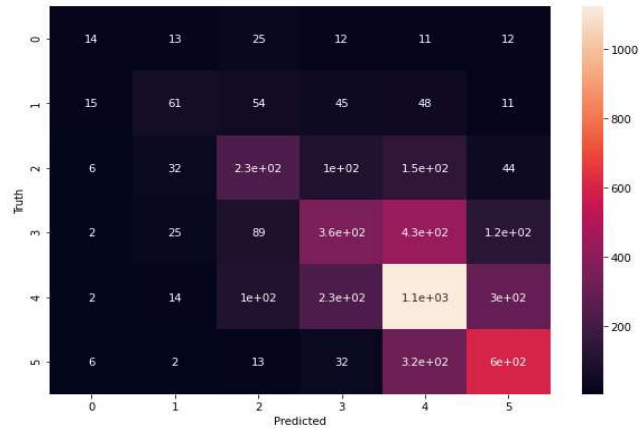


Fig. 7 Confusion matrix of random forest model

3.3 XG Boost Model

XG boost is also an ensemble type of learning algorithm. In some of the cases, it is not recommended to depend only one type of learning model. In these cases, ensemble learning becomes the first choice of the users because it systematically combines multiple learning models to ultimately give a reliable prediction. Also, it is not necessary for the base learners to be from the same machine learning algorithm. The mostly used ensemble learners are boosting and bagging, being mostly used with decision trees.

It is to be noted that in boosting, the base learners are actually weak learners, having a high bias. The purpose of the boosting technique is to combine all the weak learners to form a strong learner, having reduced bias and variance. Here, the trees are built in a sequence and every tree tries to learn from its predecessor and reduces its residual error.

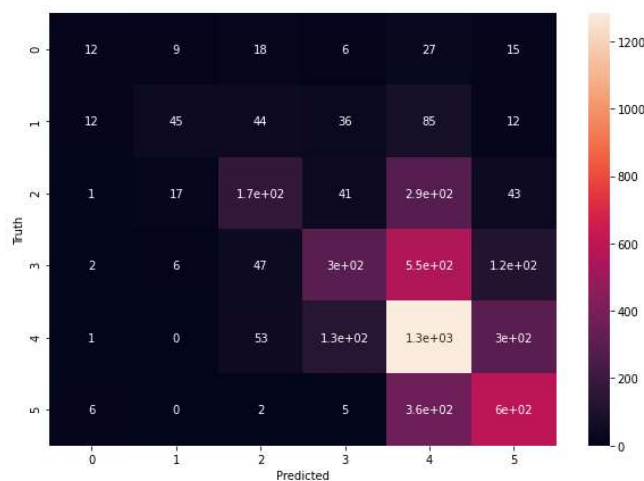


Fig. 8 Confusion matrix of XG Boost model

In random forest, the trees were grown to its maximum extent, but in boosting technique, small and highly interpretable trees are made. A large number of trees would raise the chances of overfitting. XG boost is a famous implementation of gradient boosting. It is capable of making use of multiple cores on CPU, for the sake of faster computing. It also has a provision for penalizing complex models through L1

and L2 regularizations, to prevent overfitting. Finally, it can be said that XG boost makes optimal use of the hardware.

On implementing this algorithm for the making of a thermal comfort predictive model, an accuracy score of 51.72% was achieved. A confusion matrix of this model has been shown in Fig. 8. The markings, 0 to 5, along x and y-axes, actually represent 1 to 6.

3.4 K-Nearest Neighbor Model

KNN algorithm finds its application in both, regression and classification problems. Nonetheless, it is more common in classification tasks. While analyzing the performance of any algorithm, three things must always be kept in mind, the ease with which output is obtained, the power of prediction, and the time required for the execution and calculation. KNN algorithm is known for its relatively low execution and calculation time.

As this algorithm is based on Euclidean geometry, feature scaling is pretty important, to give equal weightage to all the features. Also, determination of an optimum k value is very important. The performance of the algorithm changes significantly with change in k value. Generally, performance increases at a higher k value, but at the same time it also becomes computationally expensive.

While implementing this algorithm for the making of a thermal comfort predictive model, there was a need to determine an optimum value of k. For this purpose, a graph of Error Rate vs K Value was plot, as shown in Fig. 9, and the value of k corresponding to the minimum error was determined. The minimum error rate came to be 0.47639, and the corresponding k value was 32.

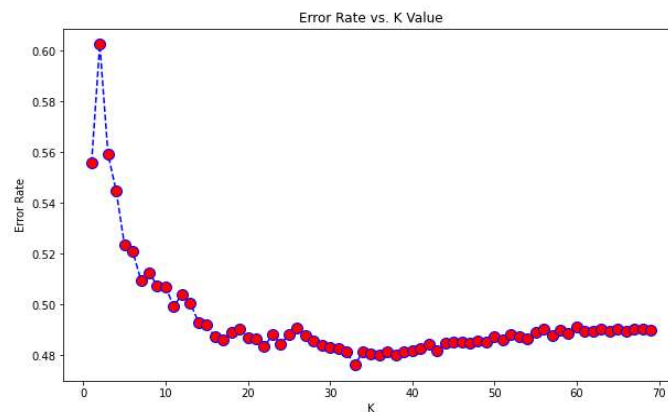


Fig. 9 Error Rate vs K Value for KNN model

Finally, the accuracy score of the model came to be 51.87%, using $k = 32$. A confusion matrix of this model has been shown in Fig. 10. The markings, 0 to 5, along x and y-axes, actually represent 1 to 6.

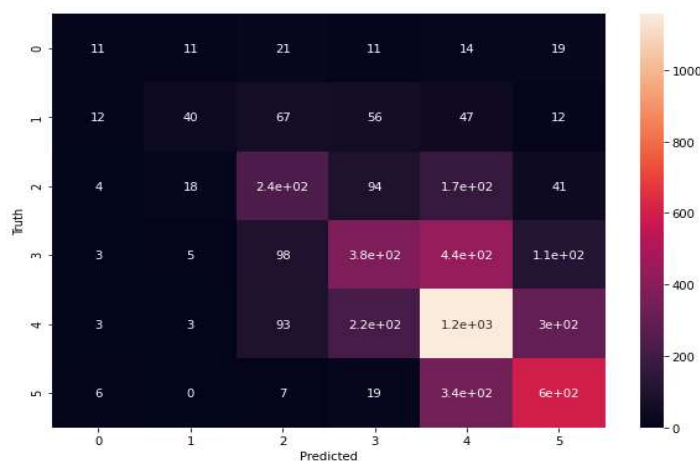


Fig. 10 Confusion matrix of K Nearest Neighbor model

3.5 Bagging Model

Bagging is an ensemble learning technique, which is also known as bootstrap aggregation. It is used for both, classification and regression problems. Here, from the training dataset, random samples are selected by bootstrapping sampling technique. Some data may also be repeated during the selection of random samples. Finally, the weak models are trained independently, with these samples. The final prediction is done by either considering the average or the majority vote of the outputs of different models. It is to be noted that the algorithm of random forest is an extension of the bagging algorithm, which uses both bagging and randomness of feature for the formation of a forest of decision trees, that is uncorrelated.

The main ensemble learning methods are bagging and boosting. The key difference between them is that in bagging, the training of base or weak learners is done in parallel, whereas in boosting, it is done in a sequence. Also, bagging technique is usually implemented on those weak learners that have low bias and high variance, whereas boosting technique is implemented in cases where the weak learners have high bias and low variance. The problems associated with bagging is that it is computationally expensive, and sometimes not precise.

On implementing this algorithm for the making of a thermal comfort predictive model, an accuracy score of 50.60% was achieved. A confusion matrix of this model has been shown in Fig. 11. The markings, 0 to 5, along x and y-axes, actually represent 1 to 6.

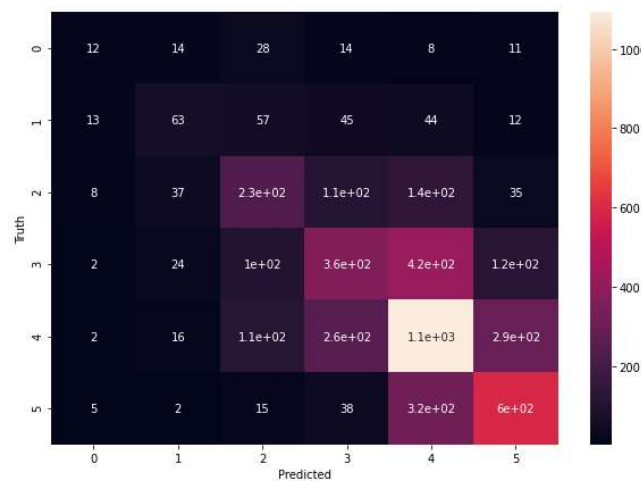


Fig. 11 Confusion matrix of Bagging model

3.6 Gaussian Naïve Bayes Model

Gaussian Naive Bayes algorithm is a type of Naive Bayes algorithm that has continuous data, along with an assumption of normal distribution of each and every class. It is used for classification problems and its theory and working is based on Bayes principle. It falls under the category of supervised machine learning, and it is both, powerful and simple. When the dataset is large enough, this algorithm shows high accuracy as well as speed.

$$\text{Bayes theorem: } P(A|B) = \frac{P(B|A)P(A)}{P(B)}$$

$P(A|B)$ is the posterior probability of class (A) given predictor (B).

$P(A)$ is the prior probability of class.

$P(B|A)$ is the probability of the predictor given class.

$P(B)$ is the prior probability of the predictor.

Posterior Probability = (Conditional Probability x Prior probability)/ Evidence

The class which has the maximum probability, is chosen as the final prediction. The problem with this algorithm is that it depends on a wrong assumption of the features being independent.

On implementing this algorithm for the making of a thermal comfort predictive model, an accuracy score of 31.55% was achieved. A confusion matrix of this model has been shown in Fig. 12. The markings, 0 to 5, along x and y-axes, actually represent 1 to 6. This model has the minimum accuracy score among the rest.

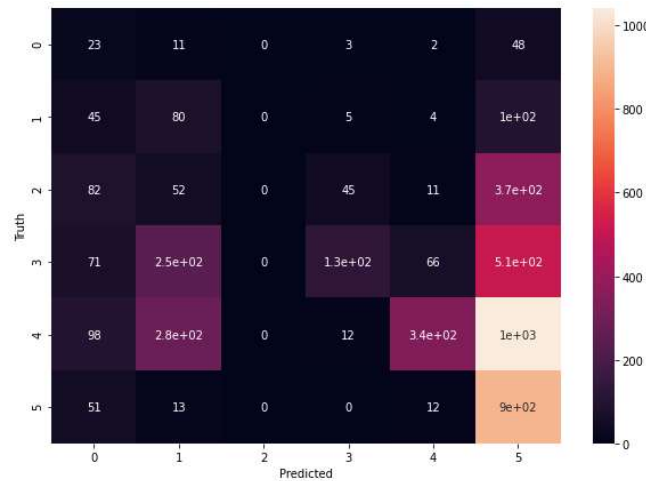


Fig. 12 Confusion matrix of Gaussian Naive Bayes model

4 Web Deployment

Web deployment is the process of deploying the codes from source control to a local or cloud server hosting platform. In this project, the web deployment was done using a streamlit package that makes it easy to create and share beautiful, custom web applications for machine learning and data science.

The K-Nearest Neighbor model was selected for web deployment, and was coded in python language, and that file was converted into a pickle file for further use. The coding of the Application was done in python language, along with HTML and CSS codes, with the help of streamlit package.

After model preparation, the pickle file was used in Application to predict the thermal comfort after getting the input from the user. Streamlit had created a local host where the Application was checked.

5 Conclusion

Six different machine learning algorithms were used to make thermal comfort predictive models. Their individual accuracy score and confusion matrix have already been demonstrated. The accuracies of different models are listed below

- Decision Tree Model → accuracy = 43.03 %
- Random Forest Model → accuracy = 51.35 %
- XG Boost Model → accuracy = 51.72 %
- K Nearest Neighbor Model → accuracy = 51.87 %
- Bagging Model → accuracy = 50.60 %
- Gaussian Naive Bayes Model → accuracy = 31.55%

It can be understood from the obtained accuracies that the best performing model is the K Nearest Neighbor model. Also, it is to be noted that there is a very small difference between the accuracy scores of random forest, XG boost, and k nearest neighbor models. Minimum accuracy score is reported for the Gaussian Naive Bayes model. Finally, because of its maximum accuracy, K Nearest Neighbor model was selected for web deployment.

The main application of the deployed model is in HVAC sector. It would be of great help to them to predict whether a certain value of features would be thermally comfortable or not. It would allow the researchers to study the actual effect of any specific feature on the thermal comfort. Also, with its help, the goal of reducing power consumption by HVAC appliances could also be addressed, perhaps by maintaining the ambient temperature at a maximum value, while cooling, that would be thermally comfortable.

6 Future Scope

This project can be further enhanced. The initial dataset had 107583 rows and 70 columns, which got reduced to 23,297 rows and 18 columns because of various data cleaning operations. A better way could be identified to fix the missing values, so that a huge dataset is available for training purpose. In this study, six different machine learning algorithms were used and their performance was compared. There is a scope to implement other algorithms as well, such as deep learning and reinforcement learning, to achieve a better reliability and accuracy score.

References

1. Lu, S., Wang, W., Lin, C., & Hameen, E. C. (2019). Data-driven simulation of a thermal comfort-based temperature set-point control with ASHRAE RP884. *Building and Environment*, 156, 137-146.
2. Wang, Z., Parkinson, T., Li, P., Lin, B., & Hong, T. (2019). The Squeaky wheel: Machine learning for anomaly detection in subjective thermal comfort votes. *Building and Environment*, 151, 219-227.
3. Gao, G., Li, J., & Wen, Y. (2019). Energy-efficient thermal comfort control in smart buildings via deep reinforcement learning. *arXiv preprint arXiv:1901.04693*.
4. Kima, J., & de Dear, R. Thermal comfort expectations and adaptive behavioural characteristics of primary and secondary school students.
5. Nkurikiyeyezu, K., Shoji, K., Yokokubo, A., & Lopez, G. (2019). Thermal Comfort and Stress Recognition in Office Environment. In *HEALTHINF* (pp. 256-263).
6. Ličina, V. F., Cheung, T., Zhang, H., De Dear, R., Parkinson, T., Arens, E., ... & Zhou, X. (2018). Development of the ASHRAE global thermal comfort database II. *Building and Environment*, 142, 502-512.

Casting Simulation, Manufacturing and Validation for Railway Coupler

Apurba Das*, Adil Wazeer, Prashna Maity, Krishna Chandra Roy, Gurudas Mondal, Arijit Sinha, Sriram Mahitha

1 Introduction

Rail transportation plays a strategic role in the transport network of countries, hence sufficient safety factors for train parts must be considered. Couplers are one of the vital parts of the train as they are used to connect wagons together, as well as for connection wagons to locomotives to transfer load or passengers. Trial-and-error methods of the past to design casting processes are finding it more and more difficult to compete. This approach is expensive and inflexible because many variables affect the solidification of the metal inside the mold [1, 2]. This mechanical casting simulation is a new technology that has been adopted in the industry as a way to reduce scrap, reduce lead times, cut costs, use less energy, have a better final design, and improve the parts design and manufacturing processes. Using simulation, the behavior of the molten aluminum during the filling, heat transfer, and solidification of different casting methods can be studied [3-5]. Casting simulation has the ability to analyze various physical phenomena occurring during the casting process. From previous research, the simulation of metal casting about fluid flow, heat transfer and solidification has been treated extensively [1, 5]. It allows researchers to observe and quantify what is not usually visible or measurable during the real casting process. The simulation produces a tremendous amount of data that characterize the transient flow behavior (e.g., velocity, temperature), as well as the final quality of the casting (e.g., porosity, grain structure). It takes a good understanding of the actual casting process, and experience in numerical simulation, for a designer to be able to relate one to the other and derive useful conclusions from the results [4]. A railway coupler is a vital part to connect the adjacent wagon or coach. These components are mainly manufactured through the casting process. However, from the past studies [8-11] it has been observed that several casting defects like mis-run, cold shuts, hot crack, and slag inclusion deteriorates the mechanical properties and reduce the life and functionality of such components. Improper and inadequate casting process responsible for fatigue crack nucleation which can result in a catastrophic failure during operation. [12]. Failure of the coupler can also lead to train derailment [13]. Zhongming [14] reported the requirement of coupler materials and strength for desired application. Soldatov et al. [15] worked on the Optimization of properties of steel 20GL for railway transport castings. However, it has been observed from the open literature that not much work is available on simulation of casting process before actual fabrication to reduce the effort and minimize the defects during fabrication.

To address this problem, the present work focuses on the evaluation of specific casting processes for coupler specific design through casting simulation before actual manufacturing. 70 BD “E” type coupler is used for the present study. A SoftCast software is used for investigates the behavior of the molten metal during the melt filling and solidification in the casting process. This software is a 3D solidification and fluid flow package used in the die casting industry to model the molten metal flow and solidification. It employs the finite difference method to solve the heat and mass transfer on a rectangular grid. It is a useful tool for simulating molten metal flow in a permanent mould since it can provide useful information about the filling pattern. It also produces reasonably accurate data on casting-related features such as premature solidification, air entrapment, velocity distribution, runner, and gate effectiveness. The developed process parameter is used for the actual fabrication of the coupler and the validation study of this process is also examined.

A. Das*, A. Wazeer, P. Maity, K. C. Roy, G. Mondal, A. Sinha, S. Mahitha
Department of Aerospace Engineering & Applied Mechanics, IEST, Shibpur, Howrah-711103, India

A three-dimensional computer model of 70 BD “E” type coupler is modeled using Creo 3.0 parametric software. The computer model is shown in Fig 1 (a) while the sectional view of the coupler is shown in Fig 1(b). This 3D model is imported in SoftCast software to perform casting simulation and evaluate the proper process parameter to be followed during fabrication of coupler through sand casting technique.

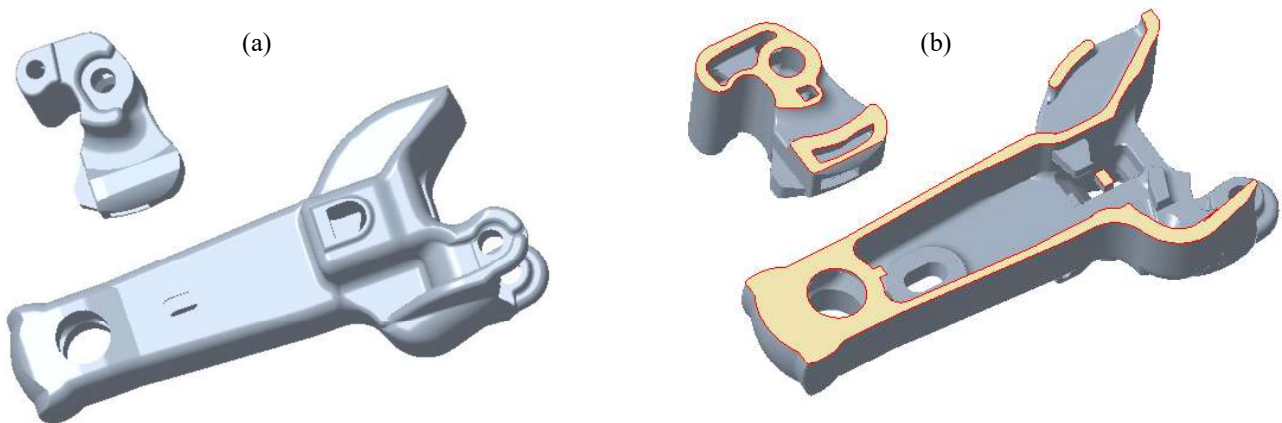


Fig. 1 (a) 3D computer model of AAR E Type coupler (b) Sectional view

2 Simulation of Casting

The 3D model developed in the computer is imported in the SoftCast software for carrying the casting simulation. Casting weight 178.35 Kg is assigned for the finished product with a material density of 7.8 g/cm³. The runner riser and the gating system are considered based on the existing method of casting practice in the industry as shown in Fig. 2. The runner is shown with a yellow head while the riser is shown in red color. The overall weight including runner, riser, and gating system is considered based on the Sofcast optimized parameter. The pouring temperature of the molten metal is considered as 1580 degrees C. Initially the poring time of 40 sec is considered. Based on the 40 sec pouring time the casting simulation is performed to see the temperature profile and overall performance of the casting (shown in Fig 3). Depending on the temperature profile entire model is divided into 5 hotspot zone as shown in Fig. 4. Hotspots are the last freezing areas in a casting. SoftCast accurately locates all hotspots and displays them in order of their intensity, on a relative temperature intensity scale, with levels ranging from 1 to 5. Major hotspots are at the lowest levels of casting quality. Medium hotspots are the moderate levels of casting quality while the minor hotspots are the good levels of casting quality. As we increase the temperature intensity minor hotspots are dropped as those are with better quality, only the larger or more intense ones are displayed with poor quality.

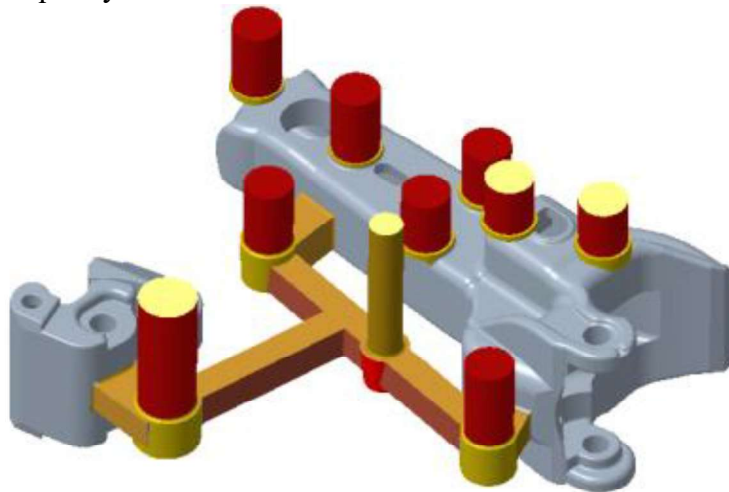


Fig. 2 Coupler and coupler pin with casting riser, runner and gating system

Viewing the hotspot data of the casting a proper method is determined. Hotspots appear or enter the casting at a certain level and they are absent inside the casting below a certain level and increase beyond that level. The assessment of the Hotspots is based on the location, intensity, and distribution of temperature, against the backdrop of the cast alloy. This is done in conjunction with the temperature distribution maps.

The temperature profile along the coupler wall is analyzed from SoftCast based on the molten metal pouring temperature 1580°C as shown in Fig. 5. The thermal gradient along the thickness direction of the coupler from the temperature profile analysis with 40 sec pouring time is shown in fig 6. (a). A smooth variation along the thickness is not observed. The thermal gradient along the thickness direction of the coupler from the temperature profile analysis with 39 sec, 38 sec, and 37-sec pouring time is shown in fig 6.(b), 6.(c), and 6.(d), respectively. It has been observed from the thermal gradient that with 37 sec pouring time gives the advantage in the casting process which will reduce the casting defects. The fluid flow and the runner dimensions are checked with the 37 sec pouring time. With a pouring time of 37 sec, the overall weight of the casting came 276.7 Kg after incorporating all the parameters. It gives a casting yield of 64.5%. After fixing the parameter for the casting based on the simulation the actual coupler is manufactured through the sand casting method. The manufacturing process is described in section 3.

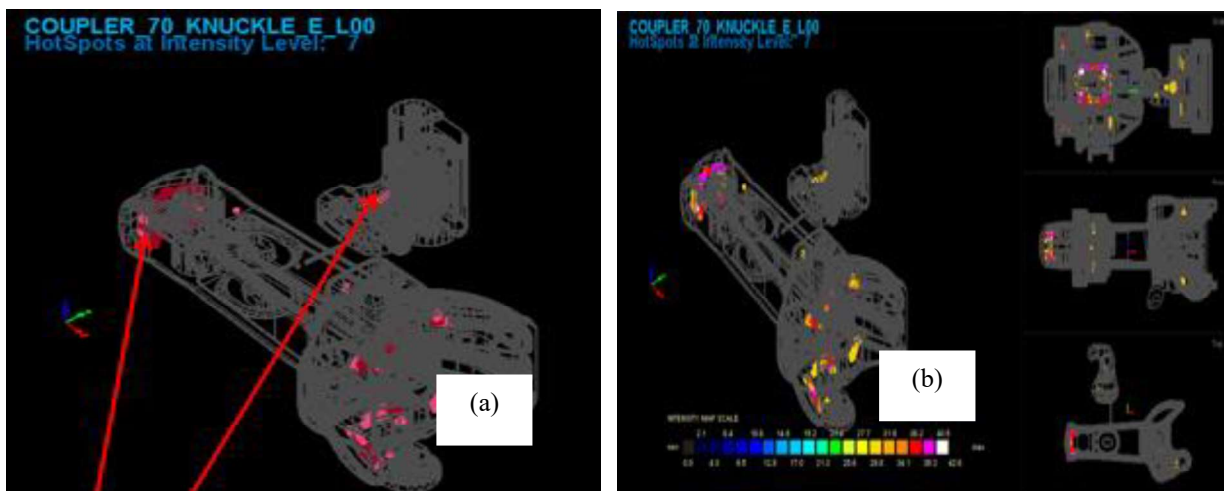


Fig. 3 Hotspot of the casting simulation based on analysis

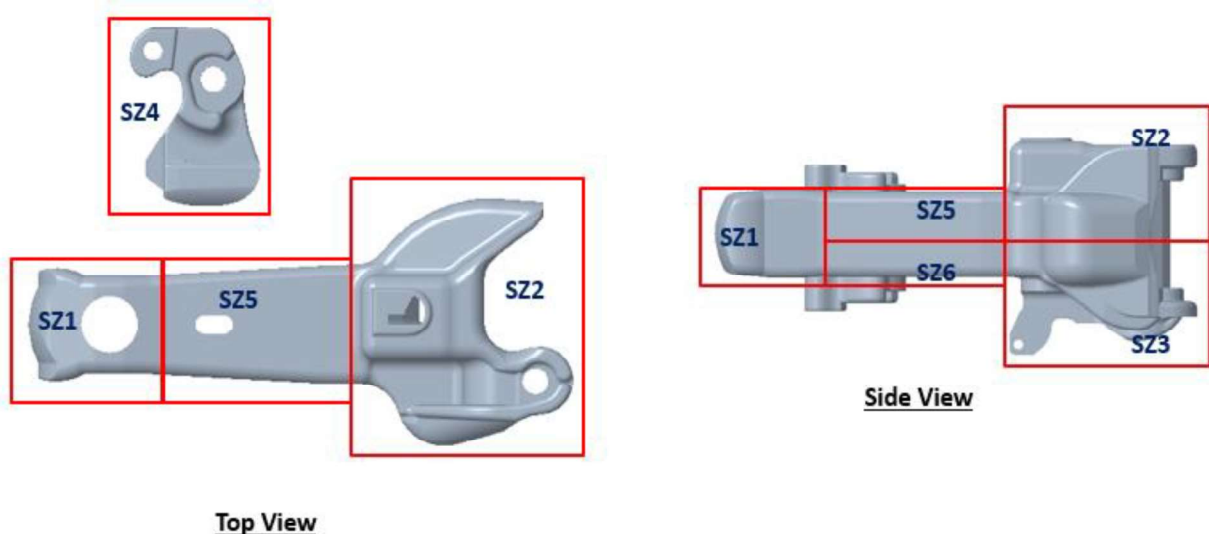


Fig. 4 Hotspot zone (1-5) casting simulation based on analysis.

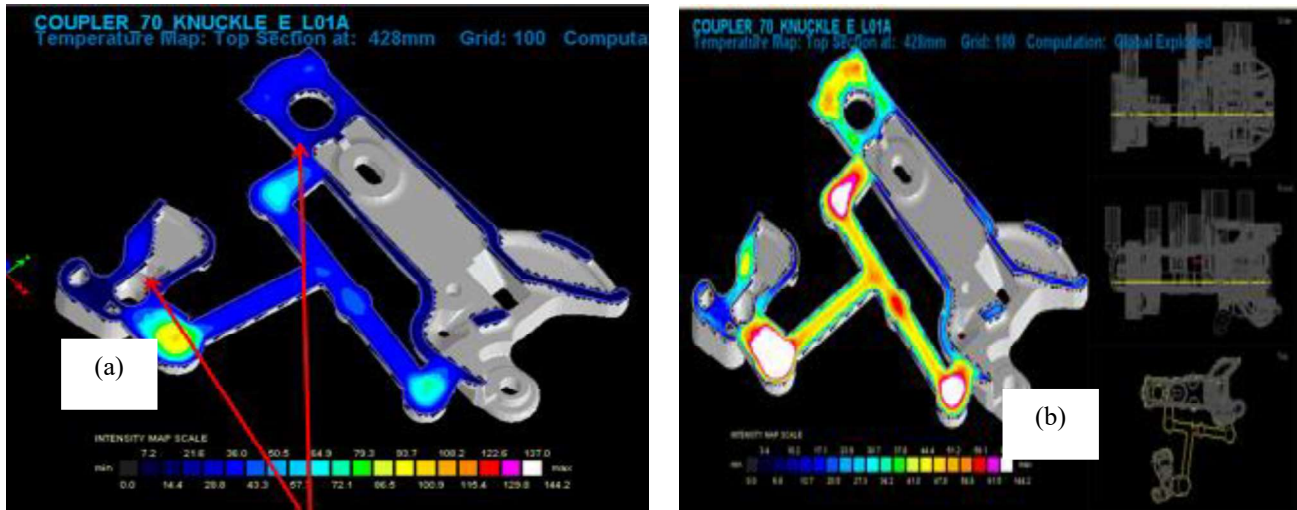


Fig. 5 temperature profile along the coupler wall is analysed from Soft Cast

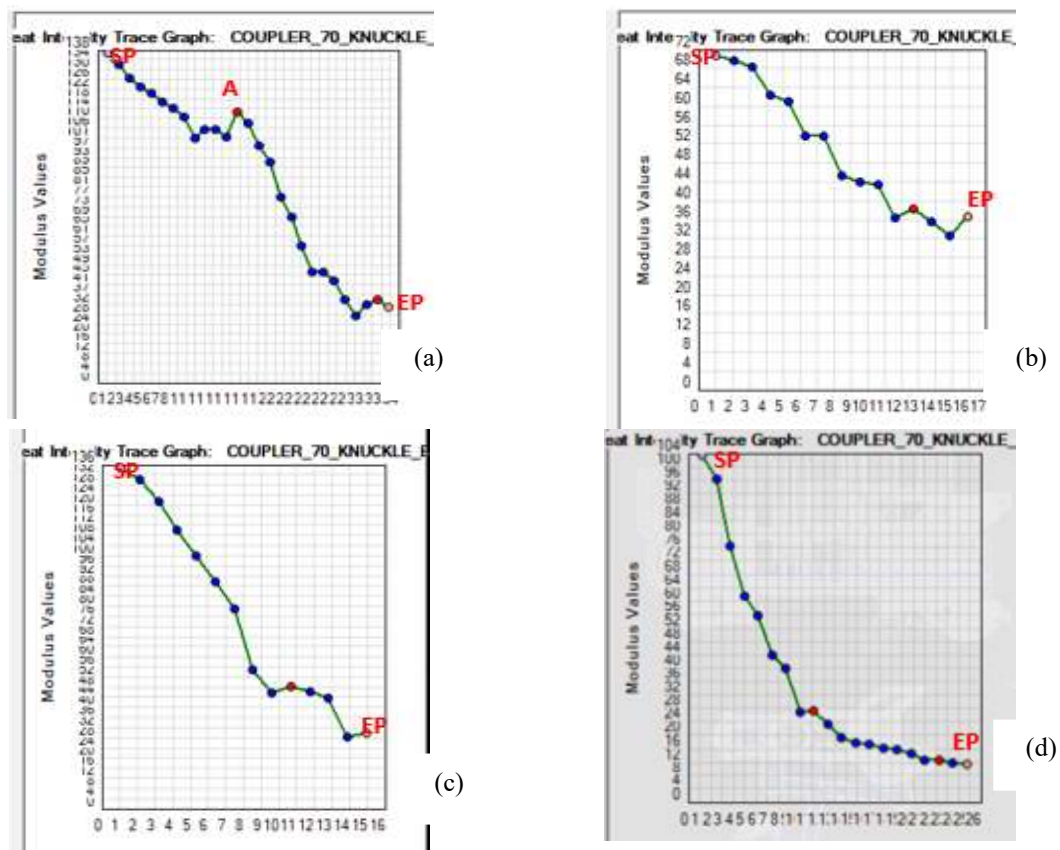


Fig. 6 Thermal gradient along the thickness direction of the coupler from the temperature profile analysis with pouring time (a) 40 sec, (a) 39 sec, (a) 38 sec, (a) 37 sec

3 Manufacturing of Coupler

A sand mould with cope and drag is prepared for the casting of the coupler. The cope and drag prepared with sand are shown in Fig. 7. The riser, runner, and gating system are minutely prepared to avoid all types of molding flaws. In some locations, the damaged portion is repaired to get a good quality mould box for further processing of the casting. The molten metal based on the specified composition is melted in an electric furnace for the pouring purpose. An overhead crane with a molten ladle is then filled in the mould

box with specified pouring time. After filling the molten metal in the mould box, it is kept for 24 hours and then the mould box is opened. After removing the sand through sandblasting the felting operation is performed to remove the riser, runner, and other additional things. Then the coupler is hand machined through a hand grinder. The finished product of the coupler is shown in Fig. 8. A total 25 number of couplers are prepared following the same process. Out of 25 samples of the coupler, anyone will be picked for the phactographic and mechanical testing as per RDSO specification.



Fig. 7 Cope and drag prepared with sand prepared for coupler casting.



Fig. 8 Casted coupler after finishing and machined

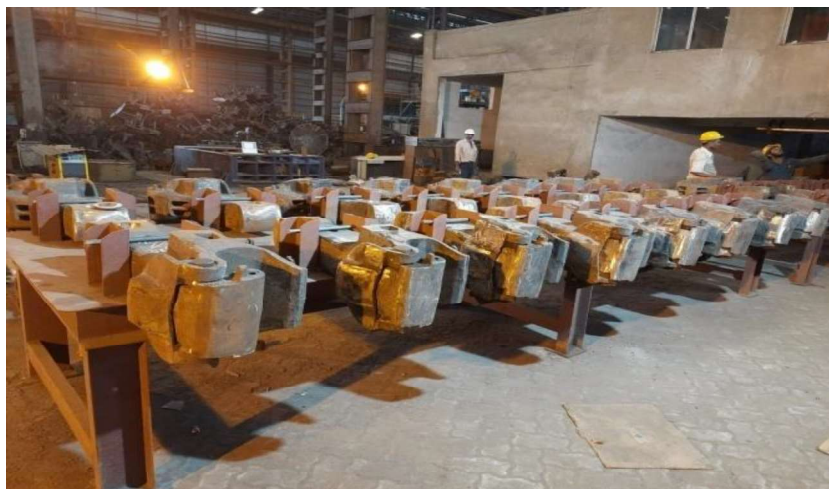


Fig. 9 Total 25 Number of coupler are casted for phactographic and mechanical testing as per RDSO specification



Fig. 10 Location of the cut sections for inspection as per RDSO specification

4 Results and Discussion

Based on the coupler casting simulation 40 sec poring time is giving the optimized value where smooth temperature profile along the thickness is obtained. Couplers are prepared based on the casting simulation data and one sample is selected randomly for spectrometer analysis. A sample coupler is also cut in several cross-sections to check the quality of the casting and observe any notable casting defects are present or not. The composition of the 70 BD “E” type coupler as per specification is given in table 1. The evaluated composition based on spectrometer analysis is also shown in table 1. It has been noted that all the chemical compositions are within the specified range. Therefore casting compositions are as per the specified range. In order to see the quality of the casting, the coupler is cut using a gas cutter in several locations as shown in Fig 10 based on RDSO specification. The details of the cut sections are shown in Fig.11 (a-e). From the inspection, it is observed that no slag inclusion, blowholes, and cold shuts are detected in the given critical cross-sections. In this present work, the photographic and mechanical testing of the coupler is excluded which will be reported in separate work.

Table 1. Chemical composition as per specification for 70 BD “E” type coupler and the comparison based on spectrometre analysis

Element (%)	Range as per Spec	Variation Percent Allowed	Spectrometer analysis Report
Carbon	0.28-0.33	±0.03	0.32
Manganese	0.60-0.90	±0.04	0.73
Phosphorus	0.03 max	±0.05	0.22
Sulphur	0.03 max	±0.005	0.25
Silicon	0.40-0.60	±0.005	0.52
Chromium	0.50-0.80	±0.04	0.67
Aluminum	0.020-0.050	±0.03	0.03
Nickel	0.50-0.60	±0.03	0.50
Molybdenum	0.15-0.25	±0.003	0.20
Iron	Balance		Balance



Fig.11 Details of the cut sections of the 70 BD coupler for inspection

5 Conclusions

In the present work, a proper methodology is established for casting and testing of couplers used in railway industries. The following conclusions can be drawn based on the present work.

1. A poring time of 37 sec gives an optimized value for casting where the smooth temperature gradient is achieved.
2. The total weight of the coupler casting is 276.7 Kg against the finished product weight of 178.35 Kg where a good yield of 64.5% is achieved.
3. Spectrometer analysis report of the coupler material shows the chemical composition within the specified range.
4. Based on the cut section evaluation of the critical location of the casting no noticeable casting defects is observed. A sound casting has confirmed from the inspection.
5. Phactographic and mechanical testing as per RDSO specification is excluded in this study. Those test analyses and reports will be followed in the next part of the work

Acknowledgements

The authors acknowledge the Brand Alloys Pvt Ltd, Serampore, West Bengal 712223, India office and Softcast Pvt Ltd and NML-Jamshedpur for providing the facility.

Disclosure statement

Authors declare no potential conflict of interest related to this work.

References

1. C. K. Jung, J. H. Jang and K. S. Han: *Metallurgical and Materials Transactions A* vol.39A (2008), p.2736-2748.
2. S. Abis, S: *Metallurgical Transactions B* vol.17B (1986), p.209-216.
3. C. E. Esparza, P. Martha, Guerrero-Mata, Z. Roger and Rios-Mercado: *Optimal design of gating systems by gradient search methods*. (2005)
4. A. Kermanpur, M. Eskandari, H. Purmohamad, M. A. Soltani and R. Shateri: *Materials Processing Technology* vol.206 (2008), p.62-68.
5. T. R. Vijayaram, S. Sulaiman, A. M. S. Hamouda and M. H. M. Ahmad: *Materials Processing Technology* vol.178 (2006), p.29-33.
6. T. R. Vijayaram: *Properties of Metal Matrix Composite of Aluminium-11.8% Silicon Reinforced with Different Particulates*. Doctor of Philosophy, University Putra Malaysia. (2006)
7. A. L. K. Hooi: *Thermal Analysis of Two and Three-Gate Sand Casting Mould*. Master of Science, University Putra Malaysia. (2001)
8. Zadeh Noughabi SM, Dehghani K, Pouranvari M. Failure analysis of automatic coupler SA-3 in railway carriages. *Engineering failure analysis*. 2007 Jul 1;14(5):903-12.
9. Chunduru SP, Kim MJ, Mirman C. Failure analysis of railroad couplers of AAR type E. *Engineering Failure Analysis*. 2011 Jan 1;18(1):374-85.
10. Mohammadi M, Rahmatfam A, Zehsaz M, Hassanifard S. Failure analysis study of railway draw-hook coupler. *Journal of Central South University*. 2019 Apr;26(4):916-24.
11. Morsy MA, Khafagy S, Mosa ES. Failure Analysis of the Semi-permanent Coupler Used in Metro Rail. In *IOP Conference Series: Materials Science and Engineering* 2019 Oct 1 (Vol. 611, No. 1, p. 012028). IOP Publishing.
12. Infante V, Branco CM, Brito AS, Morgado TL. A failure analysis study of cast steel railway couplings used for coal transportation. *Engineering Failure Analysis*. 2003 Aug 1;10(4):475-89.
13. Hou L, Peng Y, Sun D. Dynamic analysis of railway vehicle derailment mechanism in train-to-train collision accidents. *Proceedings of the Institution of Mechanical Engineers, Part F: Journal of Rail and Rapid Transit*. 2021 Sep;235(8):1022-34.
14. Zhongming S. COUPLER MATERIALS AND STRENGTH [J]. *Journal of The China Railway Society*. 1985;4.
15. Soldatov VG, Manuev MS, Ivashchenkov YM, Tupatilov EA. Optimization of properties of steel 20GL for railway transport castings. *Metal Science and Heat Treatment*. 2007 Jul;49(7):417-9.

Computer Aided Manufacturing using Fusion 360

Abhas Das, Sibsankar Dasmahapatra

1 Introduction

Computer aided manufacturing CAM can be considered as Numerical Control NC programming tool. The two dimensional 2D and three dimensional 3D models of different components used in the manufacturing industry, automobile industry, aerospace industry have been generated in the CAM. The visualization of the model before real time implementation can be done with Computer aided design CAD of the CAM software package [1]. The simulation as well as optimization can be performed with CAM package [2]. The different operations like roughing, semi-finishing, finishing and contour milling can be performed through CAM [3].

The most important CAM software's [4] which are used mostly in the industry as follows

- Fusion 360
- SolidWorks CAM
- HSM
- Solid CAM
- CAM Works
- NX CAM
- Mastercam

In this paper Fusion 360 has been considered as CAD tool. Fusion 360 is an outstanding tool to make the 2D and 3D models. The Fusion 360 can be used to render objects, simulate loads. This CAD tool can be implemented to make the models used in the CNC machining. The workspace of Fusion 360 has been discussed in the next section. The use of these software's can be implemented for the prior knowledge of the real-time fabrication works of Electrohydraulic actuation system defined by the previous researchers [5-7]. These packages are helpful for the designing of the thermometric Refrigeration System [8]. CAD and CAM are essential to design Parallel Manipulator like Stewart Platform[10-13]. These software's are helpful to get the prior knowledge about the system to design the controllers as Sliding Mode Controllers [14-17]. In the next section the workspace of Fusion 360 has been discussed followed by the tools used in the Fusion 360 in the section III. The section IV describes the results and discussion followed by the conclusion.

2 Workspaces of Fusion 360

Seven workspaces are provided by Fusion 360 to perform various functions such as Design, Generative Design, Render, Animation, Simulation, Manufacture and Drawing. Some of these have been discussed in this section.

A. Das*, S. Dasmahapatra

Department of Mechanical Engineering, Kalyani Government Engineering College, India 741235

Design: 3D geometry in this tool has been created using sketches using the “Create Sketch” button in the top left depicted in the Fig. 1. For the designing purpose, first choose a plane for the sketch, then draw the 2D sketch using lines, splines, curves, and other simple 2D elements.

Manufacture: Fusion 360 is an excellent feature to make the model produced in the CNC. Computer-aided machining (CAM) is a feature supported natively in Fusion 360. To make cuts, choose tools provided by the software and then generate the tool path. The simulation has to be done to watch the model in turn to avoid any problems that might occur during actual machining. The manufacturing button mentioned in the Fig. 2.

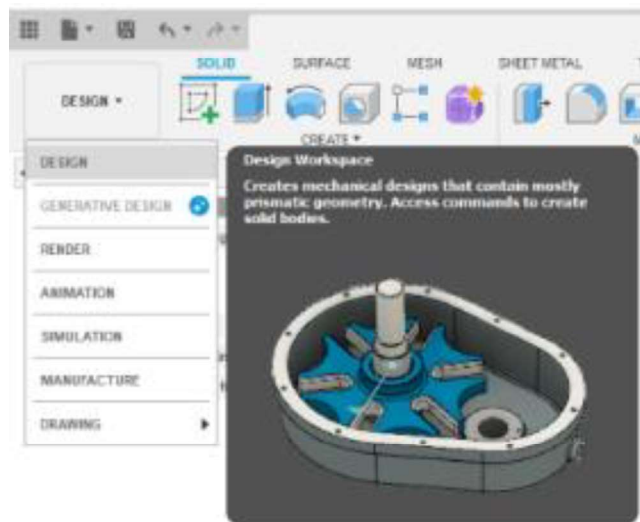


Fig. 1 Create Sketch button in the Fusion 360.

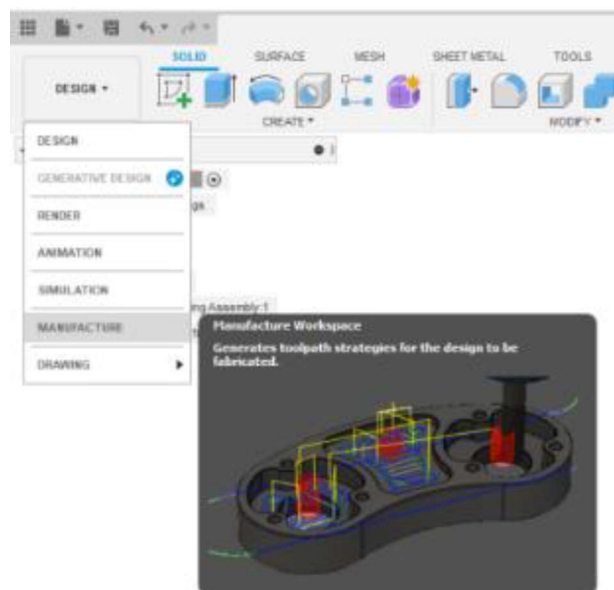


Fig. 2 Manufacture button in Fusion 360.

Render: The Render environment in the Fig. 3 provides tools that make model seem more realistic in real time applications. Specific material can be attributed to the models as an example solid bodies can be made of marble, wood, various metals, glass, and more. The rendering can be improved with various plug-ins for an even more photo-realistic result.

Animation: Fusion 360 supports key frame animation, so all kinds of animations for assemblies like engines, gearboxes can be made. Using the Transform tool, components can be moved in order to animate them in a timeline. Just keep in mind that the organization of bodies matters here and complex animations should probably be done in another tool specifically for animation. In general, Fusion 360's animation depicted in Fig. 4 feature is best-suited for simple visualization.

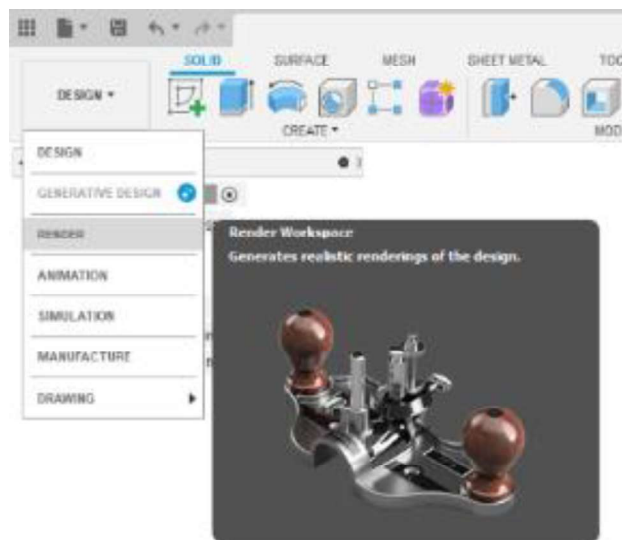


Fig. 3 Render button in Fusion 360.

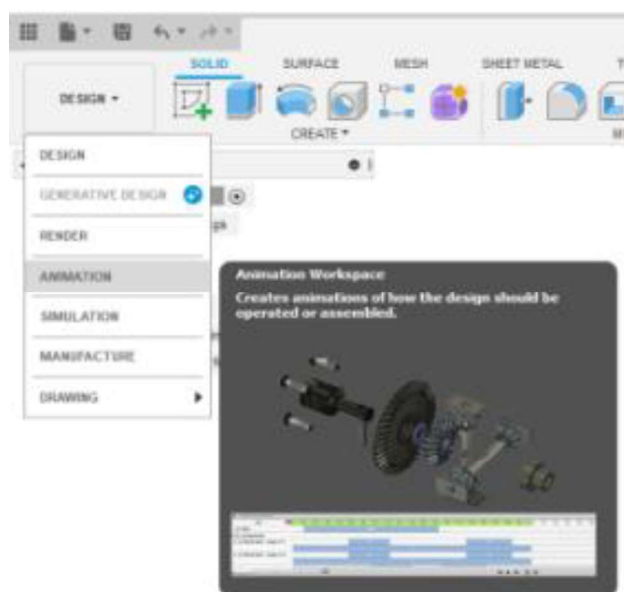


Fig. 4 Animation button in Fusion 360.

Simulation: When the weight of prototype is not distributed equally and that loads can have a negative impact on the final product then a simulation study is needed. A study of different load types or stresses can be done for the models in the simulation before real time applications. Multiple variables can be manipulated such as static stress, modal frequencies, thermal stress and nonlinear static stress. The simulation button in the Fusion 360 has been shown in the Fig. 5.

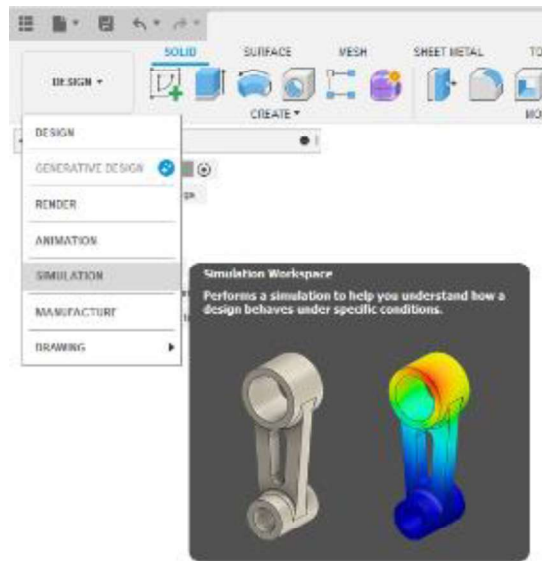


Fig. 5 Simulation button in Fusion 360.

3 Tools Used For Fusion 360

The Fusion 360 can be used to simulate all kinds of CNC manufacturing jobs option like milling, turning, additive, fabrication. In this paper the tools used for Fusion 360 CAM milling operations have been discussed.

Setup: It is simply the tool that allows to create a setup file which basically stores information regarding manufacturing operations of a particular portion to obtain designed geometry for that portion only. The setup button has been mentioned in the Fig. 6(a).

2D & 3D: These are particular tools which are only present in milling section. These provides various options to create a tool paths for a particular operation like facing, contouring, boring in a single time. The corresponding button has been depicted in Fig. 6(b).

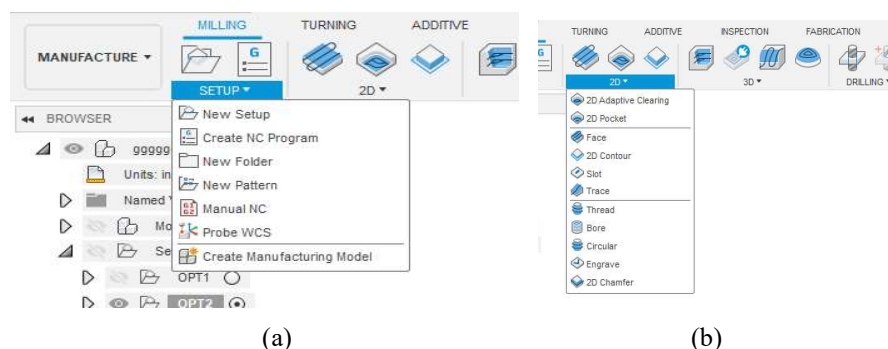


Fig. 6 (a) Setup button (b) 2D & 3D button in Fusion 360.

Drilling: This tool as its name suggests provides various hole making operations and its information is also stored in the setup file.

Actions: This tool provides various simulation options by which the manufacturing process can be visualized and the post processing operations can be done if required. Through this tool G codes can be exported.

Manage: Various cutting tools can be managed with this Manage tool. The tools can be created or edited through this tool in Fusion 360. The corresponding tool of drilling, action and manage has been mentioned in Fig. 7 (a), (b) and (c) respectively.

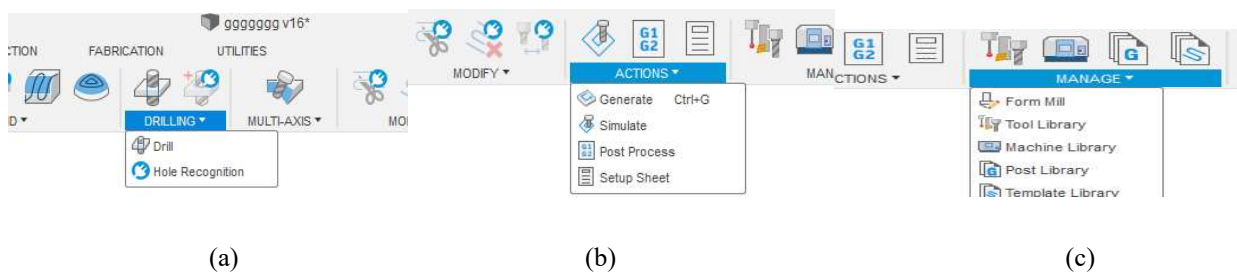


Fig. 7 (a) Drilling button (b) Action button (c) Manage button in Fusion 360.

4 Results and Discussion

The Fusion 360 has been used in this paper to simulate the following design in Fig. 8

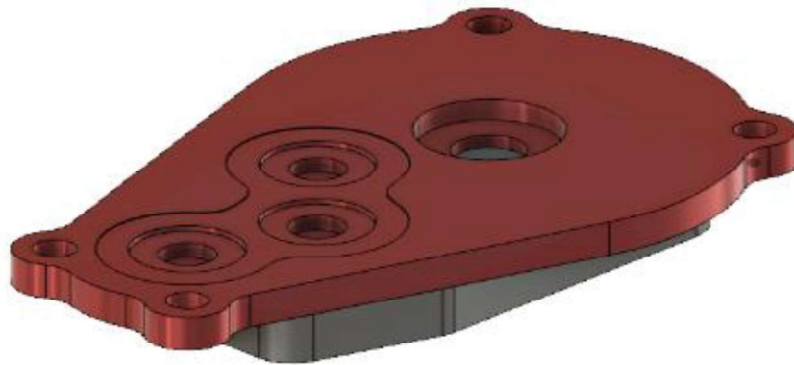


Fig. 8 The given designed has been simulated with help of Fusion 360.

The procedures have been taken into four steps as follows

1. Tool library used for this project
2. Simulation of the surface operations for the side containing the fixture
3. Simulation of the surface opposite to the fixture
4. Simulating and exporting G codes and setup sheets

Creation of Custom tool library

Step 1: From the Manage ribbon select the Tool Library option and the tool library windows will open up.

Step 2: From the option of the library selection click on Cloud and create a new cloud file.



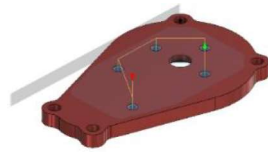
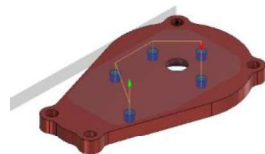
Step 3: Inside the cloud file fill it up with the necessary tools which will be used for the purpose of simulating desired job material.

Step 4: Selections will be done by copying and pasting the standard tools from the local library and creating a new tool from the Plus sign given on the top off the window. It basically signifies creation of new tool.

Step 5: Once the cloud library will be filled up with the necessary tools just click on Apply and the cloud library will be created which will contain all the tools which will be needed to create the manufacturing model.

The simulation setup of the surface containing the fixture and opposite to the fixture have been tabulated with the corresponding steps in the Table 1 and Table 2 respectively.

Table 1. Simulation setup of the surface containing the fixture

STEP	FIGURE
Step 1 Click on the Setup option in the setup ribbon and create a new setup file.	NA
Step 2 Now right click on setup file and select new to create a new setup rename it as OPT1 as operation 1.	NA
Step 3 Now desired setup file which is required for simulation of the first surface is created named OPT1.	NA
Step 4 Select the OPT1 setup by clicking on it then in order to perform the basic facing operation select the facing option from the 2D ribbon and give it the necessary information to get a facing tool path.	
Step 5 Select 2D contour option from the same 2D ribbon and then again insert the necessary information to get the shown tool path.	
Step 6 Just like step 4 and 5 repeat the same but in this case just select the drill option from the drilling ribbon.	
Step 7 Duplicate the previous drilling operation and make necessary changes in it just by right clicking and selecting the edit option and instead of spot drill make it a peck drill operation.	

Step 8 Again duplicate the previous operation and it instead of peck drill makes it tapping operation just to get the required thread and hence we are done with our first operation.

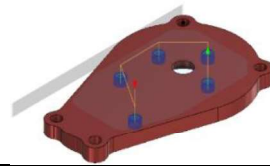
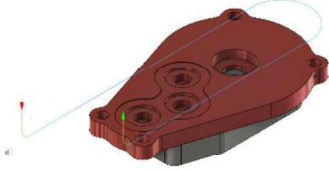
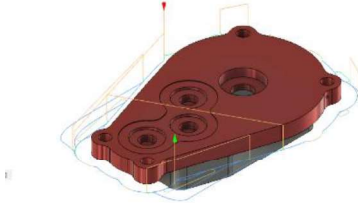
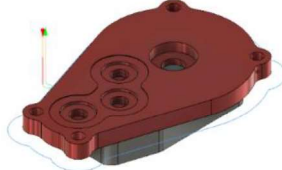
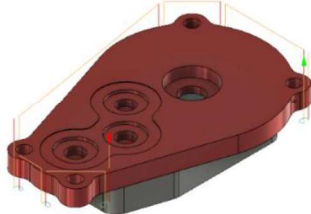
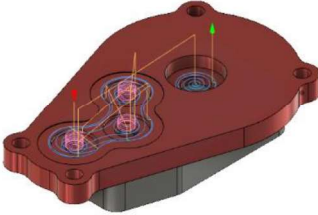
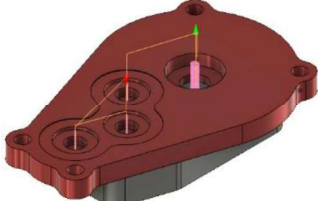
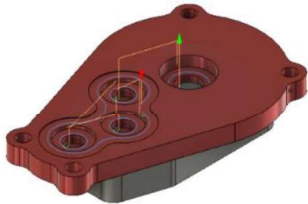
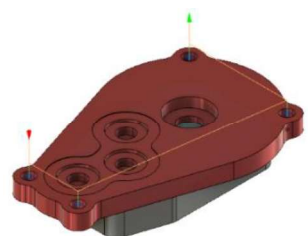
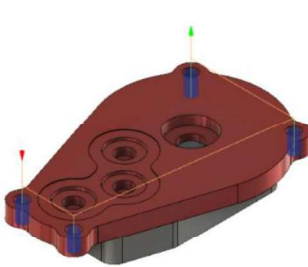
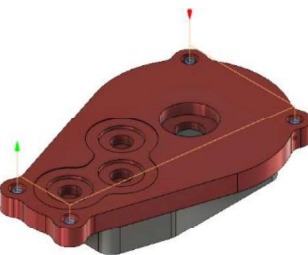


Table 2. Simulation setup of surface opposite to the fixture

STEP	FIGURE
Step 1 Create a second setup file below the setup option and name it as OPT2.	—
Step 2 In selecting the geometry select the model and in selecting the fixture select the fixture which was included into the design during the creation of the setup file.	—
Step 3 Again repeat the facing operation but this time for the different face.	
Step 4 Go for adaptive 2D surfacing and select the pocket which is to be surfaced.	
Step 5 Perform contouring operation on the below mentioned path by selecting the 2D contour tool.	
Step 6 Duplicate the previous operation and just change the contouring path and keep the rest equal.	
Step 7 Click on adaptive 2D again and select the given section and with selecting the required tool to complete this step.	
Step 8 Again selects the 2D contour option to perform the contouring operation on the given sides.	

<p>Step 9 Duplicate the previous operation again and just change that tool and the contouring surfaces and keep the rest the same.</p>	
<p>Step 10 Finally select the drilling option. The Rapid out drilling should be selected.</p>	
<p>Step 11 Duplicate the previous option and instead of rapid out just select the chip baking option so that it goes in and out through the job material.</p>	
<p>Step 12 Select the bore option from 2D ribbon and create the bore through the drill and the material is finished.</p>	

5 Conclusion

It can be concluded that the Fusion 360 tool has been successfully implemented to simulate of surface to the fixture and opposite to the fixture of a gear housing design. The Fusion 360 tool of the CAM software can be implemented to make the model of the manufacturing components used in the real time application in different automobile, production applications. The different steps involved in Fusion 360 can be now easily used to make the other models for the designing purpose. Fusion 360 can be used in different platforms whereas Procast software is used in few specific platform. CAD, CAM, CAE professionals are the users of Fusion 360 whereas the developers to simulate the casting are the users of the Procast software. So this Fusion 360 is mostly used in the industry before fabrication works. This software can be easily implemented for the designing of the hydraulic actuation systems, electrohydraulic actuation systems, parallel manipulators.

References

1. Shah, J.J. & Mantyla, M. (1995). Parametric and feature-based CAD/CAM: concepts, Techniques, and applications, 1st edn. Wiley, New York.
2. Sreedhar, R., Mahato, R., Chaturvedi, A., & Kumar Jaiswal, P. (2021). 3D PCB Designing of Protecting Circuit Using Fusion 360, Asian Journal of Convergence in Technology, vol. 7, 63-65.

3. Lennings, L. (1992). CAD/CAM integration in practice: Two cases of computer aided toolmaking, *Computers in Industry*, Vol.18, 127-134.
4. Khan, J., & Mishra, A. (2019) Role of CAD/CAM in Designing, Challenges Facing in Manufacturing Industry and Developing Manufacturing in Modern Manufacturing Technology, *International Research Journal of Engineering and Technology*, Vol. 6, pp 453-457.
5. Chaudhuri, S., Dasmahapatra, S., Chatterjee, A., Saha, R., Mookherjee S., & Sanyal, D. (2017). Adaptive Fuzzy-Sliding Mode Control with Fixed Bias Compensator for an Electrohydraulic Actuation System with Hard Nonlinearities, Springer India, A. K. Saha et al. (Eds.): FMFP 2014, Contemporary Research, LNME book series, pp. 1223-1232.
6. Dasmahapatra, S., Chaudhuri, S., Mandal, P., Mookherjee, S., & Saha, R. (2015). Fuzzy- PI control of motion tracking by an electrohydraulic system with multiple nonlinearities, *Proceeding of Michael Faraday IET International Summit: MFIIS-2015*, September 21 – 13, Kolkata, India.
7. Dasmahapatra, S., Saha, R., Sanyal, D., Sengupta, A., & Bhattacharyya, U. (2016). Adaptive PID Control for Angular Motion Tracking by Linear Electrohydraulic Actuation, *Proceeding of IEEE First International Conference on ICPEICES*, July 4-6, New Delhi, Delhi, India.
8. Bose, A., Debnath, A., & Dasmahapatra, S. (2020). Thermometric Refrigeration System, Springer Nature Switzerland AG 2020, S. Dawn et al. (Eds.): ICIMSAT 2019, LAIS 12, pp. 702–709.
9. Kundu, S., & Dasmahapatra, S. (2020). A blind stick assisting blind person to detect obstacle ahead and to alert the user, *Reason-A Technical Journal*, Vol. XIX, pp. 16-25.
10. Dasmahapatra, S., Saha, D., Saha, R., Sanyal, D., Lahiri, D., & Singh, J.P. (2016). Analysis of 6-DOF motion with PI controller in electrohydraulic Stewart platform, *Proceeding of IEEE First International Conference on CMI*, January 8-10, Jadavpur University, Kolkata, India.
11. Dasmahapatra, S., & Ghosh, M. (2020). Workspace Identification of Stewart Platform, *International Journal of Engineering and Advanced Technology*, vol. 9, pp. 1903-1907.
12. Ghosh, M., & Dasmahapatra, S. (2020). Kinematic Modeling of Stewart Platform, Springer Nature Switzerland AG, (2020), S. Dawn et al. (Eds.): ICIMSAT 2019, LAIS 12, pp. 693-701.
13. Mullick, S. H. & Dasmahapatra, S. (2020). Combined Motion Generation by Electro-Hydraulic Stewart Platform for Manufacturing Industries, Springer Nature Switzerland AG 2020, S. Dawn et al. (Eds.): ICIMSAT 2019, LAIS 12, pp. 596–604.
14. Dasmahapatra, S., Saha, R., Mookherjee, S., & Sanyal, D. (2018). Designing an Input- linearized Adaptive Sliding Mode Coupled Nonlinear Integral Controller, *IEEE/ASME Trans. Mechatronics*, vol. 23, pp. 2888-2895.
15. Dasmahapatra, S., Saha, R., Chatterjee, A., Mookherjee, S., & Sanyal, D. (2015). Design of an adaptive-fuzzy-bias-SMC and validation for a rugged electrohydraulic system, *IEEE/ASME Trans. Mechatronics*, vol. 20, pp. 2708-2715.
16. Dasmahapatra, S., Saha, R., Sanyal, D., Sengupta, A., Bhattacharyya, U., & Sanyal, S. (2016). Designing Low-Chattering Sliding Mode Controller for an Electrohydraulic System, *Proceeding of IEEE First International Conference on CMI*, January 8-10, Jadavpur University, Kolkata, India.
17. Dasmahapatra, S., Saha, R., Sanyal, D., Sengupta, A., & Sanyal, S. (2015). Designing Sliding Mode with Integral Control for Angular Rotation of a Link by Linear Electrohydraulic Actuation, *Proceeding of 12th IEEE India International Conference of INDICON*, December 17-20, 2015, Jamia Milla Islamia, new Delhi, India.

Assessment of Micro-mixing Process of Electroosmotic Flow in a Microchannel

Biswajit Gayen*, Nirmal K. Manna, Nirmalendu Biswas, Ashim Chakrabarty

1 Introduction

Electrokinetics refers to the transport of fluid/ particles due to the application of an electric field [1], [2]. Electrokinetics has plenty of applications in advances of microfluidic devices. Lab-on-a-chip [3] – [5] is one of the most familiar examples of this kind of microfluidic device. Lab-on-a-chip systems have abundant applications like drug delivery [6] – [8], DNA hybridization [9], [10], point-of-care testing [11] – [15], etc. The lab-on-a-chip system has advantages over other experimental platforms because of its miniaturization. The consumption of samples as well as test is greatly alleviated here [16], [17].

The history of electrokinetics started in the early 19th century when Reuss first studied the mixture of water/ clay and at that time he demonstrated the electrokinetic effect by externally applying an electric field using direct current (DC). Throughout the mid – 19th century, numerous developments occurred in the field of electrokinetics; however, the most distinguish was the discovery of the electrokinetic-based analytical model developed by Helmholtz, and consequently, a combined work between Smoluchowski and Pellat. They derived slip velocity, which is known as Helmholtz – Smoluchowski equation.

In general, there are two types of micromixers; active micromixers and passive micromixers. In the case of active micromixers, an external force is applied in the form of an electric field or magnetic field in a micromixer chamber, and in passive micromixing, only geometric design variations are considered [18]. But, in microfluidic devices, the hydraulic diameter is in the range of micrometers and the fluid velocity in mm per second is very low makes the flow in highly ordered laminar flow. So, it is cumbersome to attain efficient mixing in such a microfluidic device, where the mixing mainly depends on molecular diffusion. Therefore, it is our utmost desire to apply some methods by which we can achieve effective and rapid mixing of fluids [19], [20]. To improve the mixing quality, some researchers analyzed the mixing quality by considering specific geometries of microchannels [21], [22]. Some researchers applied pursuant grooves at the base of their model [23] or inserted a non-conductive plate that may be flexible or nonflexible [24]. Now – a – days AC microelectrodes are effectively and efficiently used in microfluidic devices. The advantages we get by using AC microelectrodes are that it can produce electrokinetic forces such as electroosmotic and electrophoretic forces and due to these forces microvortex are generated which helps to mix different concentrations of fluid rapidly [25]. Moreover, some researchers investigated the dependency of the magnitudes of the abovementioned forces on AC voltage, frequency of the alternating current, and the electrical properties of fluid [26]. The major difficulties they faced to fabricating this huge length, but the mixing quality they reported as 36.5% using a single optimized channel.

In this paper, three different geometry has been chosen to investigate the mixing quality. The details of this geometry have been depicted in Fig. 1. Two identical pairs of microelectrodes are located at the outer surface at an angle of 45, - 45, 135, - 135°. The microelectrodes are augmented by a sinusoidal electric field. As a result, this time-dependent electric field generates microvortex and results in rapid mixing. The microchannel is filled with diluted electrolytes solution. In our simulation, we have taken KCL and water as base fluid. The electrical properties are disclosed in TABLE I. To achieve optimum mixing quality, we simulated at different values of different parameters, such as we have considered fluid mean inlet velocity of 0.05, 0.1, 0.2 mm/s, the frequency at a range of 4, 8, 12 Hz. and different voltage amplitude of 0.05, 0.1 and 0.2 V. The main advantage to adopt this kind of methodology over past is that in a single – step the better mixing quality can be achieved with ease of fabrication.

B. Gayen*, N. K. Manna, N. Biswas, A. Chakrabarty
Department of Mechanical Engineering, Jadavpur University, India 700032

2 Methodology

COMSOL Multiphysics® 5.6 software [27] has been employed to perform all numerical simulations of electrokinetic micromixing. The COMSOL Multiphysics software utilizes Backward Euler method to analyze a large numerical part by breaking it into smaller elements and then with proper selections of governing equations and boundary conditions gives us approximate solution. In the present simulation we considered Quadratic discretization to solve all equations. The absolute tolerance is considered 1×10^{-5} . PARDISO linear solver has been employed to solve fluid flow variables (spf). For nonlinear solver, Constant (Newton) method has been considered as a method of termination and the upper limit of tolerance factor we considered in our present simulation is 0.5. Simulation workflow such as selecting the physics, setting up the model dimensions and geometry, different parameters, adding materials, incorporating mesh and finally time dependent approach has been disclosed.

2.1 Model Physics

To test our simulation model in the current study, we considered three physics i.e. electric currents (ec), laminar flow (spf), and transport of diluted species (tds) then we coupled to each physics by applying the correct boundary conditions such as Helmholtz – Smoluchowski slip velocity (electroosmotic) applied to all micro - channel boundaries except the boundaries of obstacles. In this way, we coupled the electric currents and laminar flow physics. This coupling between the necessary physics enables us to modify the mixing analysis within the model.

2.2 Model design

Fig. 1(a), Fig. 1(b), and Fig. 1(c) show 2D one ring-shaped with two obstacles at lower and upper inner surfaces, one ring-shaped with one obstacle at the center, one ring-shaped type micromixer, respectively. For every geometry, there are two inlets with concentrations of 1 mol/ m^3 and 0 mol/ m^3 entering into the microchannel, and one outlet has been considered to achieve an effective concentration of 0.5 mol/ m^3 at the outlet.

2.4 Model parameters

2.5

Different model parameters have been considered which govern the fluid flow, fluid compositions, electrical properties, physicochemical properties, etc. TABLE I shows the numerical values of different parameters.

2.4 Model meshing

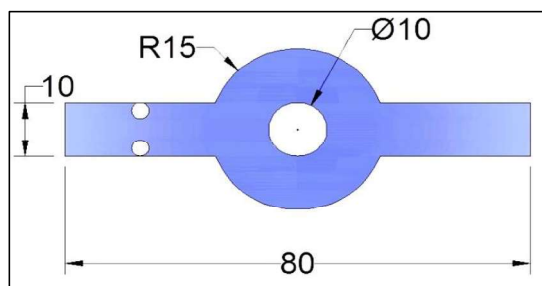
COMSOL Multiphysics® 5.6 has a provision to select various meshing elements. In this simulation, we consider extremely fine predefined mesh physics. In Fig. 2 the meshes for one ring-shaped with two obstacles have been depicted. We choose extremely fine triangular elements. For these extremely fine triangular meshing elements, we considered maximum element size of 0.8, minimum element size of 0.0016, maximum element growth rate of 1.1, curvature factor 0.2, and resolution of narrow regions of 1. The 2D model environment consists of 4794 mesh vertices, 582 edge elements, 9010 triangles, 30 vertex elements with triangular meshing.

2.5 Time-dependent approach

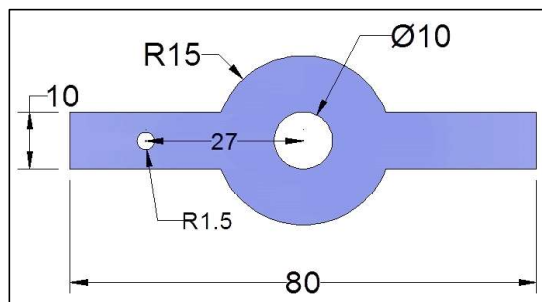
In our present simulation, we first consider a stationary step at time $t = 0 \text{ s}$. to solve for only two physics – fluid flow and transport of diluted species. Then we consider a time-dependent step and the initial conditions are the solutions we get from the stationary solution. In this way, we minimize the enormous time and memory of the simulation. We impose a step function at the middle of the inlet to smoothen the concentration differences between the fluid and we neglect the discontinuity of the Convection – Diffusion equation. We run the simulation for 0.5 s, as in an inappropriate environment most of the biological

molecules are highly unstable. Within a second it may have a possibility of chemical damage taking place before the drug delivery in the micro-mixture chamber.

(a)



(b)



(c)

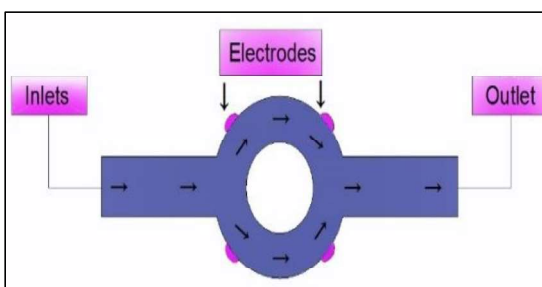


Fig. 1 (a) one ring-shaped with two obstacles (b) one ring-shaped with one obstacle (c) one ring-shaped without obstacle model with four microelectrodes at the outer surface of the micromixing – chamber wall. (All lengths are in micrometer).

Table 1. The numerical value of different parameters

Parameters	Symbol	Value
Dielectric constant	ϵ	80.2
Permittivity of vacuum	ϵ_0	8.854×10^{-12} C/ V.s
Viscosity	μ	0.9×10^{-3} Kg/ m.s
Density	ρ	1000 Kg/ m ³
Zeta potential of the channel wall	ζ_w	-0.1 V
Mean inflow velocity	U_0	0.05, 0.1, 0.2 mm/ s
Conductivity of the ionic solution	σ	0.11846 S/ m
Maximum value of the AC potential	V_0	0.2 V
Frequency of the AC	f	4, 8, 12 Hz
Start time	t	0 s
Diffusion coefficient of the silotion	D	0.6×10^{-11} m ² / s
Initial concentration	C_0	1 mol/ m ³
Maximum concentration	C_{\max}	0.5 mol/ m ³

3 Mathematical Model

The mathematical model of electric currents, flow field, and concentration field with boundary conditions are presented as follows:

3.1 Electric field

We consider the Poisson equation [28] to know the distributions of the electric field in the model, as follows:

$$\nabla^2 \phi = \frac{\rho_e}{\varepsilon \varepsilon_0} \quad (1)$$

Here, ε_0 and ρ_e signifies the permittivity of vacuum and electric charge density far away from the channel wall, respectively. Also, ε and ϕ indicates permittivity of the fluid and electric potential, respectively. As $\rho_e = 0$ far from the solid wall so that the Poisson equation takes the form of Laplace equation [28] as follows:

$$\nabla^2 \phi = 0 \quad (2)$$

The boundary conditions we considered here are as follows:

- Wall of the microchannel and obstacles:

$$\mathbf{n} \cdot \nabla \phi = 0 \quad (3)$$

- Two electrode – pairs:

$$V = V_0 \sin(2\pi ft) \quad (4)$$

- The outlet of the microchannel:

$$\phi = 0 \quad (5)$$

In Eq. (3) \mathbf{n} represents the unit normal basis vector towards the domain. In Eq. (4) V_0 and f demonstrate the maximum potential and frequency of the sinusoidal time-dependent electric field.

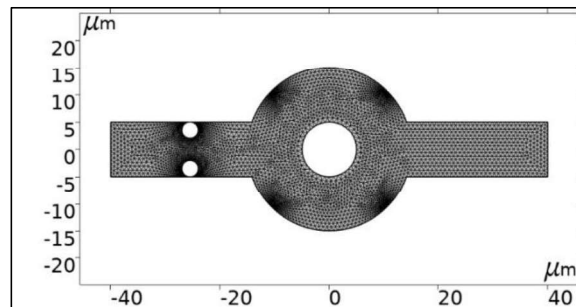


Fig. 2 Triangular meshing elements of one ring-shaped with two obstacles geometry.

3.2 Flow field

We apply continuity and Navier – Stokes equations to know the pressure and velocity vector (assuming Newtonian and incompressible fluid) as follows:

- Continuity equation [29]:

$$\nabla \cdot \mathbf{u} = 0 \quad (6)$$

- Navier – Stokes equation [30]:

$$\rho \left[\frac{\partial \mathbf{u}}{\partial t} + \mathbf{u} \cdot \nabla \mathbf{u} \right] = -\nabla P + \mu \nabla^2 \mathbf{u} + \mathbf{E} \rho_e \quad (7)$$

In Eq. (7) ρ and μ represent density and dynamic viscosity of water, respectively. Where, \mathbf{u} represents the velocity vector and ∇P is the pressure gradient. The electric field vector is represented by $\mathbf{E} = -\nabla\phi$. From the fact that counter ions are attracted by the charged surfaces as a result, at the vicinity of the microchannel chamber wall, there will be more accumulation of the counter ions and the net charge within this thin layer (electric double layer, EDL) is not zero. The thickness of EDL can be expressed by the following relation [29]:

$$\lambda_D = \sqrt{\frac{\epsilon_0 \epsilon k_B T}{2n_0 (ze)^2}} \quad (8)$$

In the above equation, e , k_B , n_0 , z and T are elementary charge, Boltzmann constant, bulk ionic concentrations, valence and absolute temperature, respectively. In microfluidic applications, for buffer solutions, the ionic concentrations remain in the range of nm [30], which is negligible as compared to other lengths of the microchannel. As a result we can neglect the term $\mathbf{E} \rho_e$ in Eq. (7). As a result, we applied Helmholtz – Smoluchowski slip boundary condition as electroosmotic flow [29]:

$$\mathbf{u} = -\frac{\epsilon_0 \epsilon \zeta_w}{\mu} \mathbf{E} \quad (9)$$

Where ζ_w represents the zeta potential of the microchannel wall.

Boundary conditions applied for solving the flow model are as follows:

- Inlet of the microchannel:

Fully developed flow with an average velocity.

- The outlet of the microchannel:

$P = P_a$ (local atmospheric pressure) with suppressed backflow.

- Wall of the microchannel, and obstacles:

Electroosmotic velocity.

3.2 Concentration field

The Convection – Diffusion equation is [29]:

$$\frac{\partial C_i}{\partial t} + \mathbf{u} \cdot \vec{\nabla} C_i = D_i \nabla^2 C_i \quad (10)$$

Where, $i = 1, \dots, n$

In the above equation, C_i represents the concentration of i^{th} fluid. Whereas, D_i represents the diffusion coefficient of i^{th} fluid. To solve the Eq. (10) we applied the boundary conditions are as follows:

- At inlet:

$C = C_0$ (for upper half) and $C = 0$ (for lower half).

- Walls of the microchannel and obstacles:

$$\frac{\partial C_i}{\partial t} = 0 \quad (t \geq 0) \quad (11)$$

a. Mixing quality factor

For finding out the performance of the micromixing we define a mixing quality (MQ) factor in Eq. (11) as follows:

$$MQ = 1 - \sqrt{\frac{\sigma_{mean}^2}{\sigma_{max}^2}} \quad (12)$$

$$\sigma_{mean}^2 = \int (C_i - C_{max})^2 dy \quad (13)$$

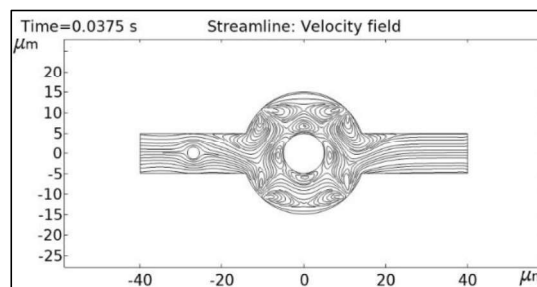
In the above equation, the integration has been evaluated at the outlet. C_i represents the concentration of i^{th} fluid at the outlet and the value of C_{max} equals 0.5 mol/ m^3 . σ_{max} is the maximum variation in the mixture. In Eq. (12) an MQ value of 1 represents 100% mixing and an MQ value of 0 represents no mixing.

4 Results And Discussion

It is noteworthy that due to change of the width of each geometry, during each period of the application of electric field the fluid from opposite sides are pulled and as shear stress acts as a barrier of backflow, this mechanism greatly influences to generate vortices near the four microelectrodes as depicted at time 0.0375 s in Fig. 3.

In this simulation, to get physical perceptions of mixing quality for the geometry of one ring-shaped without obstacle type micromixer, we presented the concentration at outlet along y-direction measured from top to bottom at the outlet at time $t = 0.5 \text{ s}$ in Fig. 4. Then we investigated the influence of the inlet velocity on mixing quality in the micro mixture for the geometry of one-ring without obstacle as depicted in Fig. 5.

(a)



(b)

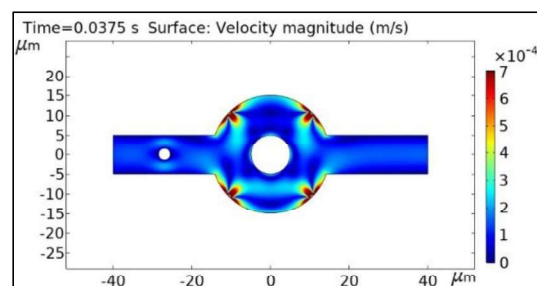


Fig. 3 (a) Streamline velocity field profile of one ring - shaped with one obstacle geometry. The instantaneous time $t = 0.0375 \text{ s}$ at $u = 0.1 \text{ mm/ s}$, $V_0 = 0.1 \text{ V}$ and $f = 8 \text{ Hz}$. (b) Velocity magnitude field as depicted in (a).

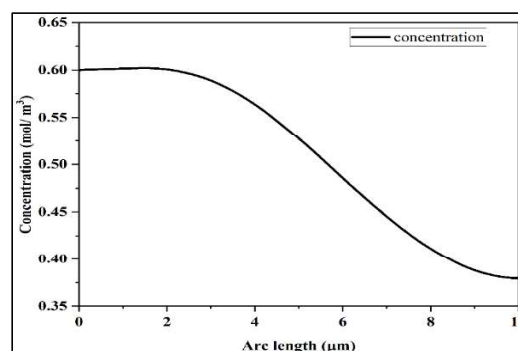


Fig. 4 The concentration profile at outlet as a function of distance measured from top to bottom for one – ring without obstacle geometry.

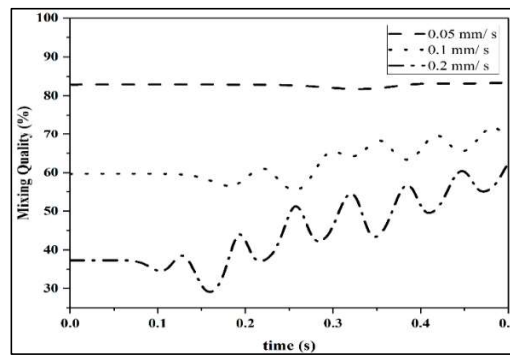


Fig. 5 MQ (%) of the one ring-shaped without obstacle model at different inlet velocities at $V_0 = 0.1$ V and $f = 8$ Hz.

From the fact that, as the inlet velocity increases the inertia forces are dominant as compared to electroosmotic force, and as a result mixing quality is not prominent due to fewer vortices being generated. From Fig. 5. we can conclude that at velocity 0.2 mm/ s the inertia forces are dominant as compared to electroosmotic forces.

In the present study, we studied the mixing quality at different frequencies for one ring – shaped type mixing chamber without obstacles configuration in Fig. 6. We observed that at frequency 4 Hz. the mixing quality is better than other frequencies. Moreover, we investigated the mixing quality at different voltages amplitude considering one ring – shaped mixing chamber without obstacles configuration. As depicted in Fig. 7, the best voltage amplitude for micro – mixing is 0.2 V.

Finally, we have investigated the best geometry by simulating the three configurations at velocity 0.05 mm/ s , frequency 4 Hz. We have concluded that one ring - shaped without obstacle configuration executes better result for micro – mixing as depicted in the Fig. 8.

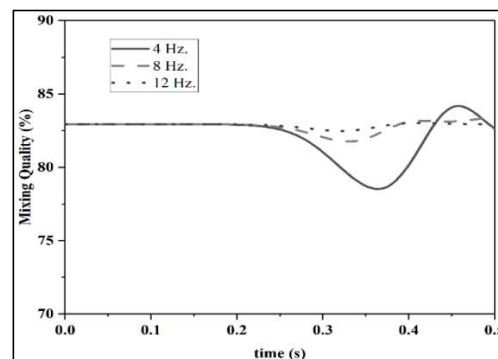


Fig. 6 MQ (%) of one ring-shaped without obstacle configuration at a various frequencies inlet velocity of 0.05 mm/ s and $V_0 = 0.1$ V.

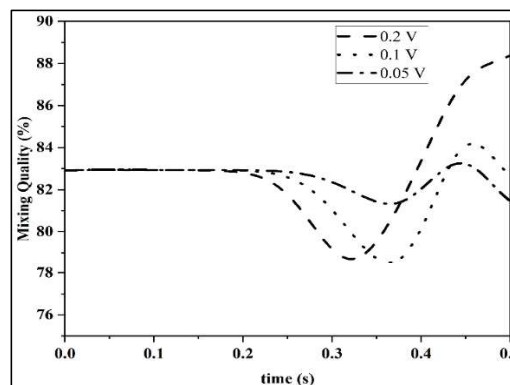


Fig. 7 MQ (%) of the one ring-shaped without obstacle geometry at various voltages at 0.05 mm/ s and $f = 4$ Hz.

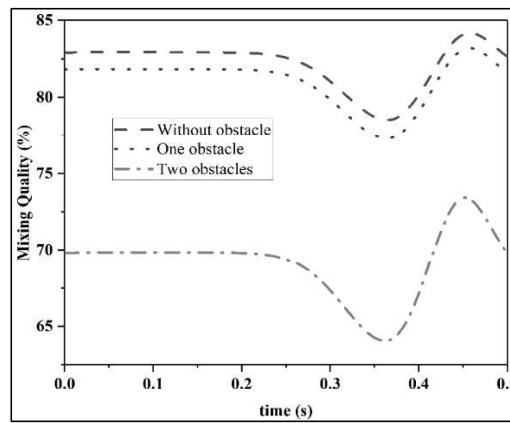


Fig. 8 MQ (%) for one ring-shaped without obstacles, with one obstacle and with two obstacles configuration at $u = 0.05$ mm/s and $V_0 = 0.1$ V.

It should be mentioned that the diagram presented in Fig. 5. is the result of integration at the outlet boundary of the criterion, mixing quality as presented in Eq. (12), derived from the concept of square deviation from the desired concentration (0.5 [mol/ m^3]). Initially, the mixing quality is not good as can be depicted in Fig. 9 and the magnified view in Fig. 10. by momentarily showing the surface concentration magnitude at time $t = 0.2375$ s at the outlet. For example, more fluid with a concentration of 1 mol/ m^3 passes across the outlet boundary as compared to fluid with 0 mol/ m^3 concentration.

But, with an increase in time, we observed a better mixing quality.

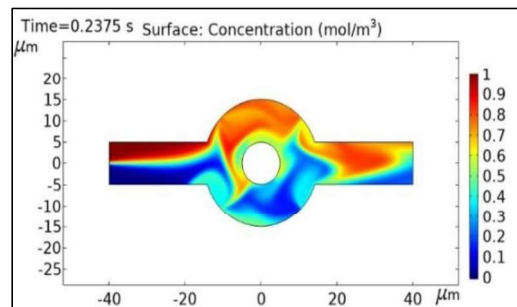


Fig. 9 The surface concentration profile at $t = 0.2375$ s, $u = 0.05$ mm/s.

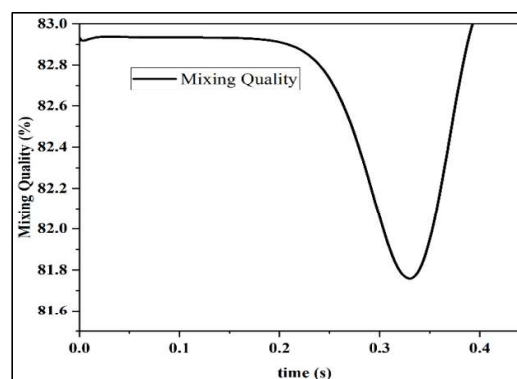


Fig. 10 Magnified mixing quality diagram for 0.05 mm/s.

5 Conclusions

The present work address three different geometry for assessing the mixing quality of electroosmotic flow in a microchannel. Following conclusions may be drawn from the present simulation:

- The best mixing chamber we observed is one ring-shaped without obstacle configuration.
- It is observed that at 0.05 mm/ s of inlet velocity the mixing quality is better than other inlet velocities.
- It is observed that when the frequency of AC is of the magnitude of 4 Hz. the best mixing quality we achieved.
- When the voltage amplitude is 0.2 V, better mixing quality is achieved compared to other amplitudes.

Nomenclature

ϕ	Electric potential distribution	μ	Dynamic viscosity of the fluid
\mathcal{E}	Dielectric constant of the medium	e	Elementary charge
ϵ_0	Permittivity of vacuum	K_B	Boltzmann constant
ρ_e	Free charge density	n_0	Bulk ionic concentrations
\mathbf{n}	Unit normal basis vector	z	Valence of the ionic charge
V	Voltage	ζ_w	Zeta potential
E	Electric field vector	C_i	Concentration of ith stream
u	Velocity vector	D_i	Diffusion coefficient of ith stream
P	Pressure	MQ	Mixing quality
ρ	Density of the fluid	σ_{\max}	Maximum variation in the mixture

References

1. C. C. Chang and R. J. Yang, "Electrokinetic mixing in microfluidic systems," *Microfluid Nanofluid*, vol. 3 (5), 2007, pp. 501–525.
2. A. V. Delgado, F. Gonzalez-Caballero, R. J. Hunter, L. K. Koopal and J. Lyklema, "Measurement and interpretation of electrokinetic phenomena," *Journal of Colloid and Interface Science*, vol. 309 (2), 2007, pp. 194–224.
3. Á. Ríos, M. Zougagh, and M. Avila, "Analytica Chimica Acta Miniaturization through lab-on-a-chip : Utopia or reality for routine laboratories ? A review," *Anal. Chim. Acta*, vol. 740, pp. 1–11, 2012.
4. J. Knight, "Honey, I shrunk the lab," *Nature*, vol. 418, no. 6897, pp. 474–475, 2002.
5. Y. Daghighi and D. Li, "Lab on a Chip Micro-valve using induced-charge electrokinetic motion of Janus particle," pp. 2929–2940, 2011.
6. Y. Chen, D. Gao, Y. Wang, S. Lin, and Y. Jiang, "A novel 3D breast-cancer-on-chip platform for therapeutic evaluation of drug delivery systems," *Anal. Chim. Acta*, 2018.
7. M. H. Wu, S. Bin Huang, and G. Bin Lee, "Microfluidic cell culture systems for drug research," *Lab Chip*, vol. 10, no. 8, pp. 939–956, 2010.
8. P. S. Dittrich and A. Manz, "Lab-on-a-chip: microfluidics in drug discovery," *Nat. Rev. Drug Discov.*, vol. 5, no. 3, p. 210, 2006.
9. D.-K. Kang et al., "Rapid detection of single bacteria in unprocessed blood using Integrated Comprehensive Droplet Digital Detection," *Nat. Commun.*, vol. 5, p. 5427, 2014.
10. T. J et al., "Accurate multiplex gene synthesis from programmable DNA microchips," *Nature*, vol. 432, no. 7020, pp. 1050–1054, 2004.
11. C.D. Chin, V. Linder, S.K. Sia, Lab-on-a-chip devices for global health: past studies and future opportunities, *Lab Chip* 7 (2007) 41–57.
12. D. Figeys, D. Pinto, Lab-on-a-chip: a revolution in biological and medical sciences, *Anal. Chem.* 72 (2000) 330A–335A.
13. S. Haeberle, T. Brenner, H.P. Schlosser, R. Zengerle, J. Duerée, Centrifugal micromixery, *Chemical Engineering & Technology* 28 (2005) 613–616.
14. S.-J. Lee, B.-K. Choi, The artificial glomerulus design using diffusion in microchannels, *Int. J. Precis. Eng. Manuf.* 13 (2012) 307–310.
15. S.-P. Ryu, J.-Y. Park, S.-Y. Han, Optimum design of an active micro-mixer using successive Kriging method, *Int. J. Precis. Eng. Manuf.* 12 (2011) 849–855.
16. R.B. Fair, Digital microfluidics: is a true lab-on-a-chip possible? *Microfluid. Nanofluid.* 3 (2007) 245–281.
17. V. Srinivasan, V.K. Pamula, R.B. Fair, An integrated digital microfluidic lab-on-a-chip for clinical diagnostics on human physiological fluids, *Lab Chip* 4 (2004) 310–315.
18. V. Hessel, H. Löwe, F. Schönfeld, Micromixers—a review on passive and active mixing principles, *Chem. Eng. Sci.* 60 (2005) 2479–2501.
19. Ahmed D, Mao X, Shi J, et al. A millisecond micromixer via single bubble - based acoustic streaming [J]. *Lab on a Chip*, 2009, 9(18):2738- 2742

20. Li J., Kleinstreuer C., Microfluidics analysis of nanoparticle mixing in a microchannel system [J]. *Microfluidics Nanofluidics*, 2009, 6(6):661- 668.
21. H. Chen, J.-C. Meiners, Topologic mixing on a microfluidic chip, *Appl. Phys. Lett.* 84 (2004) 2193–2195.
22. A.D. Stroock, S.K. Dertinger, G.M. Whitesides, A. Ajdari, Patterning flows using grooved surfaces, *Anal. Chem.* 74 (2002) 5306–5312.
23. A.D. Stroock, S.K. Dertinger, A. Ajdari, I. Mezic, H.A. Stone, G.M. Whitesides, Chaotic mixer for microchannels, *Science* 295 (2002) 647–651.
24. C.-C. Cho, Electrokinetically-driven flow mixing in microchannels with wavy surface, *J. Colloid Interface Sci.* 312 (2007) 470–480.
25. E. Biddiss, D. Erickson, D. Li, Heterogeneous surface charge enhanced micromixing for electrokinetic flows, *Anal. Chem.* 76 (2004) 3208–3213.
26. N.G. Green, A. Ramos, A. González, H. Morgan, A. Castellanos, Fluid flow induced by nonuniform ac electric fields in electrolytes on micromicroelectrodes. I. Experimental measurements, *Phys. Rev. E* 61 (2000) 4011.
27. M. Yoshimura, K. Shimoyama, T. Misaka, and S. Obayashi, “Optimization of passive grooved micromixers based on genetic algorithm and graph theory,” *Microfluid. Nanofluidics*, vol. 23, no. 3, pp. 1–21, 2019.
28. Z. Kazemi, S. Rashidi, and J. A. Esfahani, “Effect of flap installation on improving the homogeneity of the mixture in an induced-charge electrokinetic micro-mixer,” *Chem. Eng. Process. Process Intensif.*, vol. 121, pp. 188–197, 2017.
29. Z. Wu and D. Li, “Micromixing using induced-charge electrokinetic flow,” *Electrochim. Acta*, vol. 53, no. 19, pp. 5827–5835, 2008.

Quantitative Analysis of Climatic Influence on the Cooling Tower Performance

Swastika Talukder, Priyanshu Roy, Trinanjan Mandal, Souvik Mandal, Sanchayan Mukherjee

1 Introduction

A cooling tower is a typical heat exchanger used in industries in which air and water are brought into direct contact in order to reduce the water temperature. In the process, a small volume of water evaporates, reducing the temperature of the water circulating through the tower. Water, heated in a water-cooled condenser, is pumped to the cooling tower. Nozzles spray the water on to banks of packing or fill, which slows down the flow of water falling downwards, and facilitates maximum air-water contact. Water is cooled through evaporative cooling by means of heat and mass transfer. The cooled water is then pumped back to the condenser or process equipment where it absorbs heat. The cycle continues.

Several researchers have devised working relations for the tower characteristic and effectiveness for a wide range of water-to-air flow (L/G) ratio, also providing the variations of the parameters with external conditions.

An empirical formula for effectiveness was also given by [1]. In another study a L/G ratio between 0.1-0.2 for cooling systems in buildings was considered. It was shown that there is a remarkable rise in the tower characteristic for low L/G ratios [2]. The height of an induced draft cooling tower for effective water cooling was suggested in [3]. Reference [4] used Merkel's method for cooling tower design. The equation for Merkel's integration for tower characteristic (KaV/L) is

$$\frac{KaV}{L} = c_w \int_{T_{WC}}^{T_{WH}} \frac{dT}{h_s - h_a} \quad (1)$$

Where

K = Mass transfer coefficient ($\text{kg/m}^2\text{s}$)

a = Area of heat and mass transfer per unit volume (m^2/m^3)

V = Volume of exchange core or packing (m^3)

L = Water flow rate (kg/s)

G = Air flow rate (kg/s)

T_{WC} = Cold water temperature ($^{\circ}\text{C}$)

T_{WH} = Hot water temperature ($^{\circ}\text{C}$)

h_s = Enthalpy of saturated air at local water temperature (kJ/kg)

h_a = Enthalpy of local air stream (kJ/kg)

The primary parameters analysed in this study were

Range(R) = $T_{WH} - T_{WC}$

Approach (A) = $T_{WC} - WBT$

Where

WBT = Wet bulb temperature (°C)

Effectiveness (ϵ) = Range/ (Range + Approach)

$$\epsilon = \frac{(T_{WH} - T_{WC})}{(T_{WH} - \text{WBT})} \quad (2)$$

The variation of cooling tower parameters like range, approach, tower characteristic etc. were studied with the changing external parameters like specific humidity and water inlet temperature in [5]. Performance variation of an induced draft cooling tower was studied in [6], [7].

2 Experimental Set up and Procedure

Experiments have been carried out in a Triplee-make induced draft cooling tower in the Heat Transfer Laboratory of Kalyani Government Engineering College from 24th September 2019 to 26th October 2021. Fig. 1 shows the cooling tower with different components. The water volume flow rate has been measured with a rotameter and the air velocity has been measured with a digital anemometer. The air volume flow rate is calculated using continuity equation as the inlet areas are known. The water has been heated by two water heaters. The temperature of water has been displayed by a digital temperature indicator. The dry bulb and wet bulb temperatures have been read with the help of a psychrometer.

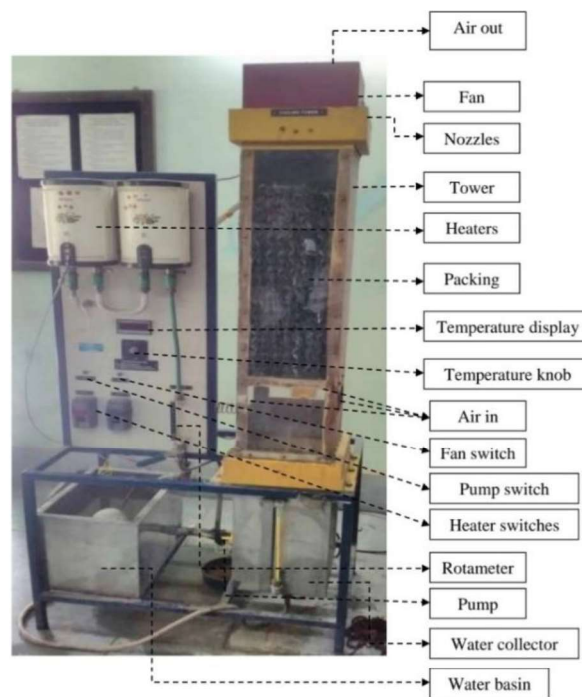


Fig. 1. The Cooling Tower Set Up

3 Sample Calculation

A sample calculation done on data collected in a day is presented as below:

- Dry bulb temperature = 24°C
- Wet bulb temperature = 22°C
- Relative humidity (ϕ) = 84% (From psychrometric chart)
- Mean water flow rate (L) = 0.01 kg/s
- Mean air flow rate (G) = 0.0810 kg/s

Therefore, mean water-to-air flow rate (L/G) = $0.01/0.0810 = 0.1234$

• Specific heat of water (c_w) = 4.186 kJ/kgK

• Temperature step = 5°C .

Table 1 shows the necessary steps leading to a sample calculation.

From Table 1,

Tower Characteristic (KaV/L) = $4.186 \times 5 \times 0.0582 = 1.218$

Average Effectiveness (ϵ) = 84.22%

4 Results and Discussion

Table 1. Sample Calculation

Serial No.	Hot Water Temperature (T_{WH}), $^\circ\text{C}$	Cold Water Temperature (T_{WC}), $^\circ\text{C}$	Mean Water Temperature ($T_w = (T_{WH} + T_{WC})/2$), $^\circ\text{C}$	Enthalpy of Saturated Air at T_w (h_s), kJ/kg	Enthalpy of Air (h_a), kJ/kg	$h_s - h_a$ (kJ/kg)	$1/(h_s - h_a)$ (kg/kJ)	Avg. $1/(h_s - h_a)$ (kg/kJ)	Effectiveness (ϵ), %
1	40	24	32.0	110.6200	72.7548	37.8652	0.0264		88.8
2	45	25	35.0	129.0000	74.8210	54.1790	0.0184	0.0224	86.9
3	50	27	38.5	153.9800	76.3707	77.6093	0.0129	0.0156	82.1
4	55	28	41.5	178.9900	78.4369	100.5531	0.0099	0.0114	81.8
5	60	29	44.5	207.9700	80.5031	127.4669	0.0078	0.0088	81.5
								Total = 0.0582	Avg. = 84.22

Calculations made on the experimental outputs have yielded significant results. MS Excel 2016 is used to plot the graphs between relevant parameters and also to find the correlations between them. Fig.2 reveals the gradual fall in tower effectiveness vis-a-vis the rise in the water-to-air flow rate (L/G). The increasing values of L/G indicates that the rise in water flow rate compared to that of the air stream allows less time for heat and mass transfer. Water falls due to gravity before it gets enough time to interact with air. The effectiveness is related with L/G ratio as

$$\epsilon = -4064.1 \left(\frac{L}{G}\right)^2 + 913.55 \left(\frac{L}{G}\right) + 32.973 \quad (3)$$

From Fig.2, it is evident that the peak occurs at an approximate L/G ratio of 0.11 for the cooling tower.

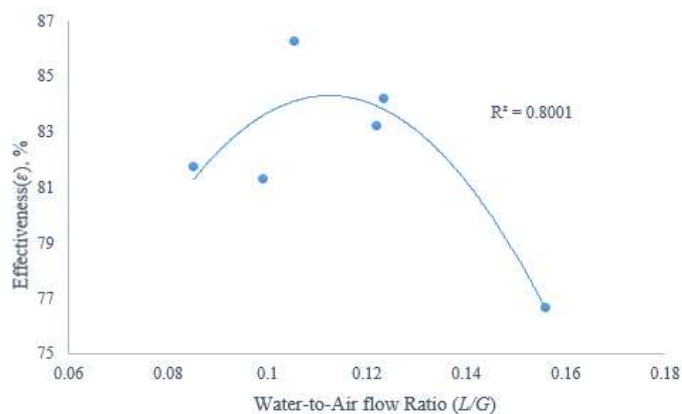


Fig. 2. Effectiveness vs. Water-to-Air flow Ratio

Fig. 3 shows the increasing trend of effectiveness (ϵ) with an increase in the relative humidity (ϕ). The more is ϕ , the more is the degree of saturation of the air, which in turn decreases the approach of the tower. Also, an increase in the degree of saturation of the air adds to the sensible heat transfer from the air to the hot water, facilitating a large range of the tower. Combination of these effects finally results in the rise of the effectiveness as per the following expression:

$$\epsilon = 40.363e^{0.0087(\phi)} \quad (4)$$

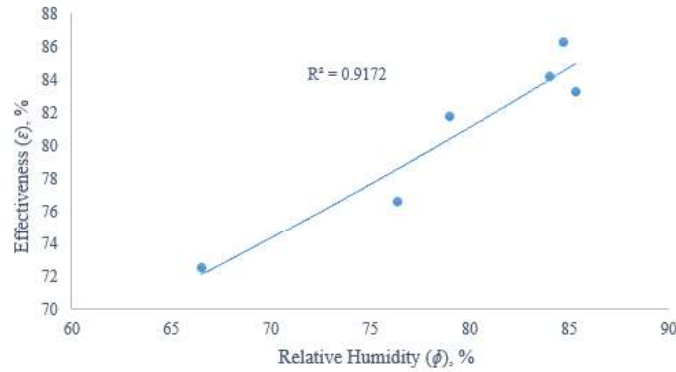


Fig. 3. Effectiveness vs. Relative Humidity

Cooling tower characteristic (KaV/L) follows a decreasing trend with an increase in the water-to-air flow ratio (L/G) as shown in Fig.4. Rise in L/G reduces the volume of the air cooling the unit mass of the hot water. As a consequence, air stream and water do not get sufficient time as well as proper contact area for evaporative cooling. Moreover, the continuous change in flow velocity responsible for the change in L/G ratio adds to the unevenness in the heat and mass transfer. A relation between KaV/L and L/G has been developed as under

$$\frac{KaV}{L} = 356.6 \left(\frac{L}{G}\right)^2 - 98.288 \left(\frac{L}{G}\right) + 7.8205 \quad (5)$$

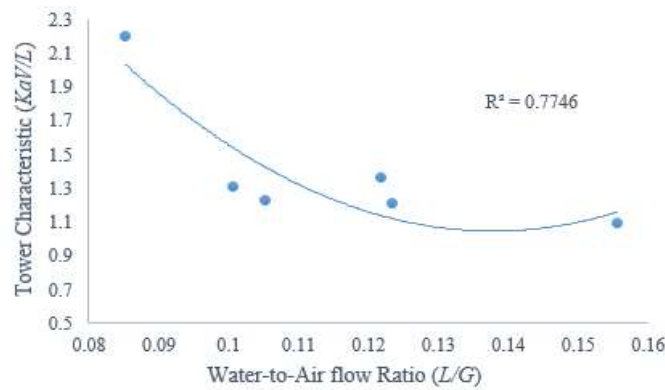


Fig. 4. Tower Characteristic vs. Water-to-Air flow Ratio

Fig.5 depicts that the tower characteristic increases as the relative humidity approaches saturation, in accordance with the following relation:

$$\frac{KaV}{L} = 0.0014(\phi)^2 - 0.2046(\phi) + 8.4687 \quad (6)$$

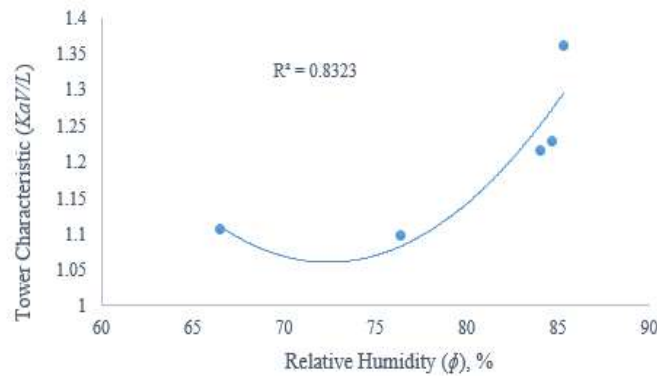


Fig. 5. Tower Characteristic vs. Relative Humidity

5 Conclusions

Following conclusions may be made from the investigation:

- Effectiveness of the tower shows significant variation with water-to-air flow ratio. Maximum effectiveness occurs at an optimum L/G ratio of 0.11 (approx.) for the cooling tower.
- Effectiveness rises exponentially with relative humidity. An increase in relative humidity, with the wet bulb temperature not being a constant, positively influences approach of the tower, increasing its effectiveness.
- The tower characteristic decays with water-to-air flow ratio. A high flow rate of water (generally indicating high velocity as well), allows less time for heat and mass transfer as water falls under gravity.
- The tower characteristic curve rises sharply after a certain value of relative humidity, unless the air is fully saturated. In this small domain of liquid flow rate in the present case, it has a positive influence on the heat and mass transfer capability of the tower.

Acknowledgment

The authors are indebted to Mr. Priyaranjan Jha and Mr. Prakash Choudhary, passed-out students of Kalyani Government Engineering College for their kind contributions during experimentation.

References

1. Q.J. Kong, X.Y. Zhao, D.Q. Xie, B. Zhang and P. Wang, "Experimental investigation of the heat and mass transfer phenomena in a counterflow wet cooling tower with foam ceramic packing". *Advances in Mechanical Engineering*, Vol. 10 (I), pp. 1-11, 2018.
2. B. Costelloe, D.P. Finn, "Heat transfer correlations for low approach evaporative cooling systems in buildings". *Applied Thermal Engineering*, Elsevier, Vol. 29 (1), pp.105-115, 2009.
3. M. Gholizadeh, M. Momayyeza, "The estimation of cooling tower height by modeling the water and air contact situation in cooling tower falling film". *Journal of Chemical Engineering and Materials Science*, Vol. 2 (2), pp. 21-27, February 2011.
4. P. Shah, N. Tailor, "Merkel's method for designing induced draft cooling tower". *International Journal of Advanced Research and Engineering and Technology*, Vol. 6 (2), pp. 63-70, February 2015.
5. R. Patel, R. Tripathi, S. Gangwar, "Conventional analysis of performance of Cooling tower used for Industrial purpose". *International Journal of Engineering and Advanced Technology*, Vol. 4 (4), pp. 133-138, April 2015.

6. S. Mukherjee, "Dependence of Cooling Tower Performance on Climatic Variation", The Innovative ACR, Vol. 15(2), pp. 44-48, April – May 2006.
7. S. Mukherjee, T. Chakraborty, R. S. Sen. & U. Kundu, "Cooling Tower Performance: How It Varies in Seasons", The Innovative ACR, Vol. 15 (5), pp. 20-28, October – November 2006.

Magneto-nanofluid flow evolution in a heart-shaped special cavity

Nirvik Hazra, Moumik Maitra, Prantik Chongdar, Nirmal K. Manna,
Nirmalendu Biswas, Dipak Kumar Mandal

1 Introduction

Cavity-like confined thermal systems undergoing natural convection find a variety of uses in widespread applications [1–9] such as heating/processing of food/food grains and materials, cooling of electronic and electrical devices, solar collectors, etc. The shape, as well as boundary conditions of the cavity, has a great role in the establishment of flow and associated transport phenomena. The present work considers a special shape of the cavity following the shape of the human heart that has not been investigated so far, although there exist many studies using complex geometries [10–18]. Magnetohydrodynamic (MHD) flow in recent times has been seriously attended to due to its versatile applications [19–22]. Magnetic fields usually act against the flow driving force; however, it is very useful to moderate/control local and global behavior of the transport phenomena. In dimensionless simulations, the magnetic field simulated through Hartmann number (Ha) is utilized to address the flow dampening impacts with the electrically conducting fluids. Another aspect of the current trend of studies is the use of mono or hybrid nanofluids [1–15,19–22] that possess superior transport capacity due to enhanced thermal conductivity. The correct choice of the volume concentration (ϕ) of the micron-order nanoparticles ($1\text{--}100\mu\text{m}$) is essential for heat transfer enhancement. The earlier mentioned literature along with review works on nanofluids [23,24] are also consulted for the preparation of the present work. The highly diluted nanofluids ($\phi < 5\%$) are more effective as realized from many studies. The physical parameter Rayleigh number (Ra) has a great impact during buoyancy-driven flow [25,26]; it formulates the buoyancy term and thus acts as a main driving force for establishing fluid flow in the closed cavity.

From the vast pool of literature on thermal convection in complex geometry, it reveals that the overall thermal performance of a device/ system is modulated significantly depending on the shape as well as boundary conditions of the geometry. The present work on this heart-shaped cavity undergoing natural convection is undertaken from a fundamental viewpoint in absence of such work in the literature. A typical differentially heated configuration is chosen for this investigation as detailed with Fig. 1. The evolutions of both fluid flow and heat transfer at different parametric conditions of magneto-thermal nanofluid flow are captured and presented.

2 Modeling

Fig. 1 shows the current problem, a differentially heated and specially designed heart-shaped enclosure of maximum height $2.5H$ and maximum width $2H$ (distance between two extremes of the sides). The length from the base of the cavity to the middle of the active walls is H . The heart-shaped cavity is geometrically symmetrical about the vertical axis. Isothermal conditions (temperature T_h for heating, T_c for cooling) for the active portions of the sidewalls are implemented for this study. The convective heat transfer of Cu-water nanofluid flow at 300K in the magneto-thermal working environment takes place inside the heart-shaped cavity (Fig. 1). The Hartmann number (Ha) is varied to alter magnetic field intensities. The buoyancy force establishes the flow that is modulated by the Rayleigh number (Ra) taking Prandtl number is $Pr = 5.83$.

N. Hazra¹, M. Maitra¹, P. Chongdar¹, N. K. Manna¹, N. Biswas^{2,*}, D. K. Mandal³

¹Department of Mechanical Engineering, Jadavpur University, Kolkata 700032, India

²Department of Power Engineering, Jadavpur University, Kolkata 700106, India

³Department of Mech. Engineering, College of Engg. and Management, Kolaghat 721171, India

*biswas.nirmalendu@gmail.com

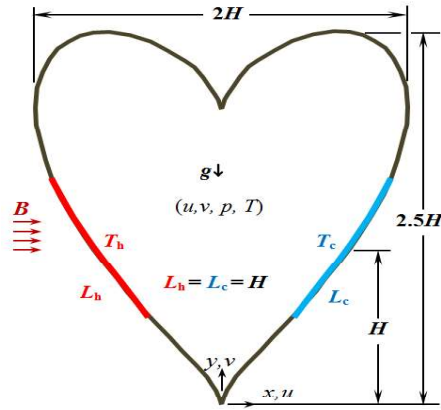


Fig. 1. Schematic of the heart-shaped cavity.

Based on the available literature [27], a single-phase homogenous model is applied by assuming a two-dimensional steady Newtonian laminar flow. The buoyancy force is added invoking the Boussinesq approximation. Applying the fundamental principles (of conservations), the mass, momentum, and energy balance equations are respectively derived as

$$\frac{\partial u}{\partial x} + \frac{\partial v}{\partial y} = 0 \quad (1)$$

$$\rho \left(u \frac{\partial u}{\partial x} + v \frac{\partial u}{\partial y} \right) = -\frac{\partial p}{\partial x} + \mu \left(\frac{\partial^2 u}{\partial x^2} + \frac{\partial^2 u}{\partial y^2} \right) \quad (2)$$

$$\rho \left(u \frac{\partial v}{\partial x} + v \frac{\partial v}{\partial y} \right) = -\frac{\partial p}{\partial y} + \mu \left(\frac{\partial^2 v}{\partial x^2} + \frac{\partial^2 v}{\partial y^2} \right) - \sigma B^2 v + \rho g \beta (T - T_c) \quad (3)$$

$$\rho C_p \left(u \frac{\partial T}{\partial x} + v \frac{\partial T}{\partial y} \right) = k \left(\frac{\partial^2 T}{\partial x^2} + \frac{\partial^2 T}{\partial y^2} \right) \quad (4)$$

The above-mentioned dimensional governing equations in the x - y plane are transformed into the non-dimensional X - Y plane as expressed below

$$\frac{\partial U}{\partial X} + \frac{\partial V}{\partial Y} = 0 \quad (5)$$

$$\left(U \frac{\partial U}{\partial X} + V \frac{\partial U}{\partial Y} \right) = -\frac{1}{\rho_r} \frac{\partial P}{\partial X} + \nu_r \text{Pr} \left(\frac{\partial^2 U}{\partial X^2} + \frac{\partial^2 U}{\partial Y^2} \right) \quad (6)$$

$$\left(U \frac{\partial V}{\partial X} + V \frac{\partial V}{\partial Y} \right) = -\frac{1}{\rho_r} \frac{\partial P}{\partial Y} + \nu_r \text{Pr} \left(\frac{\partial^2 V}{\partial X^2} + \frac{\partial^2 V}{\partial Y^2} \right) - \frac{\sigma_r}{\rho_r} \text{Pr} \text{Ha}^2 V + \frac{(\rho\beta)}{\rho\beta_f} \text{RaPr}\theta \quad (7)$$

$$\left(U \frac{\partial \theta}{\partial X} + V \frac{\partial \theta}{\partial Y} \right) = \alpha_r \left(\frac{\partial^2 \theta}{\partial X^2} + \frac{\partial^2 \theta}{\partial Y^2} \right) \quad (8)$$

The transformation of primitive variables (u, v, p, T) is made on the basis of certain scales (H for length, α_f/H for velocity) to form dimensionless velocity components, pressure and temperature (U, V, P, θ), and other associated dimensionless parameters ($\text{Pr}, \text{Ra}, \text{Ha}, \text{Nu}$) as given by

$$(X, Y) = (x, y) / H, (U, V) = H(u, v) / \alpha_f,$$

$$\theta = (T - T_c) / (T_h - T_c), P = pH^2 / \rho_f \alpha_f^2,$$

$$\text{Pr} = \frac{\nu_f}{\alpha_f}, \text{Ra} = \beta_f H^3 (T_h - T_c) \frac{g}{\nu_f \alpha_f}, \text{Ha} = BH \sqrt{\frac{\sigma_f}{\mu_f}} \quad (9)$$

$$\text{Nu} = k_r \int_{s=0}^1 \left(-\frac{\partial \theta}{\partial n} \right)_{\text{hot or cold wall}} ds \quad (10)$$

In the above equations, the base fluid properties are indicated by the subscript “*f*”. The symbols (μ , ν , σ , ρ , α , β) represent thermal volumetric thermal expansion coefficient, and kinematic viscosity, electrical conductivity, density, diffusivity, and expansion coefficient, respectively. These properties of the Cu-water nanofluid (without any subscript) taken from [27] are computed using the well-known closure relations available in many works [27,28] (therefore, the same is not reproduced here due to stringent space limitation). The effect of property changes of the working nanofluid is included in the governing equations with the appropriate property ratios (with the subscript “*r*”) as indicated in Eqs. (5) to (8). The global heat transfer from the active heating or cooling wall is assessed using the average Nusselt number, Nu, given in Eq. (10). The finite element method is applied (details can be found in [29-31]) to solve this problem numerically considering high-resolution mesh.

The associated boundary values for solving the problem are applied as $\theta = 0$ for the cold portion of the right wall, $\theta = 1$ for the left heated wall, normal gradient $d\theta/dn = 0$ for the rest of the adiabatic walls, and $U, V = 0$ implemented to the surrounding walls of the cavity.

3 Results And Discussion

The implications of our findings primarily delved into differences of flow regimes (conduction and convection modes) by varying the following parameters namely $\text{Ra} = 10^3$ - 10^6 , $\text{Ha} = 0$ -70), and nanofluid concentration ($\phi = 0, 2$, and 3%) in a heart-shaped differentially heated enclosure. The volumetric concentration is of the Cu concentration in H_2O base fluid. In the following subsections, one parameter is swept through all its values while a constant value is assigned to the remaining two and the resulting streamline and isotherm contours are obtained. Further sectional velocity and temperature plots along with the effect of the above-mentioned parameters on Nusselt number are also shown.

3.1 Effect of Rayleigh number

Fig. 2 illustrates the effect of Ra on streamline and isotherm behaviors of a differentially heated heart-shaped enclosure when the Hartmann number (Ha) remains constant at 30 and volume concentration fixed at 1%. In the figure, the first row depicts the variation of streamlines and the second row shows the variation of isotherms upon changing Ra. At a lower value of Rayleigh number ($\text{Ra} = 10^4$), the flow pattern is almost symmetric vertically due to the low buoyancy force and heat transfer mode being primarily conduction. This depicts a small circular core at the center.

Upon increasing the Rayleigh numbers to 10^5 and 10^6 , the vortices start stretching towards the periphery and the fluid flows faster from the middle portion of the cavity and thus pushing the flow field towards the boundary. Overall flow strength increases due to the increased buoyancy forces caused by the increment of the Rayleigh number. The streamlines are denser at the active wall portions. The core streamlines are stretched horizontally, particularly more prominent at the highest Ra. Therefore, it concludes that upon increasing the Rayleigh number, flow strength increases which in turn increases the convective heat transfer.

Now, for isotherm plots, at a low Ra (10^4), they are mostly vertically oriented. Upon increasing the Rayleigh number, the isotherm lines started becoming horizontal. The isotherm lines become mostly

horizontal at high Ra (10^6). Thermally conductive heat transfer drives the nanofluid flow phenomenon inside the heart-shaped cavity at low Ra . Another thermal convection mode plays the principal role when the Rayleigh number is augmented to 10^5 , 10^6 , or higher, and then it is truly called a natural convection system.

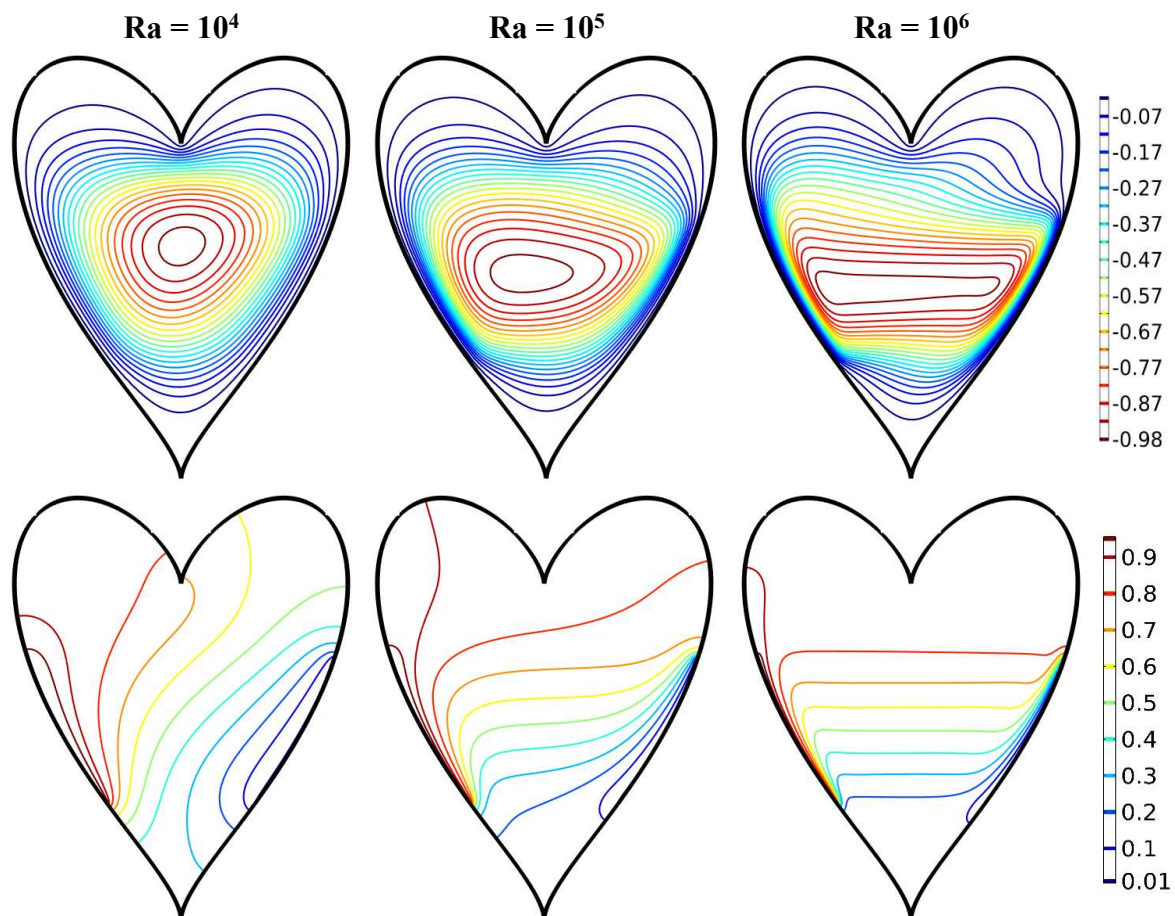


Fig. 2. Streamline (top) and isotherm plots with $Ha = 30$, $\phi = 1\%$.

3.2 Effect of Hartmann number

The change in streamline and isotherm plots shown in Fig. 3 demonstrates magnetic field effects at $Ha = 0, 50, 70$. At $Ha = 0$, the natural convection takes place with no magnetic field present. The streamlines are depicted clockwise with two small cells placed diagonally opposite to the central portion of the differentially heated heart-shaped cavity.

When we increase Ha to 50, the reduced flow-velocity becomes a smooth round core in the middle zone. The overall strength of fluid flow also reduces. This happens because the flow field is disturbed by the opposing Lorentz forces, which come into play vigorously with an increase in Hartmann number.

Now for isotherms, when the Hartmann number is 0, they are mostly horizontal and for $Ha = 70$, they are depicted as vertical mainly along the periphery, i.e., tend to get perpendicular to the magnetic field direction. The wall-adhering isotherms shift away from the walls, indicating a thickening of the thermal boundary layer. Thus, heat transfer is compromised upon an increment of Ha .

3.3 Effect of volumetric concentration

Fig. 4 shows the Streamline and Isotherm plots for $Ra = 10^6$ and $Ha = 30$ as we vary the percentage of volumetric concentration or ϕ from 0 to 2%, and 3%. As we can see from the below-given figures, there

is no noticeable change in flow through the cavity due to varying values of volumetric concentration in either streamlines or isotherms. Thus, the presence of Cu particles has a minute impact on velocity or temperature variations in a heart-shaped cavity.

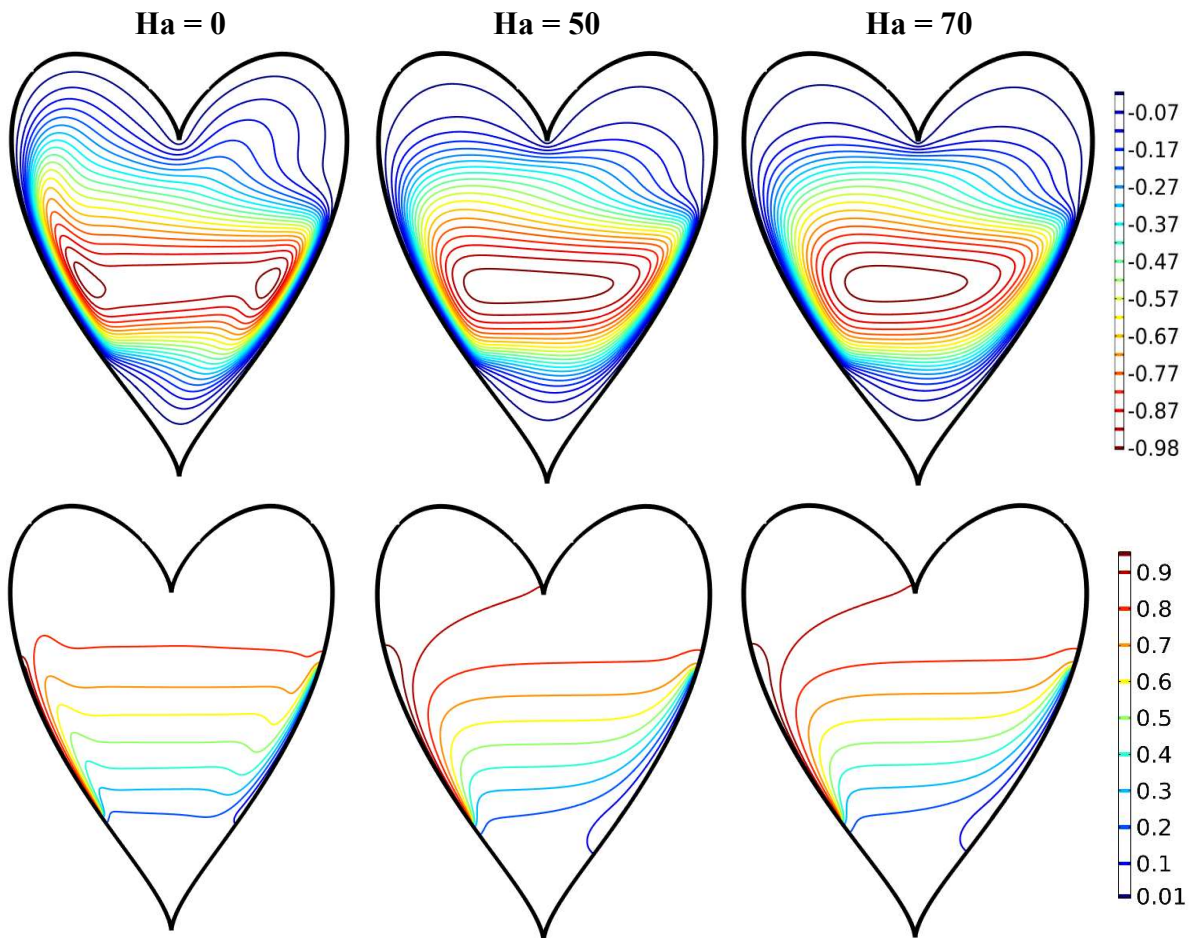


Fig. 3. Streamline (top) and isotherm plot with $Ra = 10^6$, $\phi = 1\%$.

3.4 Analysis of global estimates

The global estimates of thermofluid phenomena within the cavity are indicated in Table I. It clearly shows that the thermal performance along with the buoyancy-induced flow increases as the Ra increases. Both the Nusselt number (Nu) and the minimum streamfunction (ψ_{min}) are found to significantly increase with Ra . However, the flow-dampening effect due to the enhanced Ha is also prominently reflected from Nu and ψ_{min} listed in the table for $Ha = 0, 10, 70$. The flow dampening becomes significantly higher at $Ha = 70$.

Table 1. Average Nusselt number (Nu) and Streamfunction.

Parameters	ϕ	Ha	$Ra = 10^4$	$Ra = 10^5$	$Ra = 10^6$
Nu	1%	0	3.124	5.650	10.170
ψ_{min}	1%	0	-7.136	-12.133	-20.524
Nu	1%	10	2.581	5.291	9.963
ψ_{min}	1%	10	-5.063	-10.567	-19.587
Nu	1%	70	1.130	1.947	5.768
ψ_{min}	1%	70	-0.409	-2.923	-9.660

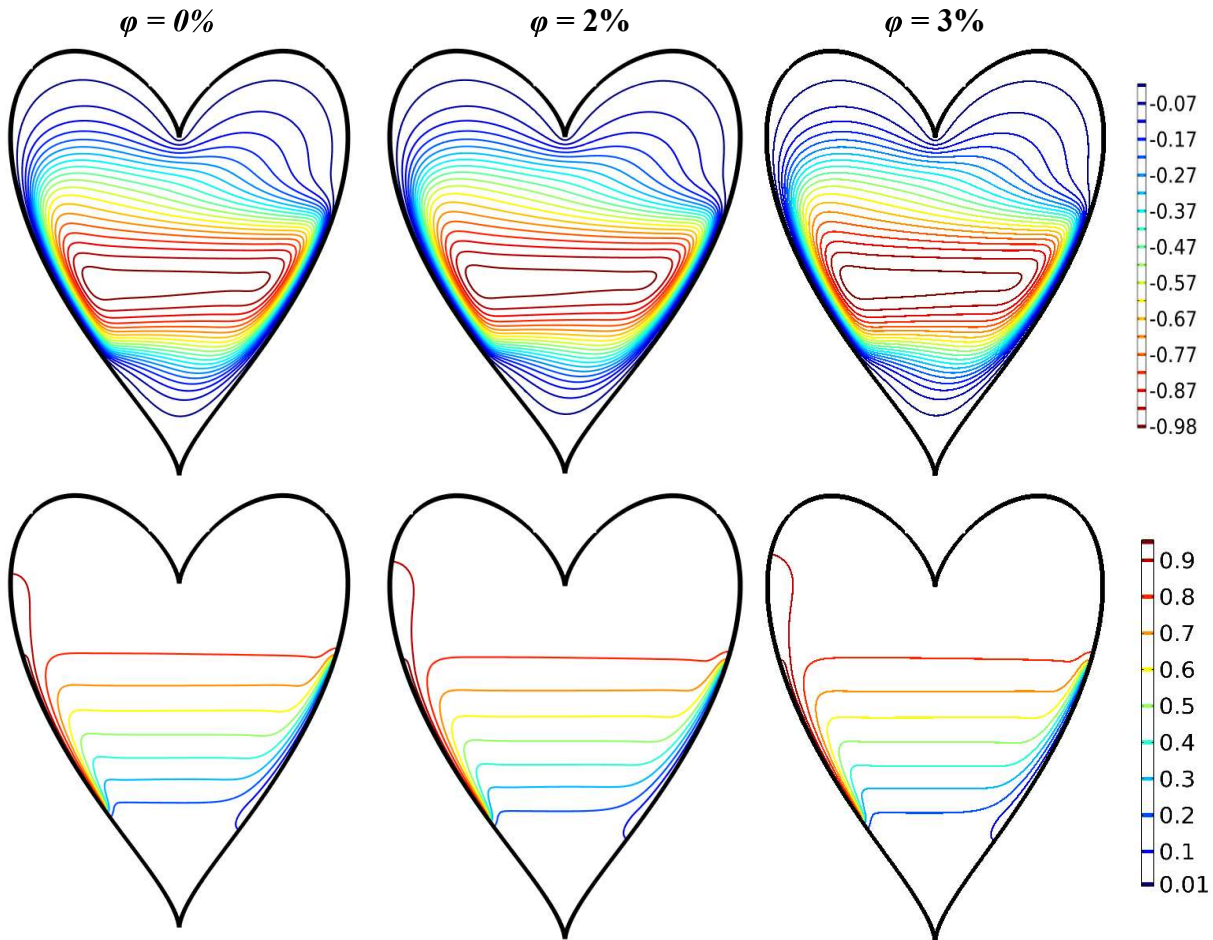


Fig. 4. Streamline (top) and isotherm plots with $Ra = 10^6$, $Ha = 30$.

The mid-sectional velocities (U , V) shown in Figs. 5 and 6 clearly reveal thin thermal boundary layer formation at higher Ra and lower Ha (Fig. 5). The positive peak of V indicates the uprising flow along the left hot wall and its opposite happens at the left cold wall. The main flow takes near the sidewalls. The middle stretch has almost zero vertical component of velocity, which is also justified from the horizontal streamline contours about the mid horizontal plane. It leads to higher Nu presented in Table I. The mid-sectional horizontal U in Fig. 6 shows the rightward flow (positive magnitude of U) taking place at the top of the cavity. Thus, a clockwise circulation occurs in the cavity.

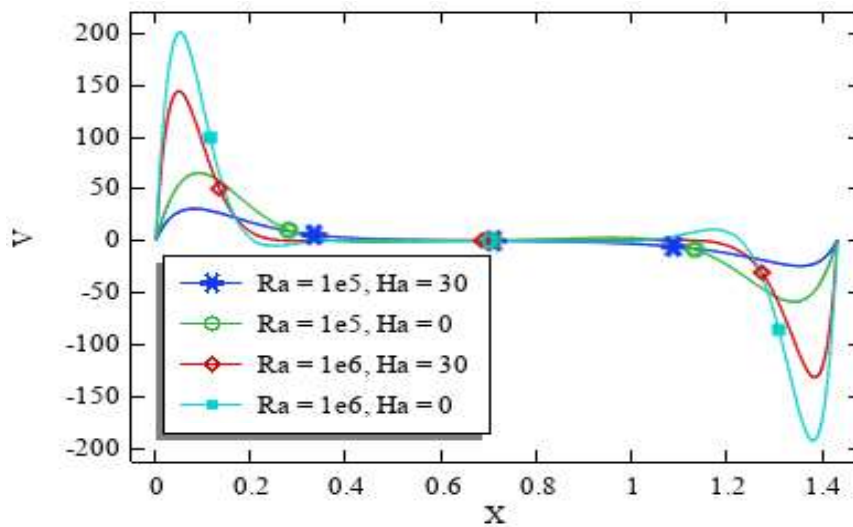


Fig. 5. Horizontal mid-active wall sectional V – velocity plot.

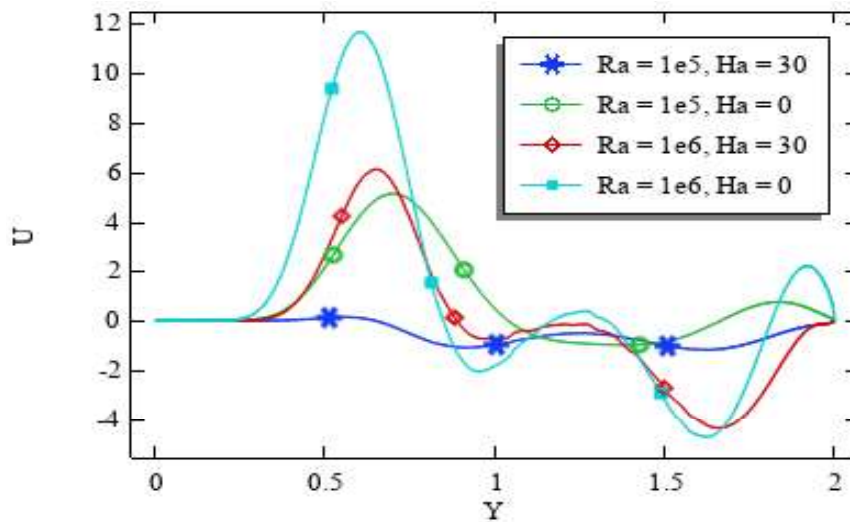


Fig. 6. Vertical mid-sectional U – velocity plot.

4 Conclusions

Magnetic field affected nanofluid flow is studied in a specially designed heart-shaped enclosure. Differential heating strategy is applied for a range of control parameters Ra and Ha . The salient points are summarized below.

- There is a direct impact between an increase in Ra and convective heat transfer domination. Both flow velocity and heat transfer rate increase as a result when Ra increases.
- The buoyancy force driving natural convection is counteracted by increasing the Lorentz force through an increment of Hartmann number. As a result not only is flow velocity compromised but heat transfer rates also get reduced.
- Within the study ranges of the present problem configuration, the effect of nanofluid concentration is less revealed.

Future study of this problem could be extended considering other multiphysical scenarios (like porous media, radiation, etc.) with modified boundary conditions like bottom heating or distributed heating/cooling.

Nomenclature

B	magnetic field, $N/A \cdot m^2$	U, V	dimensionless velocity components
H	length scale, m	X, Y	dimensionless coordinates
Ha	Hartmann number	α	thermal diffusivity, m^2/s
Nu	average Nusselt number	θ	dimensionless temperature
p	pressure, Pa	σ	electrical conductivity, $\mu S \cdot cm^{-1}$
Pr	Prandtl number	ψ_{min}	dimensionless min. stream function
Ra	Rayleigh number	ν	kinematic viscosity, m^2/s
T	temperature, K	ϕ	nanofluid volumetric concentration
T_h	temperature for heating	f	fluid-based properties
T_c	temperature for cooling	r	property ratios

References

1. Hashemi-Tilehnoee, M., Dogonchi, A. S., Seyyedi, S. M., Chamkha, A. J., & Ganji, D. D. (2020). Magnetohydrodynamic natural convection and entropy generation analyses inside a nanofluid-filled

- incinerator-shaped porous cavity with wavy heater block. *Journal of Thermal Analysis and Calorimetry*, 141, 2033–2045.
2. Izadi, M., Mohebbi, R., Chamkha, A. J. & Pop, I. (2018). Effects of cavity and heat source aspect ratios on natural convection of a nanofluid in a C-shaped cavity using Lattice Boltzmann method. *International Journal of Numerical Methods for Heat & Fluid Flow*, 28(8), 1930–1955.
 3. Abbas, Z., Rafiq, M. Y., Hasnain, J. & Umer, H. (2021). Impacts of Lorentz force and chemical reaction on peristaltic transport of Jeffrey fluid in a penetrable channel with injection/suction at walls. *Alexandria Engineering Journal*, 60(1), 1113–1122, 2021.
 4. Biswas, N., Mandal, D. K., Manna, N. K., Gorla, R. S. R. & Chamkha, A. J. (2021). Magnetohydrodynamic thermal characteristics of water-based hybrid nanofluid filled non-Darcian porous wavy enclosure: effect of undulation. *International Journal of Numerical Methods for Heat & Fluid Flow*, doi: 10.1108/HFF-03-2021-0190.
 5. Mandal, D. K., Biswas, N., Manna, N. K., Gorla, R. S. R. & Chamkha, A. J. (2021). Role of surface undulation during mixed bioconvective nanofluid flow in porous media in presence of oxytactic bacteria and magnetic fields. *International Journal of Mechanical Science*, 211, 106778.
 6. Biswas, N., Manna, N. K., Chamkha, A. J. & Mandal, D. K., (2021). Effect of surface waviness on MHD thermo-gravitational convection of Cu–Al₂O₃–water hybrid nanofluid in a porous oblique enclosure. *Physica Scripta*, 96, 105002.
 7. Mondal, M. K., Biswas, N., Manna, N. K. & Chamkha, A. J., (2021). Enhanced magnetohydrodynamic thermal convection in a partially-driven cavity packed with a nanofluid-saturated porous medium, *Mathematical Methods in Applied Science*, doi: 10.1002/mma.7280.
 8. Sarkar, U. K., Biswas, N. & Öztop H. F., (2021). Multiplicity of solution for natural convective heat transfer and entropy generation in a semi-elliptical enclosure. *Physics of Fluids*, 33, 013606.
 9. Biswas, N., Sarkar, U. K., Chamkha, A. J., & Manna, N. K. (2021). Magneto-hydrodynamic thermal convection of Cu–Al₂O₃/water hybrid nanofluid saturated with porous media subjected to half-sinusoidal nonuniform heating. *Journal of Thermal Analysis and Calorimetry*, 143, 1727–1753.
 10. Ma, Y., Rashidi, M. M., Mohebbi, R. & Yang, Z. (2021). Investigation of magnetohydrodynamics in Ag–TiO₂/water hybrid nanofluid in a Shamse knot shaped cavity. *International Journal of Numerical Methods for Heat & Fluid Flow*, 31(1), 251–272.
 11. Ghalambaz, M., Zadeh, S. M. H., Veismoradi, A., Sheremet, M. A. & Pop, I. (2021). Free convection heat transfer and entropy generation in an odd-shaped cavity filled with a Cu–Al₂O₃ hybrid nanofluid. *Symmetry*, 13, 122.
 12. Sen, K., Manna, N. K. & Biswas, N. (2021). Thermo-fluidic transport process in a double-driven cavity with triangular adiabatic obstacles. *Materials Today: Proceedings*, doi: 10.1016/j.matpr.2021.09.276.
 13. Maitra, S., Mandal, D. K., Biswas, N., Datta, A. & Manna, N. K. (2021). Hydrothermal performance of hybrid nanofluid in a complex wavy porous cavity imposing a magnetic field. *Materials Today: Proceedings*, doi: 10.1016/j.matpr.2021.09.078.
 14. Parvin, S., Roy, N. C. & Saha, L. K. (2021). Magnetohydrodynamic natural convection of a hybrid nanofluid from a sinusoidal wavy cylinder placed in a curve-shaped cavity. *AIP Advances*, 11(8), 085029.
 15. Rahmati, A. R. & Nemati, M. (2018). Investigation of magnetic field effect on nanofluid mixed convection inside lid-driven K-shaped enclosure using Lattice Boltzmann Method. *Journal of Solid and Fluid Mechanics*, 8(1), 111–126.
 16. Mandal, D. K., Manna, N. K. & Chakrabarti, S. (2010). Numerical study of blood flow through different double bell-shaped stenosed coronary artery during the progression of the disease. atherosclerosis. *International Journal of Numerical Methods for Heat & Fluid Flow*, 20(6), 670–698.
 17. Mandal, D. K., Manna, N. K. & Chakrabarti, S. (2011). Influence of different bell-shaped stenoses on the progression of the disease, atherosclerosis. *Journal of Mechanical Science & Technology*, 25(8), 1933.

18. Goswami, P., Mandal, D. K., Manna, N. K. & Chakrabarti, S. (2014). Study on the effect of steady, simple pulsatile and physiological pulsatile flows through a stenosed artery. *Heat and Mass Transfer*, 50(10), 1343–1352.
19. Biswas, N., Manna, N. K., N. K., Mandal, D. K. & Gorla, R. S. R. (2021). Magnetohydrodynamic mixed bioconvection of oxytactic microorganisms in a nanofluid-saturated porous cavity heated with a bell-shaped curved bottom. *International Journal of Numerical Methods for Heat & Fluid Flow*, 15(4), 3722–3751.
20. Biswas, N., Manna, N. K. & Chamkha, A. J. (2021). Effects of half-sinusoidal nonuniform heating during MHD thermal convection in Cu–Al₂O₃/water hybrid nanofluid saturated with porous media. *Journal of Thermal Analysis and. Calorimetry*, 143, 1665–1688.
21. Mallick, H., Mondal, H., Biswas, N. & Manna, N. K. (2021). Buoyancy driven flow in a parallelogrammic enclosure with an obstructive block and magnetic field. *Materials Today: Proceedings*, 44(2), 3164–3171.
22. Chatterjee, D., Manna, N. K., Mandal, D. K. & Biswas, N. (2021). Effect of partial magnetic field on thermo gravitational convection in an inclined cavity. *IOP Conference Series: Materials Science and Engineering*, 1080(1), 012030.
23. Bahiraei, B. & Heshmatian, S. (2018). Electronics cooling with nanofluids: a critical review. *Energy Conversion and Management*, 172, 438–56.
24. Khanafer, K. & Vafai, K. (2018). A review on the applications of nanofluids in the solar energy field. *Renewable Energy*, 123, 398–406.
25. Mahapatra, P. S., Manna, N. K. & Ghosh, K. (2015). Effect of active wall location in a partially heated enclosure. *International Communication in Heat and Mass Transfer*, 61, 69–77.
26. Biswas, N., Mahapatra, P. S. & Manna, N. K. (2016). Buoyancy-driven fluid and energy flow in protruded heater enclosure. *Meccanica*, 51(9), 2159–2184.
27. Biswas, N., Manna, N. K., Datta, P. & Mahapatra, P. S. (2018). Analysis of heat transfer and pumping power for bottom-heated porous cavity saturated with Cu-water nanofluid. *Powder Technology*, 326, 356–369.
28. Ghasemi, B. & Aminossadati, S. M. (2009). Natural convection heat transfer in an inclined enclosure filled with water–CuO nanofluid. *Numerical Heat Transfer A*, 55 (9), 807–823.
29. Lewis, R. W., Nithiarasu, P. & Seetharamu, K. N. (2004). *Fundamentals of the Finite Element Method for Heat and Fluid Flow*. John Wiley and Sons.
30. Zienkiewicz, O. C. & Taylor, R. L. (1991). *The Finite Element Method*. London: McGraw-Hill.
31. Das, D. & Basak, T. (2017). Role of distributed/discrete solar heaters for the entropy generation studies in the square and triangular cavities during natural convection. *Applied Thermal Engineering*, 113, 1514–1535.

ANN Modeling to Estimate Cutting Forces in Turning Operation

Mintu pal, Sibsankar Dasmahapatra

1 Introduction

Turning is one of the machining processes performed in lathe. It is an example of conventional machining process. Lathe consists head stock in one end and tail stock in other end. To perform the turning operation, the work piece is to be clamped with help of head stock and axially supported by tail stock. The head stock is attached to a motor through some mechanical component. Power is provided to the motor and jaw attached to the head stock provide a rotational movement to the work piece. Same time a cutting tool is attached to a tool post and when this tool comes in touch to the rotating work piece a relative motion between cutting tool and work piece is established. Which causes material removal from the work piece in the form of chip. To remove the material from the work piece forces are required which is related to the energy requirement during the process. Forces have different component such as main cutting force, feed force and thrust force [1-2]. These forces can be easily measured with help of dynamometer.

The forces developed during turning are not only depend on the material removal also depend on the geometrical structure of the cutting tool, cutting speed, feed, depth-off cut and many other condition. So the perfect combination of optimum tool geometry and cutting parameters are required to reduce the force requirement during cutting operation [1-4]. It can be said that the different cutting parameters have direct impact on the machining variables. In a single research paper it is not possible to study the effect of all the cutting parameters, due to this reason in this paper rake angle, entering angle and cutting speed have been consider to study their effect on the machining variables such as main cutting force, feed force and thrust force. To predict the cutting forces under different cutting conditions two models have been established with help of artificial neural network (ANN).

In past few years researchers viewed their interest in the field of estimation or prediction along with optimization with help of soft computing model. Sharma et al. [1] estimated the cutting forces and surface roughness by considering different machining variables such as approaching angle, speed, feed and depth of cut. Ozkan et al. [2] designed model with two tools artificial neural network (ANN) and fuzzy expert system (FES). Rao et al. [3] observed the flank wear and tool tip temperature with the help of temperature measurement sensor. Asilturk et al. [4] carried out an experiment based on prediction of surface roughness in turning operation performed under different cutting parameters. The models were based on multiple regression and ANN. According to the research the predicted result getting by ANN model has more accuracy as compared to the result getting from the multiple regression model. Altintas et al. [5] introduced a model made with multilayer feed-forward neural network to predict the tool wear in case of turning operation with tungsten carbide cutting tool and number of different work piece material under different cutting condition. With help of ANN the estimation of the control parameters can be done for the real time control of the electrohydraulic linear [6-7], angular [8] and multiple degree of freedom [9-11]. Empirical formulation for predicting the energy consumption in turning operation [12] and online monitoring in turning operation by ANN [13] are also interesting research work in present day. The modeling of the multilayer feed forward neural network-MLFFNN has been done in the next section followed by the detailed discussion of the architecture of ANN for training, testing and validation. The predictions of main cutting force, feed force and thrust force have been done in the results and discussion section. The comparison between actual values [14] and estimated values found out in this project work has been done with help of Bar Chart.

M. Pal*, S. Dasmahapatra

Department of Mechanical Engineering, Kalyani Government Engineering College, India 741235

2 Modelling of Multilayer Feedforward Neural Network-MLFFNN

In past few years Artificial neural networks (ANN) applications are gradually increased. Now a days ANN becomes one of the most popular modeling tools due to its high performance computing, accuracy, big application potential. Here the term neural network derives from human brain or it can be said that from human nervous system [15]. That's the reason it is named as artificial neural network. In actually human brain is the example of natural neural network with approximately 10 billion of neurons and 60 trillions of interconnections.

In general an ANN model consists of three different layer namely known as input layer, hidden layer and output layer [16]. The input layer is connected to the input variables. In this current work the input variables are rake angle (A), entering angle (B) and cutting speed (C). Similarly the output layer is connected to the output variables such as main cutting force F_m , feed force F_f and thrust force F_t . In this paper work MLFFNN has been used and the structure of this model with all three layers has been shown in Fig. 1. The input and output layers are interconnected through hidden layer. The number of neurons in input and output layer are equal to the number of variables in input and output layers respectively. But the selection of number of hidden layer and number of neurons in each hidden layer is complicated.

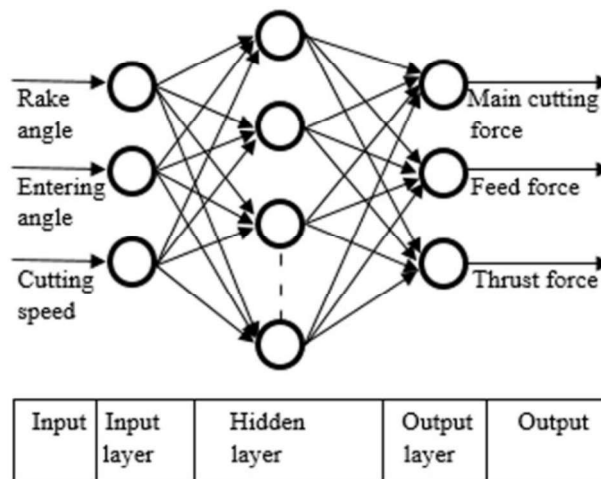


Fig. 1 Multilayer feed forward neural network architecture.

3 Architecture of Ann For Training, Validation, Testing and Evaluation

3.1 Data-set for training, validation and testing

Saglam et al. [14] conducted an experimental setup to study the effect of tool geometry and cutting speed on cutting forces. Total 64 set of data is available in the research work done by Saglam et al. (2007). For this project work 18 set of data has been chosen and used as a training data. Similarly 3 set of data has been chosen for testing and 9 set of data has been used for validation purpose. The corresponding Training data in Table 1, Validation data in Table 2 and Test data in Table 3 have been taken from Saglam et al. (2007).

3.2 Network architecture and neural network training

In this paper work two different models have been constructed to train the training data available in Table 1. The models have been made by considering different training functions, number of neurons and number of epochs. Model 1 has been constructed with 10 number of neurons and 100 epochs and training is performed with Levenberg-Marquardt training function. Model 2 has been created with 20 number of neurons and 200 epochs and training is performed with Bayesian Regularization training function.

Table 1. Training data.

Ex. No.	Rake angle (°)	Entering angle (°)	Cutting speed (m/min)	Main cutting Force (N)	Feed force (N)	Thrust force (N)
1	0	45	113	491	252	341
2	0	45	160	481	194	306
3	0	60	113	480	247	210
4	0	60	160	453	217	185
5	0	75	75	490	344	190
6	0	75	160	448	233	150
7	6	45	113	437	107	95
8	6	45	160	419	95	78
9	6	60	75	423	225	106
10	6	60	160	405	117	76
11	6	75	75	422	252	69
12	6	75	113	409	177	56
13	12	45	75	403	138	118
14	12	45	113	398	118	105
15	12	60	75	396	150	92
16	12	60	160	376	118	72
17	12	75	75	393	164	56
18	12	75	113	381	149	53

Table 2. Validation data.

Ex No.	Rake angle (°)	Entering angle (°)	Cutting speed (m/min)	Main cutting force (N)	Feed force (N)	Thrust force (N)
1	0	60	75	497	279	239
2	0	75	113	475	258	176
3	0	90	236	410	271	118
4	6	45	75	456	194	132
5	6	75	160	400	124	48
6	6	90	236	388	111	37
7	12	45	160	386	105	94
8	12	60	113	382	136	78
9	12	90	236	367	136	29

Table 3. Test data.

Ex No.	Rake angle (°)	Entering angle (°)	Cutting speed (m/min)	Main cutting force (N)	Feed force (N)	Thrust force (N)
1	0	45	75	520	267	372
2	6	60	113	411	147	82
3	12	75	160	372	142	49

The network architecture of model 1 has been depicted in Fig. 2 which reflects the number of input 3, number of hidden layer 1, number of neurons in hidden layer 10 and the number of output 3. Neural Network-NN Training of Model 1 has been given in the Fig. 3 which shows the data division as randomly, the training function Levenberg-Marquardt, the basis of performance Mean Squared Error and the number of epochs 100.

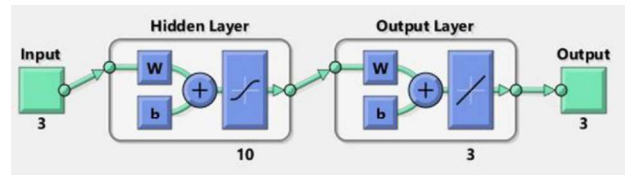


Fig. 2 Network architecture of model 1.

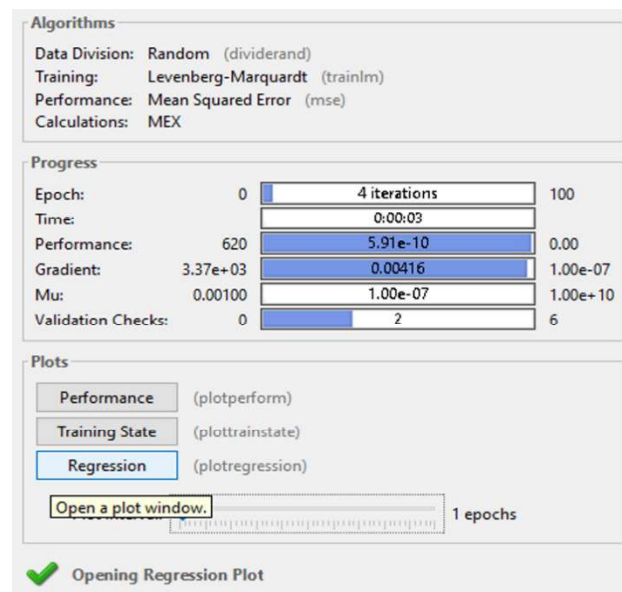


Fig. 3 Neural network training of model 1.

The network architecture of model 2 has been given in Fig. 4 which reproduces the number of input 3, number of hidden layer 1, number of neurons in hidden layer 20 and the number of output 3. Neural Network-NN Training of Model 1 has been depicted in the Fig. 5 which indicates the data division as random, the training function Bayesian Regularization, the basis of performance Mean Squared Error and the number of epochs 200.

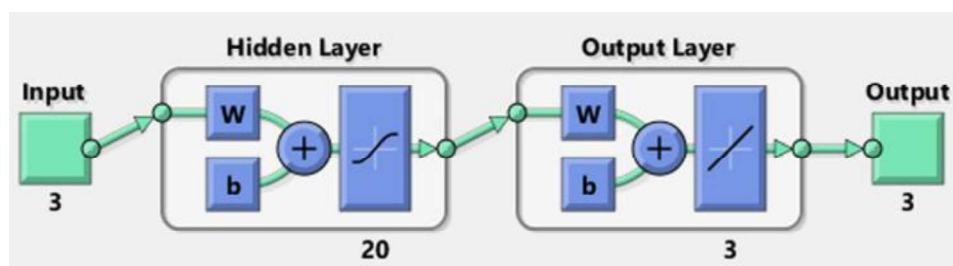


Fig. 4 Network architecture of model 2.

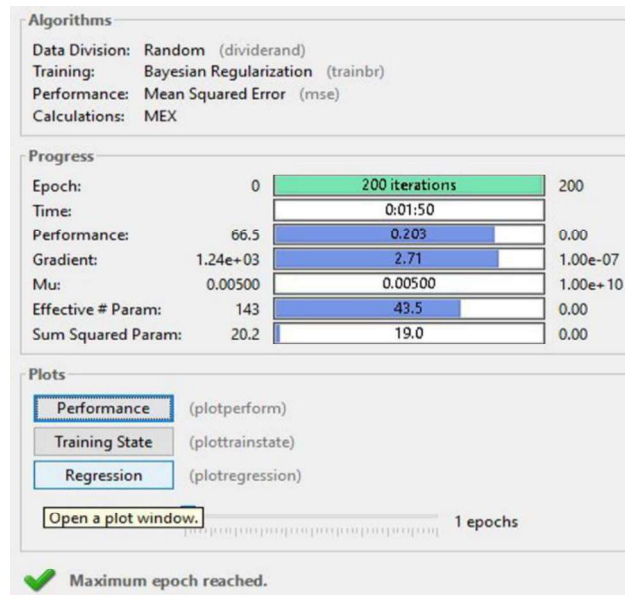


Fig. 5 Neural network training of model 2.

The regression plots and the corresponding regression analysis of Fig. 3 and Fig. 5 have been discussed in the next section.

4 Results and Discussion

In this section Regression analysis of each model have been done with help of training, testing and validation. After Regression analysis, the estimated cutting forces have been found out and compared with the actual values with help of Bar Chart.

4.1 Regression analysis

The Neural Network training regression results of Model 1 have been given in the Fig. 6. The regression plot represents that the network performance has been done with training $R=1$, testing $R=0.99185$, validation $R=0.99662$ and all $R=0.99775$.

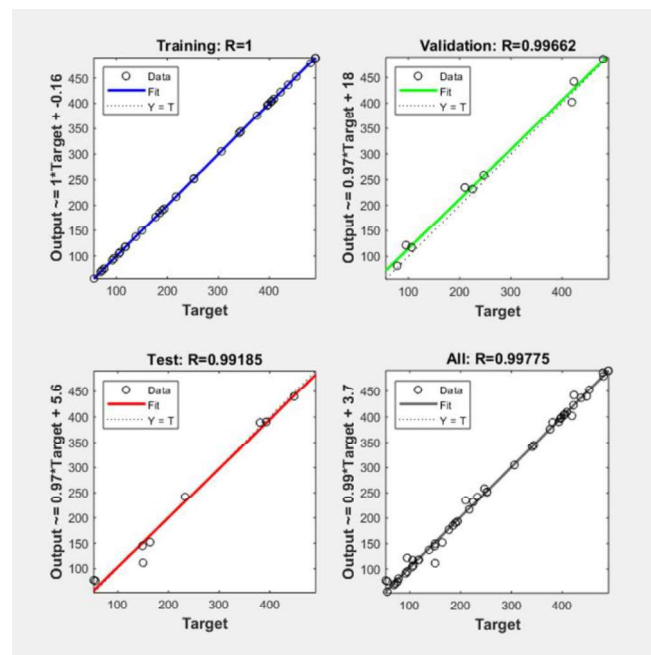


Fig. 6 Regression plot for model 1.

The regression plot of model 2 in Fig. 7 represents that the network performance has been done with training $R=1$, testing $R=0.99064$ and all $R=0.99848$.

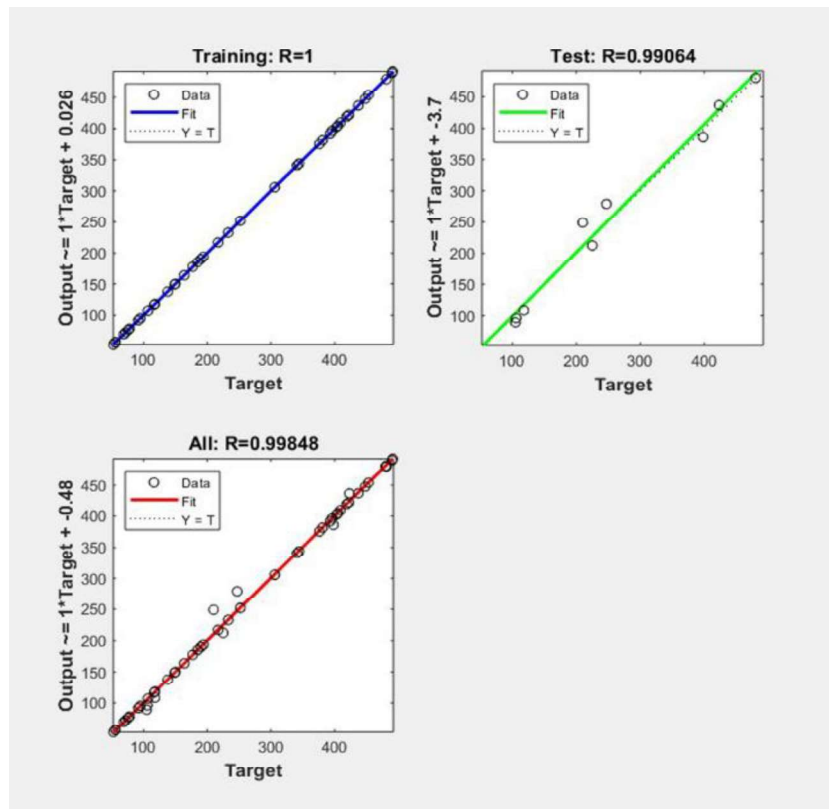


Fig. 7 Regression plot for model 2.

4.2 Comparison between actual and estimated cutting forces

After deploying the solution in the Matlab Simulink, the estimated cutting forces of the Models 1 and 2 have been tabulated in the Table 4 and Table 5 respectively. The comparison between the actual values of the cutting forces present in the Table 3 and the corresponding estimated values of the Models 1 and 2 have been depicted in Bar Chart of the Figs. 8 to 10.

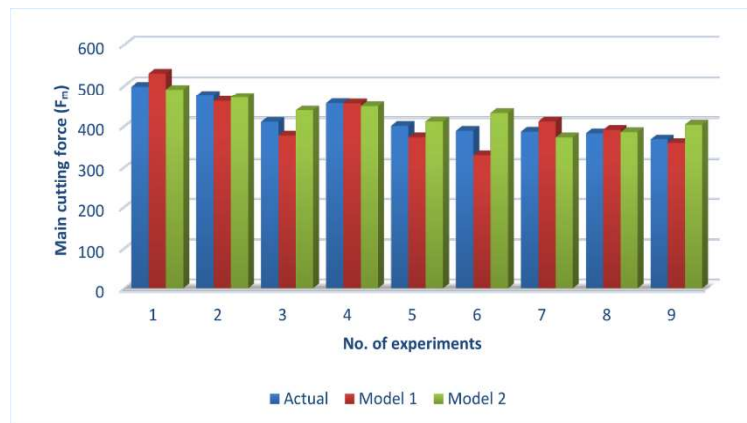
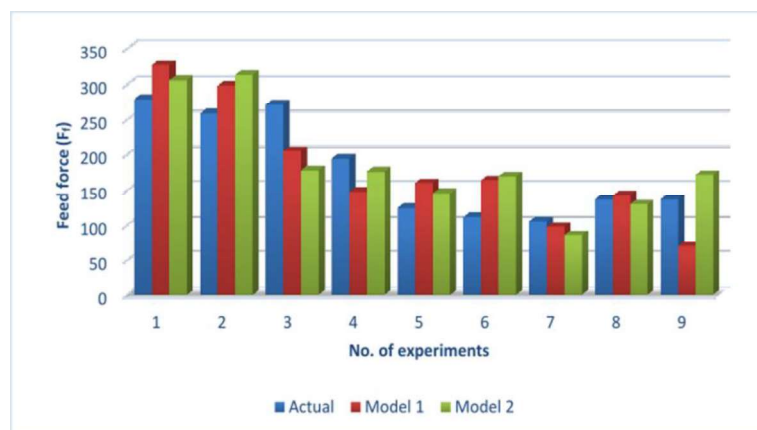
Table 4. Estimated cutting forces from model 1.

Sl. no.	Main cutting force (Fm), (N)	Feed force (Ff), (N)	Thrust force (Ft), (N)
1	529.51	326.37	285.23
2	461.72	297.89	149.39
3	376.79	205.45	10.07
4	455.35	147.43	108.83
5	372.56	159.55	44.49
6	328.39	163.18	19.04
7	410.67	97.51	91.26
8	390.40	141.81	86.26
9	358.35	69.16	38.67

Table 5. Estimated cutting forces from model 2.

Sl. no.	Main cutting force (F_m), (N)	Feed force (F_f), (N)	Thrust force (F_t), (N)
1	490.10	305.39	271.42
2	470.47	312.90	156.85
3	437.68	177.37	212.43
4	448.71	175.33	160.65
5	410.47	144.92	97.10
6	431.10	168.66	198.36
7	372.00	85.76	75.23
8	384.74	128.79	84.49
9	402.48	170.94	143.38

Fig. 8 shows the comparison between the actual and estimated values of main cutting force (F_m). In this case estimated values from model 2 is closer than that of the estimated values from model 1. Fig. 9 depicts the comparison between the actual and estimated values of feed force (F_f). Here also after carefully observation it can be said that the estimated result of model 1 is closer to the actual value. Whereas the estimated result from model 2 is also within acceptable range. Similarly Fig. 10 shows comparison between the actual and estimated thrust force (F_t) from model 1 and model 2. It can be observed that estimated values from model 2 are much higher than actual value in most of the set of data. So clearly it can be revealed that the prediction of thrust force is better by model 1 as compared to model 2.

**Fig. 8** Comparison between actual and estimated values of F_m .**Fig.9** Comparison between actual and estimated values of F_f .

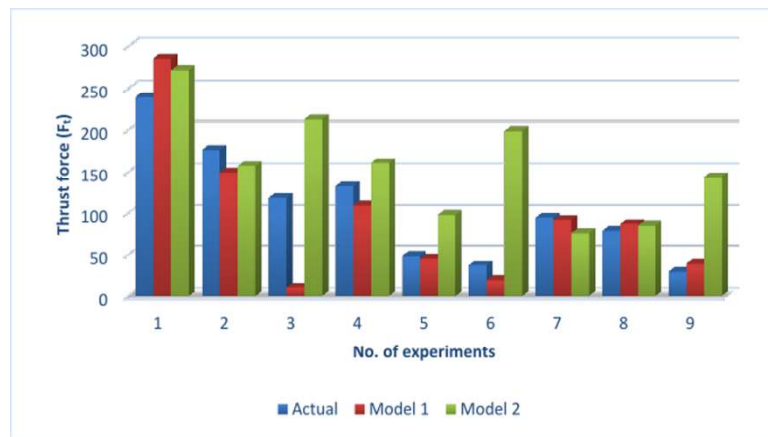


Fig.10 Comparison between actual and estimated values of F_t .

5 Conclusions

In this paper work different cutting forces of turning operation have been estimated through ANN. With help of ANN tool two different models have been taken to compare the estimated cutting forces with the actual cutting forces of the turning operation. The proposed work in this paper reveals that the Levenberg-Marquardt training function of the ANN is superior than Bayesian Regularization training function for the estimation of feed force, also for the estimation of thrust force. The Model 1- Levenberg-Marquardt training function showing better performance for the prediction purpose of main cutting force and thrust force whereas the Model 2- Bayesian Regularization training function is better for feed force. It can also be concluded that the Model 1 performs better for prediction of main cutting force compare to thrust force. The cutting parameters selection influence all the machining variables, so proper attention should be taken during selection of cutting parameters of the turning operation.

The optimization technique can be used in this work to find the best combination of the input parameters so that the output will be optimized. For this purpose, the training function, algorithm, number of neurons and epochs should be considered in a combination so that it will be able to provide estimated values with higher accuracy. It will be helpful to choose the proper cutting parameters and tool with proper geometry for different types of cutting condition. As a result, the requirement of forces will be reduced which will be helpful to reduce the cost of product.

References

1. Sharma, V.S., Dhiman, S., Sehgal, R., & Sharma, S.K. (2008). Estimation of cutting forces and surface roughness for hard turning using neural networks. *Journal of Intelligent Manufacturing*, vol. 19, 473-483.
2. Ozkan, I.A., Saritas, I., & Yaldiz, S. (2010). A comparative study of ANN and FES for predicting of cutting forces and tool tip temperature in turning. *Proceedings of the 11th International Conference on Computer Systems and Technologies and Workshop for PhD Students in Computing on International Conference on Computer System and Technologies*, 177-185.
3. Rao, C.H.S., Rao, D.N., & Rao, R.N.S. (2006). Online prediction of diffusion wear on the flank through tool tip temperature in turning using artificial neural networks. *Proceedings of the Institution of Mechanical Engineers, Part B: Journal of Engineering Manufacture*, vol. 220, 2069-2076.
4. Asilturk, I., & Cunkas, M. (2011). Modeling and prediction of surface roughness in turning operations using artificial neural network and multiple regression method. *Expert Systems with Applications*, vol. 38, 5826-5832.
5. Liu, Q., & Altintas, Y. (1999). On-line monitoring of flank wear in turning with multilayered feed-forward neural network. *International Journal of Machine Tools and Manufacture*, vol. 39(12), 1945-1959.
6. Dasmahapatra, S., Saha, R., Mookherjee, S., & Sanyal, D. (2018). Designing an Input- linearized Adaptive Sliding Mode Coupled Nonlinear Integral Controller. *IEEE/ASME Transactions on Mechatronics*, vol. 23, 2888-2895.

7. Dasmahapatra, S., Chaudhuri, S., Mandal, P., Mookherjee, S., & Saha, R. (2015). Fuzzy- PI control of motion tracking by an electrohydraulic system with multiple nonlinearities. Proceeding of Michael Faraday IET International Summit: MFIIS-2015, September 21 – 13, 2015, Kolkata, India.
8. Dasmahapatra, S., Saha, R., Chatterjee, A., Mookherjee, S., & Sanyal, D. (2015). Design of an adaptive-fuzzy-bias-SMC and validation for a rugged electrohydraulic system. IEEE/ASME Transactions on Mechatronics, vol. 20, 2708-2715, 2015.
9. Dasmahapatra, S., & Ghosh, M. (2020). Workspace Identification of Stewart Platform. International Journal of Engineering and Advanced Technology, vol. 9, 1903-1907.
10. Mullick, S.H., & Dasmahapatra, S. (2020). Combined Motion Generation by Electro-Hydraulic Stewart Platform for Manufacturing Industries. Springer Nature Switzerland AG 2020, S. Dawn et al. (Eds.): ICIMSAT 2019, LAIS 12, 596–604.
11. Ghosh, M., & Dasmahapatra, S. (2020). Kinematic Modeling of Stewart Platform. Springer Nature Switzerland AG 2020, S. Dawn et al. (Eds.): ICIMSAT 2019, LAIS 12, 693-701.
12. Li, W., & Kara, S. (2011). An empirical model for predicting energy consumption of manufacturing processes: a case of turning process. Proceedings of the Institution of Mechanical Engineers, Part B: Journal of Engineering Manufacture, vol. 225(9), 1636-1646.
13. Paulo Davim, J., Gaitonde, V.N., & Karnik, S.R. (2008). Investigations into the effect of cutting conditions on surface roughness in turning of free machining steel by ANN models. Journal of Materials Processing Technology, vol. 205(1-3), 16-23.
14. Saglam, H., Yaldiz, S., & Unsacar, F. (2007). The effect of tool geometry and cutting speed on main cutting force and tool tip temperature. Materials & design, vol. 28 (1), 101-111.
15. Tarng, Y.S., wang, T.C., Chen, W.N., & Lee, B.Y. (1995). The use of neural networks in predicting turning forces. Journal of Materials Processing Technology, vol. 47(3-4), 273-289.
16. Das, S., chattopadhyay, A.B., & Murthy, A.S.R. (1996). Force parameters for online tool wear estimation: a neural network approach. Neu-ral Networks, vol. 9(9), 1639-1645.

The Jalpaiguri Government Engineering College, abbreviated as JGEC, is a premiere public engineering institution established in 1961. It is situated in the Jalpaiguri, the divisional headquarters of the eight districts of North Bengal. The university offers bachelor's degrees (B.Tech) in six branches and master's degrees (M.Tech) in two branches of engineering. JGEC has the largest campus (165 acres) among all government engineering colleges in the state of West Bengal. With affiliation to the West Bengal University of Technology, the institute is now an autonomous engineering college under the Government of West Bengal.

www.jgec.ac.in

